CRANFIELD UNIVERSITY

Weiqun Gu

Evaluation of optimised flight trajectories for conventional and novel aircraft and engine integrated systems

SCHOOL OF ENGINEERING
DEPARTMENT OF POWER AND PROPULSION

PhD THESIS
Academic Year: 2010 - 2013

Supervisor: Dr. Vishal Sethi
April 2013

CRANFIELD UNIVERSITY

SCHOOL OF ENGINEERING
DEPARTMENT OF POWER AND PROPULSION

PhD THESIS

Academic Year 2010 - 2013

Weiqun Gu

Evaluation of optimised flight trajectories for conventional and novel aircraft and engine integrated systems

Supervisor: Dr. Vishal Sethi
April 2013

This thesis is submitted in partial fulfilment of the requirements for the degree of Doctor of Philosophy

ABSTRACT

Today, the air transport industry has become an essential element of global society by its great contributions to the wide exchanges of cultures/people and to the rapid growth in the world economy.

However, on the other hand, the adverse impacts on the environment caused by air transport, such as air pollution, noise and climate change, are drawing, increasingly, growing public concern.

In order to address the steady growth in air-travel demand in the next decades through an environmentally-friendly way and realise the ACARE 2020 environmental goals, The Clean Sky programme has been launched by European Union over the period 2008 – 2013.

The project research, described in this thesis and sponsored by the Clean Sky programme, aims at evaluating the feasibility of reducing the environmental impact of commercial aviation through the introduction of changes in the aircraft operational rules and procedures, as well as the application of the new-generation propfan (open rotor) engine, based on flight trajectory multidisciplinary optimisation and analysis of commercial aircraft.

In order to accomplish the above research objectives, a complete methodology to achieve and realise optimum flight trajectories has been initially proposed. Then, 12 component-level models which function as simulating different disciplines, such as aircraft performance, engine performance, engine gaseous emission, and flight noise, have been developed or selected/adopted. Further, nine system-level integration and optimisation models were built. These system-level models simulate flights from Amsterdam Schiphol airport in the Netherlands to Munich airport in Germany flown by different types of aircraft through different flight phases with different optimisation objectives. Finally, detailed investigations into the flight trajectory optimisations were performed, extensive optimisation results were achieved and corresponding description, analysis and comparisons were provided.

The main contributions of this work to knowledge broadly comprise the following: 1) the further development regarding the methodology of flight trajectory multidisciplinary optimisation; 2) previous work on aircraft trajectory optimisation has often considered fixed objectives over the complete flight trajectory. This research focused on representative flight phases of a flight mission with different optimisation objectives, namely, noise impact and fuel burn during the departure phase; fuel burn and flight time during en route phase; and noise impact and NOx emission during the arrival phase; 3) this research has extended the current flight trajectory optimisations to turboprop and propfan equipped aircraft. As a result, a relative complete 2D flight trajectory multidisciplinary optimisation spectrum, spanned by primary commercial aircraft types, primary flight phases and primary optimisation objectives of interest, has been built.

Although encouraging progress have been achieved, this project research, as with any other research activity, is also only ‘on the way’ rather than coming to the ‘end’ point. There are still many aspects which can be improved further and there is still much new research and exploration which can be investigated further. All these have also been suggested in this thesis.

Key words: flight trajectory, multidisciplinary, integration, optimisation, modelling, performance, gaseous emissions, flight noise.

ACKNOWLEDGMENTS

When looking at the history of science and technology, I am surprised by the intelligence of human beings and feel proud and lucky to be one of human beings.

When looking at the great achievements of aviation, I am surprised by the dramatic changes, spanning just over 100 years, from the very early Wright brothers' aeroplane to today's very large civil aircraft with 400+ seats, and feel proud and lucky to be one of the members of this society.

When looking back at the three years I stayed at Cranfield University, I am happy with my change and growth and feel proud and lucky to be one of the PhD research students in the Department of Power and Propulsion.

The three-year study changed my mind a lot and led me into a new and beautiful world of science, technology and engineering which I have never felt before. Now, I can feel and understand:

Science, technology and engineering are not only a block of theories, equations and experiences, and they are more a kind of culture, idea and belief. It is the strong belief about the power and beauty of science and technology that drives human beings to pursue them, continuously.

The product design is not only to simply apply the known theories, equations and experiences, and it is more the process that designers "melt" their passion, efforts, imagination, personality and understanding about the life, etc. into the products. Such products are no longer "cold" and "dead" issues but alive, indeed, with the souls and characteristics of designers.

Similarly, gas turbine performance is not only to simply implement some numerical simulations by means of thermodynamic software, and it is more a discipline and technology with systematic and dialectical thinking (trade-off and decision making), requiring a deep understanding and wide knowledge about gas turbine characteristics and future development trends, application and market, constraints (multi-criteria and available technology level), and new technologies, ideas and methods emerging from this field or others, etc. It can be said that the soul and characteristics of a gas turbine engine is, to a great extent, formed by its performance design at the early stage of the

product design and, correspondingly, the “destiny” of a gas turbine product in the market is, to a great extent, decided by its performance design. Indeed, gas turbine performance is an “art”!

Special thanks to my supervisor, Dr. Vishal Sethi, and Professor Pericles Pilidis, for the unique research opportunity they provided to me and their dedicated guidance and support throughout the entire research project. The invaluable guidance, suggestions and support from them in different ways not only enhanced my technology level, but also broadened my horizon greatly.

Special thanks to my wife, Xiaoling Hu, my mother, Shufeng Bai, my father, Guodong Gu, my sister, Aiqun Gu and her family, as well as my lovely son, Boren Gu, for all their loves, understanding, support and encouragement which have given me strong inner strength to overcome difficulties and accomplish my research.

Special thanks to the Department of Power and Propulsion of Cranfield University, the Aviation Industry Corporation of China (AVIC), The China Scholarship Council and the Education Section of the Chinese Embassy in Britain for the funding and support provided for the development of this research project.

I also want to thank the Gas Turbine Establishment (AVIC) for its kind help and support.

My thanks also to Mr. Devaiah Nalianda, Mr. Hugo Pervier, Mr. William Camilleri, Mr. Sander Hartjes, Mr. Matthew Sammut and Mr. Rukshan Navaratne, and so on. As my colleagues on the SGO (Systems for Green Operation) project of the Clean Sky Programme, they have kindly given me many good suggestions and support.

Last, but not least, I would like to express my appreciation to all the staff in this department and the University and all my friends who gave me help and support.

TABLE OF CONTENTS

LIST OF FIGURES

LIST OF TABLES

NOMENCLATURE

Symbol	Definition	Unit
a	Speed of sound, lift curve slope	m/s, rad.$^{-1}$
a_0	Lift curve slope of 2D thin airfoil	rad.$^{-1}$
a/c-t, a/c-HTP	Aircraft excluding HTP	
A_x	Fuselage cross-sectional area	m^2
b	Biases matrix	
C	Chord	m
C	Smoke soot	
C_{D0}	Zero-lift drag coefficient	
C_{DP}	Profile drag coefficient	
C'_{DP}	Updated profile drag coefficient	
C_f	Skin friction coefficient	
C_L	Lift coefficient	
$C_{L\alpha=0}$	Zero-AOA lift coefficient	
$C_{L,minD}$	Minimum-drag lift coefficient	
CX	Constraints in horizontal flight distance	m
D	Diameter, drag	m, N
D'	Tail (HTP) drag	N
dC_L	Lift-coefficient increment	
dh	small altitude increment	m
dp	small pressure increment	Pa
dX	Increment in independent-variable vector	
e_0, e	Oswald's efficiency factor	
E	Errors	
e^H	humidity factor	
g	Acceleration of gravity	m/s^2
F	Shape (form) factor, tail (HTP) force	N
F1	Fraction of fuel reaching the near wall mixing zone	
F2	Proportion of the swirler and dome air that goes into the flame front PaSR reactor	
F3	Fraction of the burning gases admitted into the primary near-wall reactor	
F4	Fraction of the air initially assigned to the primary zone that goes into the primary near-wall reactor	
F5	Fraction of the air initially assigned to the intermediate zone that goes into the intermediate near-wall reactor	
$F_i(\mathbf{x})$	the i^{th} objective function	
F_n	(Single) engine net thrust	N
g_i	a time-of-day dependent weighting factor	
H, h	altitude	m

H	humidity correction	
I	Identity matrix	
K	Lift-dependent drag factor	
L	Lift, length, characteristic length	N, m, m
l	Length	m
L_A	A-weighted sound level	dBA
LAMAX	A-weighted maximum sound level	dBA
L_E	Noise Metrics based on the total sound energy	dB
$\overline{L}_E$	average event level of the N events experienced during the specified time interval	dB
$L_{E,i}$	noise exposure level of the i-th noise event	dB
Leq	Equivalent sound level	dB
$L_{Aeq,night}$	8-hour night-average sound level	dBA
$L_{Aeq,day}$	16-hour day-average sound level	dBA
$L_{Aeq,24h}$	24-hour average sound level	dBA
L_{DEN}	Day-evening-night sound level	dB
L_{DN}	Day-night average sound level	dB
L_{max}	Noise Metrics based on the maximum sound intensity	dB
L_{PNT}	Tone-corrected Perceived Noise Level	EPNdB, TPNdB
m	number of objective functions	
M	Flight Mach number, average molecular weight	
mu	adaptive value	
N	number of aircraft noise events occurring over the specified reference time period T_0	
N_{Tr}	the number of days with defined scenario air traffic	
p	number of inequality constraints	
P	pressure	Pa
P_3	Air stagnation pressure at the inlet of engine combustion chamber	Pa
PSAT	Saturated vapour pressure of water at the given ambient conditions	kPa
q	number of equality constraints	
Q	Interference factor	
T	temperature	K
T_3	Air stagnation temperature at the inlet of engine combustion chamber	K
r	a random number from [0,1]	
R	perfect gas constant	J/(kg K)
R_e	Reynolds number	
S	Area	m^2
t	generation number	
t	Flight time	s
T	Thrust	N
t_0	reference time	s

t/c	thickness/chord ratio	
V_∞, V	Free stream velocity, flight speed	m/s
W	Weight matrix	
W, G	Weight	N
x	decision-variable vector	
X	Horizontal flight distance	m
x_i	The i^{th} independent variable	
$\mathbf{x}^L$	the lower boundary vector	
$\mathbf{x}^U$	the upper boundary vector	
y_j	The j^{th} dependent variable	
z	geometric altitude	m
Z	Flight altitude	m
α	Angle of attack	°, $rad.^{-1}$
$\alpha_{L=0}$	Zero-lift angle of attack	°, rad.-1
α'	Angle of attack for $C_{L,minD}$	°, rad.-1
α_1, α_2, α	exploration factor	
β	spread factor	
ω	humidity ratio	kg water/kg dry air
δ	creep size	
ρ	Mass density	kg/m^3
τ	Shearing stress	N/m^2
μ	Dynamic viscosity	$N{\cdot}s/m^2$
ν	Kinematic viscosity	m^2/s
γ	Ratio of specific heats, creep decay rate	
λ_f	Finess Ratio	
Λ, φ	Sweepback angle	°
dc/dy	Rate of change of fluid velocity along the y direction	s^{-1}
ΔT	Temperature increment	K
2D	Two-dimensional	

LIST OF ABBREVIATIONS

Symbol	Description	Unit
ACARE	the Advisory Council for Aeronautical Research in Europe	
Alt, alt., ALT	altitude	m
ANNs	Artificial Neural Networks	
ANOVA	analysis of variance	
AOA	Angle of attack	°, radian
AP	Approach	
APM	Aircraft Performance Model	
AR	Aspect ratio	
ATC	Air Traffic Control	
ATR	Aerei da Trasporto Regionale or Avions de Transport Régional	
BADA	Base of Aircraft Data	
BLX	blend crossover	
BPR	ByPass Ratio	
CA	Constraints in altitude	m
CAS	calibrated airspeed	m/s
CEA	Chemical Equilibrium with Applications	
CFD	Computational Fluid Dynamics	
CFMI	CFM International	
CO	Carbon monoxide	
CO_2	Carbon dioxide	
COT	Combustor outlet temperature	K
CR	Cruise	
CUPFDAC	Cranfield University PropFan-Driven AirCraft	
CUPROPFAN	Cranfield University Propfan	
CUTFDAC	Cranfield University TurboFan-Driven AirCraft	
CUTPDAC	Cranfield University TurboProp-Driven AirCraft	
CUTPROP	Cranfield University Turboprop	
CUTSTF	Cranfield University Twin Spool Turbofan	
dB	deciBel	
Dev.	Deviation	
DIS	distance	m
DP	Design point	
DVM	dynamic vectored mutation	

DZ	dilution zone	
Econ.	Economic	
EI	Emission Index	g/kg fuel
EICO	Emission Index of CO	g/kg fuel
EICO2	Emission Index of CO2	g/kg fuel
EINOx	Emission Index of NOx	g/kg fuel
EIH2O	Emission Index of H2O	g/kg fuel
EIUHC	Emission Index of UHC	g/kg fuel
EPNL	Effective perceived noise level	EPNdB
E.S.F.C., ESFC	Equivalent specific fuel consumption	µg/J
ESP, E.S.P	Equivalent shaft power	w
FAR	Fuel air ratio	
FF	flame front	
FFNNs	FeedForward Neural Networks	
FPA	flight path angle	°, radian
FPT	Free Power Turbine	
GA(s)	Genetic Algorithm(s)	
GATAC	Green Aircraft Trajectory under ATM Constraints	
GDP	Gross Domestic Product	
GE	General Electric	
GUI	Graphical user interface	
H_2O	Water vapour	
HP	High pressure	
HPC	High pressure compressor	
HTP	Horizontal tailplane	
IA	Instrument Approach	
IC	Initial Climb	
ICAO	International Civil Aviation Organization	
INM	Integrated Noise Model	
INMTM	Integrated Noise Model/Management of Trajectory and Missions	
ISA	International Standard Atmosphere	
ISO	International Organization for Standardization	
ITDs	Integrated Technology Demonstrators	
IZ	intermediate zone	
JTI	Joint Technology Initiative	
JX	Jacobian matrix	
LAMAX	A-weighted maximum sound level	

Leq	Equivalent sound level	
LN	Natural Logarithm	
LP	Low pressure	
LPC	Low pressure compressor	
LPT	Low pressure turbine	
MAC	Mean Aerodynamic Chord	m
Max.	Maximum	
MDO	Multi-disciplinary design optimization	
MIL 210	US Military Standard 210	
MNf	Flight Mach number	
MSDO	multidisciplinary system design optimization	
MSE	Mean Square Error	
MSL	Mean Sea Level	
NASA	National Aeronautics and Space Administration	
NNs	Neural Networks	
NoiseLAss	Noise level assessment	
NOx	Nitrogen oxide	
NPD	Noise-Power-Distance	
NSGAMO	Nondominated sorting genetic algorithm multiobjective	
NW	near-wall	
OPR	Overall pressure ratio	
P	pressure	Pa
PA	Pressure Altitude or Geopotential Altitude	
PAMB	Ambient pressure	kPa
PaSR	partially-stirred reactor	
ppb	parts per billion	
PSR	Perfectly-Stirred Reactor	
PSRS	a series of perfectly-stirred reactors	
PZ	primary zone	
TAMB, Tamb	Ambient temperature	K
PNLTM	Tone-corrected maximum perceived noise level	TPNdB
PR	Pressure ratio	
PSAT	Saturated vapour pressure of water at the given ambient conditions	kPa
R.R.	Rolls-Royce	
SBX	simulated binary crossover	
SFC	Specific fuel consumption	mg/Ns
SO_2	Oxides of sulphur	
SP, S.P.	Shaft power	w
SPD	Speed (CAS or Mach number)	m/s or -

SPL	sound pressure level	µPa
SRs	stirred reactors	
SUS	stochastic universal sampling	
T	temperature	K
TAS	True airspeed	m/s
T-O	Take-off	
TOC	Top of climb	
R	perfect gas constant	J/(kg K)
rad.	Radian	
RH	Relative humidity	%
SEL	A-Weighted Sound Exposure Level	dBA
SGO	Systems for Green Operation	
SH	Specific humidity	%
SID	Standard Instrument Departure	
SLS	Sea level static	
TET	Turbine Entry Temperature	K
TR	Taper ratio	
UHC, HC	Unburned Hydrocarbons	
VTP	Vertical tailplane	
WMO	World Meteorological Organization	

SUBSCRIPTS

Symbol	Definition
0	Standard sea level conditions
3	high pressure compressor exit/combustor diffuser inlet
25	25% chord
0.5C, 50	50% chord
11	Tropopause conditions
∞	Free stream
act	Actual
a/c	Aircraft
a/c-t, A/C-HTP, a/c-HTP	Aircraft excluding HTP
Alt	Altitude
amb	Ambient
ave	Average
c, cds	Constant diameter section part of fuselage, component
eff	Effective
eq	Equivalent
f	Fuselage
HTP	Horizontal tailplane
i	Induced
LE	Leading edge
max	Maximum
min	Minimum
n, N	Nose part of fuselage, nacelle
nose	Nose part of fuselage
p	Planform
r	Root
ref	Reference
SE	Single engine
SL	Sea level
system	System installation
t	Tail cone part of fuselage, tip
tail	Tail cone part of fuselage, HTP
VTP	Vertical tailplane
w	Main wing
wet, w	Wetted

CHAPTER ONE INTRODUCTION

1.1 Context of the Research Work

Today, the air transport industry has become an essential element of global society by its great contributions to the wide exchanges of cultures and people among different countries as well as the rapid growth in the world economy. It is reported that "air transport moves over 2.2 billion passengers annually" [1] and "generates a total of 32 million jobs globally (of which 5.5 million work directly in the aviation industry)" [1]. "Aviation's global economic impact (direct, indirect and induced) is estimated at US$ 3.560 billion representing 7.5% of world Gross Domestic Product (GDP)" [1].

However, on the other hand, the adverse impacts on the environment caused by the air transport, such as air pollution (such as NOx, CO and UHC, etc.), noise and climate change (which is related to emissions of CO_2 and H_2O), are increasingly drawing growing public concern. According to statistics, "air transport's contribution to climate change represents 2% of human-induced CO_2 emissions (and 12% of all transport sources)" [1] and "flights produce 628,000,000 tonnes of CO_2 yearly" [1], nowadays.

With the continuous and steady growth in demand for air travel ("increasing 4-5% per annum over the next 20 years" [1]), "worldwide, it is estimated that the equivalent of 1300 new international airports will be required by 2050 with a doubling in the commercial aircraft fleet" [1] and, as a result, the share in the total man-made CO_2 emissions contributed by air transport is expected to increase to 3% by 2050 [1].

Therefore, to look ahead, the mission and challenge commercial aviation will face is to meet the increasingly growing demand for air travel but through an environmentally-friendly way.

This challenge has been long realised by the European aviation industry. As a result, ACARE (the Advisory Council for Aeronautical Research in Europe), in the year 2001, established the following ambitious targets for the year 2020 (compared to 2000):

- "reduce fuel consumption and CO_2 emissions by 50% per passenger kilometre" [1]
- "reduce NOx emissions by 80%" [1]
- "reduce perceived noise by 50%" [1]

- "make substantial progress in reducing the environmental impact of the manufacture, maintenance and disposal of aircraft and related products" [1]

Aimed at the above targets, the primary contributors to achieve them have been identified by ACARE. "The predicted contributions to the 50% CO_2 emission reduction target are: efficient aircraft: 20-25%; efficient engines: 15-20%; improved air traffic management: 5-10%" [1].

In order to address the ACARE environmental objectives, "a quantum leap in performance through a consistent, coherent and holistic approach focusing on the integration of advanced technologies and validation of results in a multidisciplinary approach leading to full-scale ground and flight demonstrators" [1] is required.

The Clean Sky JTI (Joint Technology Initiative) is one of the largest European research projects ever, with a budget of €1.6 billion, equally shared between the European Commission and industry, over the period 2008 – 2013 [1], [2]. The main objective of this unique integrated and coordinated programme is to "speed up technological breakthrough developments and shorten the time to market for new solutions tested on Full Scale Demonstrators" [1] and, therefore, "make major steps towards the environmental goals set by ACARE and to be reached in 2020" [1].

The following Figure 1-1 illustrates the primary technology domains which have been defined to achieve the above ACARE goals and these technology domains also constitute the scope of the Clean Sky programme.

Figure 1-1 Technology domains of Clean Sky programme [1]

And further, all these technology domains have been integrated within Clean Sky into six Demonstrators, the ITDs (Integrated Technology Demonstrators) and one Technology Evaluator, as shown in the following Figure 1-2.

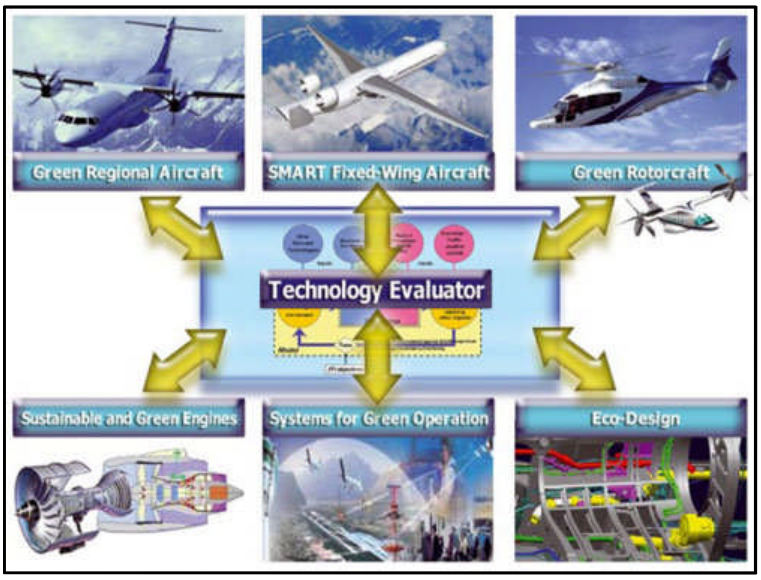

Figure 1-2 ITDs and technology evaluator [1]

Among the six ITDs [3–8], "**Green Regional Aircraft** will deliver low-weight aircraft using smart structures, as well as low external noise configurations and the integration of technology developed in other ITDs, such as engines, energy management and new system architectures; **Smart Fixed-Wing Aircraft** will deliver active wing technologies and new aircraft configuration for breakthrough, new products; **Green Rotorcraft** will deliver innovative rotor blades and engine installation for noise reduction, lower airframe drag, integration of diesel engine technology and advanced electrical systems for elimination of noxious hydraulic fluids and fuel consumption reduction; **Sustainable and Green Engines** will design and build five engine demonstrators to integrate technologies for low noise and lightweight low pressure system, high efficiency, low NOx and low weight cores and novel configurations such as open rotors and intercoolers; **Systems for Green Operation** will focus on all-electrical aircraft equipment and systems architectures, thermal management, capabilities for "green" trajectories and mission and improved ground operations to give any aircraft the capability to fully exploit the benefits of Single European Sky; **Eco-Design** will focus on green design and production, withdrawal, and recycling of aircraft, by optimal use of

raw materials and energies thus improving the environmental impact of the whole products life cycle." [1] The **Technology Evaluator** which is a simulation network will assess the performance of the technologies thus developed [1].

1.2 Content of the Research Work

The project research which is described in this thesis, sponsored by the Clean Sky programme, aims at optimising the two-dimension flight trajectories of commercial aircraft by means of a new multidisciplinary optimisation method and, in the meantime, evaluating the possible benefits brought by the introduction of the new-generation propfan (open rotor) engine. Compared with the above mentioned Clean Sky programme, this research which is mainly concerned with the flight mission & trajectory management is a part of the SGO (Systems for Green Operation) ITD (Integrated Technology Demonstrator).

This research takes the flight from Amsterdam Schiphol airport in the Netherlands to Munich airport in Germany as an example, and makes a detailed investigation into the flight trajectory optimisations for different types of commercial aircraft, including turbofan-propelled aircraft, turboprop-driven aircraft and propfan-powered aircraft. The overall horizontal flight distance covered by this flight mission is over 700 kilometres and in order to reflect the different priorities in economy and environment concerns during the different flight parts of this mission, the entire flight profile is divided into three phases, that is, the departure flight phase, the en route flight phase and the arrival flight phase with different objective functions. During the departure flight part, fuel consumption, external noise impact and pollutant emissions (here mainly the emission of NOx) are of main concern due to the usually higher engine power settings, lower flight altitude as well as the dense population distributions in the vicinity of airports (and the aerodynamic noise from aircraft high lift devices makes a contribution to the adverse impact as well) and, therefore, ideally the three parameters should be selected as the objective functions for the purpose of multidisciplinary optimisation for this flight phase. Unfortunately, under the present research conditions only two objective functions can be selected simultaneously. Based on the consideration that there is some degree of correlation between fuel consumption and NOx emission (NOx emission=EINOx × fuel consumption), fuel consumption and external noise impact (in

terms of noise-impact area or noise contour area with SEL not less than 70 dBA) are treated as the objectives for the purpose of minimisation. As for the en route flight phase, fuel consumption and flight time concerned traditionally by civil air transport are once more selected as optimisation objectives because much higher flight altitudes are implemented during this part, and the concerns about pollutant emissions and especially about external noise impact become relatively subordinate. When the flight enters into the 3rd phase (i.e., the arrival flight), again the impacts from pollutant emissions and aircraft/engine noise emerge as the primary concern with regard to the consideration of the health of the residents around airports. Therefore, in this research, NOx emission and external noise impact are taken as the optimisation objectives for the purpose of minimisation. In addition, it is worth noting that taking fuel consumption as one of the objectives in the first two flight phases for minimisation, is also helpful to reduce the production of CO_2 and H_2O which contribute to the global climate change – one of the key issues of concern to the Clean Sky programme and ACARE. The following Figure 1-3 illustrates a complete methodology (or called research chain) for the flight trajectory optimisation as well as the position of this research work in this chain. From the chart, it can be found that the entire flight trajectory optimisation can be divided into two sections, i.e., the training (or called calibration) section and execution section. In the first section (i.e., the training/calibration section), there are two parts. The first part functions to obtain the corresponding values of flight parameters such as horizontal flight distance, flight altitude, flight speed (calibrated airspeed (CAS) or flight Mach number), flight path angle (FPA), pitch angle, bank angle and heading angle from the optimised results of overall performance parameters, such as fuel consumption, flight time, external noise impact and pollutant emissions, etc., through the multidisciplinary optimisation process, and the second part further establishes the correlations between the above optimised flight parameters and operation parameters of aircraft/engine combination, such as the positions of control surfaces of aileron, elevator and rudder as well as engine power ratings. After the training/calibration section, the correlations between the overall performances expected by a certain flight mission and the corresponding operation parameters have been well established and then these correlations are arranged into the control laws especially for this expected flight. In the following second section (i.e., execution section), these specially designed control laws

are embedded into the comprehensive control system of aircraft/engine and implemented subsequently to realise the expected flight performances.

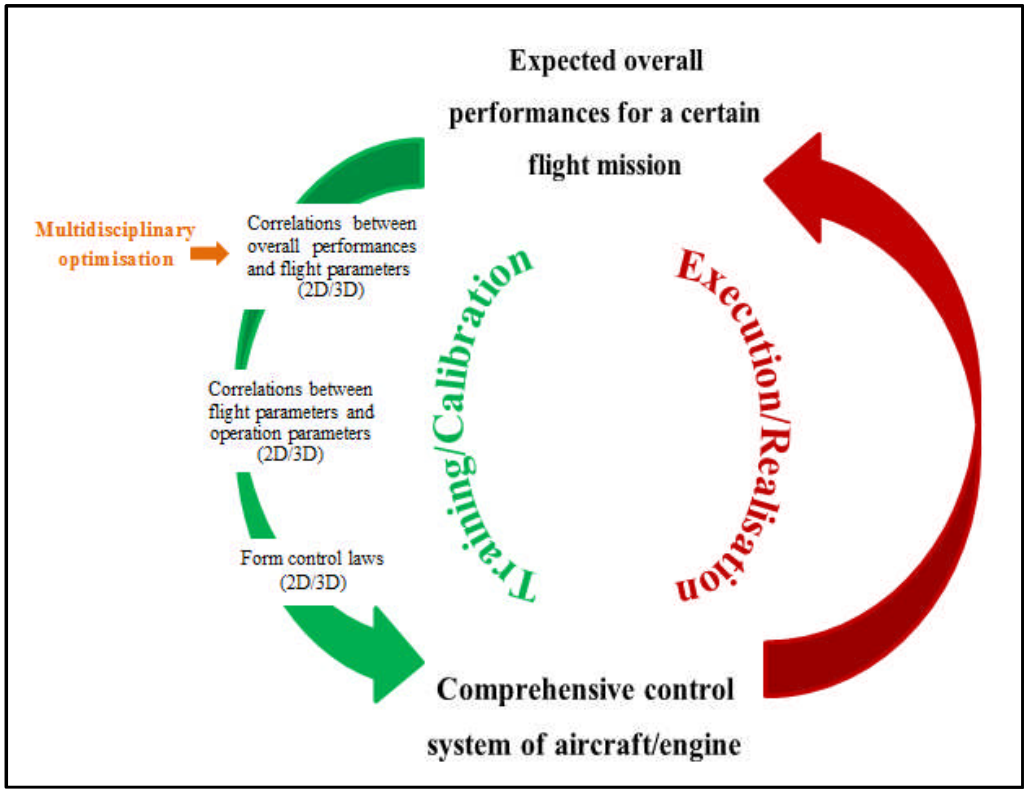

Figure 1-3 Optimisation and realisation of flight trajectory

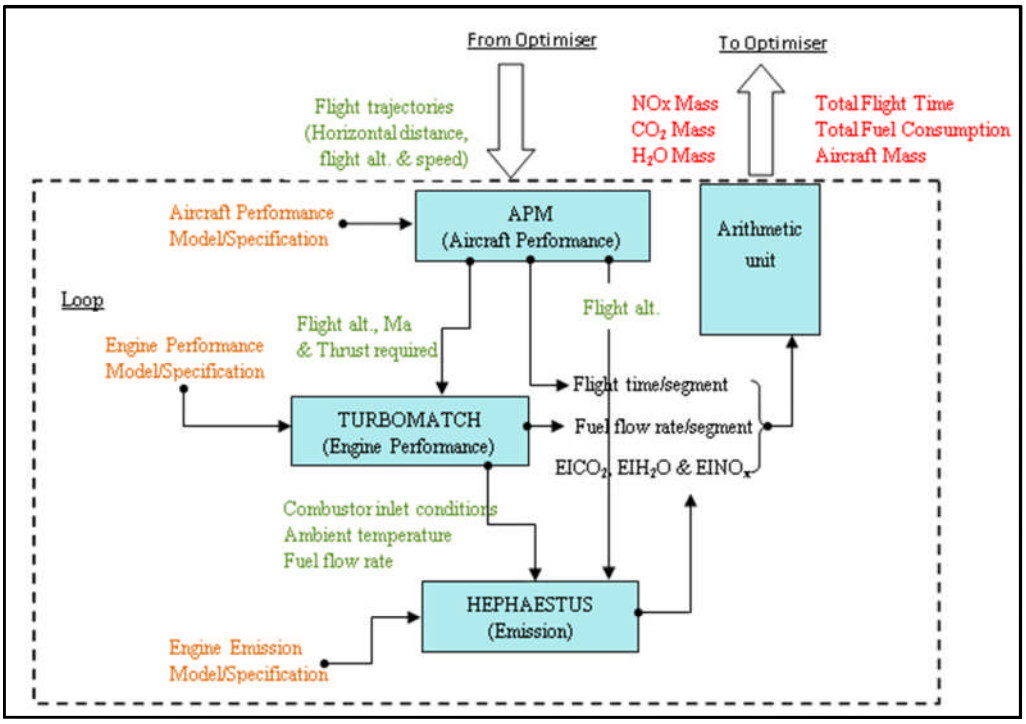

Figure 1-4 Multidisciplinary optimisation of flight trajectory

Figure 1-4 illustrates the basic idea of multidisciplinary flight trajectory optimisation used in this research work. Compared to the trajectory optimisation approach introduced in the references [9] to [12], obvious differences exist for both in terms of the modelling procedure. While trajectory optimisation is performed for climb and descent phases by means of the method described in the above references, the engine power ratings (i.e., turbine entry temperature) are given with one or a few constant values. As a result, the engine net thrust is treated as one of inputs into the aircraft performance calculation module together with flight altitude, flight speed and aircraft mass, and the horizontal flight distance covered by flight is obtained as one of calculation outputs from the aircraft performance module. This approach mainly has two disadvantages: firstly, with given value(s) in TET, the flight trajectory optimisation is in fact a strong-constraint optimisation, which will to a great extent limit the availability of 'real' optimum solutions. Secondly, during the practical flights, especially for the departure or arrival flights from or to the airports, there are usually some additional requirements to aircraft flight trajectories. For instance, aircraft are probably asked by local airports to pass some given waypoints with prescribed flight altitudes and horizontal flight distances. Under this condition, it is hard for the above optimisation method with fixed TET(s) to function due to the lack of the direct control to the parameter of horizontal flight distance. On the contrary, in the optimisation process implemented with the method used in this research, the flight trajectory is defined completely by the trajectory parameters, such as horizontal flight distance, flight altitude and flight speed, while engine net thrust is treated as one of the calculation outputs from the aircraft performance module. Although for this method there is still some constraints in engine power settings, this is only a type of 'weak' constraint with an allowed magnitude range of turbine entry temperature prescribed based on the engine life consideration, instead of one or a few fixed values as used in the above approach of references [9] to [12]. Therefore, the possibility to find 'real' optimum solutions is greatly increased. In addition, because the parameter of horizontal flight distance can be directly treated as optimisation (or design or control) variable for the trajectory definition, the flexibility of describing and modelling desired trajectories has also been improved greatly (namely, the method adopted in this research is suitable not only for the optimisations of the trajectories with strict requirements in horizontal flight distance, such as the cases with

waypoints mentioned above, but also for trajectory optimisation problems without such demands).

The modelling procedure used in this research can be also seen in the reference [13]. However, the differences between both lie in that the work introduced in the reference [13] only focused on the gaseous emission assessment under the condition of a given flight path, while this research described in this thesis not only applied the modelling procedure but also combined it with optimiser to perform multidisciplinary flight trajectory optimisation.

In this project research, a multi-objective Genetic Algorithm (GA) called NSGA- II [14] is adopted to perform the multidisciplinary optimisation calculation. This algorithm has the advantage of global searching and is especially suitable for solving nonlinear, non-smooth, non-differentiable and multi-modal (i.e., there are several local minima or maxima for an optimisation problem), complicated, multi-objective optimisation problems, such as the flight trajectory optimisation in this project research. The optimisation variables (or called design variables) involved in the 2D trajectory optimisation of this research include horizontal flight distance (X), flight altitude (Z) and flight speed (CAS used in the departure and arrival flight phases, or flight Mach number occurring in the en route flight phase). The optimisation constraints involved in optimisation processes of this research are, mainly focusing on the departure and arrival cases, from the requirements of local airports through SID (Standard Instrument Departure) chart and IA (Instrument Approach) chart.

Through several rounds of optimisation simulations, a complete set of optimised solutions, aiming at the optimisation problem spectrum spanned by different types of aircraft powered by different types of aero engines, and different flight phases with different optimisation objectives, have been achieved and provided by the research work. These optimised results are Pareto efficient (i.e., the obtained optimised solutions for the same optimisation problem are unique and not dominant over each other and any improvement in one of the two objectives will have to be realised at the cost of the degradation in the other objective), and based on these results customers are provided with the opportunity and freedom to further make their own choices according to the actual requirements in practice.

Besides the above detailed investigations into the flight trajectory optimisation, based on the achieved optimisation results, a comprehensive comparison and evaluation about the new-generation propfan (open rotor) engine, which is of higher component efficiencies and higher turbine entry temperature (TET) and will enter into service in around 2030, in terms of overall performances such as fuel consumption, flight time, noise-impact area, gaseous emissions (NOx, CO_2 and H_2O etc.), is made in this research project as well, by taking the conventional turbofan engine with 1990's technology level as the reference. The evaluation results indicate that the new-generation propfan engine has significant advantages in fuel consumption and emissions of CO_2 and H_2O due to its higher thermal efficiency and propulsive efficiency, and it can be predicted that the combination of the new-generation propfan engine with the optimised flight trajectory achieved by the global optimisation method described in this research work, will become an important contributor to ACARE 2020 goals or even beyond.

1.3 Contributions to Knowledge

Through the research work described in this thesis, the main contributions to knowledge can be identified and summarised as follows:

1) From the known literature published openly so far, it is the first time that the flight trajectories flown respectively by turboprop-driven aircraft and propfan-powered aircraft, for the purpose of city-pair air transport, are optimised based on multidisciplines with the new optimisation method and multi-objective Genetic Algorithms mentioned previously as well as actual constraints from the local airports.
2) From the known literature published openly so far, it is the first time that a relative complete set of models involving aircraft performance, engine performance, gaseous emission and noise are included when flight trajectories are optimised with the multidisciplinary optimisation method and optimisation constraints mentioned in item 1) above.
3) From the known literatures published openly so far, it is the first time that the combination of the new-generation propfan (or called open rotor) engine, which is planned into commercial service in 2030, with the optimised flight trajectory

achieved by a new multidisciplinary optimisation method is tried and evaluated to achieve more economical and greener commercial flight.

4) Inside the SGO ITD project of the Clean Sky programme, it is one of quite few cases where Artificial Neural Networks (ANNs) and P3T3 method were used to replace the complicated and time-consuming simulation models of engine performance and engine gaseous emissions, to alleviate the challenge in optimisation time costs brought by GAs and speed up the optimisation processes. By the actual application comparisons, significant benefit in terms of the optimisation time consumption has been achieved. It has been found that an optimisation example in this research project with the complicated simulation models will usually cost three or four days to reach convergence, while the similar case with substitutive models from ANNs and P3T3 method will only need around ten hours. For a long time, much longer optimisation time caused by GAs has been a main problem/obstacle for the wide application of this optimisation method. The successful usages of ANNs in engine performance modelling and multidisciplinary optimisation cases in this research project provide one promising solution.
5) Inside the SGO ITD project of the Clean Sky programme, it is the first time that compressor variable geometry and bleeding is dynamically introduced into engine off-design operations (that is, these anti-surge measures will be implemented when required). Previously, for the purpose of simplicity, when the performance of an engine was modelled, anti-surge measures were often omitted or an unchanged bleeding was adopted at all engine operating conditions (design points and all off-design points), and more attention was paid to the simulation accuracies in engine net thrust and SFC (Specific Fuel Consumption). However, such models will encounter serious difficulties when descent or arrival flights are performed because of the limitation resulted from compressor surge at lower engine power ratings (even the model with constant bleeding at all engine operations cannot also address this problem, due to the relatively small bleeding amount based on the consideration of performance loss at engine ‘normal’ working points which are free from surge risk). The shortcoming in the engine performance model will incur unnecessary constraints to the optimisation

problem so that the real optimum solutions cannot be achieved, or even possibly, no solutions can be available (especially for the descent or arrival flights). In the research work described in this thesis, the improvement to this problem has been done and the anti-surge measures can be applied according to needs, namely, during the normal flights, such as climb and cruise, where engines operate at higher power ratings and are free from the surge risk, the anti-surge measures will be switched off so that engine performance can be guaranteed, and when the descent or arrival flights are performed, where lower engine power settings are adopted and compressors possibly face the risk of surge, the anti-surge system will be switched on automatically during the optimisation process so that engine safety can be ensured and the descent or arrival flights can be continued. Doubtlessly, through this improvement, the achieved optimised solutions will be more reasonable and closer to the practical applications.

6) Compared with previous work in case modelling by the author (see the reference [15]) where the horizontal coordinates X of a flight trajectory were fixed and only flight altitudes and flight speeds can be selected as optimisation/design variables, again an obvious progress has been achieved in this research work described in this thesis, that is, when a new optimisation case is modelled, horizontal flight distance X, flight altitude Z and flight speed (CAS or Mach number) can all become the options of optimisation/design variables. This improvement is very meaningful especially for the optimisations of aircraft climb and descent flights. From the reference [15], it can be found that with given values in the horizontal coordinates and just flight altitudes and flight speeds as the optimisation/design variables, the achieved optimised results in the climb and descent phases only show the monotonous increases or decreases in flight altitude and flight speed simultaneously. However, in this research work described in this thesis, more colourful optimised solutions have been achieved by the introduction of horizontal flight distances (namely horizontal coordinates X mentioned above) as possible optimisation/design variables, which essentially increases the number of dimensions of the optimisation search space. For instance, as the result of this improvement, aircraft during the climb or descent flights not only can fly with the simultaneous increases in flight altitude and

flight speed but also can adopt other possible flight styles such as accelerated level flight, decelerated level flight, constant-CAS climb and constant-CAS descent. Therefore, through this improvement, the optimum solutions with practical application prospect can be found.

1.4 Structure of the Thesis

The thesis is mainly made up of ten chapters. They are: chapter one “introduction”; chapter two “atmosphere modelling”; chapter three “aircraft performance modelling”; chapter four “gas turbine engine performance and modelling”; chapter five “engine gaseous emissions and modelling”; chapter six “flight noise and modelling”; chapter seven “multidisciplinary optimisation and genetic algorithms”; chapter eight “system integration and optimisation modelling ─ case studies”; chapter nine “optimised results and analysis”; chapter ten “conclusions and future works”.

In the first chapter of this thesis, the author summarily introduced the background of this research work, main research content, contributions to knowledge and the structure of this thesis so as to provide readers with a good overview and an overall understanding to the whole research work described in this thesis before going into the details.

Aircraft is the vehicle which is designed to ‘swim’ in air and its power plant – aero engine - is also designed to produce thrust required by aircraft by means of air. Air properties (i.e., the atmosphere performance) have extremely important influences on design and operation of aero vehicles and are also the fundament of performance analyses performed in this thesis. Therefore, the description about atmosphere model used in this research work is firstly provided in the second chapter.

Chapter three addresses aircraft performance modelling. In this research work, totally, three different aircraft types are discussed, that is, 1) the aircraft propelled by two conventional turbofan engines, which takes the aircraft A320-200 produced by Airbus as the prototype, and is designated as CUTFDAC (Cranfield University TurboFan-Driven AirCraft); 2) the aircraft driven by two conventional turboprop engines, which takes the regional aircraft ATR72-500 built by the French-Italian aircraft manufacturer ATR (Aerei da Trasporto Regionale or Avions de Transport Régional) as the prototype, and is designated as CUTPDAC (Cranfield University TurboProp-Driven AirCraft); 3)

the aircraft powered by two new-generation propfan (or called open rotor) engines, which takes the aircraft MD90-30 (a twin-engine, short- to medium-range, single-aisle commercial jet aircraft built by the former American aerospace manufacturer, McDonnell Douglas) as the prototype, with the substitution of the original two conventional turbofan engines with two propfan engines, and is designated as CUPFDAC (Cranfield University PropFan-Driven AirCraft). The performance modelling for each aircraft includes determining the lift and drag characteristics of the aeroplane such as lift-angle of attack characteristics and lift-drag characteristics (i.e., the drag polar), as well as action positions of forces imposed on the aircraft during flight, such as lift produced by main wings and fuselage, gravity, drag, engine net thrust and tail force by means of kinds of theoretical equations and empirical data. Based on the above established aircraft performance models, and given the required flight conditions (such as the aircraft mass at the start point of a flight segment, the flight altitudes at both start and end points of this segment, the horizontal flight distance of this segment, the flight speed and the flight path angle at the start point as well as the magnitude of the flight speed at the end point), the required engine net thrust for the flight in this segment and other performance parameters can be determined by the aircraft performance simulation software APM (Aircraft Performance Model), which is based on the principle of force and moment balance and developed by Cranfield University. These calculation results output from APM will be transferred as inputs to the subsequent module of engine performance simulation and (or) the module of aircraft/engine noise calculation (if used in case studies) during the flight trajectory optimisation.

The modelling of engine performance is described in the fourth chapter. Corresponding to above different aircraft models, three different types of aero engine performance models have also been built in this research work, that is, 1) the performance model of a conventional high bypass ratio (BPR) turbofan engine which takes the CFM56-5B4 engine developed by CFM International (CFMI) as the prototype; 2) the performance model of a conventional turboprop engine which takes the PW127F engine made by Pratt & Whitney Canada as the prototype; and 3) the performance model of a new-generation propfan (or called open rotor) engine which is based on the research work from Glenn Research Centre of NASA (National Aeronautics and Space Administration) published in the reference [16]. Among them, the models of turboprop

engine and propfan engine are established by means of TURBOMATCH – an engine performance simulation software developed by Cranfield University. Since the above TURBOMATCH-based performance models require a longer calculation time when performed, which will have an important influence on the whole optimisation time cost when GAs is applied which results in that a large number of evaluations are needed , a different approach was adopted when modelling the performance of the conventional turbofan engine, that is, firstly a TURBOMATCH-based engine performance model was built and was used to produce a large database of the engine performance with the combinations of variations of flight altitude, flight Mach number and turbine entry temperature (TET), and then by means of the achieved database several two-layer Artificial Neural Networks (ANNs) can be trained, and as a result, the correlation relationships which represent the performance of this engine and are required by the investigated optimisation case can be achieved, such as TET = f_1(H, M, F_n), W_f = f_2(H, M, F_n), T_3 = f_3 (H, M, F_n), P_3 = f_4 (H, M, F_n), etc. The application of the above ANNs-based engine performance in optimisation cases and comparisons with the cases with TURBOMATCH-based models indicate that the approach can indeed speed up the calculation speed and effectively reduce optimisation time (certainly, the reduction in optimisation time in this research work is also contributed from the gaseous emission side). In addition, in this chapter, besides the above modelling, the comparisons between engine models and data from the public domain (except the propfan engine because this engine is still at the stage of paper research), in terms of engine net thrust and specific fuel consumption (SFC) at take-off and cruise conditions, as well as engine performance characteristics such as variations of engine net thrust and SFC with flight altitude, flight Mach and turbine entry temperature (TET) are also provided. In optimisation processes performed in this research project, the calculation results from engine performance models will provide required inputs to the subsequent gaseous emission prediction model.

The fifth chapter introduces in detail three gaseous emission models which are respectively used in the above turbofan engine, turboprop engine and propfan engine. During the modelling process, two different types of modelling approaches were applied and, correspondingly, two different types of gaseous emission models were achieved. The first modelling approach is known as P_3T_3 method. This is a kind of

empirical estimation method by means of which the empirical correlations between the engine gaseous emissions at actual flight conditions and the emissions at the SLS condition can be established. Therefore, in practical applications, so long as gaseous emission data of the engine at the SLS condition and the air stagnation pressure (P_3) and stagnation temperature (T_3) at the inlet of engine combustion chamber at the investigated flight condition are known, the gaseous emissions at this flight condition can be predicted. The emission data of a specific engine at SLS condition can be achieved through special engine ground test or ICAO aero engine emission databank (if applicable), and the values of P_3 and T_3 can be obtained through the relevant engine performance model. The second methodology to model gaseous emissions is a physics-based method and known as stirred reactor model which predicts gaseous emissions based on chemical equilibrium calculation and reaction kinetics. The emission predictions in those case studies where the turbofan engines are applied were performed by means of P_3T_3 model due to the availability of ground emission data for the CFM56-5B4 engine from ICAO databank, and for the other cases involving the turboprop engine and propfan engine, the gaseous emission estimations were accomplished through the stirred reactor models. By reference to the ACARE 2020 environment goals and the primary challenges air transport is facing in gaseous emissions, the predictions from the above models mainly focused on emissions of NOx, CO_2 and H_2O.

Modelling and prediction of aircraft/engine noise is the topic of the chapter six. This chapter starts with the introduction of the adverse impacts of noise on human beings and community life in terms of physiological and behavioural aspects, as well as the contribution to the impact from rapidly growing commercial air transport. Then, in the subsequent second section, noise metrics which are used to measure noise levels are described including ‘single event noise metrics’, such as ‘A-weighted sound exposure level (SEL)’, ‘A-weighted maximum sound level (LAMAX)’, ‘effective perceived noise level (EPNL)’, and ‘tone-corrected maximum perceived noise level (PNLTM)’, and ‘cumulative noise metrics’ like ‘equivalent sound level L_{eq}’ as well as kinds of modified versions of L_{eq}. The third section of this chapter briefly introduces the approaches to assess the impacts of flight noise on the community quantitatively, such as the evaluations of ‘contour area’, ‘population enclosed’, ‘houses/households enclosed’, ‘noise levels at enforcement points’, ‘awakenings’, ‘people highly annoyed’, ‘sleep

disturbance', etc. In the following sections of this chapter, two simulation software packages, for the purposes of noise calculation and impact assessment respectively, designated as INMTM (Integrated Noise Model/Management of Trajectory and Missions) and NoiseLAss developed by Delft University of Technology, the entire process of noise calculation and assessment and the noise models used respectively for cases of CUTFDAC, CUTPDAC and CUPFDAC, are introduced. These noise models are from an empirical noise database named as NPD (Noise-Power-Distance) and by means of these models, the noise levels perceived by observers can be correlated with engine power ratings as well as the slant distances between noise source (i.e. aircraft) and observers under the defined flight condition. When models are implemented in optimisation processes, the influence resulted from the differences between actual flight conditions and the defined condition can be compensated automatically by INMTM.

The seventh chapter addresses the issues of multidisciplinary optimisation problem and optimisation algorithms. In this chapter, a description about the multidisciplinary optimisation problem and corresponding mathematical expression are presented first. Then the primary optimisation algorithms available at present are summarised. Further, the mathematical characteristics of the flight trajectory optimisation problems investigated in this research project are analysed and the multi-objective genetic algorithms (GAs) selected to implement the optimisation tasks of this research project are introduced. Finally, the description about GATAC (Green Aircraft Trajectory under ATM Constraints) - a software platform (developed by the University of Malta) through which component-level models introduced previously can be integrated and optimisation can be driven - is provided.

The eighth chapter discusses the system-level integration and modelling. In this chapter, in total nine optimisation models (or cases) are developed. They are: 1) the optimisation model for the departure flight of CUTFDAC; 2) the optimisation model for the departure flight of CUTPDAC; 3) the optimisation model for the departure flight of CUPFDAC; 4) the optimisation model for the en route flight of CUTFDAC; 5) the optimisation model for the en route flight of CUTPDAC; 6) the optimisation model for the en route flight of CUPFDAC; 7) the optimisation model for the arrival flight of CUTFDAC; 8) the optimisation model for the arrival flight of CUTPDAC; and 9) the optimisation model for the arrival flight of CUPFDAC. Besides the model plots

provided in this chapter, for each optimisation case mentioned above, selected optimisation (or design) variables (and their allowed variation ranges), objective functions, optimisation constraints, GA parameter settings are described as well.

Chapter Nine provides the multidisciplinary optimisation results achieved for the above nine case studies. These results include running records of optimisation processes, plots of normalised Pareto area, Pareto frontiers, typical optimum flight trajectories, overall performances (in terms of fuel consumption, flight time, gaseous emissions as well as noise-impact area and noise distributions in the vicinity of local airports) and segment distributions of primary parameters, such as engine net thrust, turbine entry temperature (TET), emission index of NOx etc. Based on these optimised results, the corresponding analysis for each one of these case studies, as well as the comparison analysis of the application of the new-generation propfan engine with the conventional turbofan engine, is also provided in this chapter.

Chapter Ten provides conclusions and discusses future works and suggestions. Although the research work described in this thesis has made a significant step forward in the field of flight trajectory optimisation, like any other research activities, there are still many aspects which can be improved further, and there is still much new research and exploration which can be investigated further. All these are discussed in the tenth chapter.

CHAPTER TWO ATMOSPHERE MODELLING

It is well known that the performances of aircraft and gas turbine engines which take, as a type of mechanical device, atmospheric air as their working fluid are affected powerfully by local atmosphere properties (or called atmosphere conditions) in terms of ambient temperature, ambient pressure, ambient density and humidity. Naturally, the knowledge of variation and distribution of such quantities is needed for the purposes of performance analysis and design of aircraft and gas turbine engines as well as pressure altimeter calibrations and so forth.

However, the real atmosphere is extremely complicated, and "never remains constant at any particular time or place" [17], therefore, a hypothetical model - Static Atmospheric Model - has to be adopted as an approximation.

Simply speaking, "Static atmospheric models describe how the ideal gas properties (namely, pressure, temperature, density and molecular weight) of an atmosphere change, primarily as a function of altitude."[18].

There are several static atmospheric models published by different organisations and standards-making authorities for the different application purposes. Among them, two most frequently used atmospheric models for aviation purposes, namely, International Standard Atmosphere (ISA) and US Military Standard 210 (MIL 210), will be discussed here.

2.1 International Standard Atmosphere

"The International Standard Atmosphere (ISA) is an atmospheric model of how the pressure, temperature, density, and viscosity of the Earth's atmosphere change over a wide range of altitudes" [19] and "defines standard day ambient temperature and pressure up to an altitude of 30500m (100066 ft)." [20].

So far, ISA has been published as an international standard by the International Organization for Standardization (ISO) and the International Civil Aviation Organization (ICAO) and defined respectively in ISO and ICAO documents ISO 2533:1975 and ICAO 7488/2. Some other atmospheric models published by other standards organisations or standards-making authorities are the extensions or subsets of the same ISA atmospheric model. For instance, the U.S. Standard Atmosphere and

WMO (World Meteorological Organization) Standard Atmosphere are the same as the ISO International Standard Atmosphere for altitudes up to 32 km. [19]

2.1.1 Basic assumptions

The ISA model was established based on the following basic assumptions:

1）The Earth's atmosphere is comprised of perfect gas which is devoid of dust, moisture and water vapour and meets the equation of state for the perfect gas:

$$\rho = \frac{MP}{R'T} \qquad (2\text{-}1)$$

Where ρ is mass density, M is average molecular weight, P is pressure, T is temperature and R' is the universal gas constant.

2) "The gas is held in place by so called "hydrostatic" forces" [18]. That is, the force balance for a layer of gas at some altitude among "the downward (towards the planet) force of its weight, the downward force exerted by pressure in the layer above it, and the upward force exerted by pressure in the layer below" [18] is achieved, which can be mathematically expressed as follows:

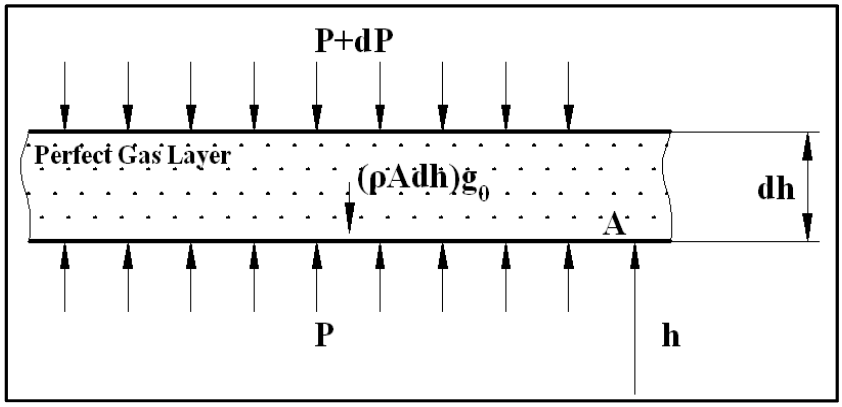

Figure 2-1 Hydrostatic forces balance

$$PA - (P + dP)A - (\rho A dh)g_0 = 0$$
$$dP = -g_0 \rho dh \qquad (2\text{-}2)$$

3) Gas properties do not change with time, namely, this is a static model.

4) The air in the model is “still” with respect to the Earth, that is, wind and turbulence is not considered.

5) Linear temperature distribution assumption.

In the ISA model, the atmosphere is divided into layers with linear temperature distributions (or called constant temperature gradient distributions), (see Figure 2-2). And then values of other properties, such as pressure and density, etc., can be calculated based on this temperature distribution and basic physical constants and relationships. Certainly, such temperature distribution is only an approximation to that of the real atmosphere and the linear distribution assumption can ease some of the maths. For instance, according to this temperature distribution assumption, ambient temperature falls with altitude at a constant lapse rate of -6.5℃/1000m (or -1.98℃/1000 ft) from Mean Sea Level (MSL) up to the tropopause with 11000 m (or 36089 ft) altitude, and then the ambient temperature remains at a constant value of -56.5℃ (or 216.65K) from the tropopause up to 20000 m (65600 ft).

Layer	Level Name	Base Geopotential Height *h* (in km)	Base Geometric Height *z* (in km)	Lapse Rate (in °C/km)	Base Temperature *T* (in °C)	Base Atmospheric Pressure *p* (in Pa)
0	Troposphere	0.0	0.0	−6.5	+15.0	101325
1	Tropopause	11.000	11.019	+0.0	−56.5	22632
2	Stratosphere	20.000	20.063	+1.0	−56.5	5474.9
3	Stratosphere	32.000	32.162	+2.8	−44.5	868.02
4	Stratopause	47.000	47.350	+0.0	−2.5	110.91
5	Mesosphere	51.000	51.413	−2.8	−2.5	66.939
6	Mesosphere	71.000	71.802	−2.0	−58.5	3.9564
7	Mesopause	84.852	86.000	—	−86.2	0.3734

Figure 2-2 Layers in the ISA [19]

6) Mean Sea Level Conditions [17].

Ambient Temperature T_0 = 288.15K (15℃).

Ambient pressure P_0 = 101325 N/m^2.

Density $\rho_0 = 1.225 kg/m^3$.

Speed of sound $a_0 = 340.294 m/sec$.

Acceleration of gravity $g_0 = 9.80665 m/sec^2$.

2.1.2 Modelling of ISA

Based on the above assumptions, modelling of ambient temperature, ambient pressure and density in ISA can be implemented as follows:

a) Temperature modelling

$$T = T_0 - 6.5 \times \frac{h(m)}{1000}, \text{ When } 0\,m \le h \le 11000\ m$$

$$T = 216.65\ K, \quad \text{When } 11000\ m \le h \le 20000\ m \qquad (2\text{-}3)$$

b) Pressure modelling

In ISA, the standard pressure p at a given altitude (Pressure Altitude (PA) or Geopotential Altitude (GA)) can be achieved by pressure modelling, that is, by using the combination of the hydrostatic equation, perfect gas law and temperature lapse rate equation.

The hydrostatic equation for a column of air can be expressed as follows based on Figure 3:

$$dp = -\rho g dh \qquad (2\text{-}4)$$

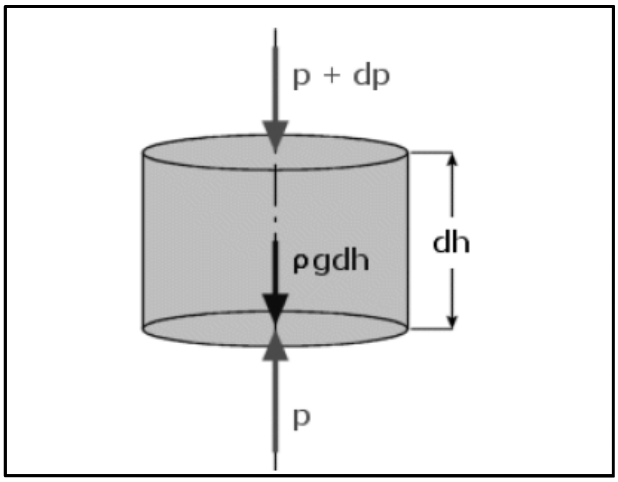

Figure 2.3 Atmosphere element [17]

The perfect gas law is:

$$p = \rho RT, \qquad (2\text{-}5)$$

Where, R is gas constant.

And then the following basic differential equation can be achieved through dividing the above equation (2-4) by the equation (2-5):

$$\frac{dp}{p} = -\frac{\rho g dh}{\rho RT} = -\frac{g}{RT} dh \qquad (2\text{-}6)$$

The above differential equation (2-6) indicates the relationship between dh (small change in pressure altitude h) and dp (small change in pressure).

Therefore, "the relationship between the pressure at a troposphere altitude and sea level pressure can be obtained by integrating equation (2-6) between h_0=0 and h:" [1]

$$\int_{p_0}^{p} \frac{dp}{p} = -\frac{g}{R} \int_{h_0=0}^{h} \frac{dh}{T_0 - 0.0065h} \qquad (2\text{-}7)$$

That is, $p = p_0 (1 - 0.0065 \frac{h}{T_0})^{5.2561}$ when $0m \le h \le 11000m$ (2-8)

Where, the units of T_0 and h are respectively K and meter.

Because of the fact that temperature vertical distribution is a piecewise function (see the above equation (2-3)), so the relationship between the pressure at an altitude above the tropopause and tropopause pressure can be achieved in a similar way but integrating the differential equation (2-6) from the tropopause to this given altitude above the tropopause:

$$\int_{p_{11}}^{p} \frac{dp}{p} = -\frac{g}{RT_{11}} \int_{h_{11}}^{h} dh \qquad (2\text{-}9)$$

That is, $p = p_{11} e^{-\frac{g}{RT_{11}}(h - h_{11})}$ when $11000m \le h \le 20000m$ (2-10)

Where, p_{11}=22632 N/m^2, T_{11}=216.65 K and h_{11}=11000 m.

Here, it should be pointed out that the constant value of gravitational acceleration g_0 (the value of gravitational acceleration at MSL) has been used during the derivation of pressure model, no matter what the given altitude is. This can be explained as follows: as a matter of fact, the acceleration of gravity 'g' does vary with the change in geometric altitude 'z' because of the varied distance from the Earth's centre accompanied by the varied geometric altitude 'z'. And the relationship between gravitational acceleration 'g' and geometric altitude 'z' can be expressed through the following equation (2-11):

$$g(z) = \frac{Gm_e}{(r_e + z)^2} \qquad (2\text{-}11)$$

During the pressure modelling, a transformation from actual geometric altitude 'z' to geopotential altitude 'h' (see equation (2-12)) is adopted so that the problem of varied 'g' with geometric altitude 'z' mentioned above is avoided.

$$h = \frac{r_e z}{r_e + z} \qquad (2\text{-}12)$$

Geopotential altitude, or called pressure altitude, is an abstraction and of the property:

$$g(z)dz = g_0 dh \qquad (2\text{-}13)$$

Where, $g_0 = g(0) = \frac{Gm_e}{r_e^2}$

The equation (2-13) indicates that a different altitude-measurement system can be so defined that the amount of work done by lifting a unit mass through a distance dz at geometric altitude z with gravitational acceleration g(z) is equal to the work done by lifting that same mass but through a distance dh and with the unchanged sea-level gravitational acceleration value g_0.

That is, the concept of geopotential altitude 'h' is based on the 'work equivalence', and when in the altitude-measurement system of geopotential or pressure altitude, the acceleration of gravity remains constant with the value of g_0.

c) Density modelling

Based on the above two models, pressure and standard temperature at a given altitude can be obtained easily and further the standard density can be calculated through the state equation of perfect gas: $\rho = \frac{p}{RT}$.

2.1.3 Atmosphere properties distribution

Figure 2-4 illustrates the assumed vertical distribution of ambient temperature and, correspondingly, the variations of standard density and ambient pressure with pressure altitude (although the figure is from the 1976 U.S. Standard Atmosphere, the distributions are the same as those from ISA up to 32 km altitude which has been mentioned previously).

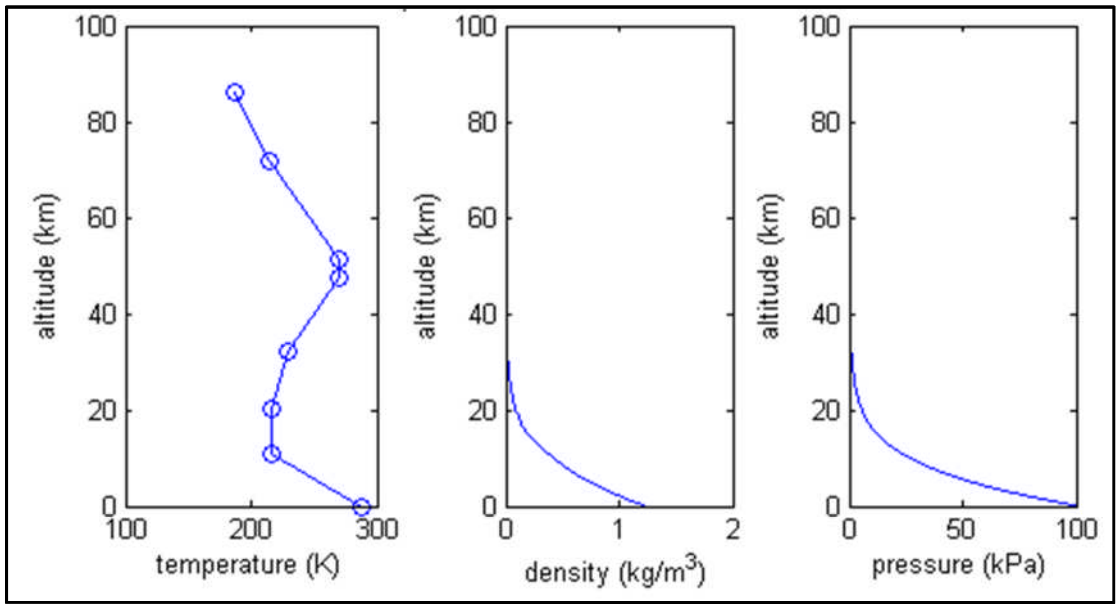

Figure 2-4 The 1976 U.S. Standard Atmosphere [18]

2.2 US Military Standard 210

"US Military Standard 210 (MIL210) is the most commonly used standard for defining likely extremes of ambient temperature versus altitude. This is primarily an aerospace standard, and is also widely used for land based applications though with the hot and cold day temperature ranges extended." [20].

Figures 2-5 and 2-6 illustrate the comparisons between MIL210 and ISA in terms of ambient temperature distribution and relative density distribution. From Figure 2-5, it can be observed that “the minimum MIL210 cold day temperature of 185.9 K (-87.38℃) occurs between 15545 m (51000 ft) and 18595 m (61000 ft). The maximum MIL210 hot day temperature is 312.6 K (39.58℃) at sea level.”[20].

Often, the actual temperature condition under non-standard atmosphere is expressed as ISA$\pm\Delta$T at a given pressure altitude h which is easy for user to know exactly the actual atmospheric condition and also the deviation from the ISA condition.

In this project research, ISA is used for performance analysis of both aircraft and gas turbine engine, and in the meantime, gas turbine performance also involves non-standard atmosphere.

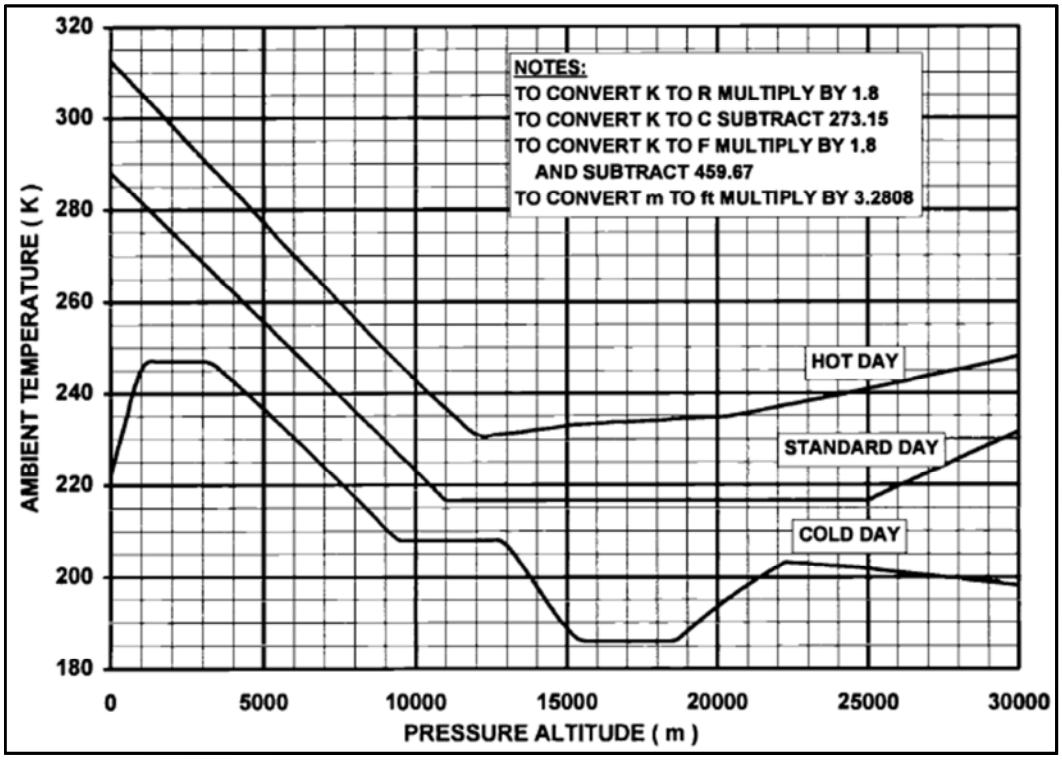

Figure 2-5 temperature distribution comparison between MIL210 and ISA [20]

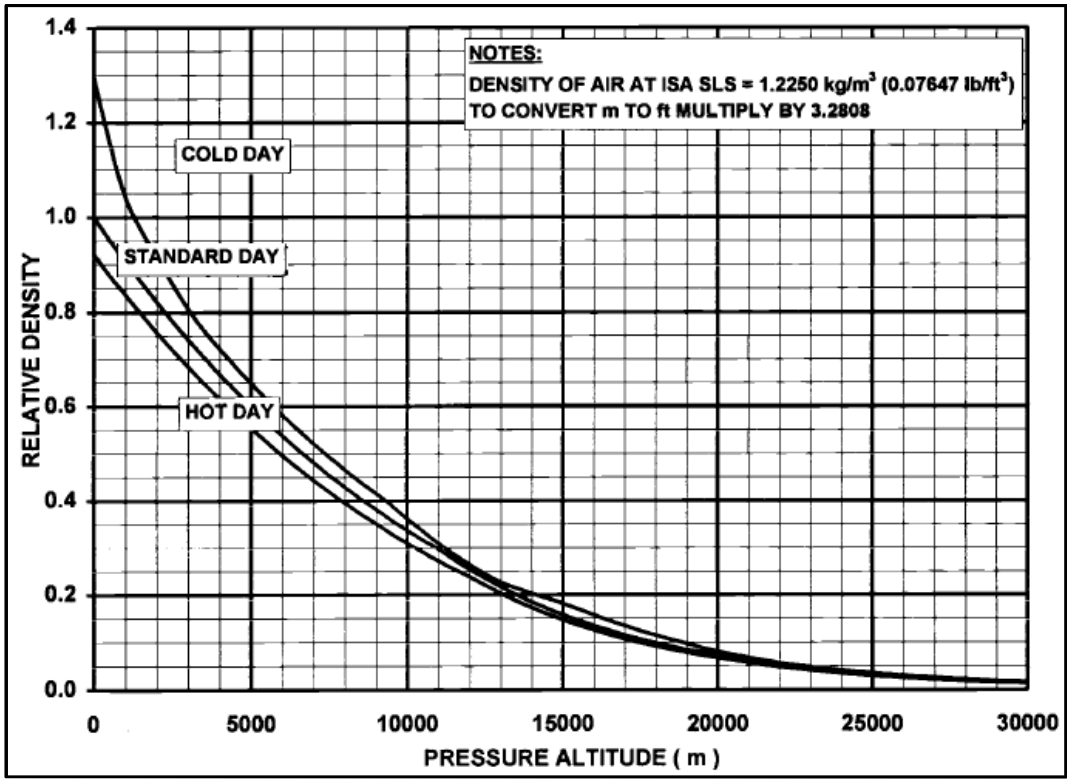

Figure 2-6 density distribution comparison between MIL210 and ISA [20]

2.3 Specific and Relative Humidity

Although "humidity has the least powerful effect upon engine performance of the three ambient parameters, its effect is not negligible in that it changes the inlet air's molecular weight, and hence basic properties of specific heat and gas constant. In addition, condensation may occasionally have gross effects on temperature." [20]. On the other hand, moisture in humid air entering the engine core and combustor also does have influence on NO_x formation rate by reducing the peak flame temperature [21], which should, and has been, considered during the project research (it will be discussed in more detail in a later chapter). Therefore, some basic knowledge about humidity property of atmosphere is still required although it is not included in current commonly-used atmosphere models.

2.3.1 Specific humidity

Atmospheric specific humidity is defined as: the ratio of water vapour to dry air by mass (see equation (2-14)), or, the ratio of water vapour to moist air by mass.

$$\text{Specific humidity (\%)} = \text{fn(water content in atmosphere)}$$
$$\Leftrightarrow \text{SH} = 100 \cdot \text{Mass of water vapor in a sample/Mass of dry air in the sample} \quad (2\text{-}14)$$

[20].

Usually, the former definition is used more widely, however, for most practical purposes the difference is small.

2.3.2 Relative humidity

Relative humidity is specific humidity divided by the saturated value for the prevailing ambient pressure and temperature (see equation (2-15)).

$$\text{Relative humidity(\%)} = \text{fn(specific humidity(\%), specific humidity if atmosphere was saturated at prevailing ambient pressure and temperature (\%))}$$
$$\Leftrightarrow \text{RH} = 100 \cdot \text{SH} / \text{SH}_{\text{sat}}$$

(2-15) [20].

2.3.3 Calculation equation of Specific humidity

The following formula (2-16) relates specific humidity with relative humidity, ambient temperature and ambient pressure, which is widely used for specific humidity calculation in practice.

$$\text{Specific humidity(\%)} = \text{fn(relative humidity(\%), ambient temperature(K), ambient pressure (kPa))}$$
$$\Leftrightarrow \text{SH} = 0.622 \cdot \text{PSAT} \cdot \text{RH}/(\text{PAMB} - \text{PSAT} \cdot (\text{RH}/100))$$

(2-16) [20].

Where, PSAT is the saturated vapour pressure of water at the given ambient conditions and expressed as:

$$\text{PSAT(kPa)} = (1.0007 + 3.46 \times 10^{-5} \cdot \text{PAMB}) \cdot 0.61121 \cdot e^{(17.502 \cdot (\text{TAMB} - 273.15)/(\text{TAMB} - 32.25))}$$

(2-17) [20].

Reference [20] provides another method to determine specific humidity (see Figure 2-7 and Figure 2-8). According to this method, firstly, the specific humidity at a given ambient temperature and relative humidity but at sea level can be determined through Figure 2-7; and then a correction factor which takes the difference between the given altitude and sea level into account can be found from Figure 2-8; finally, applying the correction factor to the specific humidity obtained from Figure 2-7 results in the specific

humidity value required at the given altitude, ambient temperature and relative humidity.

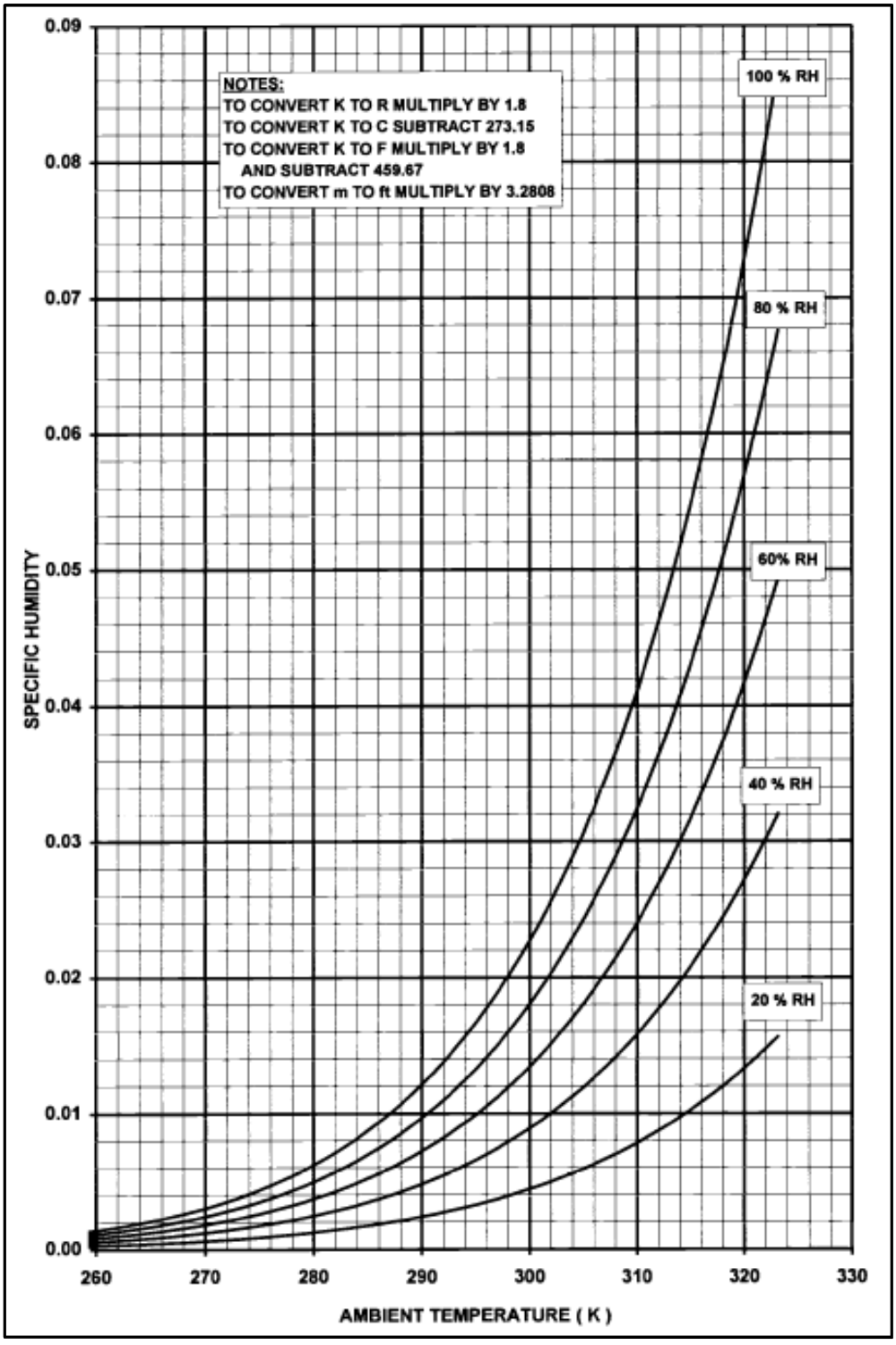

Figure 2-7 Specific humidity vs. relative humidity and ambient temperature at sea level [20]

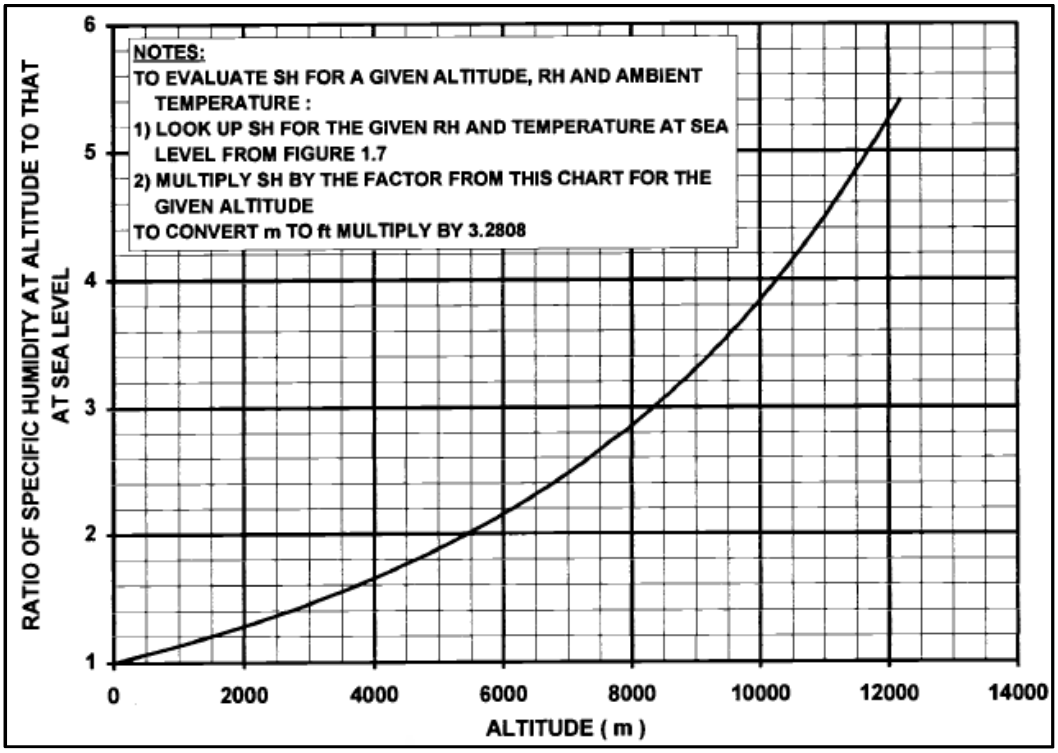

Figure 2.8 Correction factor for specific humidity [20]

2.3.4 Distribution characteristics of specific humidity in Earth's atmosphere

Figure 2-9 illustrates the variation characteristics of specific humidity with ambient temperature and pressure for the 100% relative humidity in Earth's atmosphere. From this figure, it can be observed that "for MIL 210 cold days specific humidity is almost zero for all altitudes. The maximum specific humidity will never exceed 4.8%, which would occur on MIL 210 hot day at sea level. In the troposphere, specific humidity for 100% relative humidity falls with pressure altitude, due to the falling ambient temperature. Above that, in the stratosphere, water vapour content is negligible, almost all having condensed out at the colder temperatures below." [20]. Usually, the influence of specific humidity can be ignored when the ambient temperature is below 0.8℃ or above 40.8℃ for most gas turbine performance purposes.

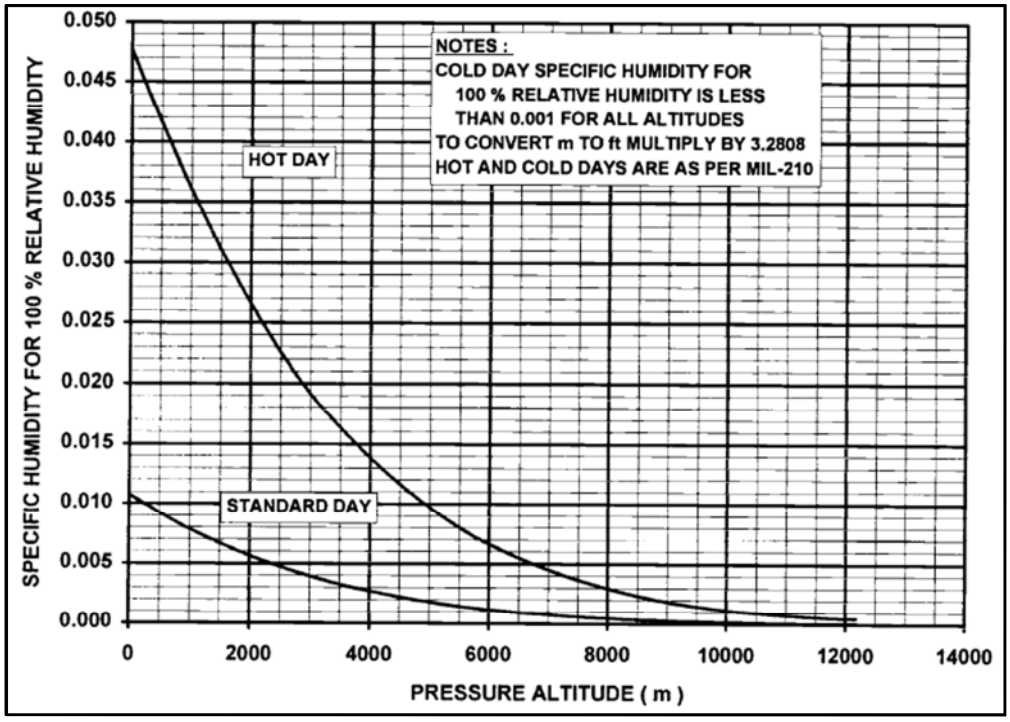

Figure 2.9 Specific humidity vs. pressure altitude with 100% relative humidity [20]

2.4 Viscosity

The viscosity of a fluid is a measure of its resistance to gradual deformation by shear stress or tensile stress and is due to friction between neighbouring parcels of the fluid that are moving at different velocities.

There exist two related measures of fluid viscosity, that is, dynamic (or absolute) viscosity and kinematic viscosity.

The dynamic or absolute viscosity is defined in the Newton Law of Friction:

$$\tau = \mu \, dc/dy \quad (2\text{-}18)$$

Where, τ, dc/dy respectively denote shearing stress and the rate of change of fluid velocity along the y direction, and μ is dynamic viscosity.

The kinematic viscosity is the dynamic viscosity μ divided by the density of the fluid ρ, that is,

$$\nu = \mu / \rho \quad (2\text{-}19)$$

"Dynamic viscosity is a function of gas composition and static temperature" [20]. The following Figure 2-10 illustrates the variations of dynamic viscosity with static temperature respectively for dry air and combustion products.

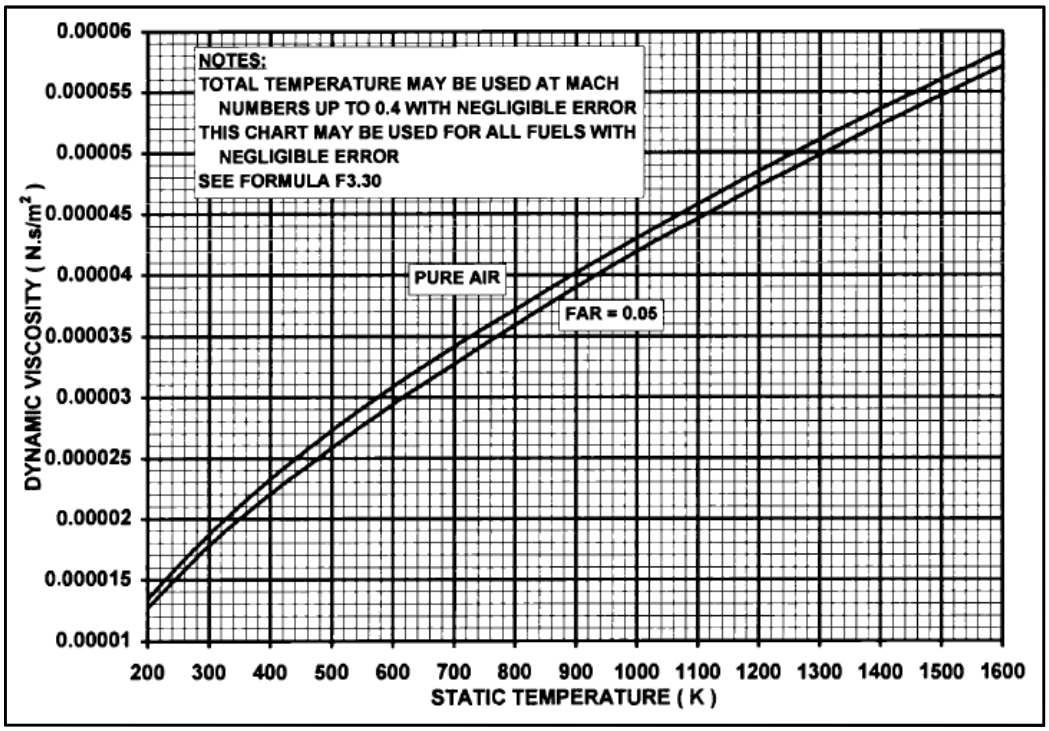

Figure 2-10 Dynamic viscosity versus temperature for pure air and kerosene combustion products [20]

However, the influence of gas composition on the dynamic viscosity can be ignored in practical applications [20] and the dynamic viscosity can be calculated through the following formula.

$$\mu = \mu_0 (\frac{TS}{273})^{1.5} \frac{273+C}{TS+C},\ (N \cdot s/m^2) \quad (2\text{-}20)\ [22]$$

Where, TS denotes static temperature, K; and for air, $\mu_0 = 1.711 \times 10^{-5}\ (N \cdot s/m^2)$ and C=122 K.

2.5 Gas Constant R

The gas constant appears extensively in formulae relating pressure and temperature changes. The gas constant for an individual gas is the universal gas constant divided by the molecular weight with the unit of J/(kg K). The value of the universal gas constant is 8314.3 J/(mol K).

In this project research, gas constant of dry air is applied. The reference [20] gives the composition of dry air as Table 2-1. And molecular weights of these related constituents listed in Table 2-1 can be found in Table 2-2.

Table 2-1 Composition of Dry Air [20]

Composition	**By mole or volume**	**By mass**
	%	%
Nitrogen (N_2)	78.08	75.52
Oxygen (O_2)	20.95	23.14
Argon (Ar)	0.93	1.28
Carbon dioxide (CO_2)	0.03	0.05
Neon (Ne)	0.002	0.001

In atmosphere, there exist trace amounts of helium, methane, krypton, hydrogen, nitrous oxide and xenon. However, for the purpose of this research, these constituents are negligible.

Table 2-2 Molecular Weights of Constituents [20]

Nitrogen (N_2)	28.013		Oxygen (O_2)	31.999
Argon (Ar)	39.948		Carbon dioxide (CO_2)	44.010
Neon (Ne)	20.183			

Therefore, the molecular weight of dry air with those constituents listed in Table 2-1 can be achieved through the average of molecular weights of these constituents on the molar basis. That is,

$$\begin{aligned} MW_{\text{dry air}} &= 28.013 \times 78.08\% + 31.999 \times 20.95\% + 39.948 \times 0.93\% + 44.010 \times 0.03\% + 20.183 \times 0.002\% \\ &= 28.9615 \end{aligned}$$

Further, gas constant of dry air can be obtained as follows:

$$R_{\text{dry air}} = \frac{R_{\text{universal}}}{MW_{\text{dry air}}} = \frac{8314.3}{28.9615} = 287.05\ \text{J}/(\text{kg K})$$

CHAPTER THREE AIRCRAFT PERFORMANCE MODELLING

3.1 Aircraft Performance Modelling

This chapter mainly discusses modelling methods and modelling results for the turbofan propelled aircraft (CUTFDAC), the propfan (open rotor) powered aircraft (CUPFDAC) and the turboprop driven aircraft (CUTPDAC) respectively, with different aircraft configurations (i.e., using or not using high lift devices, as well as the different positions of high lift devices if used. These different configurations are denoted as 'IC'- Initial Climb, 'CR'- Cruise and 'AP'- Approach respectively) for the different flight applications.

Before the detailed introduction about aircraft performance models, it is worth pointing out that due to the unavailability of BADA dataset at the early stage of the modelling process, the drag characteristics of aircraft (CUTFDAC and CUPFDAC with the 'Cruise' configuration) were estimated based on the methods recommended by the reference [23], and later related BADA data were available and applied to other modelling cases, including CUTFDAC and CUPFDAC respectively with 'Initial Climb' and 'Approach' configurations as well as CUTPDAC with the above three configurations – 'Initial Climb', 'Cruise' and 'Approach'.

3.1.1 CUTFDAC (Cranfield University TurboFan-Driven AirCraft)

CUTFDAC (Cranfield University TurboFan-Driven AirCraft) used in this research project is a hypothetical short- to medium-range, narrow-body, commercial passenger jet airliner with typical payload (150 passengers) and range (about 6000 km). This aircraft was built based on the Airbus A320-200 [24-25]. Figure 3-1 illustrates the schematic drawing of CUTFDAC and Figure 3-2 shows the geometric measurements of the A320-200 which constitute the foundation for CUTFDAC performance modelling.

Figure 3-1 CUTFDAC (Cranfield University TurboFan-Driven AirCraft)

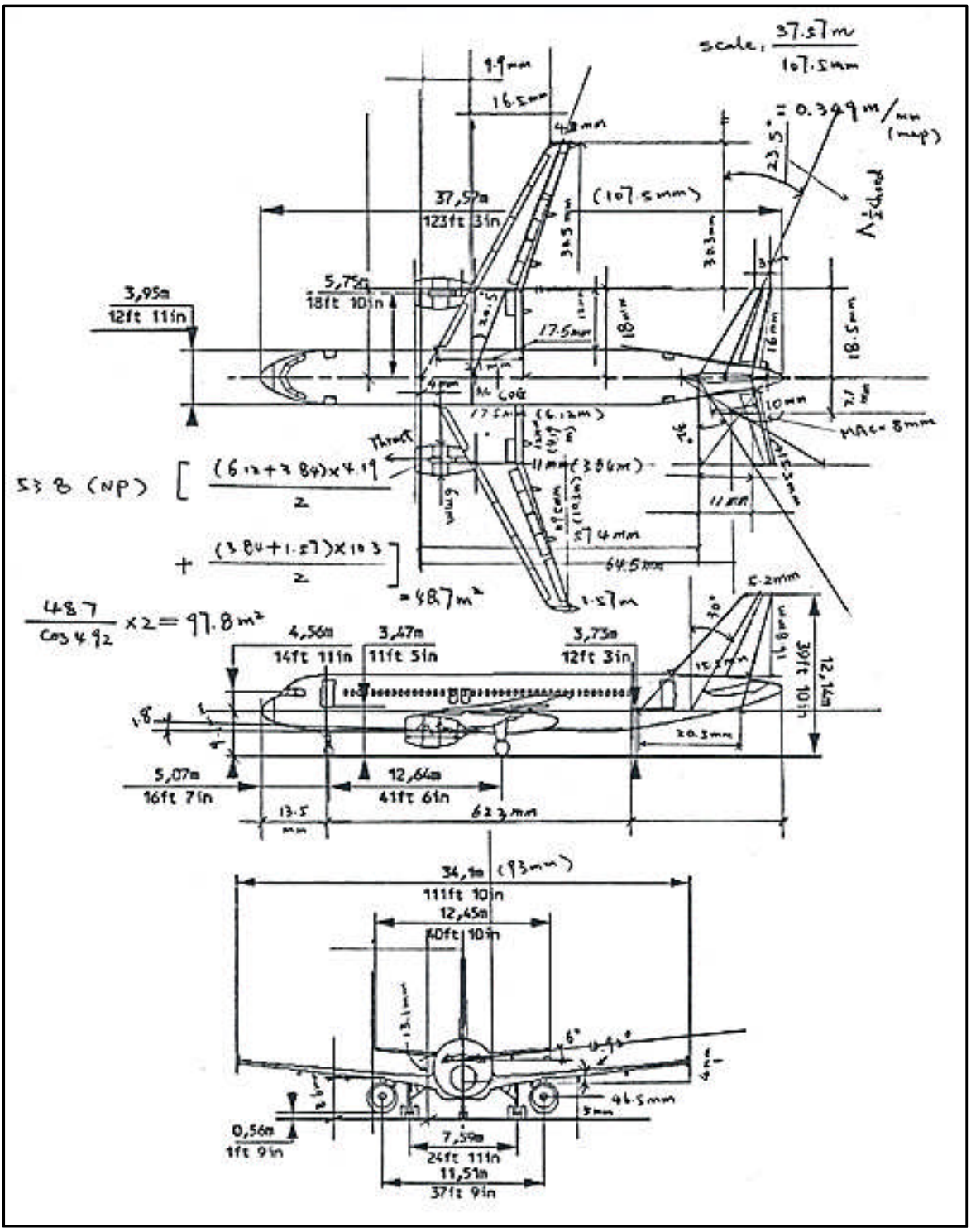

Figure 3-2 Measurements of A320-200

Take the cruise condition of A320-200 as the base to build up the aerodynamic model of CUTFDAC, that is, flight altitude 11000 meters, flight Mach number 0.78 and ISA. Further, from Chapter Two (atmosphere modelling), the following parameters can be obtained:

Ambient temperature: $T_{amb} = 216.65$ K

Ambient pressure:

$$p_{amb} = p_0(1-0.0065\frac{h}{T_0})^{5.2561} = 101325\cdot(1-0.0065\cdot\frac{11000}{288.15})^{5.2561} = 22630.6\text{Pa}$$

Ambient density: $\rho_{amb} = \frac{p_{amb}}{R\cdot T_{amb}} = \frac{22630.6}{287.05\times 216.65} = 0.36390\,\text{kg}/\text{m}^3$

Speed of sound: $a = \sqrt{\gamma R T_{amb}} = \sqrt{1.4\times 287.05\times 216.65} = 295.068$ m/s

Dynamic viscosity:

$$\begin{aligned}\mu &= 1.711\times 10^{-5}\times(\frac{T_{amb}}{273})^{1.5}\times\frac{273+122}{T_{amb}+122}\\ &= 1.711\times 10^{-5}\times(\frac{216.65}{273})^{1.5}\times\frac{273+122}{216.65+122}\\ &= 1.4109\times 10^{-5}\ (P_a\cdot s)\end{aligned}$$

Kinematic viscosity: $\upsilon = \frac{\mu}{\rho} = \frac{1.4109\times 10^{-5}}{0.36390} = 3.8772\times 10^{-5} \cong 3.9\times 10^{-5}\ \text{m}^2/\text{s}$

a) Estimation of profile drag coefficient

1) Fuselage

Shape (form) factor $F_f = 1 + 2.2/\lambda_f^{1.5} - 0.9/\lambda_f^{3.0}$ [23]

Where, finess ratio $\lambda_f = \frac{l_f}{(\frac{4}{\pi}A_x)^{0.5}} = \frac{37.57}{(\frac{4}{\pi}\cdot\frac{\pi}{4}\cdot 3.95^2)^{0.5}} = \frac{37.57}{3.95} = 9.51$ [23]

Where, l_f, A_x are overall length and cross-sectional area of fuselage respectively. And

$A_x = \frac{\pi}{4} \cdot D_f^2$, D_f is the cross-sectional diameter of fuselage. The values of l_f and D_f can be found from the above Figure 3-2.

Therefore, $F_f = 1 + \frac{2.2}{9.51^{1.5}} - \frac{0.9}{9.51^{3.0}} = 1.07$

Taking interference factor $Q_f = 1.0$ [23]

According to the above flight Mach number and the speed of sound at cruise point, the true airspeed (TAS) of the aircraft is,

$$TAS = V_\infty = a \cdot M = 295.068 \times 0.78 = 230.15 \cong 230 \text{ m/s}$$

Re number of fuselage, $R_{e,f} = \frac{V_\infty \cdot l_f}{\upsilon_\infty} = \frac{230 \times 37.57}{3.9 \times 10^{-5}} = 2.22 \times 10^8$

So, skin friction coefficient of fuselage $C_{f,f}$ can be calculated as follows：

$$\begin{aligned} C_{f,f} &= \frac{0.455}{(\log_{10} R_{e,f})^{2.58} \cdot (1 + 0.144 \cdot M^2)^{0.65}} \\ &= \frac{0.455}{(\log_{10} 2.22 \times 10^8)^{2.58} \cdot (1 + 0.144 \times 0.78^2)^{0.65}} \\ &= 1.81 \times 10^{-3} \end{aligned}$$ [23]

And further, the wetted area of fuselage $S_{wet,f}$ can be expressed as follows:

$$\begin{aligned} S_{wet,f} &= S_{wet,n} + S_{wet,c} + S_{wet,t} \\ &= 43.8 + 269 + 100 \\ &= 413 \text{ m}^2 \end{aligned}$$

Here, the entire fuselage is divided into 3 components, namely, nose part, constant section part and tail cone part, whose wetted areas are accordingly denoted as $S_{wet,n}$, $S_{wet,c}$ and $S_{wet,t}$.

By the measurements to the drawing of A320-200 (see Figure 3-2), the lengths of these three components can be calculated as follows:

$$L_{nose} = 13.5\text{mm(measured)} \times 0.349\text{m/mm(scale)} = 4.71 \text{ m}$$

$L_C = 62.3\text{mm(measured)} \times 0.349\,\text{m/mm (scale)} = 21.7\ \text{m}$

$L_{tail} = 37.57 - 4.71 - 21.7 = 11.2\ \text{m}$

Hence, the wetted areas of these three components of the fuselage can be estimated through the following simplified equations [26].

$S_{wet,nose} = 0.75 \times \pi \times D_f \times L_{nose} = 0.75 \times \pi \times 3.95 \times 4.71 = 43.8\ \text{m}^2$

$S_{wet,c} = \pi D_f L_c = \pi \times 3.95 \times 21.7 = 269\ \text{m}^2$

$S_{wet,t} = 0.72 \times \pi \times D_f \times L_{tail} = 0.72 \times \pi \times 3.95 \times 11.2 = 100\ \text{m}^2$

Finally, the contribution to aircraft profile drag coefficient from its fuselage can be obtained as follows:

$$C_{Dp,f} = \frac{C_{f,f} \cdot F \cdot Q \cdot S_{wet}}{S_{ref}} = \frac{1.81 \times 10^{-3} \times 1.07 \times 1.0 \times 413}{123.20} = 6.49 \times 10^{-3} \quad \text{(3-1) [23]}$$

Where, the wing planform area ($S_{p,w}$ = 123.20 m^2) is taken as S_{ref}.

2) Main wing

Re number $R_{e,w} = \dfrac{230 \times 4.29}{3.9 \times 10^{-5}} = 2.53 \times 10^7$ [23]

Skin friction coefficient

$$C_{f,w} = \frac{0.455}{(\log_{10} 2.53 \times 10^7)^{2.58} \cdot (1 + 0.144 \times 0.78^2)^{0.65}} = 2.46 \times 10^{-3}$$ [23]

Form (shape) factor $F_w = (F^*_w - 1) \cdot \cos^2 \Lambda_{0.5C,w} + 1$ [23]

Where,

$$\begin{aligned} F^*_w &= F^*_w(t/c_{ave,w}) = 1 + 3.3 \times (t/c_{ave,w}) - 0.008 \times (t/c_{ave,w})^2 + 27.0 \times (t/c_{ave,w})^3 \\ &= 1 + 3.3 \times 10.8\% - 0.008 \times (10.8\%)^2 + 27.0 \times (10.8\%)^3 \\ &= 1.39 \end{aligned}$$ [23]

$t/c_{ave,w}$ is wing average thickness/chord ratio, and its value of 10.8% comes from reference [27].

$\Lambda_{0.5C,w}$ is the wing sweepback angle at 50% chord, which equals 20.5° measured from

the A320-200 drawing (see Figure 3-2).

So, the form factor $F_w = (1.39-1)\times\cos^2 20.5^\circ + 1 = 1.34$

Consider A320-200 to be of well filleted low/mid wings, hence,

Interference factor $Q_w = 1.0$. [23]

Main wing wetted area $S_{w,w} = S\cdot[1.977 + 0.52\cdot(t/c_{ave,w})]$ [28]

Where, the calculation of area S is as follows:

Figure 3-3 gives the measured values of main dimensions of the main wing. From this measurement, the following calculations can be implemented.

$$S_1 = \frac{(11\times 0.349 + 17.5\times 0.349)\times(12\times 0.349)}{2} = 20.8\ (m^2)$$

$$S_2 = \frac{(4\times 0.349 + 11\times 0.349)\times(30.5\times 0.349)}{2} = 27.9\ (m^2)$$

So, $S_{12} = S_1 + S_2 = 20.8 + 27.9 = 48.7\ (m^2)$

And with the further consideration about the wing dihedral angle with the value of 4.92° measured from the aircraft configuration drawing (see the Figure 3-2), the following area can be calculated,

$$S_{12}^{'} = \frac{S_{12}}{\cos 4.92^\circ} = \frac{48.7}{\cos 4.92^\circ} = 48.9\ m^2$$

So, $S = S_{12}^{'}\times 2 = 48.9\times 2 = 97.8\ (m^2)$

Hence,

$$\begin{aligned} S_{w,w} &= S\cdot[1.977 + 0.52\cdot(t/c_{ave,w})] \\ &= 97.8\times(1.977 + 0.52\times 10.8\%) \\ &= 199\ (m^2) \end{aligned}$$

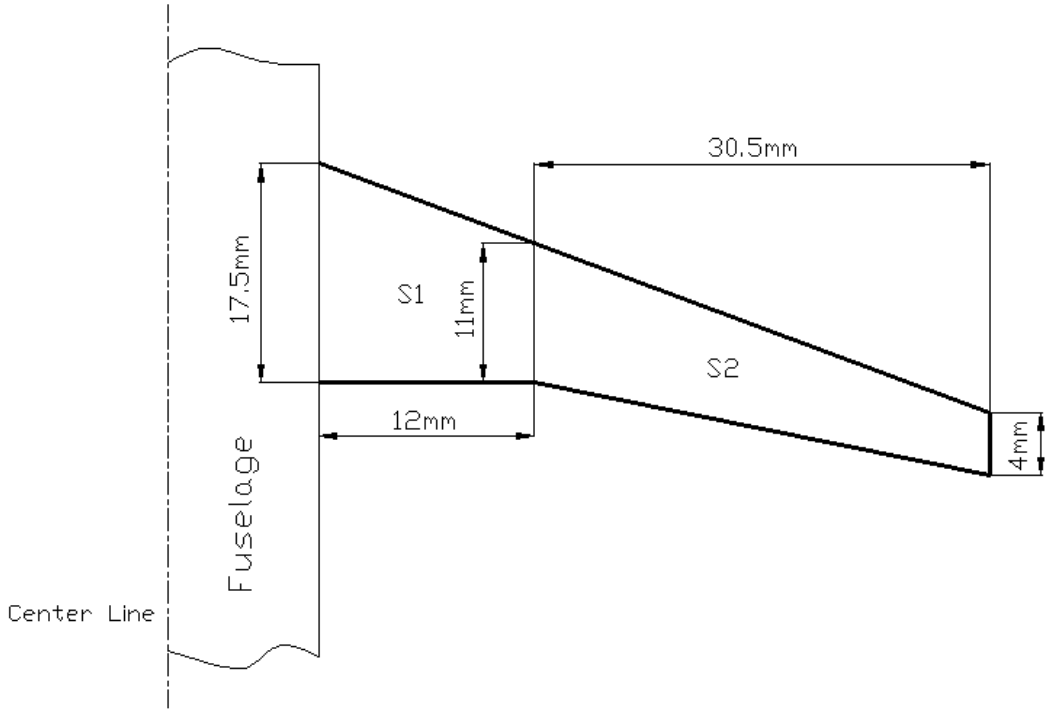

Figure 3-3 Main dimension measurements of main wing

Therefore, the contribution to the profile drag coefficient from main wing can be obtained as follows:

$$C_{DP,w} = \frac{C_{f,w} \cdot F_w \cdot Q_w \cdot S_{wet,w}}{S_{ref}} = \frac{2.46 \times 10^{-3} \times 1.34 \times 1.0 \times 199}{123.2} = 5.32 \times 10^{-3} \quad (3\text{-}2)$$

3) Vertical tailplane (VTP)

Since the horizontal tailplane (HTP) is treated separately with different reference area from the wing planform area used by other components in APM (aircraft performance model), the discussion about its profile drag coefficient will, therefore, appear later in this section, for the purpose of convenience.

The following Figure 3-4 shows the measurements of VTP from the aircraft drawing (also see Figure 3-2).

According to the measured tip chord C_t from A320-200 drawing (also see Figure 3-2) and the taper ratio (TR) of VTP provided by the reference [25] (see Figure 3-2), the value of root chord C_r of VTP can be obtained as follows:

$$TR_{VTP} = 0.303 = \frac{C_{t,VTP}}{C_{r,VTP}} = \frac{5.2 \times 0.349}{C_{r,VTP}}$$

Hence, $C_{r,VTP} = \frac{5.2 \times 0.349}{0.303} = 5.99 \text{ (m)}$

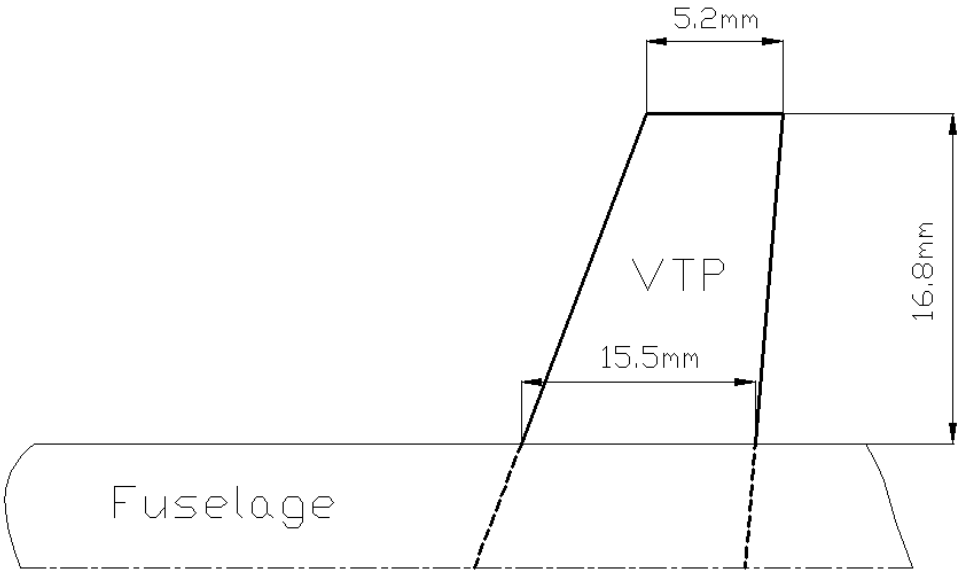

Figure 3-4 VTP measurements

And further, the Mean Aerodynamic Chord (MAC) of VTP is:

$$\begin{aligned} MAC_{VTP} &= C_{r,VTP} \times \frac{2}{3} \times \frac{1 + TR_{VTP} + TR_{VTP}^2}{1 + TR_{VTP}} \\ &= 5.99 \times \frac{2}{3} \times \frac{1 + 0.303 + 0.303^2}{1 + 0.303} \\ &= 4.27 \text{ (m)} \end{aligned}$$

So, Re number $R_{e,VTP} = \frac{V_\infty \cdot MAC_{VTP}}{\upsilon_\infty} = \frac{230 \times 4.27}{3.9 \times 10^{-5}} = 2.52 \times 10^7$

Further, the skin friction coefficient of VTP,

$$\begin{aligned} C_{f,VTP} &= \frac{0.455}{(\log_{10} R_{e,VTP})^{2.58} \times (1 + 0.144 \cdot M_\infty^2)^{0.65}} \\ &= \frac{0.455}{(\log_{10} 2.52 \times 10^7)^{2.58} \times (1 + 0.144 \times 0.78^2)^{0.65}} \\ &= 2.46 \times 10^{-3} \end{aligned}$$

Assume the average thickness/chord $(t/c)_{ave}$ of VTP is the same as that of HTP, that is, $(t/c)_{ave} = 8\%$, then factor F^*_{VTP} can be calculated as follows:

$$F^*_{VTP} = 1 + 3.52 \cdot (t/c)_{ave} = 1 + 3.52 \times 8\% = 1.2816 \cong 1.28$$

Combined with the measured sweepback angle at 50% chord, namely, $\Lambda_{0.5C} = 30^\circ$,

Form factor,

$$\begin{aligned} F_{VTP} &= (F^*_{VTP} - 1) \cdot \cos^2 30^\circ + 1 \\ &= (1.28 - 1) \times \cos^2 30^\circ + 1 \\ &= 1.21 \end{aligned} \qquad [23]$$

And taking VTP interference factor $Q_{VTP} = 1.2$. [23]

According to the measurement results from VTP (see Figure 3-4), wetted area of VTP can be calculated as follows:

$$\begin{aligned} S &= \frac{(5.2 \times 0.349 + 15.5 \times 0.349) \times (16.8 \times 0.349)}{2} \\ &= 21.2\ (m^2) \end{aligned}$$

So, the VTP wetted area

$$S_{wet,VTP} = 21.2 \times (1.977 + 0.52 \times 8\%) = 42.8\ (m^2)$$

Therefore, the contribution to profile drag coefficient from vertical tailplane is:

$$\begin{aligned} C_{DP,VTP} &= \frac{(C_{f,VTP} \cdot F_{VTP} \cdot Q_{VTP}) \cdot S_{wet,VTP}}{S_{ref}} \\ &= \frac{2.46 \times 10^{-3} \times 1.21 \times 1.2 \times 42.8}{123.20} \qquad (3\text{-}3)\ [23] \\ &= 1.24 \times 10^{-3} \end{aligned}$$

4) Nacelle

According to Figure 3-2, the length of nacelle is 4.44m. So, Re number of nacelle is,

$$R_{e,n} = \frac{230 \times 4.44}{3.9 \times 10^{-5}} = 2.62 \times 10^7$$

Then, the skin friction coefficient of nacelle is,

$$C_{f,n} = \frac{0.455}{(\log_{10} R_{e,n})^{2.58} \times (1 + 0.144 \times M_{\infty}^{2})^{0.65}}$$
$$= \frac{0.455}{(\log_{10} 2.62 \times 10^{7})^{2.58} \times (1 + 0.144 \times 0.78^{2})^{0.65}} \quad [23]$$
$$= 2.45 \times 10^{-3}$$

Take the form and interference factor $[FQ]_n = 1.25$. [23]

Approximately regard the whole propulsion system including nacelle and engine as a cylinder, so the wetted area of two nacelles is,

$$S_{wet,n} = (\pi \cdot D \cdot L_n) \times 2 = \pi \times (6 \times 0.349) \times (10.5 \times 0.349) \times 2 = 48.2\ (m^2)$$

Therefore, the contribution to profile drag coefficient from two propulsion systems is,

$$C_{DP,n} = \frac{(C_{f,n} \cdot [FQ]_n) \cdot S_{wet,n}}{S_{ref}} = \frac{2.45 \times 10^{-3} \times 1.25 \times 48.2}{123.20} = 1.20 \times 10^{-3} \quad (3\text{-}4)\ [23]$$

5) Horizontal tailplane (HTP)

The following Figure 3-5 illustrates the measurements of HTP with the same scale of 0.349m/mm as other measurements mentioned previously.

From this figure, the planform area of HTP can be determined as follows,

$$S_{planform,HTP} = \frac{(3 \times 0.349 + 10 \times 0.349) \times (16 \times 0.349)}{2} = 12.7\ (m^2)$$

And because the dihedral of HTP is 6° (measured), by this consideration, the area $S_{act,HTP}$ can be obtained,

$$S_{act,HTP} = \frac{S_{planform,HTP}}{\cos 6^\circ} = \frac{12.7}{\cos 6^\circ} = 12.8\ (m^2)$$

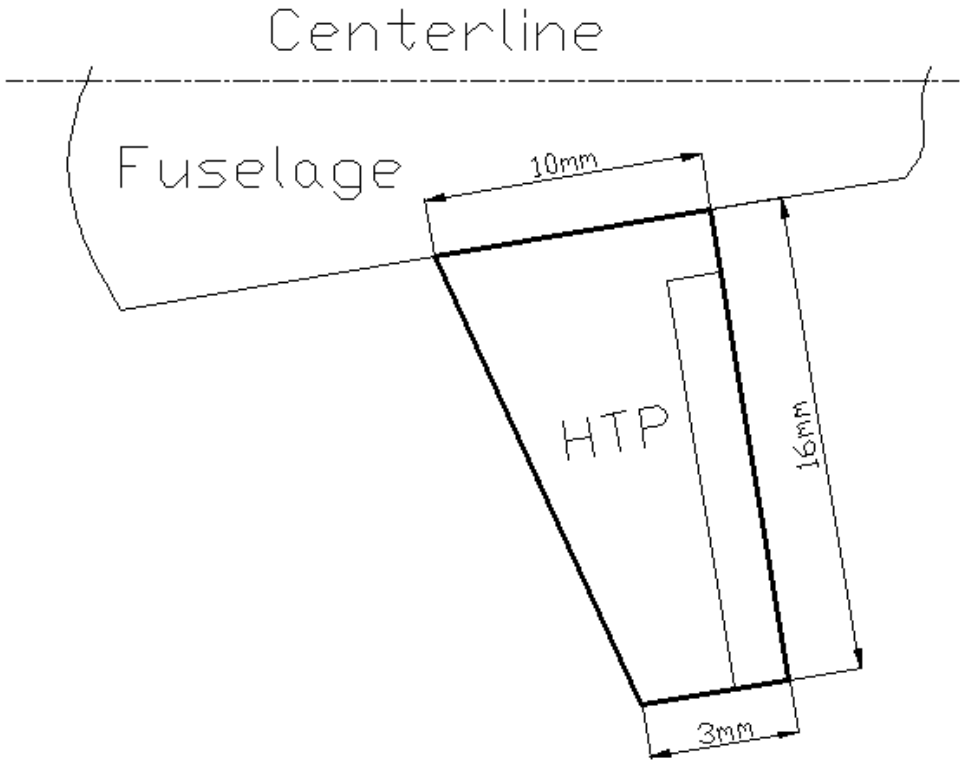

Figure 3-5 HTP measurements

Because the average thickness/chord ratio of HTP $(t/c)_{ave,HTP} = 8\%$, therefore, the total wetted area of HTP can be calculated as follows,

$$\begin{aligned} S_{wet,HTP} &= [S_{act,HTP} \times (1.977 + 0.52 \cdot (t/c)_{ave,HTP})] \times 2 \\ &= [12.8 \times (1.977 + 0.52 \times 8\%)] \times 2 \\ &= 51.7\ (m^2) \end{aligned} \qquad [28]$$

And next, the skin friction coefficient of HTP will be determined. Before this, Mean Aerodynamic Chord (MAC) and Reynolds number of HTP have to be calculated first.

$$\begin{aligned} MAC_{HTP} &= C_{r,HTP} - \frac{2 \times (C_{r,HTP} - C_{t,HTP}) \times (0.5 \times C_{r,HTP} + C_{t,HTP})}{3 \times (C_r + C_t)} \\ &= 4.02 - \frac{2 \times (4.02 - 1.03) \times (0.5 \times 4.02 + 1.03)}{3 \times (4.02 + 1.03)} \\ &= 2.82\ (m) \end{aligned}$$

Reynolds number of HTP $R_{e,HTP} = \frac{V_\infty \cdot MAC_{HTP}}{\upsilon_\infty} = \frac{230 \times 2.82}{3.9 \times 10^{-5}} = 1.66 \times 10^7$

Skin friction coefficient of HPT,

$$C_{f,HTP} = \frac{0.455}{(\log_{10} R_{e,HTP})^{2.58} \times (1 + 0.144 \cdot M_{\infty}^{2})^{0.65}} = \frac{0.455}{(\log_{10} 1.66 \times 10^{7})^{2.58} \times (1 + 0.144 \times 0.78^{2})^{0.65}} = 2.63 \times 10^{-3} \quad [23]$$

Factor $F_{HTP}^{*} = 1 + 3.52 \cdot (t/c)_{HTP} = 1 + 3.52 \times 8\% = 1.28$ [23], and by measurement, the sweepback angle at 50% chord of HTP $\Lambda_{0.5C,HTP} = 23.5^{\circ}$, so the form factor of HTP can be calculated as follows,

$$F_{HTP} = (F_{HTP}^{*} - 1) \cdot \cos^{2} \Lambda_{0.5C,HTP} + 1 = (1.28 - 1) \times \cos^{2} 23.5^{\circ} + 1 = 1.24 \quad [23]$$

Take interference factor $Q_{HTP} = 1.2$. [23]

Based on Reference [25], take the value of planform area of HTP, namely, $S_{planform,HTP} = 31.5\,(m^{2})$. And use this area as the reference area to calculate the profile (parasite) drag coefficient of HTP,

$$C_{DP,HTP} = \frac{(C_{f,HTP} \cdot F_{HTP} \cdot Q_{HTP}) \cdot S_{wet,HTP}}{S_{planform,HTP}} = \frac{2.63 \times 10^{-3} \times 1.24 \times 1.2 \times 51.7}{31.5} = 6.42 \times 10^{-3} \quad (3\text{-}5)$$

6) Drag of secondary items

As mentioned in the reference [23], the drag of secondary items may be as high as 10% of the profile drag. Therefore, the extra drag resulted from excrescence, surface imperfections and system installations is also taken into account in this research in order to provide as better a modelling accuracy as possible through the following calculations.

Updated wing profile drag coefficient,

$$C_{DP,w}^{'} = (1 + 6\%) \cdot C_{DP,w} = 1.06 \times 5.32 \times 10^{-3} = 5.64 \times 10^{-3} \quad (3\text{-}6)\ [23]$$

Updated fuselage profile drag coefficient,

$$C_{DP,f}^{'} = (1 + 7\% + 2.5\%) \cdot C_{DP,f} = (1 + 9.5\\%) \times 6.49 \times 10^{-3} = 7.11 \times 10^{-3} \quad (3\text{-}7)\ [23]$$

Updated nacelle profile drag coefficient,

$$C'_{DP,n} = (1+15\%)\cdot C_{DP,n} = 1.15\times 1.20\times 10^{-3} = 1.38\times 10^{-3} \qquad \text{(3-8) [23]}$$

The contribution to profile drag coefficient from system installation,

$$\begin{aligned} C_{DP,system} &= 3\% \times (C_{DP,f} + C_{DP,w} + C''_{DP,HTP} + C_{DP,VTP} + C_{DP,n}) \\ &= 3\% \times (6.49\times 10^{-3} + 5.32\times 10^{-3} + 1.64\times 10^{-3} + 1.24\times 10^{-3} + 1.20\times 10^{-3}) \\ &= 4.77\times 10^{-4} \end{aligned}$$

(3-9) [23]

Where, $C''_{DP,HTP}$ is calculated based on the main wing planform area $S_{planform,w}$ as follows:

$$C''_{DP,HTP} = \frac{(C_{f,HTP}\cdot F_{HTP}\cdot Q_{HTP})\cdot S_{wet,HTP}}{S_{planform,w}} = \frac{2.63\times 10^{-3}\times 1.24\times 1.2\times 51.7}{123.2} = 1.64\times 10^{-3}$$

[23]

The contribution from trim drag consideration,

$$C_{DP,trim}\times 31.50 = C''_{DP,trim}\times 123.20 = 5\times 10^{-4}\times 123.20 \quad \text{[23]}$$

Hence, $C_{DP,trim} = \frac{5\times 10^{-4}\times 123.20}{31.50} = 1.96\times 10^{-3}$ (3-10)

Where, the calculation of $C_{DP,trim}$ is based on the HTP planform area.

7) Wave drag

Because the maximum cruise Mach number of CUTFDAC can reach 0.82, therefore the additional wave drag due to compressibility was also taken into account in this research. According to the reference [23], the values of this additional drag coefficient "lie between 5 and 20 drag counts" (1 count = 1×10^{-4}). In this study, the value was assumed to be 14 counts, i.e.,

$C_{D,wave}=14\times 10^{-4}=1.4\times 10^{-3}$ (3-11)

In addition, from the reference [23], aircraft drag coefficient consists of three items, that is, profile drag coefficient C_{DP}, lift induced drag coefficient C_{Di} and wave drag $C_{D,wave}$. Since $C_{D,wave}$ is of relatively small magnitude and keeps as a constant, therefore in this research it was merged into the item of profile drag coefficient as shown in the

following formula (3-12), for the purpose of convenience.

Finally, according to the above estimation results, the profile drag coefficients for both major construction (including fuselage, main wing, VTP and nacelle) and HTP respectively can, therefore, be summarised as follows:

$$\begin{aligned} C_{DP,mc} &= \sum C_{DP,component} \qquad \text{(except HTP)} \\ &= (C'_{DP,f} + C'_{DP,w} + C_{DP,VTP} + C'_{DP,n} + C_{DP,system} + C_{D,wave}) \\ &= 7.11\times10^{-3} + 5.64\times10^{-3} + 1.24\times10^{-3} + 1.38\times10^{-3} + 4.77\times10^{-4} + 1.4\times10^{-3} \\ &= 1.72\times10^{-2} \end{aligned} \tag{3-12}$$

$$C_{DP,HTP} = 6.42\times10^{-3} + 1.96\times10^{-3} = 8.38\times10^{-3} \quad \text{(Based on HTP planform area)} \tag{3-13}$$

b) Determination of lift coefficient at zero angle of attack $C_{L,\alpha=0}$

In light of the estimation method provided in the reference [29], under the condition of cruise M=0.78 (the geometric properties of main wing required including aspect ratio AR and sweepback angle at 50% chord can be obtained from the previous section), the value of $C_{L,\alpha=0}$ can be calculated as follows:

1) Determine the lift slope $a_{wing}$with the considerations of actual 3-D flow over main wing due to the finite wing span and compressibility correction resulted from high subsonic flight.

$$a_{wing} = \frac{a_0 \cdot \cos \Lambda_{0.5C}}{\sqrt{1 - M_\infty^2 \cdot \cos^2 \Lambda_{0.5C} + \left[\frac{2\pi \cdot \cos \Lambda_{0.5C}}{\pi \cdot AR}\right]^2} + \frac{2\pi \cdot \cos \Lambda_{0.5C}}{\pi \cdot AR}} \quad [29]$$

$$a_{wing} = \frac{2\pi \times \cos 20.5^\circ}{\sqrt{1 - 0.78^2 \times \cos^2 20.5^\circ + \left[\frac{2\pi \times \cos 20.5^\circ}{\pi \times 9.39}\right]^2} + \frac{2\pi \times \cos 20.5^\circ}{\pi \times 9.39}}$$

Hence, $a_{wing} = 6.4613\ \text{rad}^{-1} \cong 6.46\text{rad}^{-1}$

2) Determine the zero-lift angle of attack $\alpha_{L=0}$

According to the reference [29], there is no difference between airfoil and actual finite wing in terms of the zero-lift angle of attack $\alpha_{L=0}$ (see Figure 3-6). Therefore, the $\alpha_{L=0}$

of the main wing can be found from its airfoil data. Unfortunately, it is also not easy to get the information about airfoil which was used by aircraft manufacturers. Reference [29] points out that the values of the zero-lift angle of attack $\alpha_{L=0}$ for airfoils with positive camber are "usually on the order of -2 or -3°". Based on this, -2° is assumed for the zero-lift angle of attack of the main wing of CUTFDAC in this research work, i.e.

$$\alpha_{L=0} = -2^{\circ}$$

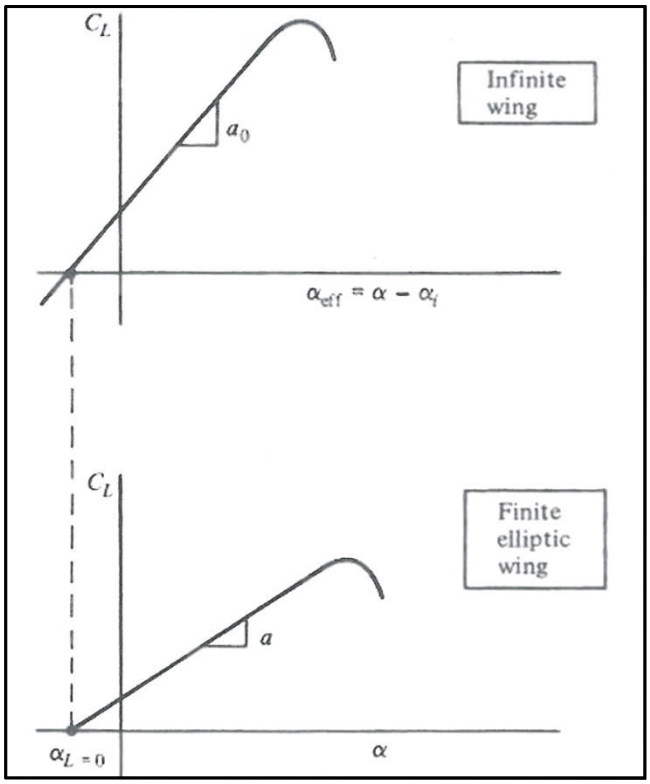

Figure 3-6 Zero-lift angle of attack for 2D airfoil and 3D wing [29]

3) Determine the variation of lift coefficient C_L with angle of attack α

$$C_L = C_L(\alpha) = \alpha_{wing} \cdot (\alpha - \alpha_{L=0}) = 6.46 \times (\alpha - (-2 \times \frac{\pi}{180}))$$ [29]

$$C_L = 6.46 \cdot \alpha + 0.225 \qquad (3\text{-}14)$$

The lift characteristics of CUTFDAC with the 'Cruise' configuration which is expressed in the above formula (3-14) can also be illustrated in the following Figure 3-

7.

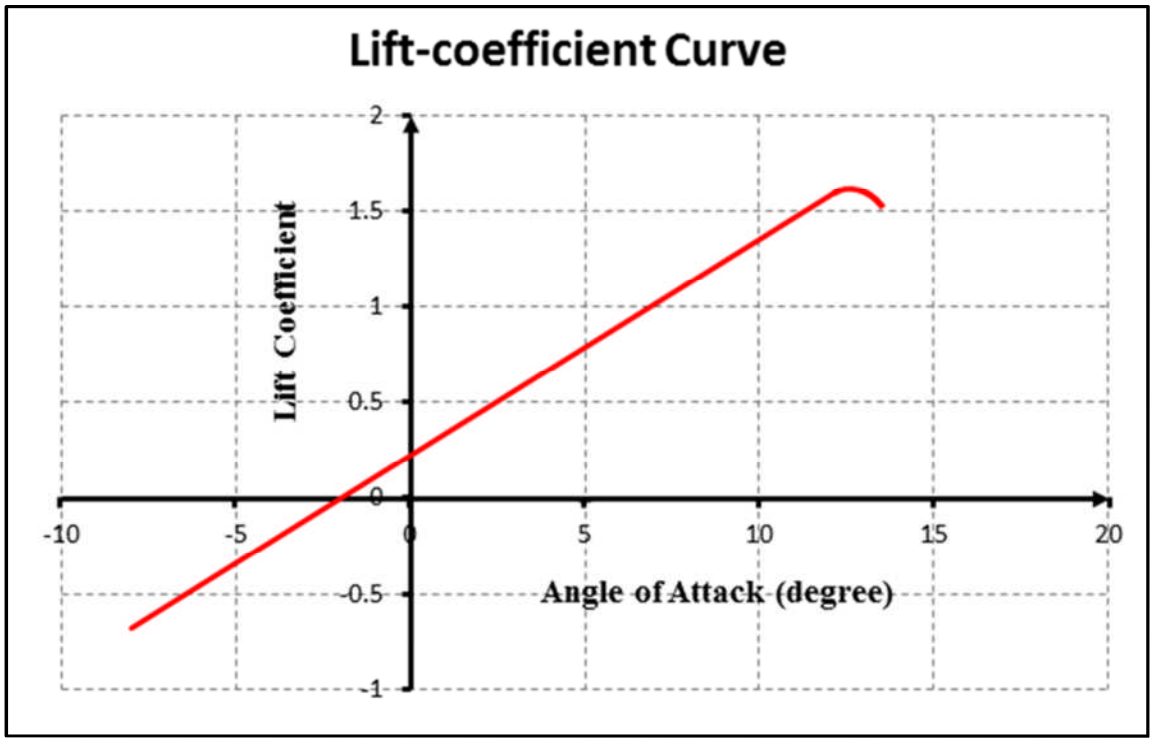

Figure 3-7 Lift characteristics of CUTFDAC

4) Determine the lift coefficient at zero angle of attack $C_{L,\alpha=0}$

From the above equation (3-14), it can be found that when the angle of attack equals zero, i.e., $\alpha = 0$, the value of lift coefficient, namely,

$$C_{L,\alpha=0} = 0.225$$

c) Determine the lift coefficient at the minimum drag coefficient $C_{L,minD}$

From the reference [30], it has been known that for the cambered airfoil the minimum drag coefficient C_{dmin} occurs at non-zero lift coefficient. Therefore, in order to determine the drag characteristics, called drag polar, of the whole aircraft except HTP in this case, the lift coefficient value at the minimum drag coefficient $C_{L,minD}$ is needed to be determined first. At present, a treatment to this issue is to assume that $C_{L,minD}$ equals $C_{L,\alpha=0}$ (i.e., zero-AOA lift coefficient). However, the reference [30] points out that "the value of $C_{L,minD}$ is determined by plotting the drag polar for the wing using actual airfoil data. If actual airfoil data is not available, as a crude approximation, assume that the airfoil generates minimum drag when it is at zero angle of attack, and

that the effect of induced drag is to move $C_{L,minD}$ to a value halfway between zero and the value of C_L when $\alpha = 0$." Further, the reference [30] also points out that "this value of $C_{L,minD}$ is then used for the entire aircraft. This is done because it is assumed that the aircraft designer will design the fuselage, strakes, etc., so that they also have their minimum drag at the angle of attack that puts the wing at its $C_{L,minD}$."

Therefore, according to the above statement, for the 2D airfoil, it can be assumed that $C_{l,mind} = C_{l,\alpha=0}$, but for the actual 3D finite wing, it will be preferred to assume $C_{L,minD} = \frac{C_{L,\alpha=0}}{2}$, and this assumption can be applied to the entire aircraft.

So, for this case,

$$C_{L,minD} = \frac{C_{L,\alpha=0}}{2} = \frac{0.225}{2} \cong 0.11 \qquad (3\text{-}15)$$

And correspondingly, the angle of attack for this $C_{L,minD}$ can be determined from the equation (3-14) as follows:

$$0.11 = 6.46 \times \alpha' + 0.225$$

So, $\alpha' = \frac{0.11-0.225}{6.46} = -0.018\ (\text{rad}) = -0.018 \times \frac{180^\circ}{\pi} = -1.03^\circ$.

d) Determine Oswald's efficiency factors for main wing and HTP

By measurement, the sweepback angle at wing leading edge $\Lambda_{LE,w} \cong 28^\circ$,

So, Oswald's efficiency factor of wing $e_{0,w}$can be calculated as follows:

$$\begin{aligned} e_{0,w} &= 1.78 \times (1 - 0.045 \times AR_w^{0.68}) - 0.64 \\ &= 1.78 \times (1 - 0.045 \times 9.39^{0.68}) - 0.64 \\ &= 0.773 \end{aligned} \qquad (3\text{-}16)\ [30]$$

As for the HTP, by measurement, the sweepback angle at HTP leading edge $\Lambda_{LE,HTP} \cong 32^\circ$, so, Oswald's efficiency factor of HTP $e_{0,HTP}$ can be obtained as follows:

$$\begin{aligned} e_{0,HTP} &= 4.61 \times (1 - 0.045 \times AR_{HTP}^{0.68}) \times (\cos \Lambda_{LE,HTP})^{0.15} - 3.1 \\ &= 4.61 \times (1 - 0.045 \times 5.0^{0.68}) \times (\cos 32^\circ)^{0.15} - 3.1 \\ &= 0.793 \end{aligned} \qquad (3\text{-}17)\ [30]$$

e) Drag characteristics (drag polar) of aircraft (except Horizontal Tailplane (HTP))

Now, based on the above calculations about $C_{D,min}$ and $C_{L,minD}$ as well as the drag polar expression for the aircraft with cambered wing, the following equation of drag polar of the aircraft in this case study can be written as follows:

$$C_D = C_{D,parasite} + C_{D,i}$$

$$= C_{D,min} + K \cdot \left(C_L - C_{L,minD}\right)^2 = C_{D,min} + \frac{1}{\pi \cdot AR_w \cdot e_{0,w}} \cdot \left(C_L - C_{L,minD}\right)^2$$

$$= 0.0172 + \frac{1}{\pi \times 9.39 \times 0.773} \times (C_L - 0.11)^2$$

$$= 0.0172 + 0.0439 \times (C_L - 0.11)^2 \qquad (3\text{-}18)$$

The drag characteristics described by the above formula (3-18) can be also illustrated in the following Figure 3-8.

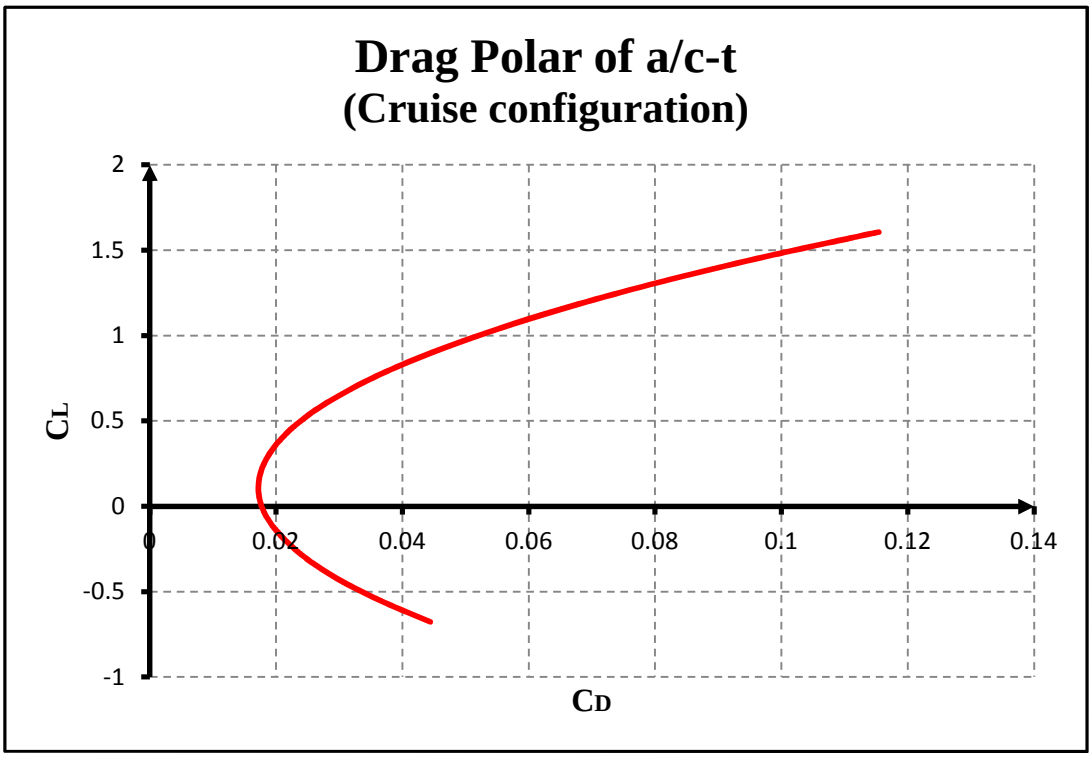

Figure 3-8 Drag polar of CUTFDAC (a/c-t) - 'Cruise' configuration

f) Drag characteristics (drag polar) of aircraft HTP (Horizontal Tailplane)

$$C_{D,HTP} = C_{D0,HTP} + C_{Di,HTP} = C_{D0,HTP} + \frac{1}{\pi \cdot AR_{HTP} \cdot e_{HTP}} \cdot C_L^2$$

$$= 0.00838 + \frac{1}{\pi \times \frac{12.46^2}{31.50} \times 0.793} \times C_L^2 = 0.00838 + 0.0814 \times C_L^2 \quad (3\text{-}19)$$

Figure 3-9 shows the drag polar of HTP expressed by the formula (3-19).

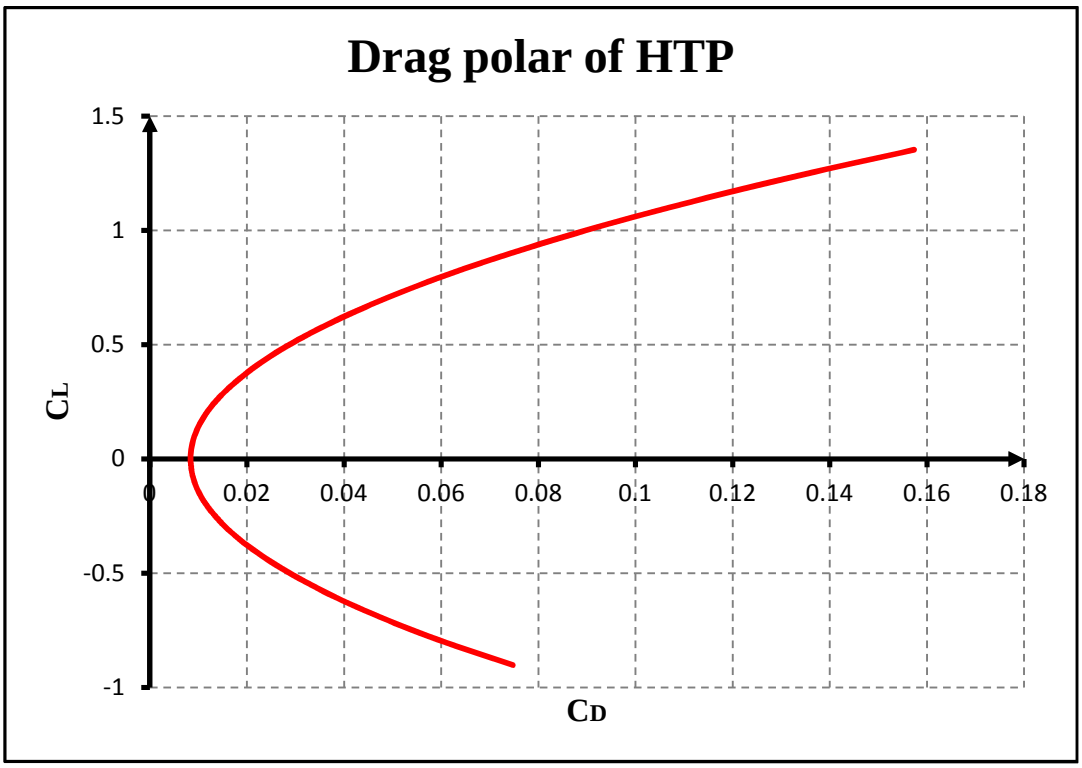

Figure 3-9 Drag polar of CUTFDAC (HTP)

Based on the above measurements, calculations and analysis, the performance model of CUTFDAC with the 'Cruise' configuration can be summarised in the following Table 3-1.

Table 3-1 CUTFDAC aircraft model (‘Cruise’ configuration)

Parameters	Units	Values
Engine section		
X-position	m	4.14
Z-position	m	1.43
Tilt	rad	0.0314
Number of engines	–	2
Horizontal Tailplane		
Span	m	12.46
Wing area	m^2	31.50
Oswald coefficient	–	0.793
Min. drag coefficient	–	0.00838
X-position	m	-16.96
Z-position	m	-1.40
Aircraft section (excluding HTP)		
Span	m	34.0
Mean aerodynamic chord	m	4.29
Wing area	m^2	123.2
Oswald coefficient	–	0.773
Min. drag coefficient	–	0.0172
Min.-drag lift coefficient	–	0.11
X-position	m	-0.43
Z-position	m	0.17
Wing sweep angle (0.5chord)	rad	0.3578
Wing setting angle	rad	0.045

Preliminary evaluation of CUTFDAC aircraft model (‘Cruise’ configuration).

Profile drag coefficient (or zero-lift drag coefficient) of the entire aircraft under ‘Cruise’ configuration:

By the above calculations,

$$C_{DP,HTP} = \frac{(C_{f,eq} \times S_w)_{HTP}}{S_{p,HTP}},$$

That is, 'drag area',

$$(C_{f,eq} \times S_w)_{HTP} = C_{DP,HTP} \times S_{p,HTP} = 0.00838 \times 31.50 = 0.264$$

So the 'equivalent' profile drag coefficient of HTP based on the planform area of main wing instead of HTP itself is:

$$C'_{DP,HTP} = \frac{(C_{f,eq} \times S_w)_{HTP}}{S_{p,wing}} = \frac{0.264}{123.2} = 0.0021$$

So, the profile drag coefficient of the entire aircraft based on the planform area of main wing with 'Cruise' configuration is:

$$C_{DP,a/c} = C_{DP,a/c-t} + C'_{DP,HTP} = 0.0172 + 0.0021 = 0.0193$$

Compared with the following Table 3-2 (for high-subsonic jet aircraft, the profile drag coefficient varies from 0.014 to 0.020), the value of $C_{DP,a/c}$ falls into this range.

Table 3-2 Typical drag values for various aircraft types [31]

		C_{D0}	e
High-subsonic jet aircraft		.014 - .020	.75 - .85
Large turbo-propeller aircraft		.018-.024	.80 -.85
Twin-engine piston aircraft		.022 - .028	.75 - .80
Small single-engine aircraft	Retractable gear	.020 - .030	.75 - .80
	Fixed gear	.025 - .040	.65 - .75
Agricultural aircraft	Spray system removed	.060	.65 - .75
	Spray system installed	.070 - .080	.65 - .75

The following Table 3-3 shows the calculation results of CUTFDAC with the above aircraft model at a typical cruise condition (flight altitude: 10668 m, flight Mach number: 0.78, ISA, initial aircraft mass: 75000 kg, 'Cruise' configuration):

Table 3-3 Cruise performance of CUTFDAC

AIRCRAFT STATES		Initial	Average	Final
Position (X) (m)	:	228612.000000	250294.000000	271976.000000
Position (Y) (m)	:	0.000000	0.000000	0.000000
Altitude (-Z) (m)	:	10668.000000	10668.000000	10668.000000
True airspeed (m/s)	:	231.439791	231.439794	231.439797
Equivalent airspeed (m/s)	:	129.171506	129.171508	129.171509
Calibrated airspeed (m/s)	:	126.951484	126.951486	126.951488
Mach no. (m/s)	:	0.780000	0.780000	0.780000
Ground speed (m/s)	:	231.439791	231.439794	231.439797
Lateral speed (m/s)	:	0.000000	0.000000	0.000000
Vertical speed (descent) (m/s)	:	0.000000	0.000000	0.000000
Flight path angle (rad)	:	0.000000	0.000000	0.000000
Heading angle (rad)	:	0.000000	0.000000	0.000000

SEGMENT			
Time interval	:	187.798939	(s)
Pitch angle	:	0.030421	(rad)
Bank angle	:	0.000000	(rad)

FORCES			
Thrust	:	37536.106693	(N)
Thrust per Engine	:	18768.053347	(N)
Weight	:	735750.000000	(N)

00 seconds 484 milliseconds

From the above calculation results, the aircraft lift to drag ratio at this typical cruise condition is:

$$\frac{L}{D} = \frac{W}{T} = \frac{735750}{37536.1} = 19.60$$

According to the reference [23], “Modern airliners using super-critical wing technology have values around 18 to 22” in terms of the lift to drag ratio (L/D) in the cruise phase.

Therefore, no matter whether from the point of view of aircraft profile drag coefficient or from the cruise lift to drag ratio, the aircraft model built for CUTFDAC with ‘Cruise’ configuration is satisfactory and reasonable.

Aircraft model of CUTFDAC with 'Initial Climb' configuration

Due to the complexity of high-lift device, this research modelled aircraft under high-lift device deployment by adopting BADA data properly.

For the 'Initial Climb' configuration of A320-200, the estimated value of the profile drag coefficient (or zero-lift drag coefficient) of the entire aircraft given by BADA dataset is 0.023, that is, $C_{DP,a/c} = 0.023$ [32].

Due to the difference of the BADA database from this project research in terms of the aircraft modelling method, the above value cannot be used directly but is helpful to determine the needed value of $C_{Dmin,a/c-t}$ as follows:

According to the definition of aircraft profile drag coefficient,

$$C_{DP,a/c} = \frac{\sum_{i=1}^{n}(C_{fc,eq}\cdot S_w)_i}{S_{P,w}} = \frac{\sum_{i=1}^{n-1}(C_{fc,eq}\cdot S_w)_i + (C_{fc,eq}\cdot S_w)_{tail}}{S_{P,w}} = C_{Dmin,a/c-t} + \frac{(C_{fc,eq}\cdot S_w)_{tail}}{S_{P,w}}$$

On the other hand,

$C_{DP,HTP} = \frac{(C_{fc,eq}\cdot S_w)_{tail}}{S_{P,t}}$, and so, $(C_{fc,eq} \cdot S_w)_{tail} = C_{DP,HTP} \cdot S_{P,t}$

So, combined with the above two equations,

$$C_{Dmin,a/c-t} = C_{DP,a/c} - \frac{(C_{fc,eq} \times S_w)_{tail}}{S_{P,w}} = C_{DP,a/c} - \frac{C_{DP,HTP} \times S_{P,t}}{S_{P,w}}$$
$$= 0.023 - \frac{0.00838 \times 31.50}{123.2} = 0.0209 \qquad (3-20)$$

So, with this configuration, the drag polar of aircraft (excluding HTP) can be expressed as the following formula (3-21) and Figure 3-10.

$$C_{D,a/c-t} = 0.0209 + 0.0439 \times (C_L - 0.11)^2 \qquad (3\text{-}21)$$

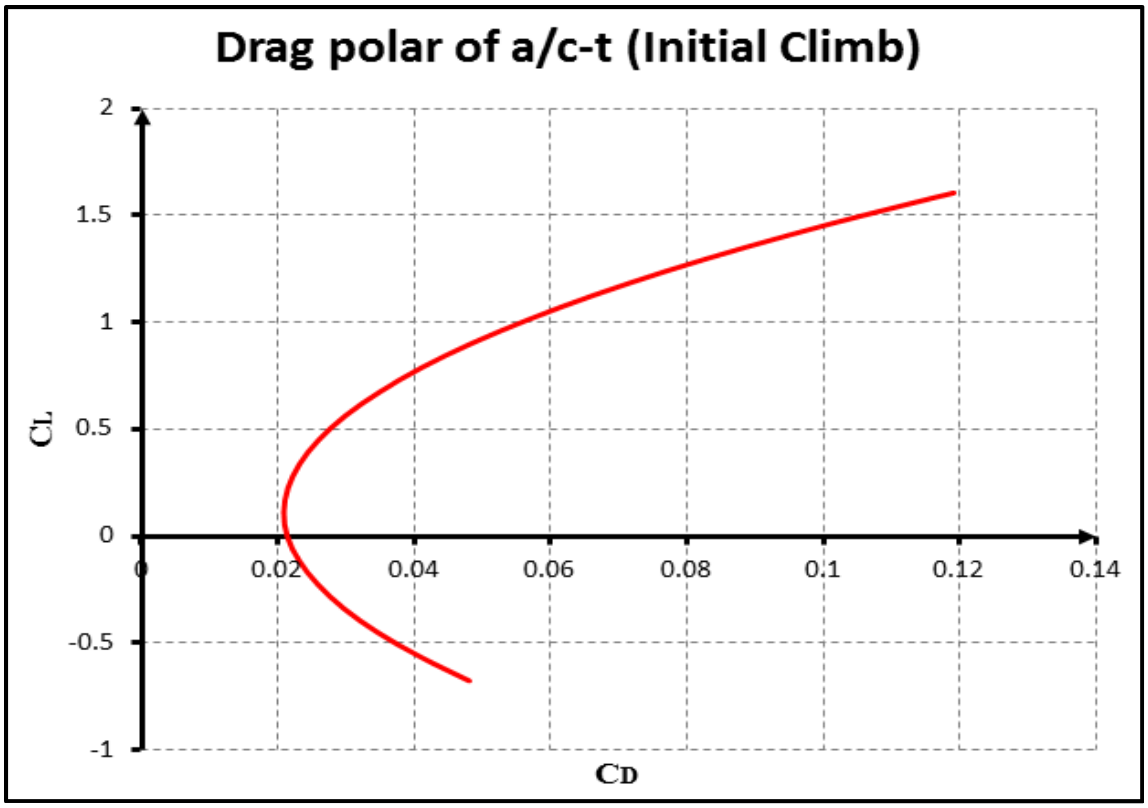

Figure 3-10 Drag polar of CUTFDAC (a/c-HTP) - 'Initial Climb' configuration

Further, the aircraft model of CUTFDAC under the 'Initial Climb' configuration can be expressed as the following Table 3-4.

Table 3-4 CUTFDAC aircraft model ('Initial Climb' configuration)

Parameters	Units	Values
Engine section		
X-position	m	4.14
Z-position	m	1.43
Tilt	rad	0.0314
Number of engines	–	2
Horizontal Tailplane		
Span	m	12.46
Wing area	m^2	31.50
Oswald coefficient	–	0.793
Min. drag coefficient	–	0.00838
X-position	m	-16.96
Z-position	m	-1.40
Aircraft section (excluding HTP)		
Span	m	34.0
Mean aerodynamic chord	m	4.29
Wing area	m^2	123.2
Oswald coefficient	–	0.773
Min. drag coefficient	–	0.0209
Min.-drag lift coefficient	–	0.11
X-position	m	-0.43
Z-position	m	0.17
Wing sweep angle (0.5chord)	rad	0.3578
Wing setting angle	rad	0.045

High-lift devices							
Parameters	Unit	Stage 0	1	2	3	4	5
dC_L	–	00.0000	0.1500	00.300	00.4500	00.6000	00.7500
C_{Lmax}	–	01.6060	1.7560	01.906	02.0560	02.2000	02.3500

(Note: the information of high-lift devices in Table 3-4 above is from the reference [33].)

Aircraft model of CUTFDAC with ‘Approach’ configuration

Similar to the ‘Initial Climb’ case, the aircraft modelling of CUTFDAC under the ‘Approach’ configuration was also achieved based on the model under the ‘Cruise’ configuration as a baseline and modified by means of the BADA dataset, as follows:

According to the BADA dataset, the profile drag coefficient (or zero-lift drag coefficient) of the entire aircraft A320-200 under the ‘Approach’ configuration equals to 0.038, that is, $C_{DP,a/c} = 0.038$ [32].

So, $C_{Dmin,a/c-t} = C_{DP,a/c} - \frac{C_{DP,HTP} \times S_{P,t}}{S_{P,w}} = 0.038 - \frac{0.00838 \times 31.50}{123.2} = 0.0359$ (3-22)

So, with this configuration, the drag polar of aircraft (excluding HTP) can be expressed as the following formula (3-23) and Figure 3-11.

$$C_{D,a/c-t} = 0.0359 + 0.0439 \times (C_L - 0.11)^2 \quad (3\text{-}23)$$

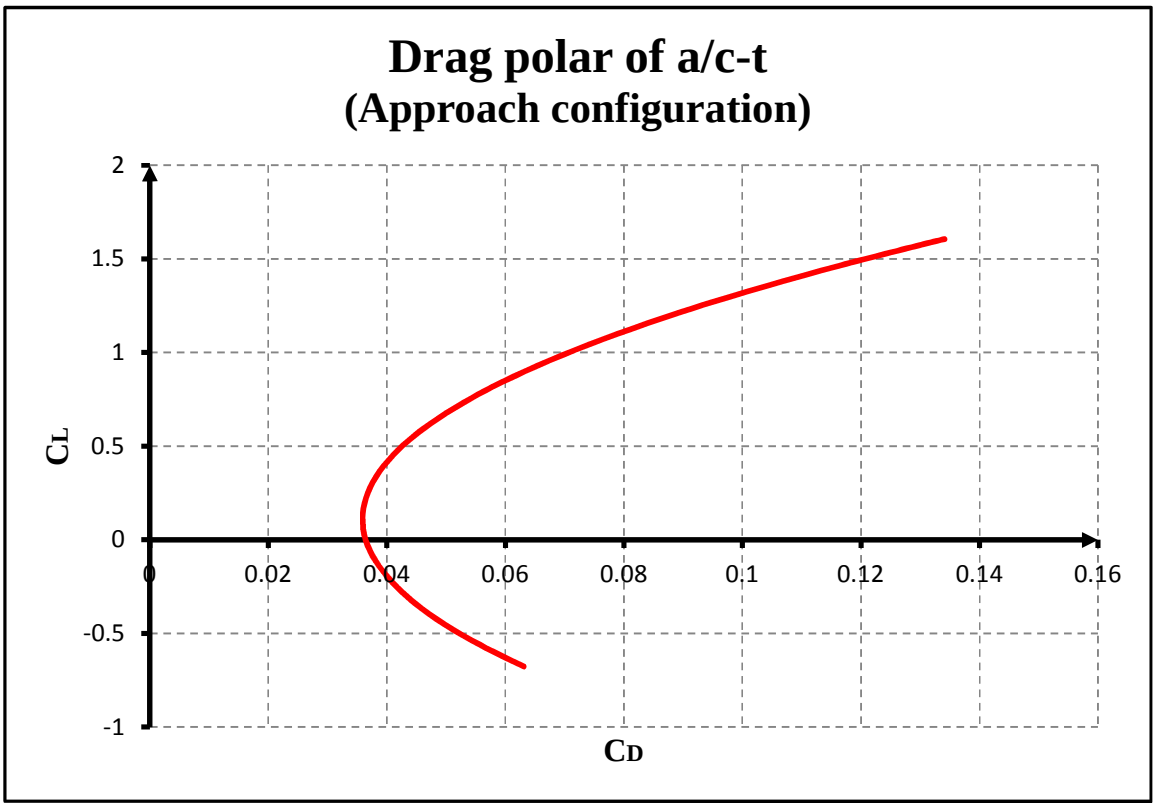

Figure 3-11 Drag polar of CUTFDAC (a/c-HTP) - ‘Approach’ configuration

Further, the aircraft model of CUTFDAC under the ‘Approach’ configuration can be expressed as the following Table 3-5.

Table 3-5 Aircraft model of CUTFDAC (Approach configuration)

Parameters	Units	Values
Engine section		
X-position	m	4.14
Z-position	m	1.43
Tilt	rad	0.0314
Number of engines	–	2
Horizontal Tailplane		
Span	m	12.46
Wing area	m^2	31.50
Oswald coefficient	–	0.793
Min. drag coefficient	–	0.00838
X-position	m	-16.96
Z-position	m	-1.40
Aircraft section (excluding HTP)		
Span	m	34.0
Mean aerodynamic chord	m	4.29
Wing area	m^2	123.2
Oswald coefficient	–	0.773
Min. drag coefficient	–	0.0359
Min.-drag lift coefficient	–	0.11
X-position	m	-0.43
Z-position	m	0.17
Wing sweep angle (0.5chord)	rad	0.3578
Wing setting angle	rad	0.045

High-lift devices							
Parameters	Unit	Stage 0	1	2	3	4	5
dC_L	–	00.0000	0.1500	00.300	00.4500	00.6000	00.7500
C_{Lmax}	–	01.6060	1.7560	01.906	02.0560	02.2000	02.3500

(Note: the information of high-lift devices in Table 3-5 above is from the reference [33].)

3.1.2 CUPFDAC (Cranfield University PropFan-Driven AirCraft)

CUPFDAC (Cranfield University PropFan-Driven AirCraft) used in this research project is a hypothetical twin-engine, short- to medium-range, single-aisle commercial jet aircraft. Its typical seating ranges from 153 to 172 passengers and the corresponding flight range is nearly 4000 km. This aircraft was built based on the McDonnell Douglas MD90-30 [24-25] but powered by two new-generation propfan (open rotor) engines instead of the original turbofan engines. Figure 3-12 illustrates the schematic drawing of CUPFDAC and Figure 3-13 shows the geometric measurements of MD90-30 which constitute the foundation for CUPFDAC performance modelling.

Figure 3-12 CUPFDAC (Cranfield University Propfan-Driven AirCraft)

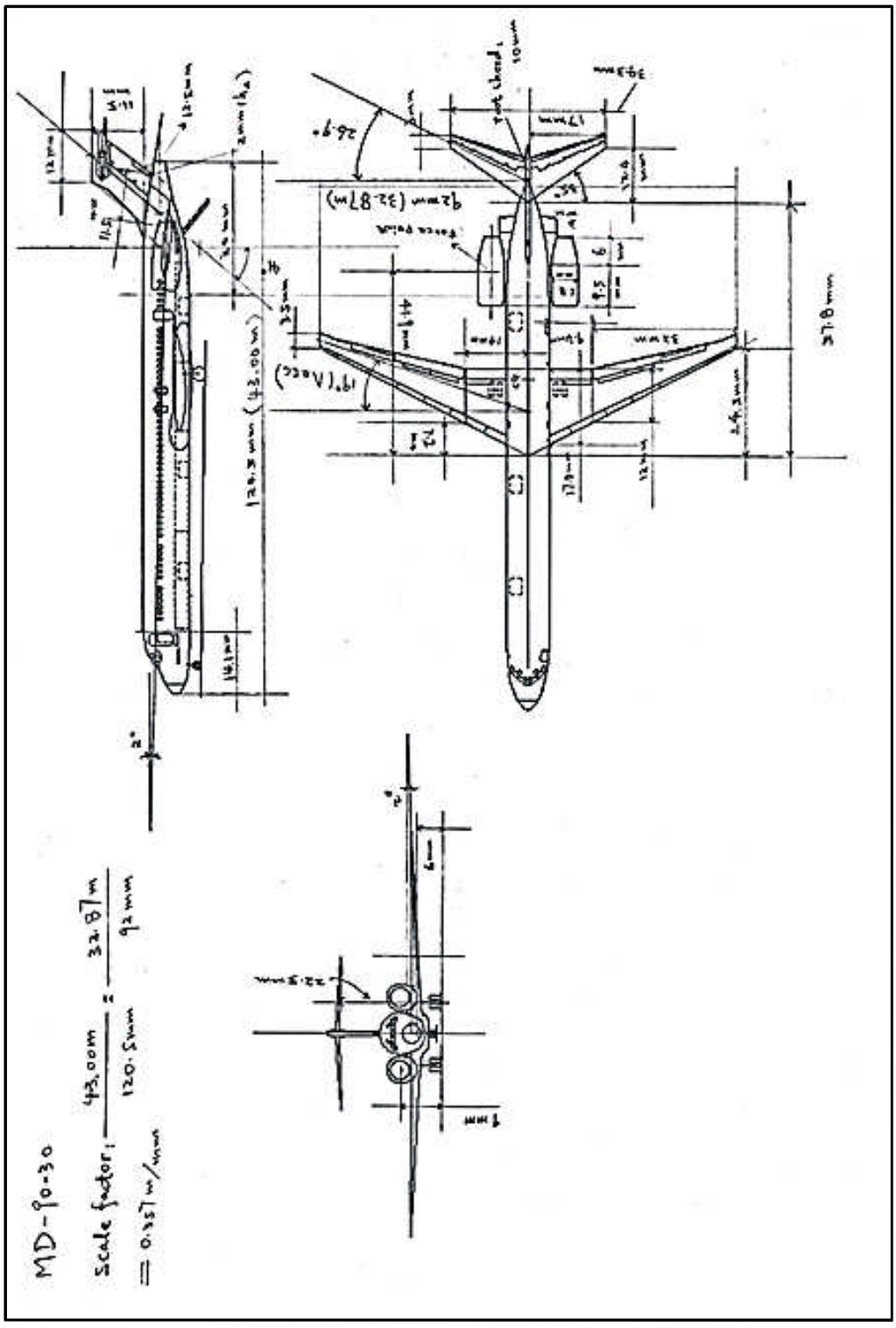

Figure 3-13 Measurements of MD90-30

Lift characteristics of CUPFDAC

The lift slope for CUPFDAC with swept wing in a compressible flow with the subsonic cruise Mach number is:

$$a_{comp} = \frac{2\pi\times\cos 19^{\circ}}{\sqrt{1-0.76^2\times\cos^2 19^{\circ}+\left[(2\pi\times\cos 19^{\circ})/(\pi\times 32.87^2/112.30)\right]^2}+(2\pi\times\cos 19^{\circ})/\left(\pi\frac{32.87^2}{112.30}\right)} = 6.46\ \text{rad}^{-1} \quad [29]$$

Similar to CUTFDAC, select $\alpha_{L=0} = -2^{\circ}$, so the lift curve of CTPFDAC is:

$$C_L = 6.46\ \text{rad}^{-1} \times \left(\alpha - (-2^{\circ}) \times \frac{\pi}{180^{\circ}}\right) = 6.46\alpha + 0.225 \qquad (3\text{-}24) \quad [29]$$

So, $C_{L,\alpha=0} = 0.225$

The lift curve of CUPFDAC expressed in the equation (3-24) is shown in the following Figure 3-14.

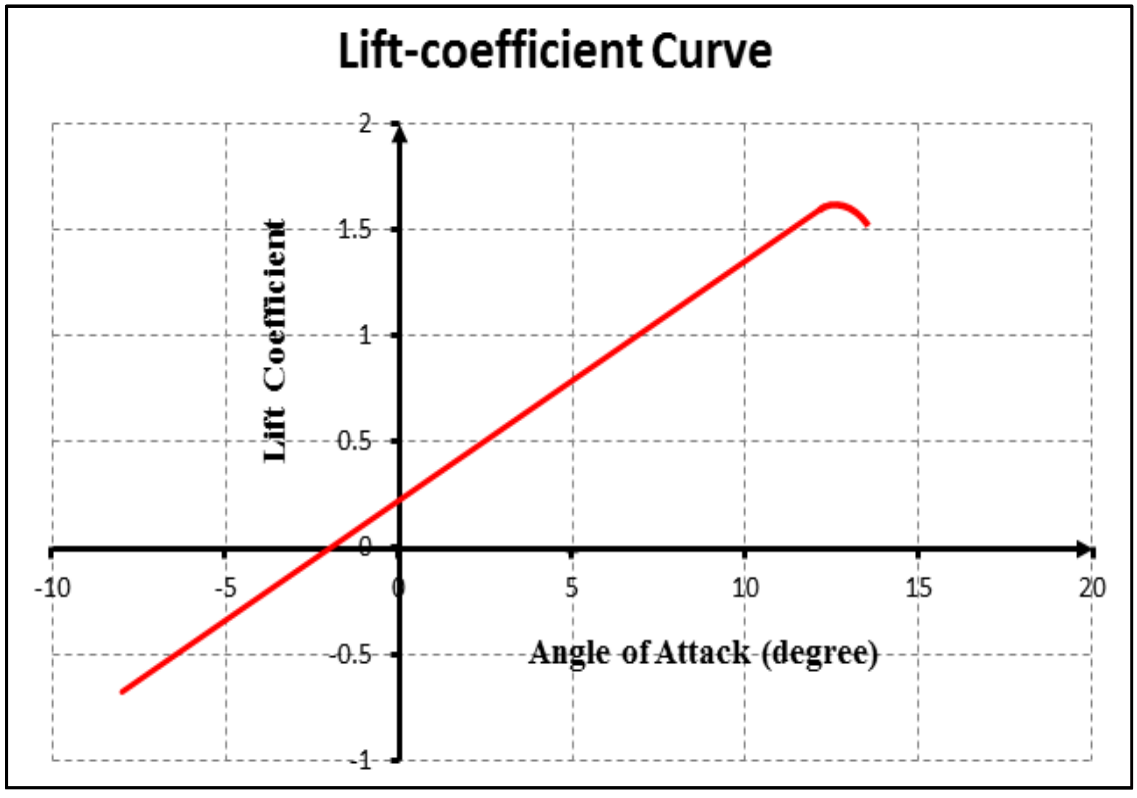

Figure 3-14 The lift characteristics of CUPFDAC

Drag characteristics of CUPFDAC

1) Profile-drag coefficient estimation of CUPFDAC

Table 3-6 Reference flight condition of profile drag coefficient estimation

Flight altitude	1.08×10^{4} m
Flight Mach number	0.76
Atmosphere condition	ISA
Air density	0.374 kg/m^3
Dynamic viscosity	1.42×10^{-5} N·s/m^2
Aircraft configuration	Clean (cruise)

Table 3-7 Main dimensions of CUPFDAC

Fuselage overall length	43.0 m
Diameter of fuselage	3.61 m
Length of nose section of fuselage	5.03 m
Length of tail section of fuselage	10.7 m
MAC of main wing	4.08 m
Average t/c of main wing	11%
$\Lambda_{0.5C}$of main wing	19°
Span of main wing	32.87 m
Area of main wing	112.30 m^2
Taper ratio of VTP	0.770
Tip chord of VTP	4.28 m
$\Lambda_{0.5C}$of VTP	41°
Tip chord of HTP	1.07 m
Root chord of HTP	3.57 m
$\Lambda_{0.5C}$of HTP	26.9°
Area of HTP	28.4 m^2
Nacelle overall length	5.75 m

Table 3-8 Main calculation equations [23]

<table>
<tr><td colspan="3">Reynolds number: $R_e = \frac{\rho V L}{\mu}$, here, L- characteristic length of investigated component</td></tr>
<tr><td colspan="3">Prandtl-Schlichting formula: $C_f = \frac{0.455}{(\log_{10} R_e)^{2.58}(1+0.144M^2)^{0.65}}$</td></tr>
<tr><td rowspan="2">Form (shape) factor:</td><td>$F = 1 + \frac{2.2}{\lambda^{1.5}} - \frac{0.9}{\lambda^{3.0}}$, here λ- Finess ratio</td><td>(for fuselage)</td></tr>
<tr><td>$F = (F^* - 1)\cos^2\Lambda_{0.5C} + 1$, here, $F^* = 1 + 3.3\left(\frac{t}{c}\right) - 0.008\left(\frac{t}{c}\right)^2 + 27.0\left(\frac{t}{c}\right)^3$</td><td>(for main wing)</td></tr>
<tr><td colspan="3">Profile drag coefficient: $C_{DP} = \frac{C_f F Q S_{wet}}{S_{ref}}$</td></tr>
</table>

a) Fuselage

Taking the overall length of fuselage as the characteristic length, that is, L=43.0 meter.

$$R_e = \frac{0.374 \times 225 \times 43.0}{1.42 \times 10^{-5}} = 2.55 \times 10^8$$

$$C_f = \frac{0.455}{(\log_{10}(2.55 \times 10^8))^{2.58} \times (1 + 0.144 \times 0.76^2)^{0.65}} = 1.78 \times 10^{-3}$$

Form (shape) factor $F = 1 + \frac{2.2}{11.91^{1.5}} - \frac{0.9}{11.91^{3.0}} = 1.05$

Interference factor Q=1.0

Calculation of wetted area $S_{wet,fuselage}$:

$S_{w,nose} = 0.75 \times \pi \times 3.61 \times 5.03 = 42.8\ (m^2)$

$S_{w,tail} = 0.72 \times \pi \times 3.61 \times 10.7 = 87.4\ (m^2)$

As in Table 3-7, the length of constant diameter section of the fuselage is:

$L_{cds} = 43.0 - 5.03 - 10.7 = 27.3\ (m)$

(Note: here, cds – constant diameter section)

$S_{w,cds} = \pi \times 3.61 \times 27.3 = 310\ (m^2)$

Therefore, $S_{w,fuselage} = 42.8 + 310 + 87.4 = 440\ (m^2)$

Then, the contribution to aircraft profile drag coefficient from fuselage is:

$$C_{DP,f} = \frac{1.78\times10^{-3}\times1.05\times1.0\times440}{112.3} = 7.32\times10^{-3} \quad (3\text{-}25)$$

b) Main wing

Taking the Mean Aerodynamic Chord (MAC) of main wing as characteristic length, that is, L=4.08 m.

$$R_e = \frac{0.374\times225\times4.08}{1.42\times10^{-5}} = 2.42\times10^{7}$$

$$C_f = \frac{0.455}{(\log_{10}(2.42\times10^{7}))^{2.58}\times(1+0.144\times0.76^2)^{0.65}} = 2.48\times10^{-3}$$

Form (shape) factor:

$$F^* = 1 + 3.3\times0.11 - 0.008\times0.11^2 + 27.0\times0.11^3 = 1.40$$

$$F = (1.40-1)\times\cos^2 19^\circ + 1 = 1.36$$

Interference factor Q=1.0

Calculation of wetted area $S_{wet,\ wing}$:

$$S_{P,panel1} = \frac{(12\text{mm}+17\text{mm})\times\frac{0.357\text{m}}{\text{mm}}}{2}\times\left(9.4\text{mm}\times\frac{0.357\text{m}}{\text{mm}}\right) = 17.4\ \text{m}^2$$

Here, S_P–planform area; the figures with the unit of 'mm' were measured from the 3-view schematic of aircraft and '0.357m/mm' is the plotting scale.

$$S_{P,panel2} = \frac{(3.5\text{mm}+12\text{mm})\times0.357\text{m/mm}}{2}\times\left(32\text{mm}\times\frac{0.357\text{m}}{\text{mm}}\right) = 31.6\ \text{m}^2$$

$$S_{P,single\ wing} = 17.4 + 31.6 = 49\ (\text{m}^2)$$

$$S_{single\ wing} = \frac{49}{\cos 2^\circ} \cong 49\ (\text{m}^2)$$

$$S_{w,single\ wing} = 49\times(1.977 + 0.52\times0.11) = 99.7\ (\text{m}^2)$$

Therefore, the total wetted area of main wing is:

$$S_{w,main\ wing} = 99.7\times2 = 199\ (\text{m}^2)$$

Then, the contribution to aircraft profile drag coefficient from main wing is:

$$C_{DP,w} = \frac{2.48\times10^{-3}\times1.36\times1.0\times199}{112.30} = 5.98 \times 10^{-3} \quad (3\text{-}26)$$

c) Vertical Tailplane (VTP)

$$\text{Root chord} = \frac{4.28}{0.770} = 5.56\ \text{m}$$

Mean Aerodynamic Chord (MAC) is:

$$\text{MAC} = 5.56 - \frac{2 \times (5.56 - 4.28) \times (0.5 \times 5.56 + 4.28)}{3 \times (5.56 + 4.28)} = 4.95\ (\text{m})$$

Taking this MAC as the characteristic length, that is L=4.95m

$$R_e = \frac{0.374 \times 225 \times 4.95}{1.42 \times 10^{-5}} = 2.93 \times 10^7$$

$$C_f = \frac{0.455}{[\log_{10}(2.93 \times 10^7)]^{2.58} \times (1 + 0.144 \times 0.76^2)^{0.65}} = 2.41 \times 10^{-3}$$

Usually, (t/c) for aircraft tail ranges from 8% to 10%, so, assume the average $(t/c)_{VTP} = 9\%$.

$$F^* = 1 + 3.52 \times 0.09 = 1.32$$

$$F = (1.32 - 1) \times \cos^2 41^\circ + 1 = 1.18$$

Interference factor Q=1.2

Calculation of wetted area:

$$S_1 = \frac{(12\text{mm} + 12.5\text{mm}) \times 0.357\frac{\text{m}}{\text{mm}}}{2} \times \left(11.5\text{mm} \times 0.357\frac{\text{m}}{\text{mm}}\right) = 18\ (\text{m}^2)$$

$$S_2 = \frac{(12.5\text{mm} \times 0.357\frac{\text{m}}{\text{mm}}) \times (2\text{mm} \times 0.357\frac{\text{m}}{\text{mm}})}{2} = 1.59\ (\text{m}^2)$$

$$S = 18 + 1.59 = 19.59\ (\text{m}^2)$$

$$S_{w,VTP} = 19.59 \times (1.977 + 0.52 \times 0.09) = 39.6\ (\text{m}^2)$$

Therefore, the contribution to aircraft profile drag coefficient from VTP is:

$$C_{DP,VTP} = \frac{2.41\times10^{-3}\times1.18\times1.2\times39.6}{112.30} = 1.20 \times 10^{-3} \quad (3\text{-}27)$$

d) Horizontal Tailplane (HTP)

$$\text{Tip chord} = 3\text{mm} \times 0.357\frac{\text{m}}{\text{mm}} = 1.07\text{m}$$

$$\text{Root chord} = 3.57\text{m}$$

$$\text{Taper ratio} = \frac{1.07}{3.57} = 0.3$$

$$\text{MAC} = 3.57 \times \frac{2}{3} \times \frac{1 + 0.3 + 0.3^2}{1 + 0.3} = 2.54\ (\text{m})$$

$$R_e = \frac{0.374 \times 225 \times 2.54}{1.42 \times 10^{-5}} = 1.51 \times 10^7$$

$$C_f = \frac{0.455}{[\log_{10}(1.51 \times 10^7)]^{2.58} \times (1 + 0.144 \times 0.76^2)^{0.65}} = 2.67 \times 10^{-3}$$

Assume average (t/c) = 8%, then,

$$F^* = 1 + 3.52 \times 0.08 = 1.28$$

$$F = (1.28 - 1) \times \cos^2 26.9^\circ + 1 = 1.22$$

Take Interference Factor Q=1.2

Calculation of wetted area:

$$S_{\text{single tail}} = \frac{1.07 + 3.43}{2} \times \left(17.0\text{mm} \times 0.357\frac{\text{m}}{\text{mm}}\right) = 13.7\ (\text{m}^2)$$

$$S_{\text{w,single tail}} = 13.7 \times (1.977 + 0.52 \times 0.08) = 27.7\ (\text{m}^2)$$

$$S_{\text{w,HTP}} = 2 \times 27.7 = 55.4\ (\text{m}^2)$$

Therefore, the profile drag coefficient, based on the planform area of HTP, is:

$$C_{DP,HTP} = \frac{2.67\times10^{-3}\times1.22\times1.2\times55.4}{28.4} = 7.63 \times 10^{-3} \quad (3\text{-}28)$$

e) Nacelle

Take nacelle overall length as the characteristic length, that is, L=5.75m

$$R_e = \frac{0.374 \times 225 \times 5.75}{1.42 \times 10^{-5}} = 3.41 \times 10^7$$

$$C_f = \frac{0.455}{[\log_{10}(3.41 \times 10^7)]^{2.58} \times (1 + 0.144 \times 0.76^2)^{0.65}} = 2.36 \times 10^{-3}$$

Combined correction factor $FQ = 1.25 \times (1 + 20\%) = 1.50$

Calculation of wetted area:

$$S_{w,1} = \pi \times \left(5.8\text{mm} \times 0.357\frac{\text{m}}{\text{mm}}\right) \times \left(9.5\text{mm} \times 0.357\frac{\text{m}}{\text{mm}}\right) = 22.1\ (\text{m}^2)$$

$$S_{w,2} = \frac{\pi \times 0.357\frac{\text{m}}{\text{mm}} \times (3\text{mm} + 5.8\text{mm})}{2} \times \left(6\text{mm} \times 0.357\frac{\text{m}}{\text{mm}}\right) = 10.6\ (\text{m}^2)$$

$S_{w,SE} = 22.1 + 10.6 = 32.7\ (\text{m}^2)$, here, SE-single engine

$S_{w,total} = 2 \times 32.7 = 65.4\ (\text{m}^2)$

Therefore, the contribution to aircraft profile drag coefficient from nacelle is:

$C_{DP,N} = \frac{2.36\times10^{-3}\times1.50\times65.4}{112.30} = 2.06 \times 10^{-3}$, here N-nacelle (3-29)

f) Contributions to aircraft profile drag coefficient from secondary items:

$C'_{DP,w} = 6\% \times 5.98 \times 10^{-3} = 3.59 \times 10^{-4}$ (3-30)

$C'_{DP,f+e} = 7\% \times 7.32 \times 10^{-3} = 5.12 \times 10^{-4}$ (3-31)

$C'_{DP,eins} = 15\% \times 2.06 \times 10^{-3} = 3.09 \times 10^{-4}$ (3-32)

$C'_{DP,cockpit} = 2.5\% \times 7.32 \times 10^{-3} = 1.83 \times 10^{-4}$ (3-33)

$C'_{DP,system} = 3\% \times (7.32 \times 10^{-3} + 5.98 \times 10^{-3} + 1.93 \times 10^{-3} + 1.20 \times 10^{-3} + 2.06 \times 10^{-3}) = 5.55 \times 10^{-4}$ (3-34)

$C'_{DP,trim} = 5 \times 10^{-4}$

$C_{DP,trim} = \frac{5\times10^{-4}\times112.30}{28.4} = 1.98 \times 10^{-3}$ (3-35)

Finally, the results are as follows:

$C_{DP,a/c-t} = 7.32 \times 10^{-3} + 5.98 \times 10^{-3} + 2.06 \times 10^{-3} + 1.20 \times 10^{-3} + 3.59 \times 10^{-4} + 5.12 \times 10^{-4} + 3.09 \times 10^{-4} + 1.83 \times 10^{-4} + 5.55 \times 10^{-4} = 1.85 \times 10^{-2}$ (3-36)

$C_{DP,HTP} = 7.63 \times 10^{-3} + 1.98 \times 10^{-3} = 9.61 \times 10^{-3}$ (3-37)

2) Oswald coefficient calculation

For main wing, $\Lambda_{LE} < 30^{\circ}$, so,

$$e_w = 1.78 \times (1 - 0.045 \times 9.62^{0.68}) - 0.64 = 0.767 \qquad (3\text{-}38)$$

For HTP, $\Lambda_{LE} > 30^{\circ}$ and $AR_{HTP} = 12.24^2/28.4 = 5.28$, so,

$$e_{HTP} = 4.61 \times (1 - 0.045 \times 5.28^{0.68}) \times (\cos 35^{\circ})^{0.15} - 3.1 = 0.75 \qquad (3\text{-}39)$$

3) Lift-dependent drag factor K_w and K_{HTP}

$$K_w = \frac{1}{\pi \times 9.62 \times 0.767} = 0.0431 \qquad (3\text{-}40)$$

$$K_{HTP} = \frac{1}{\pi \cdot AR \cdot e_{HTP}} = \frac{1}{\pi \times 5.28 \times 0.75} = 0.0804 \qquad (3\text{-}41)$$

4) Minimum-drag lift coefficient $C_{L,min.D}$

$$C_{L,min.D} = 0.5 \times 0.225 = 0.113 \cong 0.11 \qquad (3\text{-}42)$$

Therefore, based on the above calculations, the drag characteristics (drag polar) of CUPFDAC can be described as follows:

$$C_D = \begin{cases} 0.0185 + 0.0431 \times (C_L - 0.11)^2, & a/c - t \\ 0.00961 + 0.0804 \times C_L^2, & \text{HTP} \end{cases} \qquad (3\text{-}43)$$

The drag polar expressed by the above equation (3-43) is shown in the following Figure 3-15 (a) and (b).

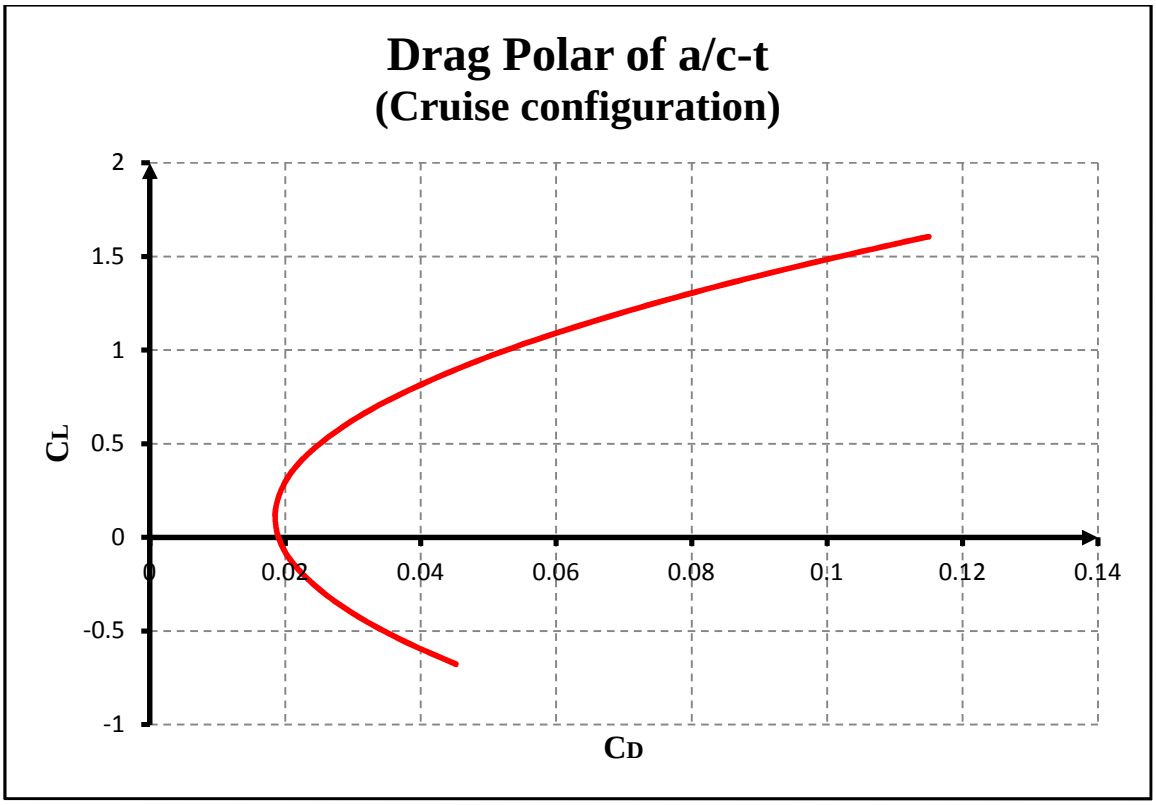

Figure 3-15 (a) Drag polar of CUPFDAC (a/c-t) - 'Cruise' configuration

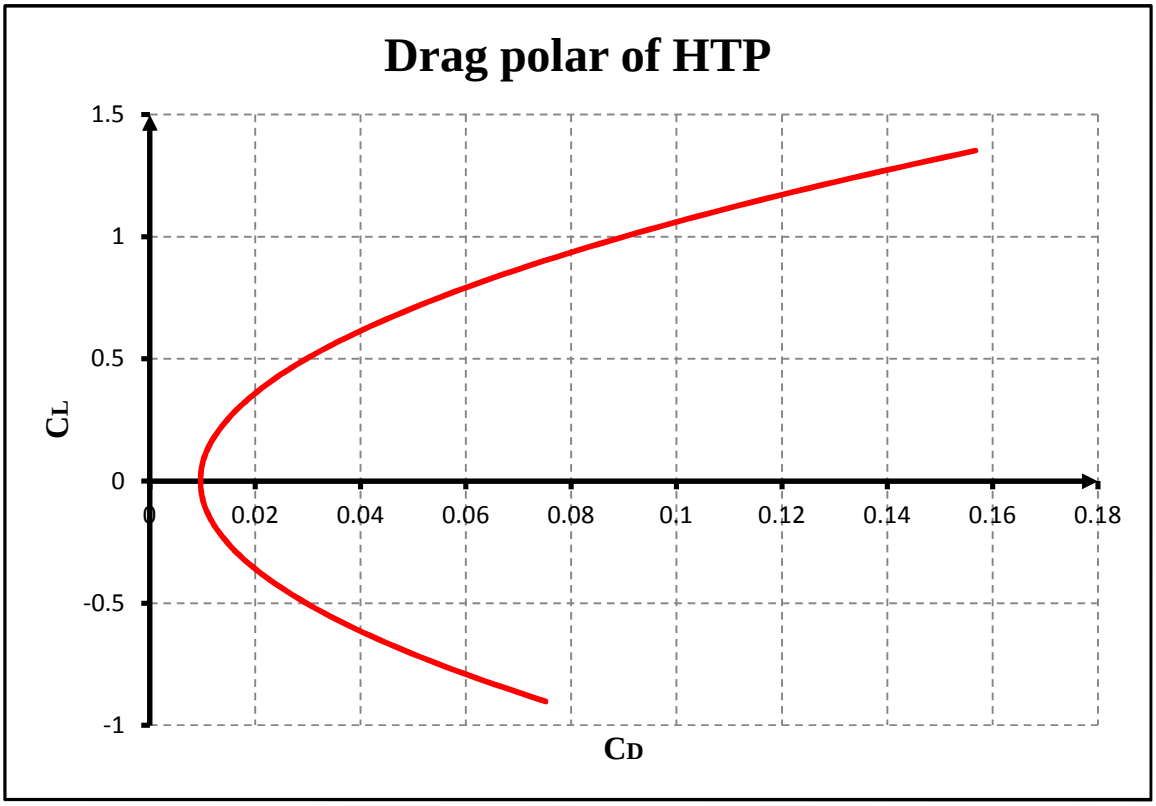

Figure 3-15 (b) Drag polar of CUPFDAC (HTP)

Therefore, based on the above measurements and calculations, aircraft performance model of CUPFDAC with 'Cruise' configuration can be summarised in the following Table 3-9.

Table 3-9 CUPFDAC aircraft model ('Cruise' configuration)

Parameters	Units	Values
Engine section		
X-position	m	-8.82
Z-position	m	-1.32
Tilt	rad	0.0349
Number of engines	–	2
Horizontal Tailplane		
Span	m	12.24
Wing area	m^2	28.4
Oswald coefficient	–	0.75
Min. drag coefficient	–	0.00961
X-position	m	-16.9
Z-position	m	-6.14
Aircraft section (excluding HTP)		
Span	m	32.87
Mean aerodynamic chord	m	4.08
Wing area	m^2	112.30
Oswald coefficient	–	0.767
Min. drag coefficient	–	0.0185
Min.-drag lift coefficient	–	0.11
X-position	m	-0.42
Z-position	m	-0.25
Wing sweep angle (0.5chord)	rad	0.332
Wing setting angle	rad	0.053

Preliminary evaluation of CUPFDAC aircraft model (‘Cruise’ configuration)

Profile drag coefficient (or zero-lift drag coefficient) of the entire aircraft under ‘Cruise’ configuration:

By the above calculations,

$C_{DP,HTP} = \frac{(C_{f,eq} \times S_w)_{HTP}}{S_{p,HTP}}$,

That is, ‘drag area’,

$$\left(C_{f,eq} \times S_w\right)_{HTP} = C_{DP,HTP} \times S_{p,HTP} = 0.00961 \times 28.4 = 0.2729$$

So the ‘equivalent’ profile drag coefficient of HTP based on the planform area of main wing instead of HTP itself is:

$$C'_{DP,HTP} = \frac{\left(C_{f,eq} \times S_w\right)_{HTP}}{S_{p,wing}} = \frac{0.2729}{112.30} = 0.0024$$

So, the profile drag coefficient of the entire aircraft based on the planform area of main wing with ‘Cruise’ configuration is:

$$C_{DP,a/c} = C_{DP,a/c-t} + C'_{DP,HTP} = 0.0185 + 0.0024 = 0.0209$$

Compared with Table 3-2 (for high-subsonic jet aircraft, the profile drag coefficient varies from 0.014 to 0.020), the value of $C_{DP,a/c}$ falls basically into this range.

The following Table 3-10 shows the calculation results of CUPFDAC with the above aircraft drag characteristics at a typical cruise condition (flight altitude: 10668 m, flight Mach number: 0.78, ISA, initial aircraft mass: 75000 kg, ‘Cruise’ configuration):

Table 3-10 Cruise performance of CUPFDAC

AIRCRAFT STATES		Initial	Average	Final
Position (X) (m)	:	228612.000000	250294.000000	271976.000000
Position (Y) (m)	:	0.000000	0.000000	0.000000
Altitude (-Z) (m)	:	10668.000000	10668.000000	10668.000000
True airspeed (m/s)	:	231.439791	231.439794	231.439797
Equivalent airspeed (m/s)	:	129.171506	129.171508	129.171509
Calibrated airspeed (m/s)	:	126.951484	126.951486	126.951488
Mach no. (m/s)	:	0.780000	0.780000	0.780000
Ground speed (m/s)	:	231.439791	231.439794	231.439797
Lateral speed (m/s)	:	0.000000	0.000000	0.000000
Vertical speed (descent) (m/s)	:	0.000000	0.000000	0.000000
Flight path angle (rad)	:	0.000000	0.000000	0.000000
Heading angle (rad)	:	0.000000	0.000000	0.000000

SEGMENT			
Time interval	:	187.798939	(s)
Pitch angle	:	0.030098	(rad)
Bank angle	:	0.000000	(rad)

FORCES			
Thrust	:	39021.816655	(N)
Thrust per Engine	:	19510.908327	(N)
Weight	:	735750.000000	(N)

From the above calculation results, the aircraft lift to drag ratio at this typical cruise condition is:

$$\frac{L}{D} = \frac{W}{T} = \frac{735750}{39021.82} = 18.85$$

Similar to the case CUTFDAC, according to the reference [3-1] (“Modern airliners using super-critical wing technology have values around 18 to 22” in terms of the lift to drag ratio (L/D) in the cruise phase).

Therefore, no matter whether from the point of view of aircraft profile drag coefficient or from the cruise lift to drag ratio, the aircraft model built for CUPFDAC with ‘Cruise’ configuration is satisfactory and reasonable.

Aircraft model of CUPFDAC with ‘Initial Climb’ configuration

As mentioned before, due to the complexity of high-lift device, this research modelled aircraft under high-lift device deployment by adopting BADA data properly.

For the ‘Initial Climb’ configuration of MD90-30, the estimated value of the profile drag coefficient (or zero-lift drag coefficient) of the entire aircraft given by BADA dataset is 0.024150, that is, $C_{DP,a/c} = 0.024150$ [34].

Due to the difference of the BADA database from this project research in terms of aircraft modelling method, the above value cannot be used directly but is helpful to determine the needed value of $C_{Dmin,a/c-t}$ as follows:

According to the definition of aircraft profile drag coefficient,

$$C_{DP,a/c} = \frac{\sum_{i=1}^{n}(C_{fc,eq}\cdot S_w)_i}{S_{P,w}} = \frac{\sum_{i=1}^{n-1}(C_{fc,eq}\cdot S_w)_i + (C_{fc,eq}\cdot S_w)_{tail}}{S_{P,w}} = C_{Dmin,a/c-t} + \frac{(C_{fc,eq}\cdot S_w)_{tail}}{S_{P,w}}$$

On the other hand,

$$C_{DP,HTP} = \frac{(C_{fc,eq}\cdot S_w)_{tail}}{S_{P,t}}, \text{ and so, } (C_{fc,eq}\cdot S_w)_{tail} = C_{DP,HTP}\cdot S_{P,t}$$

So, combined with the above two equations,

$$C_{Dmin,a/c-t} = C_{DP,a/c} - \frac{(C_{fc,eq}\times S_w)_{tail}}{S_{P,w}} = C_{DP,a/c} - \frac{C_{DP,HTP}\times S_{P,t}}{S_{P,w}}$$
$$= 0.024150 - \frac{0.00961\times 28.4}{112.30} = 0.0217 \qquad (3-44)$$

So, with this configuration, the drag polar of aircraft (excluding HTP) can be expressed as following formula (3-45) and Figure 3-16.

$$C_{D,a/c-t} = 0.0217 + 0.0431\times(C_L - 0.11)^2 \qquad (3\text{-}45)$$

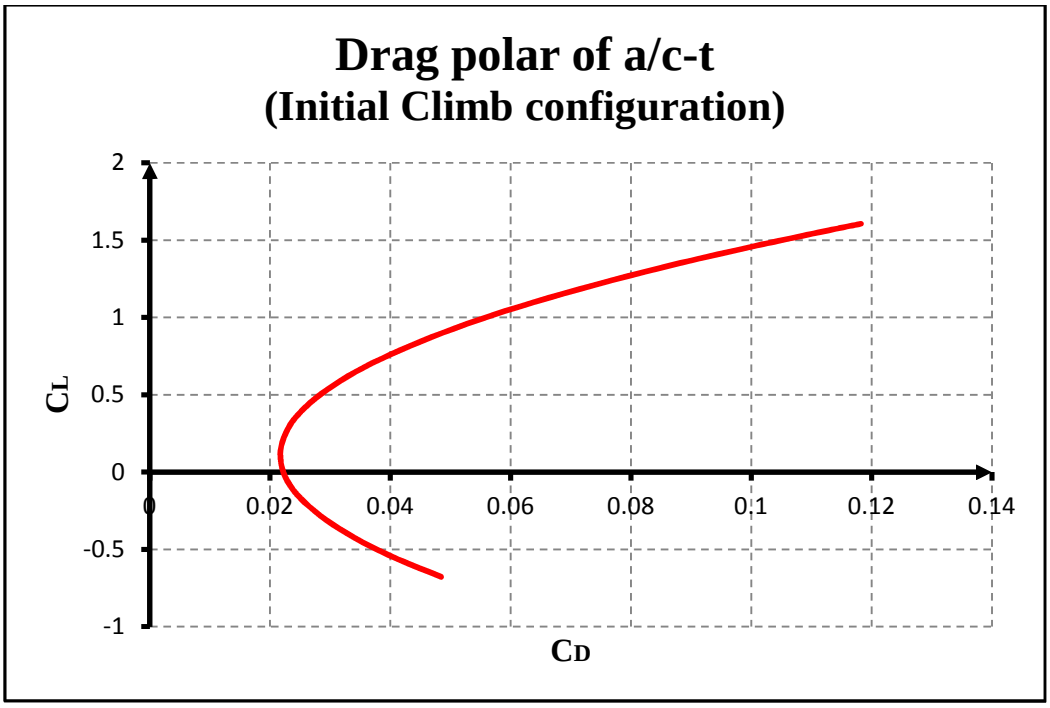

Figure 3-16 Drag polar of CUPFDAC (a/c-t) - 'Initial Climb' configuration

Further, the aircraft model of CUPFDAC under the 'Initial Climb' configuration can be expressed as the following Table 3-11.

Table 3-11 Aircraft model of CUPFDAC (Initial Climb configuration)

Parameters	Units	Values
Engine section		
X-position	m	-8.82
Z-position	m	-1.32
Tilt	rad	0.0349
Number of engines	–	2
Horizontal Tailplane		
Span	m	12.24
Wing area	m^2	28.4
Oswald coefficient	–	0.75
Min. drag coefficient	–	0.00961
X-position	m	-16.9
Z-position	m	-6.14

Aircraft section (excluding HTP)							
Span		m			32.87		
Mean aerodynamic chord		m			4.08		
Wing area		m^2			112.30		
Oswald coefficient		−			0.767		
Min. drag coefficient		−			0.0217		
Min.-drag lift coefficient		−			0.11		
X-position		m			-0.42		
Z-position		m			-0.25		
Wing sweep angle (0.5chord)		rad			0.332		
Wing setting angle		rad			0.053		
High-lift devices							
Parameters	Unit	Stage 0	1	2	3	4	5
dC_L	−	00.0000	0.1500	00.300	00.4500	00.6000	00.7500
C_{Lmax}	−	01.6060	1.7560	01.906	02.0560	02.2000	02.3500

(Note: In order to make a reasonable comparison between CUTFDAC and CUPFDAC, the same setting values about high-lift devices for CUPFDAC as those for CUTFDAC are applied in this project research.)

Aircraft model of CUPFDAC with ‘Approach’ configuration

Similar to the ‘Initial Climb’ case, the aircraft modelling of CUPFDAC under the ‘Approach’ configuration was also achieved based on the model under the ‘Cruise’ configuration as a baseline and modified by means of the BADA dataset as follows:

According to the BADA dataset, the profile drag coefficient (or zero-lift drag coefficient) of the entire aircraft MD90-30 under the ‘Approach’ configuration equals to 0.056050, that is, $C_{DP,a/c} = 0.056050$ [34].

So, $C_{Dmin,a/c-t} = C_{DP,a/c} - \frac{C_{DP,HTP} \times S_{P,t}}{S_{P,w}} = 0.056050 - \frac{0.00961 \times 28.4}{112.30} = 0.05362$ (3-46)

So, with this configuration, the drag polar of aircraft (excluding HTP) can be expressed as the following formula (3-47) and Figure 3-17.

$C_{D,a/c-t} = 0.05362 + 0.0431 \times (C_L - 0.11)^2$ (3-47)

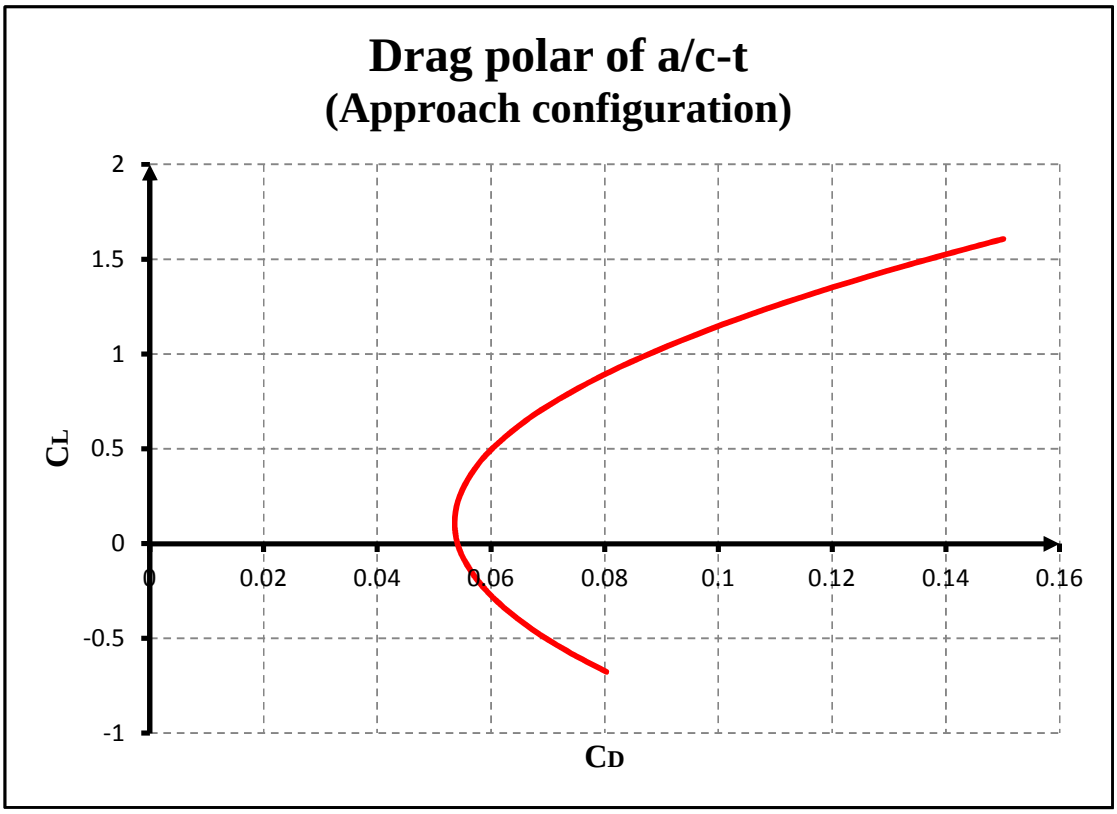

Figure 3-17 Drag polar of CUPFDAC (a/c-t) - ‘Approach’ configuration

Further, the aircraft model of CUPFDAC under the ‘Approach’ configuration can be expressed as the following Table 3-12.

Table 3-12 Aircraft model of CUPFDAC (‘Approach’ configuration)

Parameters	Units	Values
Engine section		
X-position	m	-8.82
Z-position	m	-1.32
Tilt	rad	0.0349
Number of engines	−	2
Horizontal Tailplane		
Span	m	12.24
Wing area	m^2	28.4
Oswald coefficient	−	0.75
Min. drag coefficient	−	0.00961
X-position	m	-16.9
Z-position	m	-6.14
Aircraft section (excluding HTP)		
Span	m	32.87
Mean aerodynamic chord	m	4.08
Wing area	m^2	112.30
Oswald coefficient	−	0.767
Min. drag coefficient	−	0.05362
Min.-drag lift coefficient	−	0.11
X-position	m	-0.42
Z-position	m	-0.25
Wing sweep angle (0.5chord)	rad	0.332
Wing setting angle	rad	0.053

High-lift devices							
Parameters	Unit	Stage 0	1	2	3	4	5
dC_L	−	00.0000	0.1500	00.300	00.4500	00.6000	00.7500
C_{Lmax}	−	01.6060	1.7560	01.906	02.0560	02.2000	02.3500

3.1.3 CUTPDAC (Cranfield University TurboProp-Driven AirCraft)

CUTPDAC (Cranfield University TurboProp-Driven AirCraft) used in this research project is a hypothetical twin-engine turboprop short-haul regional airliner with the seating capacity of 68 to 74 passengers and a flight range of around 1300 km. This aircraft was built based on the ATR72-500 [24-25] of the French-Italian aircraft manufacturer, ATR. Figure 3-18 illustrates the schematic drawing of CUTPDAC and Figure 3-19 shows the geometric measurements of ATR72-500 which constitute the foundation for CUTPDAC performance modelling.

Figure 3-18 CUTPDAC (Cranfield University TurboProp Driven AirCraft)

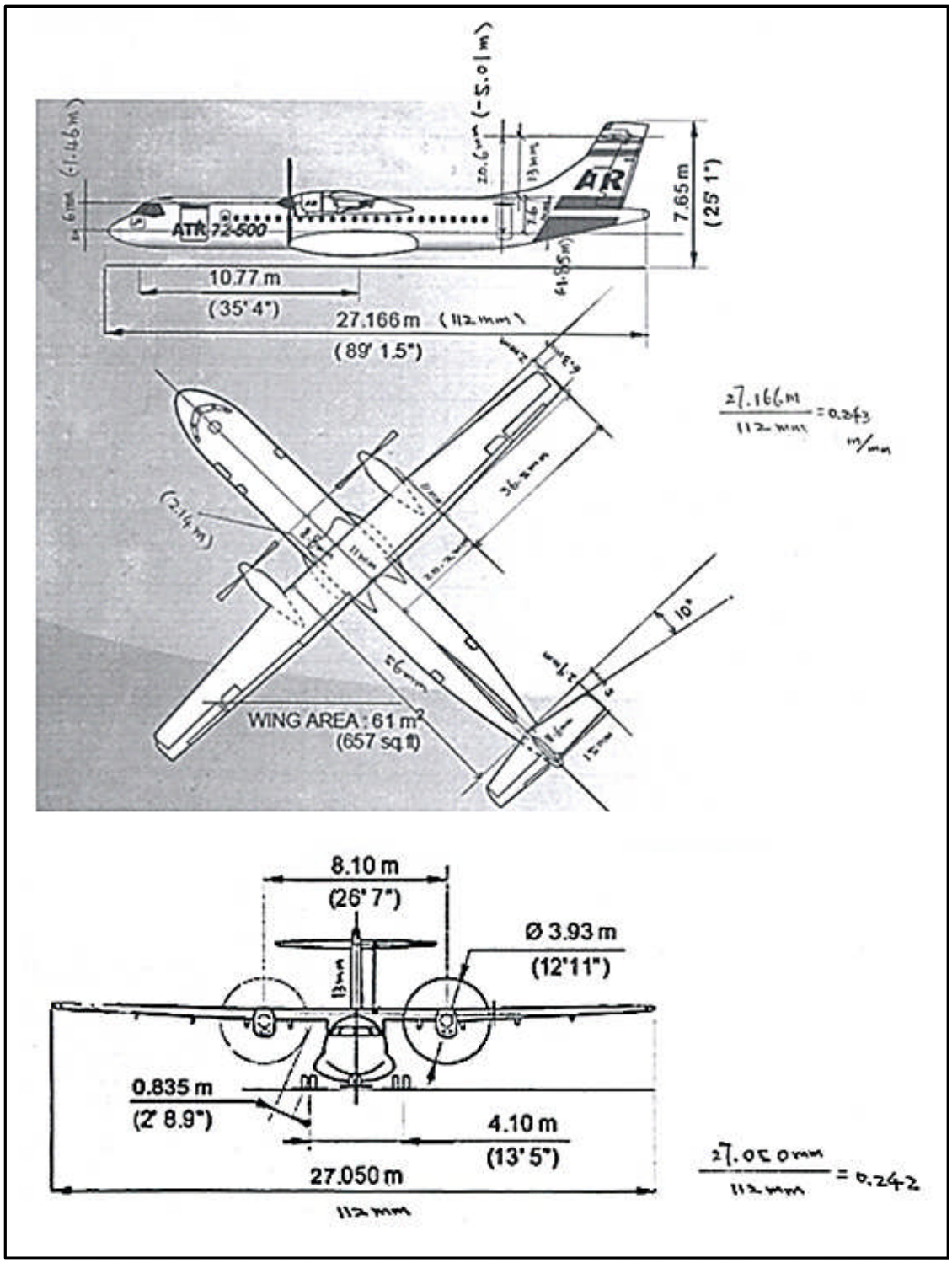

Figure 3-19 Measurements of ATR72-500

Table 3-13 Reference flight condition

Flight altitude	5181.6 m
Flight Mach number	0.44
Atmosphere condition	ISA
Air density	0.7218 kg/m^3
Dynamic viscosity	$1.6290\times\text{-}5N\cdot s/m^2$
Aircraft configuration	Clean (cruise)

Table 3-14 Main dimensions of CUTPDAC [35]

Fuselage length	27.13 m
Fuselage diameter	2.77 m
Wing span	27.32 m
Wing panel span Y	4.73 m
Wing panel span Y2	8.93 m
Wing planform area	62.187 m^2
Wing root chord A	2.626 m
Wing panel chord B	2.626 m
Wing tip chord B2	1.556 m
Wing sweep distance S	0 m
Wing sweep distance S2	0.489 m
HTP span	8.033 m
HTP planform area	10.756 m^2
HTP taper ratio	0.6
HTP sweep angle at leading edge	10°
HTP sweep distance SS	0.705 m
HTP volume ratio	1.05
Distance between both LE's D	14.2 m
VTP span	4.883 m
VTP planform area	14.904 m^2
Nacelle length	3.3 m

Lift characteristics of CUTPDAC

According to the reference [29], the lift curve slope of CUTPDAC can be calculated as follows:

$$a = \frac{2\pi \cdot AR}{2 + \sqrt{AR^2(1 + \tan^2\varphi_{50} - M^2) + 4}}$$

Here, $\tan\varphi_{50} = \tan\varphi_{25} - \frac{4}{AR}\left[\frac{50-25}{100} \cdot \frac{1-\lambda}{1+\lambda}\right] = \tan(3^\circ) - \frac{4}{12}\left[\frac{25}{100} \cdot \frac{1-0.59}{1+0.59}\right] = 0.0309$

So, $a = \frac{2\pi \times 12}{2+\sqrt{12^2(1+0.0309^2-0.443^2)+4}} = 5.823\ \text{rad}^{-1}$

Similar to CUTFDAC and CUPFDAC, assume zero-lift angle of attack $\alpha_{L=0} = -2^\circ$, and then the lift characteristics of CUTPDAC can be expressed as follows:

$$C_L = a(\alpha - \alpha_{L=0}) = 5.823 \times \left(\alpha - \left(-2^\circ \times \frac{\pi}{180^\circ}\right)\right) = 5.823 \times (\alpha + 0.0349) =$$

$$5.823\alpha + 0.2032 \qquad (3\text{-}48)$$

Hence, zero-AOA lift coefficient $C_{L,\alpha=0} = 0.2032$.

Accordingly, the lift curve of CUTPDAC is shown as follows:

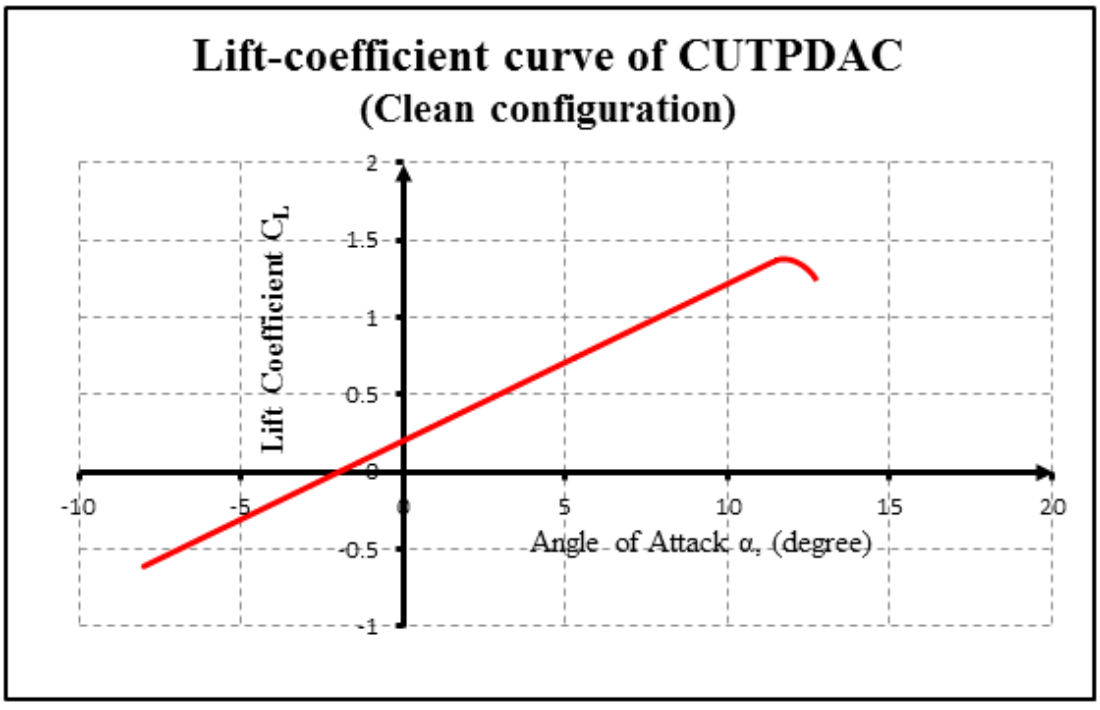

Figure 3-20 Lift curve of CUTPDAC

Due to at the later stage of aircraft performance modelling, part BADA data became available. Therefore, related information about the ATR72-500 from BADA was adopted directly.

According to the BADA dataset: AT75_.OPF (Mar. 31, 2011), for 'IC' (Initial Climb) and 'CR' (Cruise) configuration, $C_{D0} = 0.021882$ (for the entire aircraft) [36].

By the definition, the zero-lift drag coefficient C_{D0} of the entire aircraft can be expressed as follows:

$$C_{D0} = \frac{\sum_{i=1}^{n}\left(C_{f,eq} \cdot S_w\right)_i}{S_{p,w}} = \frac{\sum_{i=1}^{n-1}\left(C_{f,eq} \cdot S_w\right)_i + \left(C_{f,eq} \cdot S_w\right)_{HTP}}{S_{p,w}}$$

$$= \frac{\sum_{i=1}^{n-1}\left(C_{f,eq} \cdot S_w\right)_i}{S_{p,w}} + \frac{\left(C_{f,eq} \cdot S_w\right)_{HTP}}{S_{p,w}}$$

$$= C_{Dmin,A/C-HTP} + \frac{\left(C_{f,eq} \cdot S_w\right)_{HTP}}{S_{p,w}}$$

So, $C_{Dmin,A/C-HTP} = C_{D0} - \frac{\left(C_{f,eq} \cdot S_w\right)_{HTP}}{S_{p,w}}$

On the other hand, $C_{Dmin,HTP} = \frac{(C_{f,eq} \cdot S_w)_{HTP}}{S_{p,HTP}}$

So, $(C_{f,eq} \cdot S_w)_{HTP} = C_{Dmin,HTP} \times S_{p,HTP} = 0.00984 \times 10.756 = 0.10584$

Therefore, $C_{Dmin,A/C-HTP} = 0.021882 - \frac{0.10584}{62.187} = 0.02018 \cong 0.0202$ (3-49)

Where, the minimum drag coefficient of the aircraft excluding HTP ($C_{Dmin,A/C-HTP}$) is defined based on the wing planform area.

In addition, based on the reference [35], the minimum drag coefficient of HTP can be determined, i.e.,

$C_{Dmin,HTP} = 0.00984$ (with HTP planform area as the reference area) (3-50)

Further, according to the reference [35] and for more realistic purposes, the Oswald factor $e_{a/c-t}$ of the aircraft (excluding HTP) takes the value of 0.85 rather than its calculation value of 0.777, so the lift-dependent drag factor,

$$K_{a/c-HTP} = \frac{1}{\pi \cdot AR \cdot e_{a/c-HTP}} = \frac{1}{\pi \times 12 \times 0.85} = 0.0312 \qquad (3\text{-}51)$$

In the meantime, the minimum-drag lift coefficient can also be determined with the similar method as the CUTFDAC and CUPFDAC cases, that is,

$$C_{L,minD} = \frac{C_{L,\alpha=0}}{2} = \frac{0.2032}{2} = 0.1016$$

Because $\Lambda_{LE,HTP} = 10^{\circ} < 30^{\circ}$, therefore,

$$e_{HTP} = 1.78 \times (1 - 0.045 \times AR_{HTP}^{0.68}) - 0.64 = 1.78 \times \left(1 - 0.045 \times \left(\frac{8.033^2}{10.756}\right)^{0.68}\right) - 0.64 = 0.8691 \cong 0.87$$

$$K_{HTP} = \frac{1}{\pi \cdot AR_{HTP} \cdot e_{HTP}} = \frac{1}{\pi \times (8.033^2/10.756) \times 0.87} = 0.0610 \qquad (3\text{-}52)$$

Therefore, the drag characteristics of CUTPDAC can be expressed as the following piecewise function:

$$C_D = \begin{cases} 0.0202 + 0.0312 \times (C_L - 0.1016)^2 & a/c - HTP \\ 0.00984 + 0.0610 C_L^2 & HTP \end{cases} \qquad (3\text{-}53)$$

The drag characteristics expressed by the above formula (3-53) are also illustrated in the following Figures 3-21 (a) and (b) respectively.

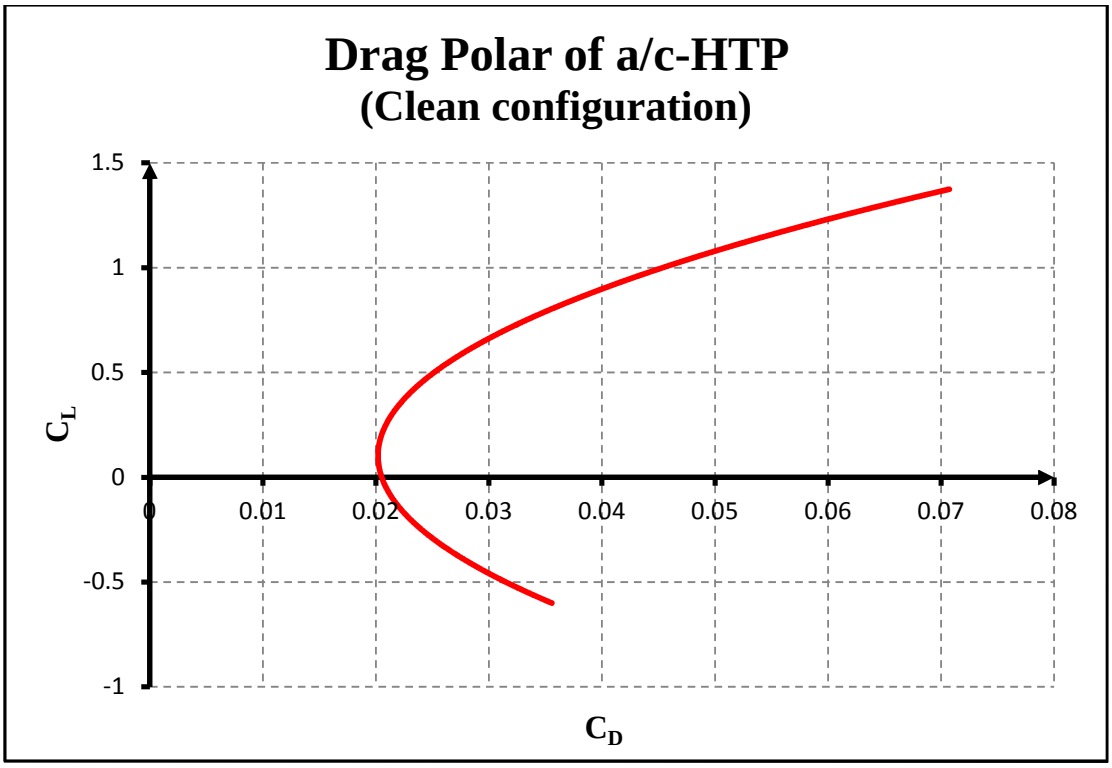

Figure 3-21(a) Drag polar of CUTPDAC (a/c-HTP) – 'clean' configuration

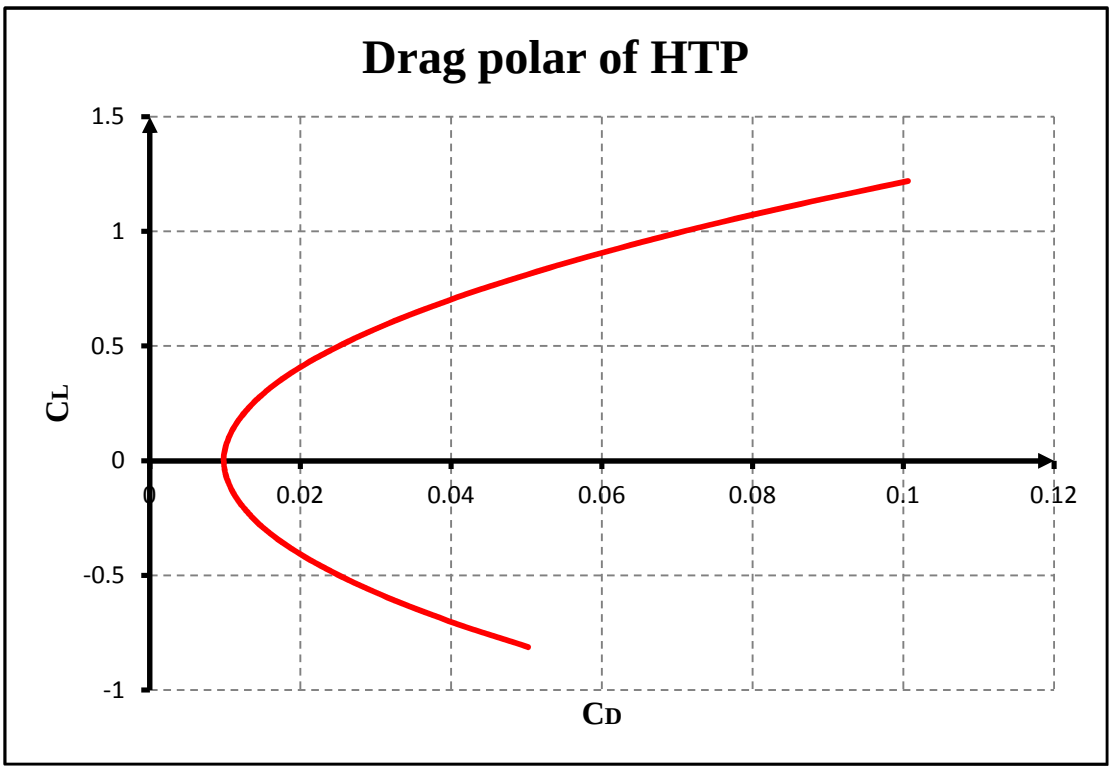

Figure 3-21(b) Drag polar of CUTPDAC (HTP)

Table 3-15 Aircraft model of CUTPDAC (‘Cruise’ configuration)

Parameters	Units	Values
Engine section		
X-position	m	3.94
Z-position	m	-1.46
Tilt	rad	0.0
Number of engines	–	2
Horizontal Tailplane		
Span	m	8.033
Wing area	m^2	10.756
Oswald coefficient	–	0.87
Min. drag coefficient	–	0.00984
X-position	m	-13.1
Z-position	m	-5.01
Aircraft section (excluding HTP)		
Span	m	27.32
Mean aerodynamic chord	m	2.33
Wing area	m^2	62.187
Oswald coefficient	–	0.777
Min. drag coefficient	–	0.0202
Min.-drag lift coefficient	–	0.1016
X-position	m	-0.24
Z-position	m	-1.85
Wing sweep angle (0.5chord)	rad	0.0309
Wing setting angle	rad	0.06

Table 3-16 Aircraft model of CUTPDAC (‘Initial climb’ configuration)

Parameters	Units	Values
Engine section		
X-position	m	3.94
Z-position	m	-1.46
Tilt	rad	0.0
Number of engines	–	2
Horizontal Tailplane		
Span	m	8.033
Wing area	m^2	10.756
Oswald coefficient	–	0.87
Min. drag coefficient	–	0.00984
X-position	m	-13.1
Z-position	m	-5.01
Aircraft section (excluding HTP)		
Span	m	27.32
Mean aerodynamic chord	m	2.33
Wing area	m^2	62.187
Oswald coefficient	–	0.777
Min. drag coefficient	–	0.0202
Min.-drag lift coefficient	–	0.1016
X-position	m	-0.24
Z-position	m	-1.85
Wing sweep angle (0.5chord)	rad	0.0309
Wing setting angle	rad	0.06

For the 'AP' (Approach) configuration of ATR72-500, from the same BADA dataset, $C_{D0} = 0.0396$ [36], through the similar treatment process as above, the following value can be obtained:

$$C_{Dmin,A/C-HTP} = 0.0396 - \frac{0.10584}{62.187} = 0.0379 \quad (3\text{-}54)$$

Therefore, the drag characteristics of CUTPDAC with the 'AP' configuration can be expressed as follows:

$$C_D = \begin{cases} 0.0379 + 0.0312 \times (C_L - 0.1016)^2 & a/c - HTP \\ 0.00984 + 0.0610 C_L^2 & HTP \end{cases} \quad (3\text{-}55)$$

The corresponding drag polar of the aircraft (excluding HTP) is illustrated in the following Figure 3-22.

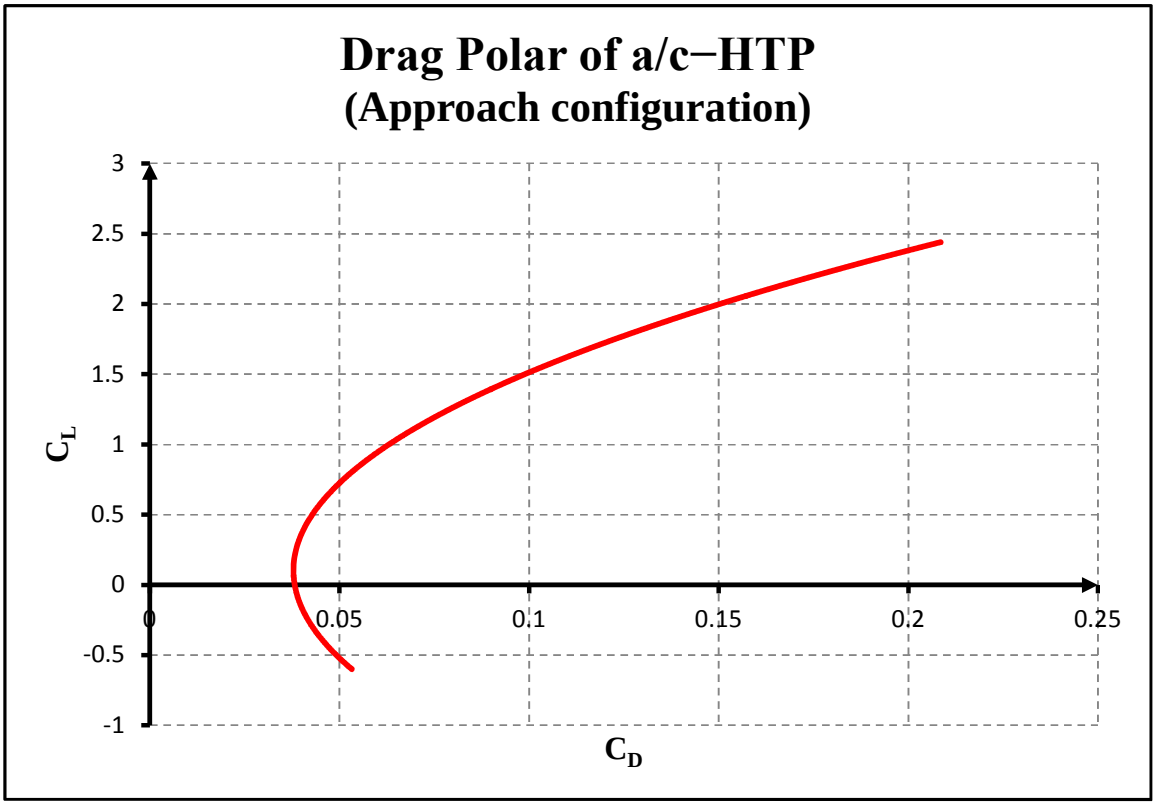

Figure 3-22 Drag polar of CUTPDAC (a/c-HTP) – 'approach' configuration

Table 3-17 Aircraft model of CUTPDAC ('Approach' configuration)

Parameters	Units	Values
Engine section		
X-position	m	3.94
Z-position	m	-1.46
Tilt	rad	0.0
Number of engines	–	2
Horizontal Tailplane		
Span	m	8.033
Wing area	m^2	10.756
Oswald coefficient	–	0.87
Min. drag coefficient	–	0.00984
X-position	m	-13.1
Z-position	m	-5.01
Aircraft section (excluding HTP)		
Span	m	27.32
Mean aerodynamic chord	m	2.33
Wing area	m^2	62.187
Oswald coefficient	–	0.777
Min. drag coefficient	–	0.0379
Min.-drag lift coefficient	–	0.1016
X-position	m	-0.24
Z-position	m	-1.85
Wing sweep angle (0.5chord)	rad	0.0309
Wing setting angle	rad	0.06

High-lift devices							
Parameters	Unit	Stage 0	1	2			
dC_L	–	00.0000	0.5780	1.0660			
C_{Lmax}	–	01.3740	1.9520	02.4400			

(Note: the information of high-lift devices in Table 3-17 above is from the reference [37].)

3.2 Aircraft Performance Simulation

Based on the aircraft models built previously and given flight missions, the aircraft flight performance can be simulated by means of the in-house simulation software at Cranfield University – the APM (Aircraft Performance Model). The following Figure 3-23 briefly illustrates the calculation process of APM for a single flight segment. For a given flight mission, which consists of many flight segments, the process is only in turn repeated with the end point of the last flight segment (and its flight data) as the start point (and calculation inputs) of the next new segment. More detailed information about APM can be obtained from the reference [33].

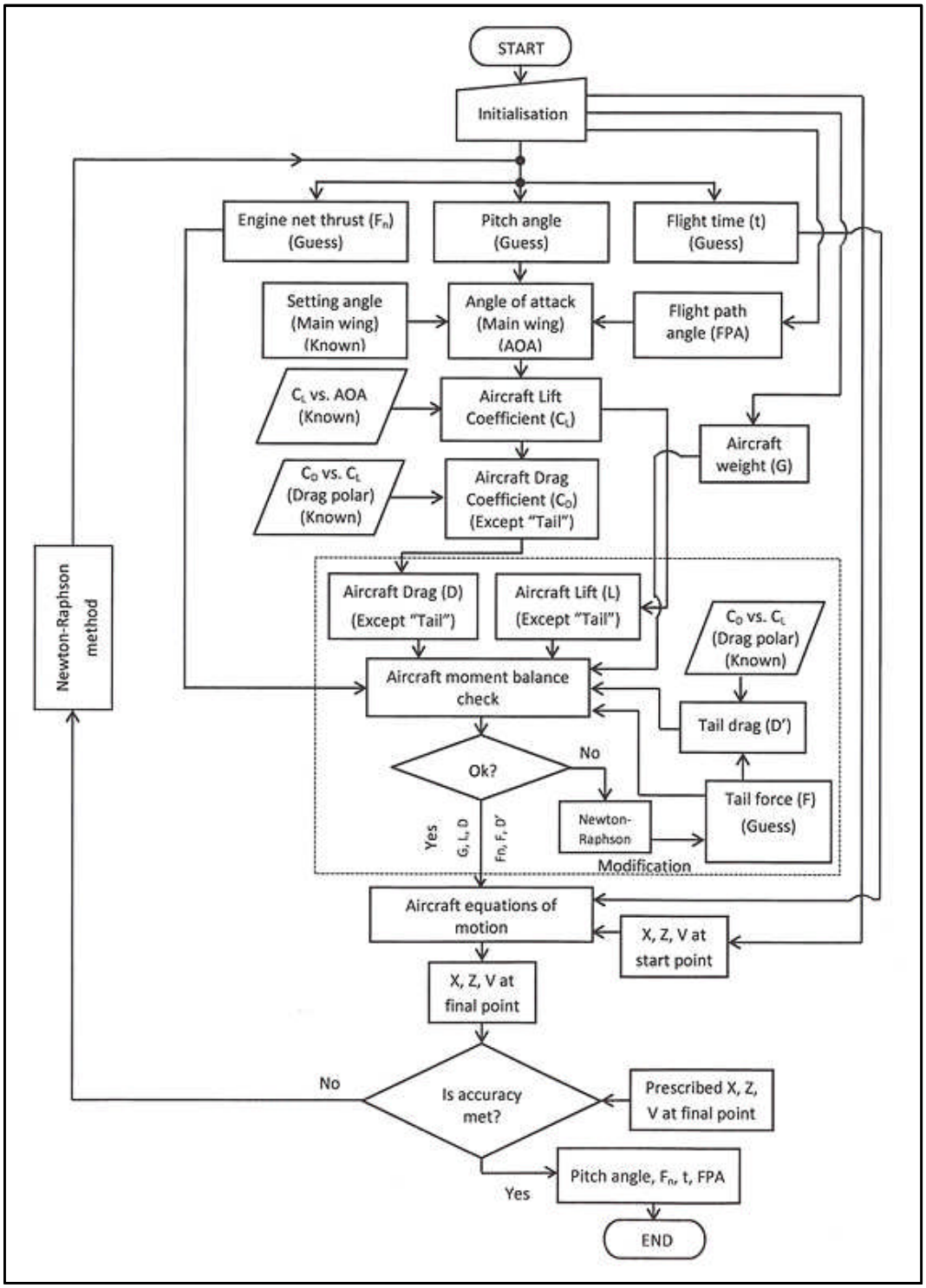

Figure 3-23 Calculation process of aircraft performance (one flight segment)

CHAPTER FOUR GAS TURBINE ENGINE PERFORMANCE AND MODELLING

4.1 Turbofan Engine Powering CUTFDAC

The turbofan engine, which is used to power the aircraft CUTFDAC, is a typical two spool, high bypass ratio turbofan aero engine with separate exhausts. The engine performance is modelled based on the CFM56-5B engine [38] which is the engine of choice for the A320 family, having been selected to power nearly 60% of the A318/A319/A320/A321 aircraft ordered. For the purpose of convenience, this engine performance model is referred as "CUTSTF" (**C**ranfield **U**niversity **T**win **S**pool **T**urbo**f**an).

Figure 4-1 illustrates a schematic of the CUTSTF engine performance model, as follows.

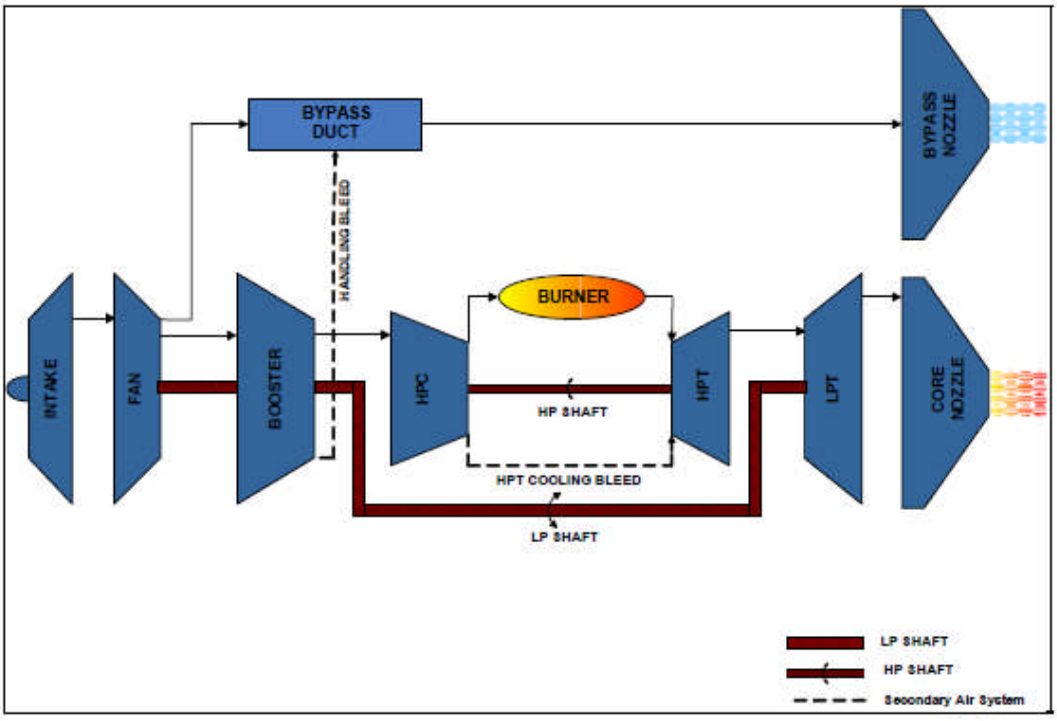

Figure 4-1 CUTSTF engine performance model [39]

The steady-state performance simulations of the CUTSTF engine including at design point and off-design points have been performed using TURBOMATCH.

TURBOMATCH [40] & [41] is an in-house gas turbine performance simulation and diagnostics software, developed by Cranfield University. TURBOMATCH comprises several pre-programmed modules, known as Bricks. Most Bricks correspond to models of individual gas turbine components, for instance, Compressors, Combustion Chamber, Turbines, Mixers, Nozzles, Heat Exchangers, Afterburners, and Power Turbines, and others. Additionally, TURBOMATCH also comprises Bricks for arithmetic operations, overall engine performance calculations and plotting of results. TURBOMATCH can be used to simulate the performance of an extensive range of both Aero and Industrial engine cycles, ranging from a simple single shaft turbojet to complex multi-spool turbofans with mixed/separate exhausts and complex secondary air systems. TURBOMATCH can also be used to simulate the performance of novel and conceptual cycles, including wave rotors, pulse detonators, constant volume combustion systems, distributed propulsion systems and intercooled/recuperated cycles. TURBOMATCH offers performance simulations ranging from steady state simulations to transient performance calculations.

TURBOMATCH encompasses all the basic capabilities of existing commercial gas turbine performance simulation software. Additionally, the following advanced performance simulation capabilities are also available from TURBOMATCH.

1) Parametric analysis
2) Engine deterioration modelling
3) Multi-fuel capabilities
4) User friendly graphical user interface (GUI)
5) High density, smooth default component characteristics
6) Ability to introduce customised (user defined) component characteristics
7) Dynamic convergence control
8) Advanced, high fidelity component zooming capabilities (coupling with high fidelity 3D software)
9) Combined cycles simulations
10) Effects of dissociation
11) Inlet flow distortion/control
12) Water/steam injection
13) Effects of humidity

14) Steam turbines
15) Engine control
16) Fuel cells

TURBOMATCH has already been applied extensively and successfully by Cranfield University in several European Union projects, including VIVACE [42] & [43], VITAL [44], NEWAC [45], DREAM and Clean Sky, etc.

The design point of the CUTSTF engine performance model is chosen at top of climb (alt. 10668m, M0.8) with the intake total pressure recovery of 0.99 and International Standard Atmosphere (ISA) condition. Several iterations were implemented at design and off-design point conditions to enable the model performance to match data obtained from the public domain. A summary of these data available through the public domain is presented in the following Table 4-1.

Table 4-1 Data of typical high by-pass ratio twin-spool turbofan (available from the Public domain) [39]

Engine type	Two-spool turbofan
Maximum take-off thrust (kN)	120.10
Take-off mass flow rate (kg/s)	408.20
Take-off bypass ratio(-)	5.70
Overall pressure ratio (at top of climb) (-)	32.60
Maximum climb thrust (kN)	25.04
Cruise SFC (mg/Ns)	16.98
Maximum cruise thrust (kN)	22.33
Fan diameter (m)	1.73

At design-point, the overall engine mass flow rate was estimated according to the measured intake area and the assumed intake average Mach number, which ranges from 0.55 to 0.65. The bypass ratio (BPR) and the turbine entry temperature (TET) were determined based on the overall pressure ratio (OPR), the net thrust and take-off BPR

available from the public domain, as well as the available technology level at the time of reference engine, and then the optimum fan pressure ratio can be further determined according to the calculated TET, OPR and BPR.

Additionally, pressure ratios of compressors, component efficiencies, compressor bleed for the purpose of turbine cooling and other parameter values were guessed and iterated to match the required engine performance at off-design conditions (take-off and cruise).

A summary of the design parameters for the CUTSTF engine performance model at design-point is illustrated in the following Table 4-2.

Table 4-2 Design parameter summary of CUTSTF engine
(DP: top of climb, alt.10668m, M0.8) [39]

Engine mass flow rate (kg/s)	180.0
Bypass ratio (-)	5.46
Overall pressure ratio (-)	32.6
Fan pressure ratio (-)	1.80
Booster pressure ratio (-)	1.811
High pressure compressor pressure ratio (-)	10.00
Fan efficiency (-)	0.90
Booster efficiency (-)	0.90
High pressure turbine cooling flow (%)	13%
Combustion efficiency (-)	0.99
Combustion fractional pressure loss (Pin-Pout)/Pin (-)	0.05
Turbine entry temperature (K)	1340.0
High pressure turbine efficiency (-)	0.91
Low pressure turbine efficiency (-)	0.91
Operating altitude (m)	10668.0
Flight Mach number (-)	0.80

Table 4-3 highlights the simulation results of the CUTSTF engine performance model at design point and some off-design points, as well as the comparisons with those values available from the public domain. As shown in the Table 4-3, the discrepancies between the results achieved from CUTSTF performance simulation and those available from the public domain are small, therefore, the CUTSTF engine performance model is deemed acceptable.

Table 4-3 Simulation results of CUTSTF performance model and comparisons [39]

Parameter	Required	CUTSTF	Discrepancies
TOC thrust (kN)-10668m and 0.8M, ISA	25.04	25.11	-0.3%
TOC SFC (mg/Ns)	Not known	17.02	---
TOC TET (K)	Not known	1340	---
T-O thrust (kN)-SLS, ISA+30	120.10	120.98	-0.7%
T-O fuel flow rate (kg/s)	1.166	1.14	2.2%
T-O air mass flow rate (kg/s)	408.2	401.4	1.7%
T-O TET (K)	Not known	1600	---
T-O BPR (-)	5.7	5.73	-0.5%

Several off-design performance simulation calculations for the CUTSTF engine performance model were implemented. These simulations yielded off-design performance charts highlighting the effects of altitude, flight Mach number, ambient temperature and turbine entry temperature on net thrust and specific fuel consumption. Figure 4-2 highlights the variation of net thrust (Fn) as a function of altitude (Alt) and flight Mach number (MNf) for a fixed value of turbine entry temperature (TET). The value of TET chosen was that at the design point (i.e., top of climb) (TET=1340K).

Similarly, Figure 4-3 presents the variation of specific fuel consumption (SFC) as a function of altitude (Alt) and flight Mach number (MNf) for the same fixed value of TET. Figure 4-4 illustrates, in turn, the variation of net thrust (Fn) as a function of ambient temperature (Tamb) and turbine entry temperature (TET) at sea level static

condition (Alt=0m, MNf=0, ISA). Finally, Figure 4-5 shows the variation of specific fuel consumption (SFC) as a function of ambient temperature (Tamb) and turbine entry temperature (TET) at sea level static condition.

All four figures broadly follow the expected trend lines. Reference [46] provides detailed qualitative descriptions of the effects of altitude, flight Mach number, ambient conditions and turbine entry temperature on gas turbine engine performance with a detailed insight into the trade-off between improved thermal and propulsive efficiency.

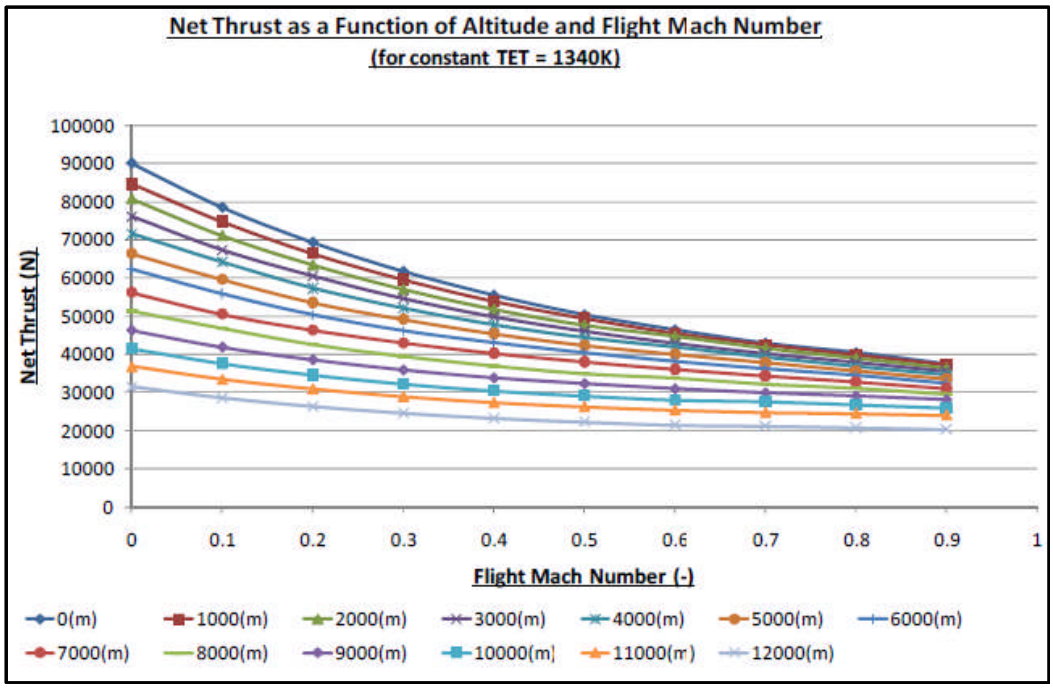

Figure 4-2 Net thrust vs. flight Mach number and altitude for a fixed TET (1340K) [39]

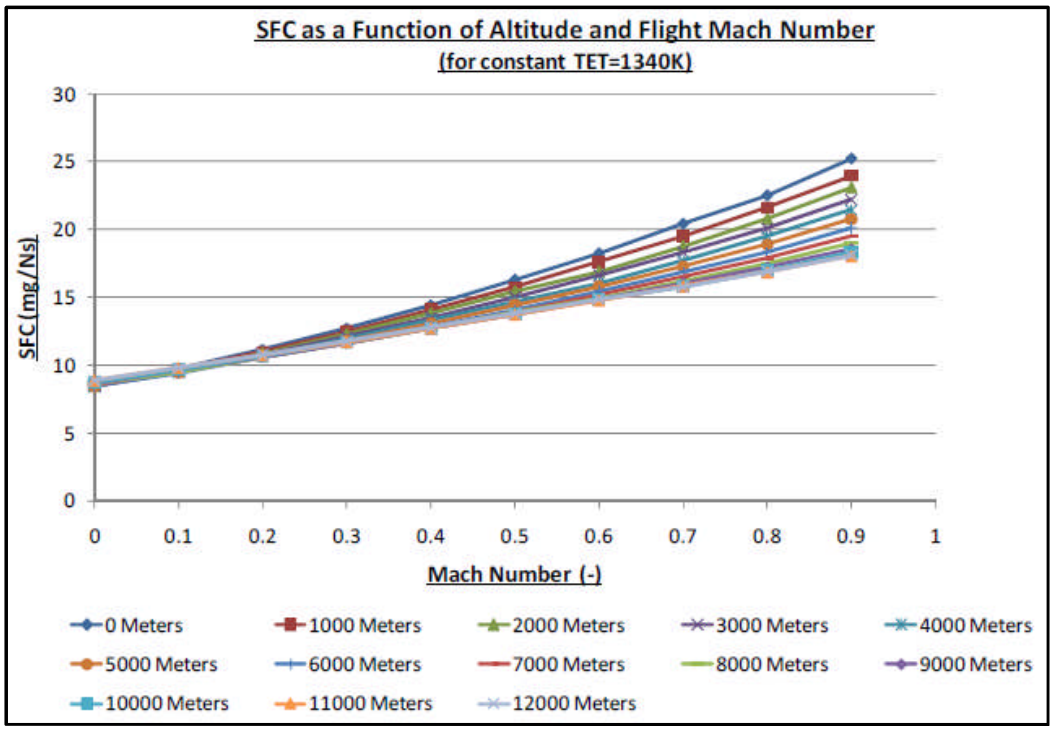

Figure 4-3 SFC vs. flight Mach number and altitude for a fixed TET (1340K) [39]

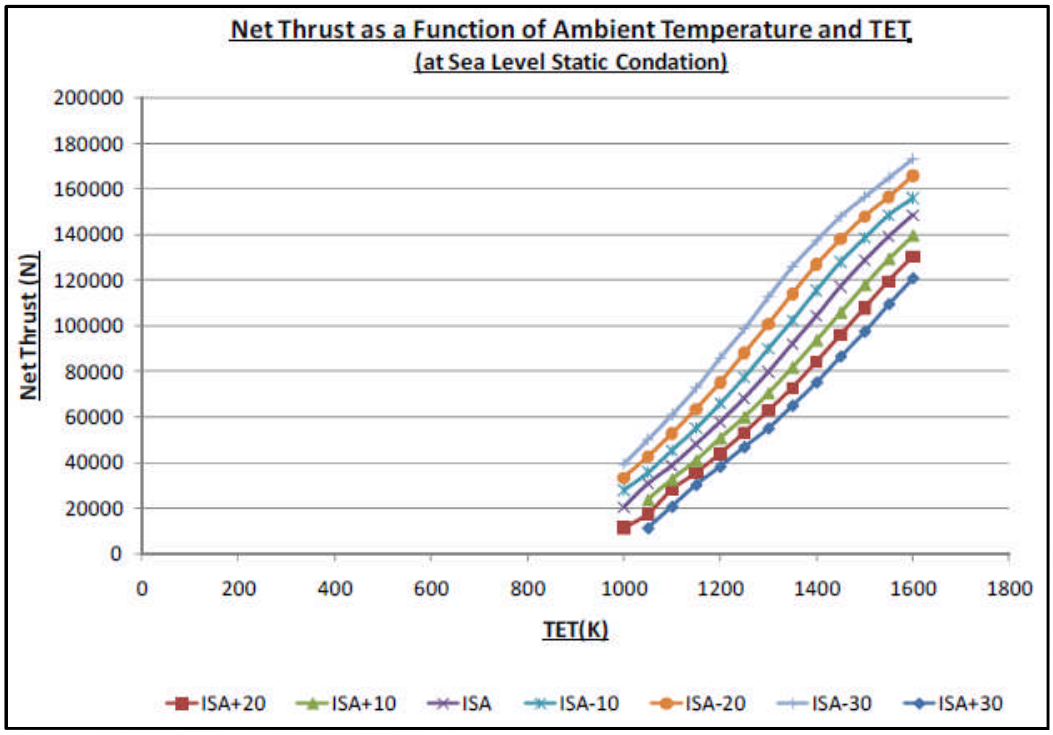

Figure 4-4 Net thrust vs. TET and ambient temperature at SLS condition [39]

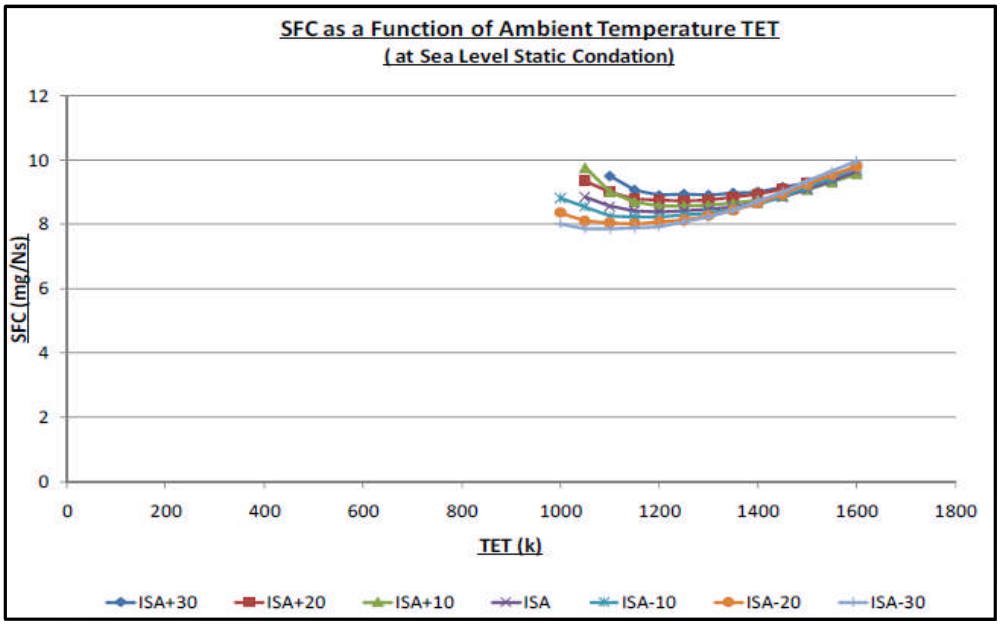

Figure 4-5 SFC vs. TET and ambient temperature at SLS condition [39]

Due to the feature of iteration calculation, TURBOMATCH needs some time to get converged results for each calculation requirement. For a single calculation task or a small number of calculations, the time consumption for each calculation from TURBOMATCH can be completely ignorable. However, when optimisation problems are implemented by means of evolution algorithms, such as Genetic Algorithms (like the flight trajectory optimisations investigated in this research work), a very large number of evaluation calculations have to be involved and, therefore, reducing the time consumption for each single calculation requirement from TURBOMATCH (as well as other calculations, for instance, engine gaseous emission calculation, etc.) can effectively contribute to the decrease in the total optimisation time.

Based on this consideration, an alternative empirical model built through Artificial Neural Networks (ANNs) and the performance database of CUTSTF which was created by means of TURBOMATCH was achieved successfully. The ANNs model replaced the actual physics-based model introduced above and was applied in the flight trajectory multidisciplinary optimisations of this research work.

The following section introduces the modelling methodology of ANNs, the entire modelling process (Figures 4-12 to 4-27) and main modelling results (Appendix A).

(Note: in the following Figure 4-6, P3T3 is an empirical emission model which was used to replace the stirred reactor emission model – a physics-based model with the same purpose to speed up the optimisation calculation. These two emission models are discussed in Chapter Five.)

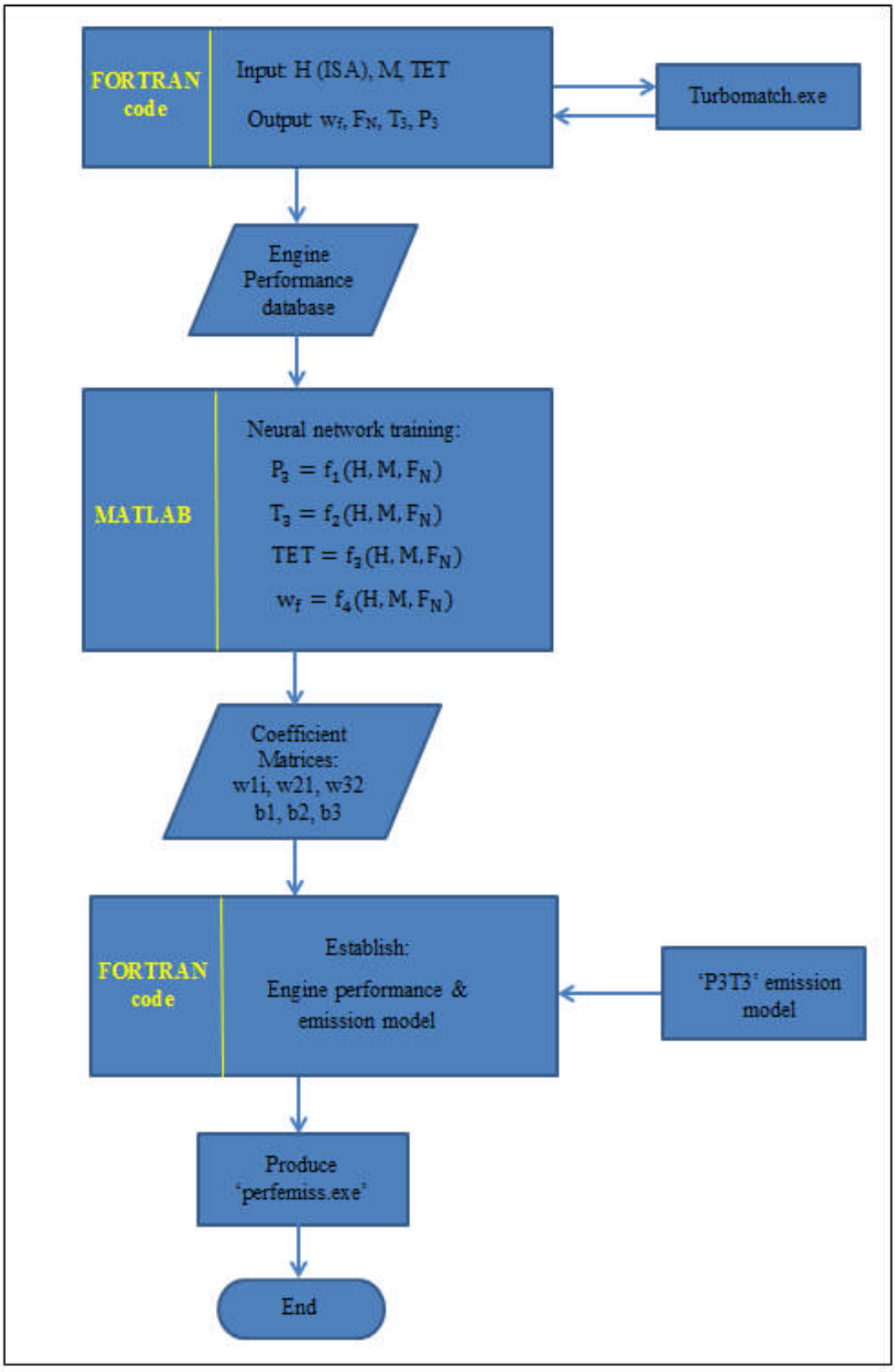

Figure 4-6 ANNs modelling of CUTSTF engine performance

Table 4-4 Performance database of CUTSTF engine (part)

```
********************************** CUTSTFEngine PROGRAM ***************************************

    This code CREATES the input file for, CALL the corresponding executable associated with,
and READS the output file produced by the CU Engine Performance Model TurboMatch.

    - Author: Weiqun Gu
              Cranfield University, 2011

*******************************************************************************************

Description of the output parameters:

POINT           Calculation point, in [--]
FLAG            TurboMatch exit flag, in [--]
WFUEL           Fuel Mass Flow rate, in [kg/s]
SFC             Specific Fuel Consumption, in [mg/Ns]
TET             Turbine Inlet Temperature, in [K]
CTAIR           Combustor Inlet Temperature (Air), in [K]
CPAIR           Combustor Inlet Pressure (Air) in [atm]
CWAIR           Combustor Inlet Mass Flow rate (Air) in [kg/s]
CTAMB           Flight Ambient Conditions - Temperature, in [K]
FNC             Engine Net Thrust Calculated, in [N]
ERR_FN          Error (in terms of Net Thrust) in predicting engine conditions, in [--]

Date (DD.MM.YYYY):      31- 3-2012
Time (HH.MM.SS)  :      12:24:27
```

POINT	ALT	MACH	Net Thrust	WFUEL	TET	CTAIR	CPAIR	CWAIR	CTAMB
[--]	[M]	[--]	[N]	[kg/s]	[K]	[K]	[atm]	[kg/s]	[K]
1	0.000000	0.000000	148740.000000	1.435200	1600.000000	846.169983	33.370998	62.465000	288.149994
2	0.000000	0.000000	147400.000000	1.411000	1590.000000	842.539978	33.047001	62.042000	288.149994
3	0.000000	0.000000	145100.000000	1.382200	1580.000000	838.140015	32.562000	61.341000	288.149994
4	0.000000	0.000000	143160.000000	1.355000	1570.000000	834.010010	32.130001	60.723999	288.149994
5	0.000000	0.000000	141200.000000	1.328100	1560.000000	829.880005	31.698000	60.102001	288.149994
6	0.000000	0.000000	139260.000000	1.301500	1550.000000	825.750000	31.268000	59.481998	288.149994
7	0.000000	0.000000	137200.000000	1.274600	1540.000000	821.369995	30.816999	58.813999	288.149994
8	0.000000	0.000000	135210.000000	1.248300	1530.000000	817.130005	30.381001	58.173000	288.149994
9	0.000000	0.000000	133220.000000	1.222300	1520.000000	812.890015	29.945000	57.528999	288.149994
10	0.000000	0.000000	131320.000000	1.197000	1510.000000	808.830017	29.528999	56.917999	288.149994
11	0.000000	0.000000	129070.000000	1.170000	1500.000000	804.320007	29.046000	56.179001	288.149994
12	0.000000	0.000000	126710.000000	1.142900	1490.000000	799.690002	28.552000	55.404999	288.149994
13	0.000000	0.000000	124270.000000	1.115600	1480.000000	794.979980	28.044001	54.603001	288.149994
14	0.000000	0.000000	121910.000000	1.089100	1470.000000	790.369995	27.554001	53.831001	288.149994
15	0.000000	0.000000	119600.000000	1.063300	1460.000000	785.789978	27.075001	53.075001	288.149994
16	0.000000	0.000000	117360.000000	1.037900	1450.000000	781.219971	26.603001	52.327999	288.149994
17	0.000000	0.000000	115200.000000	1.012500	1440.000000	776.669983	26.125999	51.563000	288.149994
18	0.000000	0.000000	112410.000000	0.984700	1430.000000	771.489990	25.551001	50.615002	288.149994
19	0.000000	0.000000	109940.000000	0.959210	1420.000000	767.059998	25.066000	49.819000	288.149994
20	0.000000	0.000000	107330.000000	0.933000	1410.000000	762.200012	24.531000	48.937000	288.149994

Artificial Neural Networks (ANNs)

Artificial Neural Networks are among the numerous data mining techniques which are used to “find pattern in data” or “extract information from a data set and transform it into an understandable structure for further use.” [47]

ANNs originated from the artificial intelligence discipline and contain key features of neurons in the human brain and process data in the manner analogous to the brain.

ANNs can be trained to identify complex relationships in data. Compared with classical statistical methods, such as regression and ANOVA (analysis of variance), ANNs “can fit data where the relationship between independent variables and dependent variables is nonlinear and where the specific form of the nonlinear relationship is unknown” [47].

Despite of the fact that many different kinds of ANNs exist, FeedForward Neural Networks (FFNNs) is undoubtedly one of the most popular. FFNN is the network

"where the signal is passed from an input layer of neurons through one or more hidden layer(s) and to an output layer of neurons" [47].

The following Figures 4-7 and 4-8 illustrate respectively the overall architecture of a FFNN with one hidden layer and the corresponding details of the hidden layer with S neurons.

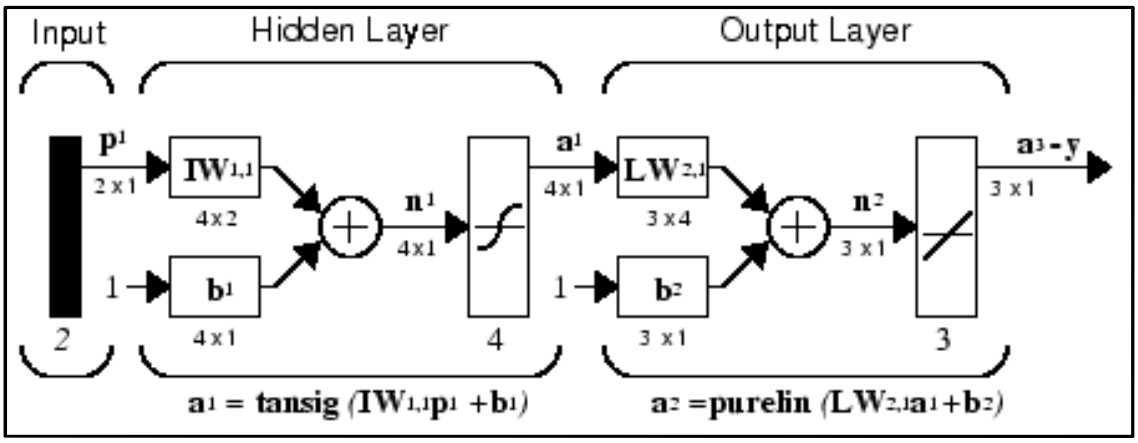

Figure 4-7 Overall architecture of a FFNN with one hidden layer [48]

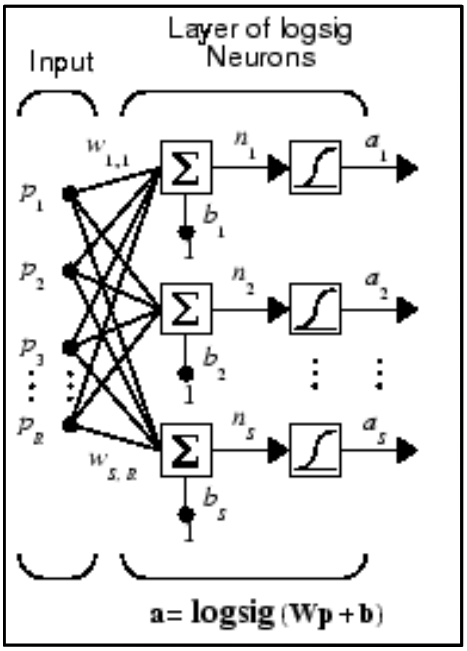

Figure 4-8 Full details of a hidden layer with S neurons [48]

From the above Figure 4-7, it can be observed that the FFNN comprises three different layers, namely, Input Layer, Hidden Layer and Output Layer. The Input Layer contains R input nodes and each node represents a separate independent variable x_i, i =

$1,2,3,\cdots,R$. These input nodes are connected to the S neurons in the intermediate (i.e., hidden) layer (where the processing to the input data through the transfer function f (or called threshold or activation function) is implemented), and further, these hidden neurons are connected to the nodes in Output Layer. Each node in Output Layer represents a separate dependent variable, $y_j, j = 1,2,3,\cdots,m$. In practice, it is more common for a FFNN to have only one dependent variable.

Commonly, during the design of FFNNs, each node in Input Layer is connected to each one in Hidden Layer and correspondingly each of nodes in Hidden Layer is also connected to each node in Output Layer.

As for the transfer function mentioned above, theoretically, neurons in either Hidden Layer or Output Layer can use any differentiable transfer function to produce their output. In practice, there are three transfer functions most-commonly used in multilayer networks, that is, 'log-sigmoid transfer function', 'tan-sigmoid transfer function' and 'linear transfer function'. And the characteristics of the three transfer functions are shown as follows.

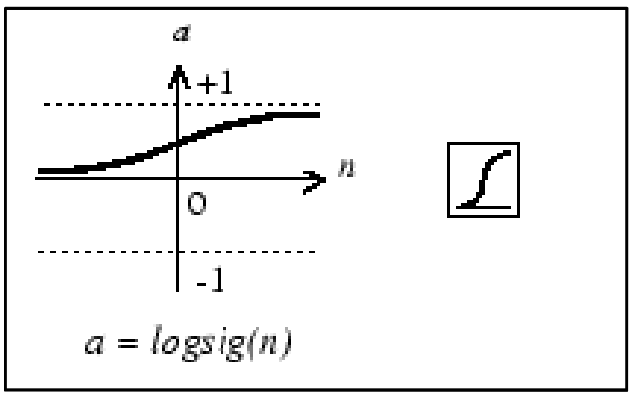

Figure 4-9 Log-sigmoid transfer function [48]

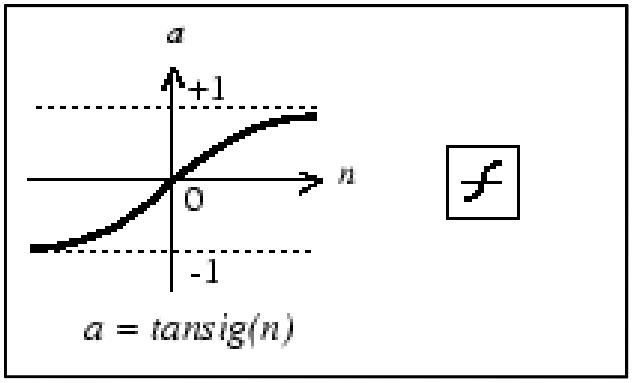

Figure 4-10 Tan-sigmoid transfer function [48]

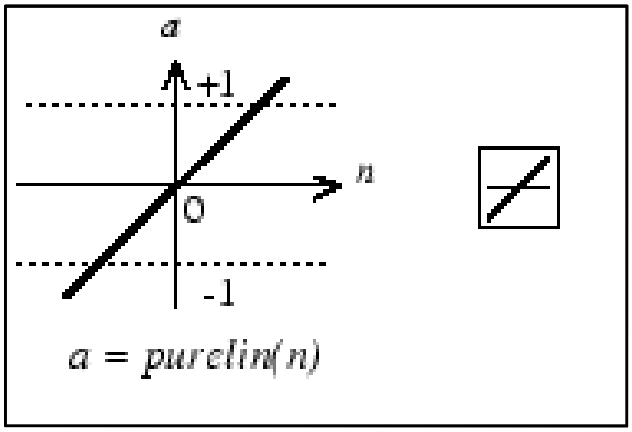

Figure 4-11 Linear transfer function [48]

For a FeedForward Neural Network, such architecture with one or more hidden layers of sigmoid neurons followed by an output layer of linear neurons is often adopted. Multiple hidden layers with non-linear transfer functions enable NN to learn non-linear relationships between independent variable(s) and dependent variable(s) and the linear output layer is usually used in function fitting problems.

After the architecture of a FFNN is created and before it can be put into actual applications, the values of all weights and biases of the network have to be determined. This can be achieved by so-called network training.

In fact, “the process of training a neural network involves tuning the values of the weights and biases of the network to optimize network performance” [48]. Usually, the network performance function for FFNNs is Mean Square Error (MSE) which is defined as “the average squared error between the network outputs a and the target outputs t as shown in the following equation (4-1).

$$\mathrm{MSE} = \frac{1}{\mathrm{N}}\sum_{\mathrm{i}=1}^{\mathrm{N}}(\mathrm{e_i})^2 = \frac{1}{\mathrm{N}}\sum_{\mathrm{i}=1}^{\mathrm{N}}(\mathrm{t_i} - \mathrm{a_i})^2 \quad (4\text{-}1)$$

Theoretically, the above optimisation process about the network performance function can be performed by any standard numerical optimisation algorithm. However, there exist some gradient- or Jacobian-based methods which have excellent performance for FFNN's training. Among them, a network training function named as 'trainlm', which is based on Levenberg-Marquardt optimisation algorithm, appears to be the fastest method and is often highly recommended as a first-choice for the training of moderate-sized (up to several hundred weights) FFNNs. The basic principle of 'trainlm' is: firstly, by a standard backpropagation technique the Jacobian matrix can be determined; and then, the increments in variables (weights and biases) can be calculated through the following equations:

$$\begin{gathered} \mathrm{JJ} = \mathrm{JX} * \mathrm{JX} \\ \mathrm{JE} = \mathrm{JX} * \mathrm{E} \\ \mathrm{dX} = -(\mathrm{JJ} + \mathrm{I} * \mathrm{mu})\backslash\mathrm{JE} \end{gathered} \quad (4\text{-}2)$$

Where, JX is Jacobian matrix determined by standard backpropagation technique; E is all errors; I denotes identity matrix; mu is the adaptive value (when mu takes the value of zero, the above Levenberg-Marquardt algorithm is just Newton's method, while mu is large, the optimisation algorithm becomes gradient descent).

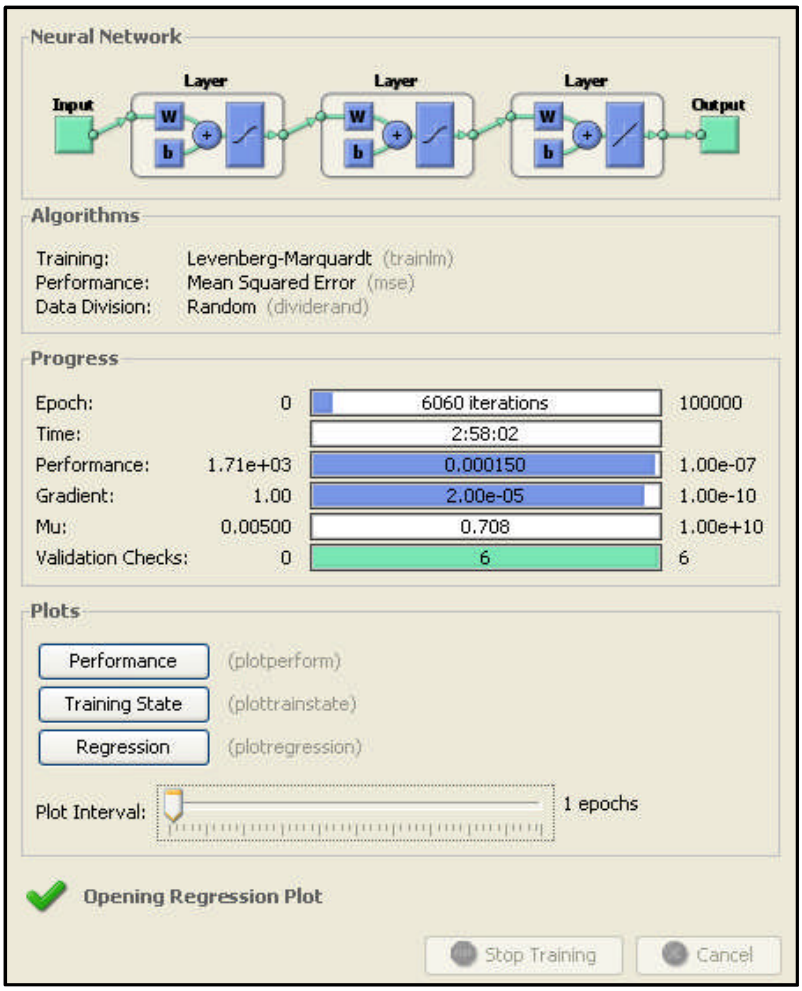

Figure 4-12 Neural Network Training for Function $P_3 = f_1(H, M, F_N)$

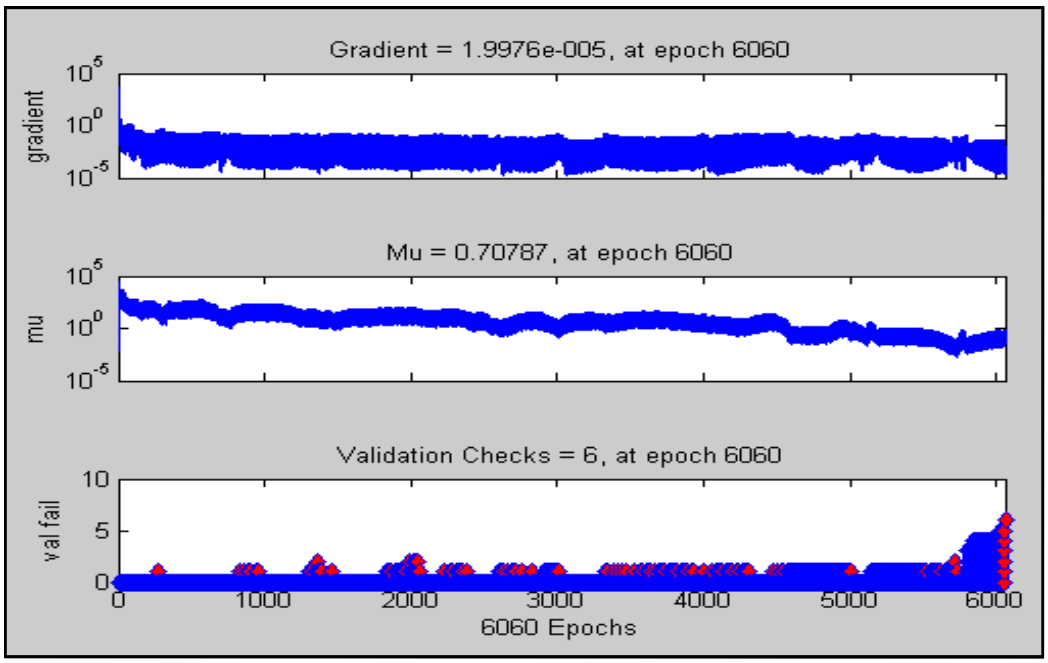

Figure 4-13 Neural Network Training State for Function $P_3 = f_1(H, M, F_N)$

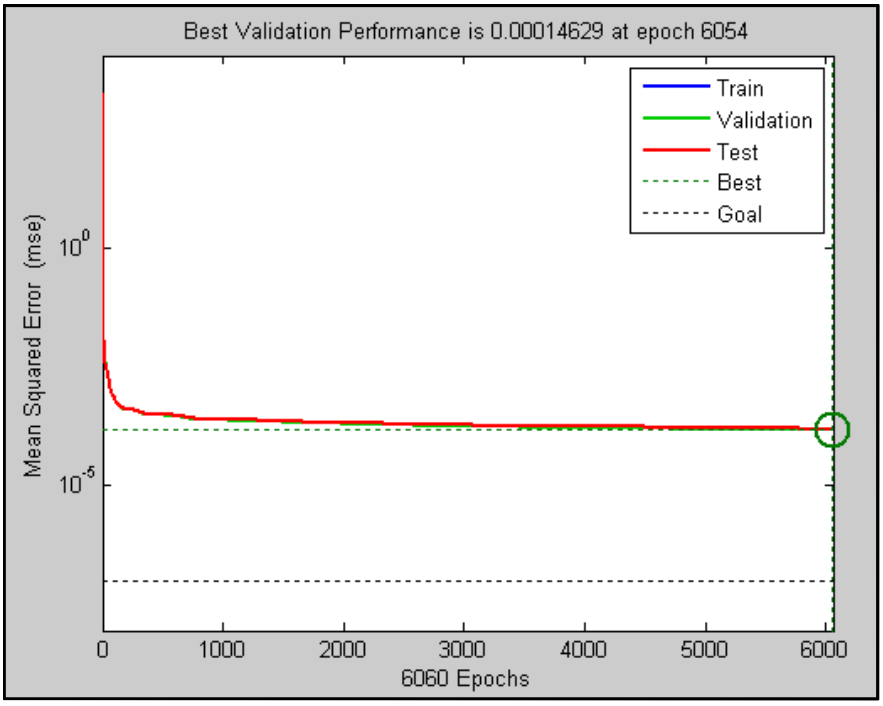

Figure 4-14 Neural Network Training Performance for Function $P_3 = f_1(H, M, F_N)$

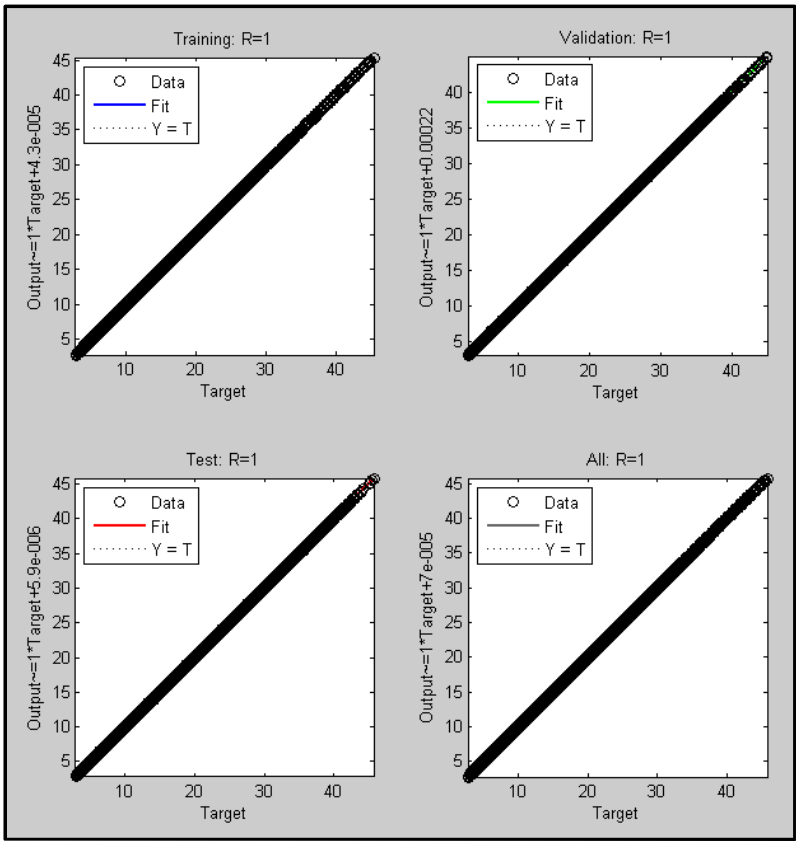

Figure 4-15 Neural Network Training Regression for Function $P_3 = f_1(H, M, F_N)$

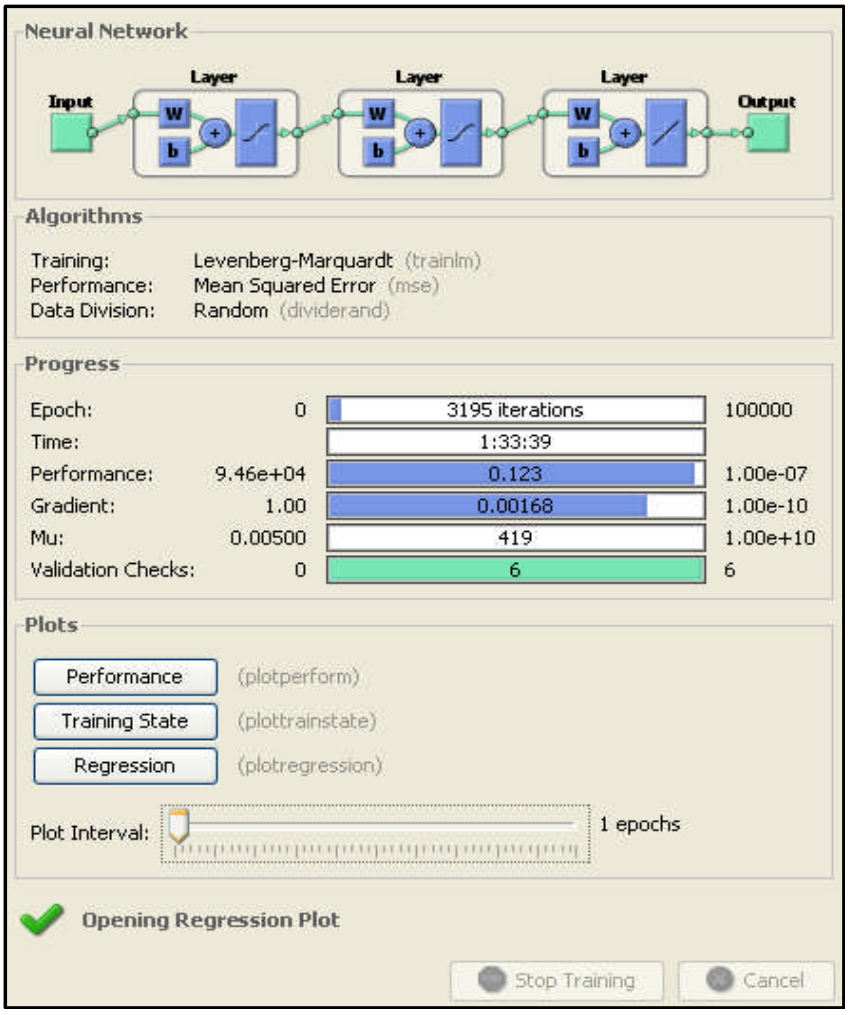

Figure 4-16 Neural Network Training for Function $T_3 = f_2(H, M, F_N)$

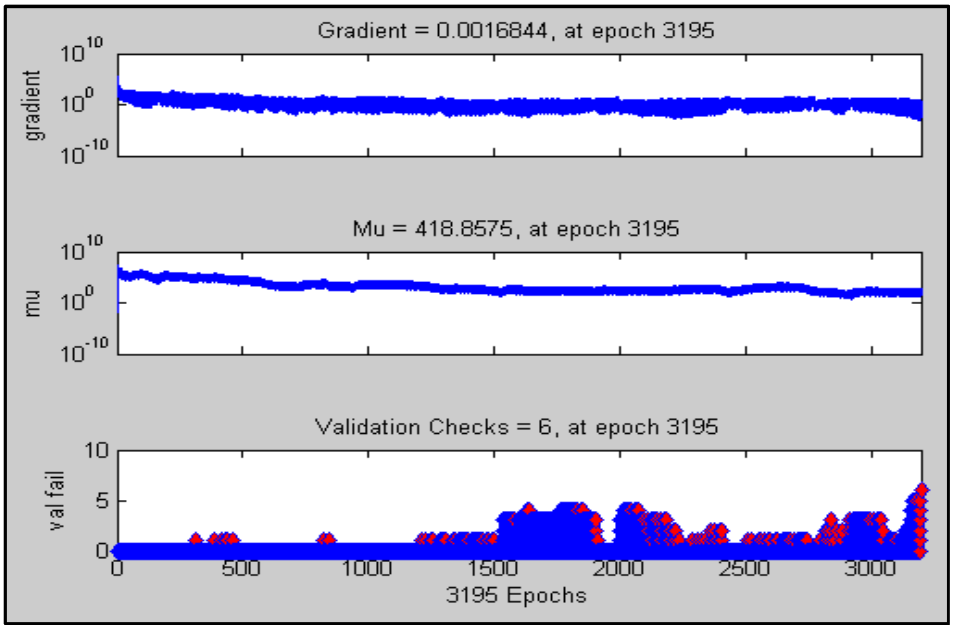

Figure 4-17 Neural Network Training State for Function $T_3 = f_2(H, M, F_N)$

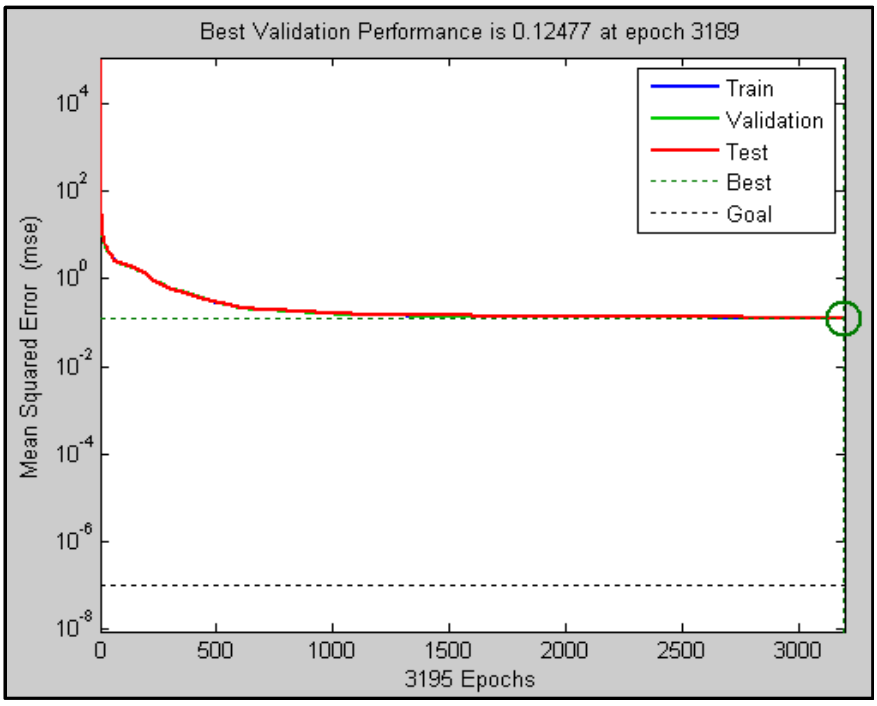

Figure 4-18 Neural Network Training Performance for Function $T_3 = f_2(H, M, F_N)$

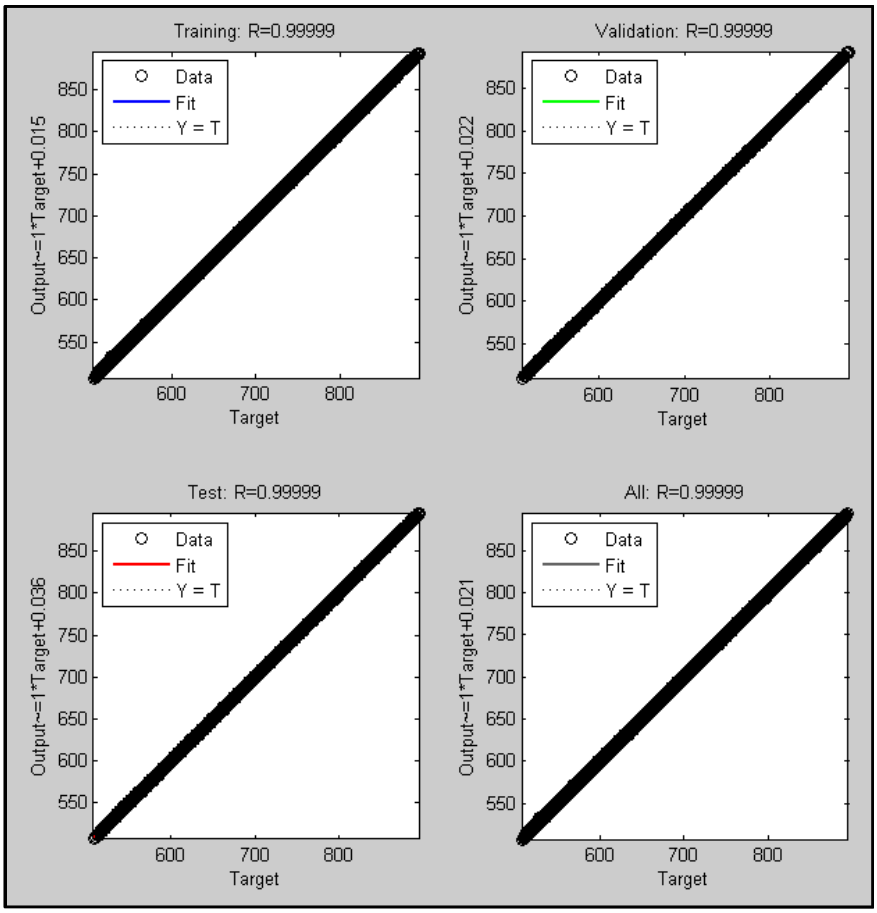

Figure 4-19 Neural Network Training Regression for Function $T_3 = f_2(H, M, F_N)$

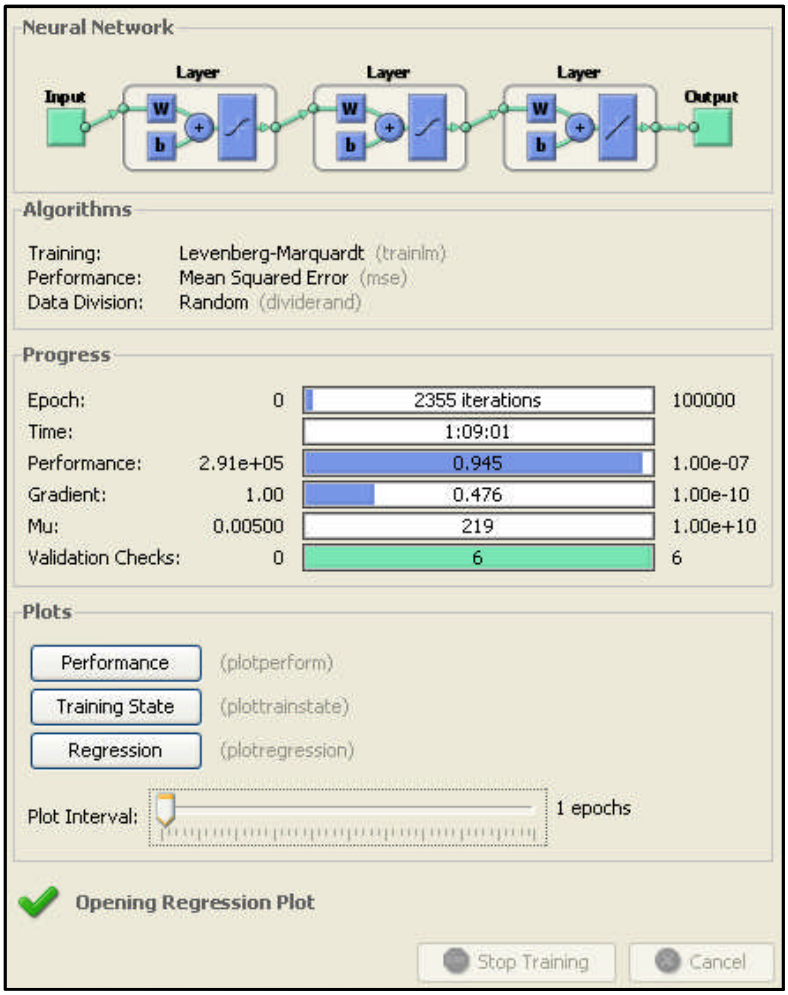

Figure 4-20 Neural Network Training for Function TET $= \mathbf{f_3(H, M, F_N)}$

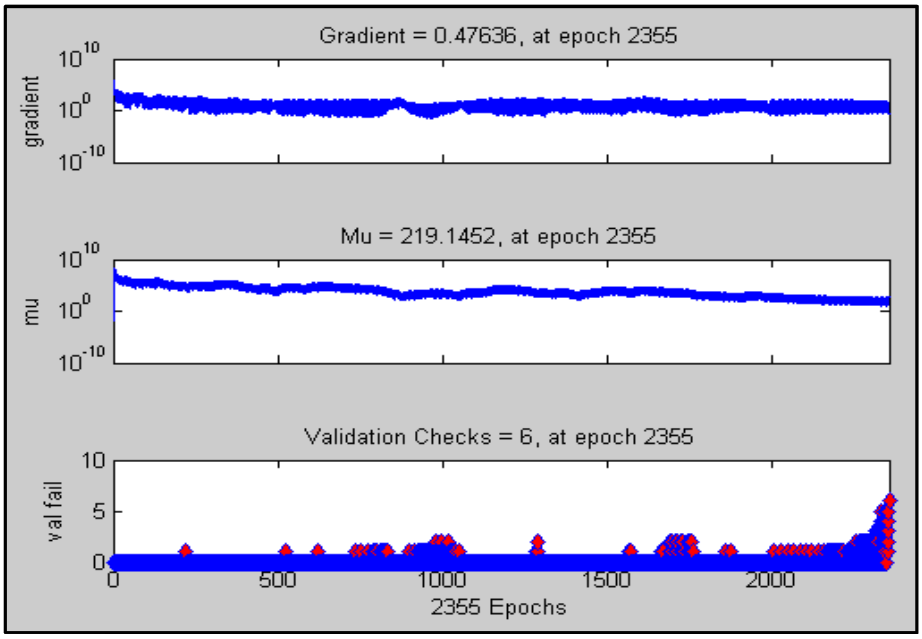

Figure 4-21 Neural Network Training State for Function TET $= \mathbf{f_3(H, M, F_N)}$

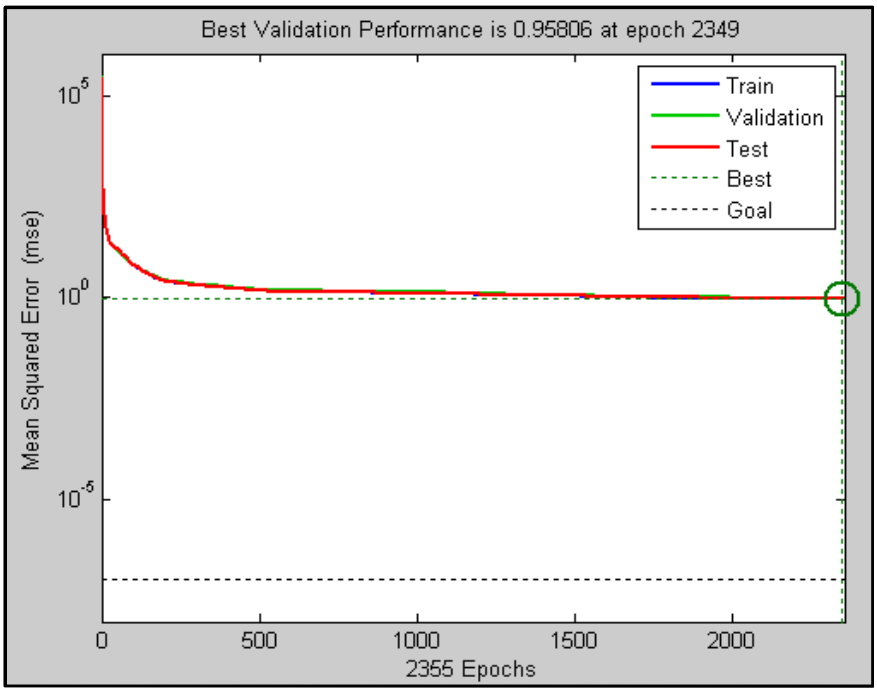

Figure 4-22 Neural Network Training Performance for Function TET = $f_3(H, M, F_N)$

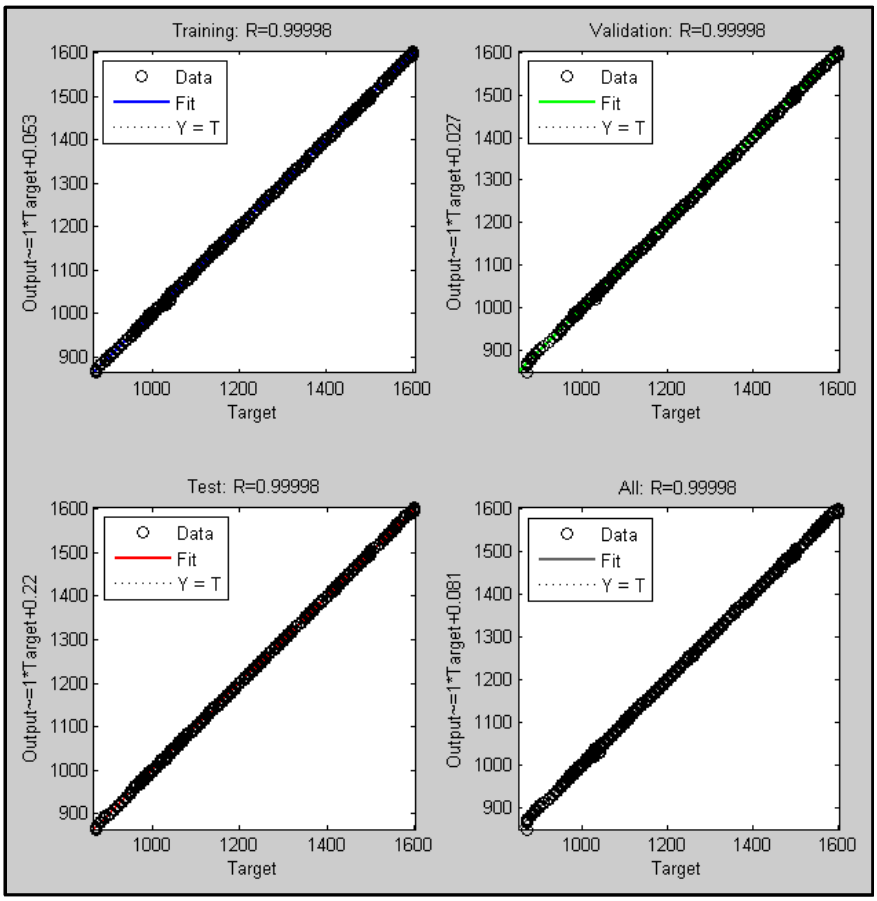

Figure 4-23 Neural Network Training Regression for Function TET = $f_3(H, M, F_N)$

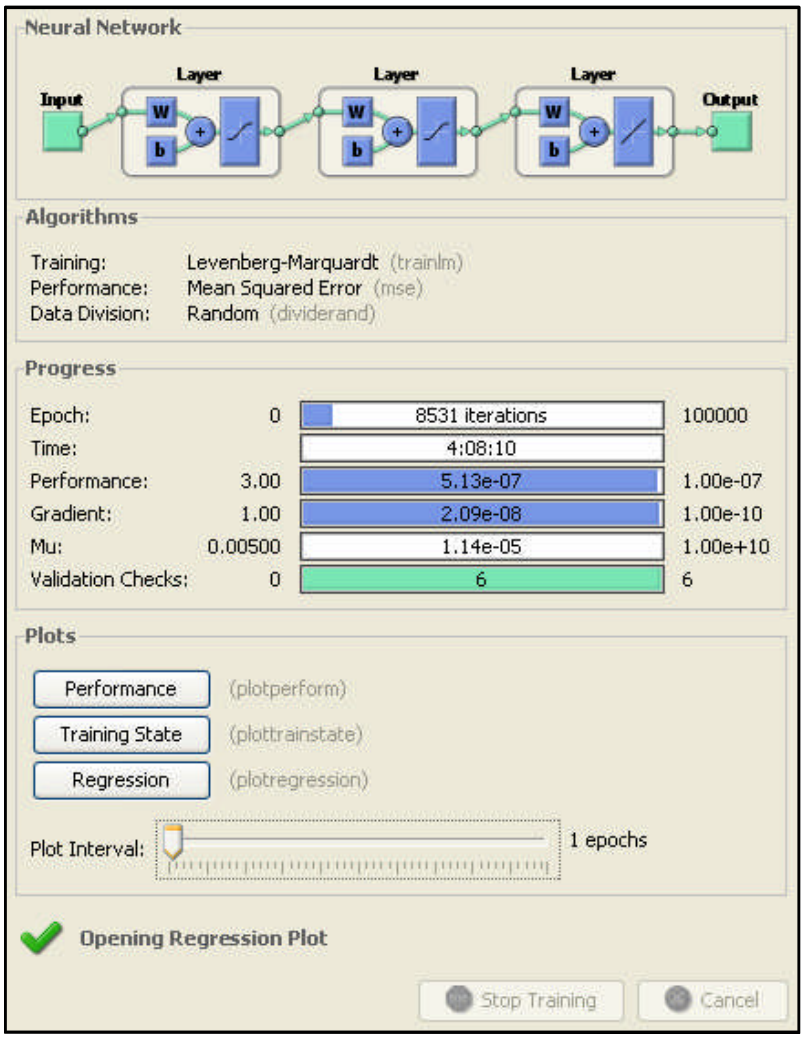

Figure 4-24 Neural Network Training for Function $W_f = f_4(H, M, F_N)$

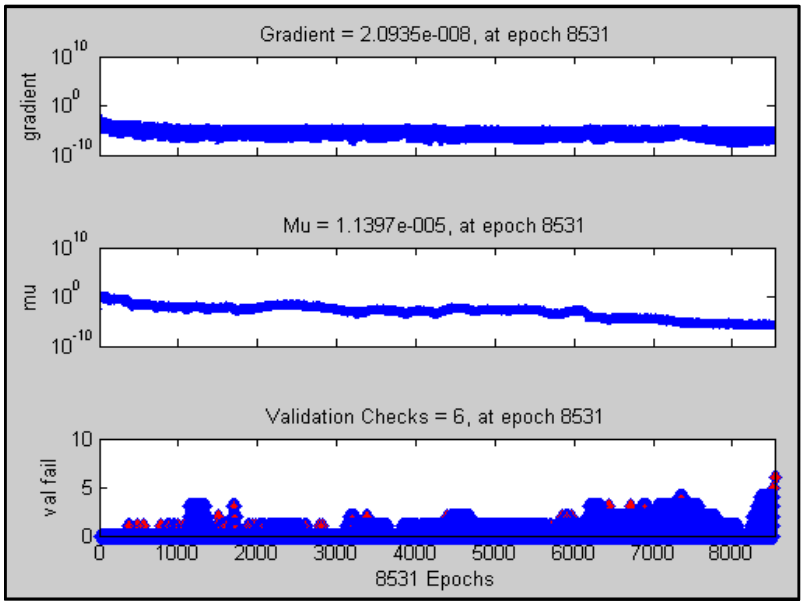

Figure 4-25 Neural Network Training State for Function $W_f = f_4(H, M, F_N)$

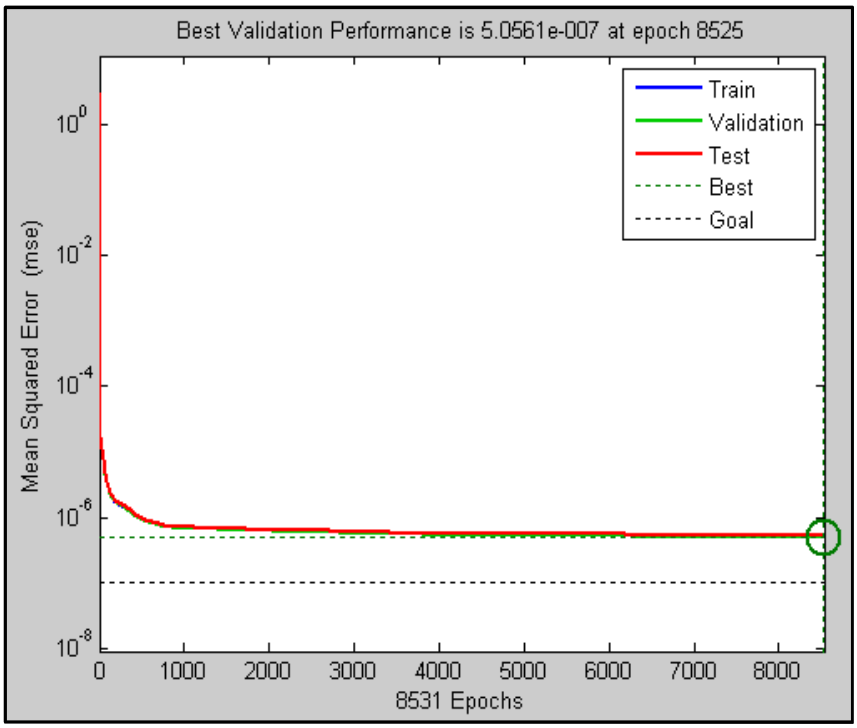

Figure 4-26 Neural Network Training Performance for Function $W_f = f_4(H, M, F_N)$

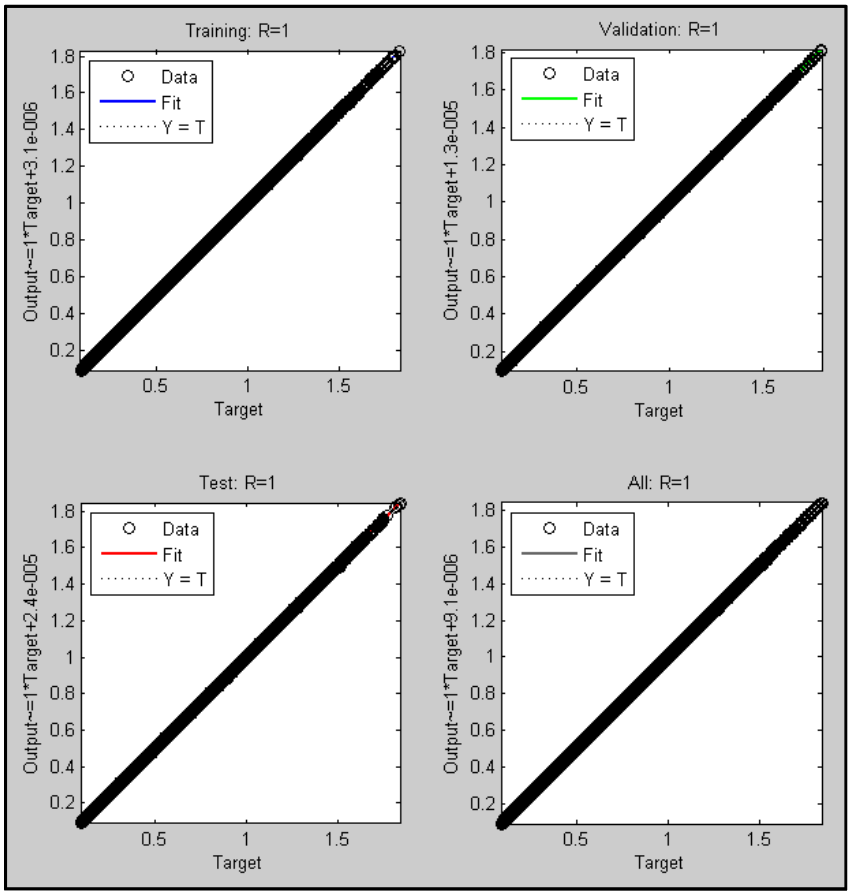

Figure 4-27 Neural Network Training Regression for Function $W_f = f_4(H, M, F_N)$

4.2 Turboprop Engine Powering CUTPDAC

The engine model which is used for driving the aircraft CUTPDAC is a three-shaft free-turbine turboprop, based on the PW127F engine which is the engine of choice for the ATR-72-500 aircraft [49, 50]. For the purpose of convenience, this engine model is referred as the CUTPROP (**C**ranfield **U**niversity **T**urbo**prop**). The following Figure 4-28 is a schematic of the CUTPROP engine model.

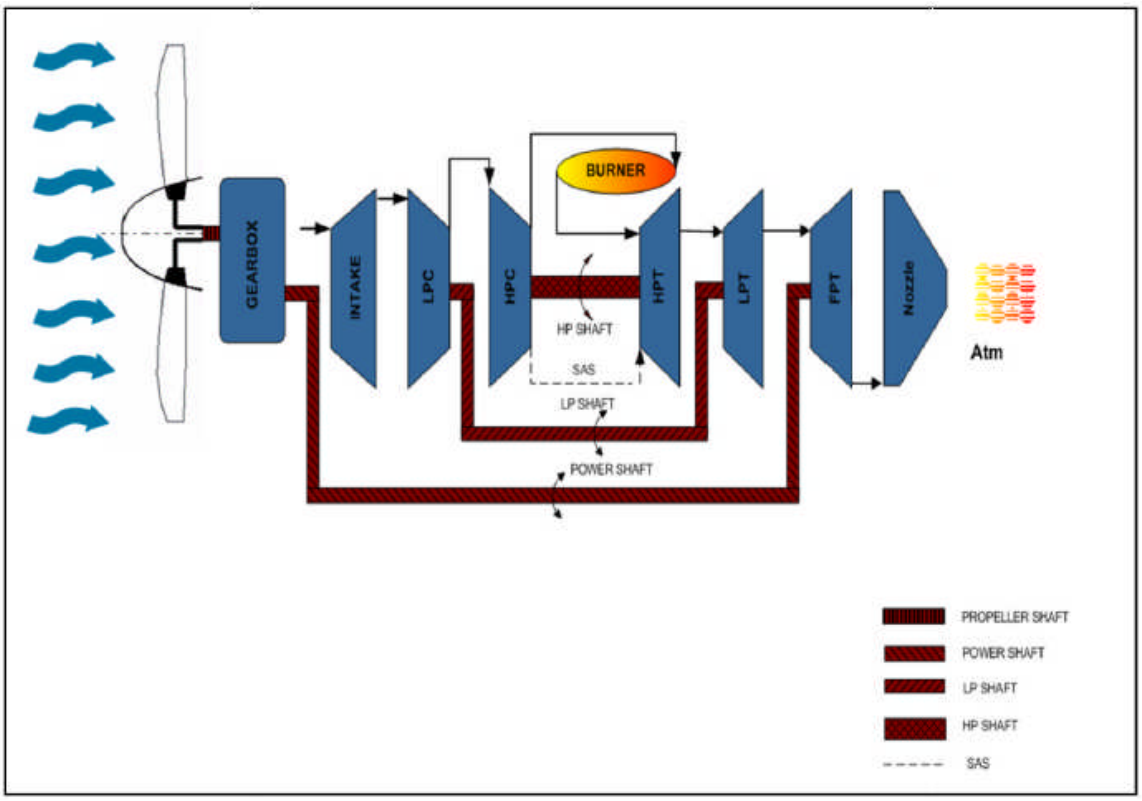

Figure 4-28 CUTPROP engine model

The design point of the CUTPROP engine model was chosen at Max. cruise point (i.e. Alt. 4876.8 m, M 0.44) with the intake total pressure recovery of 1.0 under International Standard Atmosphere (ISA) conditions. Several iterations were performed at design and off-design point conditions by using TURBOMATCH to match the performance of the model with data obtained from the public domain [49] and [50] for a three-shaft free-turbine turboprop engine. A summary of these available data is presented in the following Table 4-5.

Table 4-5 Data of a three-shaft free-turbine turboprop engine [49, 50]

Engine Type	Three-shaft free-turbine turboprop
Take-off Equivalent Shaft Power (kW), to 34.9°C	2147.6
Take-off Shaft Power (kW), to 34.9°C	2051
Equivalent Specific Fuel Consumption (μg/J)	77.6
Max cruise Equivalent Shaft Power (kW), to 22.6°C	1667
Max cruise Shaft Power (kW), to 22.6°C	1589
Econ. cruise Shaft Power (kW)	1864
Overall Pressure Ratio	14.7

At the design point, values of engine mass flow rate, turbine entry temperature (TET), component efficiencies and compressor bleed for turbine cooling, etc. were guessed and several iterations were performed to match the required engine performance at design and off-design conditions (take-off and econ. cruise). A summary of the parameters used for the CUTPROP engine model design point simulation and a comparison of the results from design point/off-design simulations with required values are presented in the following Table 4-6 and Table 4-7 respectively. It was observed that the discrepancies between the required and achieved values are small and, therefore, the CUTPROP performance model is deemed acceptable.

Table 4-6 Design point data of CUTPROP engine performance model (Max. cruise: Alt.4876.8m, M0.44, ISA)

No.	Items	Parameter Values
1	Flight Altitude	4876.8m
2	Flight Mach. Number	0.44
3	Dev. from Stand. Temp.	0.0 (ISA)
4	OPR	14.7
5	COT/TET	1185.0K
6	Air Mass Flow	8.2kg/s
7	Intake Total Pressure Recovery	1.0

8	LP compressor PR	4.03
9	LP compressor Isentropic Efficiency	0.82
10	Total Pressure Loss between LPC and HPC	1%
11	HP compressor PR	3.65
12	HP compressor Isentropic Efficiency	0.82
13	Cooling air at HPC outlet	10%
14	Combustor Total Pressure Loss	5%
15	Combustion Efficiency	0.995
16	Power take off from HP Turbine	0.0kW
17	HP Turbine Isentropic Efficiency	0.88
18	Power take off from LP Turbine	0.0kW
19	HP Turbine Isentropic Efficiency	0.9
20	Total Pressure Loss between LPT and Free Power Turbine	1%
21	Shaft Power output from FPT	1589kW
22	FPT Isentropic Efficiency	0.91
23	Propeller Efficiency	0.85
24	Fixed Convergent Nozzle	

Table 4-7 A comparison between CUTPROP simulation results and public-domain data

	Parameters	CUTPROP	Public-domain	Discrepancy
D.P. (Max Cruise, Standard Day, 15˚C)	Shaft Power (kW)	1589	1589	0.0%
	Equivalent Shaft Power (ekW)	1666.6	1667	-0.024%
	E.S.F.C. (μg/J)	66.4	Unknown	—
	COT/TET (K)	1185	Unknown	—
Max Cruise (Hot Day, 22.6˚C)	Shaft Power (kW)	1589.6	1589	0.04%
	Equivalent Shaft Power (ekW)	1665.8	1667	-0.07%
	E.S.F.C. (μg/J)	66.9	Unknown	—
	COT/TET (K)	1212	Unknown	—
T-O (Standard Day, 15˚C)	Shaft Power (kW)	2050.9	2051	-0.007%
	Equivalent Shaft Power (ekW)	2180.6	2147.6	1.54%

	E.S.F.C. (µg/J)	77.4	77.6	-0.26%
	COT/TET (K)	1242	Unknown	—
T-O (Hot day, 34.9˚C)	Shaft Power (kW)	2058.2	2051	0.35%
	Equivalent Shaft Power (ekW)	2184.1	2147.6	1.7%
	E.S.F.C. (µg/J)	78.8	Unknown	—
	COT/TET (K)	1312	Unknown	—
Econ. Cruise	Shaft Power (kW)	1864.8	1864 (Inferred)	0.04%
	Equivalent Shaft Power (ekW)	2008.6	Unknown	—
	E.S.F.C. (µg/J)	62.4	Unknown	—
	COT/TET (K)	1363	Unknown	—

Several off-design performance simulation calculations for the CUTPROP engine model were performed. These simulations yielded off-design performance charts highlighting the effects of altitude, flight Mach number, ambient temperature and turbine entry temperature on shaft power (SP), equivalent shaft power (ESP) and equivalent specific fuel consumption (ESFC).

Figure 4-29 and Figure 4-30 highlight the variation of equivalent shaft power (ESP) and shaft power (SP) respectively as a function of altitude (Alt) and flight Mach number (MNf) for a fixed value of turbine entry temperature (TET). The value of TET chosen is that at the design point (Max. cruise), i.e., TET=1185K.

Similarly, Figure 4-31 presents the variation of equivalent specific fuel consumption (ESFC) as a function of altitude (Alt) and flight Mach number (MNf) for the same fixed value of TET.

Further, Figure 4-32 and 4-33 illustrate respectively the variation of equivalent shaft power (ESP) and shaft power (SP) as a function of ambient temperature (T_{amb}) and turbine entry temperature (TET) at Econ.Cruise condition (Alt=7010m, MNf=0.41). Finally, Figure 4-34 shows the variation of equivalent specific fuel consumption (ESFC) as a function of T_{amb} and TET at Econ. Cruise condition.

All six figures follow the expected trend lines. Reference [46] provides detailed qualitative description of the effects of altitude, flight Mach number, ambient conditions and turbine entry temperature on gas turbine performance.

The integration method of the performance model of the turboprop engine and the propeller performance model, as well as the determination of TET when flight mission is performed, is illustrated in Figure 4-35 as a flow chart.

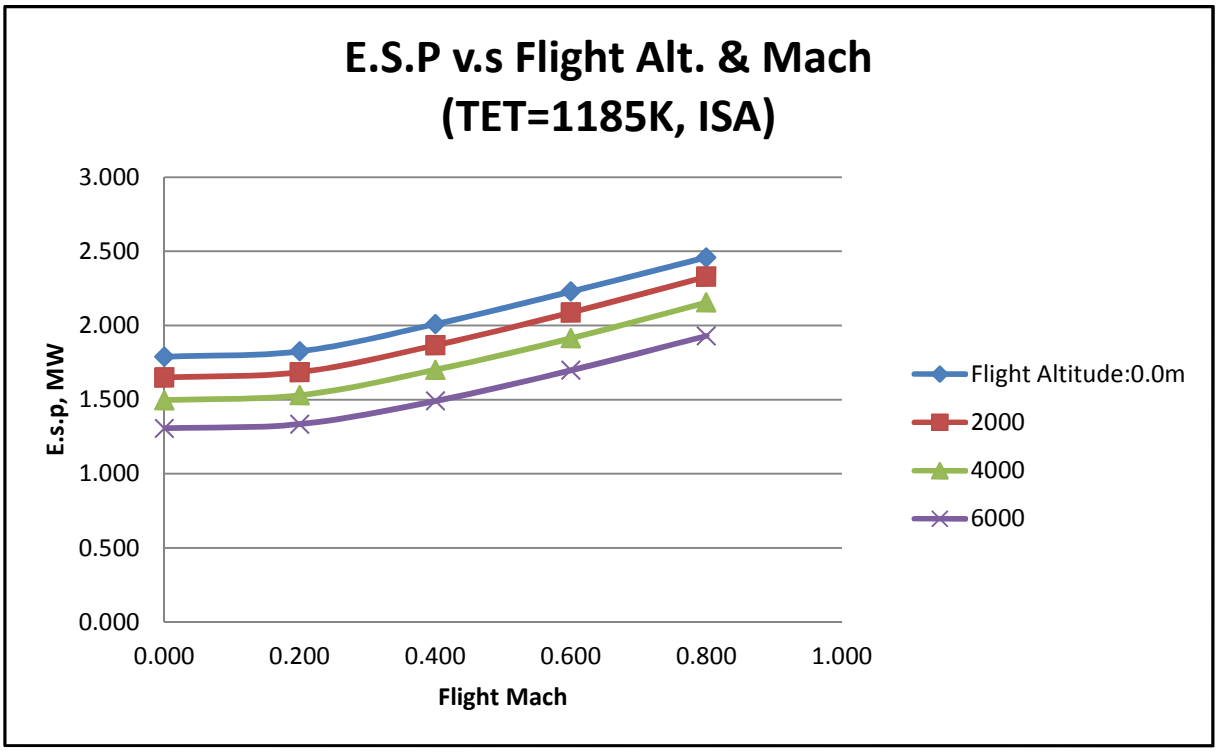

Figure 4-29 Influence of Flight Alt. & Mach on Equivalent Shaft Power

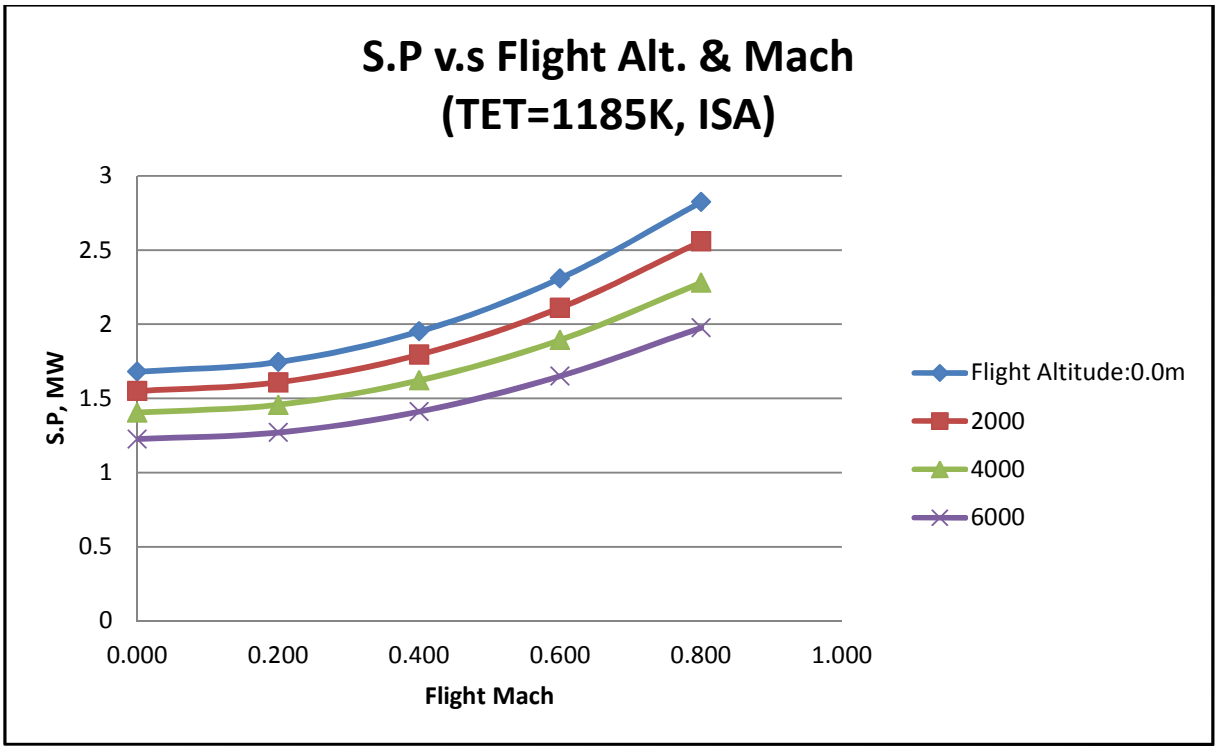

Figure 4-30 Influence of Flight Alt. & Mach on Shaft Power

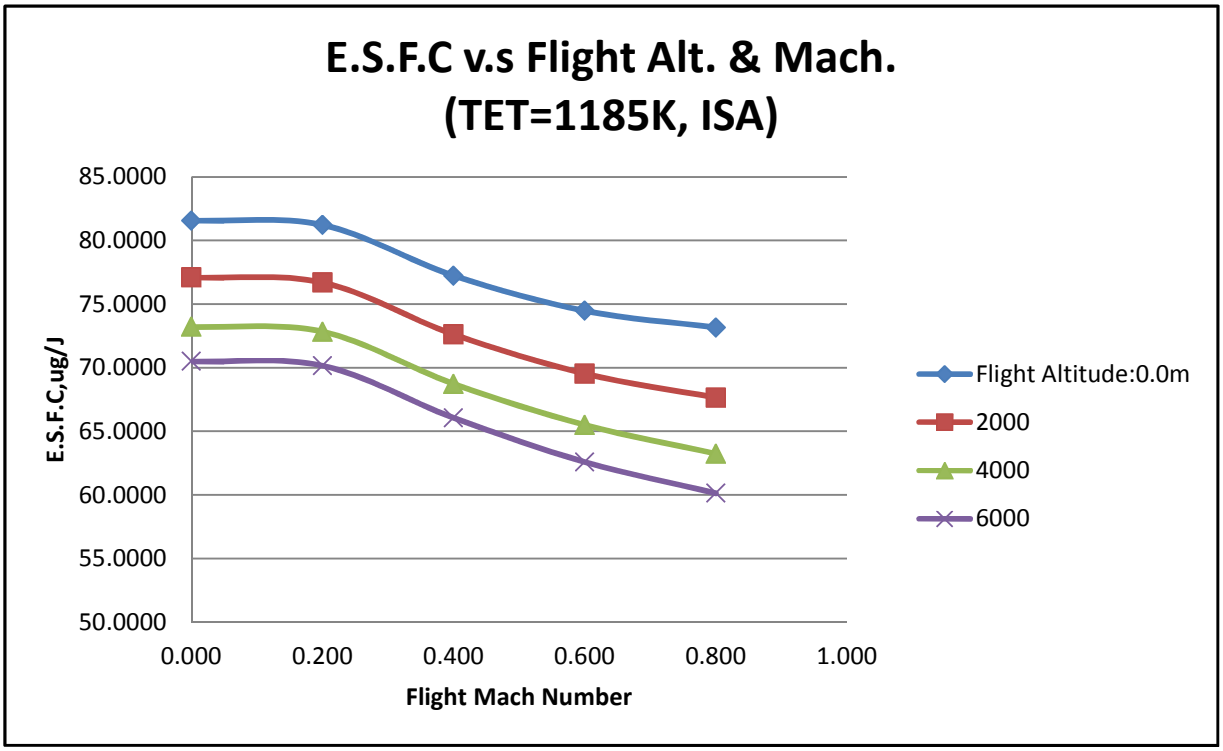

Figure 4-31 Influence of Flight Alt. & Mach on Equivalent Specific Fuel Consumption

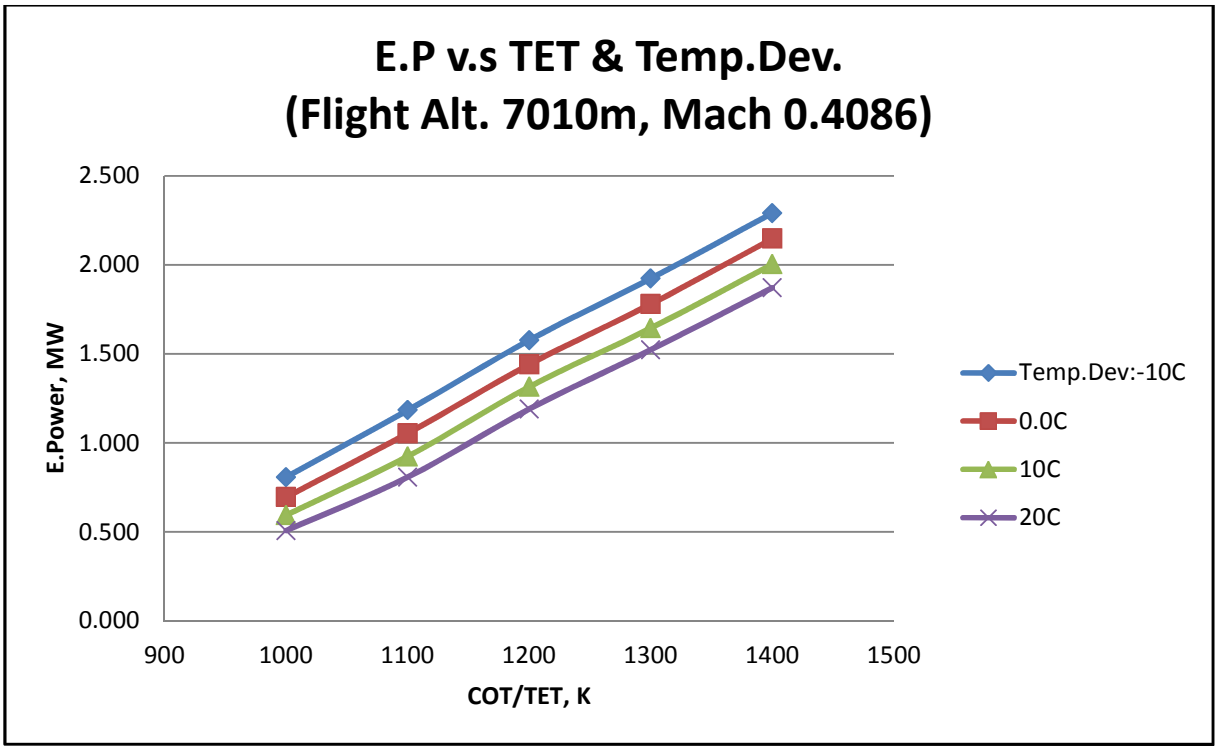

Figure 4-32 Influence of TET & temperature deviation on Equivalent Shaft Power

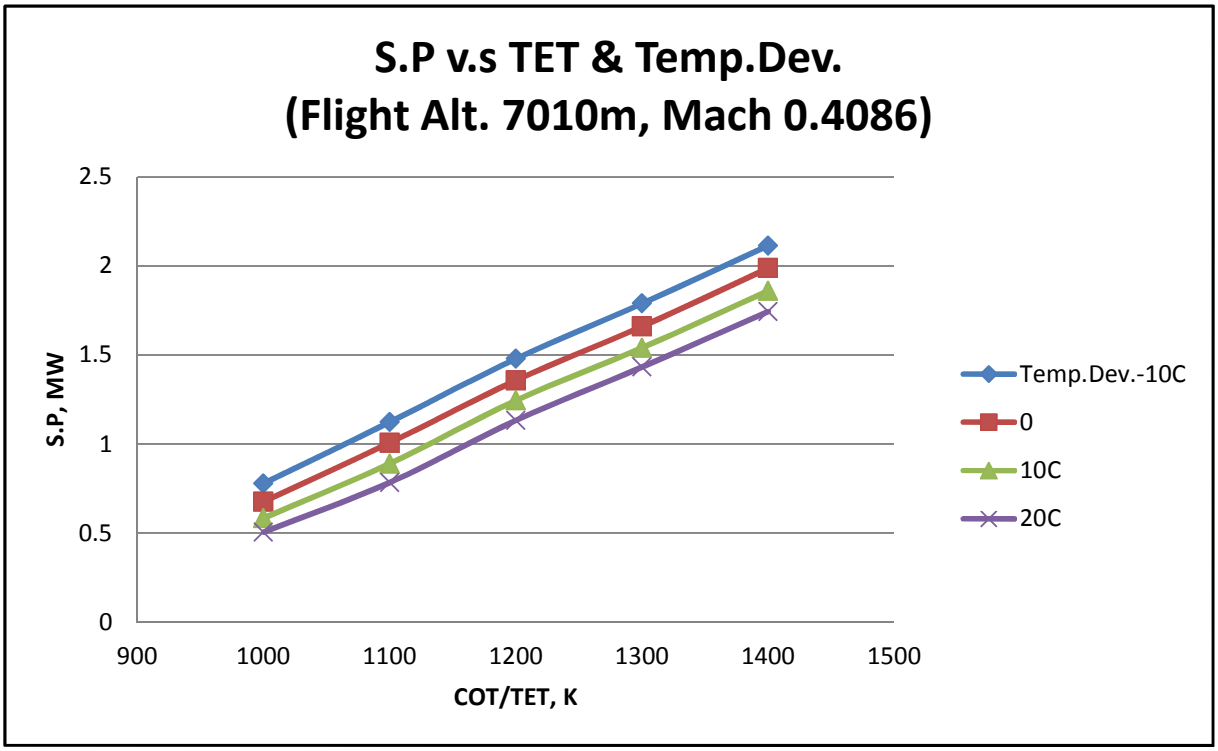

Figure 4-33 Influence of TET & temperature deviation on Shaft Power

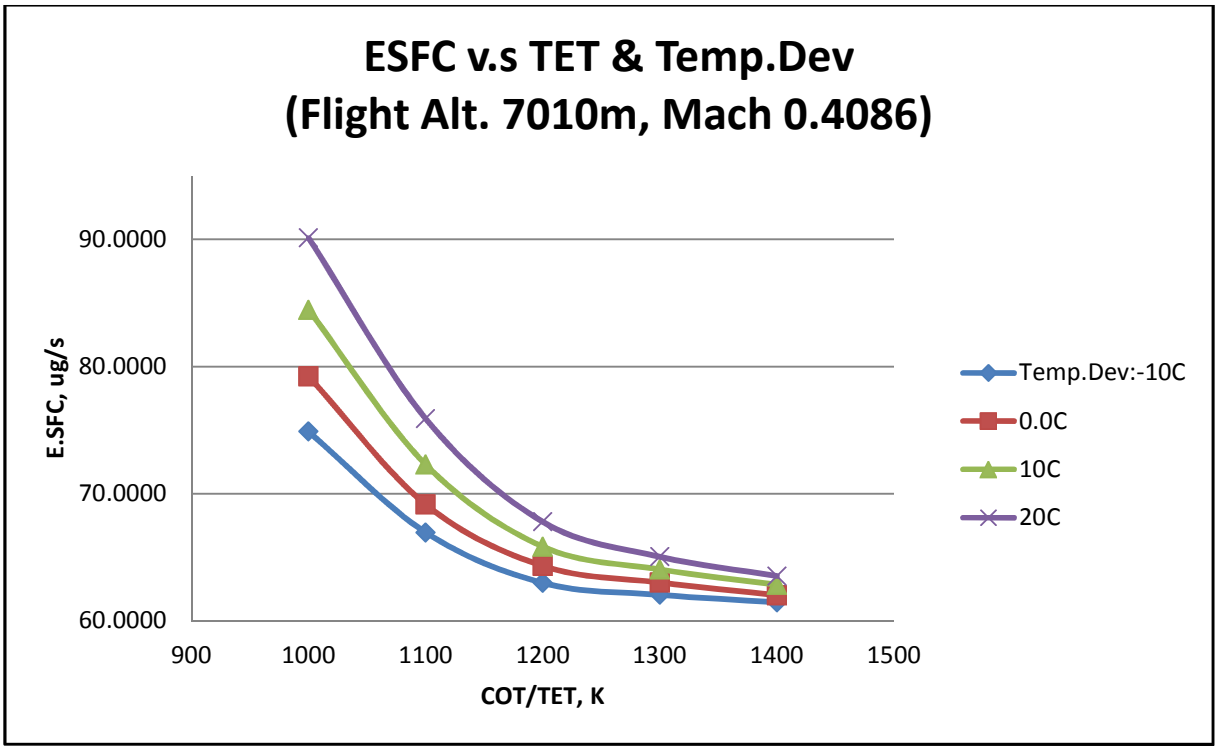

Figure 4-34 Influence of TET & temperature deviation on Equivalent Specific Fuel Consumption

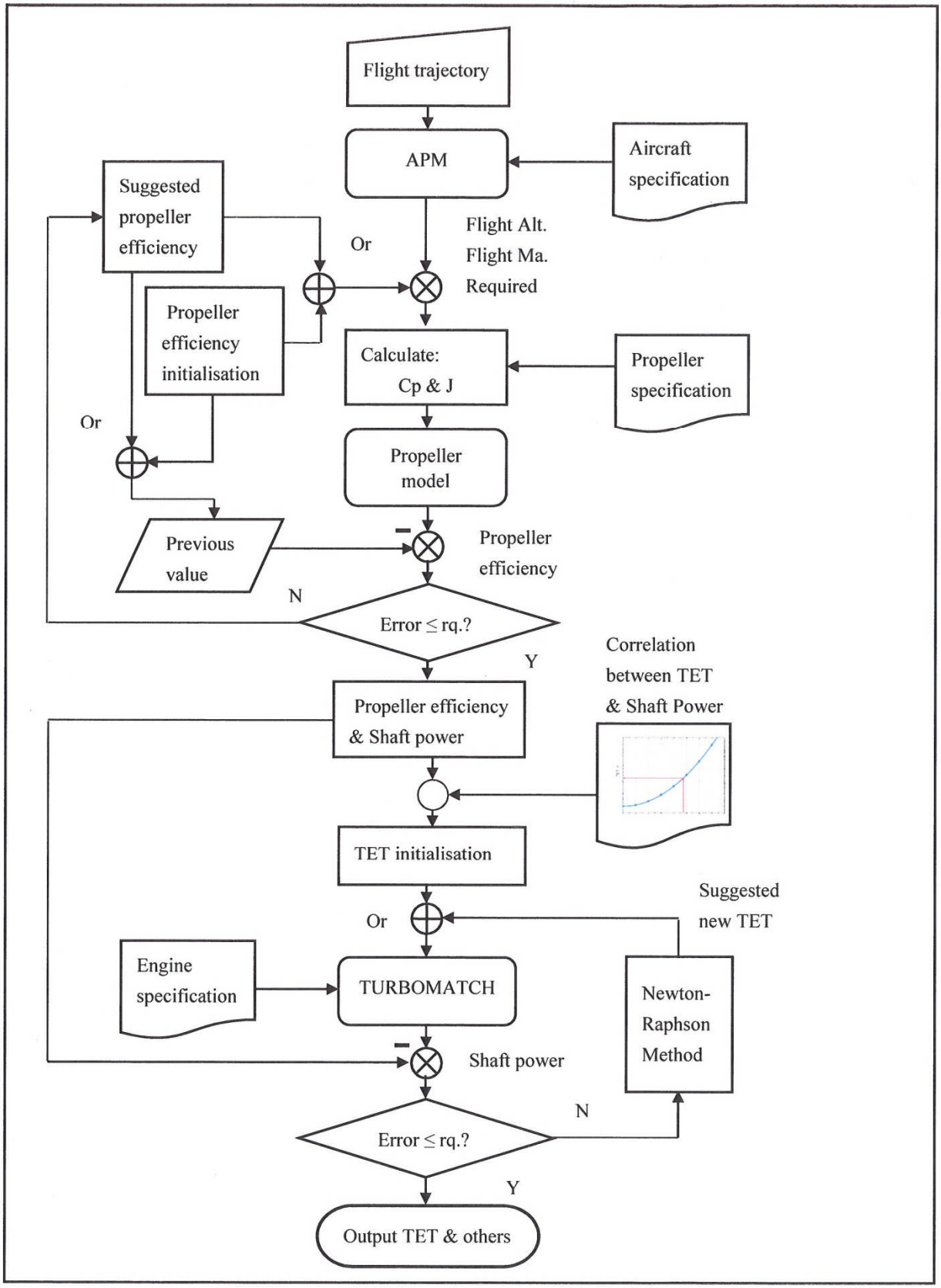

Figure 4-35 Integration of propeller/engine models and TET calculation

4.3 Propfan (open rotor) Engine Powering CUPFDAC

Propfans, also called open rotors, are advanced propeller engines that can efficiently operate at high altitude and speed (approximately 35000 ft and Mach 0.8) [51-56].

Compared with conventional propeller engines, propfan engines are more efficient at high subsonic flight speeds, since they have modern blades with thin transonic aerofoil sections and swept tips. These two features reduce the losses associated with tip transonic regimes. Propellers of propfan engine are also highly loaded (in order to achieve high thrust levels with reduced propeller diameter) and consequently they have a high number of blades (typically more than 8). Counter rotating configurations are used to further reduce propeller diameters and increase their efficiency (recovering with the rear propeller the swirl delivered by the front one) [51-56].

Usually, a propfan engine consists of a two shaft gas generator followed by a power turbine driving a set of advanced propellers. Three main features determine the configuration of a propfan engine.

1) Number of propellers: a propfan engine may have a single propeller, such as the NASA-PTA [57], or two counter-rotating propellers like the GE36 [58] or the Alison 578-DX [59]. Counter-rotating propellers can produce the same amount of thrust with smaller diameters than a single propeller. They can also achieve higher efficiencies compared with a single propeller because the rear propeller can recover the swirl delivered by the front one.
2) Position of the propellers: propellers can be located at the front of the engine (called ‘puller’ configuration) or at the rear of the engine (called ‘pusher’ configuration). The NASA-ATP and the engines on the Antonov An-70 are examples of ‘puller’ propfan, while GE36 and Allison 578-DX are classified as ‘pusher’ configuration.
3) Propeller driving mechanism: propellers can be driven by a gearbox or directly driven by the turbine (linked through a shaft in the case of a single propeller, or attached to the drums of a counter-rotating turbine in the case of counter-rotating propellers). Allison 578-DX and NASA ATP are geared propfan engines while GE36 utilises the directly-driven type.

The propfan engine model used in this research project, which is denoted CUPROPFAN (Cranfield University Propfan), is a 'pusher' geared counter-rotating type. Figure 4-36 illustrates an example of the configuration and Figure 4-37 presents the schematic created to simulate this configuration.

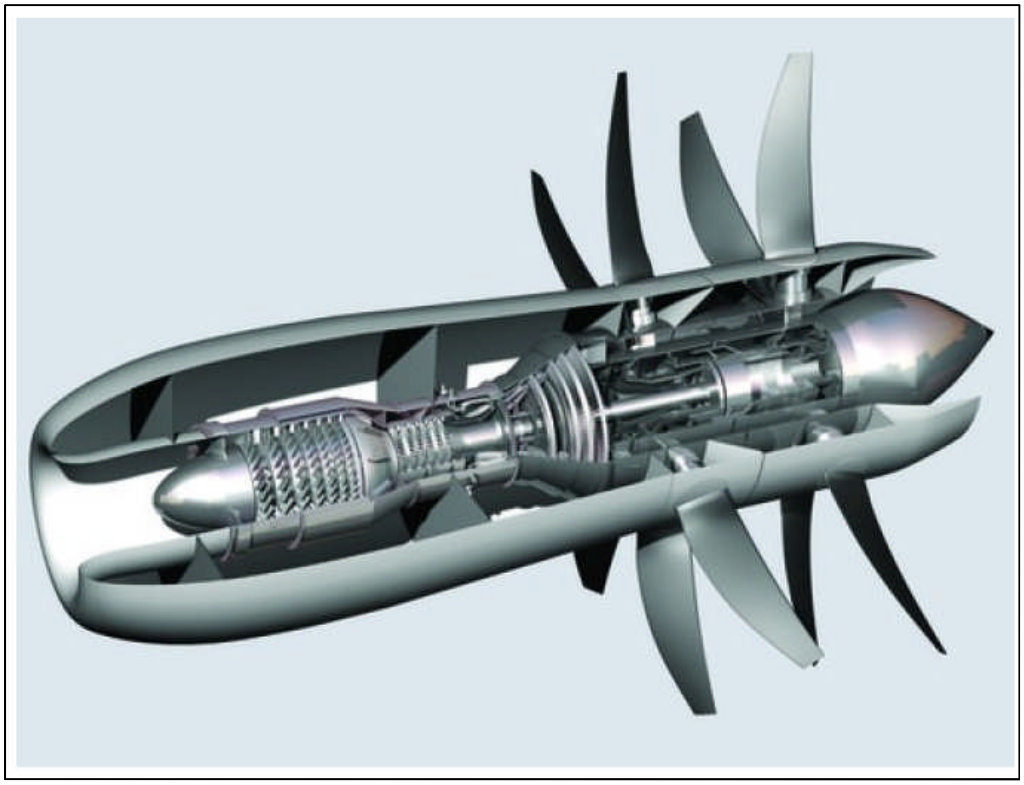

Figure 4-36 Illustration of a pusher geared counter-rotating propfan engine [60]

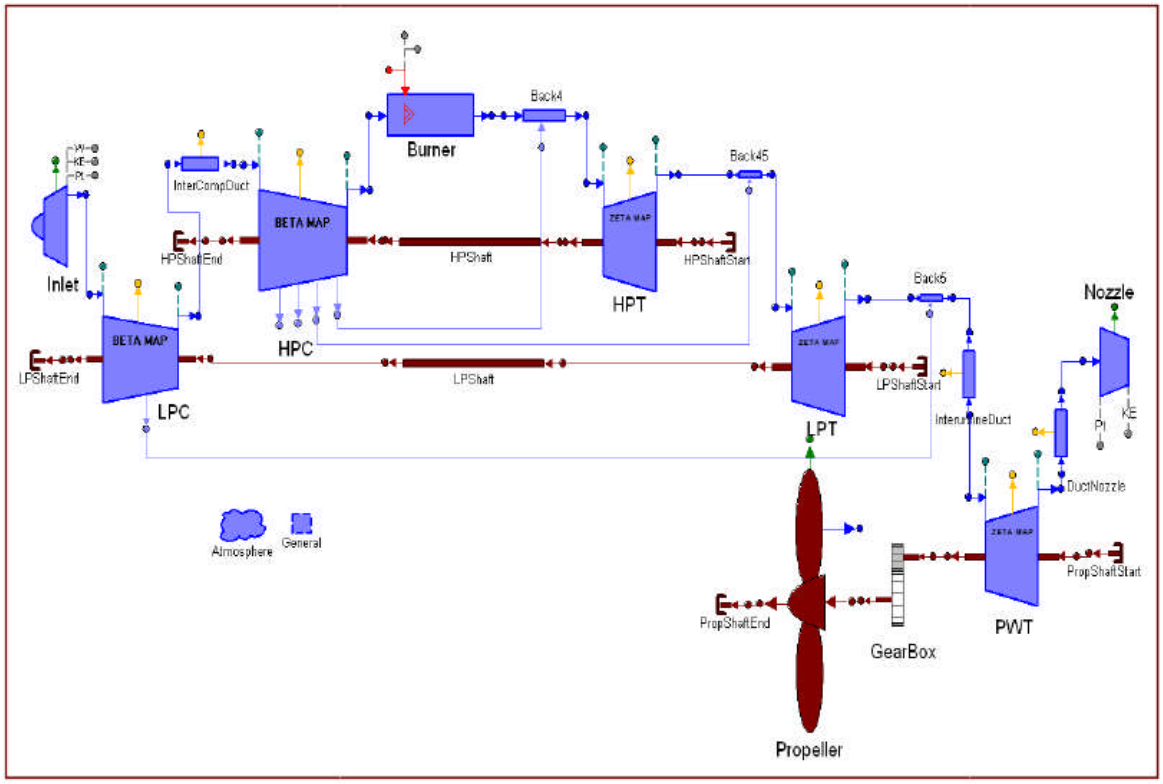

Figure 4-37 Schematic of the CUPROPFAN engine [60]

The design point of the CUPROPFAN is selected at the top of climb (TOC), i.e., flight altitude 10668 m, flight Mach number 0.8 and ISA. The main design data which are determined, based on the reference [16], are listed in the following Table 4-8.

Table 4-8 Design parameters of CUPROPFAN engine model

Flight altitude	10668 m
Atmosphere condition	ISA
Flight Mach number	0.8
Inlet total pressure recovery	1.0
LPC inlet mass flow rate	9.558 kg/s
LPC PR	4.2
LPC isentropic efficiency	0.896
Total pressure loss between LPC and HPC	0.01
HPC PR	10.0
HPC isentropic efficiency	0.886
Combustor total pressure loss	0.045
Combustion efficiency	0.995
Combustor outlet temperature	1800 K

HPT isentropic efficiency	0.919
LPT isentropic efficiency	0.942
Total pressure loss between LPT and FPT	0.01
FPT isentropic efficiency	0.94
Nozzle duct pressure loss	0.01
Propeller efficiency	0.93

Table 4-9 shows the performance outputs of this engine model at the design point by using TURBOMATCH.

Table 4-9 Performance outputs of CUPROPFAN engine model at the design point

Shaft Power	6222553 watts
Nozzle Net Thrust	857.73 Newtons
Equivalent Power	6441442 watts
Fuel Flow	0.2746 kg/s
E.S.F.C.	42.63 μg/J

Figures 4-38 to 4-40 illustrate the influences of flight altitude and flight Mach number on the engine performances in terms of shaft power, equivalent shaft power and equivalent specific fuel consumption with the design TET and International Standard Atmosphere (ISA) condition. And Figures 4-41 to 4-43, in turn, show the influences of TET and ambient temperature on the engine performances at the design flight altitude and Mach number.

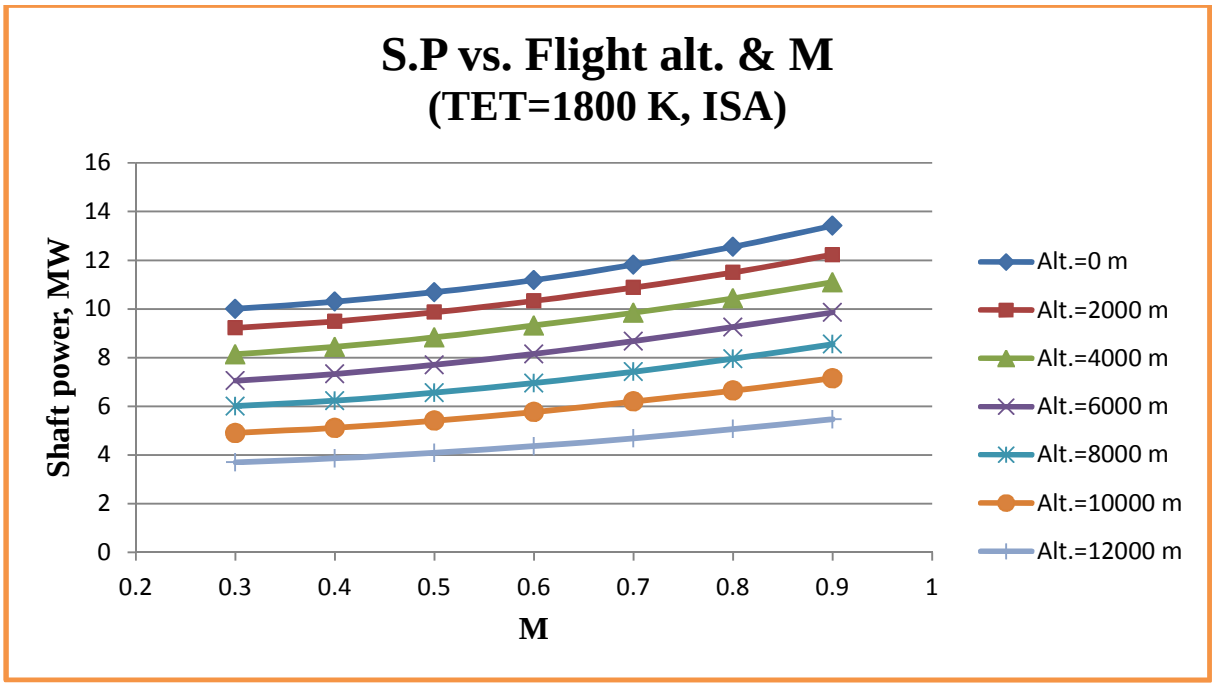

Figure 4-38 Influence of flight altitude and M on engine shaft power

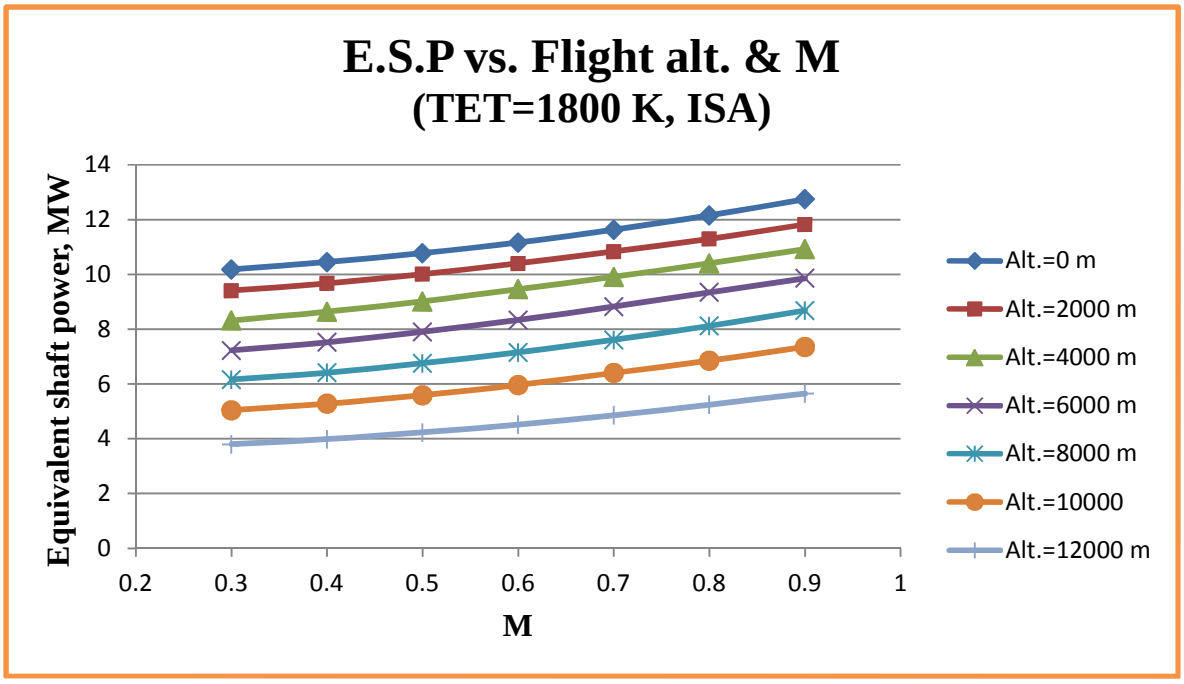

Figure 4-39 Influence of flight altitude and M on engine equivalent shaft power

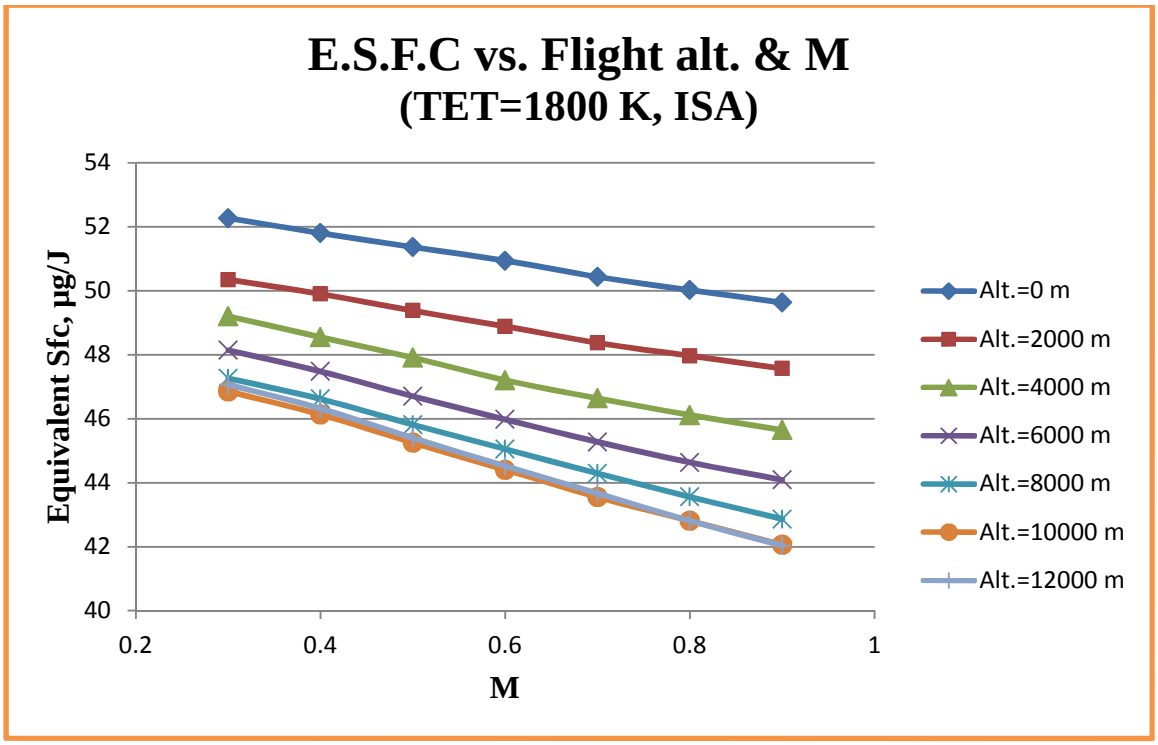

Figure 4-40 Influence of flight altitude and M on engine equivalent specific fuel consumption

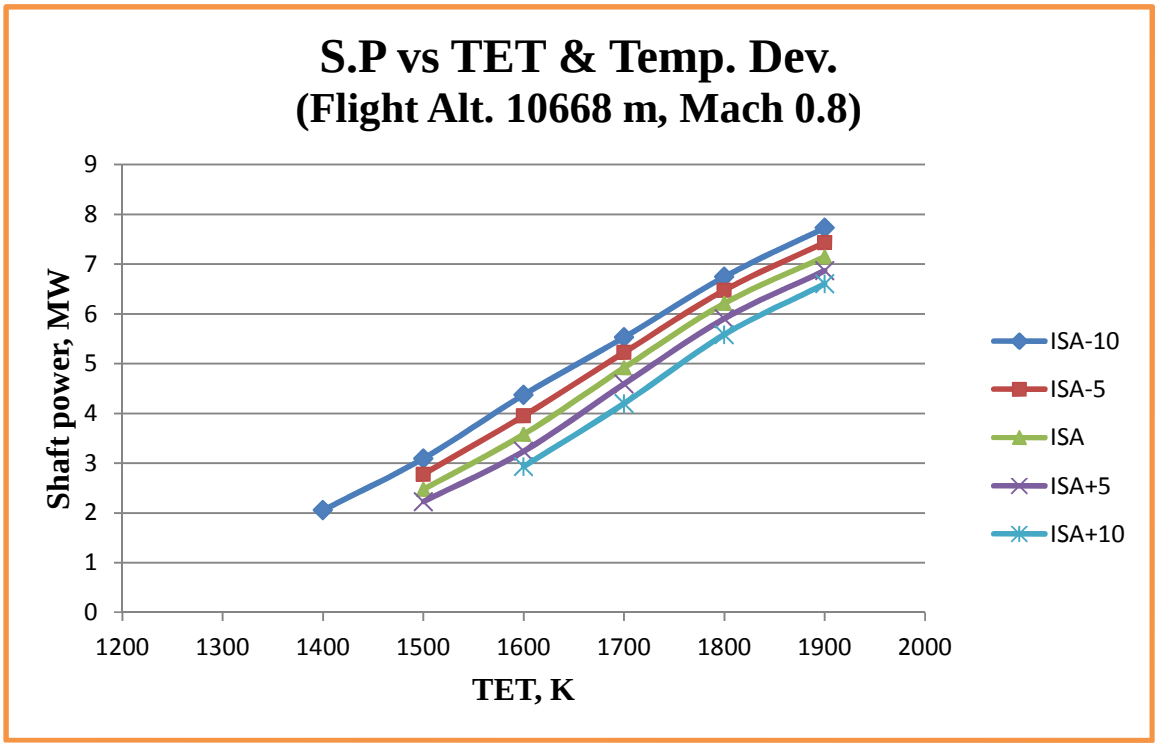

Figure 4-41 Influence of ambient temperature and TET on engine shaft power

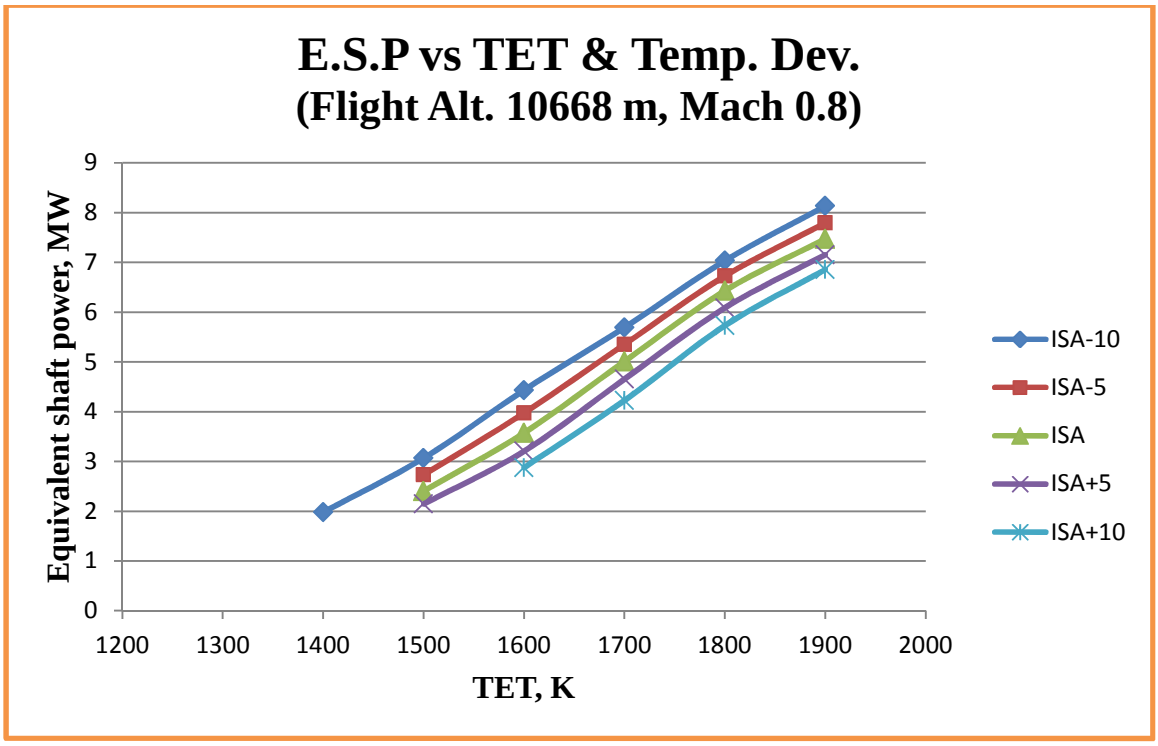

Figure 4-42 Influence of ambient temperature and TET on engine equivalent shaft power

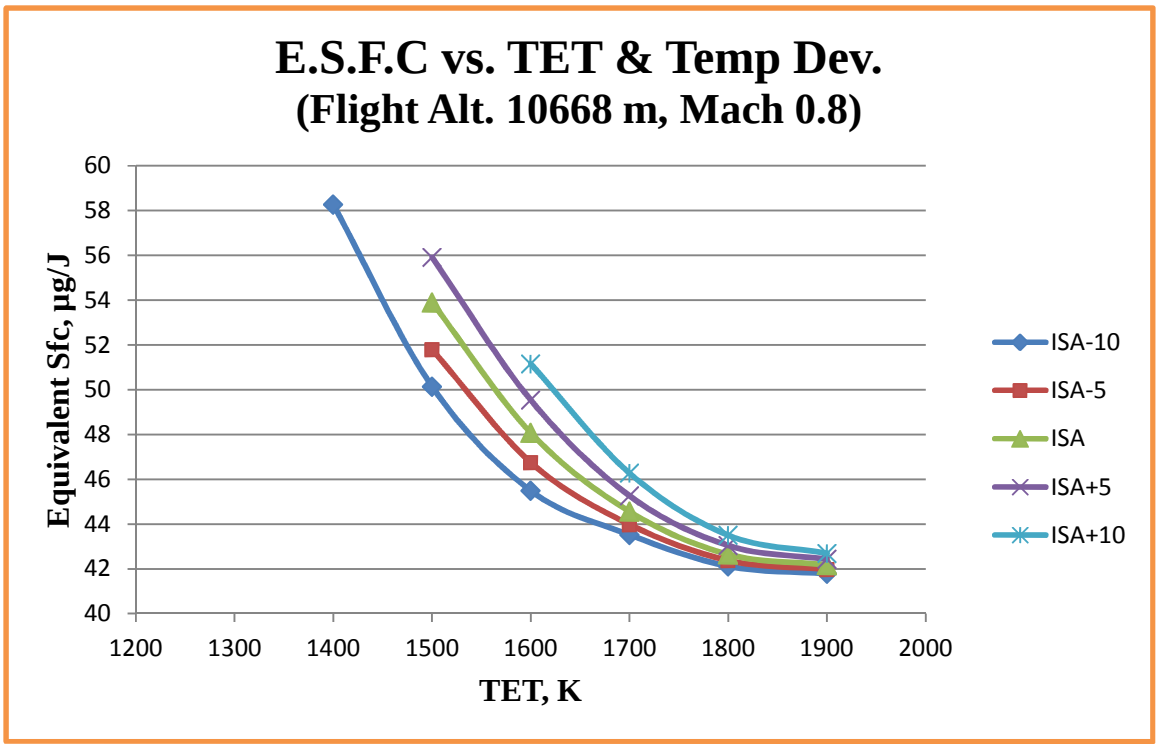

Figure 4-43 Influence of ambient temperature and TET on engine equivalent specific fuel consumption

From the above figures, it can be observed that the built propfan engine model displays the expected performance characteristics. The qualitative explanations to such behaviours are similar to those for the turboprop engine in the previous section 4.2.

CHAPTER FIVE ENGINE GASEOUS EMISSIONS AND MODELLING

5.1 Aviation Emissions and Their Consequences

Nowadays, with the rapid development of the air transport industry, more and more public attention is being drawn to the adverse impacts of aviation gaseous emissions on the environment in terms of air quality, noise and climate change.

Reference [61] briefly summarises the principal gaseous emissions from aero gas turbine engines as well as their consequences. According to [61], these emissions mainly include carbon dioxide (CO_2), oxides of sulphur (SO_2), carbon monoxide (CO), unburnt hydrocarbons (UHC), smoke soot (C) and oxides of nitrogen (NOx), etc.

CO_2 is the consequence of complete and successful combustion of a fuel containing carbon and is identified with global warming. The gas is very stable and will remain in the atmosphere for very long periods, which has led to some concern regarding global warming via the greenhouse effect. According to the reference [1], today and globally, "flights produce 628,000,000 tonnes of CO_2 yearly and air transport's contribution to climate change represents 2% of human-induced CO_2 emissions (and 12% of all transport sources)." However, in the near future, the stable and continuous growth in demand for air travel ("increasing 4-5% per annum over the next 20 years" [1]), the contribution level from commercial aviation to climate change will be increased to 3% by 2050.

SO_2 is both toxic and corrosive. All the sulphur present within a fuel is inevitably converted to oxides of sulphur. Removing as much sulphur as possible from the fuel prior to combustion is the primary way to reduce SO_2 emissions. So far, the level of oxides of sulphur permissible in fuels has already been progressively reduced over the years with some applications and regions requiring sulphur content to be limited to values as low as 0.2% [61].

Carbon monoxide and unburnt hydrocarbons are both products of partial combustion, and are formed in quantity in circumstances where the combustion zone temperature is low and/or the time available for combustion is insufficient (such as at the lower power settings for a gas turbine engine). Carbon monoxide reduces the capacity of the blood to

carry oxygen, and can cause asphyxiation and, at high concentrations, even death. UHC can themselves be toxic, and also combine with oxides of nitrogen via photochemical reactions to form toxic “smog”.

Smoke or soot is formed in local fuel-rich regions within the combustor. The propensity to produce carbon increases markedly with pressure. Therefore, engines designed to operate at high pressure ratios are likely to produce higher quantities of soot than those operating at modest pressure ratios. Whilst smoke from gas turbine combustors is visible and results in soiling, it is not toxic at the concentrations emitted. However, some smoke suppressants contain heavy metals such as barium, and whilst they may eliminate or reduce smoke produced by a gas turbine, the resulting emissions now contain the highly toxic heavy metal. Fortunately, in recent years, improvements in fuel injector technology, particularly based round the air spray and air blast sprayers, have eliminated soot or smoke production in many engines.

NOx is produced within the combustion zone if the combustion temperature is sufficiently high to dissociate molecular oxygen to atomic oxygen. The following chemical reaction equations illustrate simplified generation mechanisms of nitric oxide and nitrous oxide introduced by Zeldovich *et al*.

$$O_2 \leftrightarrows 2O \quad (5\text{-}1)$$

$$O + N_2 \leftrightarrows NO + N \quad (5\text{-}2)$$

$$N + O_2 \leftrightarrows NO + O \quad (5\text{-}3)$$

$$2NO + O_2 \leftrightarrows 2NO_2 \quad (5\text{-}4)$$

At ground level, the presence of oxides of nitrogen results in an increase in ozone concentration. Nitrogen dioxide reacts photochemically to produce nitric oxide and atomic oxygen. The atomic oxygen reacts with molecular oxygen to form ozone. This chemical reaction process can be expressed as follows:

$$NO_2 + hv \leftrightarrows NO + O \quad (5\text{-}5)$$

$$O + O_2 \leftrightarrows O_3 \quad (5\text{-}6)$$

The statistical data show that “the rate of increase of ozone in the last 20 years is now nearer 2.4% per annum, compared with about 1.6% per annum for the preceding 20

years. Of equal concern is the absolute level, now approaching 50 ppb (parts per billion) over Western Europe." [61]. Prolonged exposure, near to 100 ppb, is associated with respiratory illnesses, impaired vision, hearing disorders, headaches and allergies.

On the other hand, oxides of nitrogen can also cause damage (depletion) to the ozone layer within the stratosphere. Nitric oxide reacts with ozone to produce nitrous oxide and molecular oxygen. Nitrous oxide, in turn, reacts with atomic oxygen to form nitric oxide and molecular oxygen. Thus, the nitric oxide, having depleted the ozone, is regenerated and is hence able to continue with the damage process over very many such cycles. This mechanism is particularly effective in the stratosphere where atmospheric conditions are very stable with little or no mixing to dilute concentrations of nitric oxide once these have been deposited within the stratosphere. The ozone layer absorbs the ultra-violet radiation from the sun. The depletion of ozone then results in an increase in ground level ultra-violet radiation, which causes skin cancer and eye diseases. The chemical mechanism of ozone depletion in the stratosphere can be expressed as follows:

$$NO + O_3 \leftrightarrows NO_2 + O_2 \quad (5\text{-}7)$$

$$NO_2 + O \leftrightarrows NO + O_2 \quad (5\text{-}8)$$

5.2 Emission Prediction Modelling

References [62-65] briefly summarises the main modelling methodologies as well as their advantages and disadvantages for the purpose of emission prediction. According to these references, three different strategies can be applied to predict (or estimate) gaseous emissions from gas turbine combustors, that is, 1) empirical correlations; 2) stirred reactor models (or called physics-based models); and 3) detailed numerical simulations, for instance, by means of comprehensive CFD (Computational Fluid Dynamics) calculations.

Empirical correlations [66-68], mainly built based on experiments/measurements, usually use global expressions into which fine details of internal flow and the combustion chemistry occurring inside combustion chambers are completely subsumed. The correlation (or prediction/estimation) formulae produced by this modelling method are of the features of simplicity, easy usage and very little calculation time. However, on the other hand, this method also presents some inherent limitations. These limitations

can be observed from the facts that the prediction formulae developed by this method are usually strongly targeted (or specific) in terms of their respective applications (or, "narrow" suitability for each empirical formula built) (i.e., "different combustion concepts require the creation of new experimental databases" and "such correlations can only satisfactorily be applied to specific engine architectures and accommodate only minor design changes" [65]). In addition, another possible limitation to the wide application of this modelling method lies in that, although the methods and formulae for emission calculation are publicly available, much of data required by these calculations are proprietary and, hence, unavailable in the public domain (the application of the so called P3T3 method for emission estimation throughout the flight envelope introduced later in this section, is such an example).

The concept of stirred reactors was ever investigated widely during the 1970s and 1980s in order to achieve a better understanding about the formation process of various gaseous pollutants emitted from gas turbine combustors. Based on this, the stirred reactor based modelling method was further developed and applied to predict trends in the level of emissions produced by gas turbine combustors currently in service [69-72]. This method predicts gaseous emissions from gas turbine combustor by means of adopting a series of stirred reactors (SRs) to model combustion, mixing, steam/water injection, fuel evaporation, and their effects on emission formation based on the theories of chemical equilibrium calculations and the reaction kinetics.

Using CFD to simulate numerically the turbulent reacting flow inside the combustor [73-77] is another possible option for gaseous emission prediction. However, some inherent features of this approach limit, to some extent, its wide application. Firstly, this simulation method needs detailed geometry information of the investigated combustor, while such information is usually proprietary, and hence, it is difficult for public access; secondly, the simulation calculation based on this modelling method is in general extremely time-consuming, which inhibits the application of this method in GAs based optimisation problems, where a lot of evaluations are involved (the flight trajectory multidisciplinary optimisation performed in this research work is such an example); in addition, the lack of robustness/reliability (therefore, the validation of simulation results based on empirical data is often required) becomes another disadvantage of this simulation approach.

5.2.1 P3T3 method

P3T3 method is a semi-empirical gaseous emission prediction method. This method "utilize the entire suite of data taken during the emissions certification to calculate emissions throughout the flight envelope" [21] by means of a set of correlation formulae built semi-empirically between emission indices and the total pressure P3 and the total temperature T3 at the high compressor exit/combustor diffuser inlet.

The application procedure of this method is as follows:

1. Define a flight mission;
2. Run the mission through an aircraft performance simulation code and output engine thrust requirements at discrete flight points (defined in terms of pressure altitudes, flight speeds and ambient temperatures) along the mission;
3. Taking the information achieved in the above item 2) as inputs, the engine performance model outputs the values of P3 and T3 for each flight point;
4. For each point, "T3 is used to enter a lookup of each Emissions Index ($EINOx_{SL}$, $EIHC_{SL}$ and $EICO_{SL}$) and a reference sea level compressor exit pressure ($P3_{SL}$). The lookup is based on the sea level static, standard day emissions correlation developed from emissions certification testing" [21];
5. Achieve real values in Emission Indices corresponding to actual flight conditions by means of proper corrections to those reference values obtained in item 4) above.

The corresponding correlations for the calculation of Emission Indices at actual flight conditions are expressed as follows:

$$EICO_{Alt} = EICO_{SL} * (P3_{SL}/P3_{Alt})^{x} * (FAR_{SL}/FAR_{Alt})^{Z} \quad (5\text{-}9)$$

$$EIHC_{Alt} = EIHC_{SL} * (P3_{SL}/P3_{Alt})^{x} * (FAR_{SL}/FAR_{Alt})^{Z} \quad (5\text{-}10)$$

$$EINOx_{Alt} = EINOx_{SL} * (P3_{Alt}/P3_{SL})^{y} * e^{H} * (FAR_{Alt}/FAR_{SL})^{Z} \quad (5\text{-}11)$$

According to the reference [21], "the exponents of y and x are engine/combustor unique and are empirically derived by the manufacturers." "The value for the NOx pressure exponent y has been seen to range between 0.2 and 0.5 in rig and engine tests. Theory would suggest an exponent of 0.5, while published empirical data would suggest a typical value of 0.4[3]. The value for the HC and CO pressure exponent x, is assumed to

be 1.0. The exponent for z is effectively 0 for conventional rich front end single annular combustors. Moisture in humid air entering the engine core and combustor reduces the peak flame temperature and NOx formation rate. The NOx equation includes a humidity factor, e^H, which was originally developed from a 19 engine sample of production JT9D's." [21] (Here, H is humidity correction and defined as $H = -19 \times (\omega - 0.00634)$. ω is humidity ratio with the unit of "kg water/kg dry air".)

As for the gaseous emission prediction of turbofan-propelled aircraft involved in this research work, a set of measured data (i.e., reference data shown in the following Table 5-1) from the emission certification test of CFM56-5B4/3, which is similar to the engine model built in this research work, are available and, therefore, the P3T3 prediction method can be applied.

Table 5-1 Emission measured data of CFM56-5B4/3 engine [78]

MODE	POWER SETTING ($\%F_{oo}$)	TIME minutes	FUEL FLOW kg/s	EMISSIONS INDICES (g/kg) HC	CO	NOx	SMOKE NUMBER
TAKE-OFF	100	0.7	1.142	0.02	0.25	21.57	13.4
CLIMB OUT	85	2.2	0.939	0.02	0.16	17.23	9.9
APPROACH	30	4.0	0.316	0.05	3.24	8.85	2.1
IDLE	7	26.0	0.102	1.92	32.07	4.22	2.1
LTO TOTAL FUEL (kg) or EMISSIONS (g)			407	314	5386	4511	-
NUMBER OF ENGINES				3	3	3	3
NUMBER OF TESTS				7	7	7	7
AVERAGE D_p/F_{oo} (g/kN) or AVERAGE SN (MAX)				2.61	44.84	37.56	13.4
SIGMA (D_p/F_{oo} in g/kN, or SN)				0.36	2.4	1.1	4.5
RANGE (D_p/F_{oo} in g/kN, or SN)				2.21 to 2.9	42.0 to 46.6	36.6 to 38.8	8.4 to 16.9

Based on the reference data in the above Table 5-1 and the performance model of the CUTSTF engine described in chapter four, the empirical correlations between EIHC, EICO, EINOx and P_3 (total pressure at HPC exit) and T_3 (total temperature at HPC exit) under the reference condition of SLS (sea level static) and standard day can be established in principle.

In fact, during the establishment of these relationships, some investigations about the ways how these parameters can be correlated better have to be made. These works are shown in the following Figures 5-1 to 5-12.

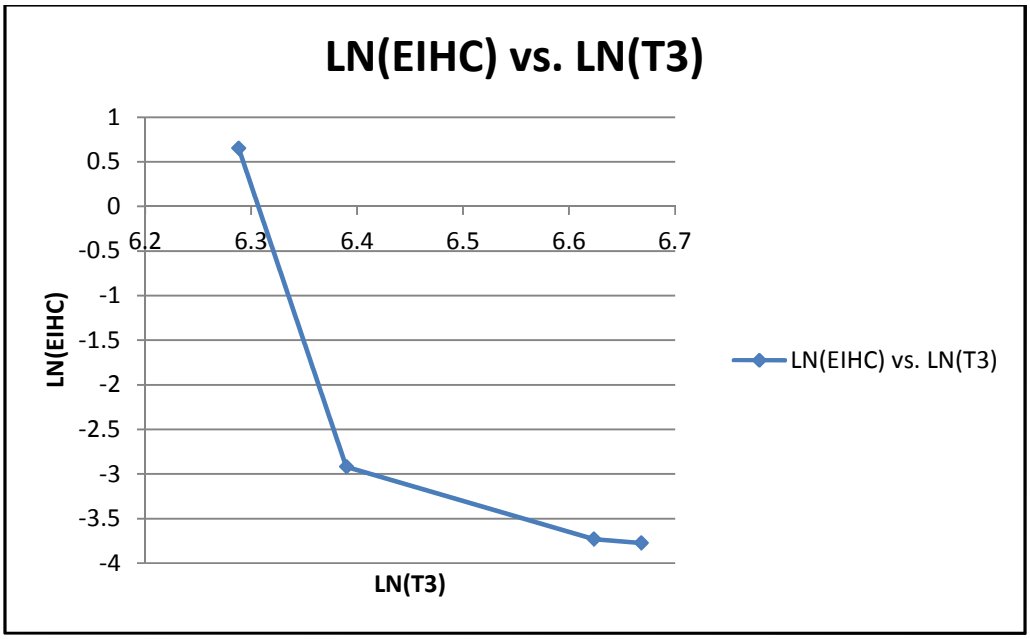

Figure 5-1 Logarithm correlation between EIHC and T_3

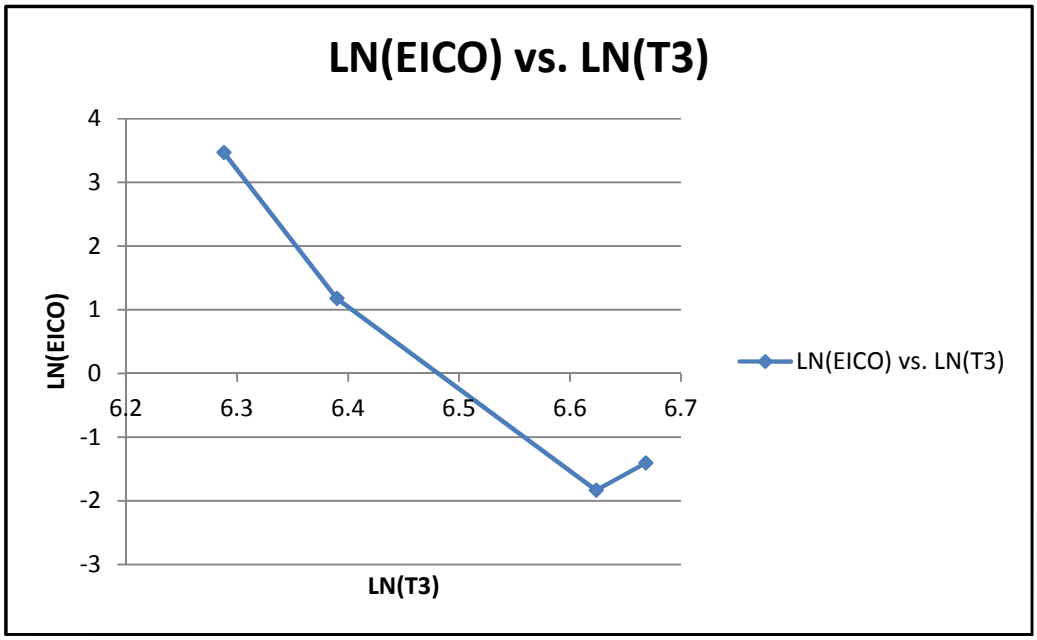

Figure 5-2 Logarithm correlation between EICO and T_3

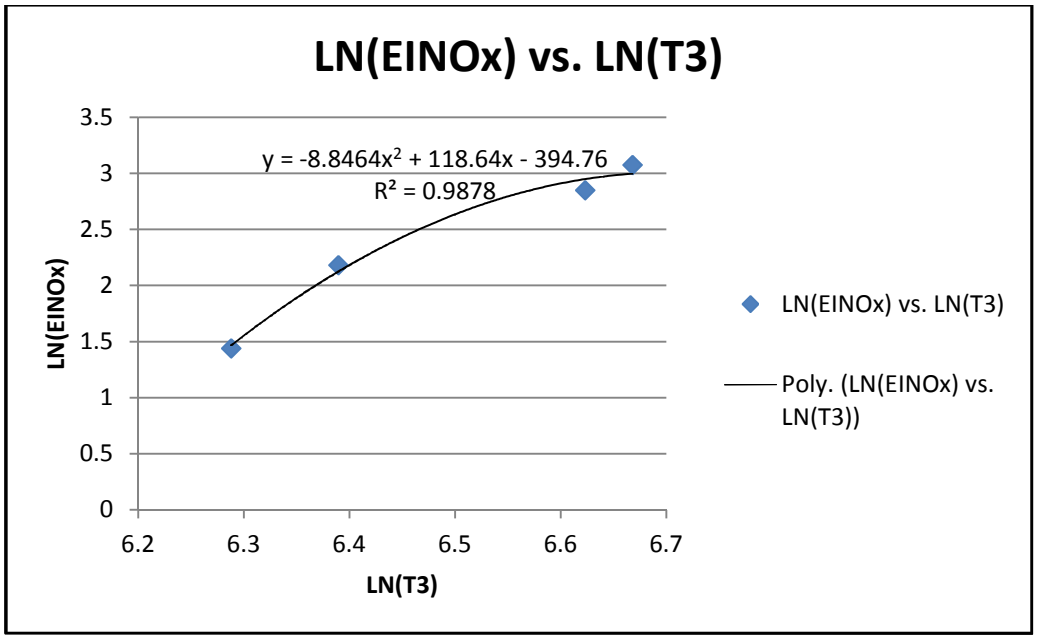

Figure 5-3 Logarithm correlation between EINOx and T_3

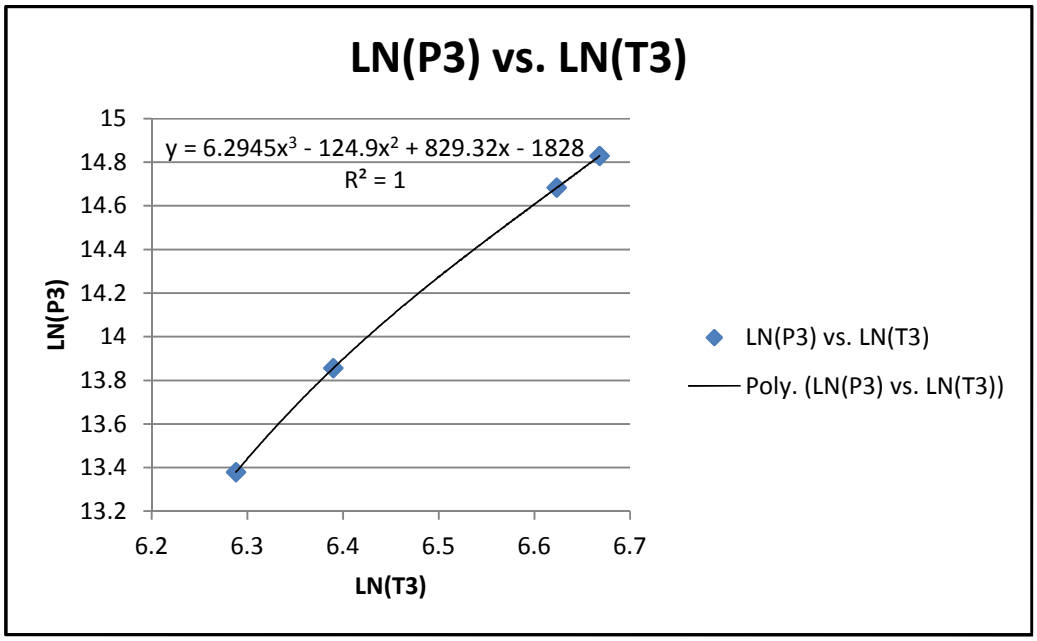

Figure 5-4 Logarithm correlation between P_3 and T_3

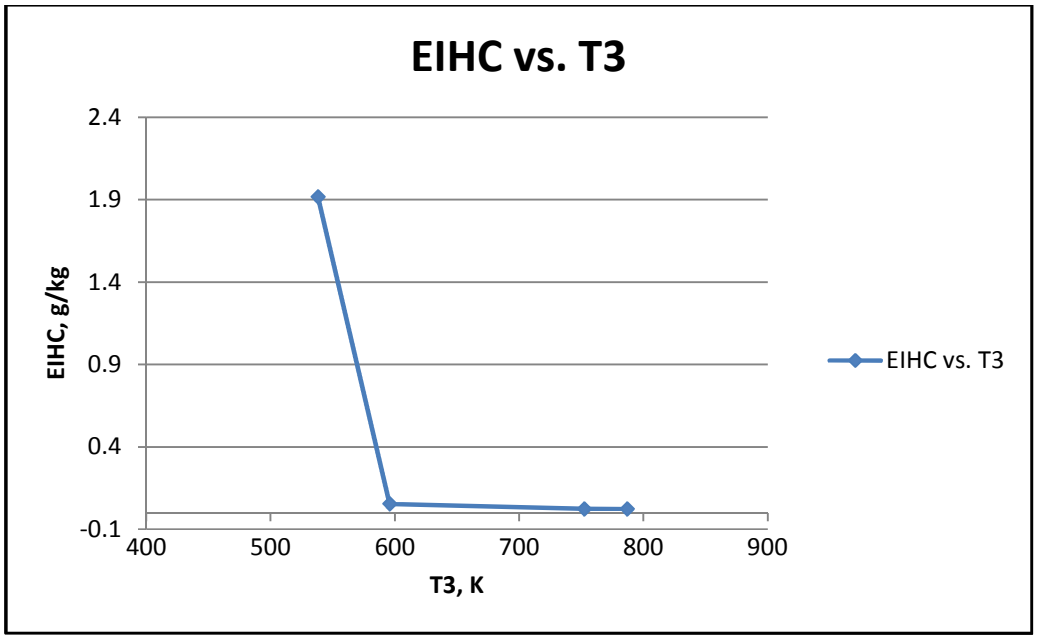

Figure 5-5 Direct correlation between EIHC and T_3

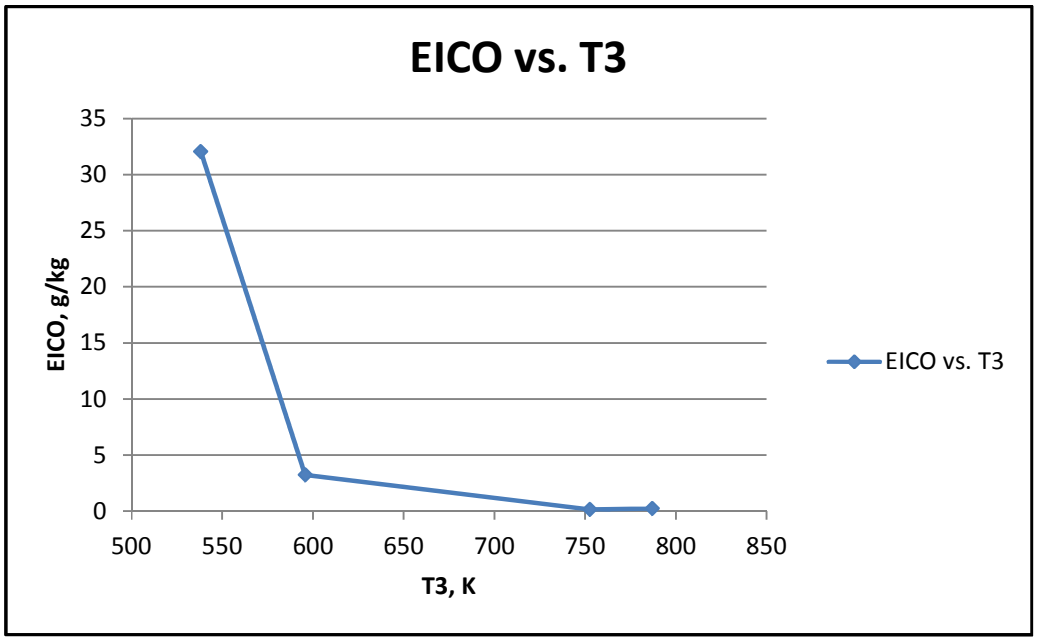

Figure 5-6 Direct correlation between EICO and T_3

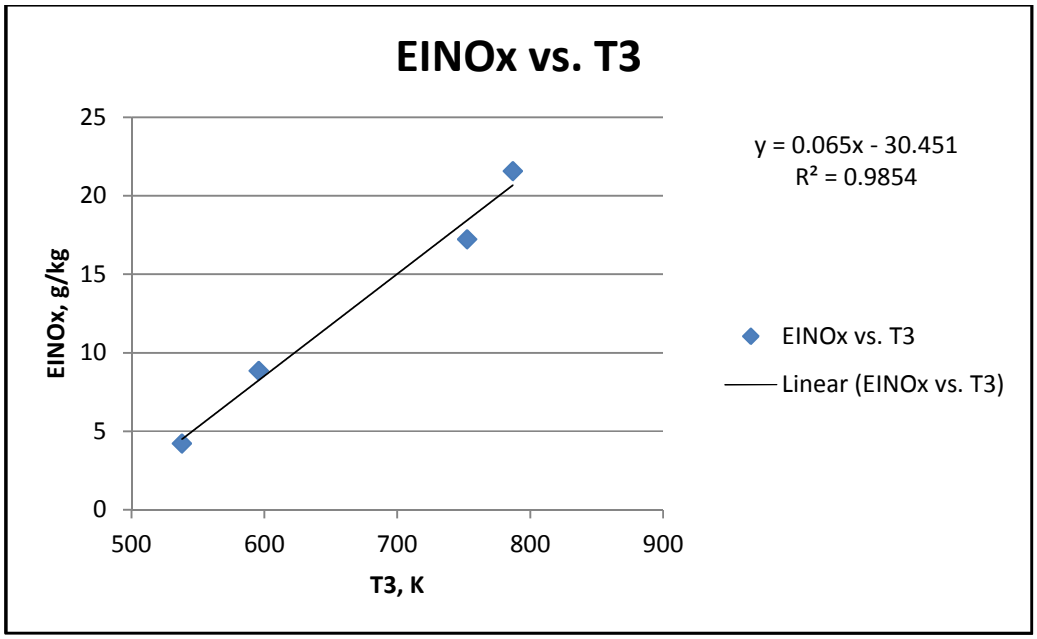

Figure 5-7 Direct (linear) correlation between EINOx and T_3

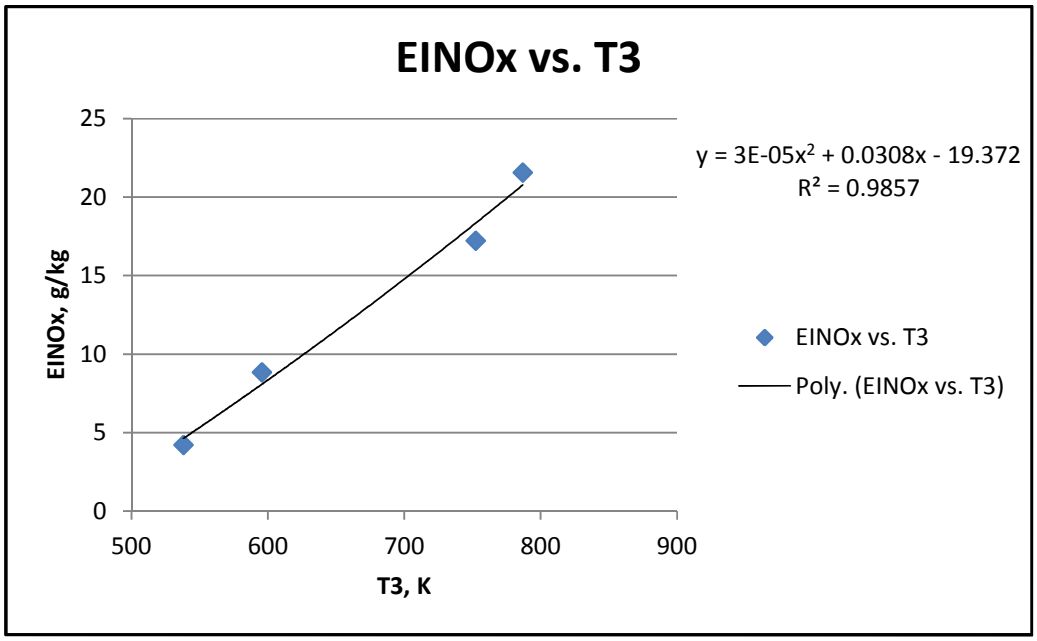

Figure 5-8 Direct (quadratic) correlation between EINOx and T_3

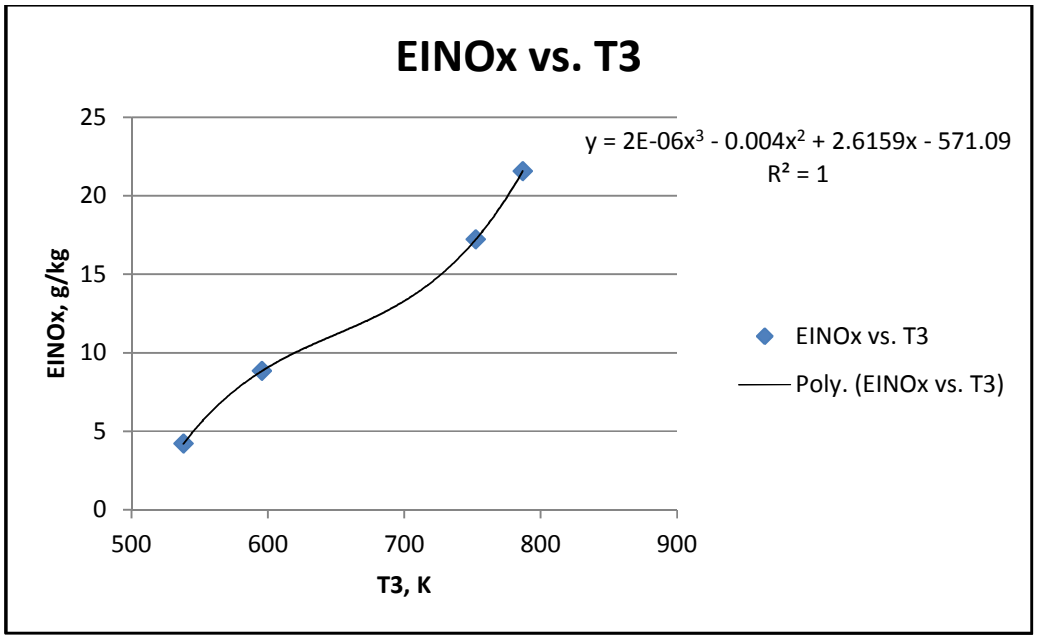

Figure 5-9 Direct (cubic) correlation between EINOx and T_3

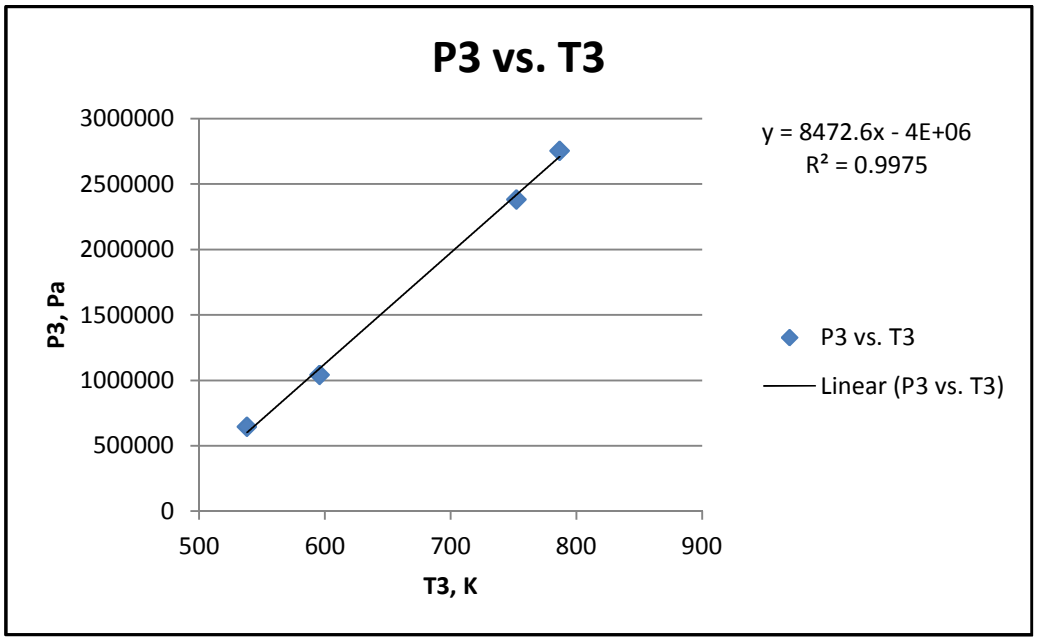

Figure 5-10 Direct (linear) correlation between P_3 and T_3

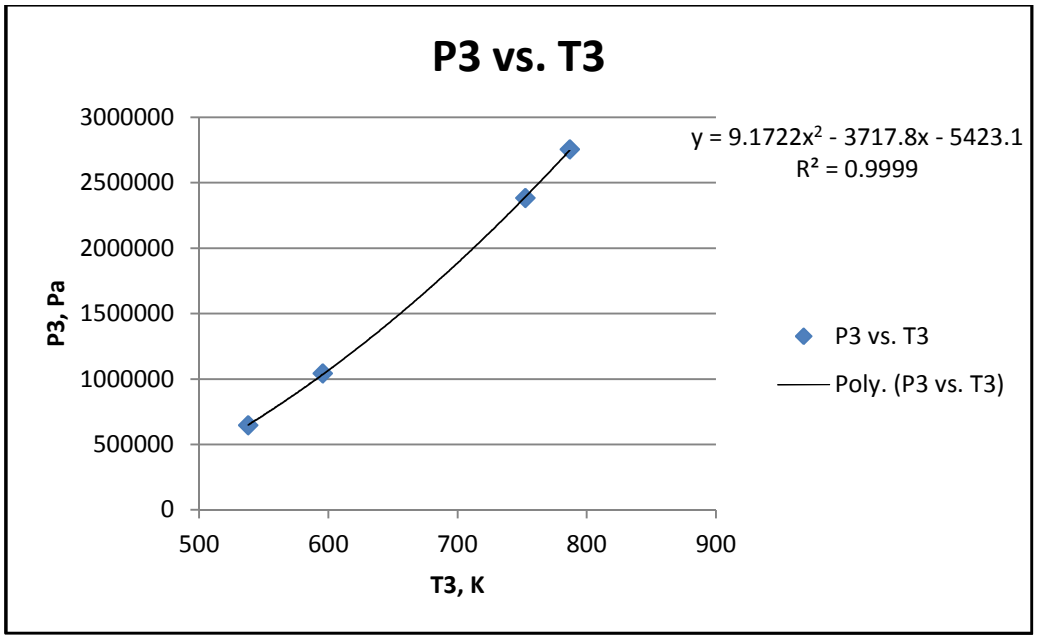

Figure 5-11 Direct (quadratic) correlation between P_3 and T_3

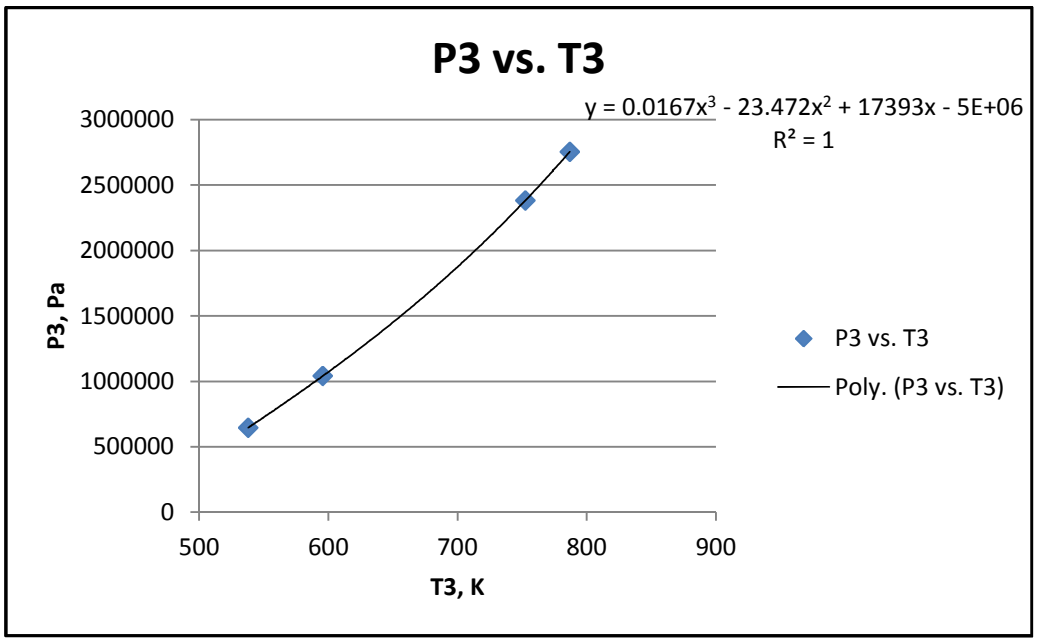

Figure 5-12 Direct (cubic) correlation between P_3 and T_3

After the comparisons among different correlation methods, the direct correlations seem to show more advantages than the logarithm correlation and, therefore, were adopted in this project research. Among them, EIHC and EICO were calculated by piecewise linear interpolation (as shown in Figures 5-5 and 5-6), while the calculations of EINOx and P_3 were implemented respectively by their own quadratic correlations (although cubic correlations show the highest values in R^2 (R^2=1), the shape of the correlation curve resulted from this method (for instance, Figure 5-9) is not preferred.), as shown in Figures 5-8 and 5-11.

CO_2 and H_2O are produced under the chemical equilibrium conditions, and hence based on these equilibrium conditions, the values of emission indices of the two emissions (i.e., $EICO_2$ and EIH_2O) can be derived as follows:

Assuming the composition of fuel is given by:

$$C_mH_nS_r$$

If ignoring 'S' (sulphur), the above composition expression of fuel becomes C_mH_n (for instance, the fuel of Jet-A is expressed as $C_{12}H_{23}$). Therefore, based on the composition, the following chemical equilibrium equation (using 'Mole' scale) can be achieved:

$$1C_mH_n + \frac{4m+n}{4}O_2 = mCO_2 + \frac{n}{2}H_2O \quad (5\text{-}12)$$

Since 1 mole C_mH_n corresponds to $(m \times 12.011 + n \times 1.0079)$ gramC_mH_n, m mole CO_2corresponds to $m \times (12.011 + 2 \times 15.9994)$ gramCO_2, and $\frac{n}{2}$ mole H_2O corresponds to $\frac{n}{2} \times (2 \times 1.0079 + 15.9994)$gram H_2O, therefore, the production rate (or Emission Index) of CO_2 and H_2O (by the definition with 'mass' scale) can be expressed as:

$$EICO_2 = \frac{m\times(12.011+2\times15.9994)\times1000}{m\times12.011+n\times1.0079} \left(^{g}/_{kg}\right) \quad (5\text{-}13)$$

$$EIH_2O = \frac{\frac{n}{2}\times(2\times1.0079+15.9994)\times1000}{m\times12.011+n\times1.0079} \left(^{g}/_{kg}\right) \quad (5\text{-}14)$$

From the above two equations, it can be concluded that the values of emission indices of CO_2 and H_2O only rely on the used fuel type (i.e., fuel composition) and they are independent of operational parameters.

Further, assume the fuel Jet-A ($C_{12}H_{23}$) is used in this research work, so the $EICO_2$ and EIH_2O can be determined as follows:

$$EICO_2 = \frac{12\times(12.011+2\times15.9994)\times1000}{12\times12.011+23\times1.0079} = 3156.5 \text{ g/kg fuel} \quad (5\text{-}15)$$

$$EIH_2O = \frac{\frac{23}{2}\times(2\times1.0079+15.9994)\times1000}{12\times12.011+23\times1.0079} = 1238.2 \text{ g/kg fuel} \quad (5\text{-}16)$$

5.2.2 Stirred reactor model

In this research work described in this thesis, emission predictions from turboprop and propfan engines were made through the stirred reactor models developed by Hugo Pervier (see references [79] and [80]), instead of the P3T3 method adopted in the previous case of turbofan engine due to the unavailability of related reference data from ICAO emission databank.

The following Figures, 5-13 and 5-14, illustrate the basic principle of the two stirred reactor models used in this research work.

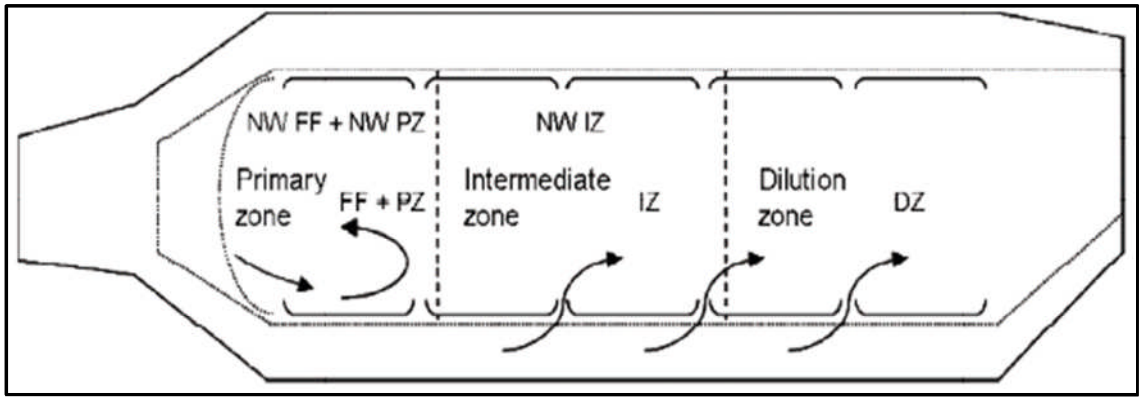

Figure 5-13 Conventional combustor schematic representation [79, 80]

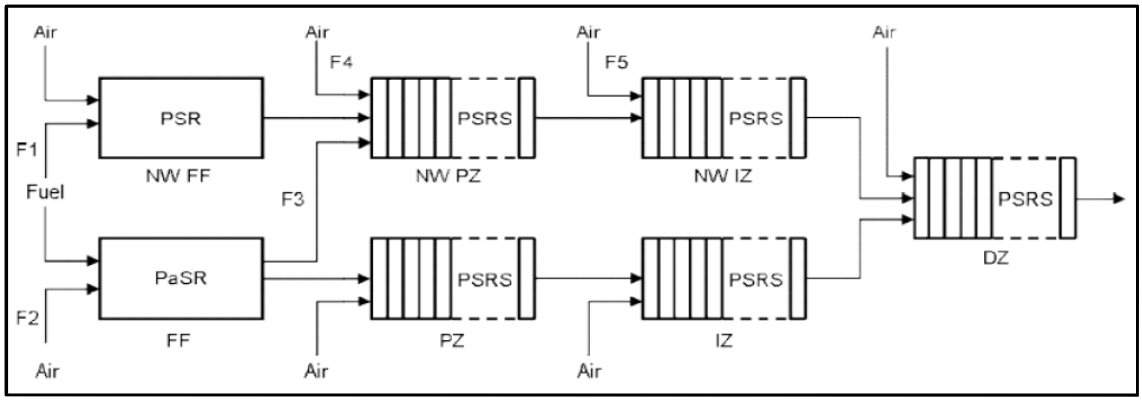

Figure 5-14 Conventional combustor – multi-reactor model [79, 80]

From the above two figures, it can be observed that: 1) the entire combustor is divided into three zones, that is, primary zone (PZ), intermediate zone (IZ), and dilution zone (DZ); 2) the combustor primary zone is subdivided into two parts, i.e., flame front (FF) and primary zone (PZ) itself. The flame front (FF) which simulates the initial mixing and reaction of the fuel with the nozzle and swirler air is modelled through a partially-stirred reactor (PaSR), rather than the commonly-used Perfectly-Stirred Reactor (PSR) so that the inhomogeneity in the distribution of fuel-air-ratio (FAR) in this combustor region, which has significant impacts on the formations of most of the pollutants of interest, can be taken into account properly; 3) The second part of the combustor primary zone, i.e., PZ, the combustor intermediate (or secondary) zone (IZ), and the dilution zone (DZ) are modelled by a series of perfectly-stirred reactors (PSRS); 4) Except the dilution zone (DZ), FF, PZ and IZ are all simulated by two generic reactor models in parallel which respectively occupy the core and the near-wall (NW) regions of each of these zones; 5) The outcomes from both core and near-wall reactors of IZ mix together as one of inputs to enter into a single PSRS model which functions to simulate the combustor DZ.

The following Figure 5-15 illustrates the code structure and calculation procedure of stirred reactor based emission prediction model.

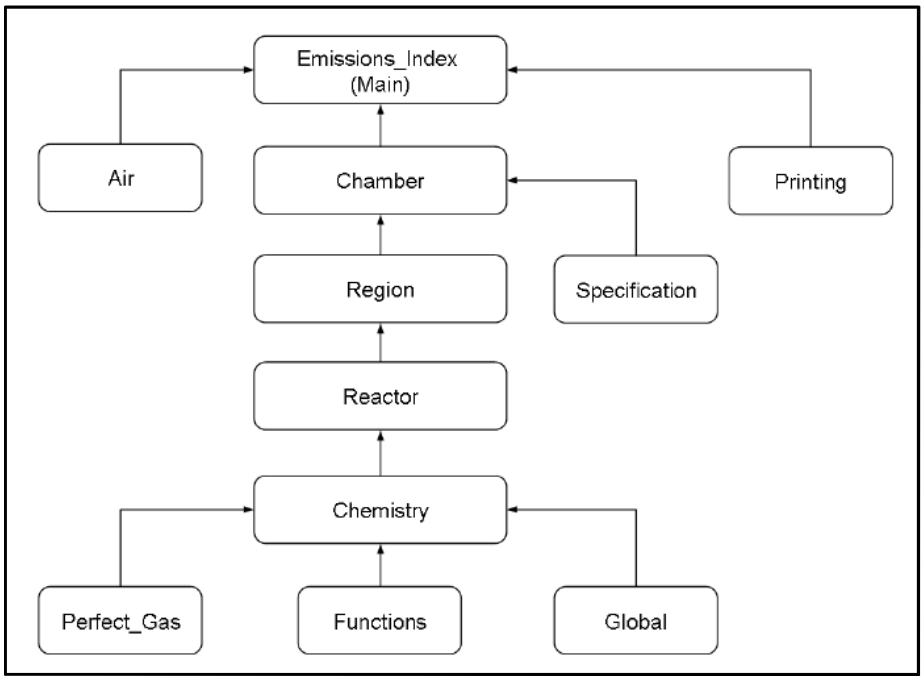

Figure 5-15 Emission prediction model - code structure and calculation procedure [65]

As shown in the above Figure 5-15, the stirred reactor based emission prediction model is coded with two types of modules, i.e., five primary modules and several secondary modules. The five primary modules are, respectively, 'Emissions_Index' module, 'Chamber' module, 'Region' module, 'Reactor' module, and 'Chemistry' module. Among them, the 'Emissions_Index' module functions as a control module responsible for reading data from the input file, driving the computation process and writing results to output files; the 'Chamber' module is designed to code different combustion chamber configurations; the 'Region' module is built for modelling the different regions of combustion chambers such as primary zone, intermediate zone, and dilution zone; 'Reactor' module is developed for modelling the generic chemical reactors; and 'Chemistry' module which contain the algorithms is utilised for simulating the formation of the main pollutants of interest. During the calculation, the calculation data flow logically from the bottom 'Chemistry' module, in turn, through the 'Reactor' module, 'Region' module and 'Chamber' module, until reaching the top 'Emissions_Index' module by one invoking another from top to bottom reversely. As for the secondary modules, they mainly include 'Air' module, 'Specification' module, 'Perfect_Gas' module, 'Functions' module, and 'Global' module, etc. Among them, 'Air' module is used to determine air composition; 'Specification' module contains parameters considered constant during the calculations; 'Perfect_Gas' module is designed to determine thermodynamic properties of ideal gases; 'Functions' module comprises those functions for calculating reaction rate coefficients, and 'Global' module comprises common parameters to all modules.

As for the stirred reactor based emission prediction model, besides the above discussion, the following points should be highlighted:

1. In the reactor models mentioned above, normally, two input streams are involved: gas stream (air or combustion products) and fuel/air stream. It is assumed that mixing of these two streams occurs instantaneously in the reactors;
2. The emissions of interest in this research work are mainly CO_2, H_2O and NOx which are directly related to the research objectives of the Clean Sky project. Among them, it is considered that CO_2 and H_2O are produced under chemical equilibrium conditions and, hence, their emission indices $EICO_2$ and EIH_2O are

respectively determined from equilibrium calculations performed by using the NASA CEA (Chemical Equilibrium with Applications) program.

3. NOx is not formed in local chemical equilibrium. Therefore, more detailed representation of finite rate chemistry and correspondingly kinetic calculations of this type of emission are included in the prediction model used in this research.

References [79] and [80] respectively give geometry data and model parameters of the combustors used in the stirred reactor models developed for the gaseous emission predictions of turboprop-driven aircraft (CUTPDAC research case) and propfan-powered aircraft (CUPFDAC research case). These data and parameter values are listed respectively in the following Tables 5-2 to 5-5.

Table 5-2 Combustor geometry data (for CUTPDAC case) [79]

Zone	FF	PZ	IZ	DZ
Flow area (m^2)	0.36	0.36	0.36	0.36
Length (m)	0.048	0.048	0.144	0.144
Air inflow fraction	0.2	0.2	0.2	0.4

Table 5-3 Model parameters (for CUTPDAC case) [79]

F1	F2	F3	F4	F5
0.20	0.75	0.25	0.20	0.40

Table 5-4 Combustor geometry data (for CUPFDAC case) [80]

Zone	FF	PZ	IZ	DZ
Flow area (m^2)	0.20617	0.20617	0.20617	0.20617
Length (m)	0.03125	0.03125	0.09375	0.09375
Air inflow fraction	0.2	0.2	0.2	0.4

Table 5-5 Model parameters (for CUPFDAC case) [80]

F1	F2	F3	F4	F5
0.15	0.60	0.15	0.20	0.20

Here, these model parameters are defined, respectively, as follows:

F1 - Fraction of fuel reaching the near wall mixing zone.

F2 - Proportion of the swirler and dome air that goes into the flame front PaSR reactor.

F3 - Fraction of the burning gases admitted into the primary near-wall reactor.

F4 - Fraction of the air initially assigned to the primary zone that goes into the primary near-wall reactor.

F5- Fraction of the air initially assigned to the intermediate zone that goes into the intermediate near-wall reactor.

In addition, reference [79] also mentioned that since no data were available to compare the outputs of this prediction model, only a preliminary check was made as shown in the following Figures 5-16, 5-17 and 5-18 (It is noted that the relative value in emission index (EI) in these figures is defined as the ratio of the EI value of a certain emission at actual engine operating rating to the corresponding one at engine full power).

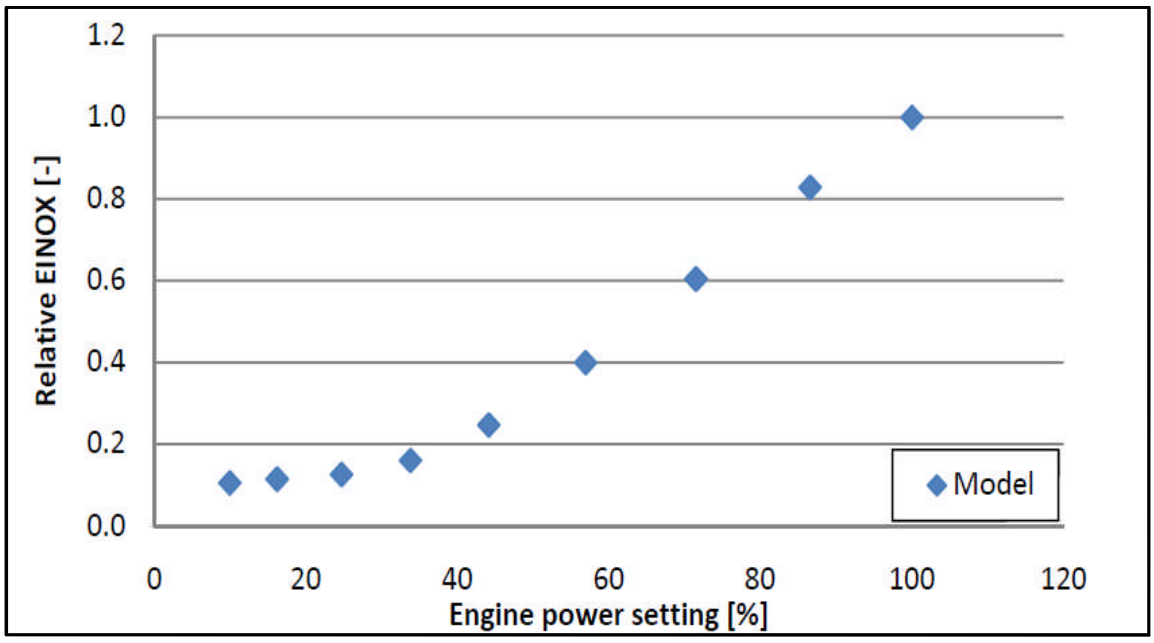

Figure 5-16 Relative NOx emission index against engine power setting [79]

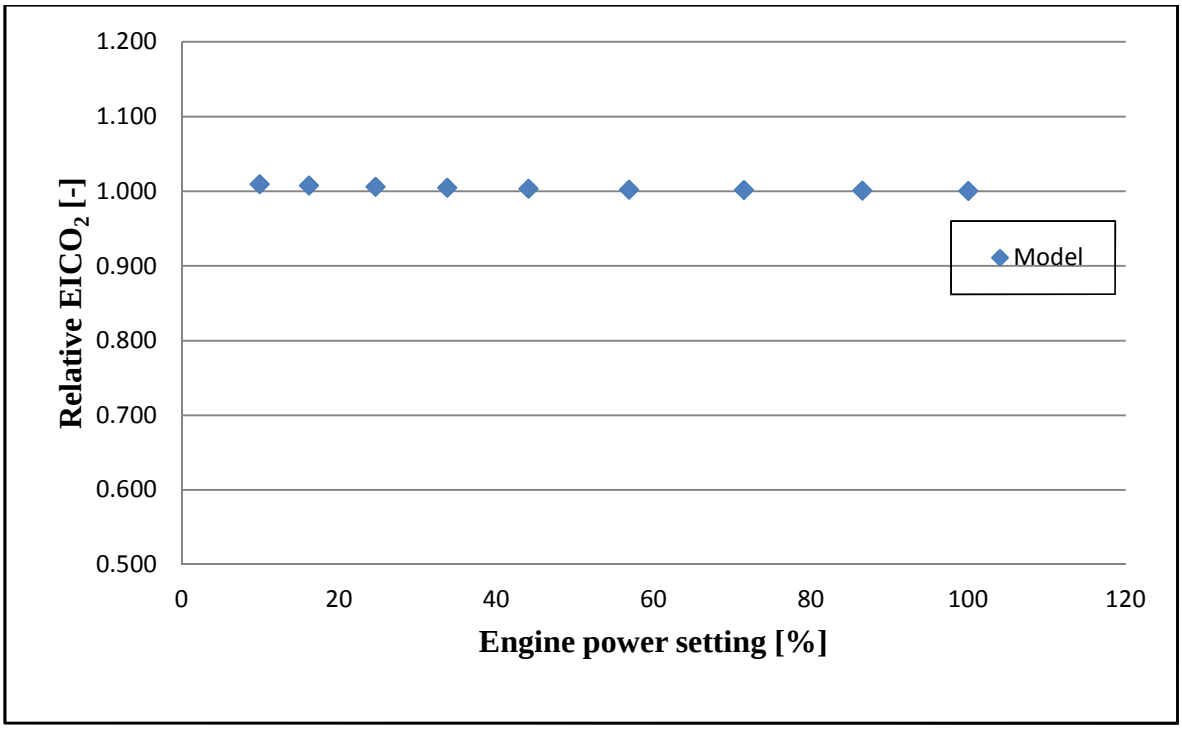

Figure 5-17 Relative CO_2 Emission Index against Power setting [79]

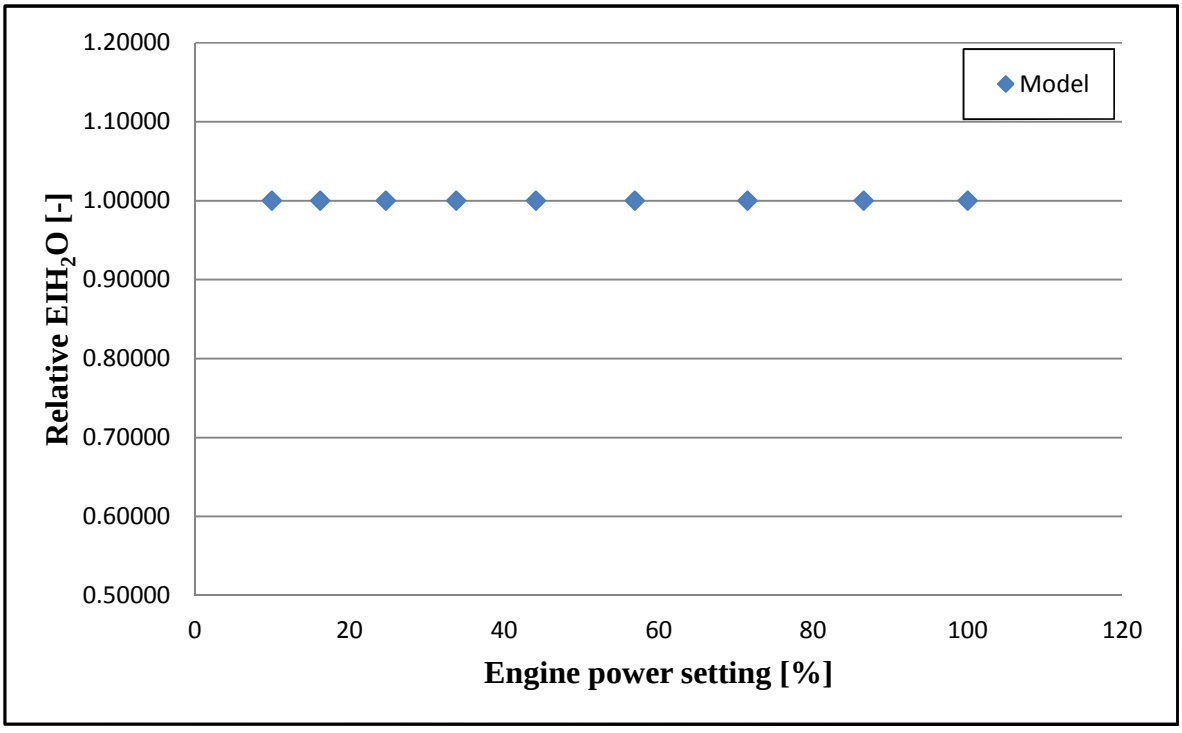

Figure 5-18 Relative H_2O Emission Index against Power setting [79]

As seen from the formation mechanism of NOx mentioned previously, the production rate of NOx is highly dependent on the flame temperature in the combustor. Therefore, it can be expected that “an increase of the engine power setting will increase the emission index of NOx” [79]. This predicted trend represented in Figure 5-16 from the stirred reactor model shows agreement with what is expected.

As for the predictions of $EICO_2$ and EIH_2O from the stirred reactor model, reference [79] states that due to the direct relationships between emissions of CO_2 and H_2O and fuel burnt, as well as the definition way of the emission index (i.e., mass of emission/mass of fuel), the $EICO_2$ and EIH_2O remain constant as the power setting changes (as a matter of fact, this point has been discussed in the previous section), which is also in agreement with what is expected.

CHAPTER SIX FLIGHT NOISE AND MODELLING

Noise, like other annoying factors such as litter, local strong lighting, may cause an uncomfortable emotional reaction in human beings (see Figure 6-1) and is often regarded as one of the most undesirable features of life in urban community. Among types of noise, aircraft noise [81-83] is second only to the traffic noise in cities and usually rise to the top of the list in rural areas "in its unsociable levels, frequency and time of occurrence" [81].

Although aircraft have been becoming increasingly quieter due to the significant progress in technology during the last several decades, especially the displacement of turbojet by turbofan engine and adoption of high bypass ratio, the achievement has not sufficiently offset the progressively-increased adverse impact of noise resulted from the rapid growth of commercial aviation operations. As a matter of fact, the fast expansion of civil aviation transport today has intensified the problem and "given rise to much greater intrusion on community life and, hence, to noise exposure" [81].

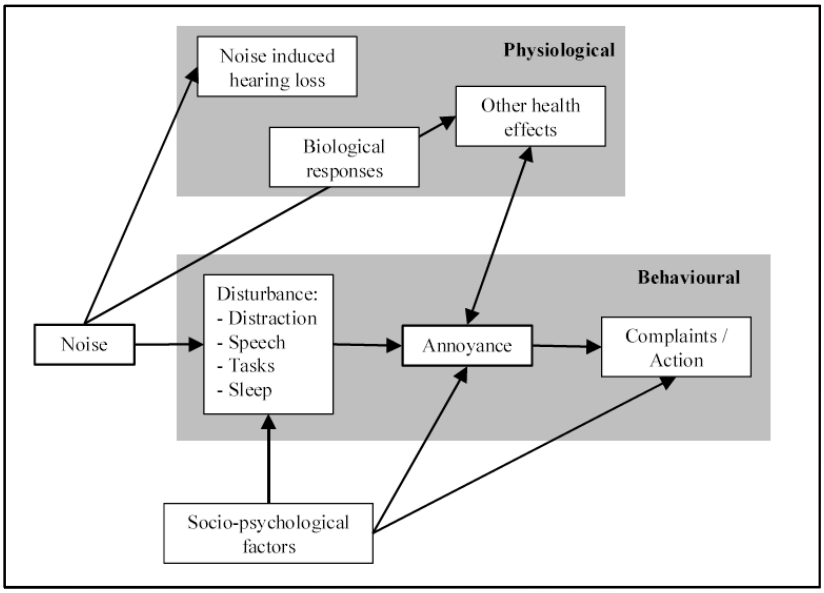

Figure 6-1 Impact of Noise [84]

Noise level is measured through Noise Metrics, with the unit of deciBel (dB) which "addresses the wide range of sound intensities accommodated by the human species by using a logarithmic ratio of the actual sound pressure level (SPL) to a nominal value, the "threshold" of hearing, set at 20 μP_a" [81], that is, $(10 \log_{10} \frac{\text{actual SPL}}{20\mu P_a})$ dB.

(Note: the deciBel concept is also used to express the relative change in two sound intensities or noise levels, that is, $(10\log_{10}\frac{I_2}{I_1})$ dB).

Noise metrics are usually divided into two types, 'Single Event Noise Metrics' and 'Cumulative Noise Metrics'.

Single Event Noise Metrics "describe the acoustic event caused by a single aircraft movement." [84]. There are two commonly-used types: L_{max} and L_E. The former one is based on the maximum sound intensity during the event, and the latter is based on the total sound energy in the event (here, the total sound energy is expressed as the product of the maximum sound intensity and the effective duration of the event defined in the following equation (6-1)). The following Figure 6-2 and equations (6-2) and (6-3) give the illustration, definition and interrelation of these two noise metrics.

$$t_e \cdot 10^{L_{max}/10} = \int_{t_1}^{t_2} 10^{L(t)/10} dt \qquad (6\text{-}1)\ [84]$$

$$L_E = 10 \cdot \lg\left(\frac{1}{t_0}\int_{t_1}^{t_2} 10^{L(t)/10} dt\right) \qquad (6\text{-}2)\ [84]$$

Where, t_0 is a reference time, and the determination of the integration interval $[t_1, t_2]$ should "guarantee that all significant sounds of the stated event is encompassed" [84].

$$L_E = L_{max} + 10 \cdot \lg\left(\frac{t_e}{t_0}\right) \qquad (6\text{-}3)\ [84]$$

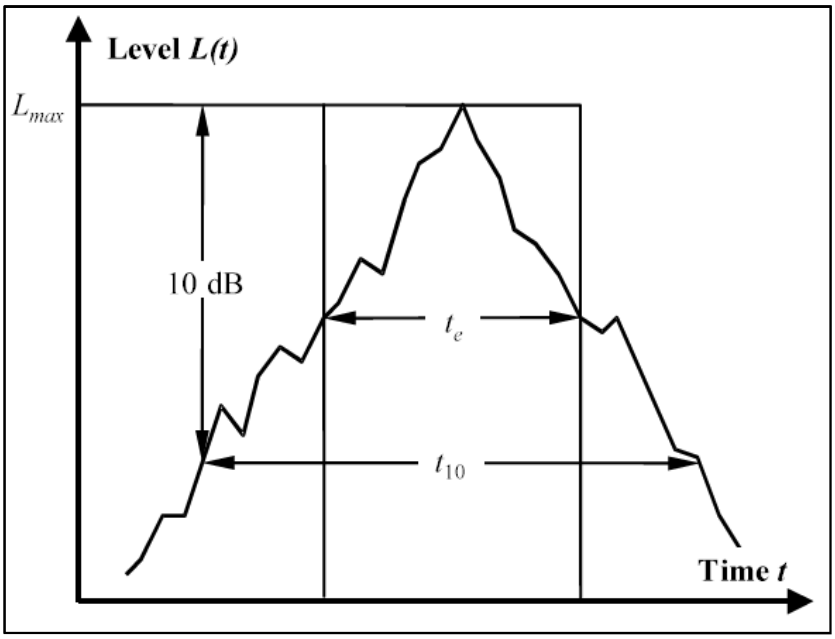

Figure 6-2 Level-Time History of a Noise Event and L_{max} [84]

Based on the facts that the acoustic energy of sound is distributed over a wide frequency range (approximately from 20Hz to 20KHz) — the frequency-spectrum property of sound, and human beings have different responses to sounds with the same intensity but different frequencies, frequency-domain treatment techniques which account for the role of sound frequency in the noise-impact assessment are adopted and, correspondingly, the so-called Noise Scales are introduced. Among them, the most important and commonly-used are 'A-weighted sound level (usually denoted as 'L_A')' and 'Tone-corrected Perceived Noise Level (denoted as 'L_{PNT}')'.

"The A-weighting is a simple filter applied to sound measurements which applies more or less emphasis to different frequencies to mirror the frequency sensitivity of the human ear at moderate sound energy levels" [84], while 'Tone-corrected Perceived Noise Level' considers "intricacies of human perception of noise from broadband sources containing pure tones or other spectral irregularities" [84].

'Tone-corrected Perceived Noise Level' is determined from 1/3-octave spectra and uniquely applied for precise measurement of aircraft noise, while 'A-weighted sound level' is a universally used scale of environmental noise level.

Therefore, combined with the above two noise scales, the four commonly-used noise metrics are available, shown in the following Table 6-1, and related expressions are further listed in equations (6-4)−(6-7).

Table 6-1 Commonly-used noise metrics with different frequency-weightings

Noise metrics / Noise scales	L_{max}	L_E
L_A	$L_{A,max}$	L_{AE}
L_{PNT}	$L_{PNT,max}$	L_{EPN}

$$L_{AE} = 10 \cdot \lg\left(\frac{1}{t_0}\int_{t_1}^{t_2} 10^{L_A(t)/10} dt\right) \qquad (6\text{-}4)\ [84]$$

$$L_{AE} = L_{A,max} + 10 \cdot \lg\left(\frac{t_e}{t_0}\right) \qquad (6\text{-}5)\ [84]$$

where, t_0=1 second.

$$L_{EPN} = 10 \cdot \lg(\frac{1}{t_0}\int_{t_1}^{t_2} 10^{L_{PNT}(t)/10}dt) \qquad (6\text{-}6)\ [84]$$

$$L_{EPN} = L_{PNT,max} + 10 \cdot \lg(\frac{t_e}{t_0}) \qquad (6\text{-}7)\ [84]$$

where, t_0=10 second.

Different from the above 'Single Event Noise Metrics', 'Cumulative Noise Metrics' are used to describe the total noise experienced during longer time periods. 'Equivalent Sound Level' (denoted as 'L_{eq}') based on the energy principle is the most commonly-used cumulative noise metric, which accounts for the contributions to annoyance from both event levels and numbers of events. The expression of 'L_{eq}' is as follows:

$$L_{eq} = \overline{L}_E + 10\lg N - \text{const.} \qquad (6\text{-}8)\ [84]$$

Where, $\overline{L}_E$ is the average event level of the N events experienced during the specified time interval. The constant term relies on the time interval ($=10 \cdot \lg[\text{number of seconds in the time interval}]$).

(Note: the energy principle is that the adverse effects of noise rely on the total amount of noise energy involved.)

In recent years, weightings have been introduced into 'Equivalent Sound Level' (L_{eq}) to consider a change of community noise sensitivity over the 24-hour day (i.e., the tolerance to noise by community falls from the daytime to the evening and further to the night). It, therefore, gave rise to modified versions of L_{eq}, such as '24-hour average sound level' ($L_{Aeq,24h}$) , '16-hour day-average sound level' ($L_{Aeq,day}$), '8-hour night-average sound level' ($L_{Aeq,night}$), 'Day-night average sound level' (L_{DN}), and 'Day-evening-night sound level' (L_{DEN}) etc..

The following equation (6-9) and Table 6-2 give the calculation methods of these modified versions of L_{eq} (or called 'Time-weighted equivalent sound levels').

$$L_{eq,W} = 10 \cdot \lg\left[\frac{t_0}{T_0} \cdot \sum_{i=1}^{N} g_i \cdot 10^{L_{E,i}/10}\right] + C \qquad (6\text{-}9)\ [84]$$

where, N denotes the number of aircraft noise events occurring over the specified reference time period T_0. $L_{E,i}$ is the noise exposure level of the i-th noise event. The coefficient g_i denotes a time-of-day dependent weighting factor.

Table 6-2 Parameters for the determination of $L_{eq,W}$ [84]

L_{eq}	$L_{E,i}$ [dB]	t_o [s]	C [dB]	T_O [1] [s]	g_i [2]		
					day	evening	night
$L_{Aeq,24h}$	L_{AE}	1	0	86400 N_{Tr}	1	1	0
$L_{Aeq,day}$ [3]	L_{AE}	1	0	57600 N_{Tr}	1	0	0
$L_{Aeq,night}$	L_{AE}	1	0	28800 N_{Tr}	0	0	1
L_{DN}	L_{AE}	1	0	86400 N_{Tr}	1	1	10
L_{DEN} [4]	L_{AE}	1	0	86400 N_{Tr}	1	3.162[5]	10

As for the impacts of aircraft noise on community, despite the announcement illustrated in Figure 6-1(above) involving both physiological and behavioural sides, scientific conclusions about the possibility of 'health effects' are much less clear [84]. Therefore, so far, the practical assessment about noise impact is to adopt 'community annoyance' as the principal response measure, such as, 'Contour Area', 'Population Enclosed', 'Houses/Households Enclosed', 'Noise Levels at Enforcement Points', 'Awakenings', 'People Highly Annoyed', 'Sleep Disturbance', etc.

In this project research, due to the research scope of single-noise-event impact assessment and actual unavailability of some statistical data, like population or house distribution around investigated airports, the four single-event noise metrics ($L_{A,max}$, L_{AE}, $L_{PNT,max}$ and L_{EPN}) and 'Contour Area' are used to measure aircraft noise level and assess its influence on the vicinity of airports during 'Departure' and 'Arrival' phases of aircraft.

The calculation of noise metrics and its impact assessment [85, 86] in this project research were completed through two simulation software packages, 'INMTM_v3.exe' (INMTM-Integrated Noise Model/Management of Trajectory and Missions) and 'NoiseLAss_v2.0' provided by Delft University of Technology [87, 88].

The 'INMTM_v3.exe' is a replication of the FAA's standard noise assessment tool INM (Integrated Noise Model) [89-91] version 7.0b. This software can provide the capability

to calculate the noise exposure of a single event flyover on a user-defined grid of observer locations below the flight trajectory for four noise metrics, i.e., $L_{A,max}$, L_{AE} (SEL), $L_{PNT,max}$ (PNLTM) and L_{EPN} (EPNL).

The methodology employed in INMTM is based on the empirically obtained Noise-Power-Distance (NPD) database (see Figure 6-5), and its calculation process can be divided into two steps [87]:

1) By the interpolation for the current thrust level and slant distance (aircraft-observer), find the uncorrected noise metrics.
2) Correction calculation.

   Since the creation of NPD is based on the assumption that the aircraft flies on an infinitely long segment at a given reference speed, and that the observer is standing directly below the flight path, several corrections are correspondingly needed. They include:

   a) 'Duration adjustment' (considering that aircraft are not flying at the reference speed, and just suitable to exposure based (i.e., time-dependent) trajectories.
   b) 'Noise fraction adjustment' (considering finite segment lengths as well as observers being ahead or aft flight segments).
   c) 'Lateral attenuation adjustment' (considering observers being astride the segment and the impact from ground reflection).

The following Figure 6-3 illustrates the entire calculation/assessment process of noise metrics and noise impact. Figure 6-4 shows the establishment of 3D flight path based on the ground track and vertical flight profile which is required by the calculation and assessment of flight noise.

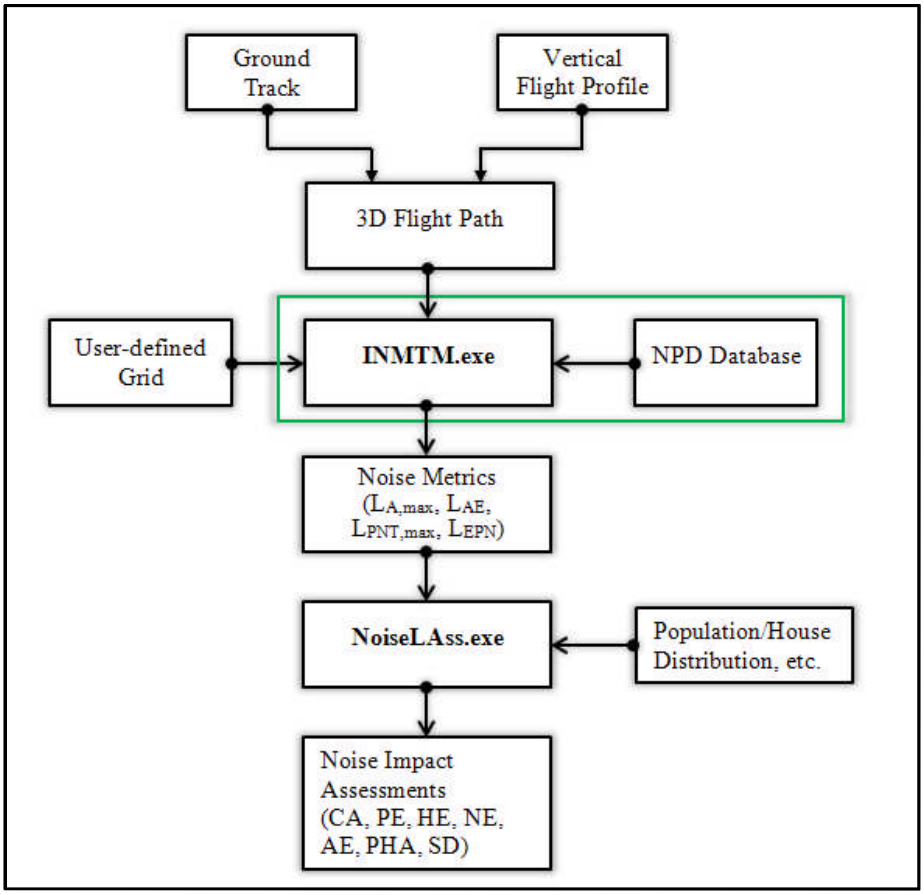

Figure 6-3 Noise Calculation and Assessment

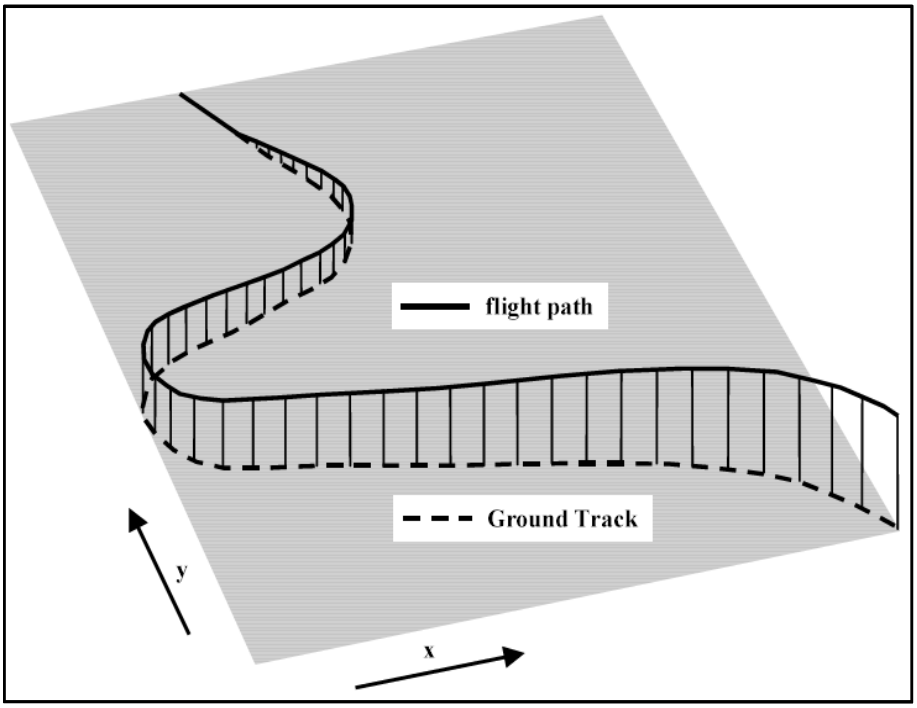

Figure 6-4 3D Flight Path [84]

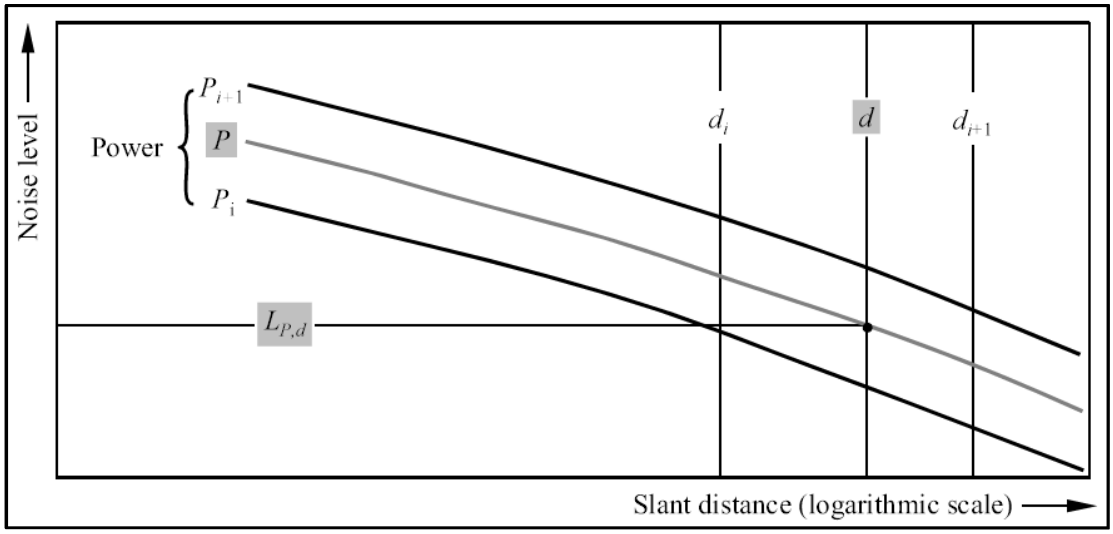

Figure 6-5 Noise-Power-Distance (NPD) Curves [84]

The following Tables 6-3 and 6-4 are the flight noise models selected from the NPD database respectively for the case studies of CUTFDAC and CUTPDAC.

Table 6-3 Noise Model of CUTFDAC [87]

NPD_ID	MET	OP	THR	200	400	630	1000	2000	4000	6300	10000	16000	25000	C
CFM565	E	A	1500	97.4	91.6	87.5	82.9	76.0	68.3	62.5	55.3	46.5	33.4	J
CFM565	E	A	3000	98.8	93.4	89.2	84.7	77.6	69.7	63.9	56.7	47.7	35.5	J
CFM565	E	A	5000	100.8	95.2	91.0	86.4	78.6	70.3	64.3	57.2	48.4	35.7	J
CFM565	E	D	12000	108.2	104.2	99.8	95.1	86.9	78.2	72.8	65.1	57.4	47.4	J
CFM565	E	D	15500	110.7	106.0	102.0	97.2	89.6	81.5	76.2	69.8	62.2	53.2	J
CFM565	E	D	19000	110.9	106.7	103.2	99.1	92.1	85.1	80.1	73.5	66.4	57.9	J
CFM565	E	D	22500	113.2	108.4	105.0	101.3	94.9	88.4	83.6	77.0	70.4	62.1	J
CFM565	M	A	1500	87.9	80.9	76.2	71.3	63.3	54.5	48.0	40.9	32.9	24.6	J
CFM565	M	A	3000	90.4	83.2	78.3	73.1	64.9	55.7	49.0	41.7	33.9	26.1	J
CFM565	M	A	5000	92.3	84.7	79.4	73.8	65.3	56.0	49.3	42.0	34.3	26.3	J
CFM565	M	D	12000	100.3	92.0	86.2	80.3	71.1	61.7	55.4	48.6	40.9	33.1	J
CFM565	M	D	15500	102.5	94.9	89.5	83.6	74.0	65.0	58.8	52.1	44.7	36.8	J
CFM565	M	D	19000	104.3	96.6	91.1	85.7	77.2	68.2	62.2	55.5	47.9	40.0	J
CFM565	M	D	22500	105.9	98.9	94.1	88.9	80.9	72.5	66.1	59.4	51.7	43.3	J
CFM565	P	A	1500	102.4	94.5	89.2	83.3	74.2	64.3	56.9	48.6	38.3	24.2	J
CFM565	P	A	3000	105.0	97.0	91.3	85.2	75.5	65.2	57.7	50.0	40.2	29.0	J
CFM565	P	A	5000	107.3	99.3	93.7	87.2	76.6	65.8	58.2	50.5	39.1	26.0	J
CFM565	P	D	12000	120.5	112.3	106.1	98.7	87.8	75.1	68.2	57.8	48.4	37.4	J
CFM565	P	D	15500	119.5	111.8	106.3	100.0	88.7	78.8	72.1	63.1	54.3	42.9	J
CFM565	P	D	19000	121.8	114.2	108.6	102.6	92.4	81.9	75.7	66.2	57.5	47.3	J
CFM565	P	D	22500	122.8	115.5	110.2	104.4	94.9	85.9	79.5	70.7	62.2	52.2	J
CFM565	S	A	1500	92.7	87.4	84.1	80.7	75.1	68.8	64.1	58.8	52.6	46.1	J
CFM565	S	A	3000	94.1	89.0	85.5	82.0	76.3	69.9	65.2	59.8	53.4	46.9	J
CFM565	S	A	5000	95.2	90.0	86.5	82.7	76.7	70.2	65.5	60.2	54.2	47.4	J
CFM565	S	D	12000	100.9	96.2	92.4	88.3	81.9	75.5	71.1	66.0	60.0	53.8	J
CFM565	S	D	15500	103.6	99.0	95.3	91.5	85.6	79.3	74.9	69.9	64.2	57.9	J
CFM565	S	D	19000	104.7	100.5	97.3	93.9	88.3	82.4	78.1	73.2	67.3	61.0	J
CFM565	S	D	22500	106.5	102.4	99.6	96.4	91.4	85.7	81.5	76.5	70.8	64.3	J

Table 6-4 Noise Model of CUTPDAC [87]

NPD_ID	MET	OP	THR	200	400	630	1000	2000	4000	6300	10000	16000	25000	C
RDA532	E	A	32	106.5	101.2	96.8	91.5	81.1	69.6	61.9	53.8	45.7	34.2	P
RDA532	E	A	73	107.3	102.2	98.1	94.5	88.5	81.3	75.5	69.2	62.9	54.6	P
RDA532	E	D	73	107.3	102.2	98.1	94.5	88.5	81.3	75.5	69.2	62.9	54.6	P
RDA532	E	D	100	107.7	103.3	100.2	96.8	91.2	84.7	79.9	74.2	67.8	59.2	P
RDA532	M	A	32	96.4	88.7	82.9	76.2	65.3	55.1	48.3	41.3	34.1	26.4	P
RDA532	M	A	73	98.2	91.1	86.2	81.2	73.6	65.9	60.5	54.7	48.2	40.7	P
RDA532	M	D	73	98.2	91.1	86.2	81.2	73.6	65.9	60.5	54.7	48.2	40.7	P
RDA532	M	D	100	98.6	92.2	87.8	83.4	76.4	68.9	63.4	57.3	50.3	42.0	P
RDA532	S	A	32	98.9	93.5	89.1	84.0	75.3	67.3	62.0	56.5	50.8	44.6	P
RDA532	S	A	73	100.2	95.4	92.0	88.4	83.1	77.7	73.8	69.5	64.5	58.5	P
RDA532	S	D	73	100.2	95.4	92.0	88.4	83.1	77.7	73.8	69.5	64.5	58.5	P
RDA532	S	D	100	101.3	97.2	94.3	91.4	86.7	81.4	77.5	72.8	67.3	60.6	P

As for the flight noise modelling of the aircraft powered by the new generation propfan (open rotor) engines (in this research work, the aircraft is denoted as CUPFDAC), it is indeed a difficult job. Ideally, the state-of-the-art propeller blade designs (for instance, those being developed by GE, RR and SNACMA in recent years) should be adopted. However, obviously, the proprietary information from these manufacturers is unavailable in this research work. Therefore, alternative approximation methods have to be considered. One possible option is to use the blade design information of the first generation open rotor engine GE36 (such as SR-7) which has been published openly. However, GE36 was designed in the 1980s (i.e., around 30 years ago) and compared to the out-of-date design, the present blade profile is of much better acoustic performance and the new-generation open rotor engine with newly-developed propellers will tend to be much quieter [92, 93]. Reference [92] briefly introduces the great progress achieved recently in this aspect. According to the reference [92], “initial performance and noise studies conducted in the wind tunnel show that an open rotor engine with counter-rotating propellers in pusher configuration will have margin for Stage 4 operations and will likely meet and exceed the more stringent Stage 5 levels to be set by ICAO next year and implemented by 2020”. Therefore, applying the old GE36 propeller technology to predict the noise impact of the aircraft powered by the new-generation propfan engine is actually not very reasonable. In this research, the main interest is in the overall impact of flight noise on the areas in the vicinity of local airports instead of the detailed noise characteristics, therefore from the point of view of similar noise levels

(magnitudes) and installation (fuselage mounted engines), as well as the availability from the noise database of NPD, the noise data from the combination MD-90/V2528-D5 (ACFT_ID: MD9028 and NOISE_ID: V2525 in the NPD database) were selected as the alternative approximation noise model (see the following Table 6-5). From the reference [94], the certificated noise levels (magnitudes) of MD-90/V2528-D5 is about 6-9 EPNdB less than the corresponding limit values of ICAO stage-3 noise standard and basically approaches the threshold values of the stage-4 requirements. Therefore, from this point of view, the combination MD-90/V2528-D5 can be, to some extent, assumed as an “equivalent” alternative of CUPFDAC (or say, in this research, the CUPFDAC is assumed to be of the noise variation characteristics with the engine power setting and the slant distance provided by NOISE_ID: V2525 in the NPD database). Certainly, due to the above reason, the optimisation results related to this model are only for the purpose of reference.

Table 6-5 Noise Model of CUPFDAC [87]

NPD_ID	MET	OP	THR	200	400	630	1000	2000	4000	6300	10000	16000	25000	C
V2525	E	A	3000	94.0	89.2	86.0	82.0	75.8	68.8	63.0	56.5	47.9	37.0	J
V2525	E	A	6950	96.7	92.0	88.3	84.5	78.5	71.5	65.9	59.5	50.5	39.5	J
V2525	E	D	10500	99.3	95.0	91.5	88.0	81.8	74.4	69.2	63.1	56.0	47.6	J
V2525	E	D	13150	101.0	96.5	93.0	89.5	83.5	77.0	72.0	66.0	59.0	51.2	J
V2525	E	D	18500	105.0	100.3	97.0	94.0	88.2	82.0	77.3	72.0	65.0	57.8	J
V2525	E	D	23000	109.8	105.2	102.5	99.0	93.0	87.0	82.6	77.0	70.8	63.5	J
V2525	M	A	3000	89.2	83.0	78.2	73.7	66.0	57.5	51.0	44.1	36.5	28.3	J
V2525	M	A	6950	91.0	84.5	80.0	75.0	67.7	58.9	53.0	46.0	38.2	30.0	J
V2525	M	D	10500	93.1	86.5	82.0	77.2	69.9	61.1	55.3	48.7	41.2	33.4	J
V2525	M	D	13150	95.2	88.8	84.0	79.5	72.1	63.5	57.9	51.0	43.8	36.0	J
V2525	M	D	18500	100.0	93.4	88.8	84.0	76.7	68.1	62.2	56.0	48.6	40.8	J
V2525	M	D	23000	104.8	98.5	93.9	89.0	81.8	73.3	67.8	61.0	53.5	45.4	J
V2525	S	A	3000	91.9	88.5	85.4	81.9	76.7	71.2	66.9	61.7	55.7	49.1	J
V2525	S	A	6950	94.3	90.2	86.6	83.5	78.3	72.8	68.4	63.7	57.5	51.5	J
V2525	S	D	10500	95.8	91.6	88.5	85.3	80.2	74.7	70.2	65.7	59.5	54.1	J
V2525	S	D	13150	98.1	94.0	91.0	87.9	82.7	76.9	72.7	68.2	62.7	56.7	J
V2525	S	D	18500	102.4	98.5	95.7	92.7	87.7	82.2	78.2	73.2	67.8	61.7	J
V2525	S	D	23000	106.2	102.7	99.7	97.0	92.2	86.7	82.7	78.0	72.7	66.5	J

CHAPTER SEVEN MULTIDISCIPLINARY OPTIMISATION AND GENETIC ALGORITHMS

7.1 Introduction of Multidisciplinary Optimisation Problem

So far, design approach of the aviation industry has roughly experienced three different historical stages. The first stage took place before the 1970s. During that stage, the design goals of engineering projects were generally performance-related, for instance, aircraft designs sought for maximum speed, minimum drag, or minimum structural weight, and aero engine designs preferred to higher thrust and lower SFC (specific fuel consumption). Between 1970 and 1990, with the appearance of computer-aided design and changes in the procurement policy of most airlines and military organisations (from a performance-centred approach to one that emphasised lifecycle cost issues), the approach of aircraft/engine design engineers to their design problems was changed accordingly, with an increased concentration on economic factors and the attributes such as manufacturability, reliability, maintainability, etc. This was the second stage of engineering design approach. Today, aviation design is experiencing its third stage and design considerations are further being expanded to the environment field, and reducing emissions of gaseous pollutants (such as NOx, CO and UHC, etc.) and noise, as well as the adverse impacts resulting in climate change from emissions of CO_2 and H_2O, have become an important design criterion for aviation products.

On the other hand, “the high-performance personal computer has largely replaced the centralized supercomputer and the Internet and local area networks have facilitated sharing of design information” [95]. Disciplinary design software in many disciplines has become very mature and many optimisation algorithms, in particular the population-based algorithms, have advanced significantly [95].

All these led to the appearance and wider and wider applications of multidisciplinary design optimisation in the present aviation industry.

“Multi-disciplinary design optimization (MDO) is a field of engineering that uses optimization methods to solve design problems incorporating a number of disciplines. It is also known as multidisciplinary optimization and multidisciplinary system design optimization (MSDO).” [95]

"MDO allows designers to incorporate all relevant disciplines simultaneously. The optimum of the simultaneous problem is superior to the design found by optimizing each discipline sequentially, since it can exploit the interactions between the disciplines. However, including all disciplines simultaneously significantly increases the complexity of the problem." [95]

7.2 Mathematic Description of Multidisciplinary Optimisation Problem

From the point of view of mathematics, a multidisciplinary design optimisation problem can be expressed as a multi-objective optimisation problem which "is an area of multiple criteria decision making that is concerned with mathematical optimization problems involving more than one objective function to be optimized simultaneously" and can be formulated as follows:

$$\begin{aligned}
&\min \quad \mathbf{F}(\mathbf{x}) = [F_1(\mathbf{x}), F_2(\mathbf{x}), \ldots, F_m(\mathbf{x})]^T \\
&\text{subject to} \\
&\mathrm{g}_j(\mathbf{x}) \le 0, \quad j = 1, 2, \ldots, p \\
&\mathrm{h}_k(\mathbf{x}) = 0, \quad k = 1, 2, \ldots, q \\
&\mathbf{x}^L \le \mathbf{x} \le \mathbf{x}^U
\end{aligned}$$

Where m is the number of objective functions, p and q are respectively the number of inequality and equality constraints, $\mathbf{x}$ is a vector of decision variables, $F_i(\mathbf{x})$ is the i^{th} objective function, $\mathbf{x}^L$ and $\mathbf{x}^U$ are respectively the lower and upper boundary vectors.

"For a nontrivial multi-objective optimization problem, there does not exist a single solution that simultaneously optimizes each objective. In that case, the objective functions are said to be conflicting, and there exists a (possibly infinite number of) Pareto optimal solutions." [96]

"A solution is called nondominated, Pareto optimal, Pareto efficient or noninferior, if none of the objective functions can be improved in value without impairment in some of the other objective values" [96]. "In mathematical terms, a feasible solution $x^1 \in X$ is said to (Pareto) dominate another solution $x^2 \in X$, if

1. $f_i(x^1) \le f_i(x^2)$ for all indices $i \in \{1, 2, \ldots, k\}$ and
2. $f_j(x^1) < f_j(x^2)$ for at least one index $j \in \{1, 2, \ldots, k\}$.

A solution $x^1 \in X$ (and the corresponding outcome $f(x^*)$) is called Pareto optimal, if there does not exist another solution that dominates it. The set of Pareto optimal outcomes is often called the Pareto front." [96].

"Without additional preference information, all Pareto optimal solutions can be considered mathematically equally good." [96].

Due to the characteristics of multiple Pareto optimal solutions for multi-objective optimisation problems, in practice there are usually two categories of treatment methodologies.

The first one can be named as the "scalarization" method which converts the original problem with multiple objectives into a single objective optimisation problem. With careful scalarization, optimal solutions to the single-objective optimisation problem can be guaranteed to be Pareto optimal solutions to the multi-objective optimisation problem, and when different values in scalarization parameters are applied, different Pareto optimal solutions can be produced. The so-called linear scalarization (shown below) is an application example of the "scalarization" method.

$$\min_{x \in X} \sum_{i=1}^{k} w_i f_i(x),$$

Where, the weights of the objectives $w_i > 0$ are the scalarization parameters [96].

The other methodology to cope with multi-objective optimisation problem is that "a representative set of Pareto optimal solutions is first found and then the decision maker must choose one of them" [96] according to his/her preferences. The typical schedule for this method is as follows:

"(1) computer approximates the Pareto frontier, i.e. the Pareto optimal set in the objective space;

(2) the decision maker studies the Pareto frontier approximation;

(3) the decision maker identifies the preferred point at the Pareto frontier;

(4) computer provides the Pareto optimal decision, which output coincides with the objective point identified by the decision maker." [96].

The second method can provide full information (or a whole picture) on all (or representative) Pareto optimum values in optimisation objectives and on objective tradeoffs, which inform how improving one objective is related to deteriorating the others while moving along the Pareto frontier, which will be helpful for the decision maker to specify the preferred Pareto optimal objective point by taking this information into account.

In this research work described in this thesis, the above second optimisation methodology was applied, that is, sets of representative Pareto optimum solutions were achieved for the multidisciplinary optimisation problems investigated in this thesis.

7.3 Optimisation Algorithms

"Operations research is the branch of mathematics concerned with both the application of scientific methods and techniques to decision making problems, and the establishment of the best or optimal solutions" [65]. "As expected, there is no a single method available for efficiently solving all optimisation problems. Thus a number of optimisation methods have been developed in the past, many of which are customised for a specific problem." [65]. The following Table 7-1 provides a list of currently available methods of operations research.

Table 7-1 Methods of operations research [97]

Mathematical Programming Techniques	Stochastic Process Techniques	Statistical Methods
Calculus methods	Statistical decision theory	Regression analysis
Calculus of variations	Markov processes	Cluster analysis, pattern recognition
Nonlinear programming	Queuing theory	Design of experiments
Geometric programming	Renewal theory	Discriminate analysis (factor analysis)
Quadratic programming	Simulation methods	
Linear programming	Reliability theory	
Dynamic programming		
Integer programming		
Stochastic programming		
Separable programming		
Multiobjective programming		
Network methods: CPM and PERT		
Game theory		
Simulated annealing		
Genetic algorithms		
Neural networks		

From Table 7-1, it can be observed that the methods of operations research can fall into three categories, namely, mathematical programming techniques, stochastic process techniques, and statistical methods. According to the reference [65], "stochastic process

techniques and statistical methods are used to analyse, respectively, problems described by a set of random variables and experimental data", while mathematical programming techniques are of particular importance since they are usually used to achieve the minimum of a function of several variables under a given set of constraints.

Among mathematical programming techniques, evolutionary algorithms taking genetic algorithms as representatives are receiving more and more attention, especially for multi-objective optimisation problem. Reference [96] states that "evolutionary algorithms are popular approaches to generating Pareto optimal solutions to a multi-objective optimization problem", and "The main advantage of evolutionary algorithms, when applied to solve multi-objective optimisation problems, is the fact that they typically generate sets of solutions, allowing computation of an approximation of the entire Pareto front."

Since the above feature of evolutionary algorithms matches very well with the methodology adopted by this research work for multi-objective optimisation problems (the methodology has been introduced already in section 7.2), evolutionary algorithms (specifically, genetic algorithms) was, therefore, selected as the optimisation algorithms for the purpose of this project research, and accordingly, the following introductions to optimisation algorithms will only focus on evolutionary algorithms, in particular, genetic algorithms.

"Evolutionary techniques are inspired by nature and mimic biological structures and processes that can be observed in natural environments with the object of solving technical problems" [65]. So far, the most primary evolutionary techniques which have been developed include evolutionary programming, evolution strategies, genetic programming, and genetic algorithms. Among them, GAs is probably the method with the most widespread use, and they have had a significant impact on optimisation [98].

Genetic algorithms (GAs) are a stochastic approach utilised for optimisation and search processes based on the mechanisms of natural selection and Darwin's main principle: survival of the fittest [99]. The operation mechanism (or procedure) of genetic algorithms for solving an optimisation problem can be briefly described as follows: firstly, the problem needs to be encoded; secondly, a judgment criterion of differentiating good solutions from bad solutions should be established, so as to direct

the evolution process of future generations; the third step is called the problem initialisation, that is, to create an initial ‘population’ of encoded solutions, and then the ‘selection’ operator and the ‘genetic’ operator will be applied iteratively to drive the evolution process of the solutions from generation to generation until a prescribed ‘stopping criterion’ (or ‘stopping criteria’) is (are) satisfied. “At the end, the final population will contain, hopefully, better solutions than those present in the initial population” [65]. The following Figure 7-1 illustrates the operation process of genetic algorithms for solving an optimisation problem.

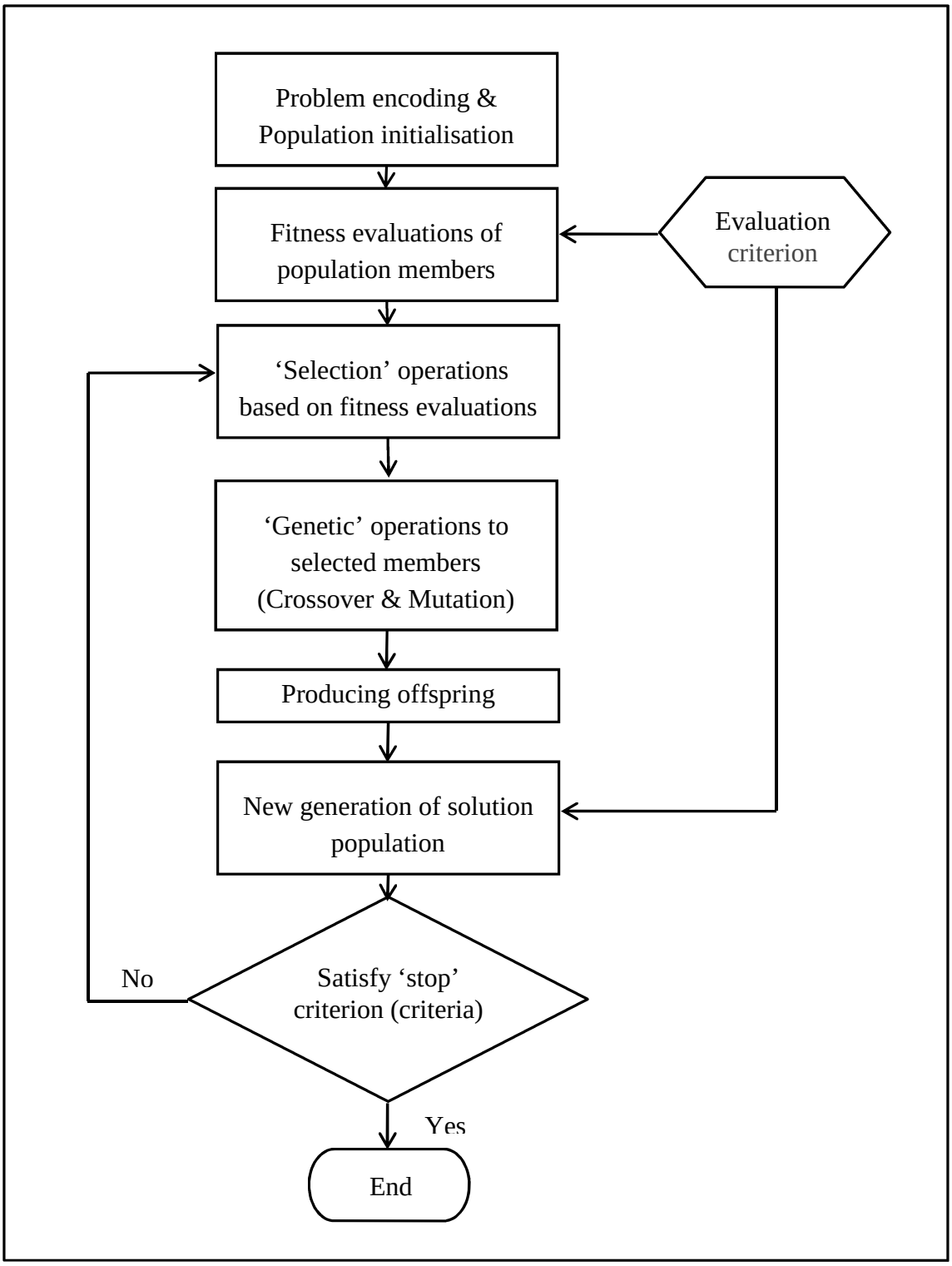

Figure 7-1 Operation process of genetic algorithms

Reference [65] described in detail the main elements contained in the above operation process of genetic algorithms and these descriptions can be briefly listed in the following sections.

7.3.1 Problem encoding

During the past several decades, different encoding techniques have been developed so that different problems can be coped with effectively by GAs. These encoding techniques, according to the reference [100], can be classified as “binary encoding”, “real-number encoding”, “integer encoding”, and “general data structure encoding”.

Binary encoding is a common encoding technique used by GAs. This technique uses “0” and/or “1” to represent genes and, accordingly, expresses chromosomes by binary strings composed of 0s and 1s. “Binary encoding for engineering optimisation problems is known to have severe drawbacks due to the existence of Hamming cliffs” [65].

“Integer encoding is best used for combinatorial optimisation problems, while that data structure encoding is suggested for more complex real-world problems” [65].

While “real-number encoding is more appropriate for engineering optimisation problems, since the parameters involved are usually expressed as real numbers. This type of encoding avoids all difficulties associated with the use of a binary (discrete) encoding when optimising ‘continuous’ search spaces”, and “currently it is widely accepted that real-number encoding performs much better than binary encoding for function optimisation and constrained optimisation problems” [65].

7.3.2 Problem initialisation

A GAs-based optimisation is essentially an evolutionary (or iterative) process of solutions and creating an initial population of encoded solutions is the starting point of this process.

Usually, the initial solution population “can be created by randomly choosing values for the genes from the search space, or by using good potential solutions that have been previously determined” by other optimisation works. [65].

An important fact implied from the population initialisation is that the optimisation process implemented by GAs starts from a population of solutions rather than from a single one.

7.3.3 Selection operation

"The principle of survival of the fittest imposed in GAs implies discarding the chromosomes with the lowest fitness at each generation. This process is carried out through the selection operator which allocates more offspring to better individuals." [65].

"Selection provides the driving force in GAs: with too much force, the genetic search will converge prematurely; and with too little force, the evolutionary process will take longer than necessary." [65].

Although "roulette wheel selection" and "stochastic universal sampling" (SUS) are two common selection methods for the purpose of the determination of parent chromosomes, the selection method based on "Pareto ranking" is usually applied for the multi-objective optimisation problem required with the output of a set of representative Pareto-efficient solutions. "This method involves sorting the population based on Pareto ranking, and assigning selection probabilities to individuals according to this ranking. The ranking procedure is as follows: (i) assign rank 1 to all nondominated individuals and remove them from contention; (ii) find the nondominated individuals from the remaining ones, assign rank 2 to them, and remove them from contention; and (iii) follow the same process until the entire population is ranked. Following this procedure, all nondominated solutions are assigned an identical fitness value, which provides them an equal reproduction probability". [65].

7.3.4 Crossover (Recombination)

In genetic algorithms, "the selection mechanism exploits accumulated information to guide the search process towards optimum solutions by allocating more offspring to the fittest chromosomes; whereas, genetic operators explore new regions of the search space." [65].

"Crossover or recombination is a genetic operator that combines traits of two or more parental solutions to form new and possibly better offspring." [65].

"For search processes involving binary encoding, there are four recombination methods commonly utilised: 'single-point crossover', 'double point crossover', 'multipoint crossover', and 'uniform crossover'." [65].

For optimisation processes using real-number encoding, 'weighted averaging crossover', 'blend crossover' (BLX), and 'simulated binary crossover' (SBX) are typical crossover approaches mainly applied.

Assume the real-number chromosome (potential solution) for an optimisation problem can be expressed as:

$$X=\{x_1, x_2,\ldots, x_k\}$$

The operation of 'weighted averaging crossover' is defined by Gen and Cheng [100] as follows:

$$X_1'=l_1X_1+l_2X_2$$

$$X_2'=l_2X_1+l_1X_2$$

Where, l_1 and l_2 are weights and satisfy the condition of $l_1 + l_2=1$.

"The averaging crossover suffers from contraction effects due to the fact that it allows the creation of offspring only along the line generated between the two parental chromosomes." [65].

The BLX crossover introduced by Eshelman and Schaffer [101] uses 'exploration factors' (α) and "randomly creates offspring within a hyper-rectangular region defined by the parental points" [65].

The reference [100] gives an example of a one-dimensional case (one variable) for the explanation of BLX crossover. In this example, the two parental points are respectively designated as p_1 and p_2 with $p_1 < p_2$ and exploration factors α_1 and α_2 which satisfy the condition of $0 < \alpha_1, \alpha_2 < 1$. In this case, an offspring can be created by the BLX operator through randomly selecting a point in the range $[p_1 - \alpha_1 (p_2 - p_1), p_2 + \alpha_2 (p_2 - p_1)]$. Sometimes, it can be found that α_1 is equal to α_2 (i.e., $\alpha_1 = \alpha_2$) and under this condition the BLX operator is designated as BLX- α. In practice, BLX-0.5 ($\alpha = 0.5$) is often adopted due to its better performance when compared to other BLX- α operators using different values in parameter α [101].

The crossover operator of SBX was introduced by Deb and Agrawal [102]. The operator "utilises a probability of creating an arbitrary child solution from a given pair of parental solutions similar to that used in binary crossover operators" [65], and is primarily characterised by the applications of the 'spread factor' β and a distribution

function to implement the recombination operations of the parental solutions (here, 'spread factor' β is defined as the ratio of the absolute differences of the children points to that of the parental points [102] and is used to "control the spread of the children with respect to that of their parents" [65]). The crossover operator of SBX has shown a better performance when compared with other real-encoded recombination operators [102].

7.3.5 Mutation

Besides the above crossover (recombination), another genetic operator named as 'mutation' is also applied, typically by GAs, for the purpose of exploration of the search space.

"In a fundamental sense, a mutation process allows the whole search space to be sampled before the process converges (prematurely). This is done by forcing the algorithm to explore other areas of the search space by randomly introducing changes, or mutations, in some of the variables comprising a given chromosome." [65].

For binary-encoded problems, the 'mutation' can be operated through simply changing gene values of chromosomes from 0 to 1, and vice versa. However, with the real-encoded optimisations, the 'mutation' process will be more complicated.

For real-number encoding problems, 'uniform mutation', 'non-uniform mutation', 'creep mutation with and without decay', and 'dynamic vectored mutation' (DVM) are main mutation methods typically used in GAs.

For a given parent chromosome $X=\{x_1, x_2, \ldots, x_i, \ldots, x_k\}$, when one of its genes x_i is chosen for mutation, and if a random change to this gene value within a prescribed domain spanned by the lower and upper bounds (respectively designated as LB_i and UB_i) is implemented and, accordingly, a new chromosome is produced (shown as follows), then this approach for mutation is referred as a 'random mutation method'.

$$X=\{x_1, x_2, ..., x_i, \ldots, x_k\} \rightarrow X'=\{x_1, x_2, ..., x_i', \ldots, x_k\}, x_i, x_i' \in [LB_i, UB_i]$$

Compared with the above 'random mutation method', as for uniform mutation, the reference [65] (based on the reference [103]) summarised that "uniform mutation involves, in turn, a process in which the values of x_i' are drawn uniformly randomly from $[LB_i, UB_i]$. A position wise mutation probability is usually utilised with this mutation method".

In the operation of non-uniform mutation, the following two choices can be randomly selected as the value of x_i':

$x_i' = x_i + \Delta(t, UB_i - x_i)$ or $x_i' = x_i - \Delta(t, x_i - LB_i)$

"The function $\Delta(t,y)$ returns a value in the range [0,y], which approaches to 0 as t increases (t represents the generation number). This property causes the mutation operator to search the space uniformly initially (when t is small), and very locally at later stages" [65]. And this function $\Delta(t,y)$ is defined as:

$$\Delta(t,y) = y \cdot \left(1 - r^{\left(1-\frac{t}{t_{max}}\right)^b}\right)$$

Where, "r is a random number from [0,1], t_{max} the maximum generation number, and b a parameter determining the degree of non-uniformity" [65].

"Creep mutation basically operates by adding or subtracting a random number to a gene of the chromosome selected for mutation." [65]. By means of this method, a mutated gene x_i' can be achieved based on the following formula:

$$x_i' = x_i + (2r-1)\Delta_{max}$$

With $\Delta_{max} = d(UB_i - LB_i)$.

In the above formula, "Δ_{max} is the maximum size used for the creep mutation, δ the range ratio, and r a random number from [0,1]. The level of disruption produced by the mutation process is controlled by the creep size δ." [65]

"In the creep mutation with decay method, the creep size is altered as a function of the stage of the search process" [65], that is,

$$\delta_{t+1} = \delta_t (1-\gamma)$$

Where, "γ represents the creep decay rate (t is the generation number)" [65].

The method of creep mutation with decay "allows the use of large values of δ in the beginning of the search process and small ones at the end; balancing in this way the exploration and exploitation capabilities required during the process" [65].

Dynamic vectored mutation (DVM) introduced by Rogero [104] "was developed in an attempt to solve some limitations present in other operators. It allows mutation in all directions of a multi-dimensional search space and not only along a single dimension

axis." [65]. (Reference [65] gives a brief summary about this method and more information can be found in other related references.)

7.3.6 Stopping criteria

As an iterative algorithm, a GAs-based optimisation evolves solutions from generation to generation until a stopping criterion (or stopping criteria) is (or are) satisfied. "Three termination criteria are most frequently utilised: maximum number of generations, maximum number of evaluations (i.e., maximum number of chromosomes or potential solutions to be evaluated during a given search or optimisation process), and maximum fitness value." [65]. In addition, reference [100] also suggests some alternative stopping strategies such as "population convergence criteria (e.g., sum of deviations among individuals smaller than a specified threshold), and lack of improvement in the best solution over a given number of generations" [65].

As for the main characteristics of GAs as well as the differences with traditional optimisation methods, reference [65] also makes a brief summary (based on [97]) as follows:

a) A population of points is utilised for starting the procedure instead of a single design point;
b) GAs use only the values of the objective function, i.e., the derivatives are not used in the search procedure;
c) In GAs, the design variables are represented as strings of binary (or real) variables that correspond to the chromosomes in natural genetics;
d) The objective function value corresponding to a design vector plays the role of fitness in natural genetics;
e) In every new generation, a new set of strings is produced by using selection and genetic operators to the old generation;
f) GAs are extremely robust which makes them very suitable for problems in which the functions relating inputs to outputs are unknown and may have an unexpected behaviour.

Besides, reference [65] also analysed the main characteristics of flight trajectory optimisation problems and they can be briefly listed as follows:

a) Constrained – design constraints will be used to limit the range of the design variables;
b) Complexity – the function (s) relating inputs (design variables) and outputs (objective function) is (are) unknown and it (they) is (are) presumed to be nonlinear, non-smooth, and non-differentiable;
c) Real-valued – most of the design variables will be permitted to take any real value;
d) Deterministic – most of the parameters involved are deterministic;
e) Multi-objective – more than one criterion (objective function) will need to be satisfied simultaneously;
f) Multi-modal – it is assumed that there are several local minima (or maxima);
g) Multi-variable – a number of design variables will be involved during the optimisation process.

Based on the above characteristics analysis of genetic algorithms and flight trajectory optimisation problem respectively, the conclusion that GAs are very suitable candidates for solving the flight trajectory optimisation problem [65] can be achieved.

7.4 Applications of GAs

The genetic algorithm adopted in this research work is called as NSGAMO (Non-dominated Sorting Genetic Algorithm Multi-Objective) [14, 105]. The following two test examples show the applications of this optimisation method, as well as its capability to cope with multi-objective optimisation problems without and with constraints respectively.

7.4.1 ZDT1 function [106]

The ZDT1 Function can be expressed as follows:

$$F_1(X) = x_1$$

$$F_2(X) = g(X)[1 - \sqrt{x_1/g(x)}]$$

$$g(X) = 1 + \frac{9(\sum_{i=2}^{n} x_i)}{(n-1)}$$

$$X = [x_1, x_2, \cdots, x_n], x_i \in [0, 1] \text{ and } n = 30$$

The optimisation objective for this test case is to find a set of Pareto-efficient solutions (trade-offs) for the minimisation of $F = [F_1, F_2]$.

The main optimiser settings are listed in the following Table 7-2.

Table 7-2 Main optimiser settings for the optimisation of ZDT1 Function [106]

1	Population size	100
2	Initialisation factor	5.0
3	Creation schemes	Trilinear and Simulated Binary Crossover (SBX) crossover and Dynamic vector Mutate
4	Creations selectors	Stochastic universal sampling for both crossover and random selection for the mutation operator
5	Creation rates	0.45, 0.45, 0.10 respectively
6	Selection pressure	2.0
7	Stopping criteria	maximum generation only (max generation = 200)

The optimisation results from NSGAMO and the comparison with the known theoretical values are illustrated in the following Figure 7-2.

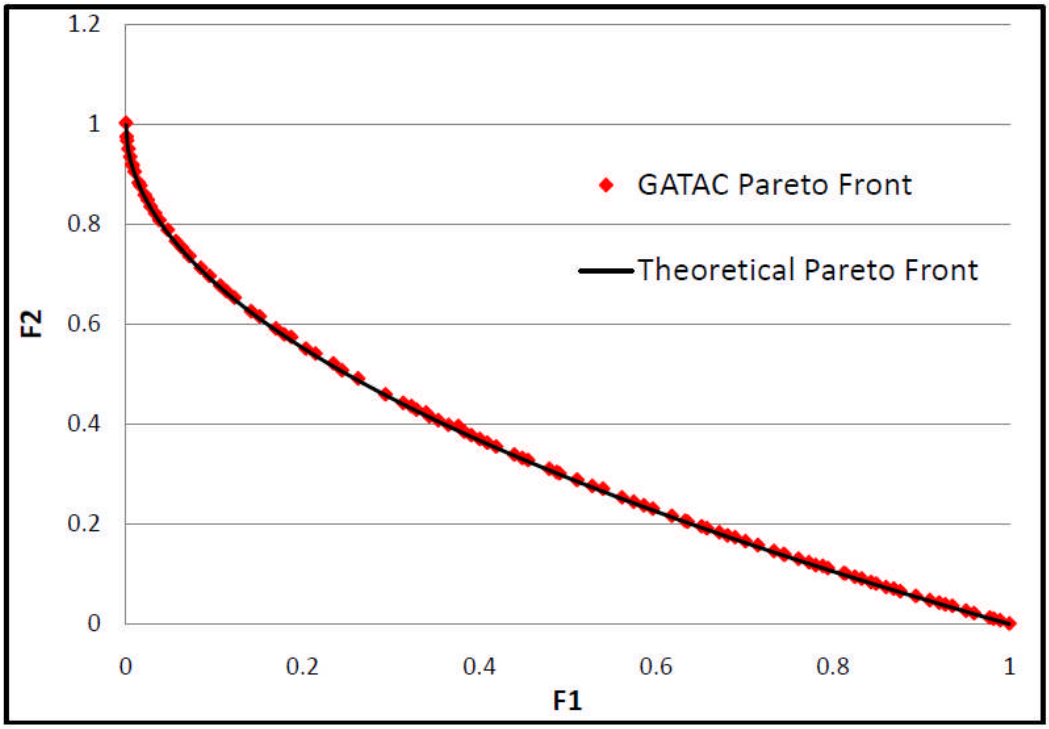

Figure 7-2 Comparison of NSGAMO results with theoretical Pareto front for ZDT1 [106]

7.4.2 CONSTR function [106]

The CONSTR Function can be expressed as follows:

$$F_1(X) = x_1$$

$$F_2(X) = \frac{1 + x_2}{x_1}$$

Constraints:

$$g_1(X) = x_2 + 9x_1 \geq 6$$

$$g_2(X) = -x_2 + 9x_1 \geq 1$$

Where, $X = [x_1, x_2]$, $x_1 \in [0.1, 1.0]$ and $x_2 \in [0, 5]$

The optimisation objective for this test case is to find a set of Pareto-efficient solutions (trade-offs) for the minimisation of $F = [F_1, F_2]$ under the above constraints $G = [g_1, g_2]$.

The main optimiser settings for this test case are listed in the following Table 7-3.

Table 7-3 Main optimiser settings for the optimisation of CONSTR Function [106]

1	Population size	100
2	Initialisation factor	2.0
3	Creation schemes	Trilinear and SBX crossover and Dynamic vector Mutate
4	Creations selectors	Stochastic universal sampling for both crossover and random selection for the mutation operator
5	Creation rates	0.45, 0.45, 0.10 respectively
6	Selection pressure	2.0
7	Stopping criteria	maximum generation only (max generation = 200)

The optimisation results from NSGAMO and the comparison with the known theoretical values are illustrated in the following Figures 7-3 and 7-4.

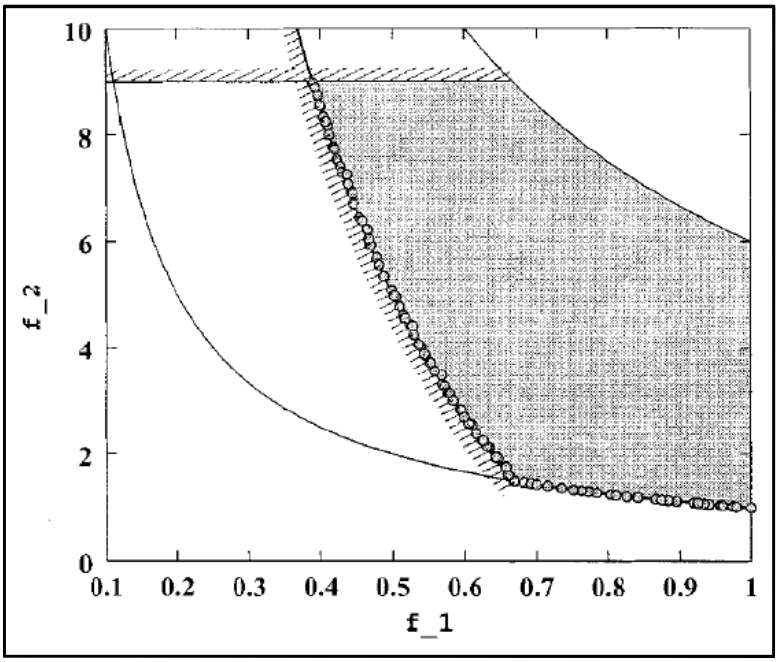

Figure 7-3 Theoretical Pareto front from the optimisation of CONSTR function [106]

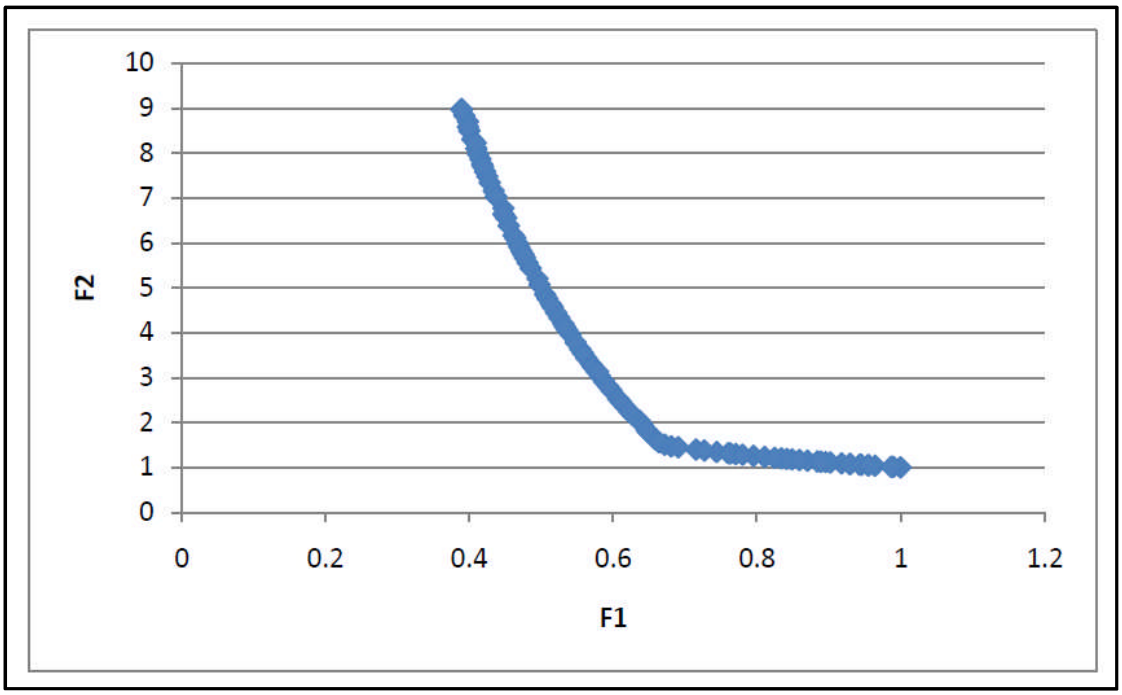

Figure 7-4 NSGAMO results for the optimisation of CONSTR function [106]

The above two typical test cases show the good agreements between the optimisation results from NSGAMO and the expected theoretical ones and, thus, confirm that the multi-objective optimisation problems (at least the two-objective optimisation, as shown in the above two test cases) without and with constraints can be effectively handled by NSGAMO which has been adopted in this research work.

7.5 GATAC Overview

GATAC (Green Aircraft Trajectories under ATM Constraints) is an integrated optimisation framework developed by the University of Malta, Cranfield University and other European partners for the purpose of flight trajectory multidisciplinary optimisation. It is also the fundamental platform used for this project research.

Reference [106] gives a detailed description about this integrated multidisciplinary optimisation framework and some main statements from [106] can be listed briefly as follows:

The architecture of the GATAC framework is made up of two system-level components, namely, the GATAC Core and the Model Suite. The GATAC Core is where the optimisation process takes place. The Model Suite services the GATAC Core

on request by executing models and transferring data to the GATAC Core. The architecture is depicted in Figure 7-5.

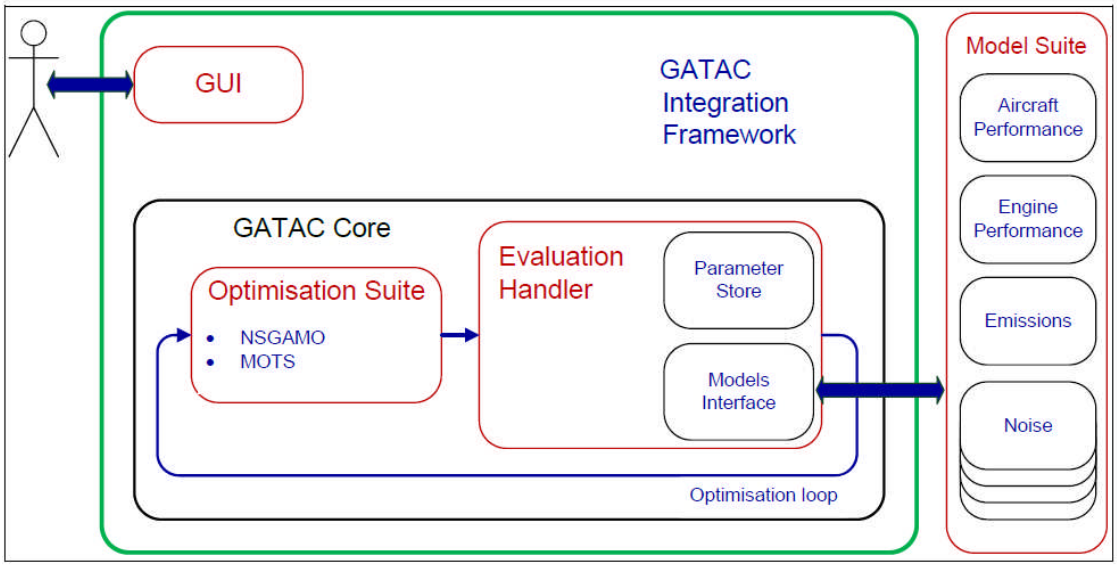

Figure 7-5 GATAC Integration Framework Architecture [106]

The GATAC Core is the heart of the optimisation framework. It is made up of an Optimization Suite and an Evaluation Handler.

The Optimization Suite is the module that defines the values of the variable parameters and analyses the resulting constraints and criteria values. The suite is further broken down into an Optimization Technique Suite, an Objective Handling Module and a Constraints Handling Module.

The Optimization Technique Suite hosts the optimisation algorithms, allowing the user to select particular optimisation techniques for specific MDO problems at hand. The optimisation algorithms that can be incorporated vary from modern evolutionary-based algorithms to classical numerical techniques.

The Evaluation Handler is the unit that handles the models and controls the direct data transfer between the models in the Model Suite, the Optimization Suite and other modules in the GATAC Integration Framework. On request from the Optimization Core, the Evaluation Handler invokes the relevant model through the Models Interface to obtain the required data.

The data flow between the Optimization Core and the Evaluation Handler takes place in the form of data structures, called dictionaries.

The Model Suite is made up of a number of models which are, in turn, used by the GATAC Core for optimisation purposes, such as aircraft performance model, engine performance model, engine gaseous emission model, and flight noise model, etc.

The GATAC software is designed to run either on a single stand-alone machine or a distributed system with multiple computers. In its simplest setup, a stand-alone system runs on a single machine that hosts both the GATAC Integration Framework and the Model Suite. When set up on a distributed system, the GATAC Integration Framework resides on a machine, henceforth called the Central Server. The Model Suite is then distributed on one or more machines acting as hosts, as shown in Figure 7-6.

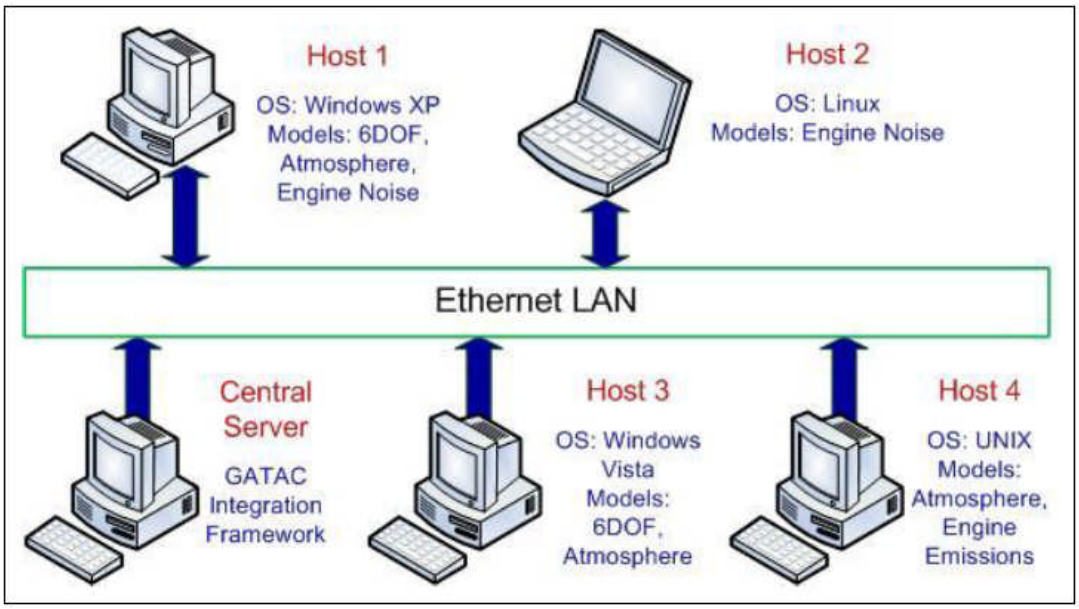

Figure 7-6 Distributed System [106]

CHAPTER EIGHT SYSTEM INTEGRATION AND OPTIMISATION MODELLING – CASE STUDIES

8.1 Overall Introduction

This chapter mainly aims to introduce the case studies completed in this project research with system-level integration and optimisation modelling. These case studies took the flight mission from Amsterdam Schiphol airport in the Netherlands to Munich airport in Germany (see Figure 8-1) as an example, and were created through the systematic integrations of component-level models (such as the atmosphere model, aircraft performance models, engine performance models, gaseous emission models, and flight noise models) described in previous chapters, based on the software platform of integration and optimisation - GATAC.

The flight mission spans 758.15 km in terms of the horizontal flight distance and was divided into three flight phases, i.e., the departure phase (34.95 km), en route phase (637 km) and arrival phase (86.2 km) with different optimisation objectives for each one. For the departure phase, the selected objective functions are fuel consumption and flight noise; during the en route flight, fuel consumption and flight time were optimised simultaneously; and for the arrival phase, NOx emission and flight noise were selected.

Flights in each flight phase were optimised under the condition of three different aircraft types, i.e., turbofan propelled aircraft (CUTFDAC case), turboprop driven aircraft (CUTPDAC case), and propfan-powered aircraft (CUPFDAC case). So in total, there are nine optimisation cases which produce a spectrum of flight trajectory optimisations spanned by aircraft types and flight phases (see Table 8-1).

Figures 8-2 and 8-3 respectively are the Instrument Standard Departure (ISD) chart for the runway 18L at Schiphol airport [107] and Instrument Approach (IA) chart for the runway 26R at Munich airport [108], which were both delivered practically by the authorities of Air Traffic Control (ATC). These two figures provide both the guidance to the case modelling and corresponding constraints to the trajectory optimisation problems implemented in these case studies.

Figures 8-4 to 8-6 are the overall schematics of these nine case studies which translate the practical city-pair trajectory optimisation problems into 2D graphical expressions in

terms of flight altitude Z and flight speed V versus horizontal flight range X (in the meantime, the available design variables and optimisation constraints are also displayed in these graphs).

Thereafter, from sections 8.2 to 8.4, the information of the systematic integration and optimisation modelling for each case study is provided including the available design variables and their setting-up, the selected objective functions and their setting-up, the adopted optimisation constraints and their setting-up, as well as the plot of system-level integration and optimisation model (see Tables 8-2 to 8-34, and Figures 8-7 to 8-15).

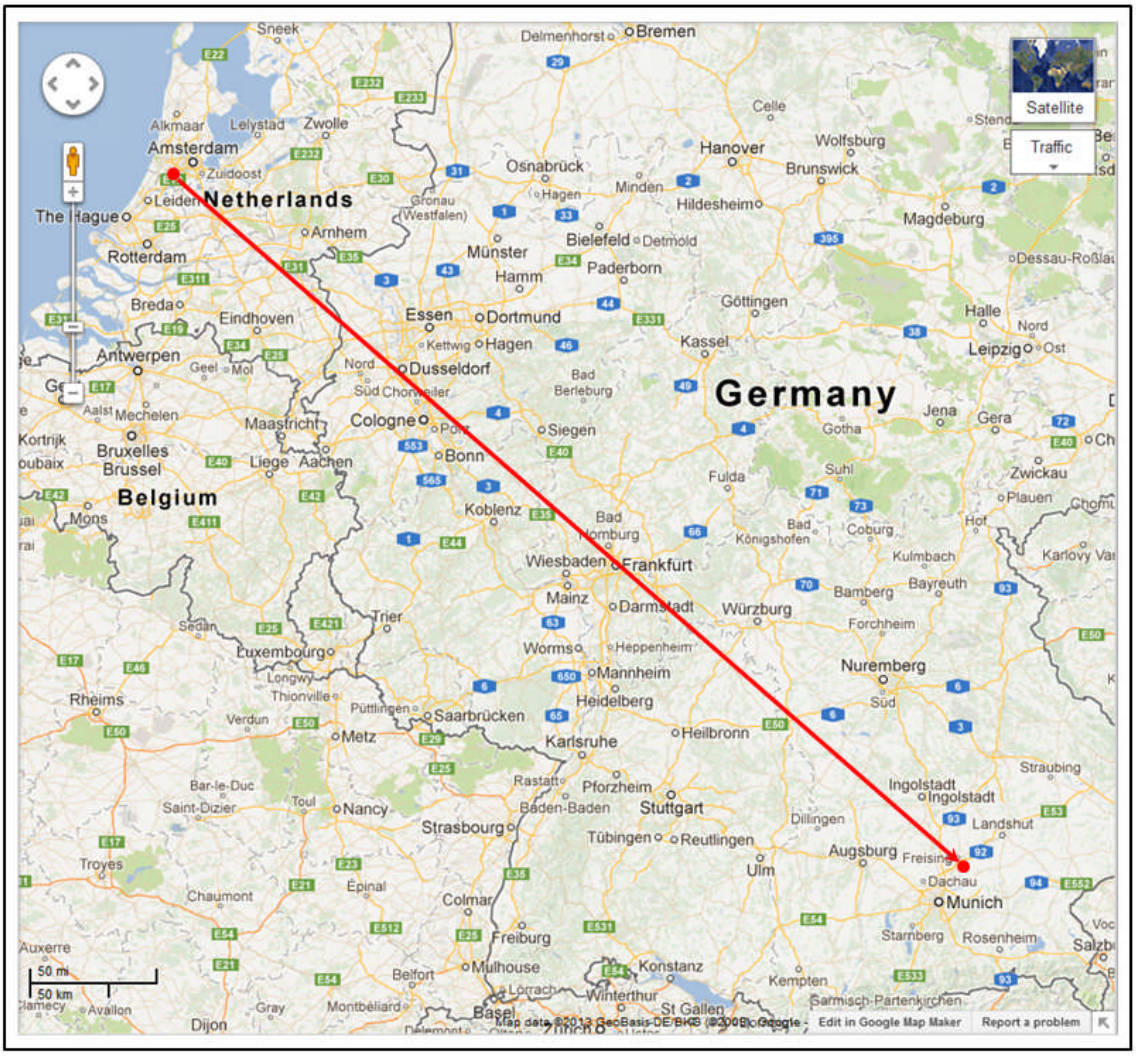

Figure 8-1 Overview of the flight mission
(Amsterdam Schiphol Airport, the Netherlands → Munich Airport, Germany)

Table 8-1 Overview of case studies

Aircraft types / Flight phases	CUTFDAC	CUTPDAC	CUPFDAC	Optimisation objectives	Disciplines
Departure	✓	✓	✓	Fuel & Noise	Aerodynamics Thermodynamics Chemistry Aeroacoustics Applied mathematics
En route	✓	✓	✓	Fuel & Time	
Arrival	✓	✓	✓	NOx & Noise	

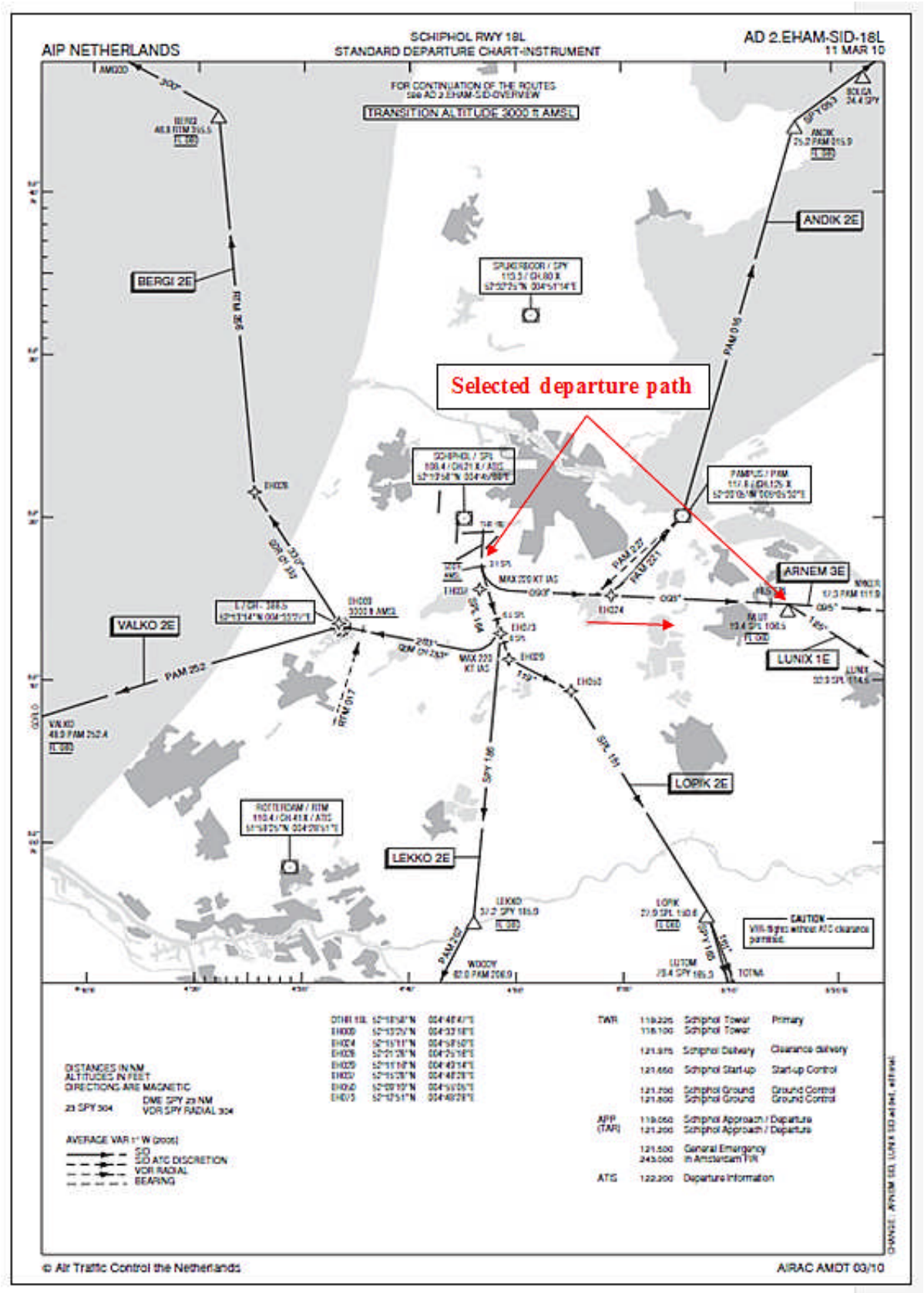

Figure 8-2 Standard departure chart – instrument (Schiphol RWY 18L) [107]

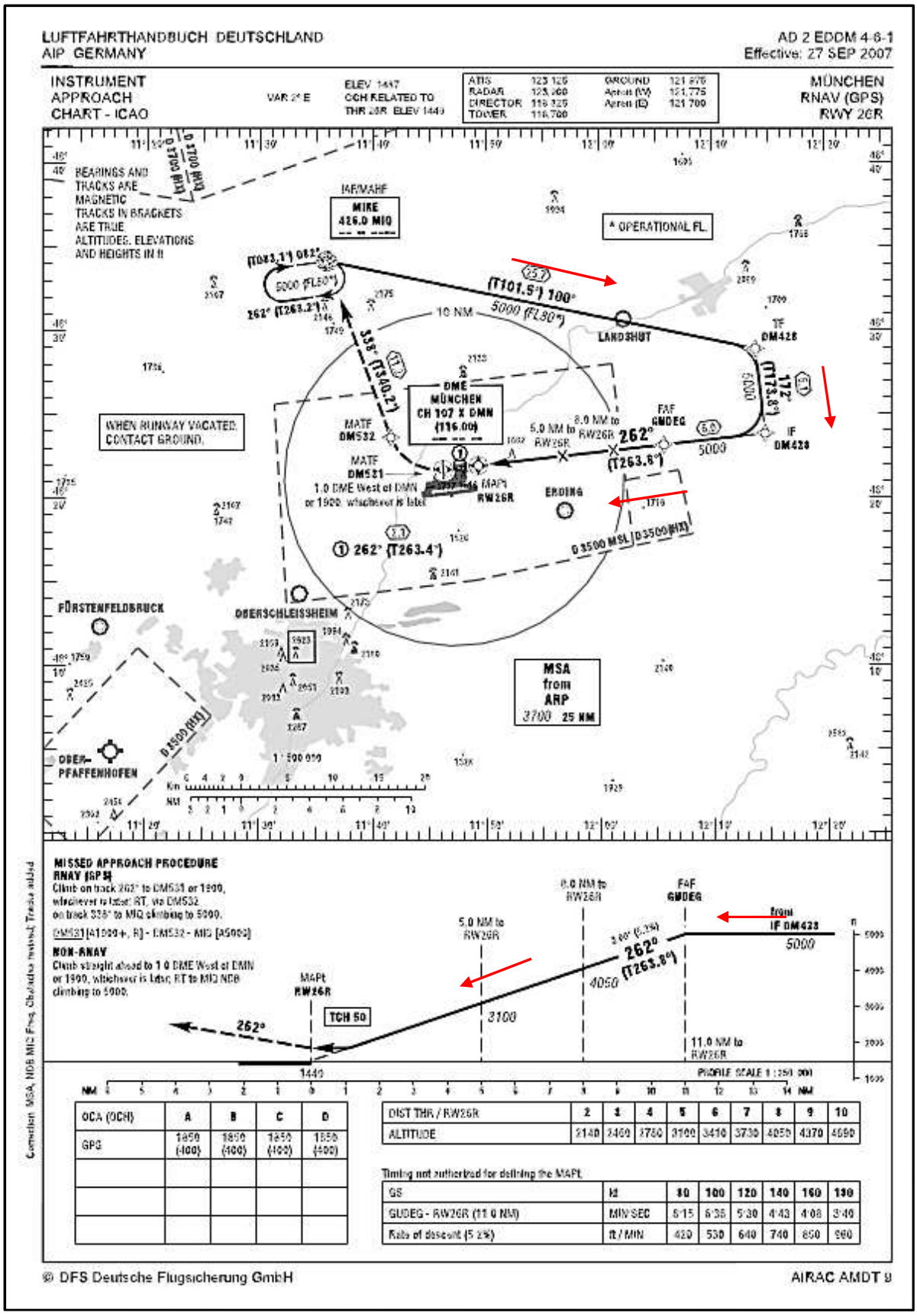

Figure 8-3 Instrument approach chart – ICAO (Munich RWY 26R) [108]

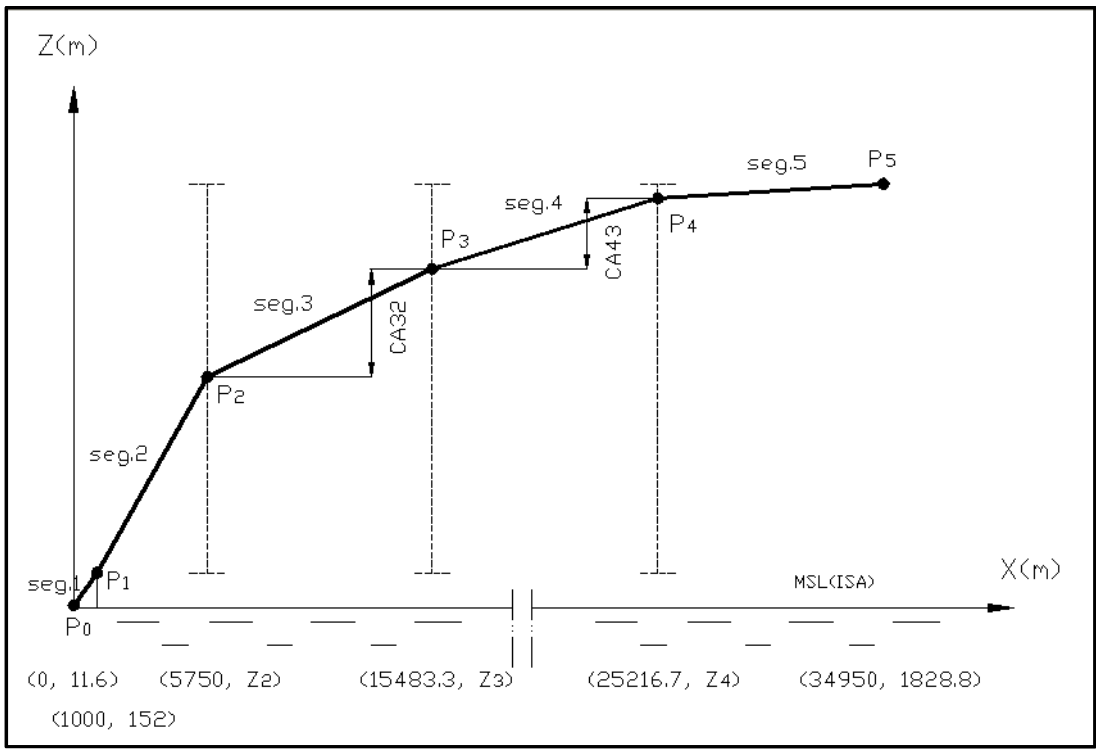

Figure 8-4 (a) 2D schematic of departure flight phase (Z vs. X)

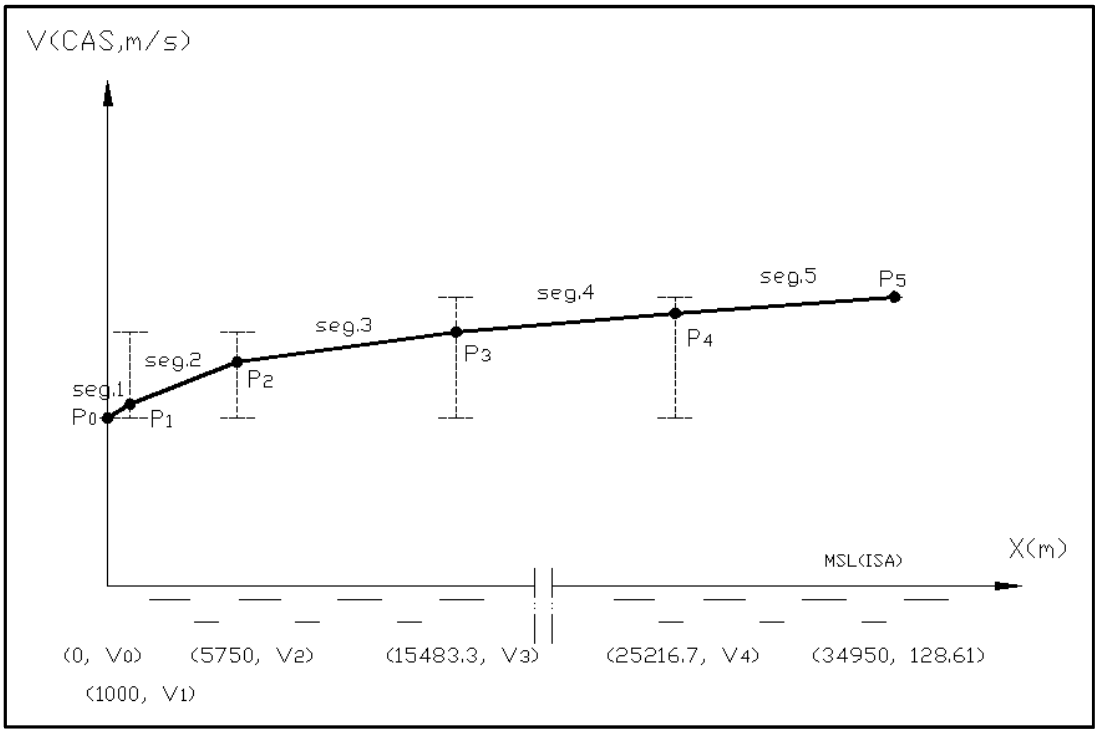

Figure 8-4 (b) 2D schematic of departure flight phase (V vs. X)

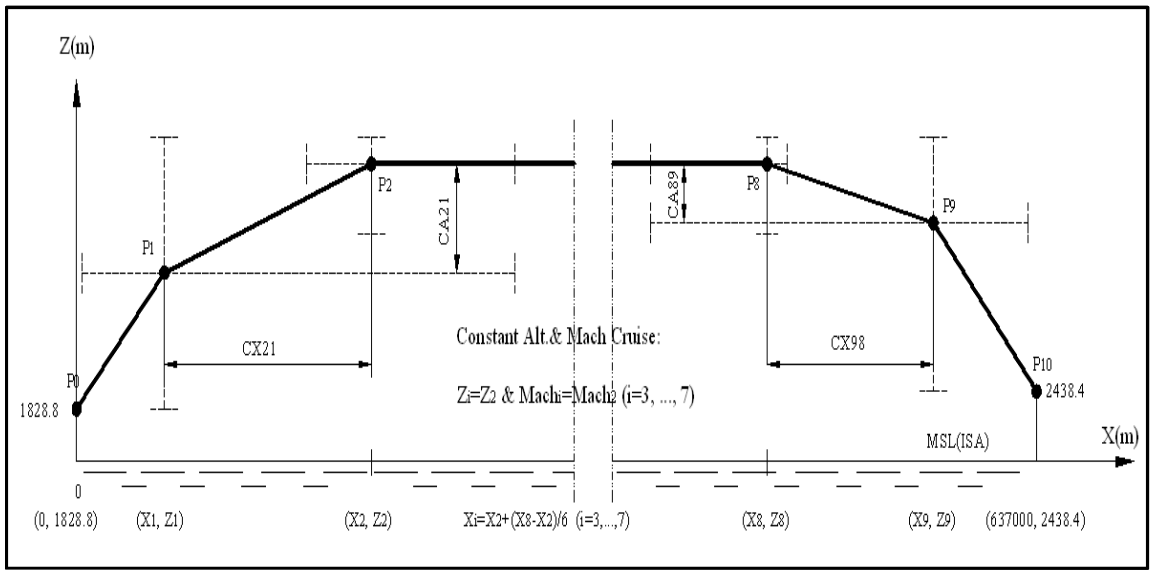

Figure 8-5 (a) 2D schematic of en route flight phase (Z vs. X)

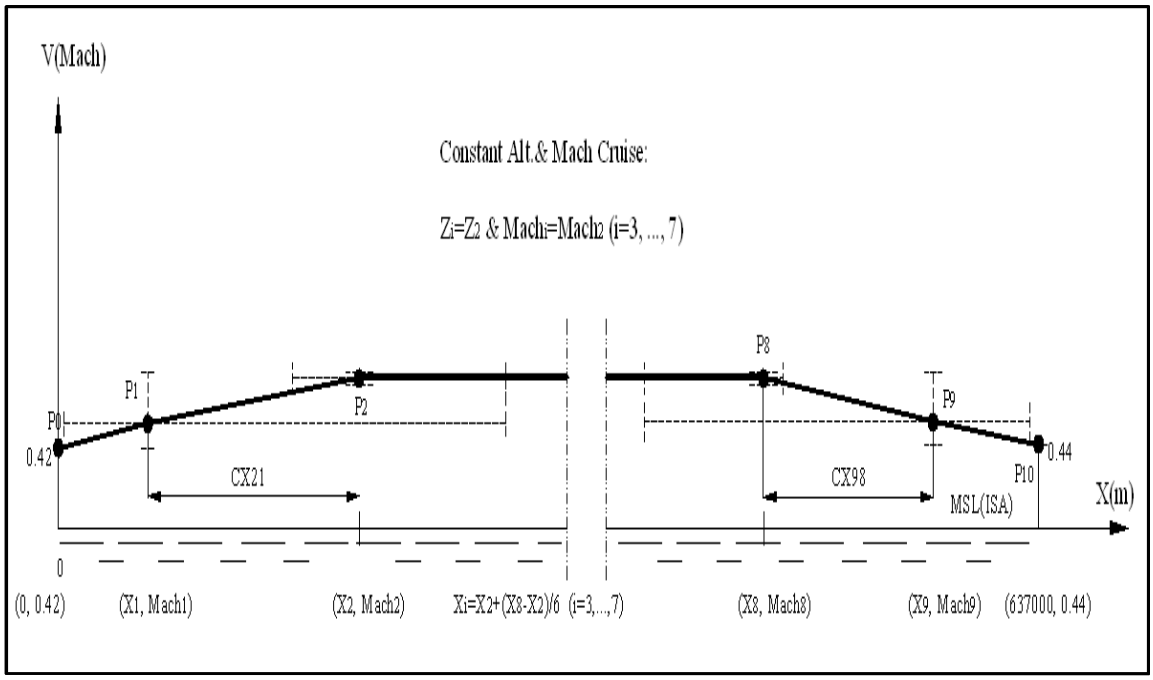

Figure 8-5 (b) 2D schematic of en route flight phase (V vs. X)

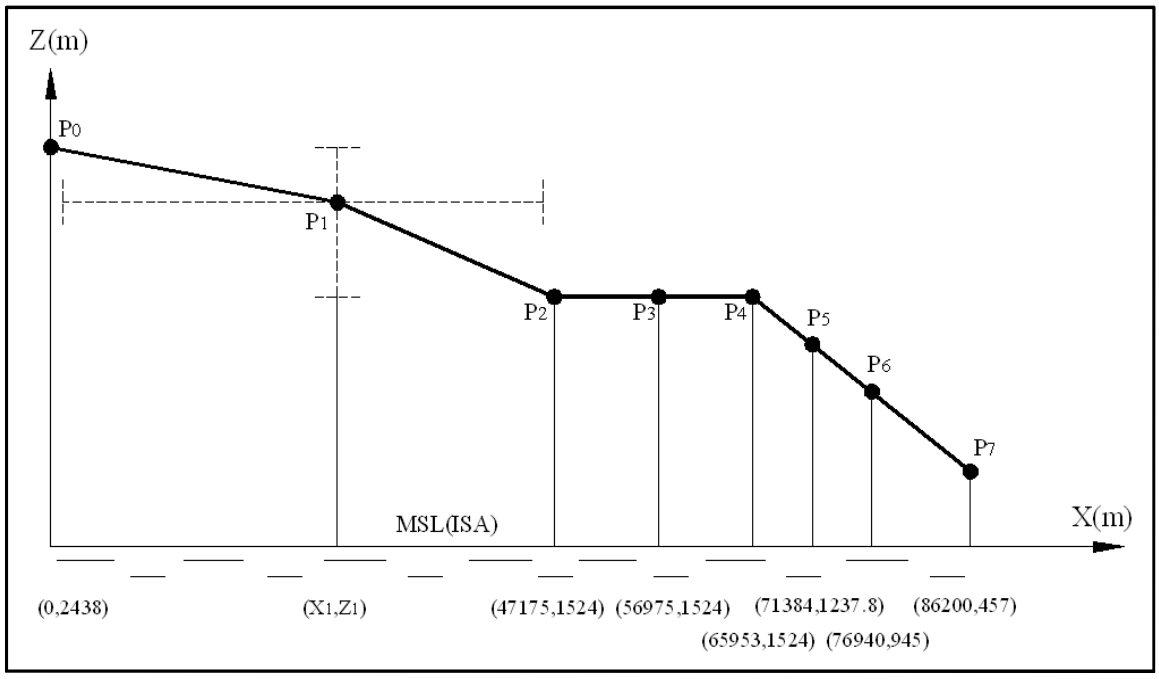

Figure 8-6 (a) 2D schematic of arrival flight phase (Z vs. X)

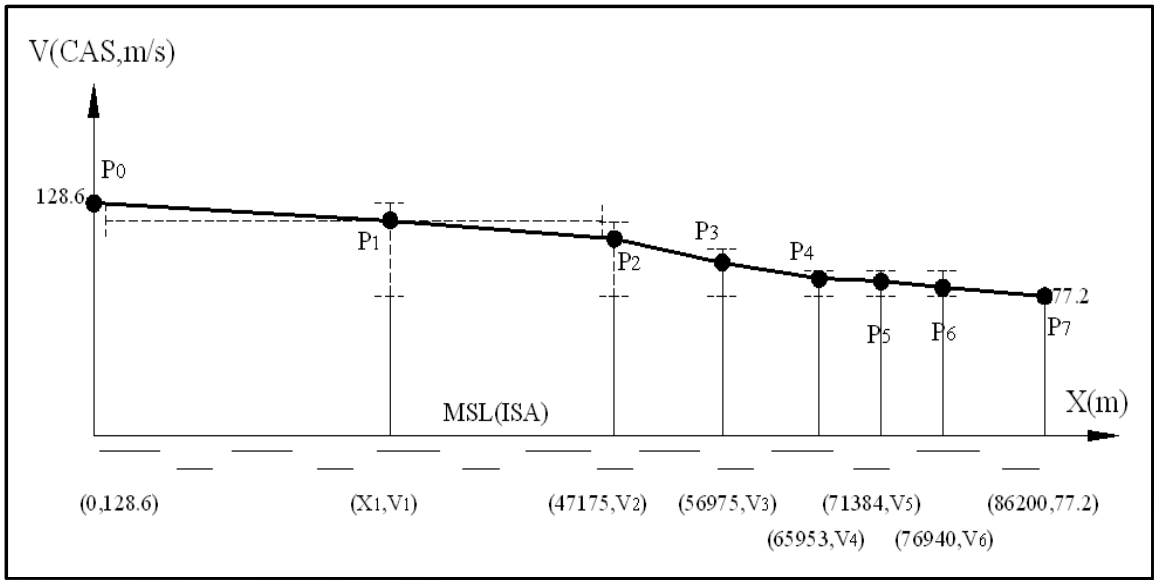

Figure 8-6 (b) 2D schematic of arrival flight phase (V vs. X)

8.2 Systematic Integration and Optimisation Modelling of CUTFDAC Flight

8.2.1 Departure phase of CUTFDAC

Table 8-2 Design variables and setting-up for CUTFDAC departure

Design variables	Description	Denormalisation function	Minimum	Maximum
ALT2	Altitude at node 2, (m)	Linear	152	1828.8
ALT3	Altitude at node 3, (m)	Linear	152	1828.8
ALT4	Altitude at node 4, (m)	Linear	152	1828.8
SPD1	Calibrated Airspeed at node 1, (m/s)	Linear	76	113.2
SPD2	Calibrated Airspeed at node 2, (m/s)	Linear	76	113.2
SPD3	Calibrated Airspeed at node 3, (m/s)	Linear	76	128.61
SPD4	Calibrated Airspeed at node 4, (m/s)	Linear	76	128.61

Table 8-3 Objective functions and setting-up for CUTFDAC departure

Objectives	Description	Optimisation type	Normalisation Function	Minimum	Maximum
FUEL	Total fuel consumption, (kg)	Minimisation	ObjectiveMin	100	2000
NOISE	Noise-impact area (SEL ≥ 70 dBA), (m^2)	Minimisation	ObjectiveMin	100	1000000000

Table 8-4 Optimisation constraints and setting-up for CUTFDAC departure

Constraints	Description	Constraint type	Normalisation Function	Minimum	Maximum
CA32	ALT3 – ALT2, (m)	Greater than minimum	GreaterThan	0	2000
CA43	ALT4 – ALT3, (m)	Greater than minimum	GreaterThan	0	2000

Table 8-5 Setting-up of GAs parameters for CUTFDAC departure

Population size	150
Initialisation factor	60
Creation schemes	Trilinear and SBX crossover and Dynamic vector Mutate
Creations selectors	Stochastic universal sampling for both crossover and random selection for the mutation operator
Creation rates	0.45, 0.45, 0.10 respectively
Selection pressure	2.0
Stopping criteria	Max. generation = 450

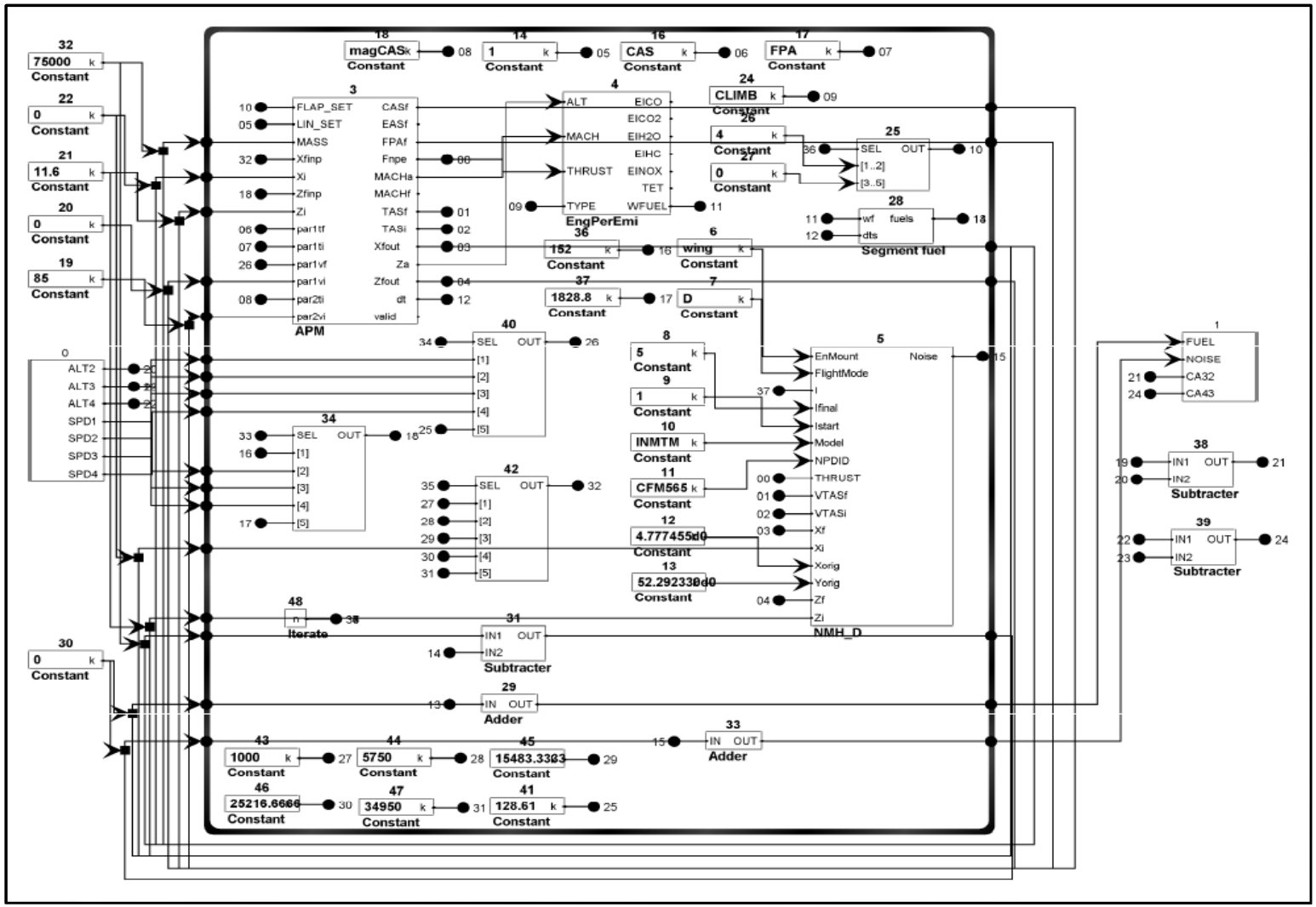

Figure 8-7 Systematic integration and modelling for CUTFDAC departure

8.2.2 En route phase of CUTFDAC

Table 8-6 Design variables and setting-up for CUTFDAC en route

Design variables	Description	Denormalisation function	Minimum	Maximum
ALT1	Altitude at node 1, (m)	Linear	1828.8	11887.2
ALT2	Altitude at node 2, (m)	Linear	7924.8	11887.2
ALT9	Altitude at node 9, (m)	Linear	2438.4	11887.2
DIS1	Distance at node 1, (m)	Linear	50	335000
DIS2	Distance at node 2, (m)	Linear	140000	335000
DIS8	Distance at node 8, (m)	Linear	402000	539000
DIS9	Distance at node 9, (m)	Linear	402000	636950
SPD1	Mach number at node 1	Linear	0.42	0.82
SPD2	Mach number at node 2	Linear	0.75	0.82
SPD9	Mach number at node 9	Linear	0.44	0.82

Table 8-7 Objective functions and setting-up for CUTFDAC en route

Objectives	Description	Optimisation type	Normalisation Function	Minimum	Maximum
FUEL	Total fuel consumption, (kg)	Minimisation	ObjectiveMin	10	100000
TIME	Total flight time, (s)	Minimisation	ObjectiveMin	10	100000

Table 8-8 Optimisation constraints and setting-up for CUTFDAC en route

Constraints	Description	Constraint type	Normalisation Function	Minimum	Maximum
CA21	ALT2 – ALT1, (m)	Greater than minimum	GreaterThan	0	10060
CA89	ALT8 – ALT9, (m)	Greater than minimum	GreaterThan	0	9450
CX21	DIS2 - DIS1, (m)	Greater than minimum	GreaterThan	50	335005

CX98	DIS9 – DIS8, (m)	Greater than minimum	GreaterThan	50	235005
CO_2	(g)	Less than maximum	LessThan	100	100000000
NOx	(g)	Less than maximum	LessThan	100	1000000

From the above Table 8-8, it can be observed that the upper boundaries of CO_2 and NOx were set very high, so in this case study, as well as the other two en route flights flown respectively by CUTPDAC and CUPFDAC described in later sections (see Tables 8-19 and 8-30), the constraints from the emissions of CO_2 and NOx were not actually considered at this stage (due to time constraints, the main objective in this research for the en route flight optimisations is to obtain baseline optimisation results). However, these case models have the capability to take these issues into account (only by reducing the two emission upper-boundary values to the expected levels) and the new optimisations with these constraints, as well as their comparisons to the optimisation results achieved currently, have been planned for the future.

Table 8-9 Setting-up of GAs parameters for CUTFDAC en route

Population size	150
Initialisation factor	60
Creation schemes	Trilinear and SBX crossover and Dynamic vector Mutate
Creations selectors	Stochastic universal sampling for both crossover and random selection for the mutation operator
Creation rates	0.45, 0.45, 0.10 respectively
Selection pressure	2.0
Stopping criteria	Max. generation = 400

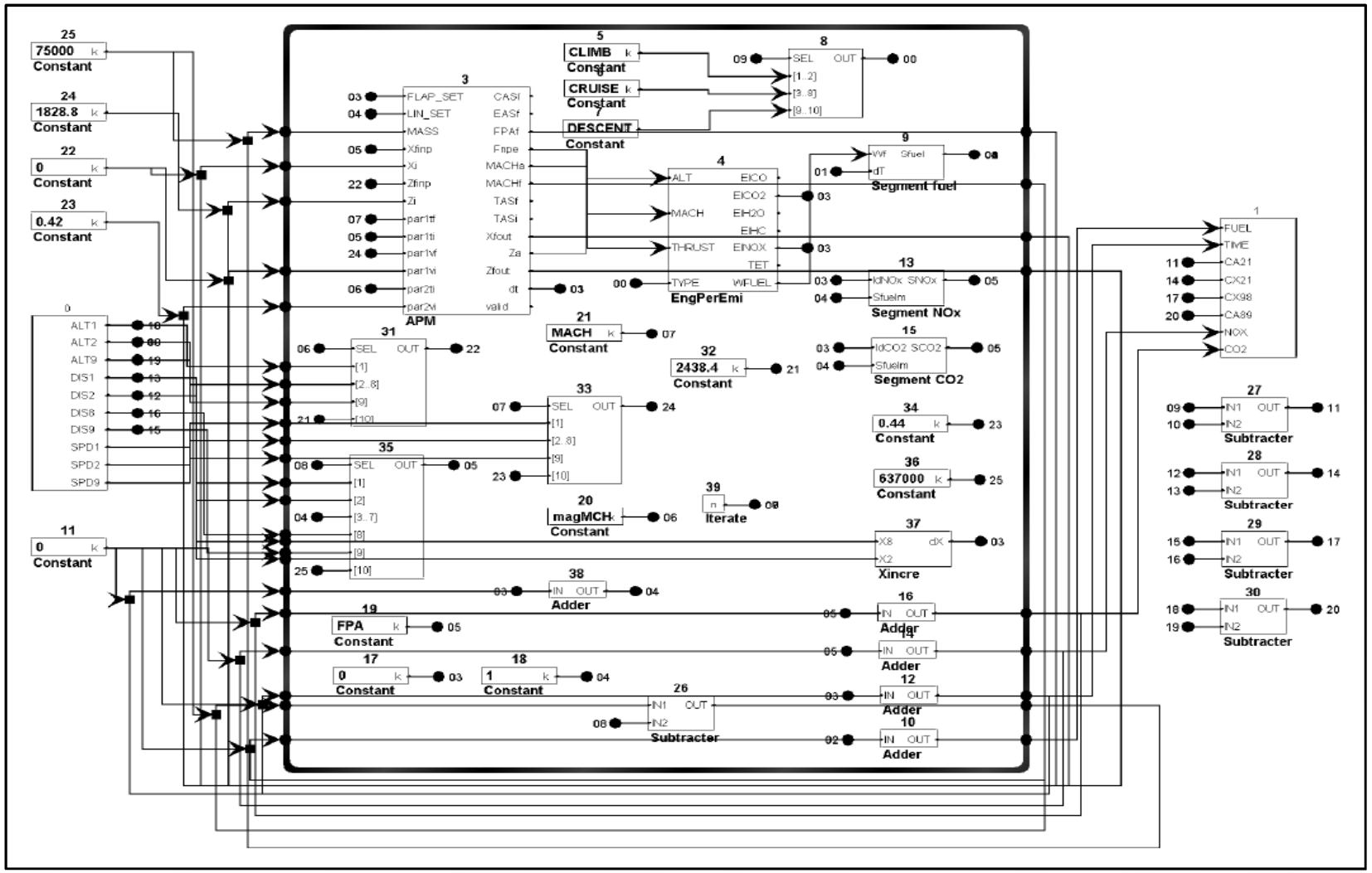

Figure 8-8 Systematic integration and modelling for CUTFDAC en route

8.2.3 Arrival phase of CUTFDAC

Table 8-10 Design variables and setting-up for CUTFDAC arrival

Design variables	Description	Denormalisation function	Minimum	Maximum
ALT1	Altitude at node 1, (m)	Linear	1524	2438
DIS1	Distance at node 1, (m)	Linear	50	47596
SPD1	Calibrated Airspeed at node 1, (m/s)	Linear	77.2	128.6
SPD2	Calibrated Airspeed at node 2, (m/s)	Linear	77.2	118.3
SPD3	Calibrated Airspeed at node 3, (m/s)	Linear	77.2	102.9
SPD4	Calibrated Airspeed at node 4, (m/s)	Linear	77.2	91.1
SPD5	Calibrated Airspeed at node 5, (m/s)	Linear	77.2	91.1
SPD6	Calibrated Airspeed at node 6, (m/s)	Linear	77.2	91.1

Table 8-11 Objective functions and setting-up for CUTFDAC arrival

Objectives	Description	Optimisation type	Normalisation Function	Minimum	Maximum
NOx	(g)	Minimisation	ObjectiveMin	10	100000
NOISE	Noise-impact area (SEL $\geq$ 70 dBA), (m^2)	Minimisation	ObjectiveMin	100	1000000000

Table 8-12 Setting-up of GAs parameters for CUTFDAC arrival

Population size	150
Initialisation factor	80
Creation schemes	Trilinear and SBX crossover and Dynamic vector Mutate
Creations selectors	Stochastic universal sampling for both crossover and random selection for the mutation operator

Creation rates	0.45, 0.45, 0.10 respectively
Selection pressure	2.0
Stopping criteria	Max. generation = 350

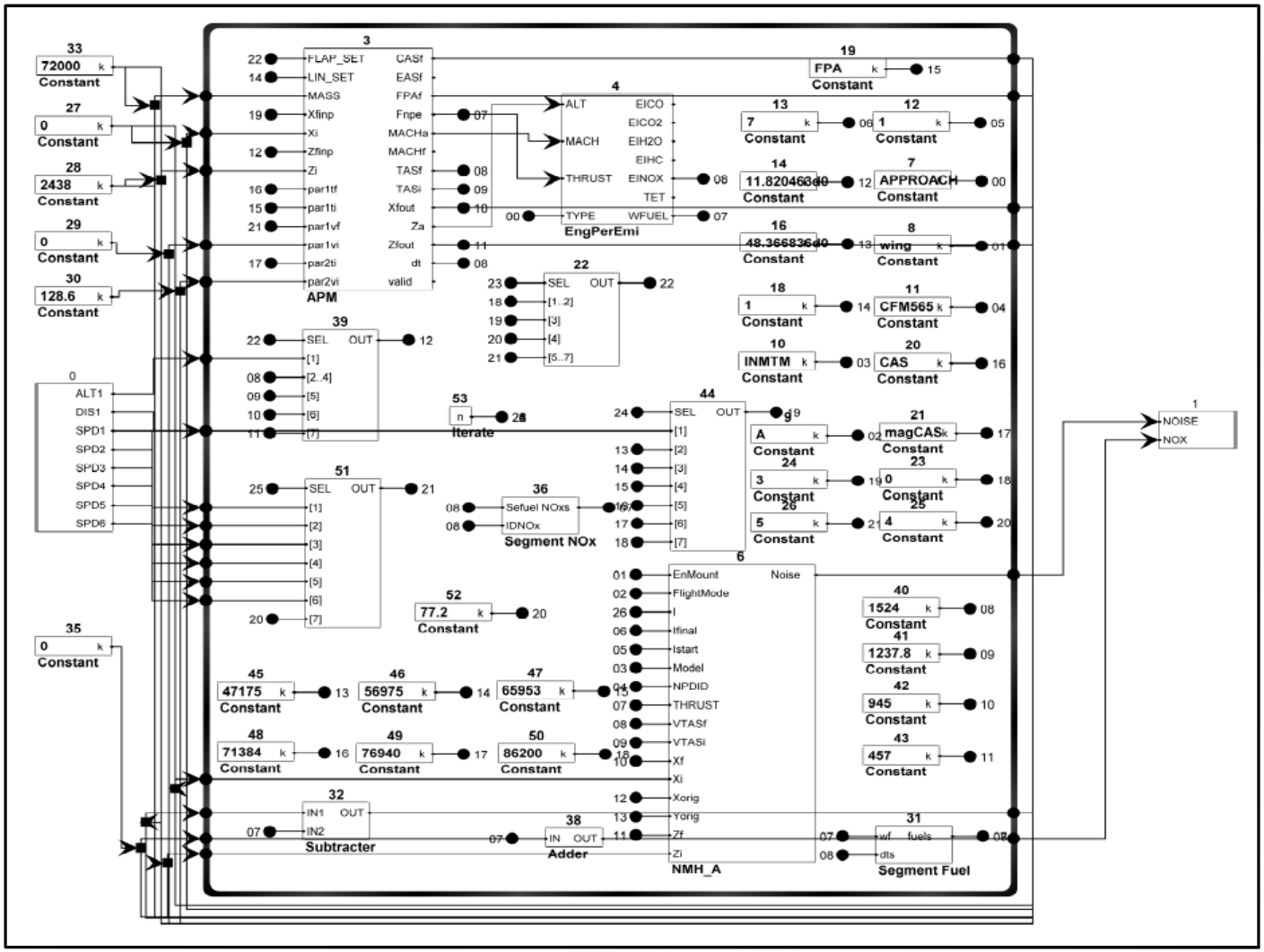

Figure 8-9 Systematic integration and modelling for CUTFDAC arrival

8.3 Systematic Integration and Optimisation Modelling of CUTPDAC Flight

8.3.1 Departure phase of CUTPDAC

Table 8-13 Design variables and setting-up for CUTPDAC departure

Design variables	Description	Denormalisation function	Minimum	Maximum
ALT2	Altitude at node 2, (m)	Linear	152	1828.8
ALT3	Altitude at node 3, (m)	Linear	152	1828.8
ALT4	Altitude at node 4, (m)	Linear	152	1828.8
SPD1	Calibrated Airspeed at node 1, (m/s)	Linear	65	113.2
SPD2	Calibrated Airspeed at node 2, (m/s)	Linear	65	113.2
SPD3	Calibrated Airspeed at node 3, (m/s)	Linear	65	128.61
SPD4	Calibrated Airspeed at node 4, (m/s)	Linear	65	128.61

Table 8-14 Objective functions and setting-up for CUTPDAC departure

Objectives	Description	Optimisation type	Normalisation Function	Minimum	Maximum
FUEL	Total fuel consumption, (kg)	Minimisation	ObjectiveMin	10	2000
NOISE	Noise-impact area (SEL $\geq$ 70 dBA), (m^2)	Minimisation	ObjectiveMin	100	10000000000

Table 8-15 Optimisation constraints and setting-up for CUTPDAC departure

Constraints	Description	Constraint type	Normalisation Function	Minimum	Maximum
CA32	ALT3 – ALT2, (m)	Greater than minimum	GreaterThan	0	2000
CA43	ALT4 – ALT3, (m)	Greater than minimum	GreaterThan	0	2000

Table 8-16 Setting-up of GAs parameters for CUTPDAC departure

Population size	150
Initialisation factor	40
Creation schemes	Trilinear and SBX crossover and Dynamic vector Mutate
Creations selectors	Stochastic universal sampling for both crossover and random selection for the mutation operator
Creation rates	0.45, 0.45, 0.10 respectively
Selection pressure	2.0
Stopping criteria	Max. generation = 400

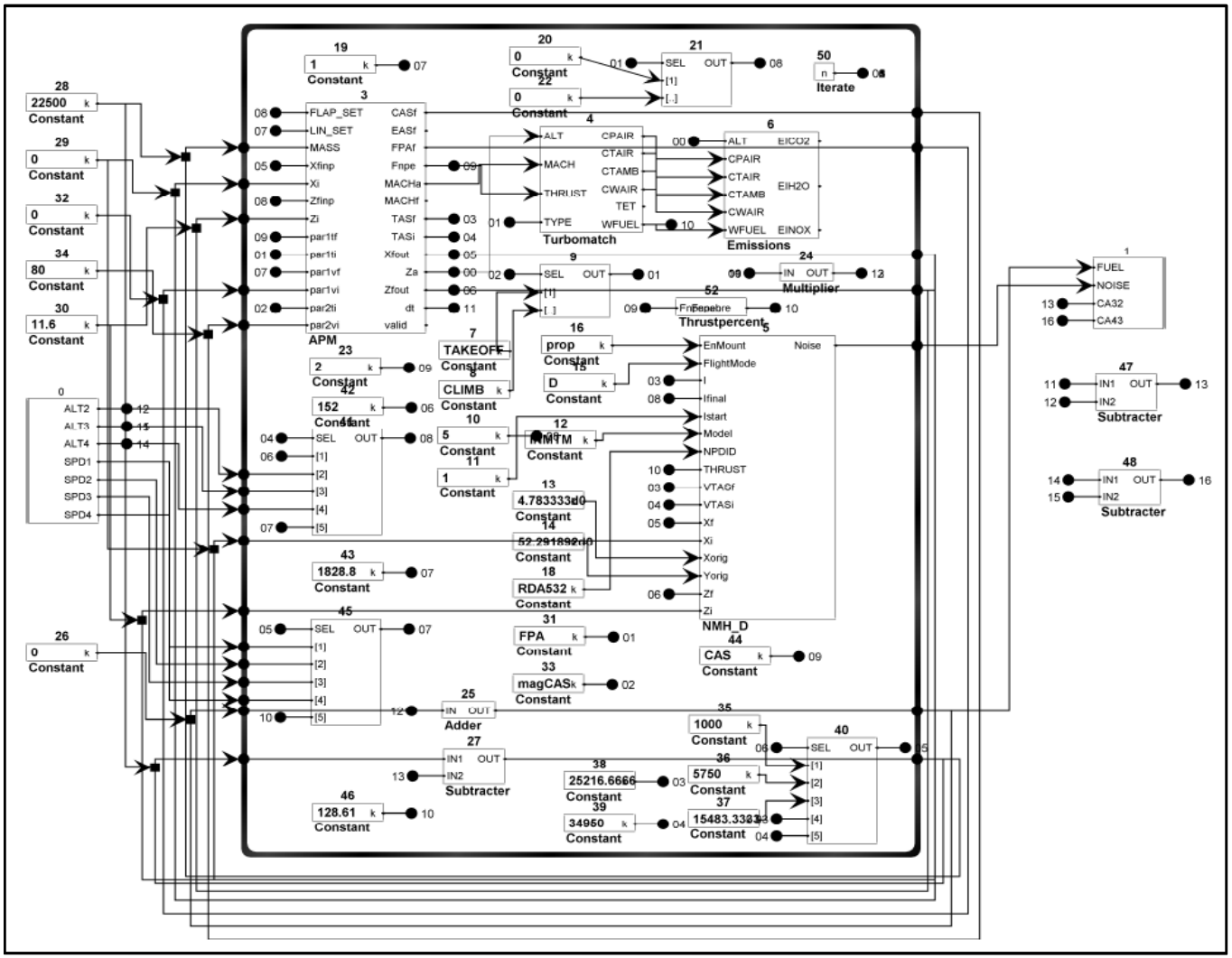

Figure 8-10 Systematic integration and modelling for CUTPDAC departure

8.3.2 En route phase of CUTPDAC

Table 8-17 Design variables and setting-up for CUTPDAC en route

Design variables	Description	Denormalisation function	Minimum	Maximum
ALT1	Altitude at node 1, (m)	Linear	1828.8	7620
ALT2	Altitude at node 2, (m)	Linear	4500	7620
ALT9	Altitude at node 9, (m)	Linear	2438.4	7620
DIS1	Distance at node 1, (m)	Linear	50	335000
DIS2	Distance at node 2, (m)	Linear	140000	335000
DIS8	Distance at node 8, (m)	Linear	402000	539000
DIS9	Distance at node 9, (m)	Linear	402000	636950
SPD1	Mach number at node 1	Linear	0.42	0.6
SPD2	Mach number at node 2	Linear	0.45	0.6
SPD9	Mach number at node 9	Linear	0.44	0.6

Table 8-18 Objective functions and setting-up for CUTPDAC en route

Objectives	Description	Optimisation type	Normalisation Function	Minimum	Maximum
FUEL	Total fuel consumption, (kg)	Minimisation	ObjectiveMin	10	100000
TIME	Total flight time, (s)	Minimisation	ObjectiveMin	10	100000

Table 8-19 Optimisation constraints and setting-up for CUTPDAC en route

Constraints	Description	Constraint type	Normalisation Function	Minimum	Maximum
CA21	ALT2 – ALT1, (m)	Greater than minimum	GreaterThan	0	5800
CA89	ALT8 – ALT9, (m)	Greater than minimum	GreaterThan	0	5200
CX21	DIS2 - DIS1, (m)	Greater than minimum	GreaterThan	50	335050

CX98	DIS9 – DIS8, (m)	Greater than minimum	GreaterThan	50	235050
CO_2	(g)	Less than maximum	LessThan	100	100000000
NOx	(g)	Less than maximum	LessThan	10	100000

Table 8-20 Setting-up of GAs parameters for CUTPDAC en route

Population size	150
Initialisation factor	40
Creation schemes	Trilinear and SBX crossover and Dynamic vector Mutate
Creations selectors	Stochastic universal sampling for both crossover and random selection for the mutation operator
Creation rates	0.45, 0.45, 0.10 respectively
Selection pressure	2.0
Stopping criteria	Max. generation = 450

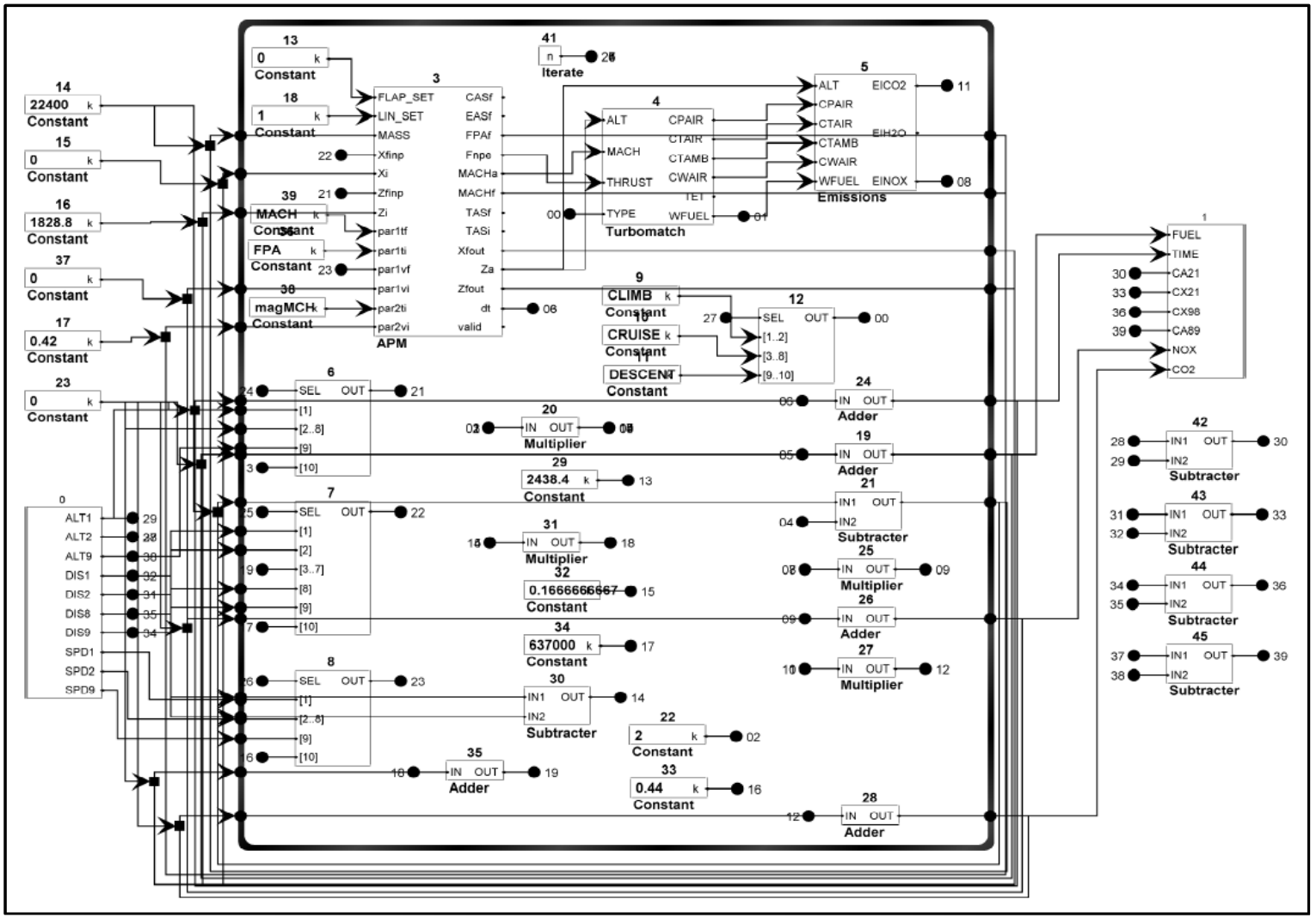

Figure 8-11 Systematic integration and modelling for CUTPDAC en route

8.3.3 Arrival phase of CUTPDAC

Table 8-21 Design variables and setting-up for CUTPDAC arrival

Design variables	Description	Denormalisation function	Minimum	Maximum
ALT1	Altitude at node 1, (m)	Linear	1524	2438
DIS1	Distance at node 1, (m)	Linear	50	47596
SPD1	Calibrated Airspeed at node 1, (m/s)	Linear	77.2	128.6
SPD2	Calibrated Airspeed at node 2, (m/s)	Linear	77.2	118.3
SPD3	Calibrated Airspeed at node 3, (m/s)	Linear	77.2	102.9
SPD4	Calibrated Airspeed at node 4, (m/s)	Linear	77.2	91.1
SPD5	Calibrated Airspeed at node 5, (m/s)	Linear	77.2	91.1
SPD6	Calibrated Airspeed at node 6, (m/s)	Linear	77.2	91.1

Table 8-22 Objective functions and setting-up for CUTPDAC arrival

Objectives	Description	Optimisation type	Normalisation Function	Minimum	Maximum
NOx	(g)	Minimisation	ObjectiveMin	10	10000
NOISE	Noise-impact area (SEL $\geq$ 70 dBA), (m^2)	Minimisation	ObjectiveMin	100	1000000000

Table 8-23 Setting-up of GAs parameters for CUTPDAC arrival

Population size	150
Initialisation factor	60
Creation schemes	Trilinear and SBX crossover and Dynamic vector Mutate
Creations selectors	Stochastic universal sampling for both crossover and random selection for the mutation operator

Creation rates	0.45, 0.45, 0.10 respectively
Selection pressure	2.0
Stopping criteria	Max. generation = 450

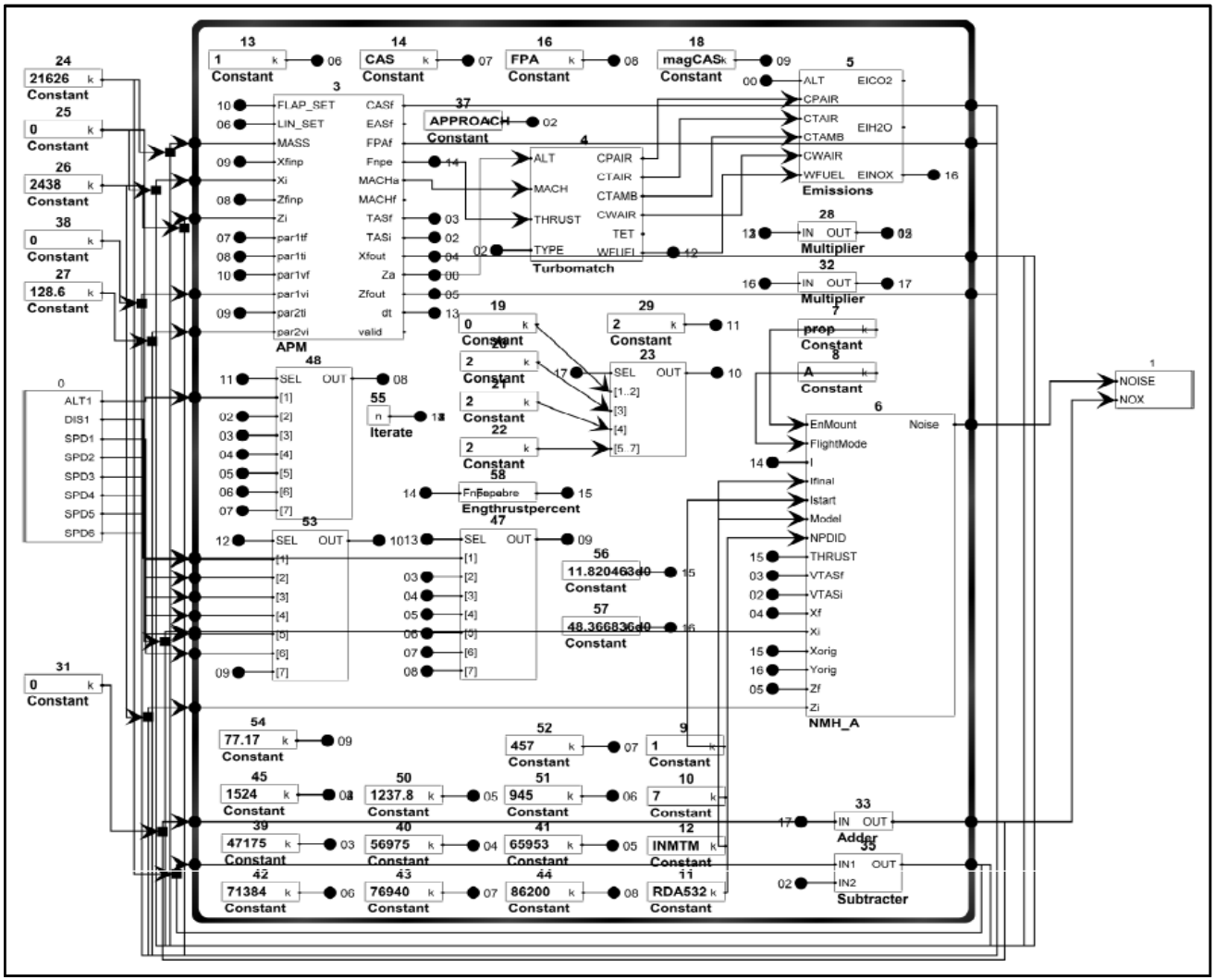

Figure 8-12 Systematic integration and modelling for CUTPDAC arrival

8.4 Systematic Integration and Optimisation Modelling of CUPFDAC Flight

8.4.1 Departure phase of CUPFDAC

Table 8-24 Design variables and setting-up for CUPFDAC departure

Design variables	Description	Denormalisation function	Minimum	Maximum
ALT2	Altitude at node 2, (m)	Linear	152	1828.8
ALT3	Altitude at node 3, (m)	Linear	152	1828.8
ALT4	Altitude at node 4, (m)	Linear	152	1828.8
SPD1	Calibrated Airspeed at node 1, (m/s)	Linear	79	113.2
SPD2	Calibrated Airspeed at node 2, (m/s)	Linear	79	113.2
SPD3	Calibrated Airspeed at node 3, (m/s)	Linear	79	128.61
SPD4	Calibrated Airspeed at node 4, (m/s)	Linear	79	128.61

Table 8-25 Objective functions and setting-up for CUPFDAC departure

Objectives	Description	Optimisation type	Normalisation Function	Minimum	Maximum
FUEL	Total fuel consumption, (kg)	Minimisation	ObjectiveMin	10	2000
NOISE	Noise-impact area (SEL ≥ 70 dBA), (m^2)	Minimisation	ObjectiveMin	100	10000000000

Table 8-26 Optimisation constraints and setting-up for CUPFDAC departure

Constraints	Description	Constraint type	Normalisation Function	Minimum	Maximum
CA32	ALT3 – ALT2, (m)	Greater than minimum	GreaterThan	0	2000
CA43	ALT4 – ALT3, (m)	Greater than minimum	GreaterThan	0	2000

Table 8-27 Setting-up of GAs parameters for CUPFDAC departure

Population size	150
Initialisation factor	40
Creation schemes	Trilinear and SBX crossover and Dynamic vector Mutate
Creations selectors	Stochastic universal sampling for both crossover and random selection for the mutation operator
Creation rates	0.45, 0.45, 0.10 respectively
Selection pressure	2.0
Stopping criteria	Max. generation = 450

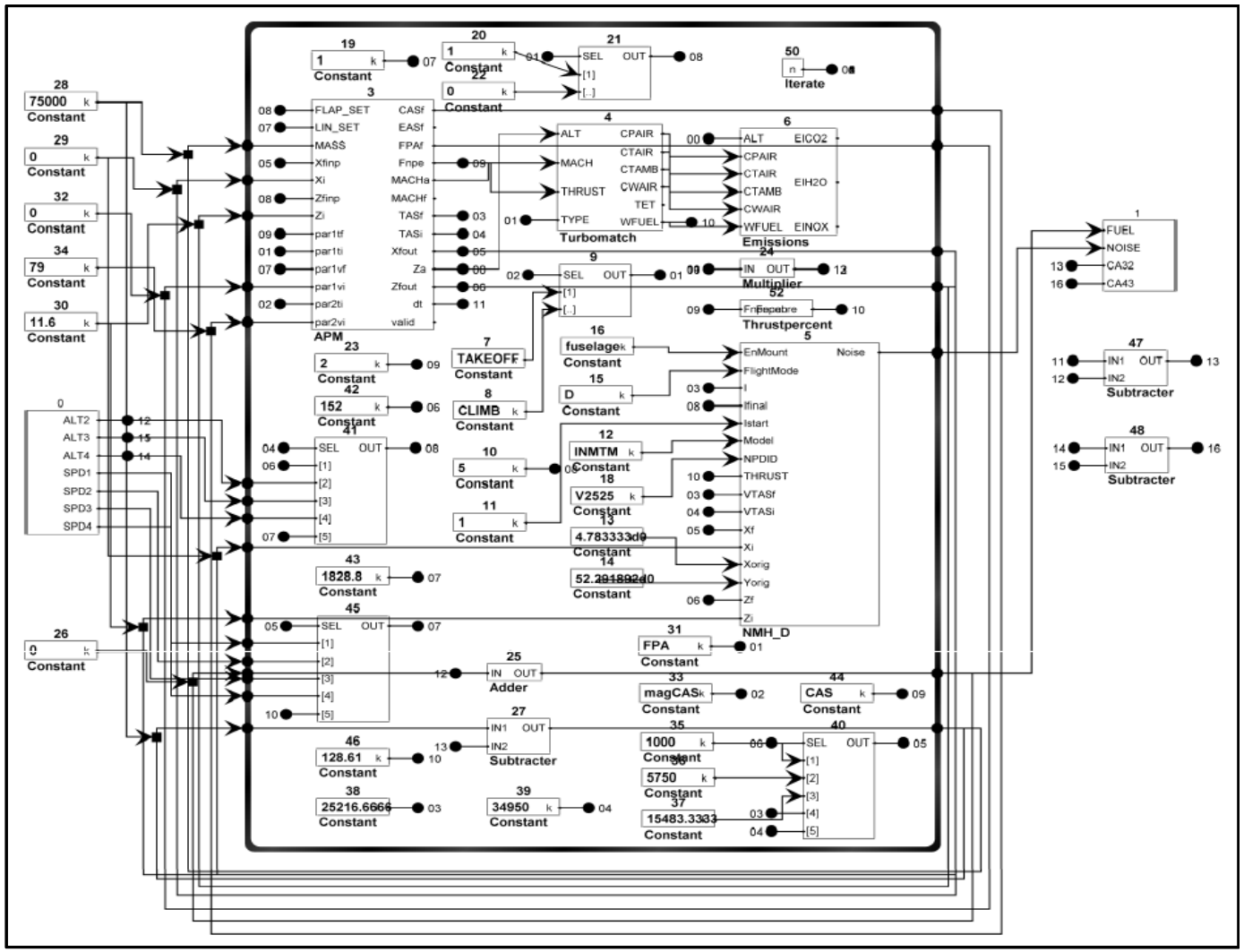

Figure 8-13 Systematic integration and modelling for CUPFDAC departure

8.4.2 En route phase of CUPFDAC

Table 8-28 Design variables and setting-up for CUPFDAC en route

Design variables	Description	Denormalisation function	Minimum	Maximum
ALT1	Altitude at node 1, (m)	Linear	1828.8	11887.2
ALT2	Altitude at node 2, (m)	Linear	7924.8	11887.2
ALT9	Altitude at node 9, (m)	Linear	2438.4	11887.2
DIS1	Distance at node 1, (m)	Linear	50	335000
DIS2	Distance at node 2, (m)	Linear	140000	335000
DIS8	Distance at node 8, (m)	Linear	402000	539000
DIS9	Distance at node 9, (m)	Linear	402000	636950
SPD1	Mach number at node 1	Linear	0.42	0.75
SPD2	Mach number at node 2	Linear	0.7	0.75
SPD9	Mach number at node 9	Linear	0.44	0.75

Table 8-29 Objective functions and setting-up for CUPFDAC en route

Objectives	Description	Optimisation type	Normalisation Function	Minimum	Maximum
FUEL	Total fuel consumption, (kg)	Minimisation	ObjectiveMin	10	100000
TIME	Total flight time, (s)	Minimisation	ObjectiveMin	10	100000

Table 8-30 Optimisation constraints and setting-up for CUPFDAC en route

Constraints	Description	Constraint type	Normalisation Function	Minimum	Maximum
CA21	ALT2 – ALT1, (m)	Greater than minimum	GreaterThan	0	10100
CA89	ALT8 – ALT9, (m)	Greater than minimum	GreaterThan	0	9500
CX21	DIS2 - DIS1, (m)	Greater than minimum	GreaterThan	50	335050

CX98	DIS9 – DIS8, (m)	Greater than minimum	GreaterThan	50	235050
CO_2	(g)	Less than maximum	LessThan	100	100000000
NOx	(g)	Less than maximum	LessThan	10	1000000

Table 8-31 Setting-up of GAs parameters for CUPFDAC en route

Population size	150
Initialisation factor	40
Creation schemes	Trilinear and SBX crossover and Dynamic vector Mutate
Creations selectors	Stochastic universal sampling for both crossover and random selection for the mutation operator
Creation rates	0.45, 0.45, 0.10 respectively
Selection pressure	2.0
Stopping criteria	Max. generation = 450

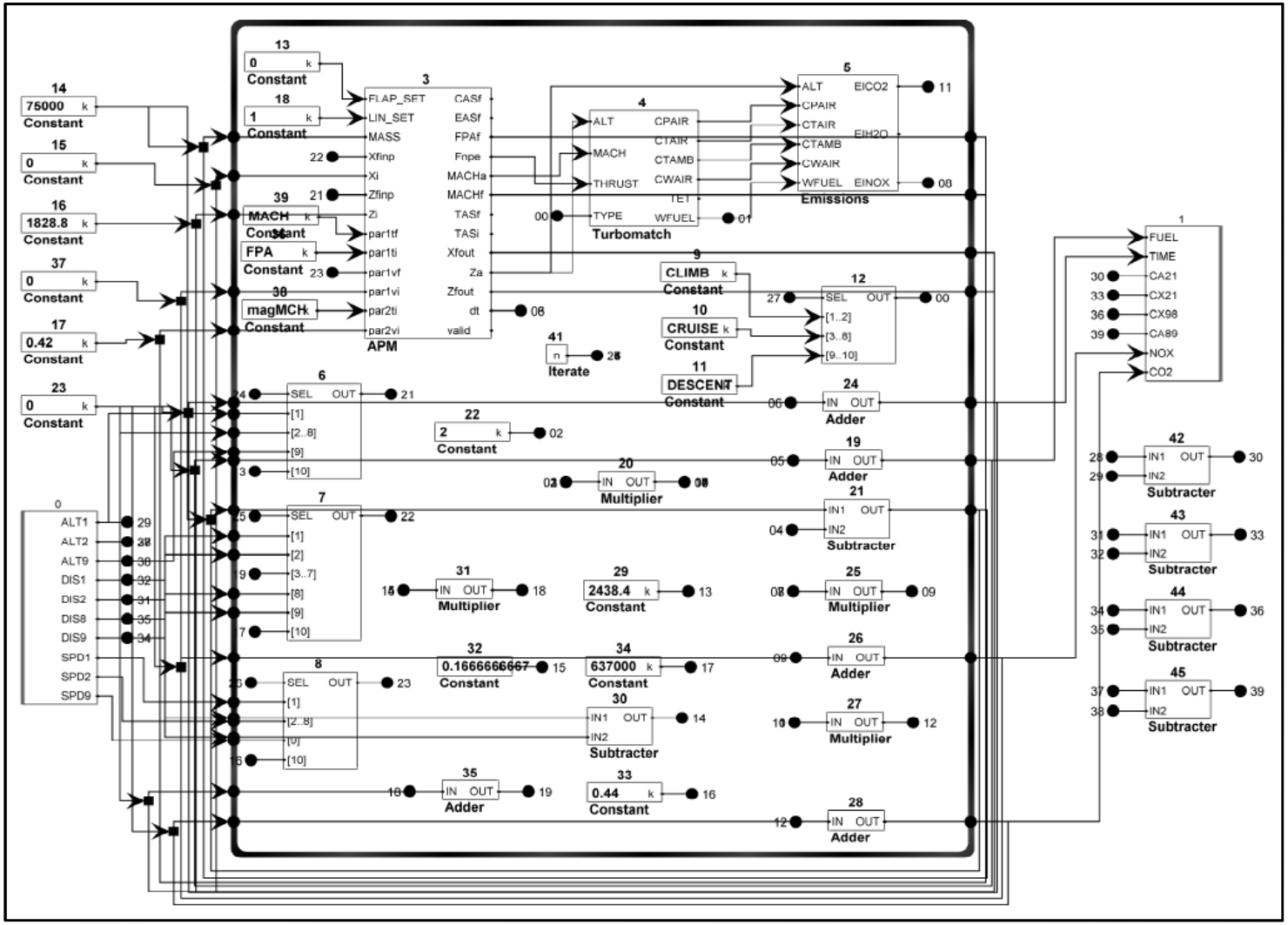

Figure 8-14 Systematic integration and modelling for CUPFDAC en route

8.4.3 Arrival phase of CUPFDAC

Table 8-32 Design variables and setting-up for CUPFDAC arrival

Design variables	Description	Denormalisation function	Minimum	Maximum
ALT1	Altitude at node 1, (m)	Linear	1524	2438
DIS1	Distance at node 1, (m)	Linear	50	47596
SPD1	Calibrated Airspeed at node 1, (m/s)	Linear	77.2	128.6
SPD2	Calibrated Airspeed at node 2, (m/s)	Linear	77.2	118.3
SPD3	Calibrated Airspeed at node 3, (m/s)	Linear	77.2	102.9
SPD4	Calibrated Airspeed at node 4, (m/s)	Linear	77.2	91.1
SPD5	Calibrated Airspeed at node 5, (m/s)	Linear	77.2	91.1
SPD6	Calibrated Airspeed at node 6, (m/s)	Linear	77.2	91.1

Table 8-33 Objective functions and setting-up for CUPFDAC arrival

Objectives	Description	Optimisation type	Normalisation Function	Minimum	Maximum
NOx	(g)	Minimisation	ObjectiveMin	10	100000000
NOISE	Noise-impact area (SEL $\geq$ 70 dBA), (m^2)	Minimisation	ObjectiveMin	100	10000000000

Table 8-34 Setting-up of GAs parameters for CUPFDAC arrival

Population size	150
Initialisation factor	60
Creation schemes	Trilinear and SBX crossover and Dynamic vector Mutate
Creations selectors	Stochastic universal sampling for both crossover and random selection for the mutation operator

Creation rates	0.45, 0.45, 0.10 respectively
Selection pressure	2.0
Stopping criteria	Max. generation = 450

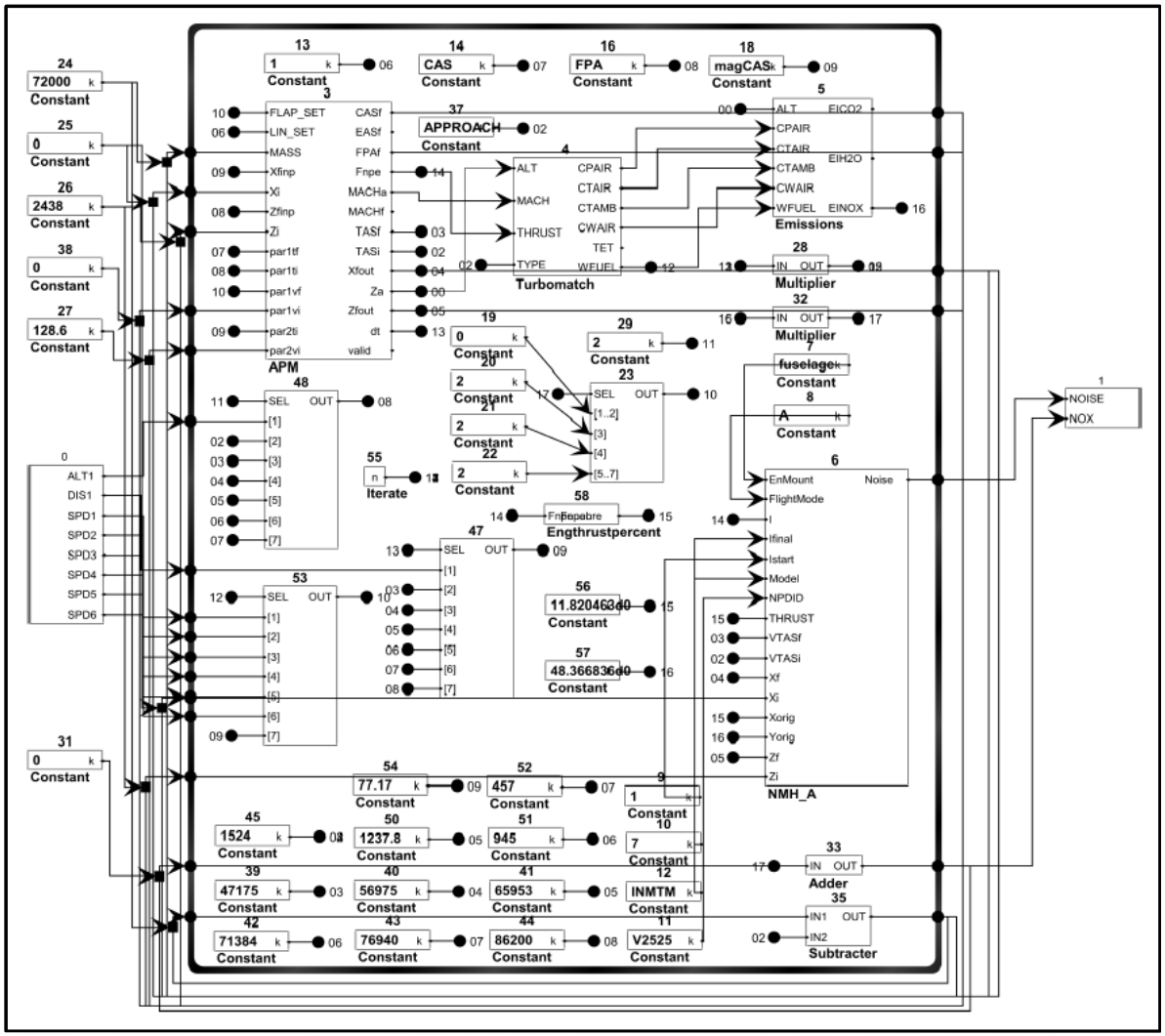

Figure 8-15 Systematic integration and modelling for CUPFDAC arrival

CHAPTER NINE OPTIMISED RESULTS AND ANALYSIS

In this chapter, the optimised results from different aircraft/engines (CUTFDAC, CUTPDAC and CUPFDAC) and different flight phases (Departure, En route and Arrival), which are based on the component-level and system-level models described in the previous chapters, and corresponding preliminary analysis, are provided.

These results include: 1) running records of optimisation processes; 2) normalised Pareto areas; 3) Pareto front lines; 4) optimised flight trajectories from typical flight modes (for instance, minimum fuel consumption mode, minimum flight time mode, minimum noise-impact area mode and/or minimum NOx emission mode) in terms of trajectory descriptions (such as flight altitude vs. flight distance, flight speed vs. flight distance and flight path angle vs. flight distance), overall performances and comparisons (involving fuel consumption, flight time, flight noise impact area and main gaseous emissions like CO_2, H_2O and NOx), as well as segment distributions, or called segment breakdown, of some main parameters (such as per engine net thrust, engine turbine entry temperature, NOx emission index, fuel consumption, flight time, CO_2 emission, H_2O emission and NOx emission, etc.).

9.1 Departure Flight Phase

9.1.1 CUTFDAC (Cranfield University Turbofan-Driven Aircraft)

Table 9-1 Running record of CUTFDAC-Departure optimisation

1	Running start time/date	Sun Oct 14 12:23:01 BST 2012
2	Running end time/date	Mon Oct 15 00:06:46 BST 2012
3	Total running time	11 hours 43 minutes 46 seconds
4	Generation number	450
5	Total number of evaluations	75207

From the above Table 9-1, it can be seen that the entire optimisation process cost 11 hours 43 minutes 46 seconds with 450 generations or 75207 evaluations. That is, on average, 93.84 seconds/generation or 0.56 seconds/evaluation.

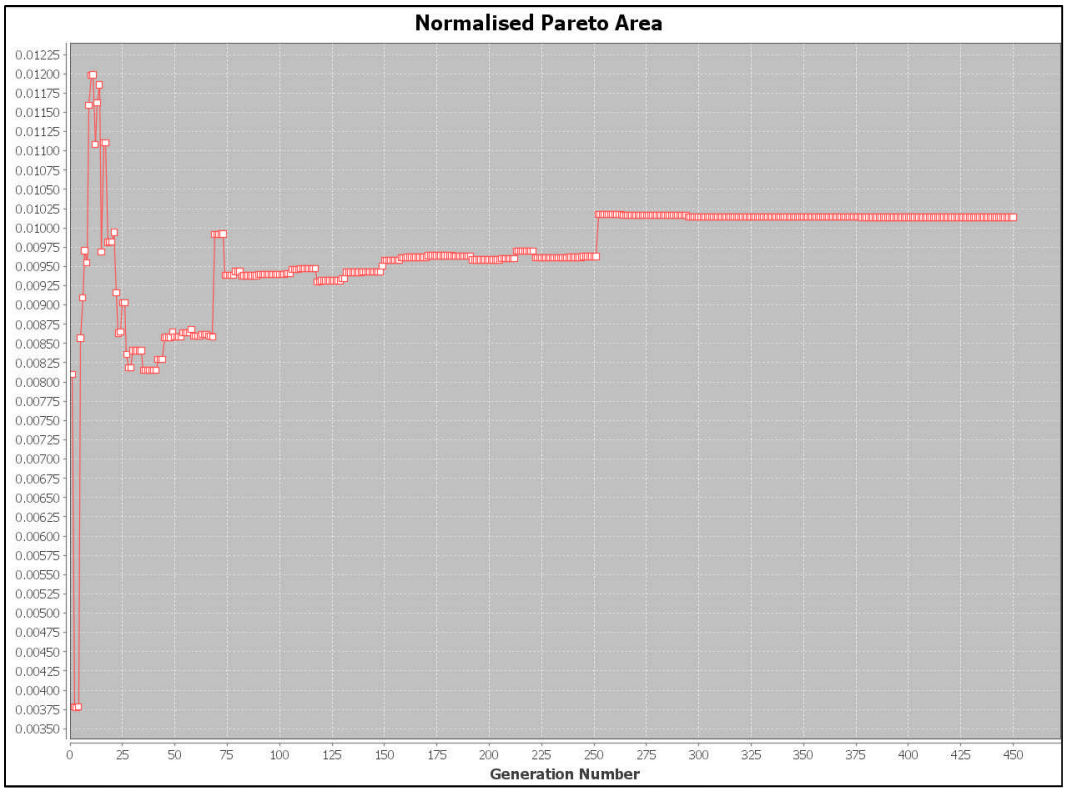

Figure 9-1 Normalised Pareto Area (CUTFDAC-Departure)

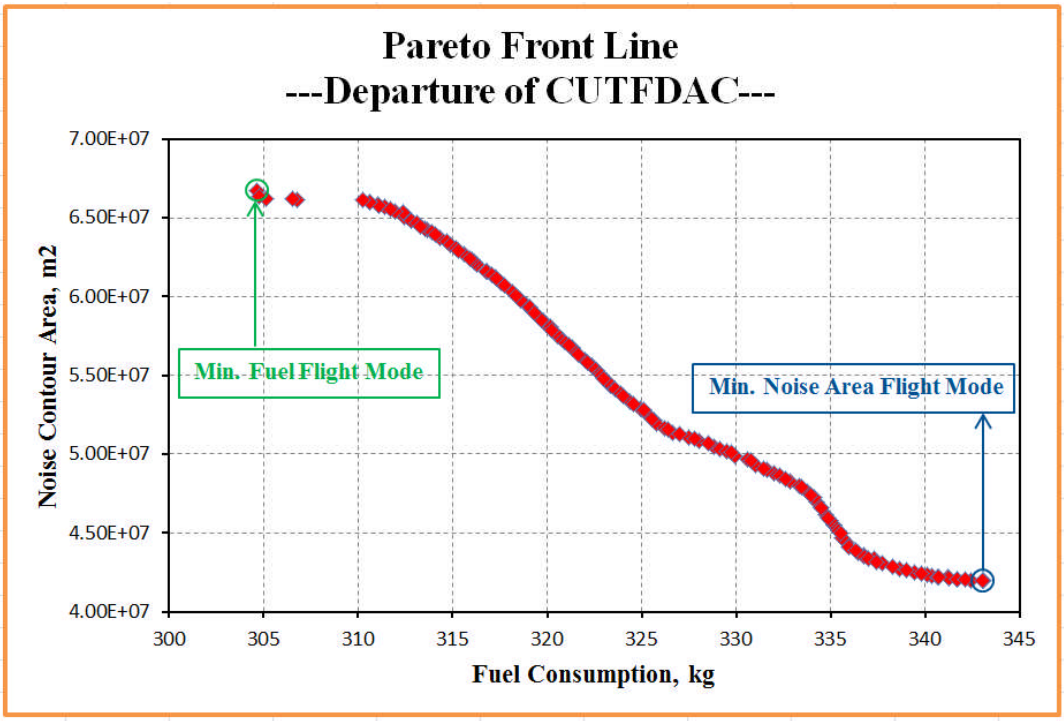

Figure 9-2 Pareto Front Line (CUTFDAC-Departure)

From the plots of normalised Pareto area and Pareto front line, respectively shown in the above Figures 9-1 and 9-2, it can be concluded that the convergence of this optimisation process after 450 generations has been achieved.

Table 9-2 Optimised results of two typical flight trajectories

		Minimum Fuel Flight Mode	**Minimum Noise Area Flight Mode**
Design variables	ALT2, (m)	152.08	152.57
	ALT3, (m)	189.84	1367.27
	ALT4, (m)	189.89	1439.66
	SPD1, (CAS, m/s)	100.66	87.19
	SPD2, (CAS, m/s)	113.20	113.20
	SPD3, (CAS, m/s)	128.61	128.54
	SPD4, (CAS, m/s)	128.61	106.02
Objective functions	Fuel consumption, (kg)	304.65	343.07
	Noise area, (m^2)	66716700	41983500
Optimisation constraints	CA32, (m)	37.76	1214.71
	CA43, (m)	0.05	72.39

Table 9-3 Flight trajectory of 'Min. Fuel Mode'

Point	**X (m)**	**Z (m)**	**CAS (m/s)**	**TAS (m/s)**	**FPA (rad.)**
1	0	11.6	85	85.71	0
2	1000	152	100.66	102.51	0.14
3	5750	152.1	113.20	115.62	1.70E-05

4	15483.33	189.8	128.61	132.12	0.004
5	25216.67	189.9	128.61	132.12	5.00E-06
6	34950	1828.8	128.61	143.20	0.17

Table 9-4 Flight trajectory of 'Min. Noise Area Mode'

Point	X (m)	Z (m)	CAS (m/s)	TAS (m/s)	FPA (rad.)
1	0	11.6	85	85.71	0
2	1000	152	87.19	88.55	0.14
3	5750	152.6	113.20	115.62	1.19E-04
4	15483.33	1367.3	128.54	139.87	0.12
5	25216.67	1439.7	106.02	115.12	0.007
6	34950	1828.8	128.61	143.20	0.04

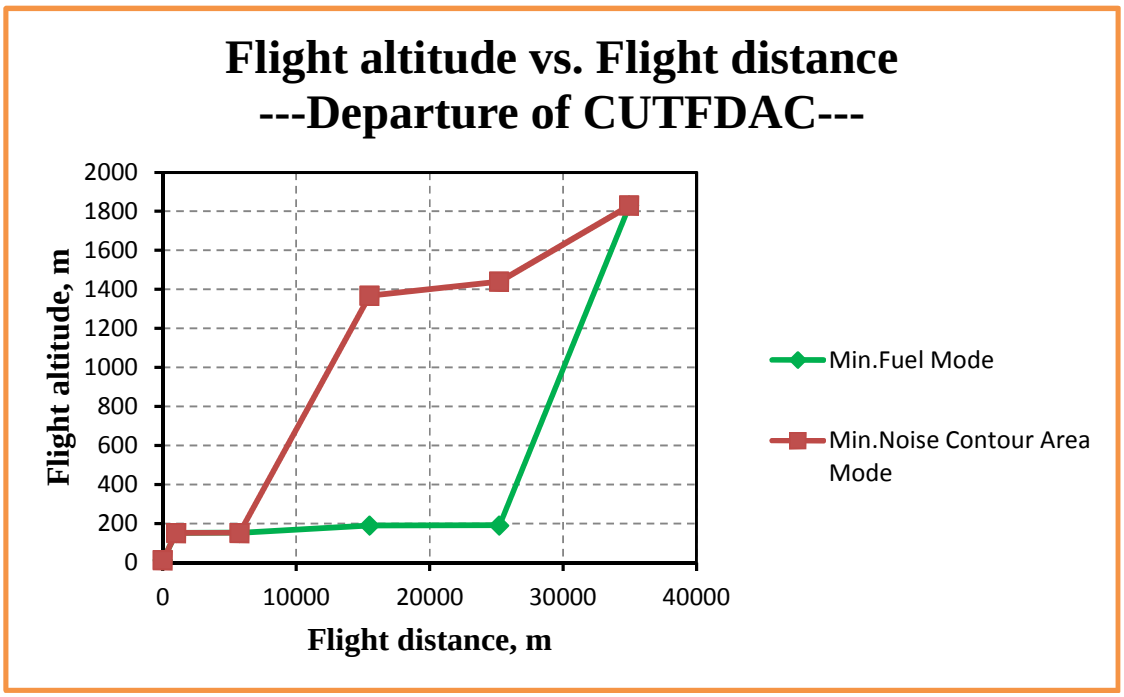

Figure 9-3 Flight altitude vs. Flight distance (CUTFDAC-Departure)

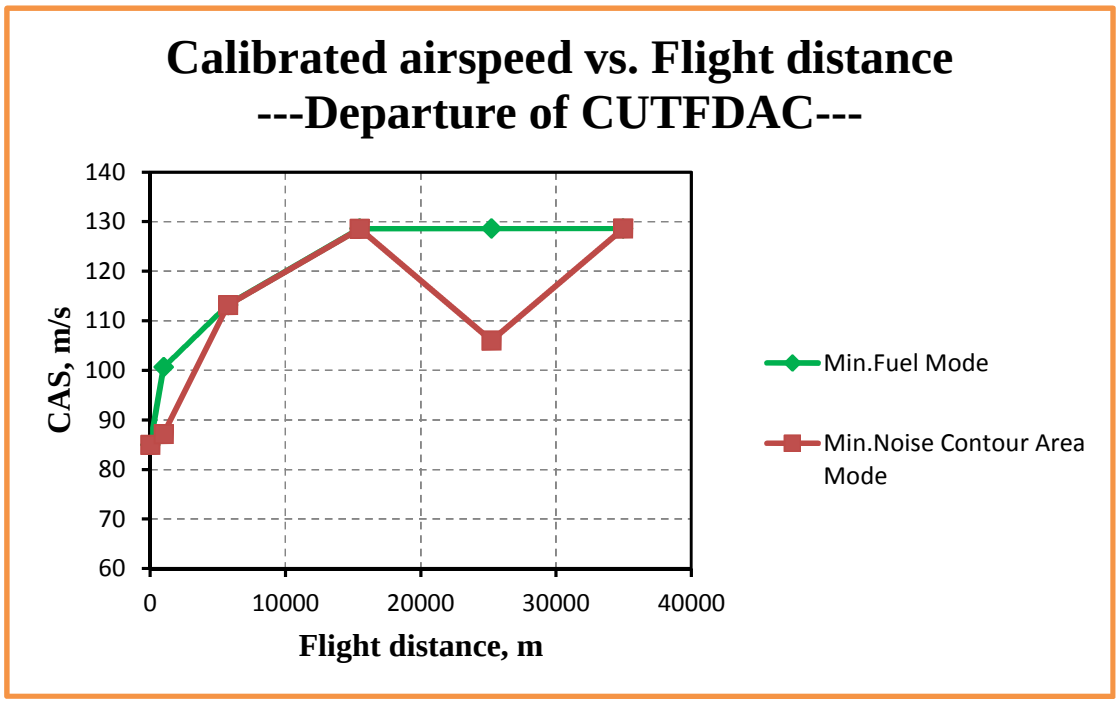

Figure 9-4 Calibrated airspeed vs. Flight distance (CUTFDAC-Departure)

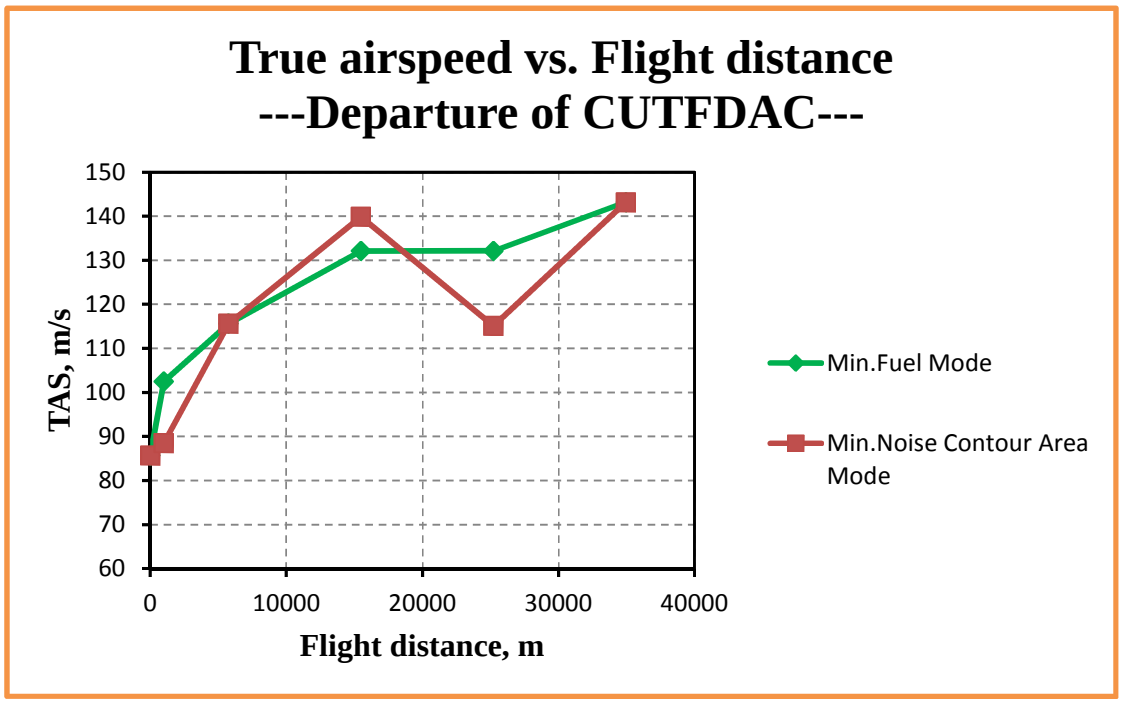

Figure 9-5 True airspeed vs. Flight distance (CUTFDAC-Departure)

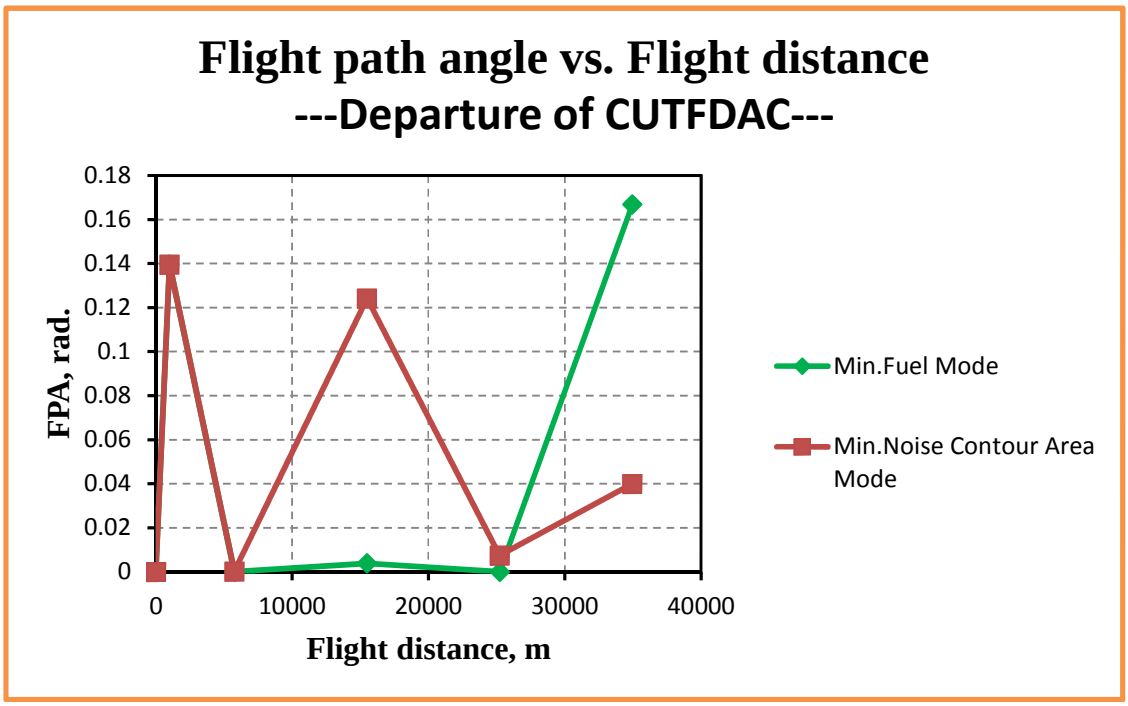

Figure 9-6 Flight path angle vs. Flight distance (CUTFDAC-Departure)

From the above tables 9-2 to 9-4 and figures 9-3 to 9-6, for the 'minimum fuel consumption' flight mode, the optimised results suggest that the flight trajectory which CUTFDAC should follow is that, firstly for the 1st segment, CUTFDAC can climb and accelerate from the given initial status point 1 (Z=11.6 m, CAS=85 m/s, FPA=0 rad.) to point 2 (Z=152 m, CAS=100.66 m/s, FPA=0.1395 rad.) with the horizontal flight distance ΔX=1000 m; during the 2nd segment, CUTFDAC will adopt 'level flight and accelerate' method to arrive at the status point 3 (Z=152 m, CAS=113.20 m/s, FPA=1.70E-05 rad.) with ΔX=4750 m; when CUTFDAC flies in the 3rd segment, the flight style of 'climb and acceleration' which is used in segment 1 is restored until the status point 4 (Z=189.84 m, CAS=128.61 m/s, FPA=0.0039 rad.) is reached, and the 3rd-segment flight will cover the horizontal distance ΔX=9733.33 m; for the 4th-segment flight, CUTFDAC needs to use another flight style, that is, constant altitude and constant speed flight, the flight in this segment will be kept in Z=190 m and CAS=128.61 m/s with the horizontal flight distance ΔX=9733.34 m; during the last (i.e., the 5th) segment, CUTFDAC flies with the style of constant-CAS climb, namely, while flying in this segment, CAS is kept as 128.61 m/s and, in the meantime, the flight

altitude Z is continuously increased to 1828.8 m from 190 m, and the last flight segment will cover the rest of horizontal flight distance for the departure phase, that is, ΔX=9733.33 m.

Different from the 'minimum fuel consumption' flight mode, the optimised results suggest that the flight trajectory, when CUTFDAC flies in the 'minimum noise contour area' mode, is that, firstly for the 1st segment, the aircraft, starting from the given initial status point 1 (Z=11.6 m, CAS=85 m/s, FPA=0 rad.), should reach the required flight altitude Z=152 m within the given horizontal flight distance ΔX=1000 m, and at the same time, a slight increase in flight speeds in terms of CAS (=87.19 m/s) and TAS (=88.55 m/s); in the following 2nd segment flight, 'level and acceleration' flight is applied, that is, the flight altitude is basically kept at 152 m, while CAS and TAS is respectively increased to 113.20 m/s and 115.62 m/s with FPA=1.19E-04 at the end of this segment; the 3rd flight segment can witness the obvious increases in both flight altitude and flight speeds, especially for the flight altitude – from 152.57 m to 1367.27 m, in the meantime, CAS increases from 113.20 m/s to 128.54 m/s, and TAS from 115.62 m/s to 139.87 m/s and all these changes take place within the horizontal flight distance ΔX=9733.33 m; during the 4th segment flight, the optimised results require the aircraft implement 'climb but deceleration' operation. According to this requirement, the flight altitude will be further increased from 1367.27 m to 1439.66 m, while CAS will be decelerated from 128.54 m/s to 106.02 m/s, and correspondingly, TAS will decrease from 139.87 m/s to 115.12 m/s; in the last (the 5th) flight segment, CUTFDAC will continue to climb and accelerate to the given flight status (Z=1828.8 m, CAS=128.61 m/s) with the required horizontal flight distance ΔX=9733.33 m.

From the above descriptions of flight trajectories resulted from two flight modes, it can be found that an obvious difference between two trajectories lies in the variation of flight altitude along flight distance. Compared to the 'min. fuel consumption' mode, 'min. noise area' mode chooses to climb to higher flight altitudes at earlier segments of the departure phase, naturally, this choice can effectively increase the distances between the aircraft (noise source) and the ground (observers) as soon as possible and reduce the noise contour area. In addition, during the departure flight by 'min. noise area' mode, a reduced flight speed is also introduced at the 4th segment. The reduced flight speed can

result in decreased engine power setting in terms of engine net thrust and turbine entry temperature (TET), therefore, lower noise contour area because, according to the flight noise theory, the distance between noise source and observer as well as engine power setting are two prime contributors to noise level.

Table 9-5 Overall performance of two typical flight trajectories (CUTFDAC-Departure)

	Fuel burnt	**Noise area**	**Flight time**	**CO emission**	**CO_2 emission**	**H_2O emission**	**UHC emission**	**NOx emission**
	(kg)	(m^2)	(s)	(g)	(g)	(g)	(g)	(g)
Min. Fuel Mode	304.65	66716700	277.91	414.58	961635.16	377220.53	11.02	4426.96
Min. Noise Area Mode	343.07	41983500	286.83	428.50	1082912.08	424793.82	12.28	5112.07
Δ	38.42	-24733200	8.92	13.92	121280	47573	1.26	685.11
δ	12.6%	-37.07%	3.21%	3.36%	12.6%	12.6%	11.43%	15.48%

(Note: In the above Table 9-5, Δ, δ denotes respectively the absolute and relative differences of the achieved results between 'Min. Fuel Mode' and 'Min. Flight Time Mode', based on the results from 'Min. Fuel Mode' as the reference.)

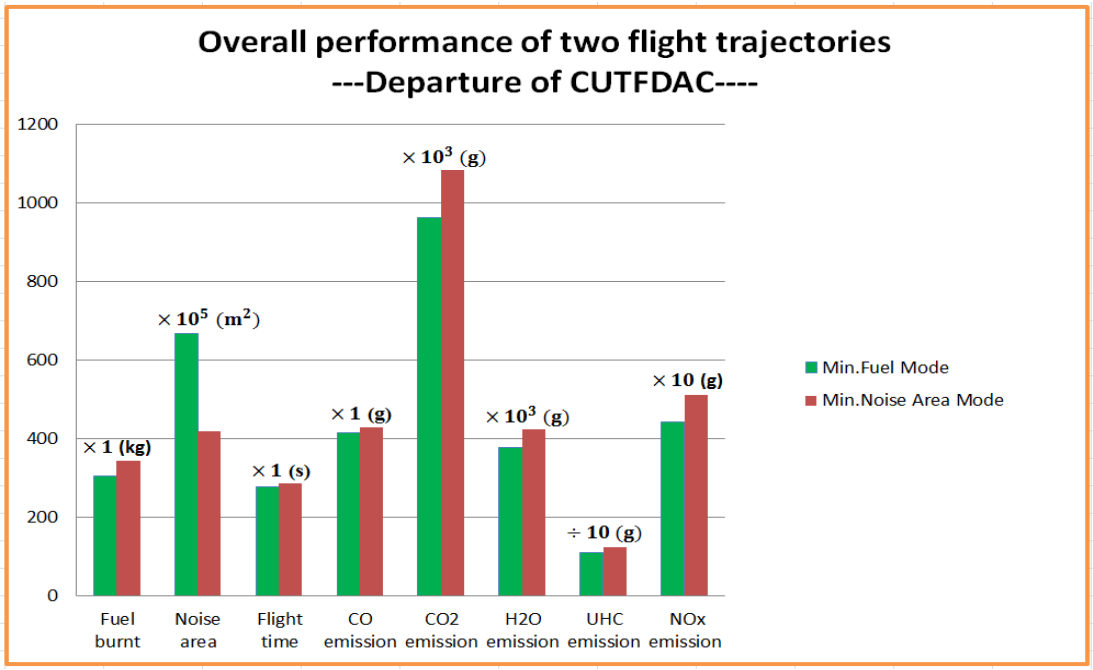

Figure 9-7 Overall performance of two typical flight trajectories (CUTFDAC-Departure)

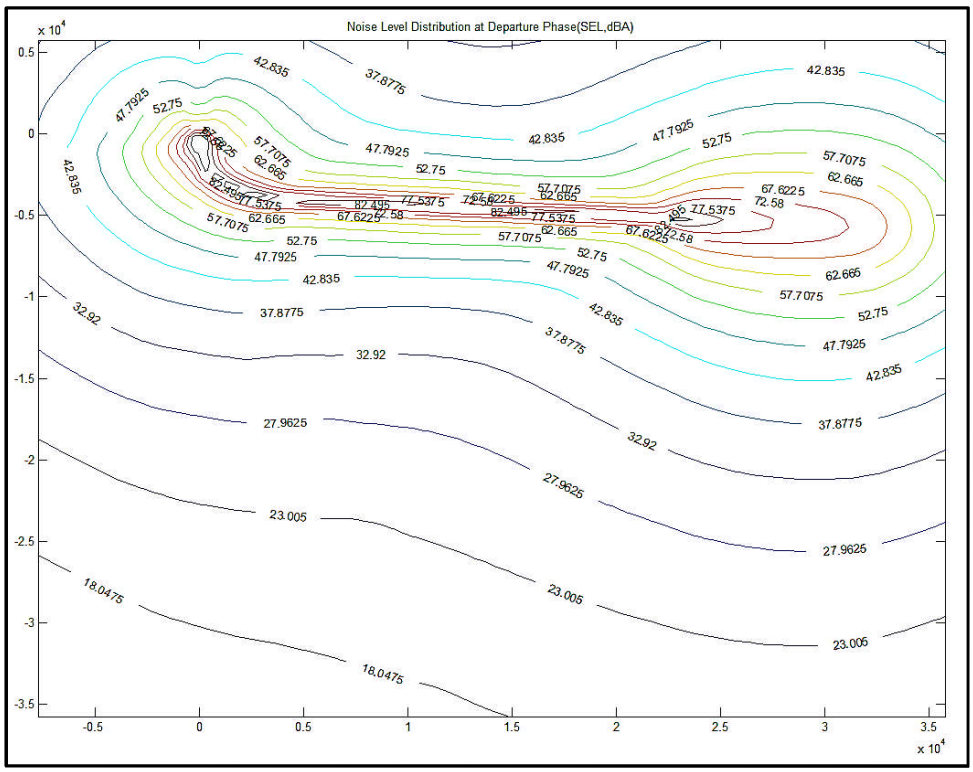

Figure 9-8 (a) Noise-level distribution contour of 'Min. Fuel Mode' (CUTFDAC-Departure)

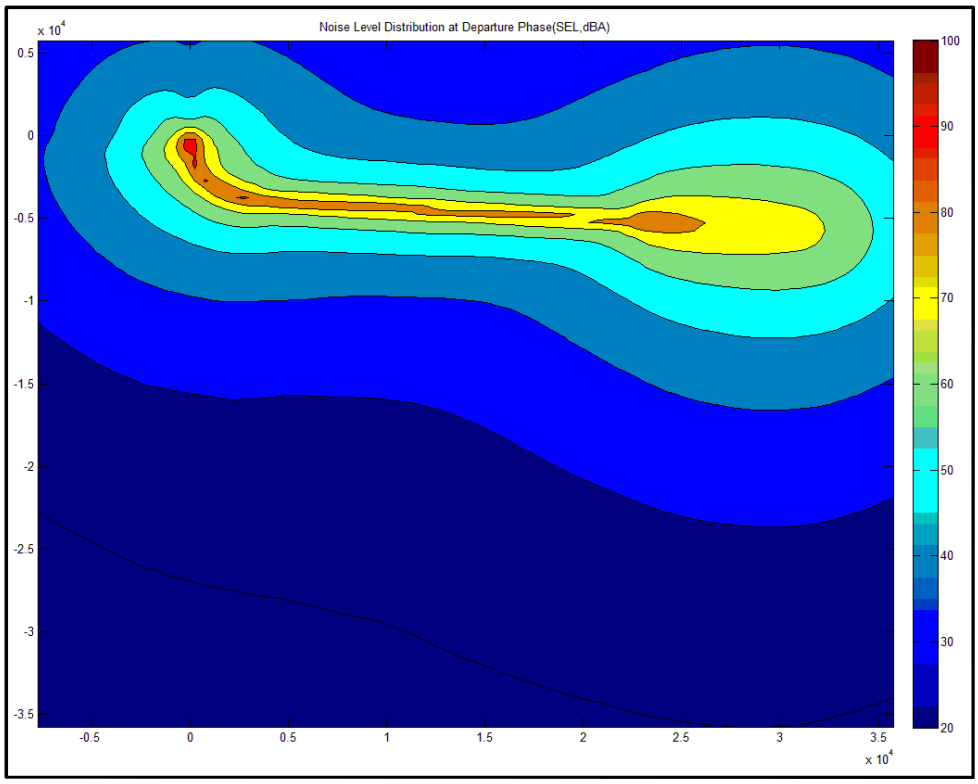

Figure 9-8 (b) Noise-level distribution filled contour of 'Min. Fuel Mode' (CUTFDAC-Departure)

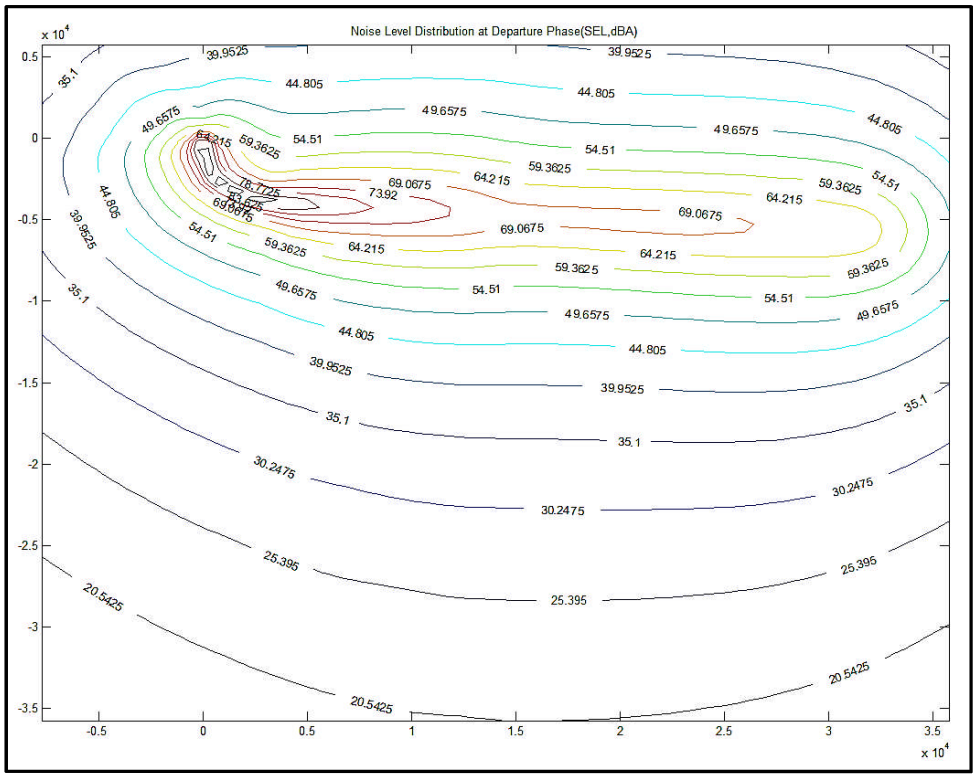

Figure 9-9 (a) Noise-level distribution contour of 'Min. Noise Area Mode' (CUTFDAC-Departure)

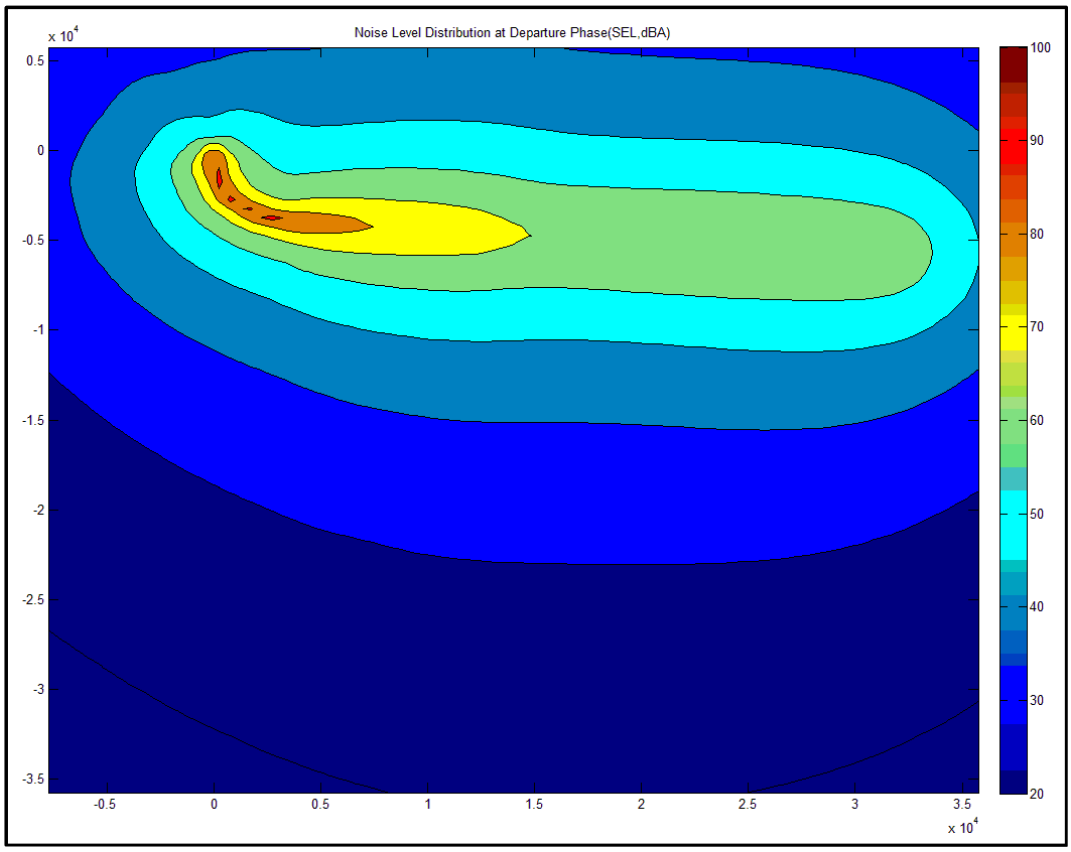

Figure 9-9 (b) Noise-level distribution filled contour of 'Min. Noise Area Mode' (CUTFDAC-Departure)

Table 9-6 Parameter segment distributions of 'Min. Fuel Mode' (part)

Segment	Fn	TET	EINOx	Fuel burnt	Flight time	CO_2 emission	H_2O emission	NOx emission
	(N)	(K)	(g/kg fuel)	(kg)	(s)	(g)	(g)	(g)
1	80008.72	1417.75	19.77	20.80	10.68	65647.03	25751.36	411.12
2	46250.44	1261.88	14.63	54.07	43.75	170672.39	66949.64	791.20
3	25344.89	1140.63	10.89	64.71	78.58	204251.32	80121.65	704.93
4	20350.60	1109.34	9.93	53.90	73.67	170143.58	66742.21	535.17
5	55546.55	1347.66	17.85	111.17	71.22	350920.84	137655.69	1984.54

Table 9-7 Parameter segment distributions of 'Min. Noise Area Mode' (part)

Segment	Fn	TET	EINOx	Fuel burnt	Flight time	CO_2 emission	H_2O emission	NOx emission
	(N)	(K)	(g/kg fuel)	(kg)	(s)	(g)	(g)	(g)
1	55419.23	1288.74	15.34	15.41	11.53	48642.25	19080.89	236.32
2	49936.01	1275.53	15.02	60.08	46.73	189642.17	74390.92	902.41
3	51367.47	1313.16	16.55	108.43	76.52	342254.54	134256.16	1794.79
4	36320.47	1226.64	13.60	79.94	76.67	252318.04	98976.77	1087.19
5	36719.36	1232.59	13.78	79.22	75.39	250055.08	98089.08	1091.36

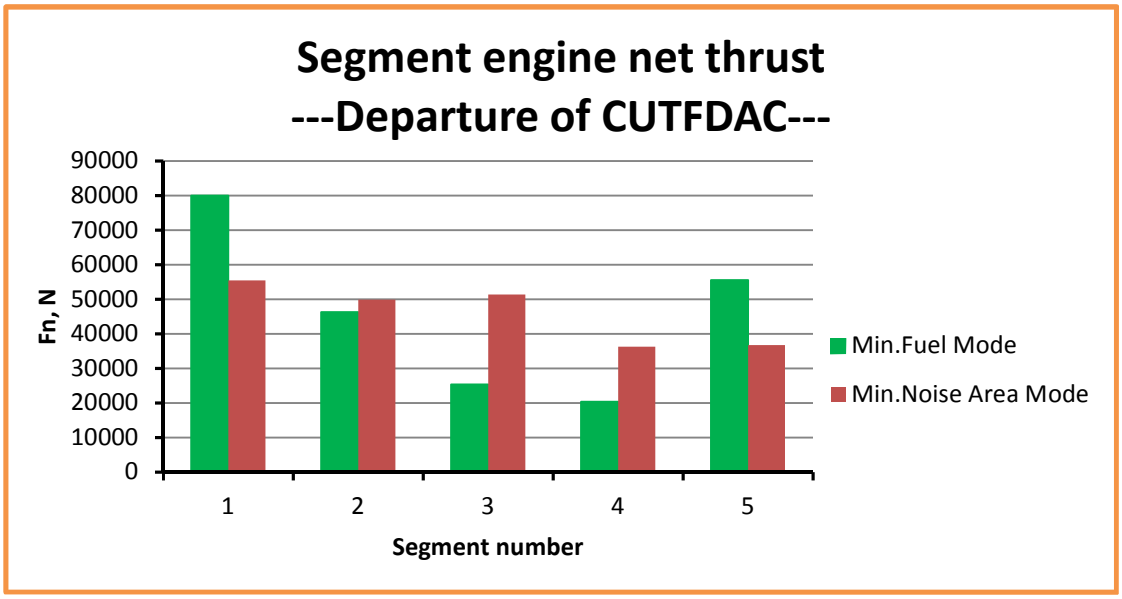

Figure 9-10 Segment engine net thrust (CUTFDAC-Departure)

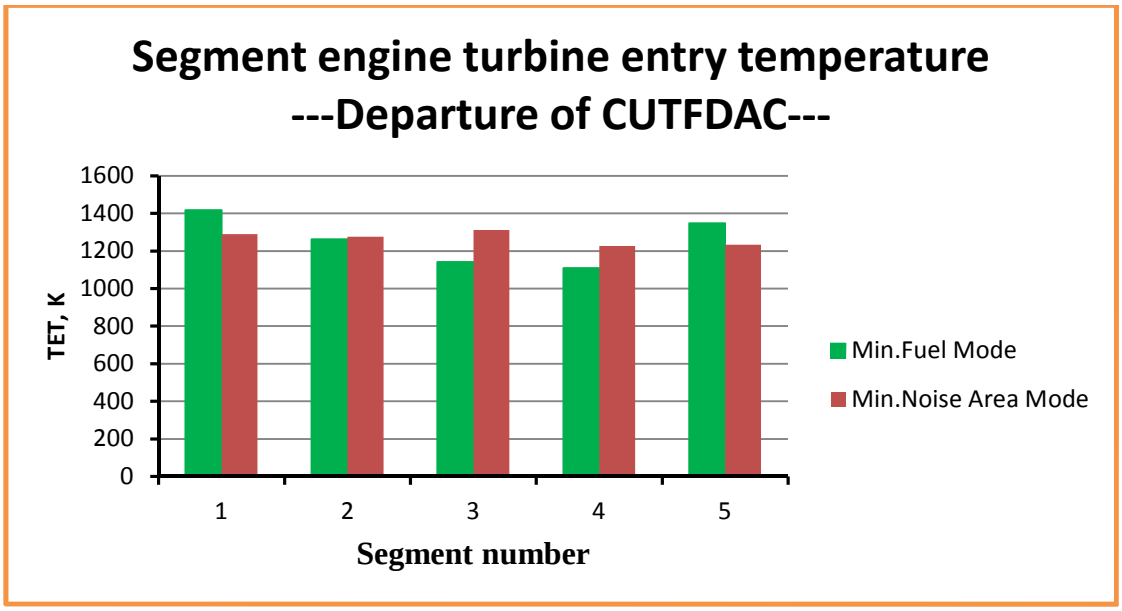

Figure 9-11 Segment engine turbine entry temperature (CUTFDAC-Departure)

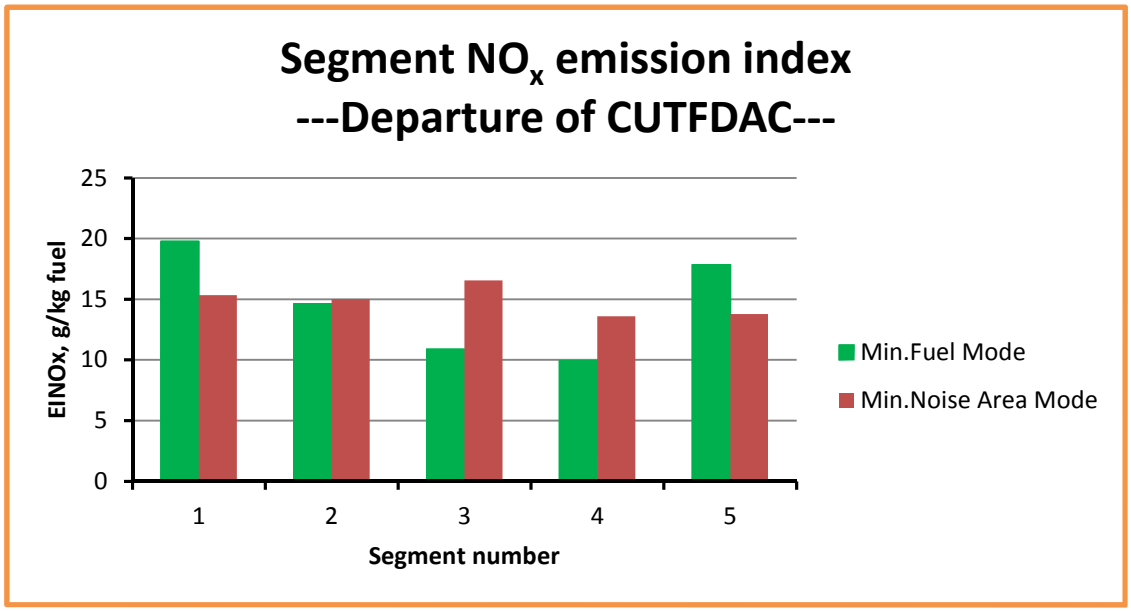

Figure 9-12 Segment NOx emission index (CUTFDAC-Departure)

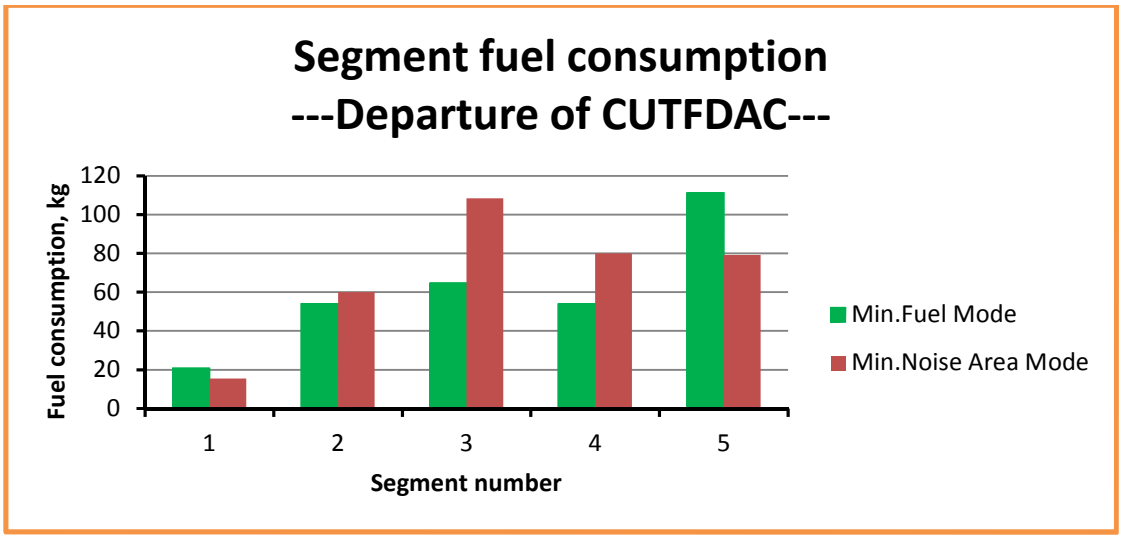

Figure 9-13 Segment fuel consumption (CUTFDAC-Departure)

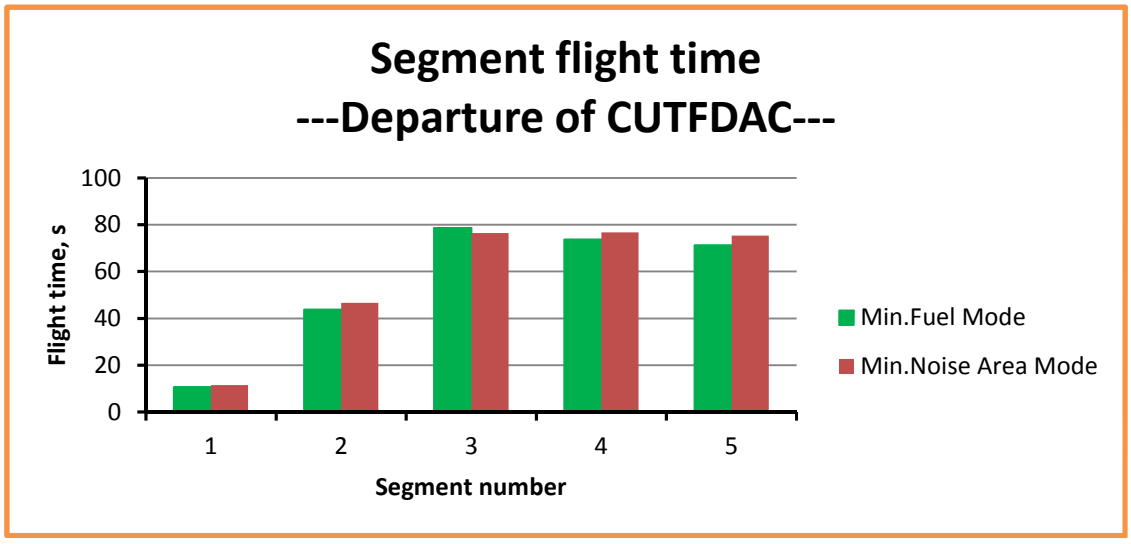

Figure 9-14 Segment flight time (CUTFDAC-Departure)

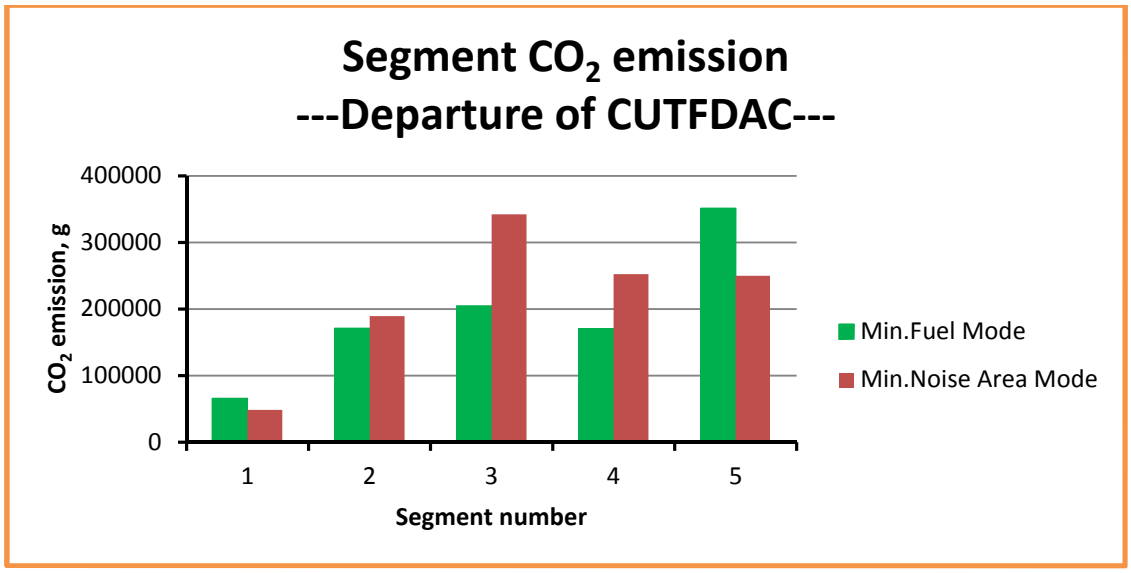

Figure 9-15 Segment CO_2 emission (CUTFDAC-Departure)

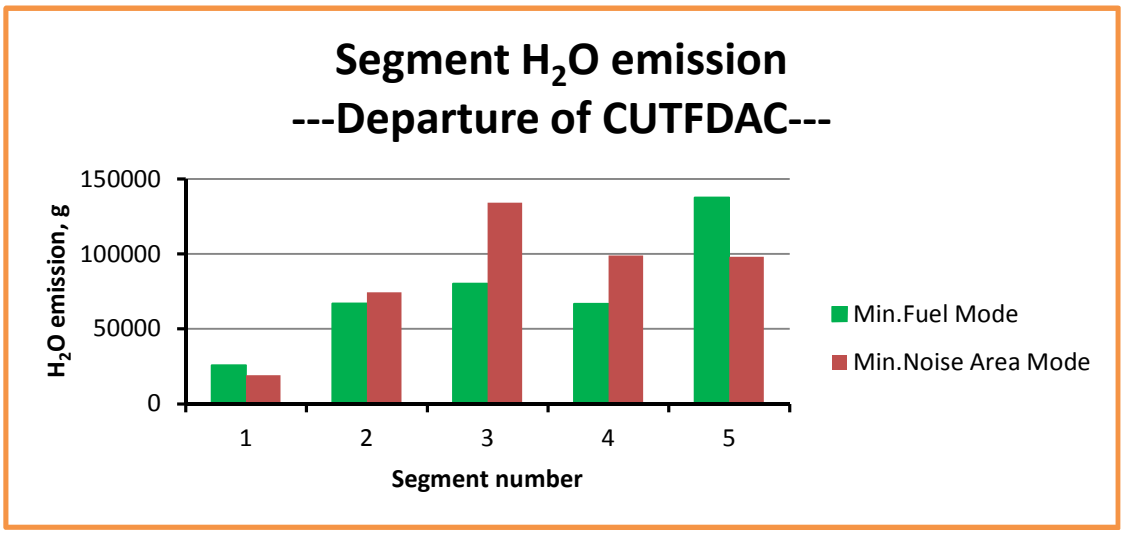

Figure 9-16 Segment H_2O emission (CUTFDAC-Departure)

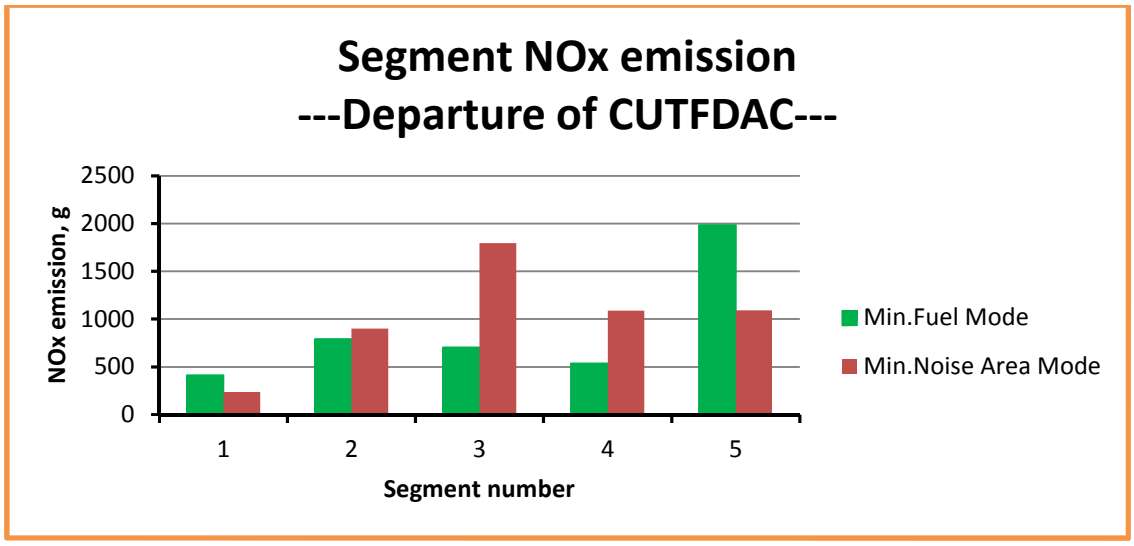

Figure 9-17 Segment NO_x emission (CUTFDAC-Departure)

Table 9-5 and Figures 9-7 to 9-9 provide a comprehensive comparison between the two 'extreme' flight modes/trajectories ('min. fuel consumption' flight mode and 'min. noise area' flight mode) for this departure phase of CUTFDAC respectively from fuel consumption, noise contour area and noise-level distribution, flight time and gaseous emissions based on the results from 'min. fuel consumption' flight mode as the reference. From the table and figures, it can be found that when CUTFDAC flies in the 'min. noise area' mode, the noise-impact area (namely, that area within which values of SEL are not less than 70 dBA) is 41983500 m^2 (i.e., around 42 km^2), and a significant reduction when compared to the noise area (66716700 m^2, i.e., around 67 km^2) resulted from 'min. fuel consumption' flight mode is achieved with the absolute decrease 24733200 m^2 (i.e., around 25 km^2) and relative decrease 37%. Certainly, the gain cannot be achieved for free. As a matter of fact, compared to 'min. fuel consumption' flight mode, 'min. noise area' flight mode does consume more fuel (38.42 kg, 12.6%) and produce more gaseous emissions. For instance, the emissions of CO_2 and H_2O will increase 121280 g (i.e., around 121 kg) and 47573 g (i.e., around 48 kg) respectively, amounting to 12.6% which is the same as the previous the relative change in fuel consumption (since emission index of CO_2 and H_2O are kept constant respectively during combustor combustion, therefore, the relative changes in CO_2 and H_2O emissions only depend on and equal to the relative change in fuel consumption), besides, NOx emission, compared to the 'min. fuel consumption' flight mode, also increases 685 g, amounting to 15.48% and the increase can be attributed to higher value

of NOx emission index (because of higher average engine operation temperature – TET=1267.33 K, while average TET=1255.45 K for the ‘min. fuel consumption’ flight mode. These can be obtained from the distributions of engine TET and NOx emission index along the flight segments provided in Tables 9-6 and 9-7 or Figures 9-11 and 9-12) and more fuel consumption from the ‘min. noise area’ flight mode, but the latter one is main contributor. From the above comparisons between two different flight modes, it can be observed that the two modes are indeed of their own characteristics (or advantages and disadvantages): the ‘min. fuel consumption’ flight mode costs less fuel and simultaneously produces less gaseous emissions but more significant noise impact (i.e., increased noise contour area), while the ‘min. noise area’ flight mode is just at the opposite position. These differences in the characteristics indicate that the two flight modes can be applied to different situations. For example, for daytime departure flights of aircraft or/and departure flights from airports which are away from populated areas, the noise impact is not a prime issue and therefore the ‘min. fuel consumption’ flight mode will be a good option, while on the other hand, if departure flights take place at night or/and aircraft depart from airports very close to densely-populated communities, noise impact will be of main concern doubtlessly, and in this situation, the ‘min. noise area’ flight mode can be adopted.

9.1.2 CUTPDAC (Cranfield University Turboprop-Driven Aircraft)

Table 9-8 Running record of CUTPDAC-Departure optimisation

1	Running start time/date	Sat Oct 27 19:12:42 BST 2012
2	Running end time/date	Mon Oct 29 17:36:44 GMT 2012
3	Total running time	46 hours 24 minutes 2 seconds
4	Generation number	400
5	Total number of evaluations	64759

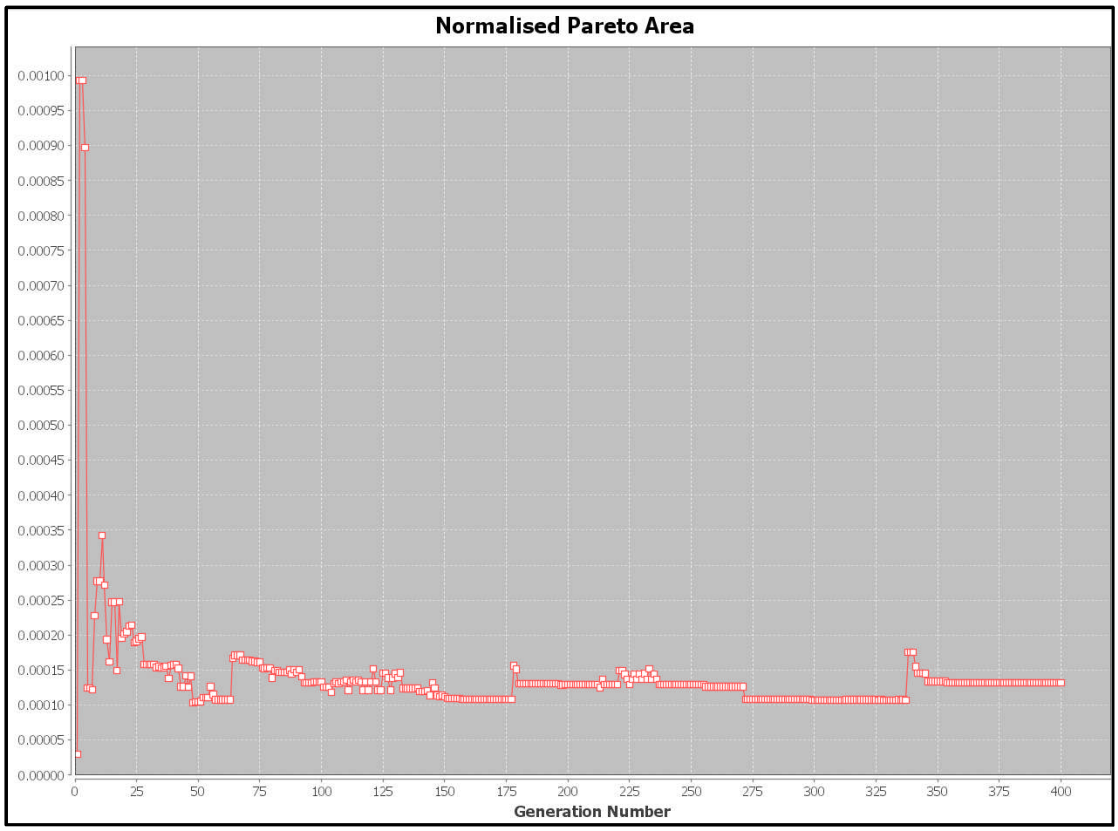

Figure 9-18 Normalised Pareto Area (CUTPDAC-Departure)

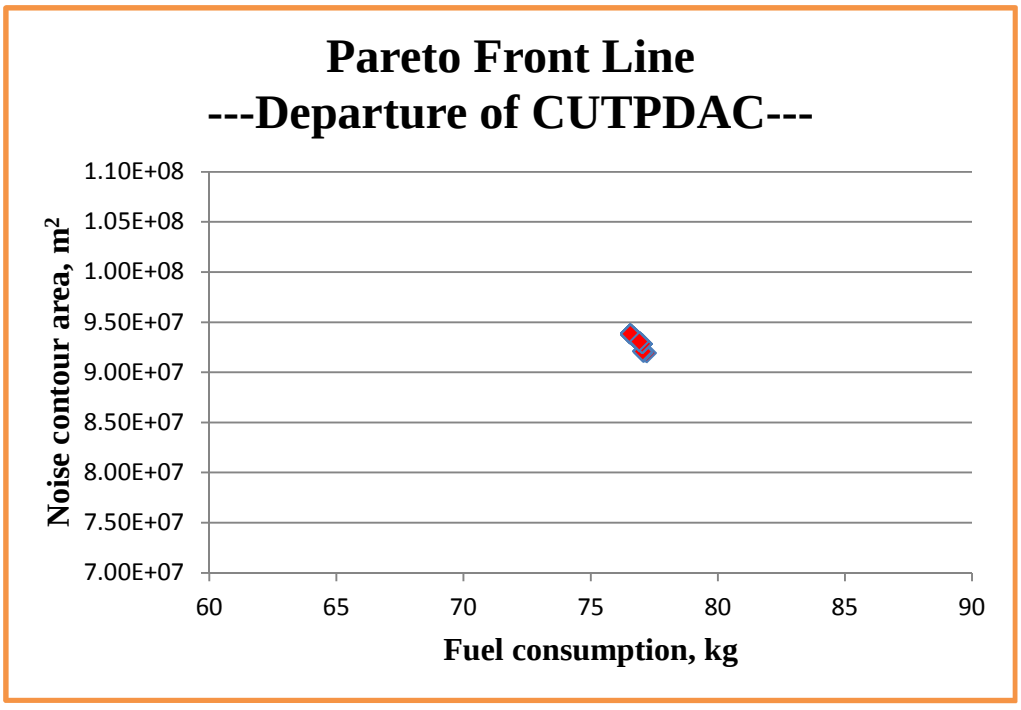

Figure 9-19 Pareto Front Line (CUTPDAC-Departure)

Table 9-9 'Consistency' analysis of optimum solutions (CUTPDAC-Departure)

	Fuel consumption, kg	**Noise contour area, m^2**
Maximum value	77.20	93831700
Minimum value	76.56	91901100
Average value	76.76	93332546.67
Maximum relative deviation	0.84%	2.07%

Table 9-10 Optimised results of two extreme flight trajectories (CUTPDAC-Departure)

		Minimum Fuel Flight Mode	**Minimum Noise Area Flight Mode**	**Δ**	**δ**
Design variables	ALT2, (m)	152.21	152.14	-0.07	-0.05%
	ALT3, (m)	152.23	152.23	0	0
	ALT4, (m)	152.83	152.83	0	0
	SPD1, (CAS, m/s)	65.07	70.42	5.35	8.22%
	SPD2, (CAS, m/s)	113.19	113.14	-0.05	-0.04%
	SPD3, (CAS, m/s)	108.61	119.86	11.26	10.36%
	SPD4, (CAS, m/s)	128.49	128.57	0.08	0.06%

Objective functions	Fuel consumption, (kg)	76.56	77.20	0.64	0.84%
	Noise area,(m^2)	93831700	91901100	-1930600	-2.06%
Optimisation constraints	CA32, (m)	0.0234	0.0948	-	-
	CA43, (m)	0.5981	0.5981	-	-

Table 9-11 Flight trajectory of 'Min. Fuel Mode' (CUTPDAC-Departure)

points	X, m	Z, m	CAS, m/s	FPA, rad
1	0	11.6	80	0
2	1000	152	65.07	0.1395
3	5750	152.21	113.19	4.40E-05
4	15483.33	152.23	108.61	2.00E-06
5	25216.67	152.83	128.49	6.10E-05
6	34950	1828.8	128.61	0.1705

Table 9-12 Flight trajectory of 'Min. Noise Area' Mode (CUTPDAC-Departure)

points	X, m	Z, m	CAS, m/s	FPA, rad
1	0	11.6	80	0
2	1000	152	70.42	0.1395
3	5750	152.14	113.14	2.90E-05
4	15483.33	152.23	119.86	1.00E-05
5	25216.67	152.83	128.57	6.10E-05
6	34950	1828.8	128.61	0.1705

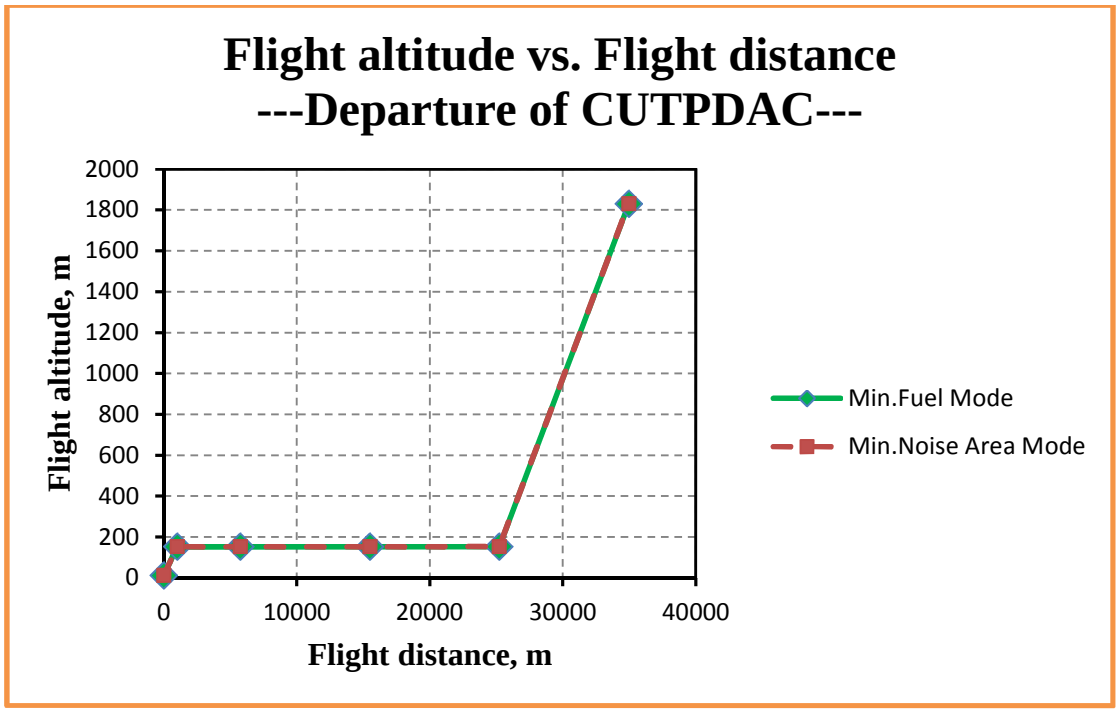

Figure 9-20 Comparison of two extreme flight trajectories (CUTPDAC-Departure) (Flight altitude vs. Flight distance)

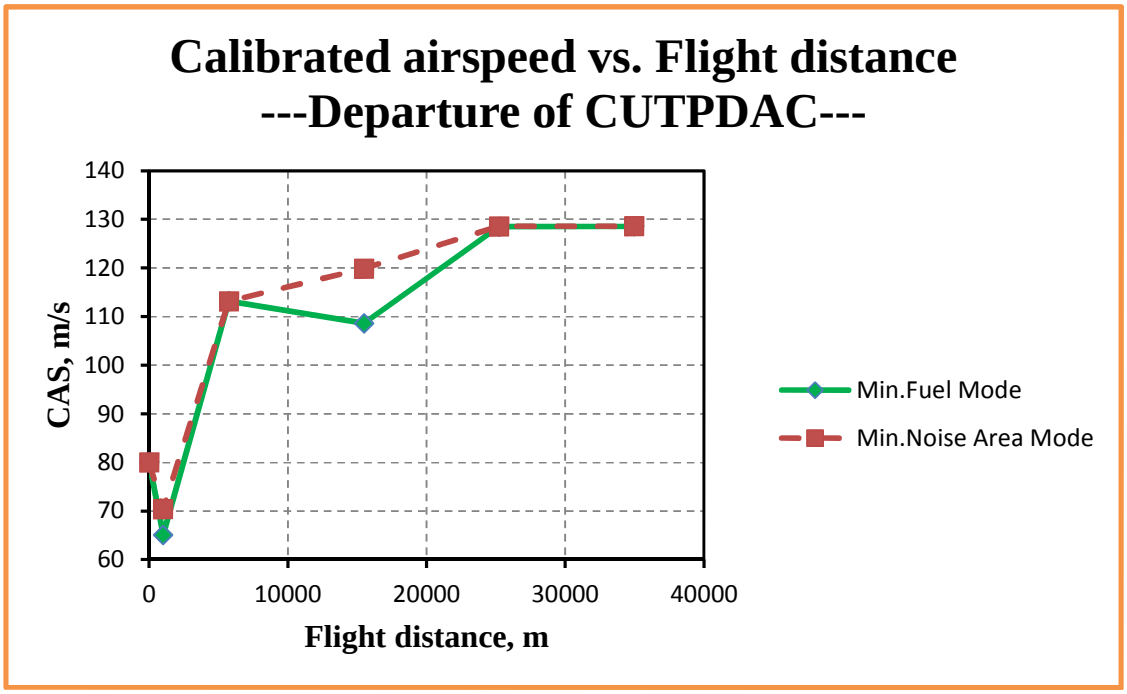

Figure 9-21 Comparison of two extreme flight trajectories (CUTPDAC-Departure) (Calibrated airspeed vs. Flight distance)

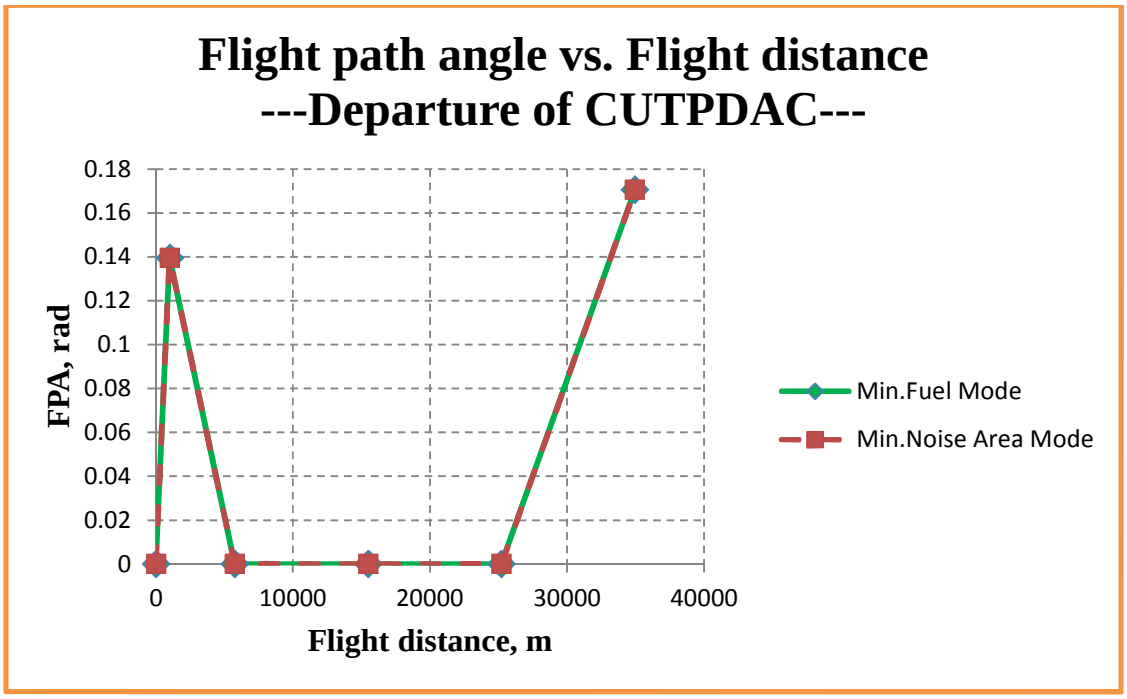

Figure 9-22 Comparison of two extreme flight trajectories (CUTPDAC-Departure) (Flight path angle vs. Flight distance)

Table 9-13 Optimised results of 'average' flight trajectory (CUTPDAC-Departure)

		'Average' flight trajectory
Design variables	ALT2, (m)	152.09
	ALT3, (m)	152.28
	ALT4, (m)	152.72
	SPD1, (CAS, m/s)	66.54
	SPD2, (CAS, m/s)	113.08
	SPD3, (CAS, m/s)	116.13
	SPD4, (CAS, m/s)	128.57

Objective functions	Fuel consumption, (kg)	76.92
	Noise area, (m^2)	93037000
Optimisation constraints	CA32, (m)	0.1925
	CA43, (m)	0.4341

Table 9-14 'Average' flight trajectory (CUTPDAC-Departure)

Points	X, m	Z, m	CAS, m/s	TAS, m/s	FPA, rad.
1	0	11.6	80	80.60	0
2	1000	152	66.54	67.35	0.1395
3	5750	152.09	113.08	115.49	1.90E-05
4	15483.33	152.28	116.13	118.69	2.00E-05
5	25216.67	152.72	128.57	131.84	4.50E-05
6	34950	1828.8	128.61	143.20	0.1705

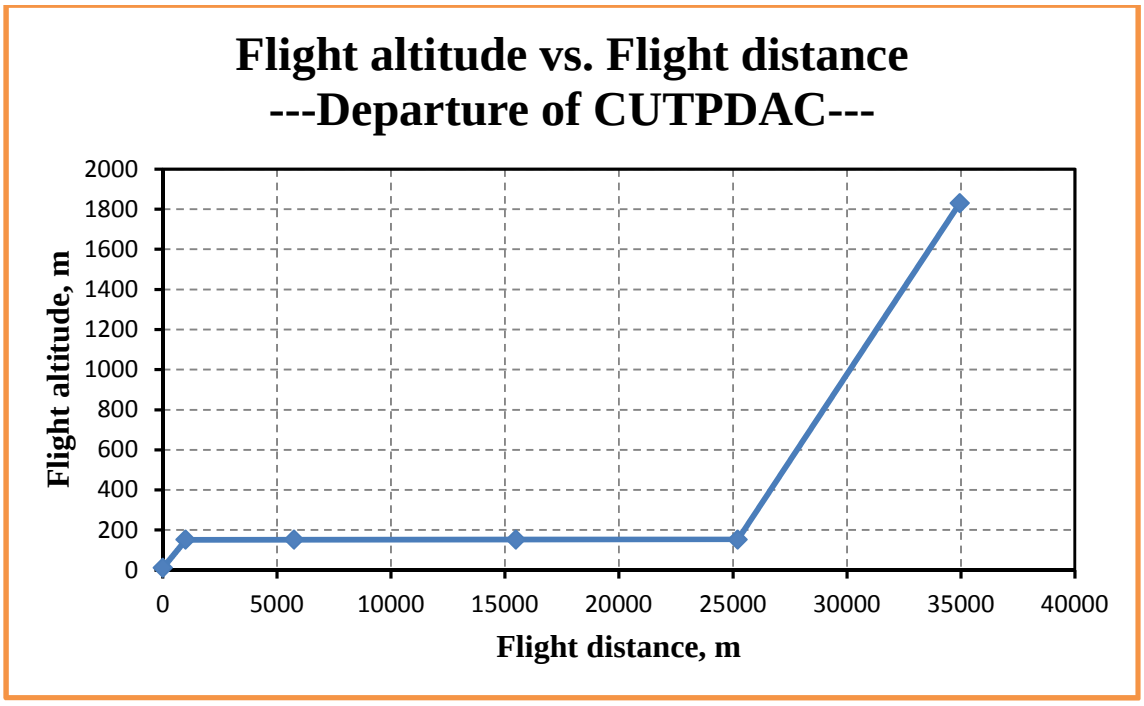

Figure 9-23 Flight altitude vs. Flight distance (CUTPDAC-Departure)

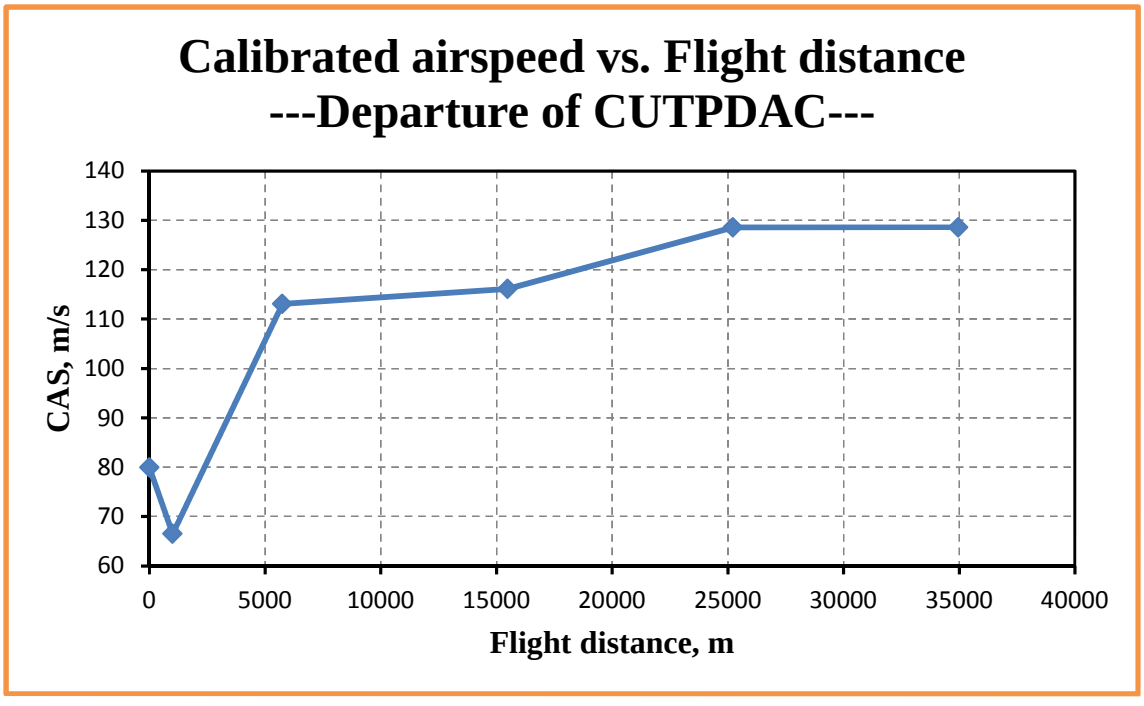

Figure 9-24 Calibrated airspeed vs. Flight distance (CUTPDAC-Departure)

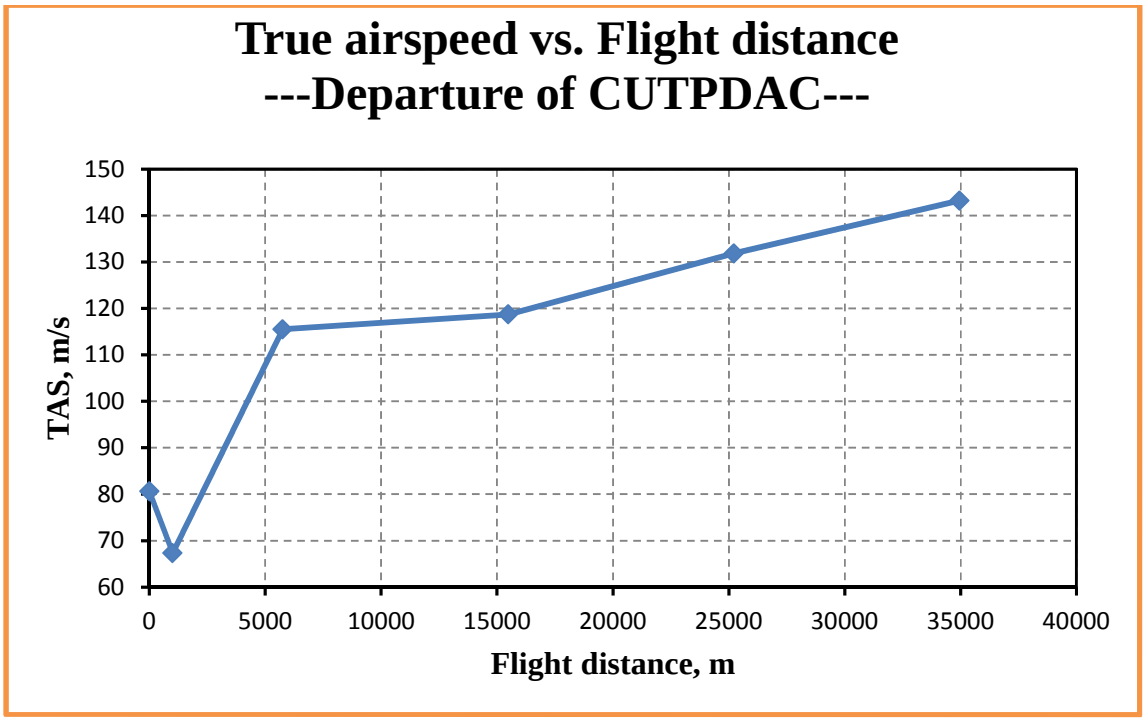

Figure 9-25 True airspeed vs. Flight distance (CUTPDAC-Departure)

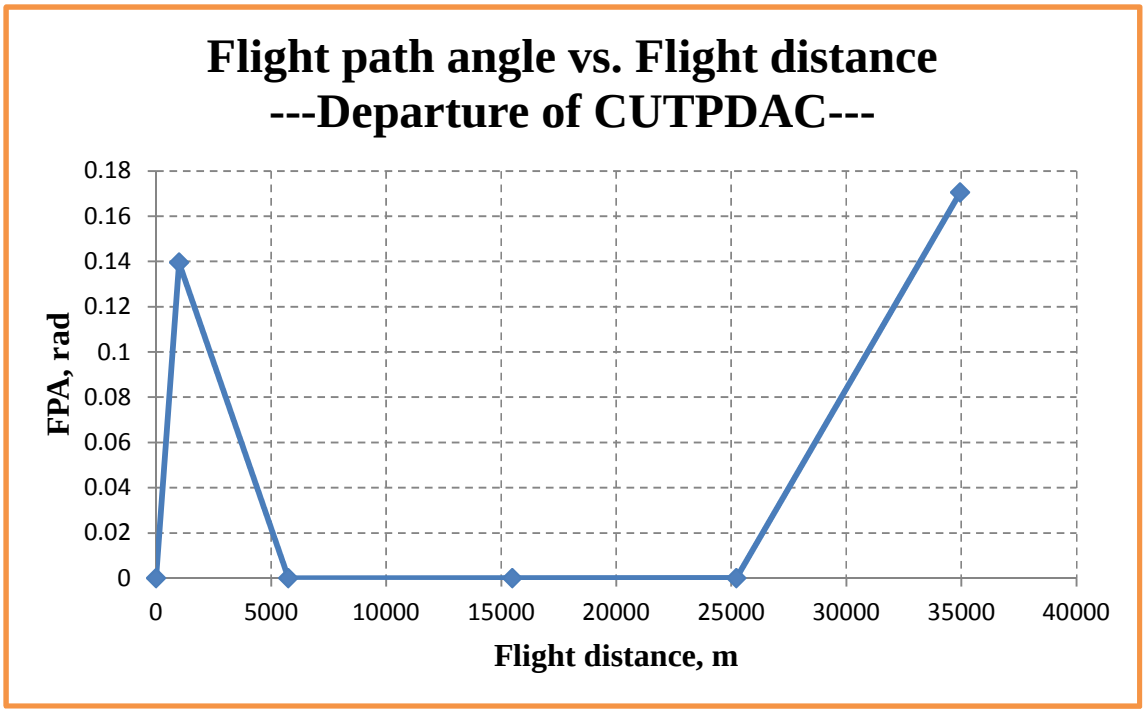

Figure 9-26 Flight path angle vs. Flight distance (CUTPDAC-Departure)

Table 9-15 Overall performance of 'average' flight trajectory (CUTPDAC-Departure)

Fuel burnt	Noise area	Flight time	CO_2	H_2O	NO_x
(kg)	(m^2)	(s)	(g)	(g)	(g)
76.92	93037000	297.86	247152.2	95892.01	374.57

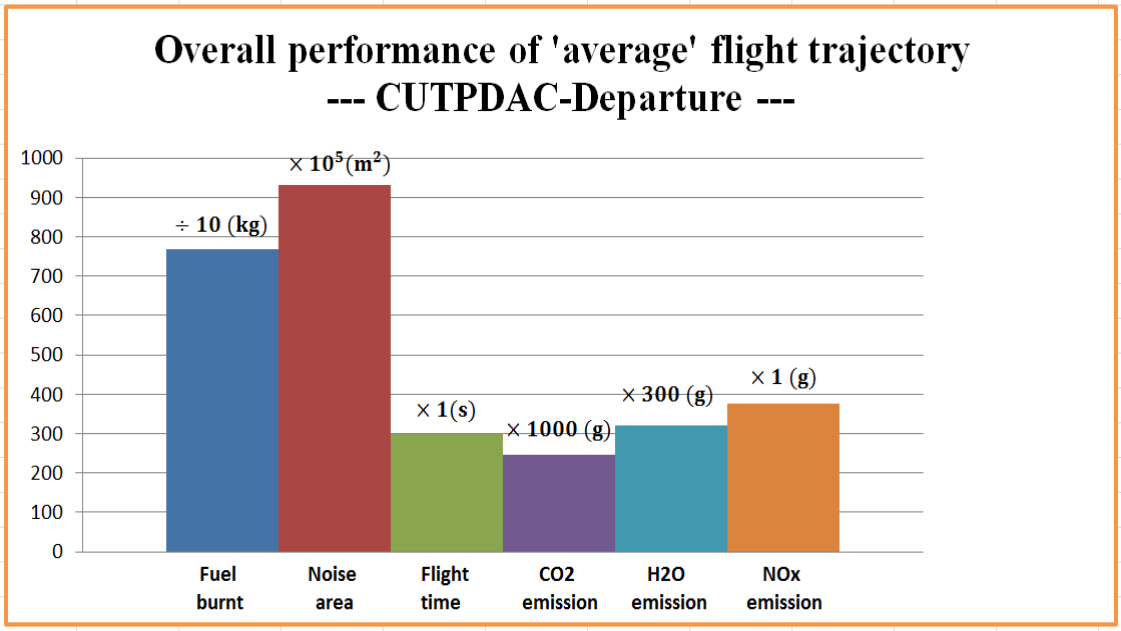

Figure 9-27 Overall performance of 'average' flight trajectory (CUTPDAC-Departure)

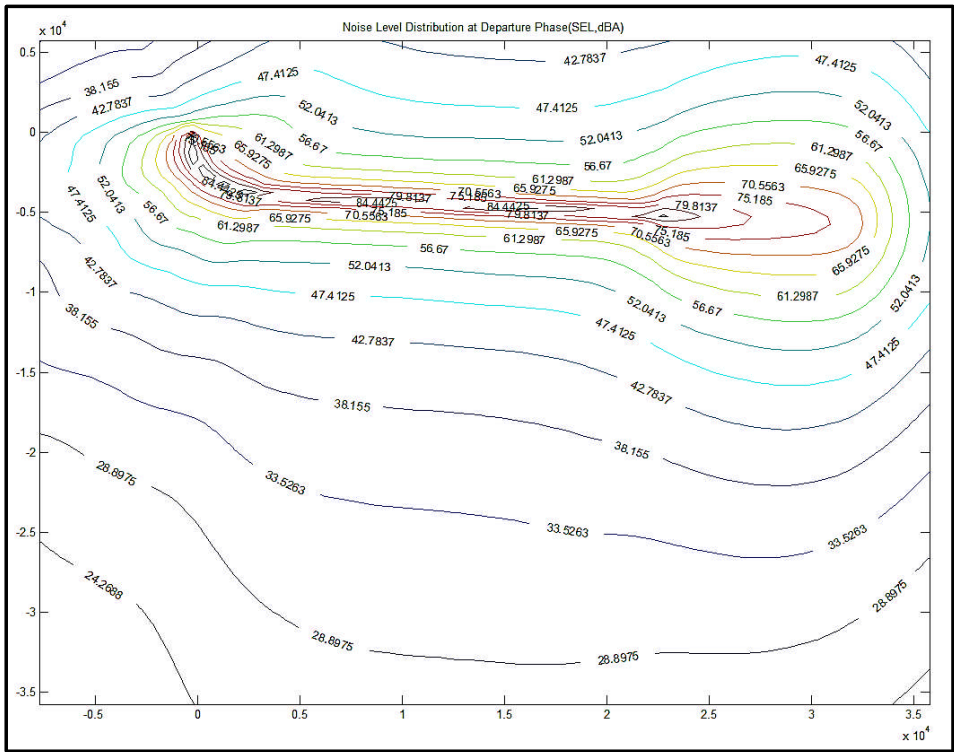

Figure 9-28 (a) Noise-level distribution contour of 'average' flight trajectory (CUTPDAC-Departure)

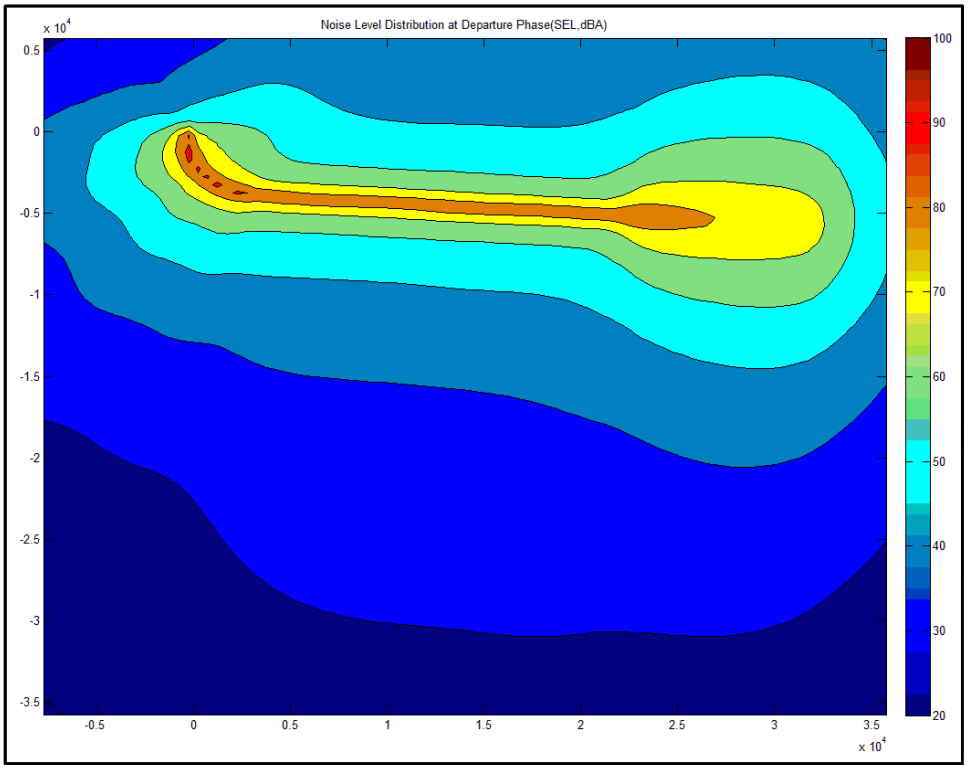

Figure 9-28 (b) Noise-level distribution filled contour of 'average' flight trajectory (CUTPDAC-Departure)

Table 9-16 Parameter segment distributions of 'average' flight trajectory (part) (CUTPDAC-Departure)

Segment	Fn	TET	EINOx	Fuel burnt	Flight time	CO_2 emission	H_2O emission	NOx emission
	(N)	(K)	(g/kg fuel)	(kg)	(s)	(g)	(g)	(g)
1	7380.00	1019.78	2.57	2.46	13.58	7914.01	3063.64	6.32
2	15401.27	1151.35	4.04	14.14	52.15	45366.32	17606.09	57.10
3	6837.72	1027.97	2.76	15.73	83.13	50676.11	19619.24	43.42
4	8187.88	1073.27	3.20	16.99	77.70	54705.88	21200.19	54.40
5	18402.91	1300.67	7.73	27.60	71.31	88489.88	34402.85	213.33

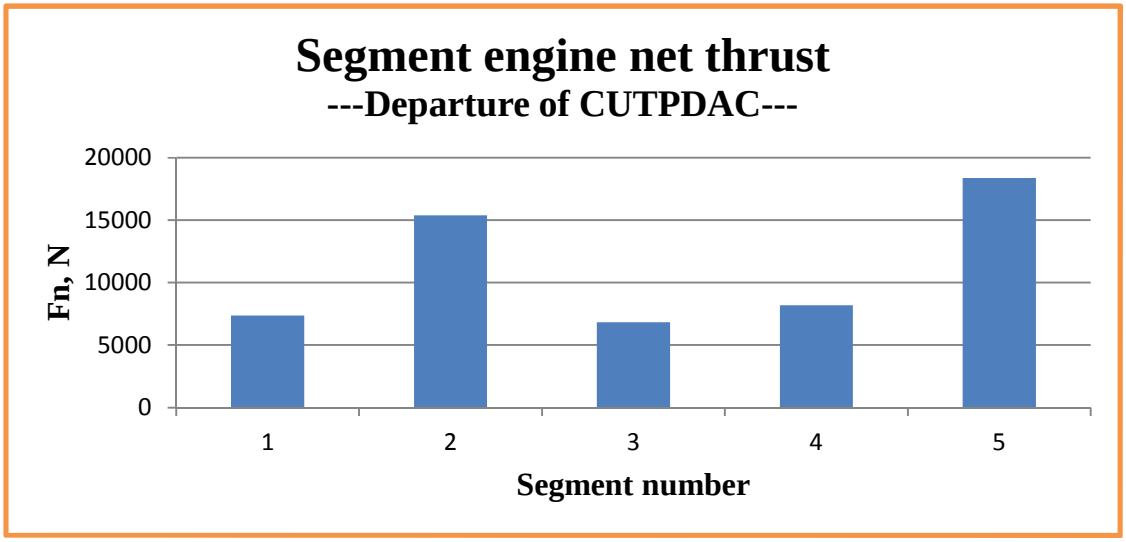

Figure 9-29 Segment engine net thrust (CUTPDAC-Departure)

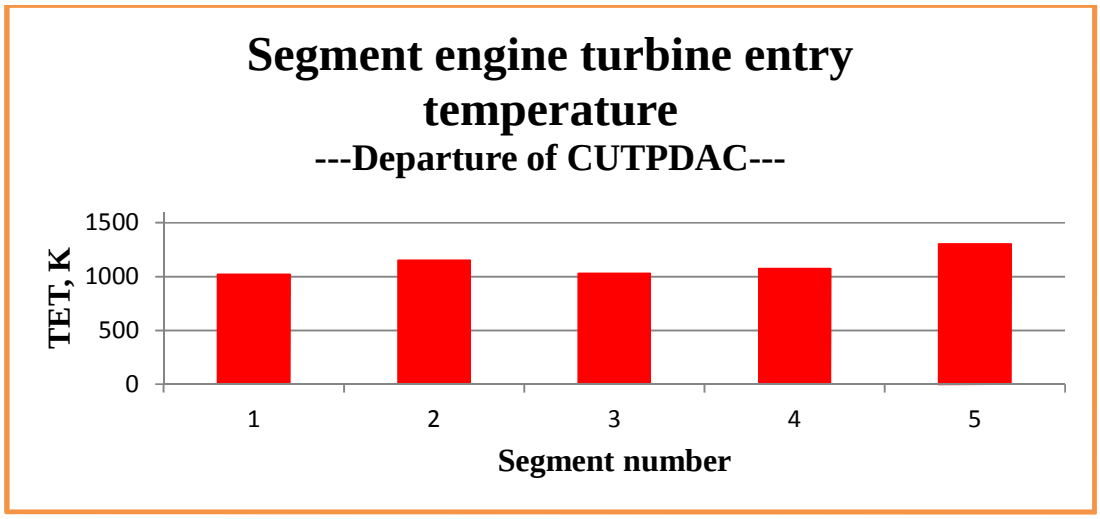

Figure 9-30 Segment engine turbine entry temperature (CUTPDAC-Departure)

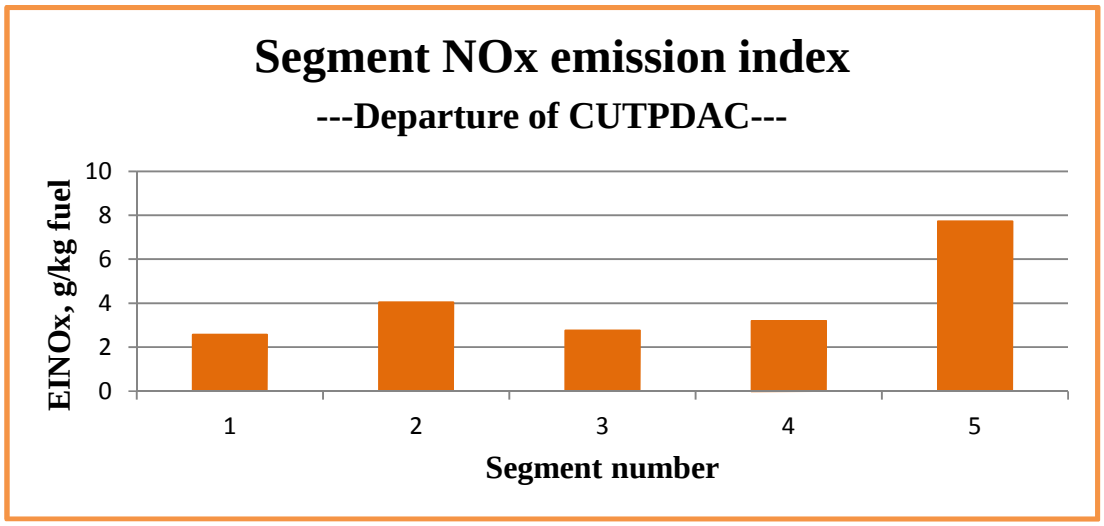

Figure 9-31 Segment NOx emission index (CUTPDAC-Departure)

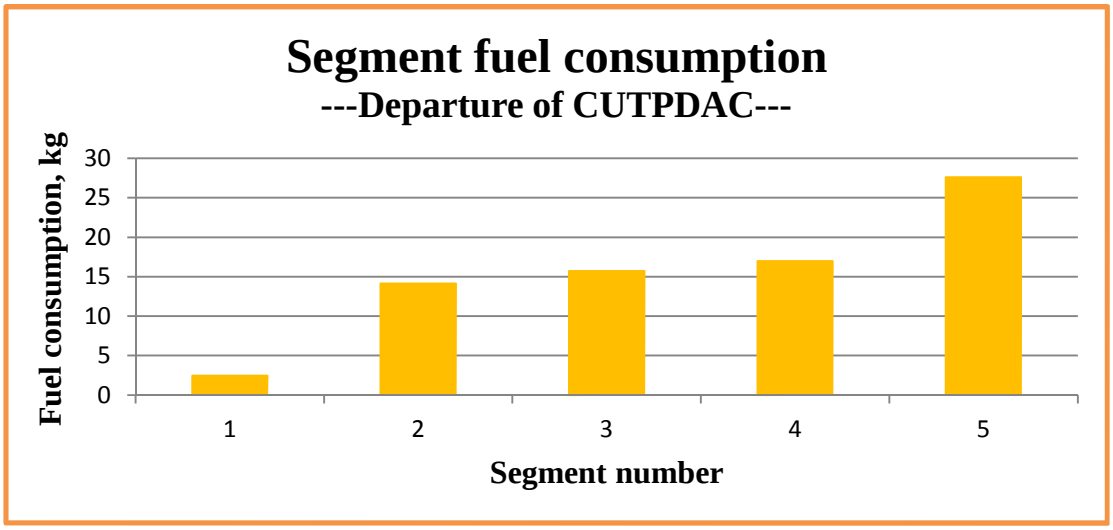

Figure 9-32 Segment fuel consumption (CUTPDAC-Departure)

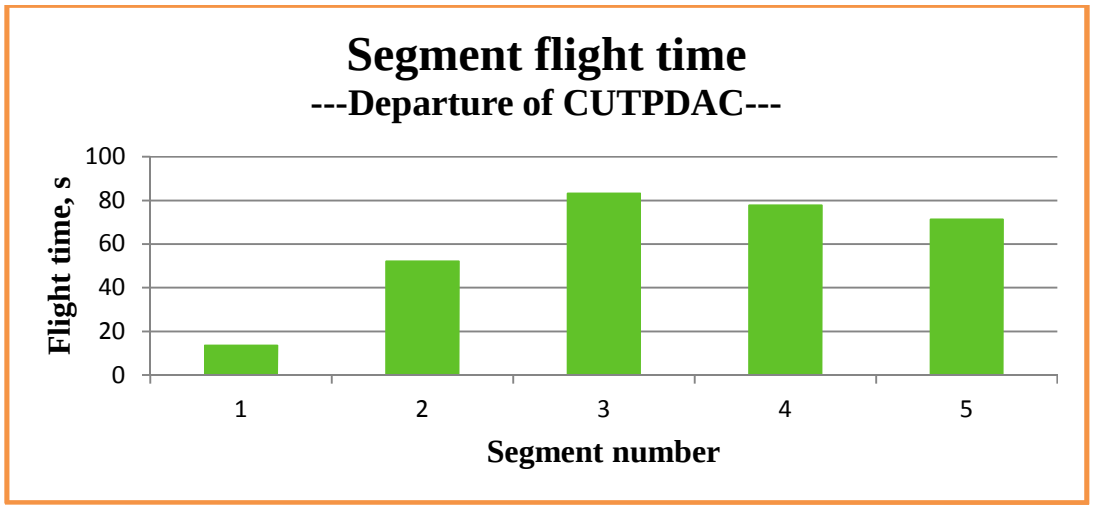

Figure 9-33 Segment flight time (CUTPDAC-Departure)

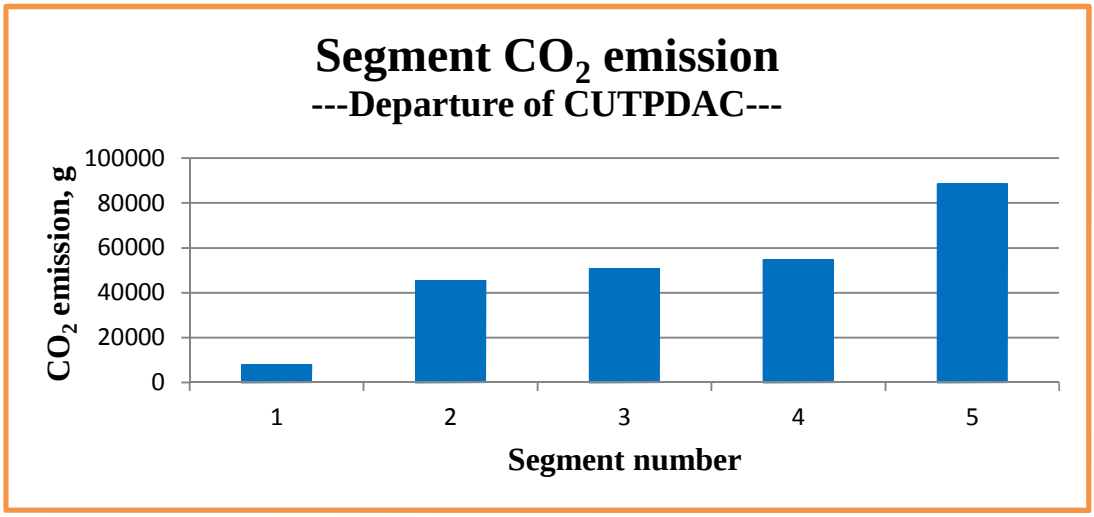

Figure 9-34 Segment CO_2 emission (CUTPDAC-Departure)

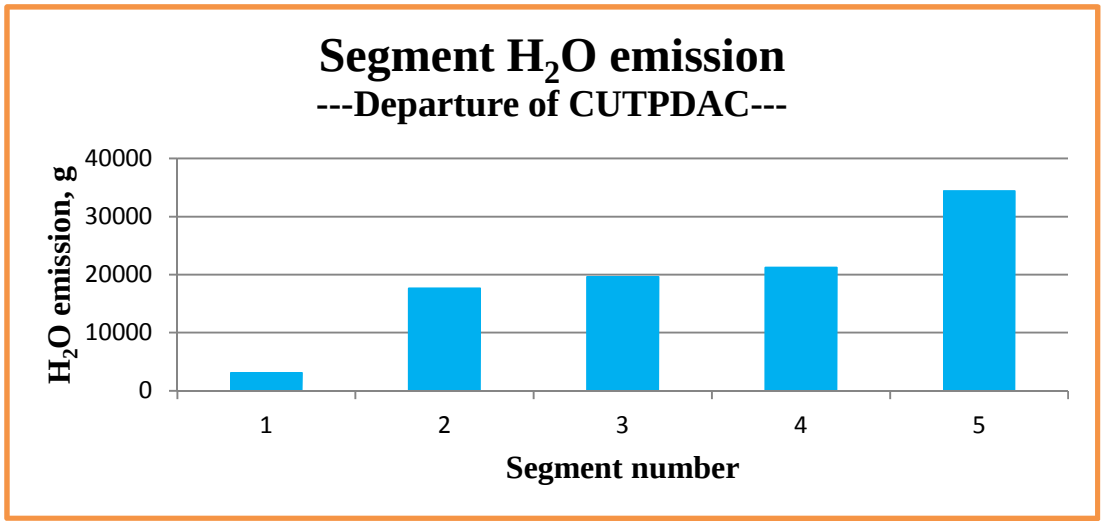

Figure 9-35 Segment H_2O emission (CUTPDAC-Departure)

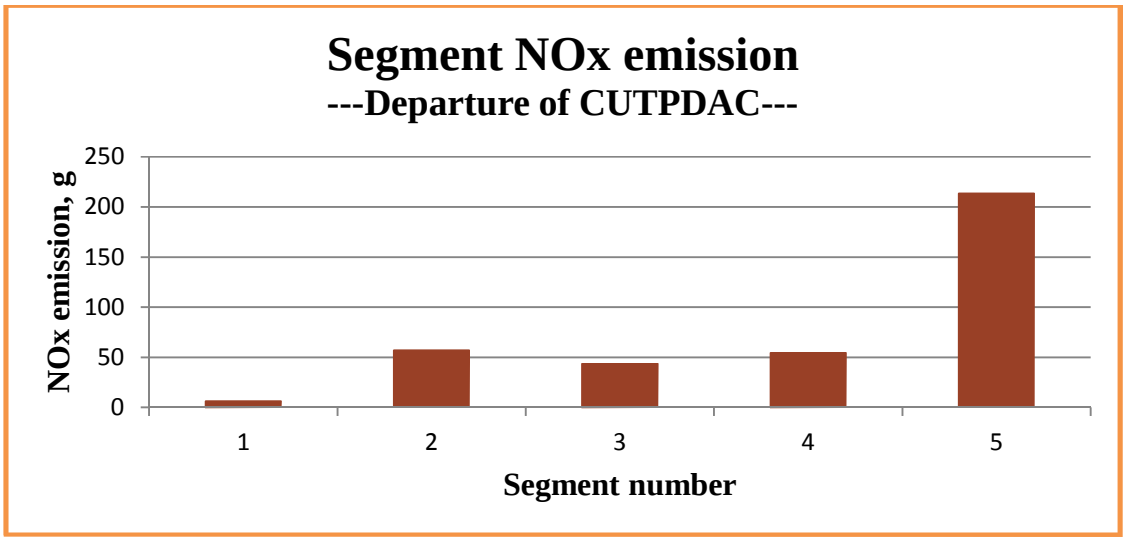

Figure 9-36 Segment NOx emission (CUTPDAC-Departure)

As for the departure flight of CUTPDAC, correspondingly, the following points can be summarised:

1) From the plot of normalised Pareto area shown in the Figure 9-18, it can be preliminarily concluded that the convergence of this optimisation process has basically been achieved.
2) Different from the departure flights respectively by CUTFDAC which has been analysed in the previous section, and CUPFDAC which will be discussed in the next section, the optimised results achieved for the departure flight of CUTPDAC are very 'close' to each other. This is clearly shown in Figure 9-19. Table 9-9 quantitatively describes this type of 'close' among all these optimum solutions. According to Table 9-9, among a total of 150 optimum solutions, maximum value of fuel consumption is 77.20 kg, and the minimum value is 76.56 kg, so the maximum relative deviation which is defined as '(max.-min.)/average' is only 0.84%, on the other hand, for the noise contour area, the maximum value equals to 93831700 m^2 and the minimum value is 91901100 m^2, therefore, the maximum relative deviation is 2.07%. The two deviation values are very small when compared to the magnitude levels provided respectively by CUTFDAC and CUPFDAC (according to the calculations, the max. relative deviations of fuel consumption and noise contour area from CUTFDAC are respectively 12% and 46%, and for CUPFDAC, the two maximum values are 12.6% and 28% respectively). Tables 9-10 to 9-12 and

Figures 9-20 to 9-22 provide the further comparisons between two extreme points among 150 optimum solutions – 'min. fuel consumption' flight mode and 'min. noise area' flight mode. From these tables and figures, it can be found that two flight trajectories from two different flight modes are very close to each other, especially in terms of the variations of flight altitude and flight path angle along the horizontal flight distance, the two trajectories almost overlap one another. There exist some differences between these two flight modes in terms of flight speed profile, 'min. noise area' mode is of higher flight speeds (CAS) at points 2 and 4 (70.42 m/s and 119.86 m/s respectively) compared to the 'min. fuel consumption' mode (65.07 m/s and 108.61 m/s respectively). Higher flight speed can reduce the flight time during the departure phase, hence the noise exposure time to ground observers, which can reduce the noise contour area correspondingly (according to the calculation, for the departure flight phase, 'min. noise area' mode will take 293.8 seconds which is 10 seconds less when compared to the 'min. fuel consumption' flight mode). However, these differences in the flight speed profile do not bring significant influence on the overall performance of two flight modes in terms of fuel consumption and noise contour area as shown before.

3) The entire optimisation process cost 46 hours 24 minutes 2 seconds with 400 generations or 64759 evaluations (Table 9-8). That is, on average, 417.6 seconds/generation or 2.6 seconds/evaluation.
4) Based on the fact that all achieved optimum solutions are 'close' to each other described in the above item 2), an 'average' solution/point was selected as the representative to describe the optimised flight trajectory of CUTPDAC for the departure flight phase mainly through variations of flight altitude, flight speed and flight path angle along the horizontal flight distance. Tables 9-13 and 9-14, as well as Figures 9-23 to 9-26, provide basic information of this 'average' optimum trajectory. These tables and figures show that when CUTPDAC makes the departure flight, the following trajectory should be followed in order to minimise fuel consumption and noise impact area: firstly for the 1st segment, it can be observed from the achieved optimum trajectory that the aircraft is suggested to fly at a 'decelerated climb' style, namely, flight altitude will

increase from initial 11.6 m to 152 m while the calibrated airspeed dropping from the initial value of 80 m/s to 66.54 m/s (correspondingly, the true airspeed decreasing to 67.35 m/s from the initial 80.60 m/s). This deceleration seems to lack a good reason. As a matter of fact, this deceleration was not desired originally. According to the design of this departure case study, the lower boundary of CAS at point 2 (i.e., the ending point of the segment 1) equals to the CAS value at point 1 (i.e., the starting point of the segment 1) which is a fixed number depending on the initial aircraft mass, wing area and the position of high-lift devices (hence the maximum lift coefficient C_{Lmax}). At the early stage of the case modelling, the CAS value at point 1 was determined as 65 m/s and correspondingly the lower boundary of CAS at point 2 was also set as 65 m/s. Thereafter, the recalculation revised the fixed number to 80 m/s, however, the lower boundary of CAS at point 2 was not updated correspondingly, therefore, the 'decelerated climb' appears in the optimised flight trajectory. However, because of the very short horizontal flight distance covered by segment 1, the influence on the overall optimised results will be very limited. In addition, due to the limitation of research time, the revision and improvement about this problem will be put into future work; segments 2, 3 and 4 will undergo the same flight style – 'level flight and acceleration'. During these 3 flight segments with the total horizontal flight distance ΔX=24217 m, the flight altitude will be always kept at about 152 m, while the calibrated airspeed will witness a continuous increase from 66.54 m/s, 113.08 m/s, 116.13 m/s to 128.57 m/s (correspondingly, the true airspeed will also be increased from 67.35 m/s, 115.49 m/s, 118.69 m/s to 131.84 m/s), and the flight path angle will also correspondingly change from initially around 0.14 rad. to approximately approaching zero; finally, when CUTPDAC enters into the 5^{th} segment, the 'constant-speed (CAS) climb' mode will be adopted, namely, the calibrated airspeed will be kept unchanged (around 128.6 m/s) and the flight altitude will be increased to required 1828.8 m from around 152 m (correspondingly, the true airspeed will also rise from 131.84 m/s to 143.20 m/s), besides, the flight path angle will change from 4.50×10^{-5} rad. to 0.1705 rad. as well.

5) Table 9-15 and Figures 9-27 and 9-28 illustrate the achieved overall performance through the 'average' optimum trajectory flown by CUTPDAC, that is, along this path, CUTPDAC will consume around 77 kg fuel and produce about 247 kg CO_2, 96 kg H_2O and 375 g NOx, besides, noise contour area (with SEL $\geq$ 70 dBA) amounts to around 93 km^2 and the entire departure flight lasts for 5 minutes. The further breakdown of these overall-performance parameters and the distributions of some other parameters along these flight segments can be found in Table 9-16 and Figures 9-29 to 9-36.

9.1.3 CUPFDAC (Cranfield University Propfan-Driven Aircraft)

Table 9-17 Running record of CUPFDAC-Departure optimisation

1	Running start time/date	Thu Nov 15 22:19:37 GMT 2012
2	Running end time/date	Sun Nov 18 06:23:32 GMT 2012
3	Total running time	56 hours 3 minutes 55 seconds
4	Generation number	450
5	Total number of evaluations	72113

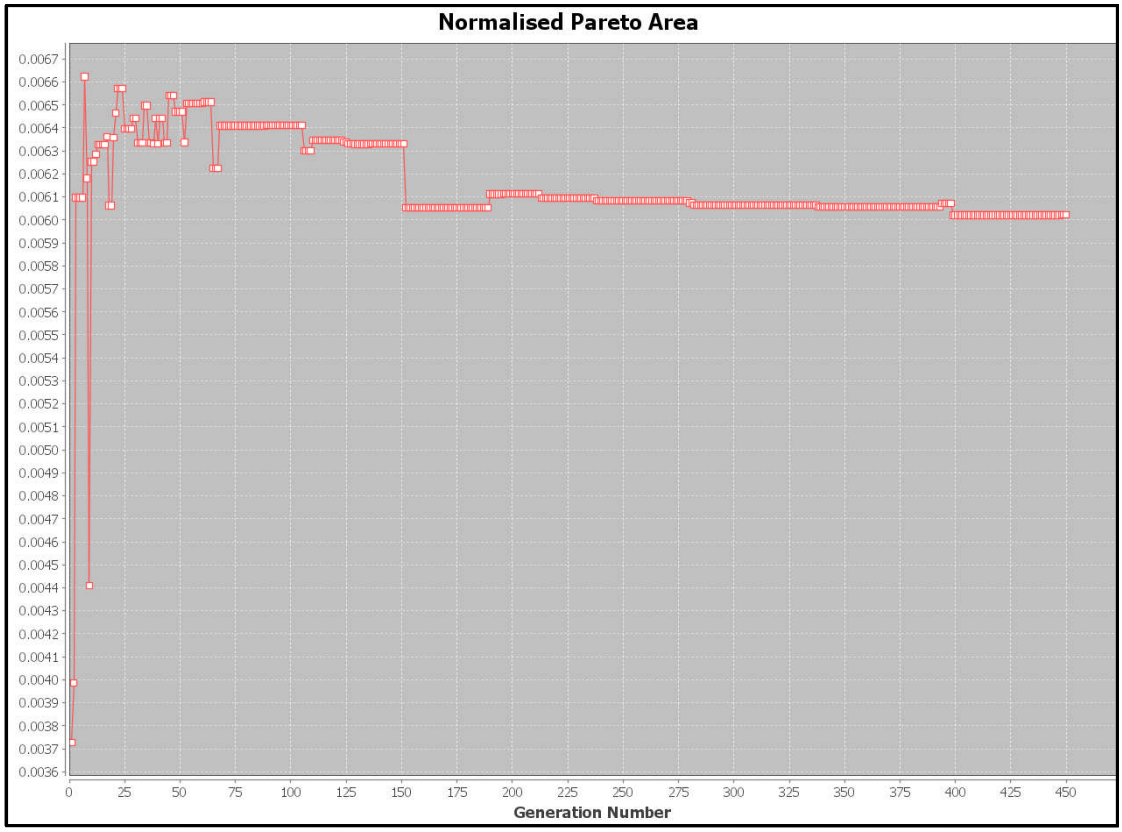

Figure 9-37 Normalised Pareto area (CUPFDAC-Departure)

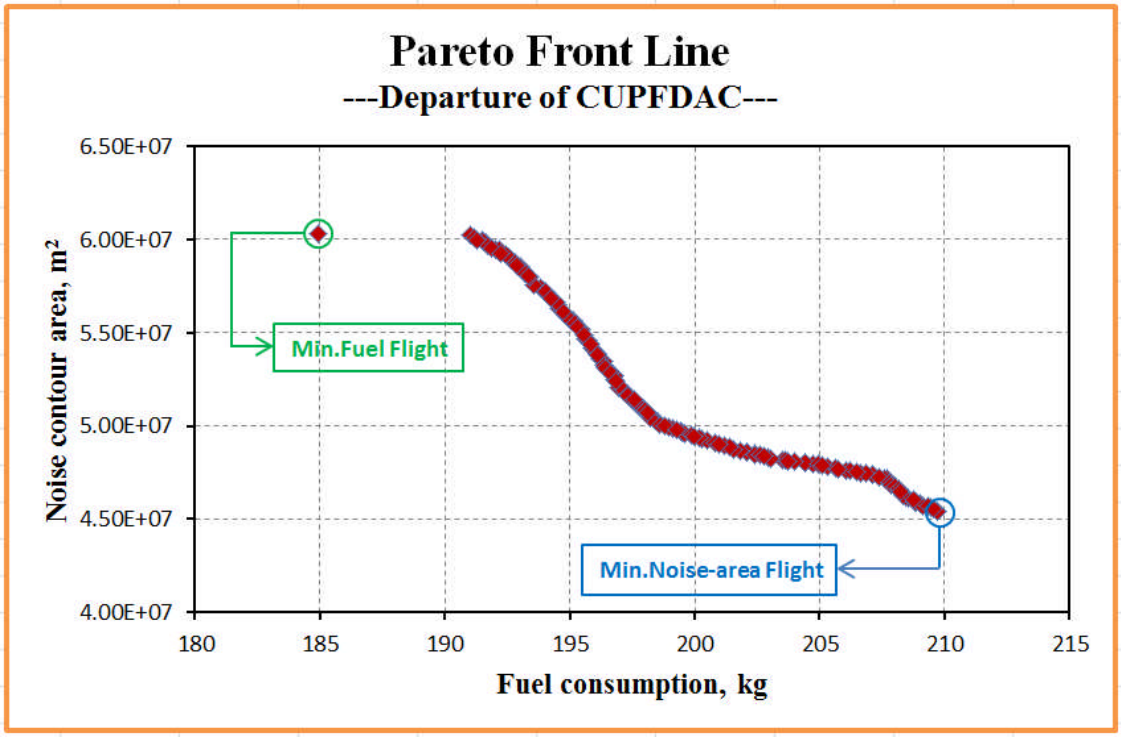

Figure 9-38 Pareto Front Line (CUPFDAC-Departure)

Table 9-18 Optimised results of two typical flight trajectories (CUPFDAC-Departure)

		Minimum Fuel Flight Mode	Minimum Noise Area Flight Mode
Design variables	ALT2, (m)	152.38	292.35
	ALT3, (m)	160.73	1473.10
	ALT4, (m)	161.19	1542.03
	SPD1, (CAS, m/s)	81.20	89.78
	SPD2, (CAS, m/s)	113.15	113.19
	SPD3, (CAS, m/s)	128.39	128.61
	SPD4, (CAS, m/s)	128.60	105.62
Objective functions	Fuel consumption, (kg)	184.94	209.71
	Noise area, (m^2)	60292300	45440000
Optimisation constraints	CA32, (m)	8.35	1180.76
	CA43, (m)	0.45	68.93

Table 9-19 Flight trajectory of 'Min. Fuel Mode' (CUPFDAC-Departure)

points	X, m	Z, m	CAS, m/s	TAS, m/s	FPA, rad.
1	0	11.6	79	79.58	0
2	1000	152	81.20	82.37	0.1395
3	5750	152.38	113.15	115.57	8.10E-05
4	15483.33	160.73	128.39	131.70	8.58E-04

5	25216.67	161.19	128.60	131.92	4.60E-05
6	34950	1828.8	128.61	143.20	0.1697

Table 9-20 Flight trajectory of 'Min. Noise Area Mode' (CUPFDAC-Departure)

points	X, m	Z, m	CAS, m/s	TAS, m/s	FPA, rad.
1	0	11.6	79	79.58	0
2	1000	152	89.78	91.23	0.1395
3	5750	292.35	113.19	116.40	0.0295
4	15483.33	1473.10	128.61	140.68	0.1207
5	25216.67	1542.03	105.62	115.26	0.0071
6	34950	1828.8	128.61	143.20	0.0295

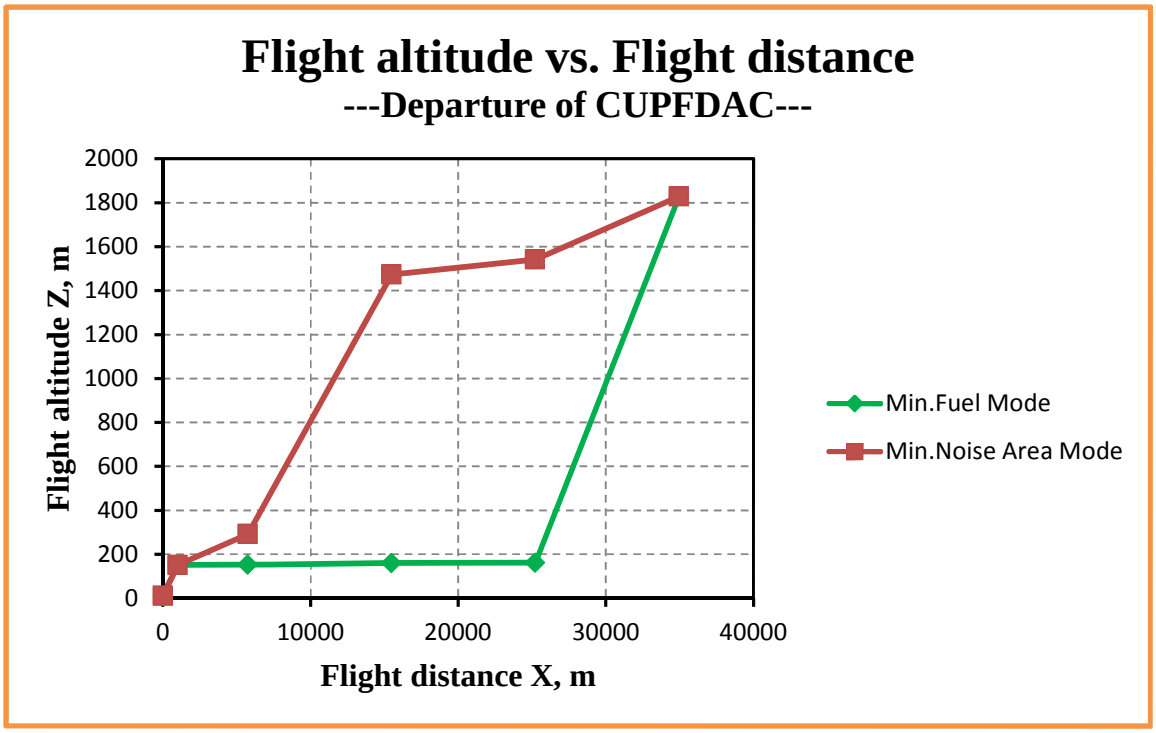

Figure 9-39 Flight altitude vs. Flight distance (CUPFDAC-Departure)

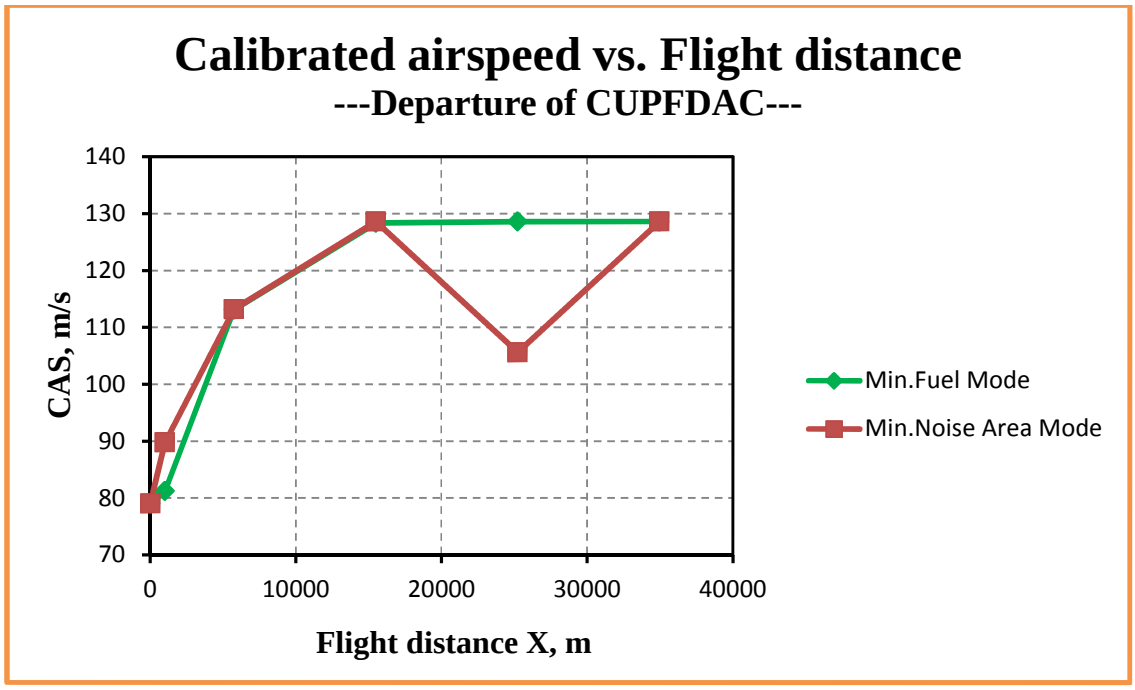

Figure 9-40 Calibrated airspeed vs. Flight distance (CUPFDAC-Departure)

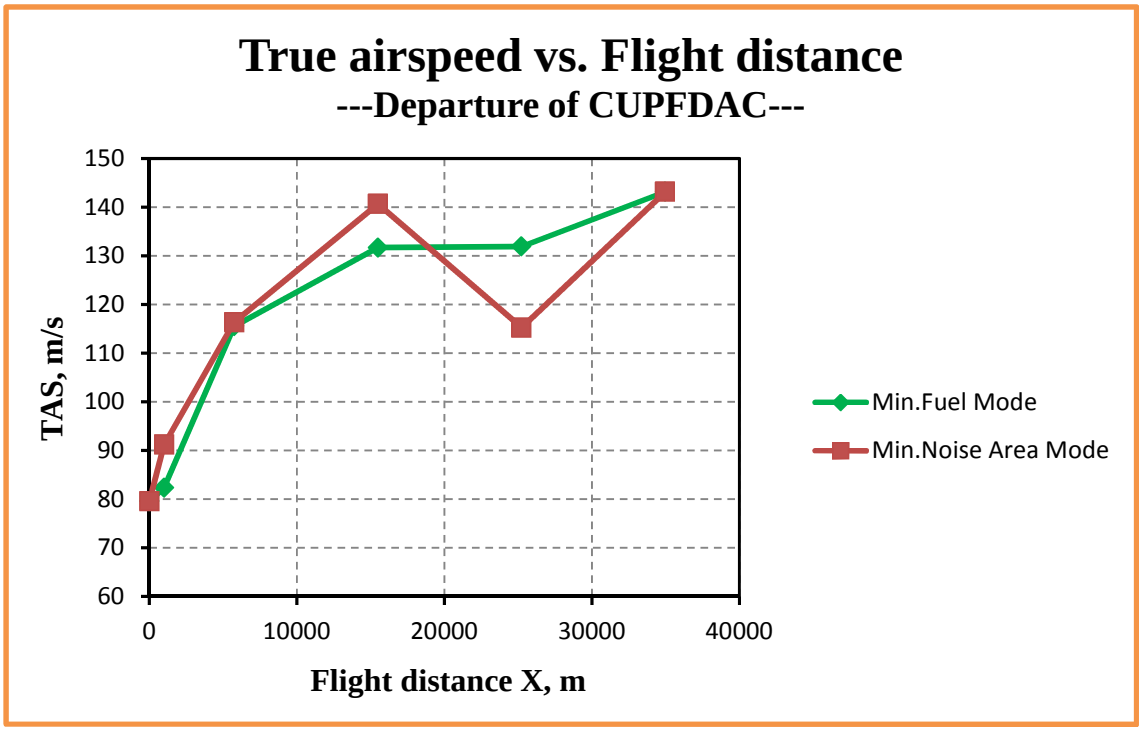

Figure 9-41 True airspeed vs. Flight distance (CUPFDAC-Departure)

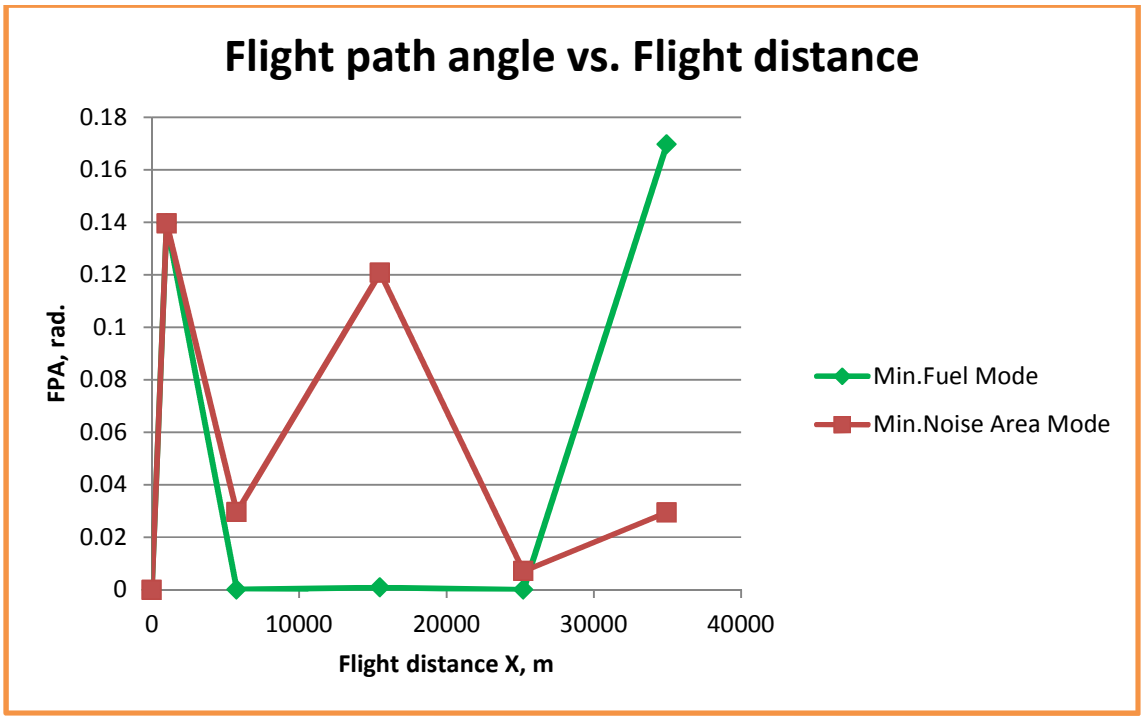

Figure 9-42 Flight path angle vs. Flight distance (CUPFDAC-Departure)

Table 9-21 Overall performance of two typical flight trajectories (CUPFDAC-Departure)

	Fuel burnt	**Noise area**	**Flight time**	**CO_2 emission**	**H_2O emission**	**NOx emission**
	(kg)	(m^2)	(s)	(g)	(g)	(g)
Min. Fuel Mode	184.94	60292300	284.46	589152.47	229570.69	8660.86
Min. Noise Area Mode	209.71	45440000	285.47	667262.70	260050.09	11179.90
Δ	24.77	-14852300	1.01	78110	30479	2519
δ	13.39%	-24.63%	0.36%	13.26%	13.28%	29.09%

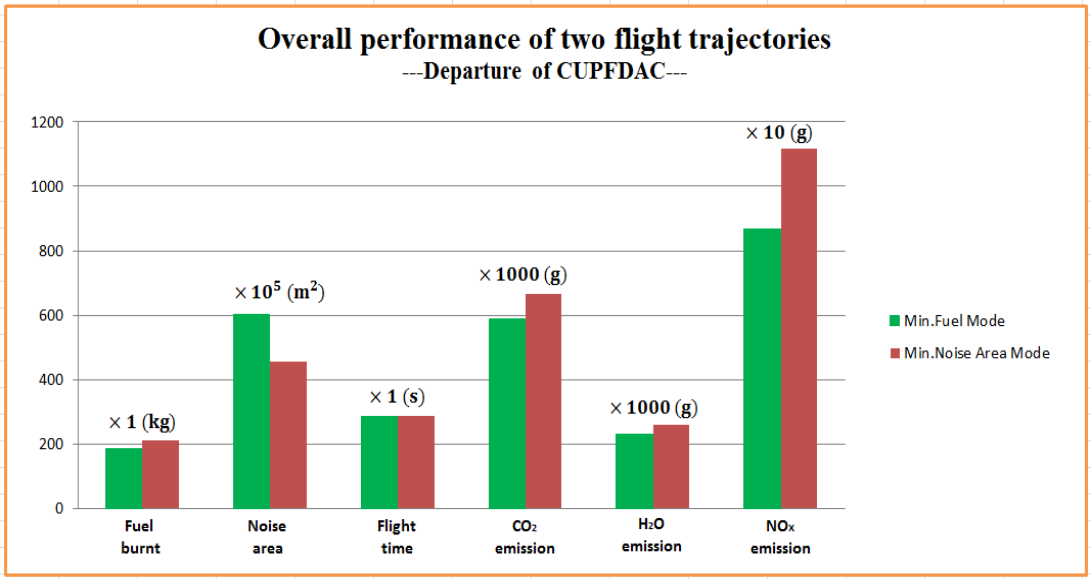

Figure 9-43 Overall performance of two typical flight trajectories (CUPFDAC-Departure)

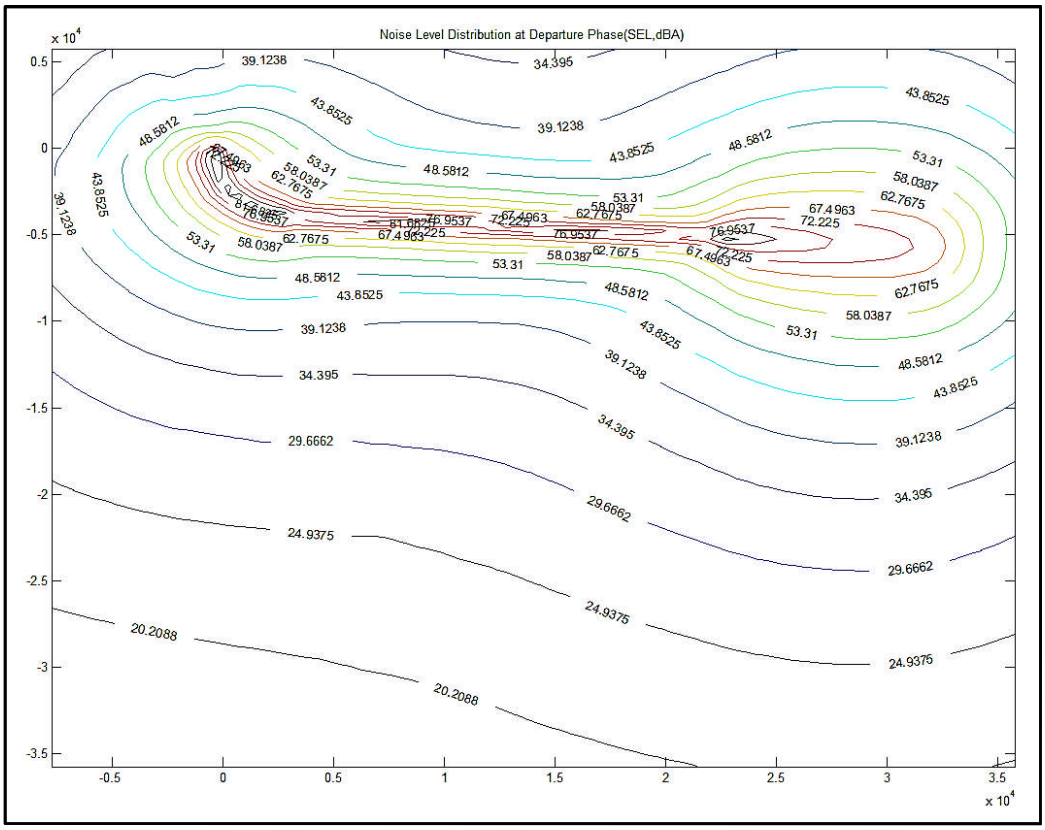

Figure 9-44 (a) Noise-level distribution contour of 'Min. Fuel Mode' (CUPFDAC-Departure)

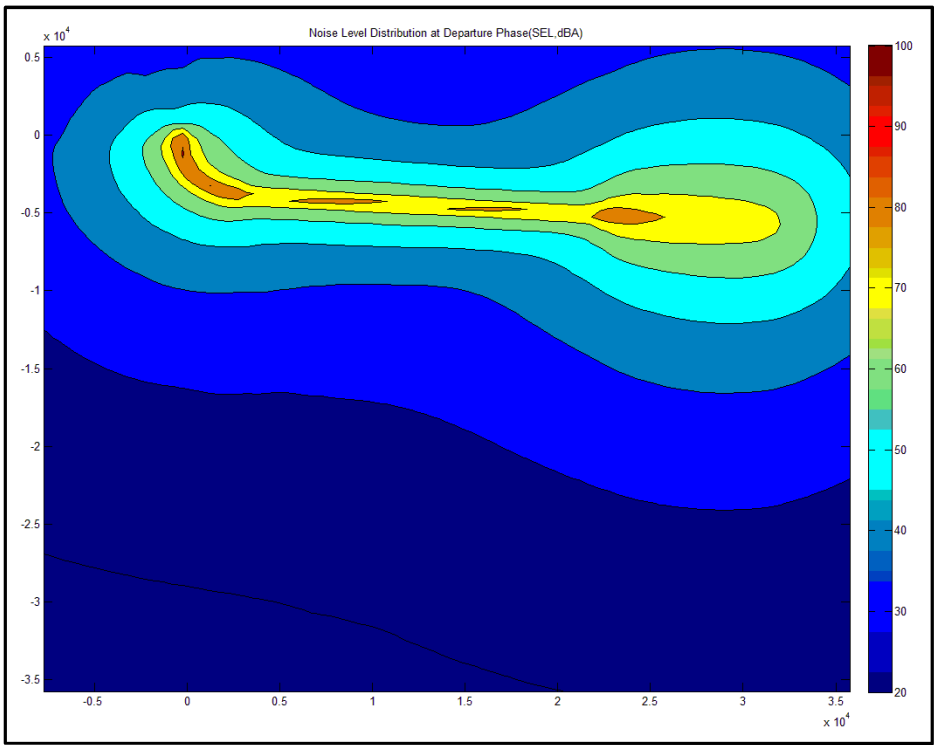

Figure 9-44 (b) Noise-level distribution filled contour of 'Min. Fuel Mode' (CUPFDAC-Departure)

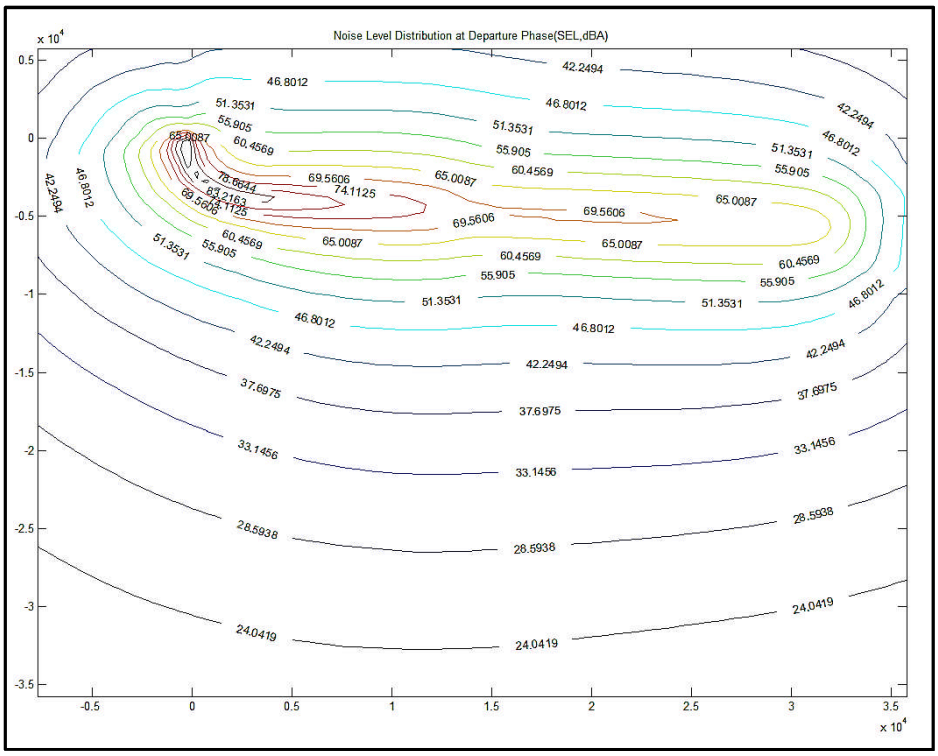

Figure 9-45 (a) Noise-level distribution contour of 'Min. Noise Area Mode' (CUPFDAC-Departure)

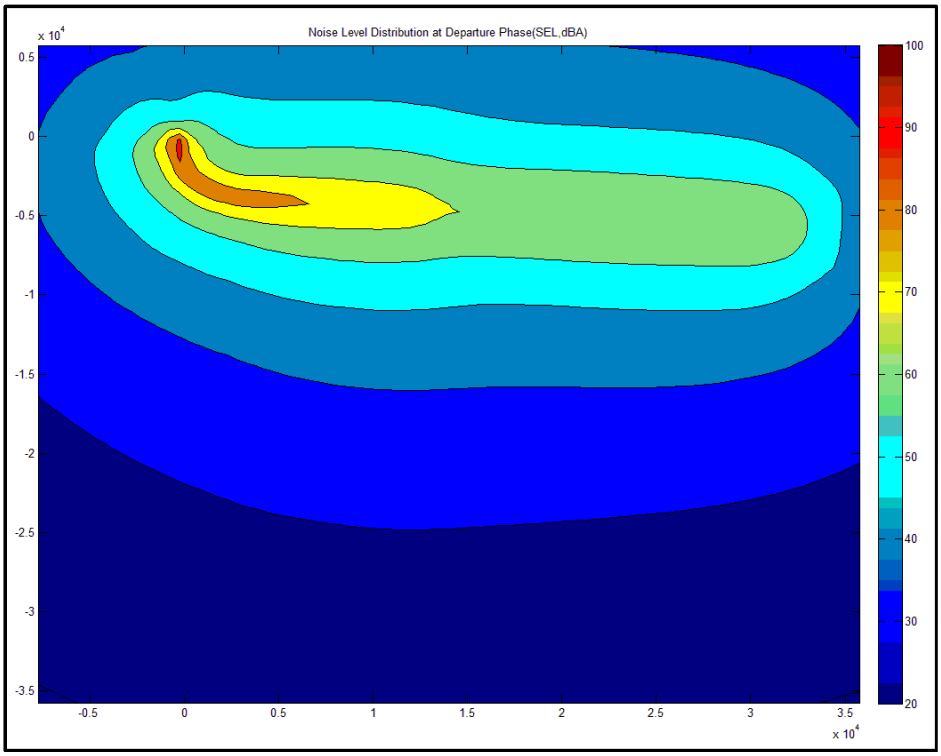

Figure 9-45 (b) Noise-level distribution filled contour of 'Min. Noise Area Mode' (CUPFDAC-Departure)

Table 9-22 Parameter segment distributions of 'Min. Fuel Mode'(part) (CUPFDAC-Departure)

Segment	Fn	TET	EINOx	Fuel burnt	Flight time	CO_2 emission	H_2O emission	NOx emission
	(N)	(K)	(g/kg fuel)	(kg)	(s)	(g)	(g)	(g)
1	59808.14	1708.28	60.87	10.41	12.41	33153.36	12920.92	633.45
2	52362.96	1642.80	47.64	34.06	48.19	108533.82	42302.03	1622.68
3	25139.36	1499.08	24.50	39.24	78.73	125170.59	48769.58	961.29
4	21622.49	1478.23	21.61	34.97	73.84	111546.03	43456.50	755.65
5	56689.19	1758.35	70.75	66.26	71.29	210748.67	82121.65	4687.78

Table 9-23 Parameter segment distributions of 'Min. Noise Area Mode' (part) (CUPFDAC-Departure)

Segment	Fn	TET	EINOx	Fuel burnt	Flight time	CO_2 emission	H_2O emission	NOx emission
	(N)	(K)	(g/kg fuel)	(kg)	(s)	(g)	(g)	(g)
1	73325.23	1784.78	76.72	11.98	11.77	38154.57	14866.27	919.17
2	59950.36	1691.77	57.86	37.02	45.96	117940.77	45966.36	2142.11
3	56313.68	1738.35	66.24	67.16	76.04	213673.38	83267.40	4449.20
4	35972.36	1615.52	39.59	47.40	76.36	150750.25	58755.81	1876.37
5	35205.89	1613.78	38.85	46.15	75.34	146743.73	57194.26	1793.05

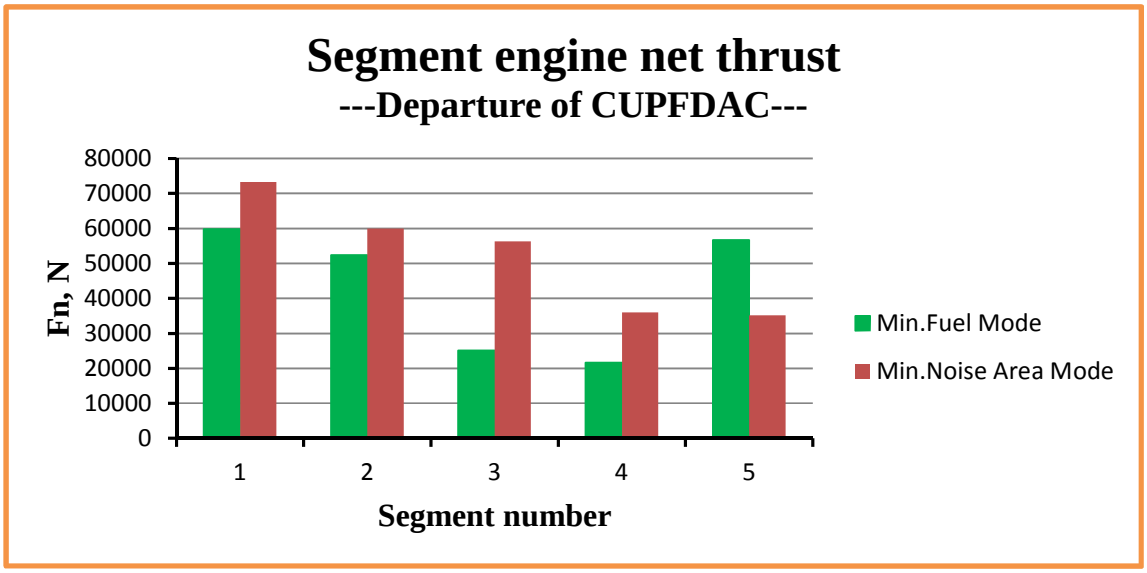

Figure 9-46 Segment engine net thrust (CUPFDAC-Departure)

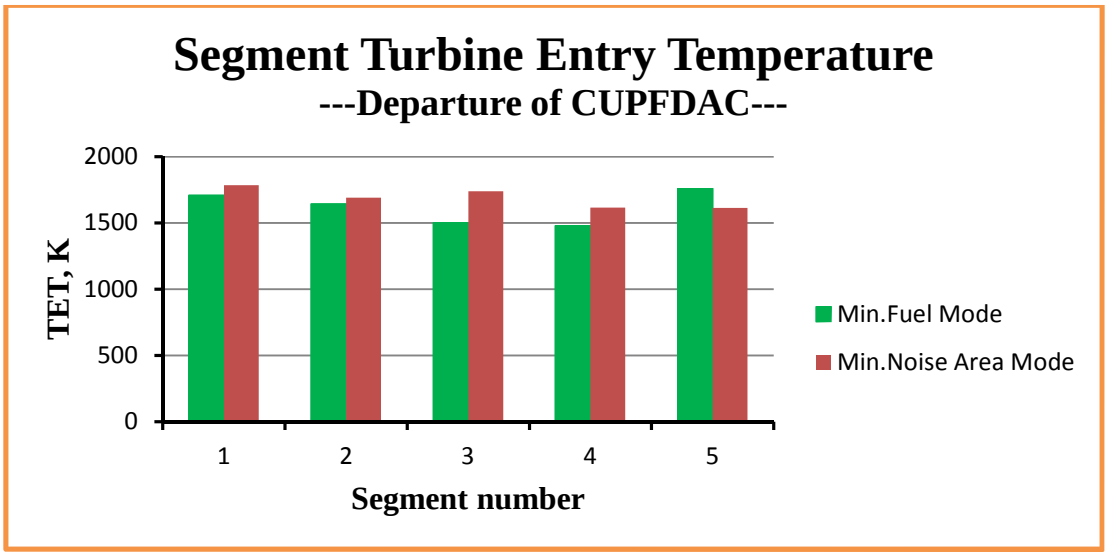

Figure 9-47 Segment engine turbine entry temperature (CUPFDAC-Departure)

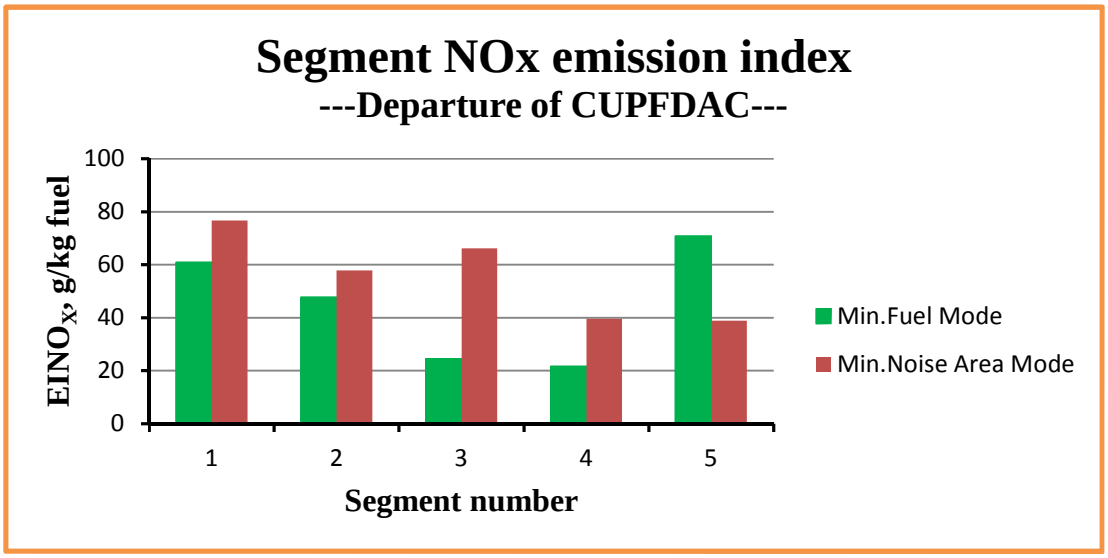

Figure 9-48 Segment NOx emission index (CUPFDAC-Departure)

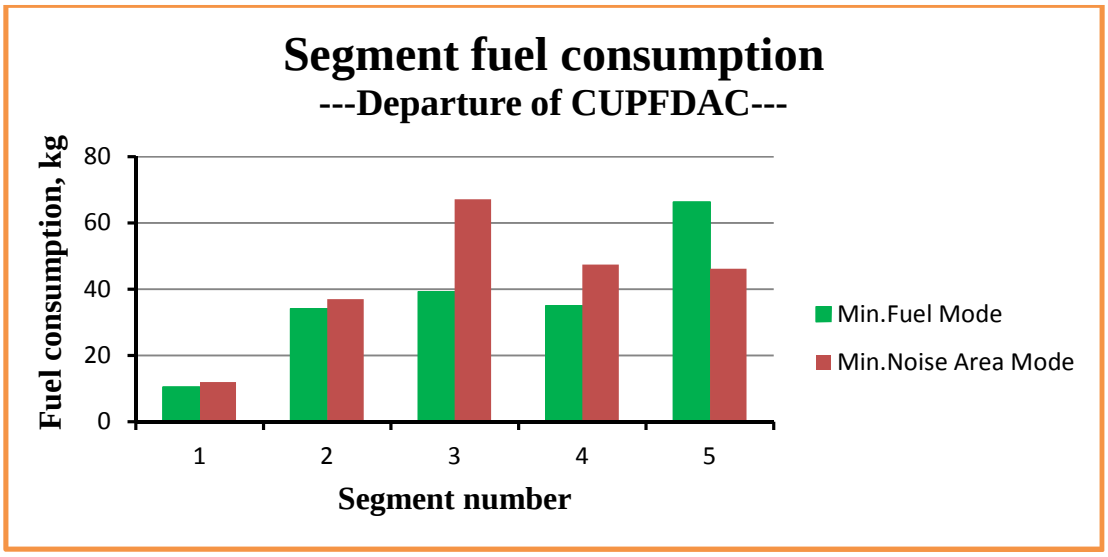

Figure 9-49 Segment fuel consumption (CUPFDAC-Departure)

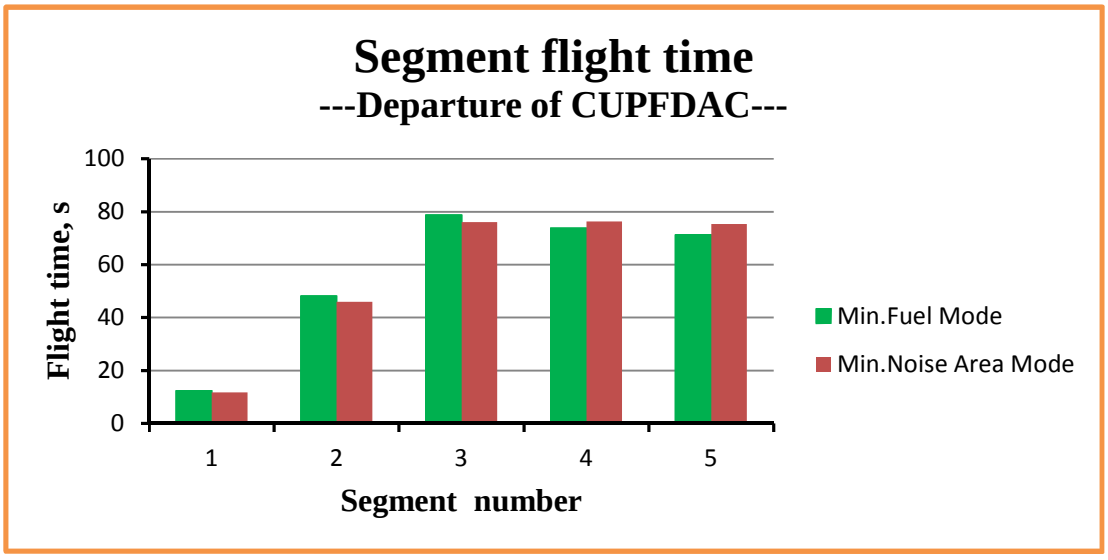

Figure 9-50 Segment flight time (CUPFDAC-Departure)

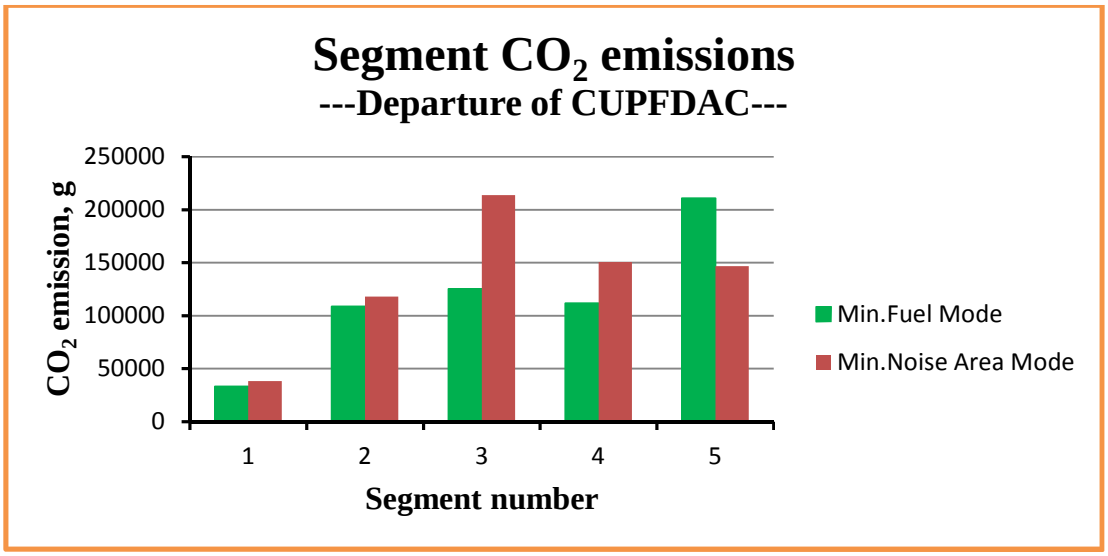

Figure 9-51 Segment CO_2 emissions (CUPFDAC-Departure)

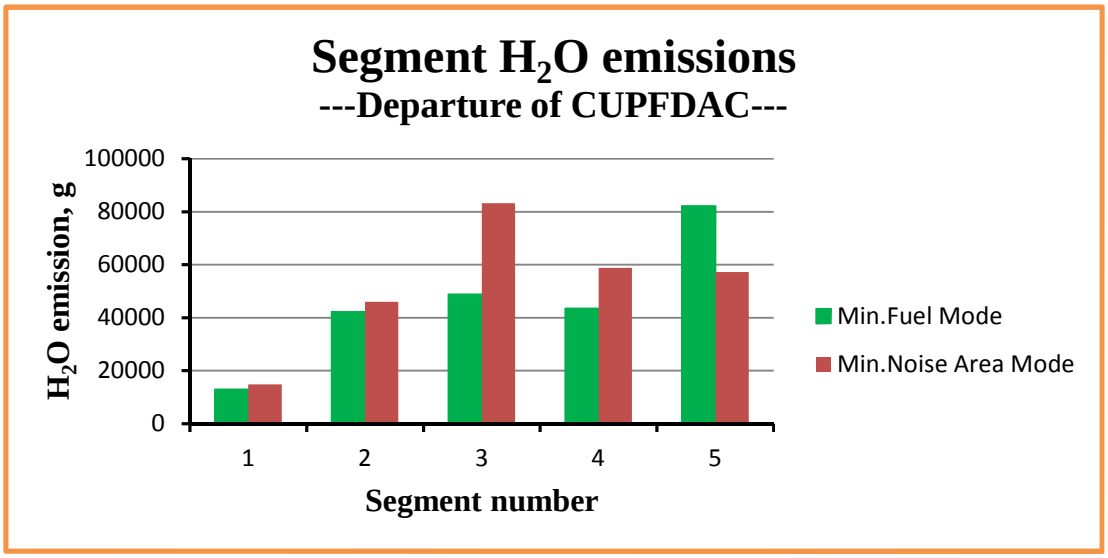

Figure 9-52 Segment H_2O emissions (CUPFDAC-Departure)

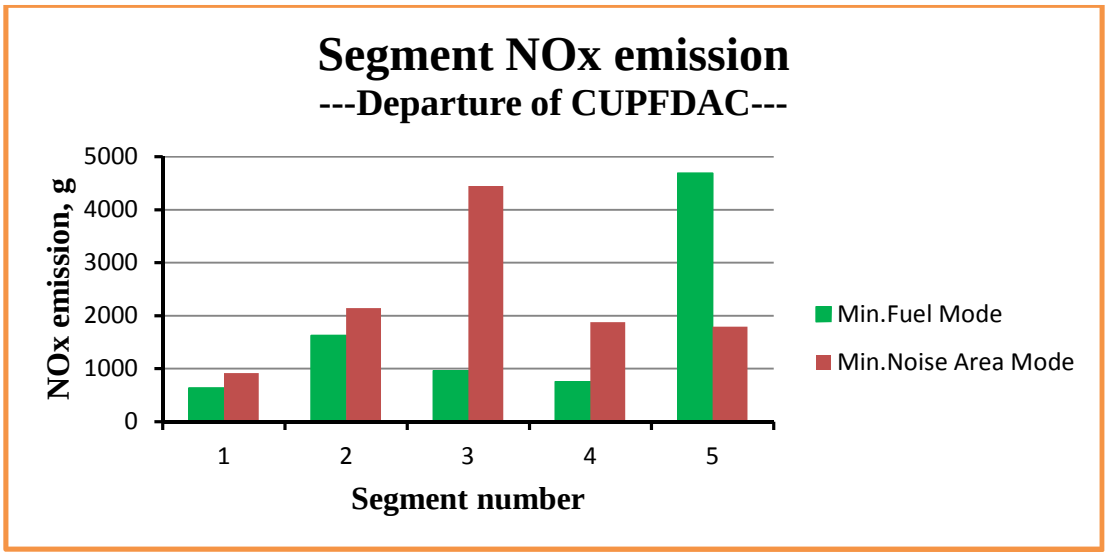

Figure 9-53 Segment NOx emission (CUPFDAC-Departure)

As for the departure flight of CUPFDAC, similar observations to the achieved optimum results can be implemented as before and correspondingly the following points can be summarised.

1) The convergence of this optimisation process has been obtained, which can be proved from the basically stable value of normalised Pareto area shown in Figure 9-37 and the smooth shape of achieved Pareto front line illustrated in Figure 9-38.
2) The entire optimisation process totally cost 56 hours 3 minutes 55 seconds with 450 generations or 72113 evaluations implemented (Table 9-17), that is, 448.5 seconds/generation or 2.8 seconds/evaluation.
3) Similarly, two extreme (also typical) points – 'min. fuel consumption' flight mode and 'min. noise area' flight mode, among all achieved optimum solutions, were selected for the convenience of analysis.
4) As for the departure trajectory resulted from the 'min. fuel' flight mode, the optimised results suggest that, for the 1st segment, a slight acceleration climb should be used so that the aircraft can, within the given horizontal flight distance of 1000m, climb from the initial altitude 11.6 m to 152 m required by ATC and, in the meantime, obtain a small increase in flight speeds (CAS increasing from 79 m/s to 81.20 m/s and correspondingly TAS increasing from 79.58 m/s to 82.37 m/s). During this flight segment, the flight path angle of CUPFDAC will

experience a relative large increase from the initial value of zero to around 0.14 radians; When the flight enters into the 2nd segment, the flight style of level flight and acceleration will be adopted, that is, the flight altitude will be kept at 152 m and the excess propulsive power of the aircraft will be only used to increase aircraft's kinetic energy or flight speeds. As a result, CAS will increase from 81.20 m/s to 113.15 m/s and correspondingly TAS will also increase from 82.37 m/s to 115.57 m/s, and this segment will cover the horizontal flight distance of 4750 m; The flight in the 3rd segment will again experience the similar flight style as that in the 1st segment – climb and acceleration. Through the flight segment, the altitude will reach 160.73 m and flight speeds will amount to 128.39 m/s (CAS) and 131.70 m/s (TAS) respectively; Constant altitude and speed flight will be the nature of the 4th-segment flight. During the flight in this segment, the flight altitude will be kept at around 161 m, flight speeds at around 128 m/s (CAS) and 132 m/s (TAS), and the flight path angles will almost approach zero radian; CUPFDAC will complete its final flight segment of the departure phase by applying constant CAS climb style, namely, during this flight segment, the calibrated airspeed will be hold at 128.6 m/s and the flight altitude will be continuously increased from around 161 m to 1828.8 m also required by ATC (correspondingly, the true airspeed will also go up from around 132 m/s to 143.20 m/s), and naturally, due to the relatively sharp increase in the flight altitude, the flight path angle will also experience a large change (rising from nearly zero radian to around 0.17 radians).

5) As for the departure trajectory resulted from the 'min. noise area' flight mode, the optimised results suggest that, for the 1st segment, the accelerated climb will be used, that is, with the given horizontal flight distance of 1000 m, the aircraft will climb from 11.6 m to 152 m and at the same time increase its calibrated airspeed from 79 m/s to nearly 90 m/s (correspondingly, the true airspeed will also rise to around 91 m/s from the initial value of nearly 80 m/s) and as a consequence the flight path angle will experience a large increase (from the initial zero radian to around 0.14 radians); When the aircraft enters into the 2nd segment, the same flight style as that in the 1st segment will continue. During this flight segment, the flight altitude and flight speeds will continue to increase,

reaching around 292 m, 113 m/s (CAS) and 116 m/s (TAS) respectively; The following 3rd segment will continue to witness the acceleration and climb of the aircraft with the flight altitude obviously increased to around 1473 m and CAS increased to 128.61 m/s (correspondingly, TAS going up to nearly 141 m/s); Different from flights in the previous three segments, the flight in the 4th segment will apply the decelerated climb flight style, that is, CAS of the aircraft will be reduced to around 106 m/s from 128.6 m/s but the flight altitude will continue to rise to 1542 m (correspondingly, TAS of the aircraft will also be decreased to around 115 m/s); In the 5th-segment flight, the flight altitude and the flight speeds of the aircraft will be both increased again. Finally, through this flight segment with the horizontal flight distance of around 9733 m, CUPFDAC will reach the flight altitude of 1828.8 m and CAS of 128.61 m/s (correspondingly, TAS equals to 143.20 m/s) which are required by ATC.

6) By the comparison between the above two typical flight trajectories respectively from the 'min. fuel' flight mode and 'min. noise area' flight mode, an obvious difference in the departure flight profiles achieved through optimisation process in terms of the variation of flight altitude with horizontal flight distance can be noticed. That is, when the 'min. noise area' mode is implemented, CUPFDAC will be required to fly at higher altitudes from earlier segments of the departure flight phase when compared to the corresponding profile resulted from 'min. fuel' mode. In addition, in the flight speed profiles from the 'min. noise area' mode which illustrate the variations of CAS and TAS with the horizontal flight distance, a decelerated climb will be required in the 4th flight segment. These differences are understandable and the reason as explained in the section of CUTFDAC lies in the fact that higher flight altitude (i.e., greater distance between noise source – the aircraft and observer – the ground) and reduced flight speed (hence reduced engine power settings) will be helpful to reduce the noise level perceived by ground observers and, therefore, the noise-impact area with SEL≥70 dBA.

7) Table 9-21 and Figures 9-43 to 9-45 further provide the overall performances of the above two typical flight modes and their comparisons. Compared to the 'min. fuel consumption' flight mode, when CUPFDAC flies along the departure

profile prescribed by the 'min. noise area' flight mode, the lower noise-impact area (around 45 km^2) with SEL ≥70 dBA can be achieved, about 15 km^2 or 25% less than the result from the 'min. fuel consumption' mode, but with more fuel consumption (around 25 kg or 13% more) and higher gaseous emissions in terms of CO_2 (around 78 kg or 13% higher), H_2O (around 30 kg or 13% higher) and NOx (around 2.5 kg or 29% higher). The increases in CO_2 and H_2O are only related to the increase in the fuel consumption, but for the NOx emission, besides the contribution from more fuel burnt, higher values of NOx emission index during the departure flight which result from higher engine power settings for the 'min. noise area' mode are also an important reason (see Tables 9-22 and 9-23 as well as Figures 9-46 to 9-49). In addition, in the aspect of flight time, there hardly exists any difference between the two flight modes in fact (the difference in flight time is only 1 second or 0.36%).

9.1.4 Departure-flight comparisons between CUPFDAC and CUTFDAC

Based on the previous descriptions about the optimised flight trajectories, especially of CUPFDAC and CUTFDAC flown through 'min. fuel consumption' mode and 'min. noise area' mode, it is now possible to compare and discuss the performances of these two aircraft respectively driven by propfan engine (or open rotor) and conventional turbofan engine during the departure flight phase. The following Tables 9-24 to 9-29 and Figures 9-54 to 9-59 provide the relevant information to this comparison.

Table 9-24 Overall comparisons between CUPFDAC and CUTFDAC ('min. fuel consumption' departure flight mode)

	Fuel burnt	**Noise area**	**Flight time**	**CO_2 emission**	**H_2O emission**	**NOx emission**
	(kg)	(m^2)	(s)	(g)	(g)	(g)
CUTFDAC	304.65	66716700	277.91	961635.16	377220.53	4426.96
CUPFDAC	184.94	60292300	284.46	589152.47	229570.69	8660.86
Δ	-119.71	-6424400	6.55	-372482.69	-147649.84	4233.9
δ	-39.29%	-9.63%	2.36%	-38.73%	-39.14%	95.64%

Table 9-25 Overall comparisons between CUPFDAC and CUTFDAC ('min. noise area' departure flight mode)

	Fuel burnt	**Noise area**	**Flight time**	**CO_2 emission**	**H_2O emission**	**NOx emission**
	(kg)	(m^2)	(s)	(g)	(g)	(g)
CUTFDAC	343.07	41983500	286.83	1082912.08	424793.82	5112.07
CUPFDAC	209.71	45440000	285.47	667262.70	260050.09	11179.90
Δ	-133.36	3456500	-1.36	-415649.38	-164743.73	6067.83
δ	-38.87%	8.23%	-0.47%	-38.38%	-38.78%	118.70%

Table 9-26 TET comparisons between CUPFDAC and CUTFDAC ('min. fuel' departure flight mode)

	TET, K		**Δ**	**δ**
	CUTFDAC	**CUPFDAC**	**K**	**-**
1	1417.75	1708.28	290.53	20.49%
2	1261.88	1642.80	380.92	30.19%
3	1140.63	1499.08	358.45	31.43%
4	1109.34	1478.23	368.89	33.25%
5	1347.66	1758.35	410.69	30.47%

Table 9-27 EINOx comparisons between CUPFDAC and CUTFDAC ('min. fuel' departure flight mode)

	EINOx, g/kg fuel		Δ	δ
	CUTFDAC	**CUPFDAC**	**g/kg fuel**	**-**
1	19.77	60.87	41.1	207.89%
2	14.63	47.64	33.01	225.63%
3	10.89	24.50	13.61	124.98%
4	9.93	21.61	11.68	117.62%
5	17.85	70.75	52.9	296.36%

Table 9-28 TET comparisons between CUPFDAC and CUTFDAC ('min. noise area' departure flight mode)

	TET, K		Δ	δ
	CUTFDAC	**CUPFDAC**	**K**	**-**
1	1288.74	1784.78	496.04	38.49%
2	1275.53	1691.77	416.24	32.63%
3	1313.16	1738.35	425.19	32.38%
4	1226.64	1615.52	388.88	31.70%
5	1232.59	1613.78	381.19	30.93%

Table 9-29 EINOx comparisons between CUPFDAC and CUTFDAC ('min. noise area' departure flight mode)

	EINOx, g/kg fuel		Δ	δ
	CUTFDAC	CUPFDAC	g/kg fuel	-
1	15.34	76.72	61.38	400.13%
2	15.02	57.86	42.84	285.22%
3	16.55	66.24	49.69	300.24%
4	13.60	39.59	25.99	191.10%
5	13.78	38.85	25.07	181.93%

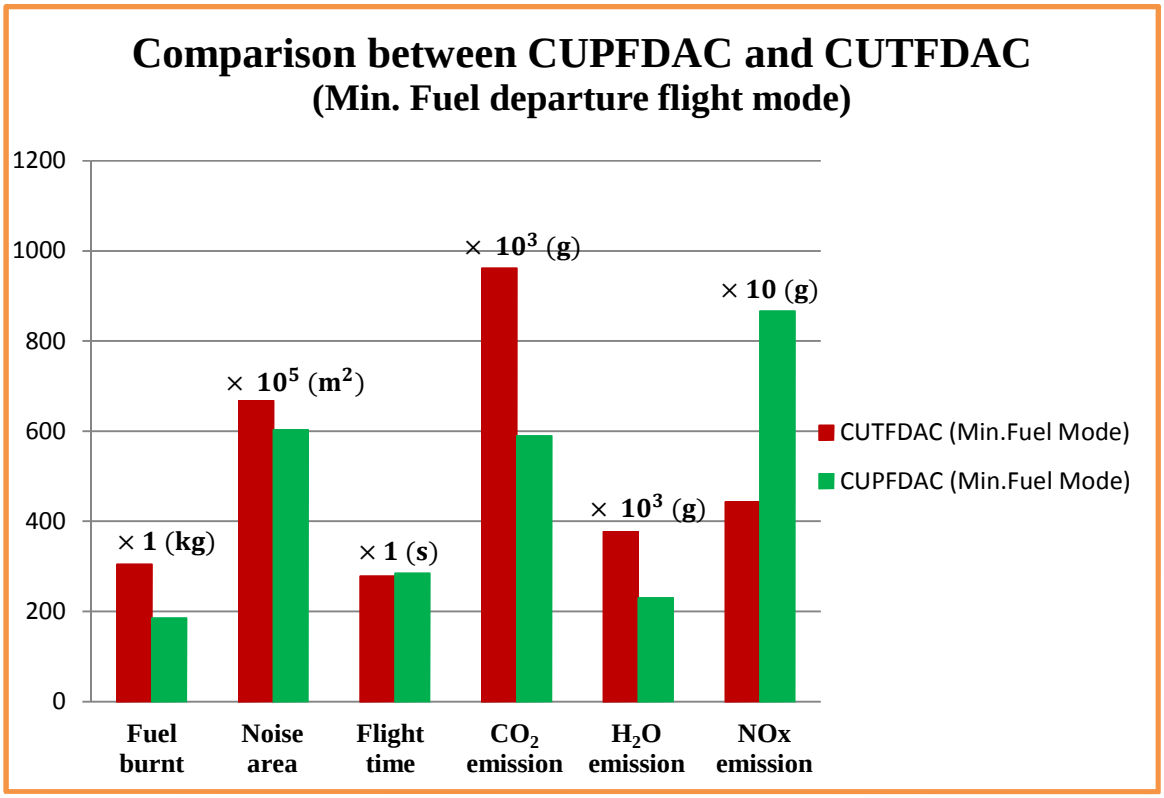

Figure 9-54 Overall comparisons between CUPFDAC and CUTFDAC ('min. fuel consumption' departure flight mode)

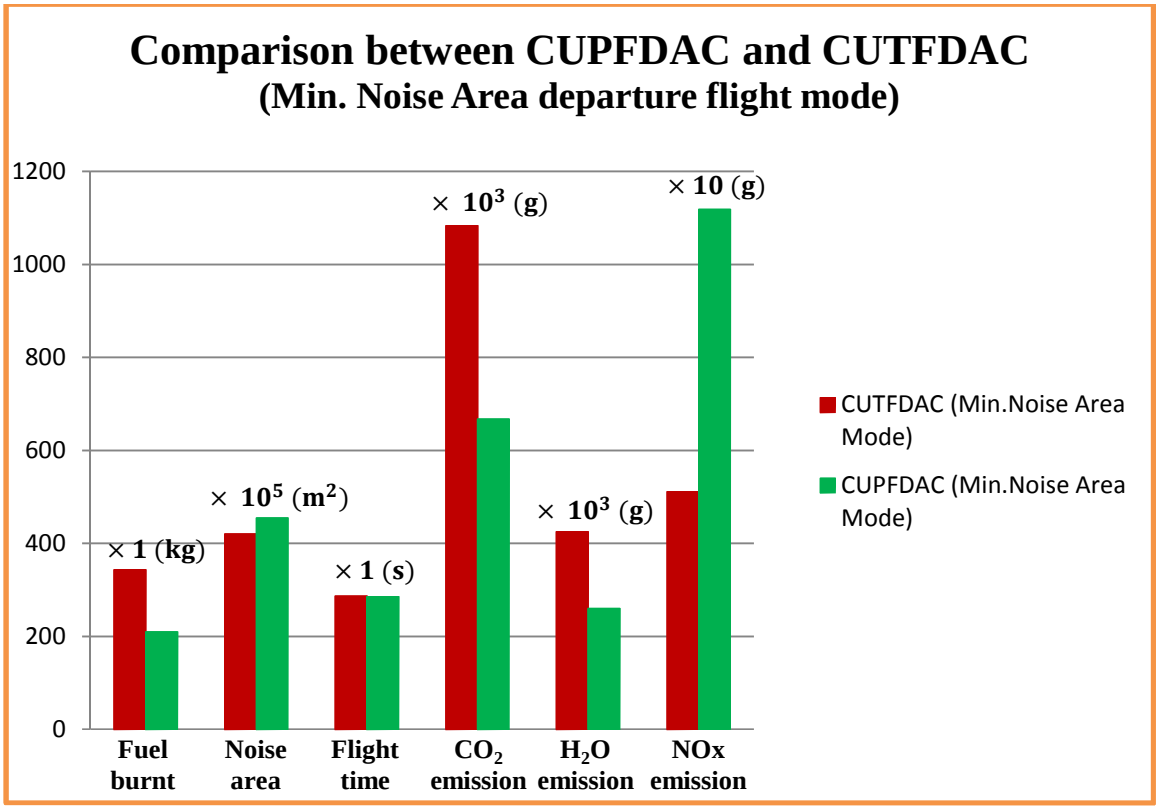

Figure 9-55 Overall comparisons between CUPFDAC and CUTFDAC ('min. noise area' departure flight mode)

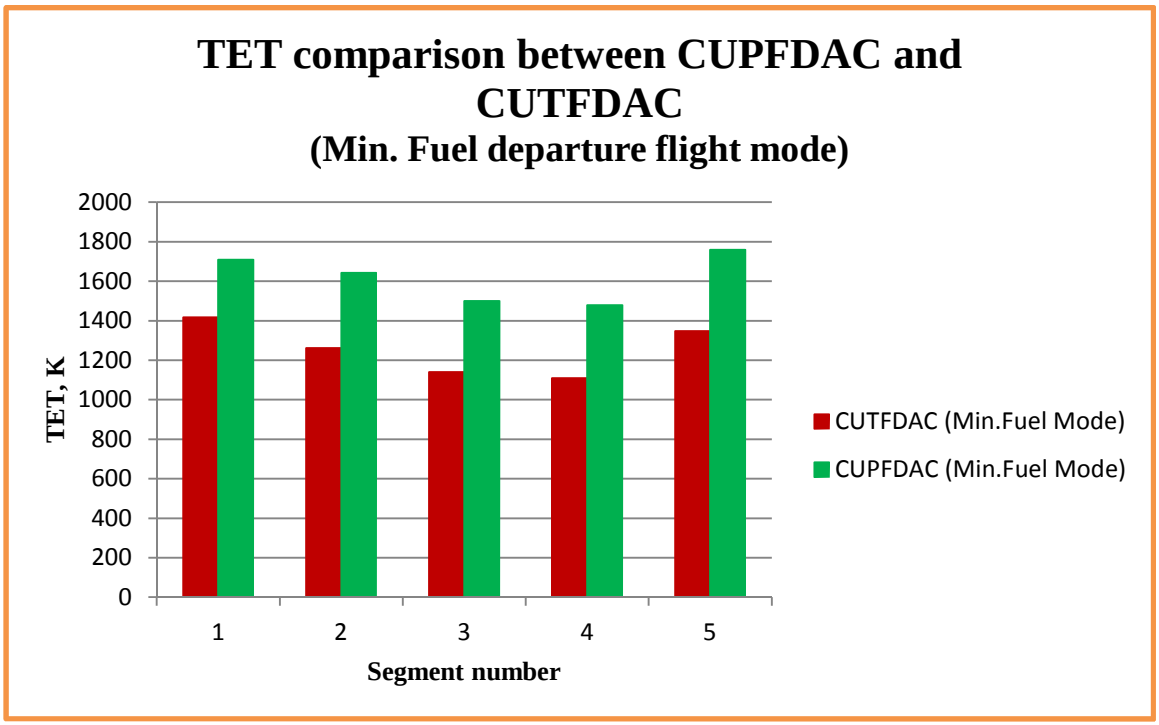

Figure 9-56 TET comparisons between CUPFDAC and CUTFDAC ('min. fuel' departure flight mode)

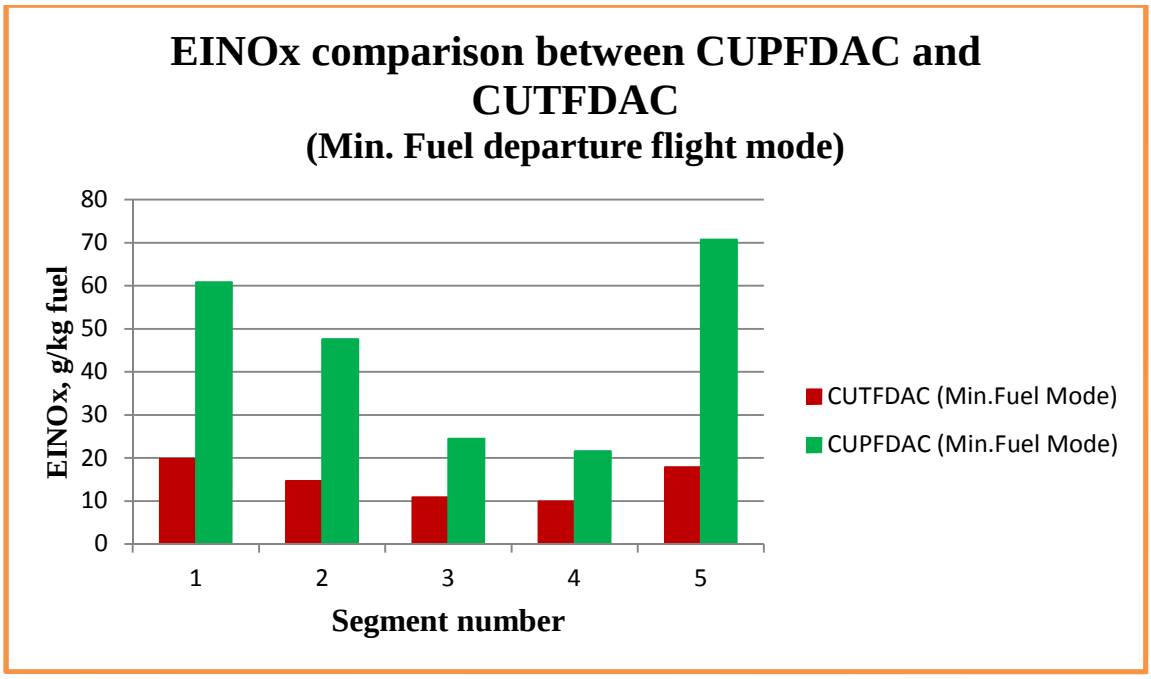

Figure 9-57 EINOx comparisons between CUPFDAC and CUTFDAC ('min. fuel' departure flight mode)

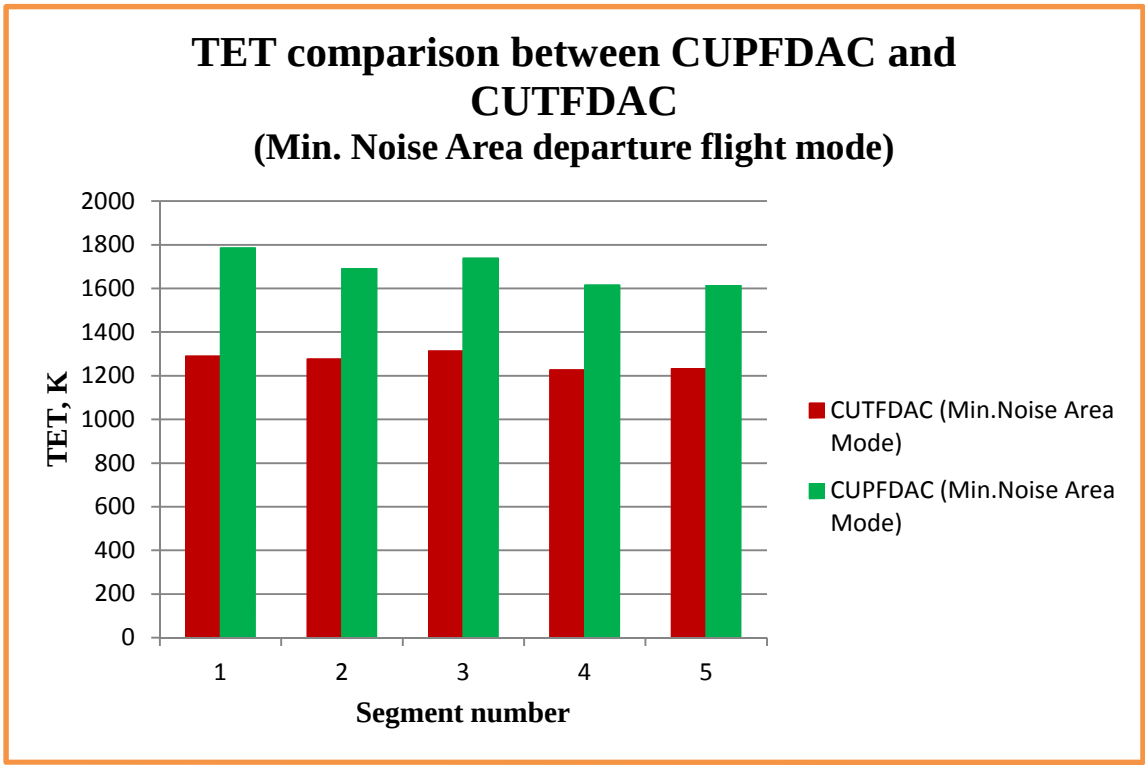

Figure 9-58 TET comparison between CUPFDAC and CUTFDAC ('min. noise area' departure flight mode)

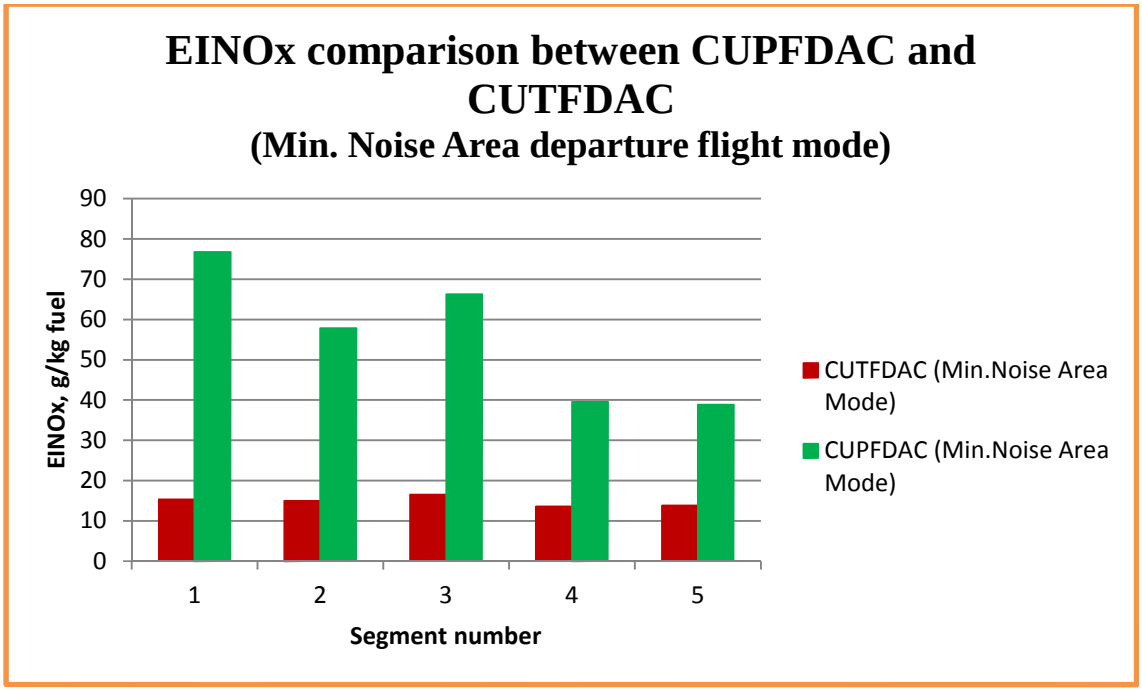

Figure 9-59 EINOx comparison between CUPFDAC and CUTFDAC ('min. noise area' departure flight mode)

From these above tables and figures, some points can be observed and summarised as follows:

1) Firstly, with the 'min. fuel consumption' departure flight mode, CUPFDAC and CUTFDAC separately reached their own minimum fuel consumptions by flying the optimised flight trajectories. However, the much lower value of minimum fuel consumption (around 120 kg or 39% less) and hence much better operation economy can be achieved when the propfan (open rotor) engine is applied compared to the turbofan case. Consequently, the emissions of CO_2 and H_2O can also be greatly reduced, the decreased magnitudes respectively amounting to 372 kg (39%) and 148 kg (39%) only due to the basically constant emission indices and the same reduced fuel consumption. In light of this calculation and adopted noise models, less noise-impact area (6.4 km^2 or 9.6%) can be obtained by CUPFDAC as well. The flight times separately spent by CUPFDAC and CUTFDAC are very close to each other and the slight difference in flight time (less than 7 seconds) can be ignored. Unfortunately, an obvious problem CUPFDAC is facing in this case study is the very high level of NOx emission (4 kg or 96% more than the emission from CUTFDAC). This is attributed to very

high value of NOx emission index in the CUPFDAC case (12-53 g/kg fuel or 118-296% higher compared to the CUTFDAC case) due to the very high engine power settings during the departure phase (290-410 K or 20-33% higher compared to the CUTFDAC case) which are shown in Tables 9-26 and 9-27 as well as in Figures 9-56 and 9-57.

2) Secondly, with the 'min. noise area' departure flight mode, a quite similar phenomenon can also be observed. That is, more fuel (133 kg or 39%) can be saved and more emissions of CO_2 and H_2O (416 kg or 38% and 165 kg or 39% respectively) can be reduced by flying CUPFDAC instead of CUTFDAC. Different from the above 'min. fuel' mode, CUPFDAC can produce more noise-impact area than CUTFDAC in the 'min. noise area' mode with the increased amount of 3.5 km^2 or 8%. The tiny difference in the flight time (only about 1 second) between the two aircraft continues to be held in this flight mode as in the 'min. fuel' flight mode and the challenge from NOx emission for CUPFDAC remains even for this 'min. noise area' mode (around 6 kg or 119% more than that from CUTFDAC).

3) Therefore, according to the above comparisons between CUPFDAC and CUTFDAC respectively under the 'min. fuel consumption' mode and 'min. noise area' mode, such a conclusion can be derived, that is, the adoption of the new-generation propfan (or open rotor) engine whose technologies will be ready around 2025 to 2030 as the power plant can significantly reduce the fuel consumption and the emissions of CO_2 and H_2O during the departure flight phase (nearly 40%), compared to the 1990s' technology level represented by the conventional turbofan engine in CUTFDAC. These impressive achievements are the results naturally derived from the combination of higher engine thermal efficiency (due to the applications of higher turbine entry temperature, higher component efficiencies) and higher propulsive efficiency which the propfan engine has inherently. On the other hand, from the above discussion, it can also be found that the challenge from NOx emission will be increasingly severe with higher operation temperatures of the future propfan engine, and traditional combustion technology and combustor design cannot any longer meet the requirements from this novel engine, hence new low emission technologies

under high engine power settings, such as fuel staged combustor etc., will have to be explored and applied.

9.2 En route Flight Phase

9.2.1 CUTFDAC (Cranfield University Turbofan-Driven Aircraft)

Table 9-30 Running record of CUTFDAC-En route optimisation

1	Running start time/date	Mon Oct 15 08:09:52 BST 2012
2	Running end time/date	Mon Oct 15 14:52:33 BST 2012
3	Total running time	6 hours 42 minutes 41 seconds
4	Generation number	400
5	Total number of evaluations	67817

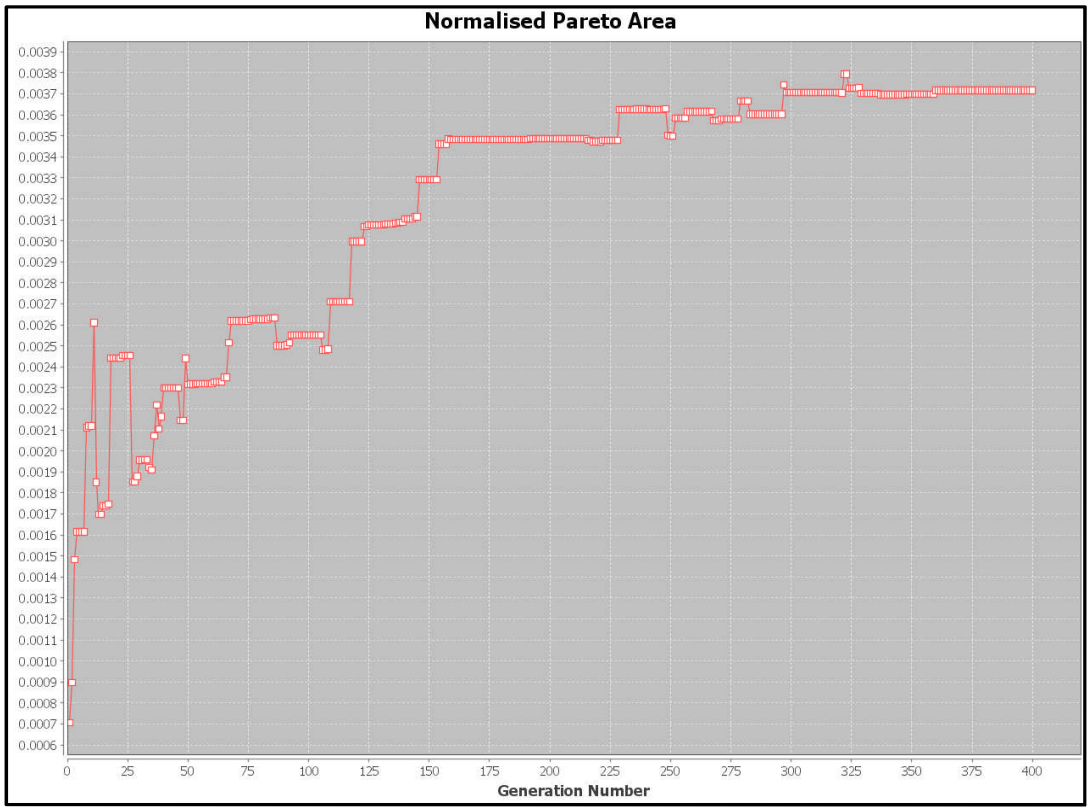

Figure 9-60 Normalised Pareto area (CUTFDAC-en route)

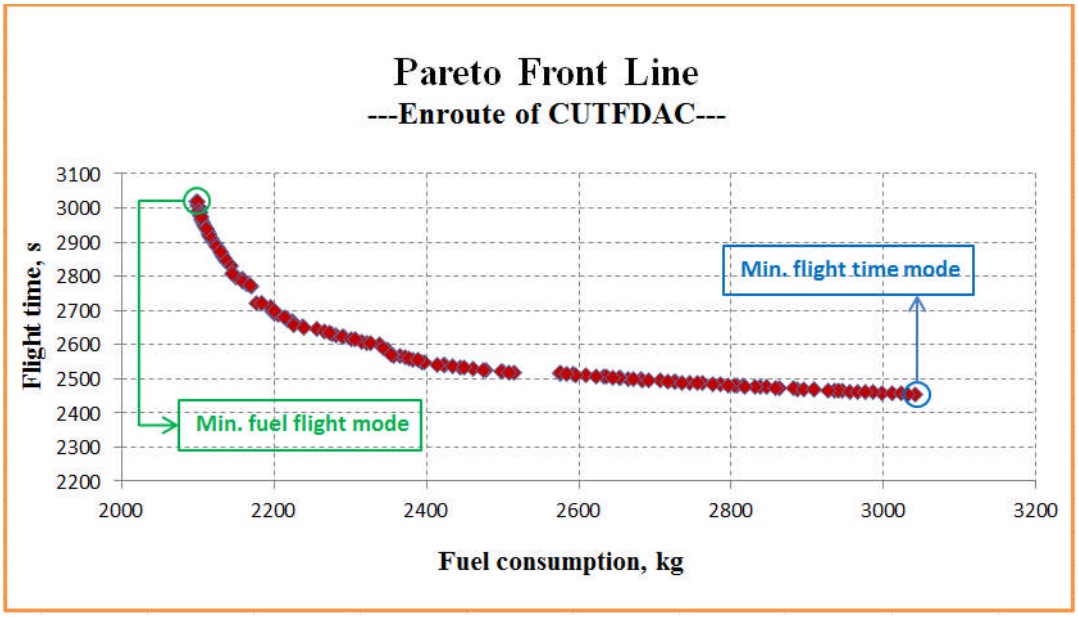

Figure 9-61 Pareto Front line (CUTFDAC-en route)

Table 9-31 Optimised results of two typical flight trajectories (CUTFDAC-en route)

		Minimum Fuel Flight Mode	Minimum Time Flight Mode
Design variables	ALT1, (m)	1828.80	1828.97
	ALT2, (m)	10050.75	7924.8
	ALT9, (m)	9774.85	2438.68
	DIS1, (m)	3954.34	11808.14
	DIS2, (m)	140000	335000
	DIS8, (m)	403904.84	407590.82
	DIS9, (m)	416480.83	631151.53
	MACH1, (-)	0.60	0.82
	MACH2, (-)	0.75	0.82
	MACH9, (-)	0.82	0.82

Objective functions	Fuel consumption, (kg)	2098.53	3040.71
	Flight time, (s)	3020.51	2454.41
Optimisation constraints	CA21,(m)	8221.95	6095.83
	CX21,(m)	136045.66	323191.86
	CX98,(m)	12575.99	223560.70
	CA89,(m)	275.91	5486.12
	NOx, (g)	26522.36	53652.68
	CO_2, (g)	6624013.66	9598013.85

Table 9-32 Flight trajectory of 'Min. Fuel Consumption' mode (CUTFDAC-en route)

Point	X (m)	Z (m)	MACH (-)	TAS (m/s)	FPA (rad.)
0	0	1828.8	0.42	139.94	0
1	3954.34	1828.80	0.60	199.55	1.00×10^{-6}
2	140000	10050.75	0.75	225.02	0.0604
3	183984.14	10050.75	0.75	225.02	0
4	227968.28	10050.75	0.75	225.02	0
5	271952.42	10050.75	0.75	225.02	0
6	315936.56	10050.75	0.75	225.02	0
7	359920.70	10050.75	0.75	225.02	0
8	403904.84	10050.75	0.75	225.02	0

9	416480.83	9774.85	0.82	245.16	-0.0219
10	637000	2438.4	0.44	145.55	-0.0333

Table 9-33 Flight trajectory of 'Min. Flight Time' mode (CUTFDAC-en route)

Point	X (m)	Z (m)	MACH (-)	TAS (m/s)	FPA (rad.)
0	0	1828.8	0.42	139.94	0
1	11808.14	1828.97	0.82	273.21	1.40×10^{-5}
2	335000	7924.8	0.82	252.89	0.0189
3	347098.47	7924.8	0.82	252.89	0
4	359196.94	7924.8	0.82	252.89	0
5	371295.41	7924.8	0.82	252.89	0
6	383393.88	7924.8	0.82	252.89	0
7	395492.35	7924.8	0.82	252.89	0
8	407590.82	7924.8	0.82	252.89	0
9	631151.53	2438.68	0.82	271.12	-0.0245
10	637000	2438.4	0.44	145.55	-4.80×10^{-5}

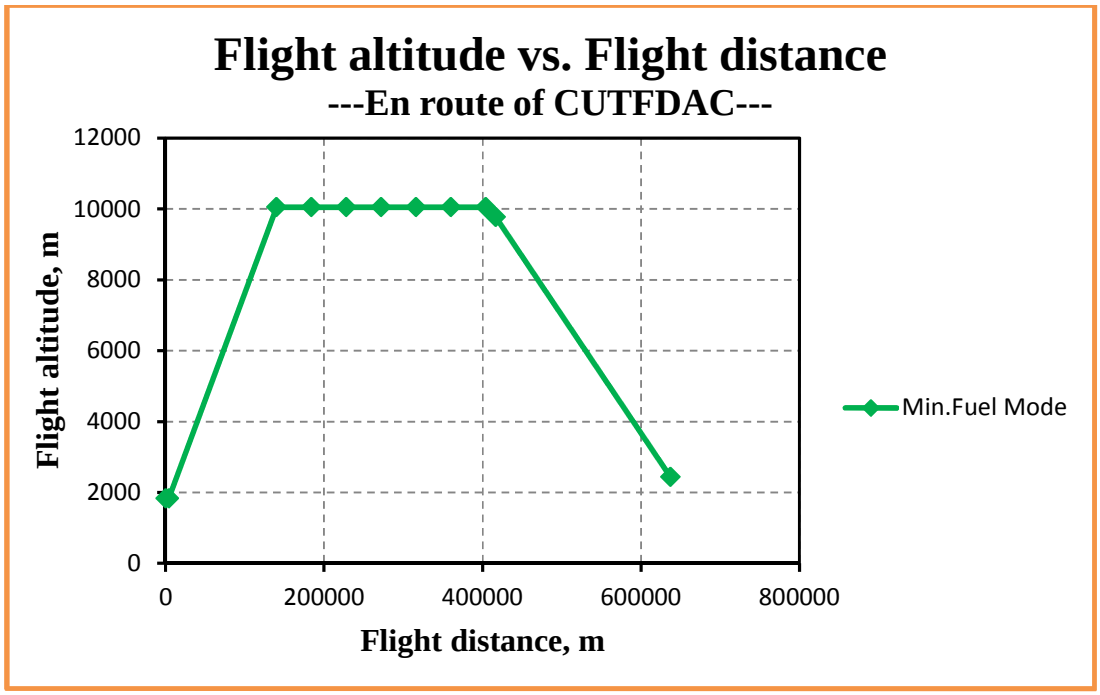

Figure 9-62 Flight altitude vs. Flight distance – 'min. fuel' mode (CUTFDAC-en route)

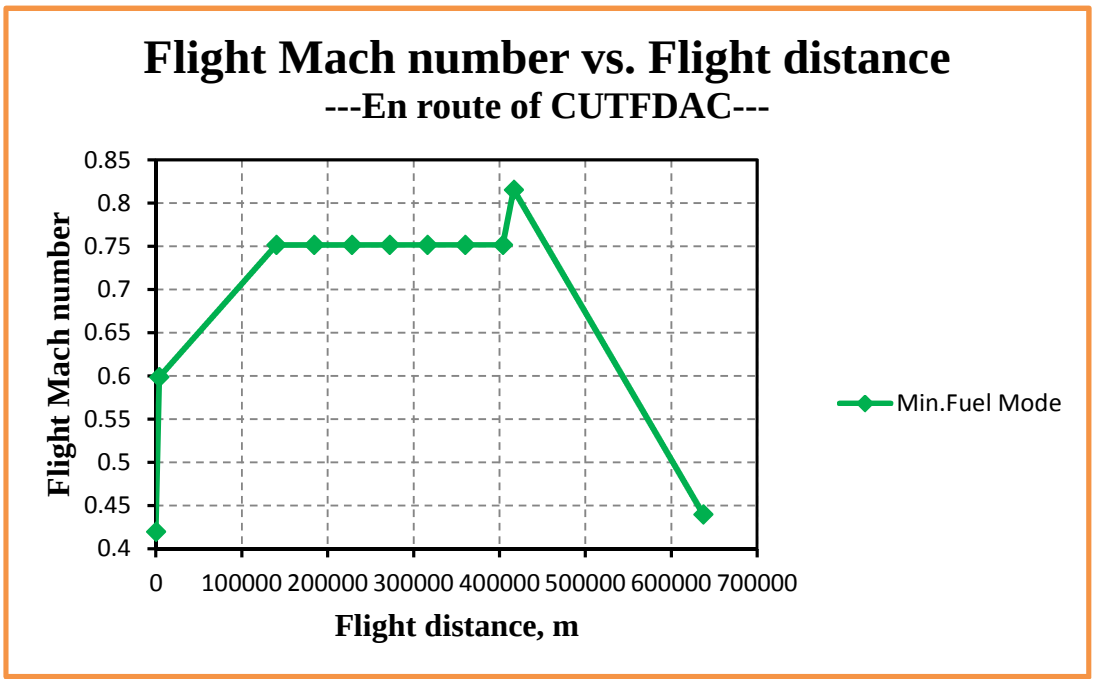

Figure 9-63 Flight Mach number vs. Flight distance – 'min. fuel' mode (CUTFDAC-en route)

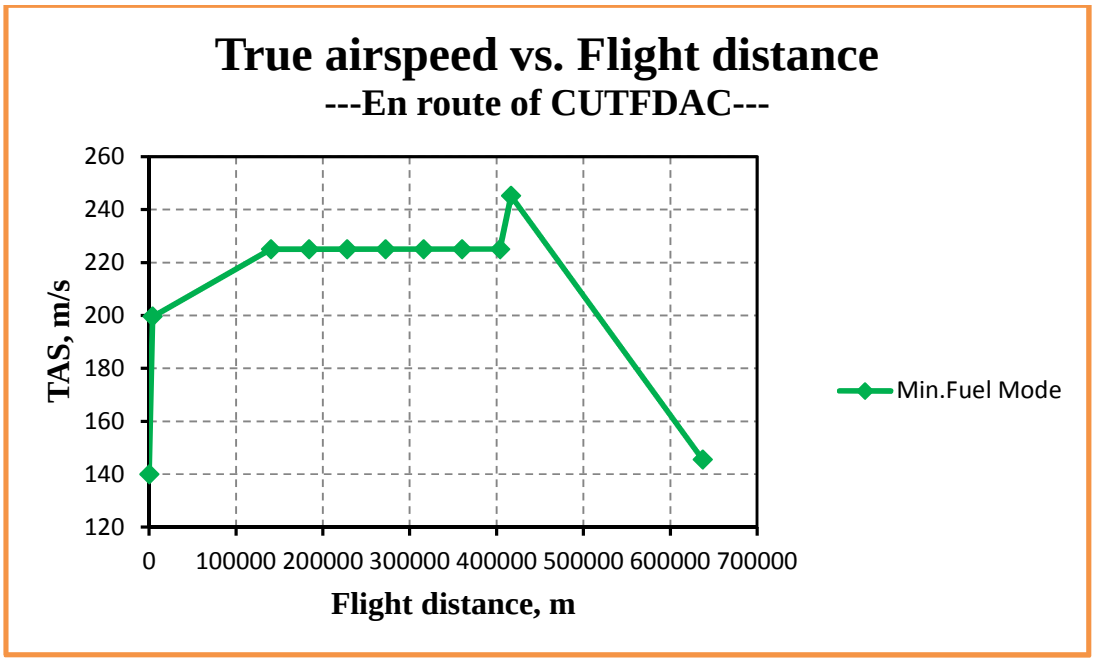

Figure 9-64 True airspeed vs. Flight distance – 'min. fuel' mode (CUTFDAC-en route)

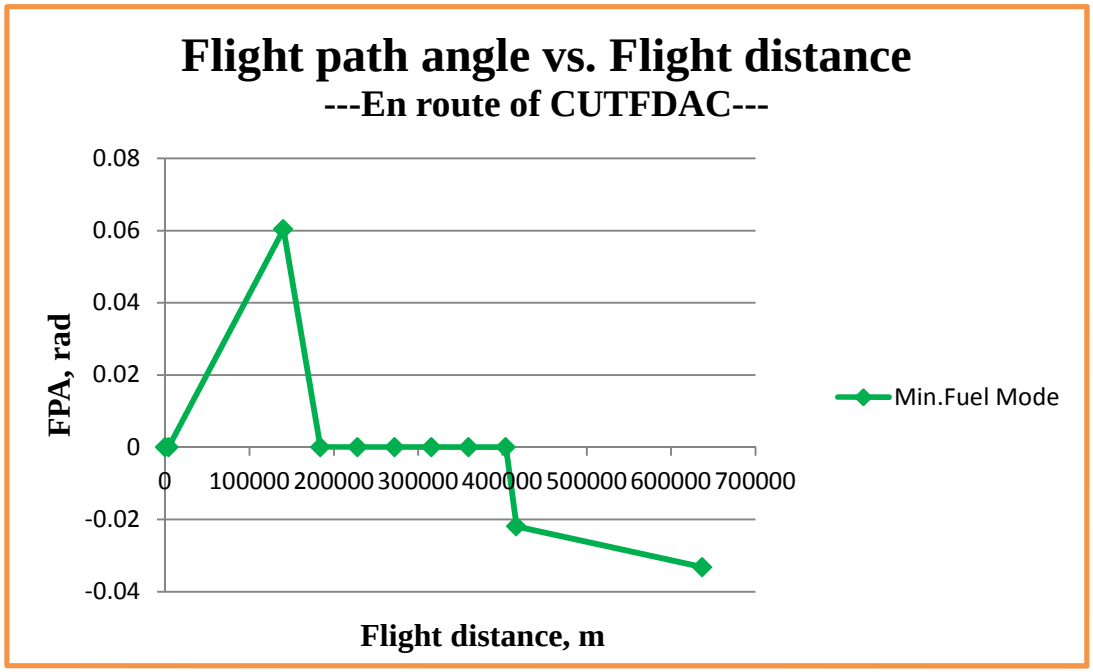

Figure 9-65 Flight path angle vs. Flight distance – 'min. fuel' mode (CUTFDAC-en route)

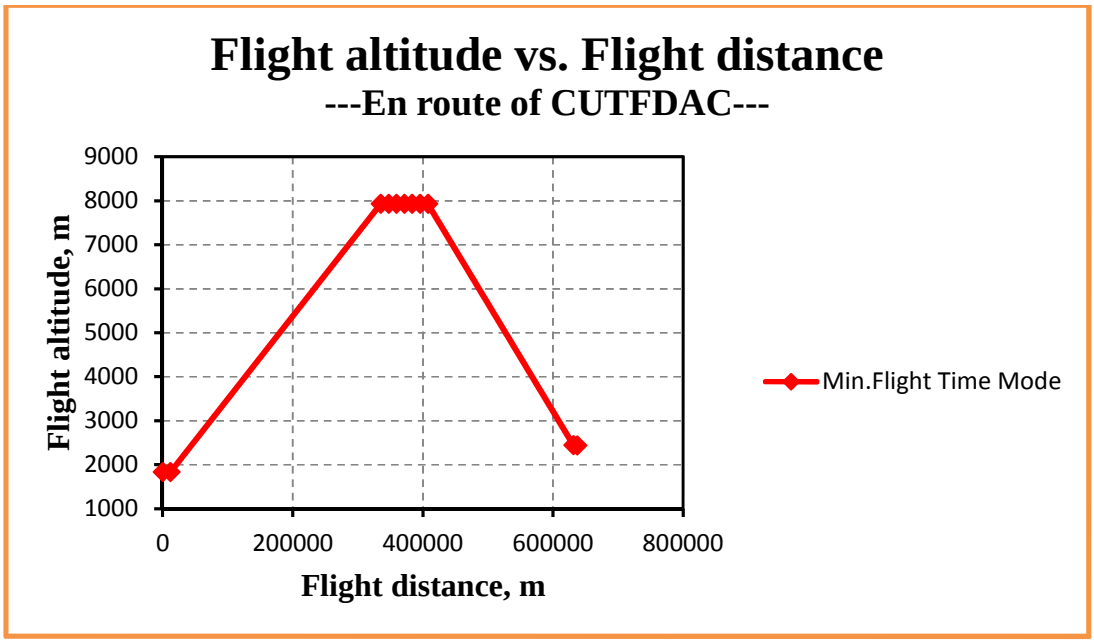

Figure 9-66 Flight altitude vs. Flight distance – 'min. flight time' mode (CUTFDAC-en route)

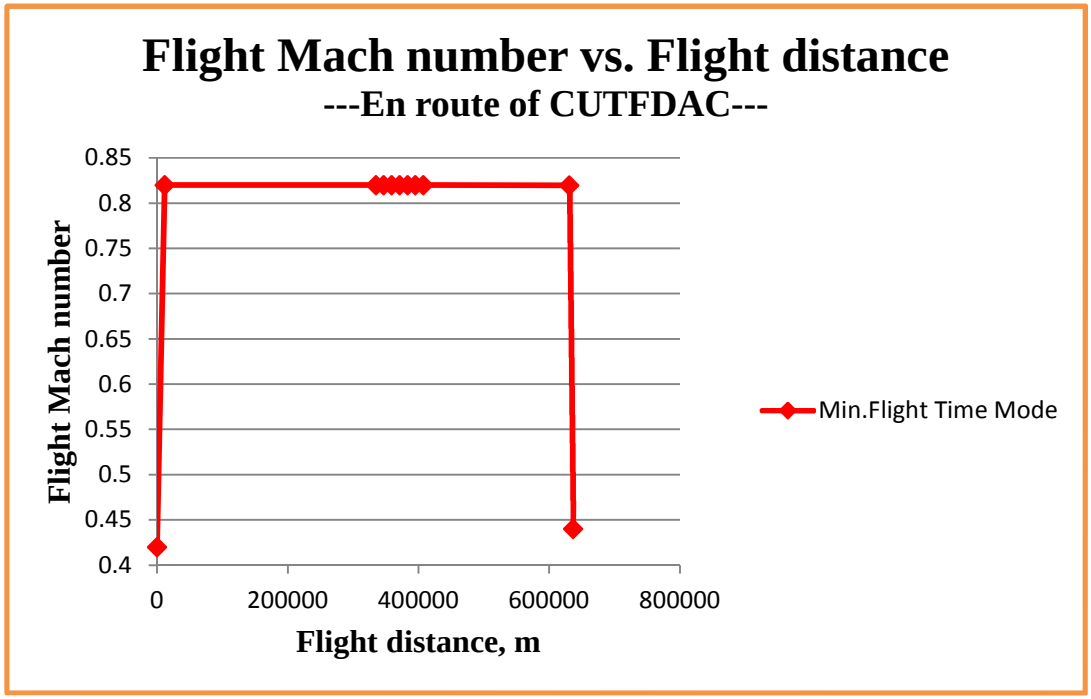

Figure 9-67 Flight Mach number vs. Flight distance – 'min. flight time' mode (CUTFDAC-en route)

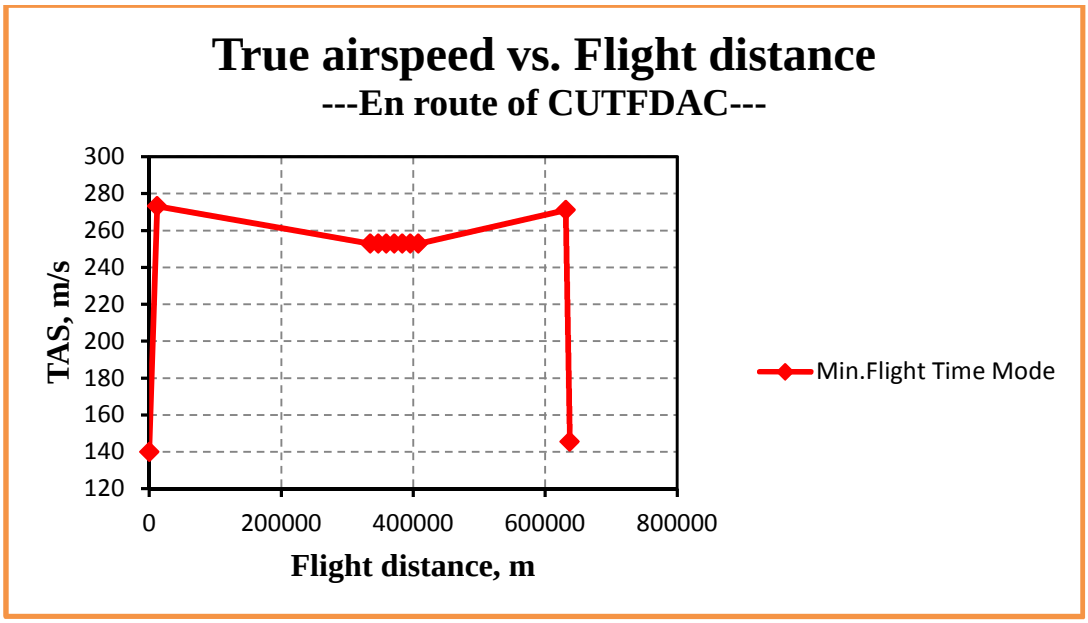

Figure 9-68 True airspeed vs. Flight distance – 'min. flight time' mode (CUTFDAC-en route)

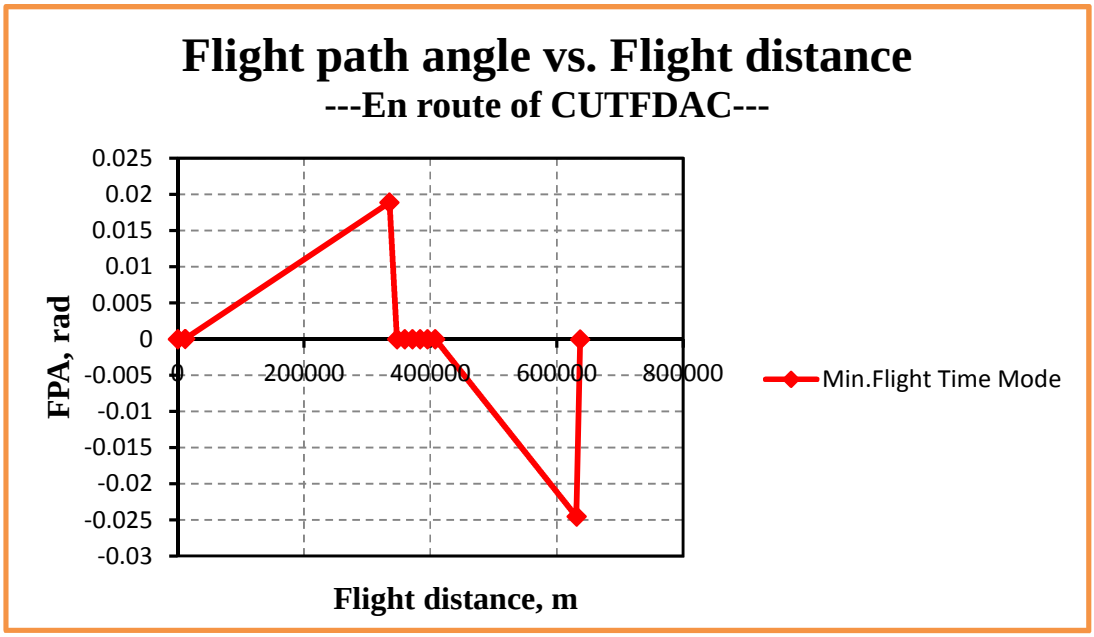

Figure 9-69 Flight path angle vs. Flight distance – 'min. flight time' mode (CUTFDAC-en route)

Table 9-34 Overall performance of two typical flight trajectories (CUTFDAC-en route)

	Fuel burnt	Flight time	CO emission	CO_2 emission	H_2O emission	UHC emission	NOx emission
	(kg)	(s)	(g)	(g)	(g)	(g)	(g)
Min. Fuel Mode	2098.53	3020.51	7571.15	6624013.66	2598401.20	296.97	26522.36
Min. Flight Time Mode	3040.71	2454.41	1760.07	9598013.85	3765011.97	100.33	53652.68
Δ	942.18	-566.09	-5811.08	2974000.19	1166610.77	-196.64	27130.31
δ	44.90%	-18.74%	-76.75%	44.90%	44.90%	-66.22%	102.29%

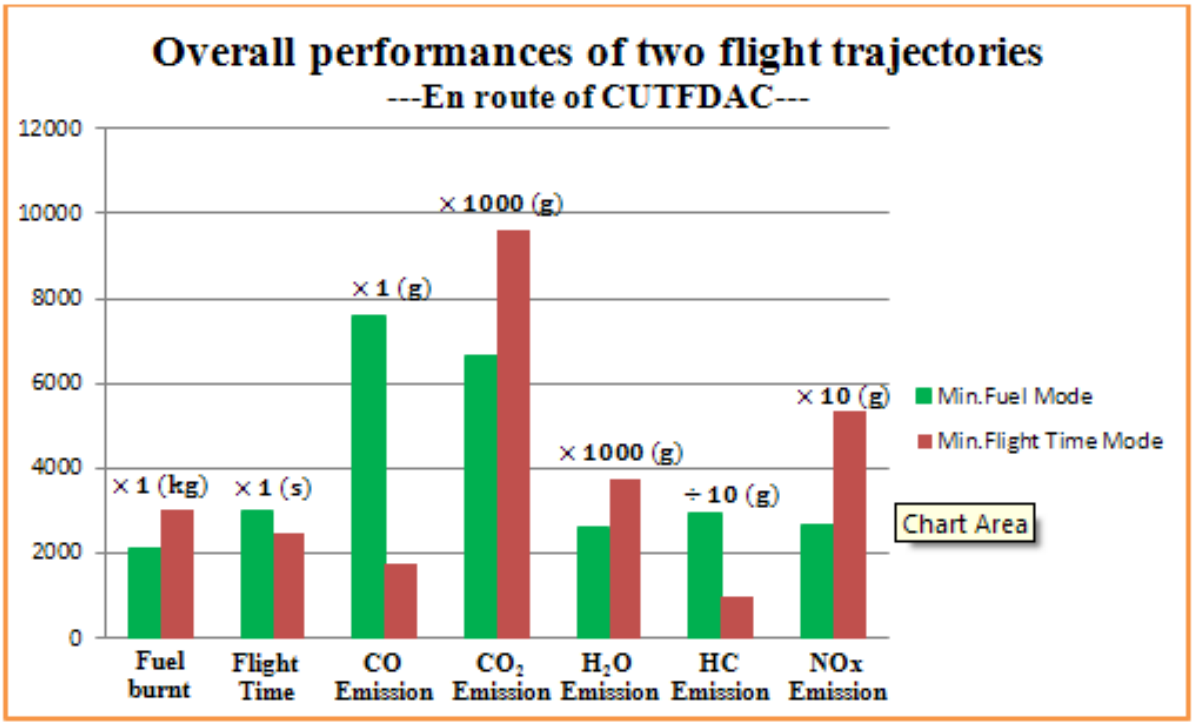

Figure 9-70 Overall performance of two typical flight trajectories (CUTFDAC-en route)

Table 9-35 Parameter segment distributions of 'Min. Fuel Consumption' mode (part) (CUTFDAC-en route)

Segment	Fn	TET	EINOx	Fuel burnt	Flight time	CO_2 emission	H_2O emission	NOx emission
	(N)	(K)	(g/kg fuel)	(kg)	(s)	(g)	(g)	(g)
1	69179.52	1462.59	22.13	48.37	23.30	152676.08	59890.23	1070.63
2	34906.93	1321.39	16.29	740.03	641.50	2335906.97	916306.00	12052.22
3	29634.03	1393.16	14.94	193.03	195.65	609293.64	239007.56	2883.22
4	18621.90	1207.46	10.83	121.96	195.47	384952.94	151005.45	1320.64
5	18596.85	1207.08	10.82	121.82	195.47	384512.40	150832.64	1317.97
6	18571.88	1206.71	10.81	121.68	195.47	384073.09	150660.31	1315.33
7	18546.98	1206.34	10.80	121.54	195.47	383630.08	150486.54	1312.67
8	18522.17	1205.97	10.79	121.40	195.47	383190.77	150314.21	1310.04
9	21733.73	1255.81	12.28	39.36	53.50	124229.81	48731.62	483.48
10	8968.21	1030.05	7.36	469.36	1129.20	1481547.88	581166.64	3456.16

Table 9-36 Parameter segment distributions of 'Min. Flight Time' mode' (part) (CUTFDAC-en route)

Segment	Fn	TET	EINOx	Fuel burnt	Flight time	CO_2 emission	H_2O emission	NOx emission
	(N)	(K)	(g/kg fuel)	(kg)	(s)	(g)	(g)	(g)
1	71513.75	1499.82	24.17	134.70	57.16	425194.36	166790.95	3256.11
2	36136.85	1344.59	18.61	1702.71	1228.73	5374589.55	2108289.72	31693.79
3	26340.39	1288.45	14.75	45.72	47.84	144302.03	56605.34	674.15
4	22937.21	1248.57	13.64	40.66	47.84	128336.09	50342.39	554.39
5	22932.90	1248.51	13.63	40.65	47.84	128316.46	50334.69	554.24
6	22928.60	1248.46	13.63	40.65	47.84	128296.53	50326.87	554.10
7	22924.30	1248.41	13.63	40.64	47.84	128275.99	50318.81	553.95
8	22920.00	1248.36	13.63	40.63	47.84	128255.76	50310.87	553.81
9	27480.92	1270.28	16.10	936.06	853.40	2954658.08	1159023.44	15068.29
10	12922.19	1090.46	10.37	18.31	28.08	57789.00	22668.88	189.86

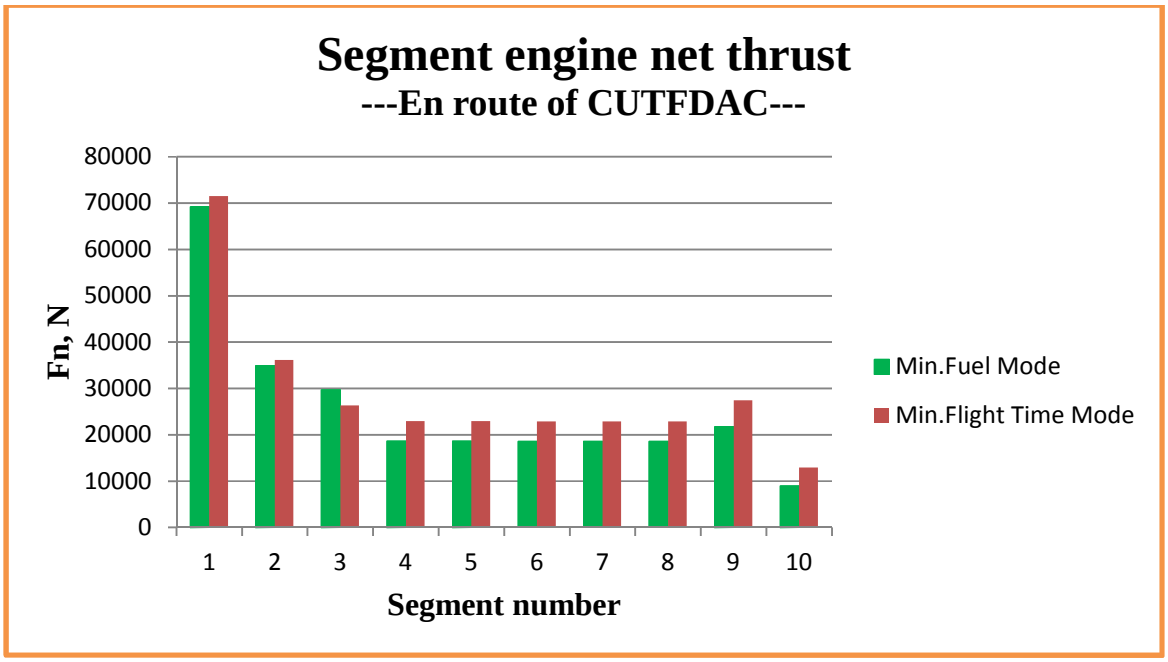

Figure 9-71 Segment engine net thrust (CUTFDAC-en route)

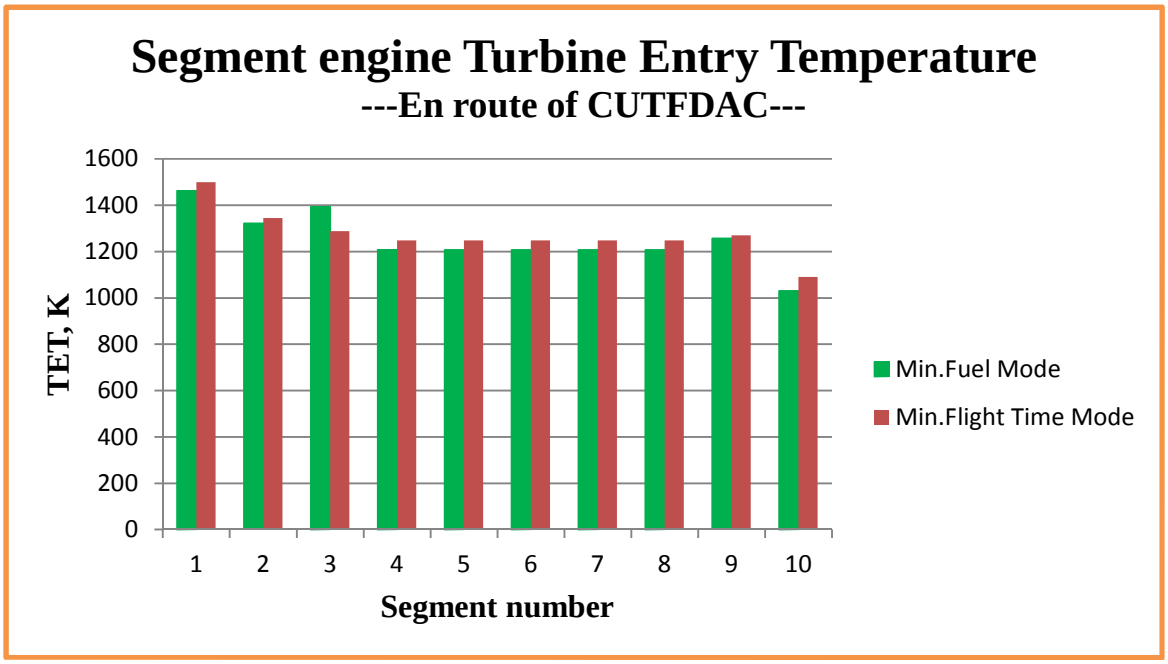

Figure 9-72 Segment engine turbine entry temperature (CUTFDAC-en route)

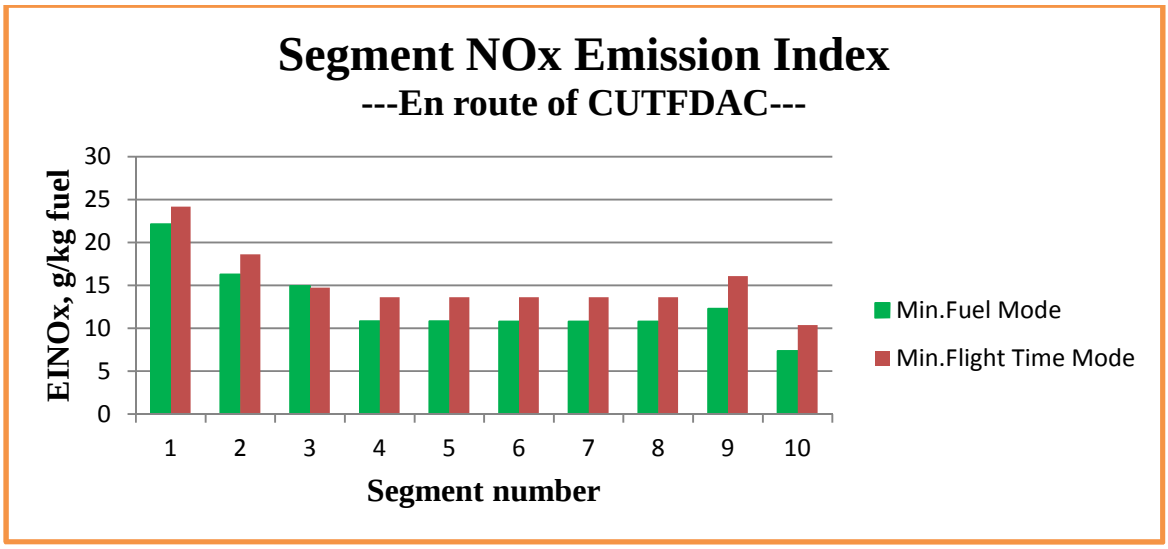

Figure 9-73 Segment NOx emission index (CUTFDAC-en route)

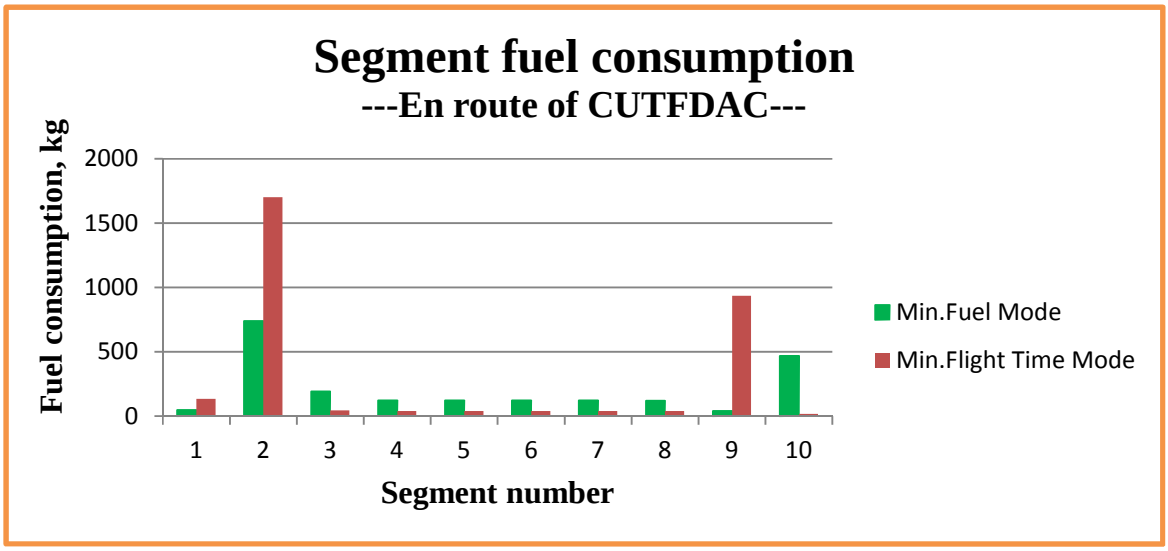

Figure 9-74 Segment fuel consumption (CUTFDAC-en route)

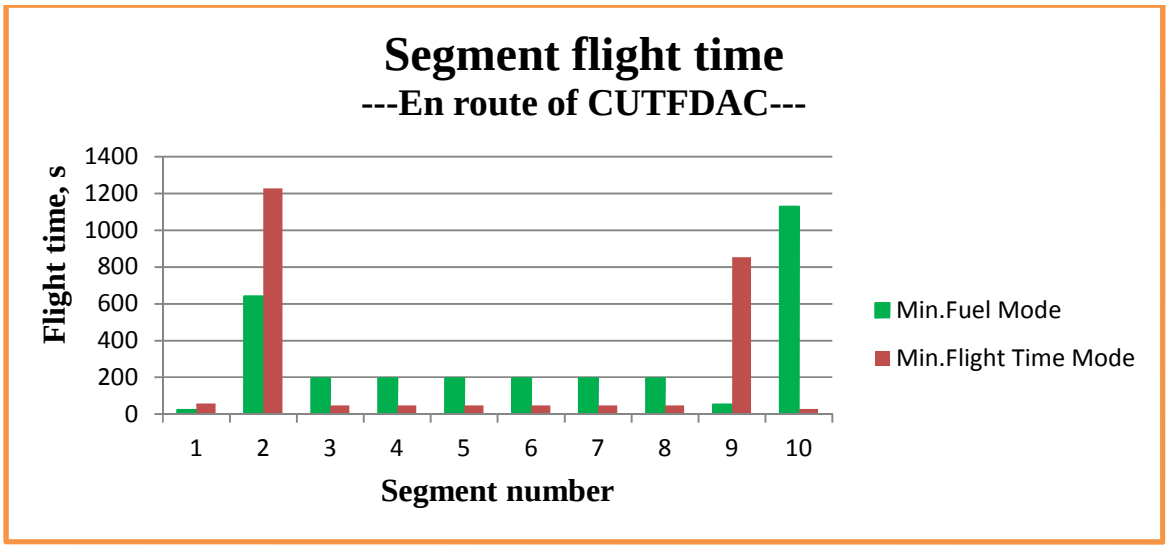

Figure 9-75 Segment flight time (CUTFDAC-en route)

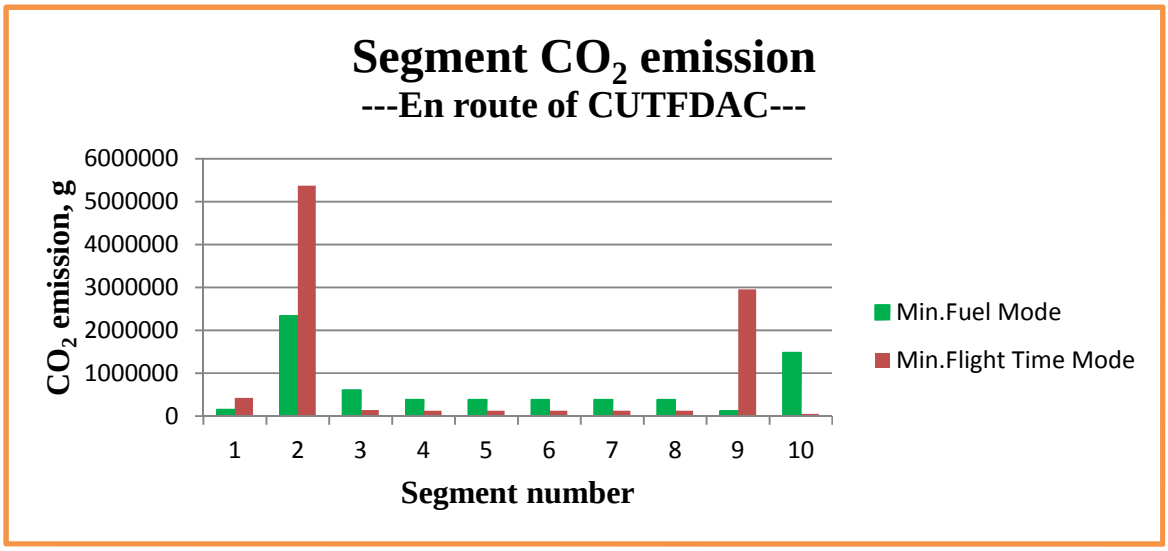

Figure 9-76 Segment CO_2 emission (CUTFDAC-en route)

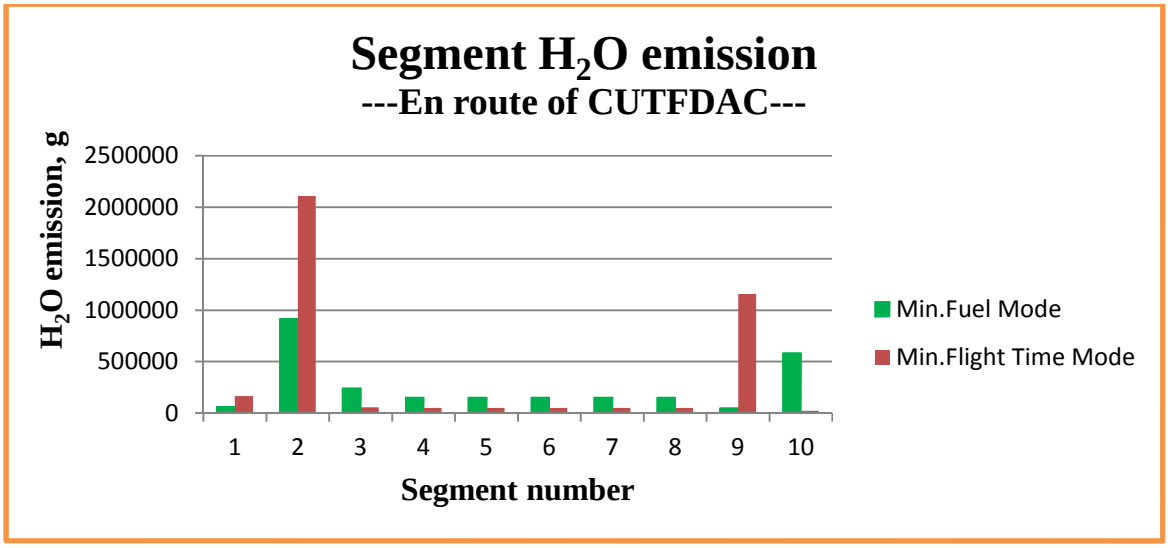

Figure 9-77 Segment H_2O emission (CUTFDAC-en route)

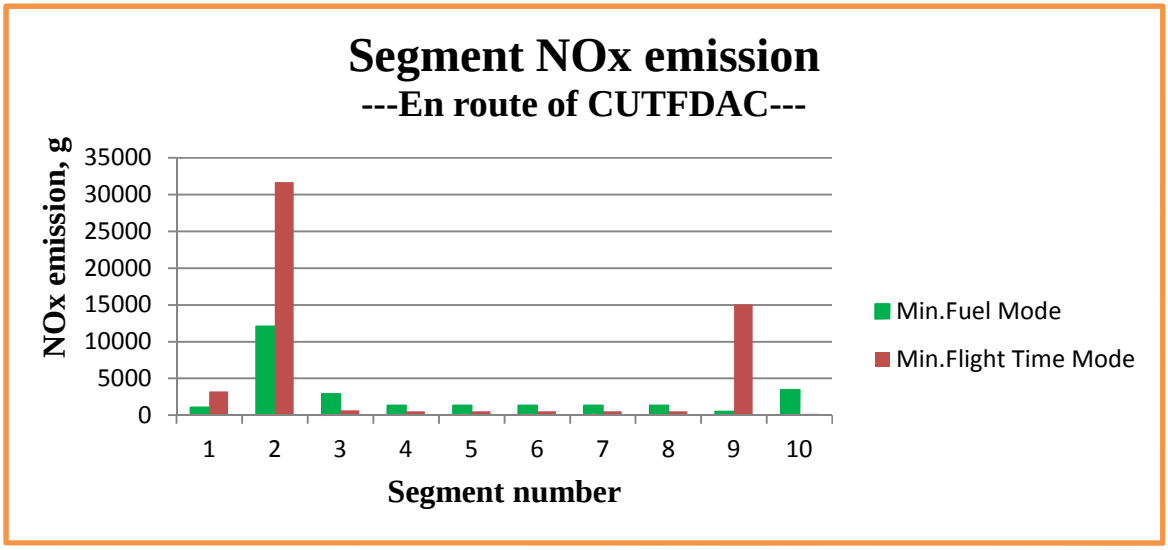

Figure 9-78 Segment NOx emission (CUTFDAC-en route)

As for the en route flight of CUTFDAC (Cranfield University Turbofan-Driven Aircraft), the following points can be observed and summarised:

1) According to the obtained plot of normalised Pareto area and the Pareto front line shown respectively in Figures 9-60 and 9-61, it can be inferred that the convergence of this optimised process has been basically achieved after the iteration of 400 generations (totally 67817 evaluations) listed in Table 9-30, that

is, a set of optimum solutions which are unique and not dominant over each other have been achieved with different trade-offs between two objectives – fuel consumption and flight time.

2) From Table 9-30, it can be found that the total time cost paid for this optimisation process with the iteration of 400 generations (totally 67817 evaluations) is 6 hours 42 minutes 41 seconds, therefore, on average, 60.4 seconds/ generation, or 0.36 seconds/ evaluation.
3) Table 9-32 and Figures 9-62 to 9-65 highlight the flight trajectory optimised for the flight mode (or purpose) of minimum fuel consumption and described through horizontal flight distance X, flight altitude Z, flight Mach number, true airspeed and flight path angle. The entire en route flight trajectory comprises ten flight segments, and according to the optimised results, when CUTFDAC flies at the 1st segment, the flight style of level flight and acceleration will be adopted, namely, the flight altitude will be kept at 1828.8 m, same as that value given by ATC at the starting point of the whole en route flight phase, but the flight Mach number will be increased from the originally given 0.42 to 0.60 and correspondingly the true airspeed will also go up to nearly 200 m/s from the initial 139.94 m/s, and this flight segment will cover the horizontal flight distance of 3954.34 m (i.e., nearly 4 km); When the flight enters into the 2nd segment, the excess propulsive power of this aircraft will be used to increase both its potential energy and kinetic energy, i.e., climb and acceleration. As a result, within the horizontal flight distance of around 136 km, CUTFDAC will climb to 10050.75 m and increase its flight Mach number and TAS respectively to 0.75 and 225.02 m/s. Naturally, the flight path angle of CUTFDAC will also witness a large increase (from nearly zero radian to 0.0604 radians); During the following six flight segments (i.e., from the 3rd segment to the 8th segment), CUTFDAC will go through the cruise flight with constant altitude and constant flight Mach number, that is, the flight altitude will be kept at 10050.75 m, the flight Mach number and TAS kept respectively at 0.75 (the lower-boundary value of this optimisation variable) and 225.02 m/s, and the FPA will remain as zero radian. The whole cruise flight will last 263904.84 m (i.e., around 264 km); From the 9th segment, the aircraft starts to descend. According to the optimised

results, in this flight segment, CUTFDAC will fly the horizontal distance of around 12.6 km with the flight altitude reduced to 9774.85 m from the previous cruise altitude 10050.75 m, however on the other hand, the flight Mach number will surprisingly rise to 0.82 from its cruise value of 0.75 (correspondingly, the TAS increased to 245.16 m/s), that is, the flight style of descent and acceleration will be required in this segment. So far, no good explanation to this phenomenon has been achieved and more investigation about it will be implemented in future work. In addition, during this segment, the FPA of this aircraft will also be changed to a negative value (-0.0219 radians) from its cruise value of zero radian, and certainly it is the natural result of aircraft descent; The last segment (i.e., the 10^{th} segment) will be a common flight segment with the decreases in both flight altitude and flight speeds (flight altitude and flight Mach number will be respectively reduced to 2438.4 m and 0.44 required by ATC, and correspondingly the TAS will also be decreased to 145.55 m/s). The last segment will cover the horizontal flight distance of 220519.17 m (i.e., around 220 km).

4) The optimised trajectory achieved for the flight mode (or purpose) of minimum flight time is expressed in Table 9-33 and Figures 9-66 to 9-69. These optimised results show that when the aircraft of CUTFDAC starts its en route flight (i.e., flying in the 1^{st} segment), the flight style of level flight and acceleration will be applied first, that is, the flight altitude will be kept at around 1829 m while the flight Mach number will increase quickly and directly from the initially given value of 0.42 by ATC to the maximum possible value 0.82 set in this case study and correspondingly the value of TAS will also rise from 139.94 m/s to 273.21 m/s. This segment will cover the horizontal flight distance of nearly 12 km; The following 2^{nd} segment will witness the increase in flight altitude (from around 1829 m to 7924.8 m which is the minimum possible value set for cruise flight in this case study) with the constant flight Mach number (Mach=0.82). Certainly, the TAS of the aircraft will go down naturally (to 252.89 m/s) because of the higher flight altitude hence the lower ambient temperature and the lower speed of sound. The flight path angle in this segment will also have a large increase from the previous nearly zero radian to 0.0189 radians. In light of the optimised

results, this climb segment will be completed within the horizontal flight distance of around 323 km; During the next six flight segments which span from the 3rd segment to the 8th segment totally covering the horizontal flight distance of 72590.82 m (around 73 km), CUTFDAC will experience the cruise flight with maximum possible flight Mach number 0.82 and minimum possible flight altitude 7924.8 m. In the cruise flight, the TAS of aircraft will amount to 252.89 m/s and the FPA will remain zero radian reasonably; When the flight enters into the 9th segment with the horizontal flight distance of around 223 km, the flight style of constant-Mach descent will be used, namely, the flight Mach number will be kept at the maximum possible value 0.82 while the flight altitude will be reduced to 2438.68 m. Correspondingly, the TAS will rise up to 271.12 m/s due to the lower flight altitude and hence higher ambient temperature and the higher speed of sound, and besides the FPA will also naturally change from zero radian in previous cruise flight to a negative value (-0.0245 radians); Finally, when CUTFDAC flies during the last segment (i.e., the 10th segment), the flight style of constant-altitude deceleration (or level-flight deceleration) will be adopted, that is, the flight altitude will remain at around 2438 m while the flight Mach number will be directly decreased from the maximum possible value 0.82 to 0.44 - the value required by ATC and correspondingly the TAS of the aircraft will be also reduced to 145.55 m/s. This flight segment will cover the horizontal flight distance of 5848.47 m.

5) Based on the above trajectory descriptions, it can be found that there are significant differences between the two typical flight trajectories optimised respectively for the different flight purposes. From the point of view of minimum-time flight, the aircraft is required, in order to save the flight time, to fly at the maximum possible flight Mach number 0.82 as long time as possible, and in the meantime, to select the lowest possible cruise altitude (7924.8 m). Obviously, the requirements are reasonable and both contribute to the significant reduction in flight time because the maximum possible flight Mach number and the lowest possible flight altitude (hence higher ambient temperature and correspondingly higher speed of sound) mean the maximum possible true airspeed which the aircraft can achieve during its flight and on the other hand the

selection of the lowest possible cruise altitude also means less time spent in climb and descent flights. However, the benefit in flight-time saving is not free but with the cost of higher fuel consumption and more emissions of CO_2, H_2O and NOx because greater flight drag contributed by both higher air density and aircraft true airspeed ($D = C_D \cdot \frac{1}{2}\rho(TAS)^2 \cdot S$) needs to be overcome through engines providing greater power . In contrast to the above minimum-time flight, when CUTFDAC flying for the purpose of minimum fuel consumption, the higher flight altitude (10050.75 m) and the lowest possible flight Mach number (0.75) are selected for the cruise. The selection is also understandable because higher flight altitude and lower flight Mach number mean lower air density and aircraft true airspeed. This will result in less flight drag and correspondingly lower engine thrust requirement, and therefore the fuel consumption can be reduced.

6) Table 9-34 and Figure 9-70 further provide the comparisons of overall performance from the two typical flight modes in terms of fuel consumption, flight time and gaseous emissions. From the table and figure, it can be found that compared to the results from minimum-fuel-consumption flight, the minimum-time flight will consume 942.18 kg (or 44.90%) more fuel and produce 2974 kg (or 44.90%) more CO_2, around 1167 kg (or 44.90%) more H_2O and around 27 kg (or 102.29%) more NOx to complete this en route flight but with 566 seconds (or 18.74%) less flight time, 5.8 kg (or 76.75%) less CO emission and 197 g (or 66.22%) less UHC emission. The reason for the difference in fuel consumption has been explained in the above item 5). Emissions of CO_2 and H_2O depend on only the fuel consumption due to their almost constant emission-index values and, therefore, the increase in fuel consumption from the minimum-time flight naturally causes the increases in CO_2 and H_2O emissions and with the same percentage. The significant increase in NOx emission can be attributed to the increases in both fuel consumption and emission-index value due to the higher engine operation temperature for the minimum-time flight case. In addition, from the table and figure, it can also be found that although more fuel is consumed, the significant reductions in emissions of CO and UHC have been still achieved, which has resulted from lower emission-index values of both

pollutants when engine operates at higher power settings for the case of minimum-time flight mode.

9.2.2 CUTPDAC (Cranfield University Turboprop-Driven Aircraft)

Table 9-37 Running record of CUTPDAC-En route optimisation

1	Running start time/date	Tue Oct 23 22:45:46 BST 2012
2	Running end time/date	Sat Oct 27 14:55:20 BST 2012
3	Total running time	88 hours 9 minutes 34 seconds
4	Generation number	450
5	Total number of evaluations	72115

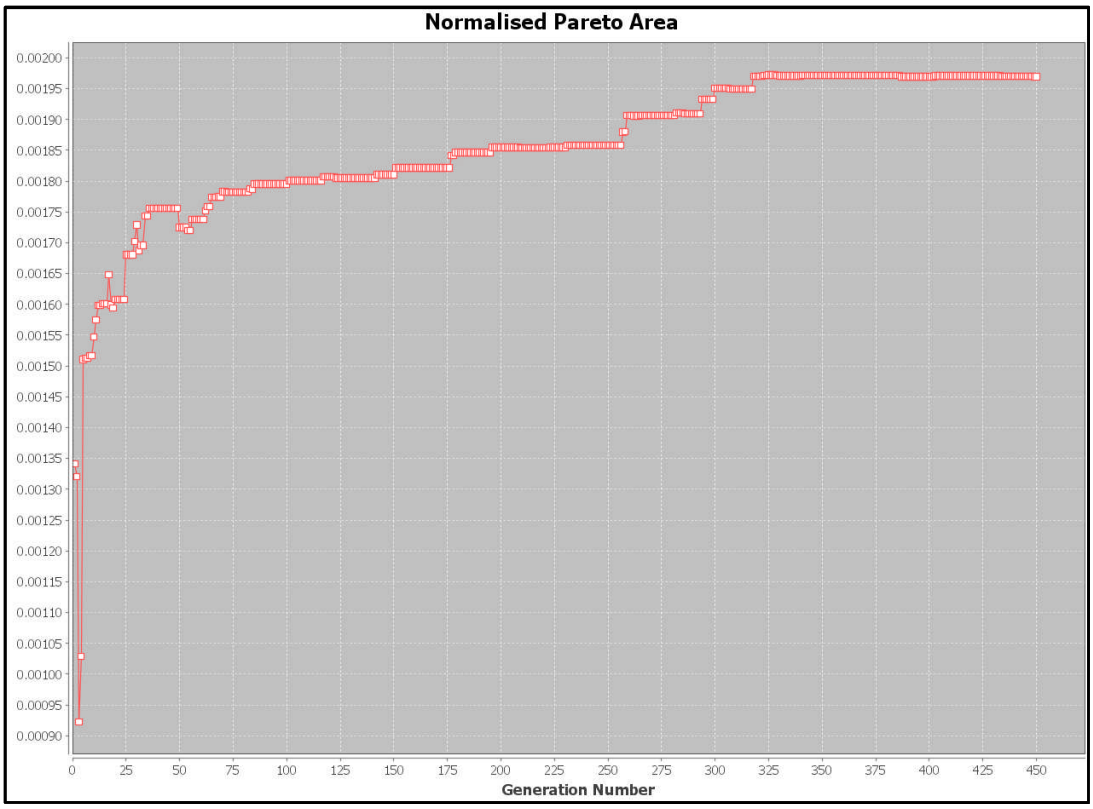

Figure 9-79 Normalised Pareto area (CUTPDAC-en route)

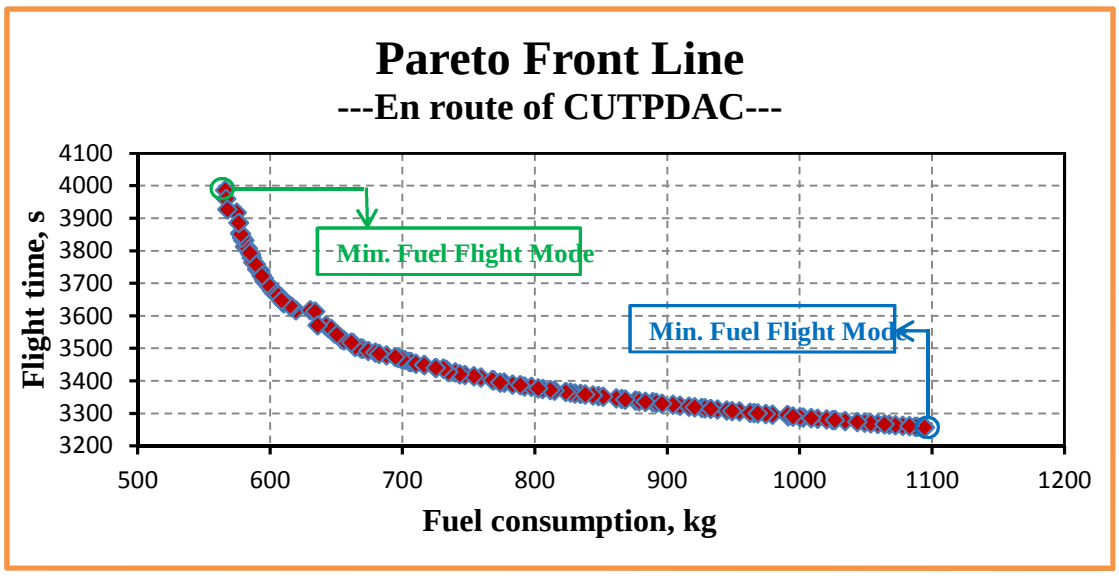

Figure 9-80 Pareto Front line (CUTPDAC-en route)

Table 9-38 Optimised results of two typical flight trajectories (CUTPDAC-en route)

		Minimum Fuel Flight Mode	Minimum Time Flight Mode
Design variables	ALT1, (m)	7569.34	1828.82
	ALT2, (m)	7589.28	4500.03
	ALT9, (m)	4177.88	2444.34
	DIS1, (m)	114078.48	5749.55
	DIS2, (m)	140327.50	334070.32
	DIS8, (m)	402000	402821.28
	DIS9, (m)	432359.51	631514.61
	MACH1, (-)	0.52	0.60
	MACH2, (-)	0.54	0.60
	MACH9, (-)	0.52	0.60
Objective functions	Fuel consumption, (kg)	566.17	1094.47
	Flight time, (s)	3985.93	3256.64
Optimisation constraints	CA21,(m)	19.94	2671.21
	CX21,(m)	26249.02	328320.77
	CX98,(m)	30359.51	228693.33
	CA89,(m)	3411.40	2055.69
	NOx, (g)	1344.43	7611.31
	CO_2, (g)	1810186.01	3506091.57

Table 9-39 Flight trajectory of 'Min. Fuel Consumption' mode (CUTPDAC-en route)

Point	X (m)	Z (m)	MACH (-)	TAS (m/s)	FPA (rad.)
0	0	1828.8	0.42	139.94	0
1	114078.48	7569.34	0.52	161.61	0.0503
2	140327.50	7589.28	0.54	166.02	7.60×10^{-4}
3	183939.59	7589.28	0.54	166.02	0
4	227551.67	7589.28	0.54	166.02	0
5	271163.75	7589.28	0.54	166.02	0
6	314775.83	7589.28	0.54	166.02	0
7	358387.92	7589.28	0.54	166.02	0
8	402000	7589.28	0.54	166.02	0
9	432359.51	4177.88	0.52	167.96	-0.1119
10	637000	2438.4	0.44	145.55	-0.0085

Table 9-40 Flight trajectory of 'Min. Flight Time' mode (CUTPDAC-en route)

Point	X (m)	Z (m)	MACH (-)	TAS (m/s)	FPA (rad.)
0	0	1828.8	0.42	139.94	0
1	5749.55	1828.82	0.60	199.92	4.00×10^{-6}
2	334070.32	4500.03	0.6	193.55	0.0081
3	345528.81	4500.03	0.6	193.55	0
4	356987.31	4500.03	0.6	193.55	0

5	368445.80	4500.03	0.6	193.55	0
6	379904.29	4500.03	0.6	193.55	0
7	391362.79	4500.03	0.6	193.55	0
8	402821.28	4500.03	0.6	193.55	0
9	631514.61	2444.34	0.60	198.46	-0.0090
10	637000	2438.4	0.44	145.55	-0.0011

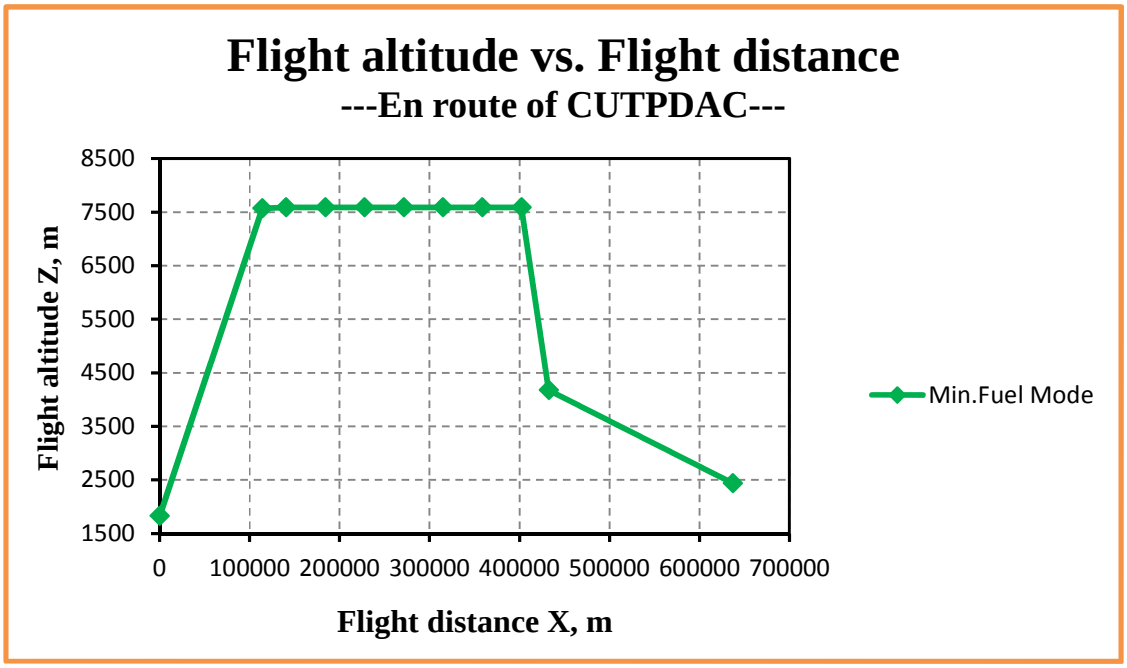

Figure 9-81 Flight altitude vs. Flight distance – 'min. fuel' mode (CUTPDAC-en route)

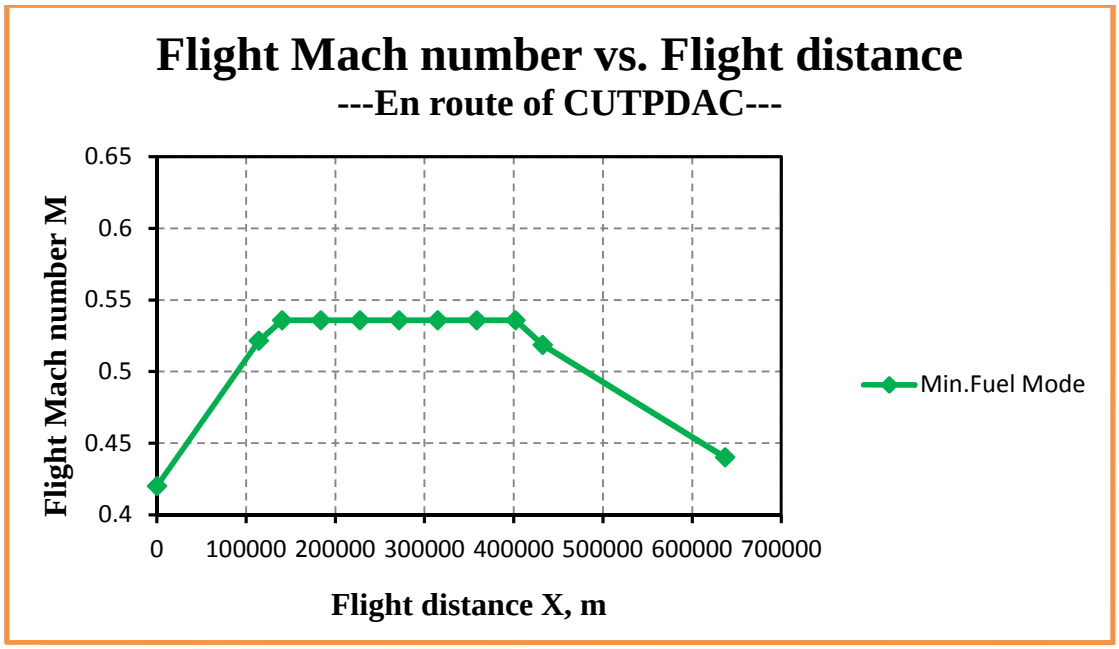

Figure 9-82 Flight Mach number vs. Flight distance – 'min. fuel' mode (CUTPDAC-en route)

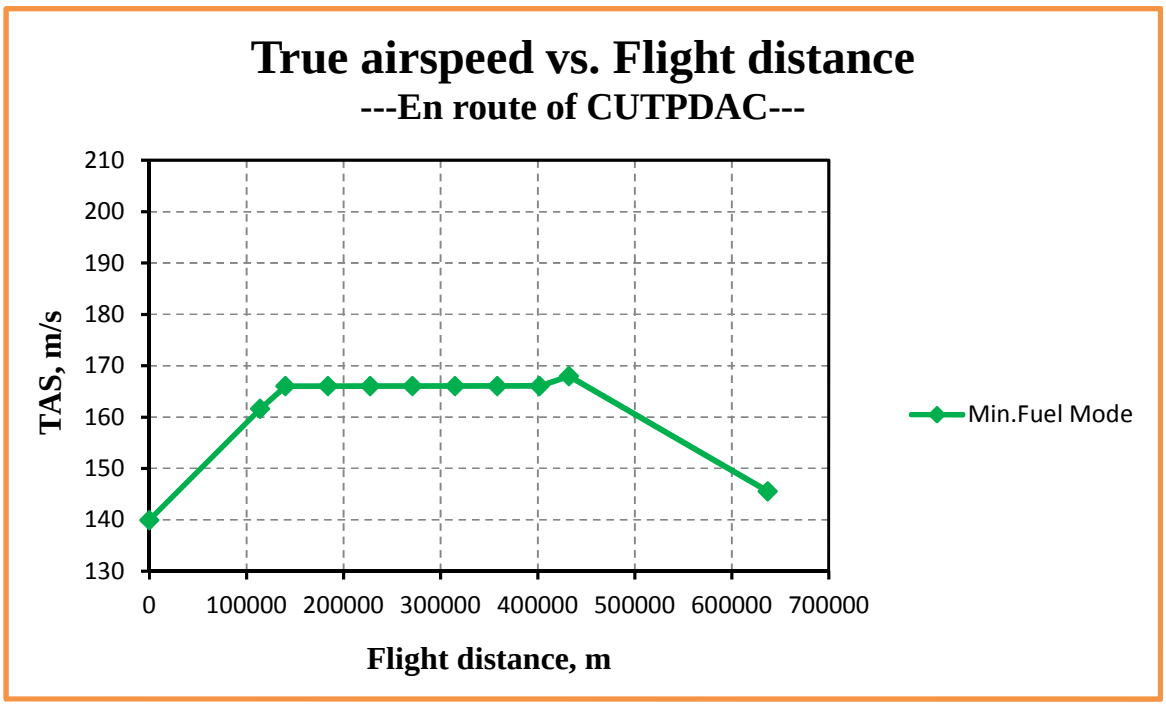

Figure 9-83 True airspeed vs. Flight distance – 'min. fuel' mode (CUTPDAC-en route)

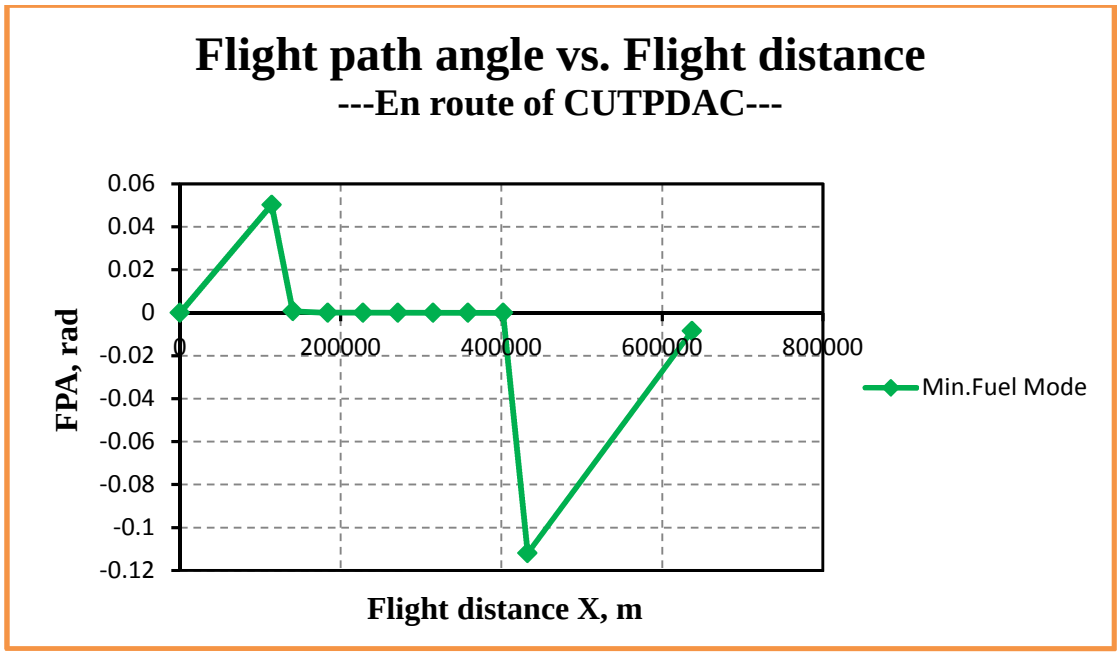

Figure 9-84 Flight path angle vs. Flight distance – 'min. fuel' mode (CUTPDAC-en route)

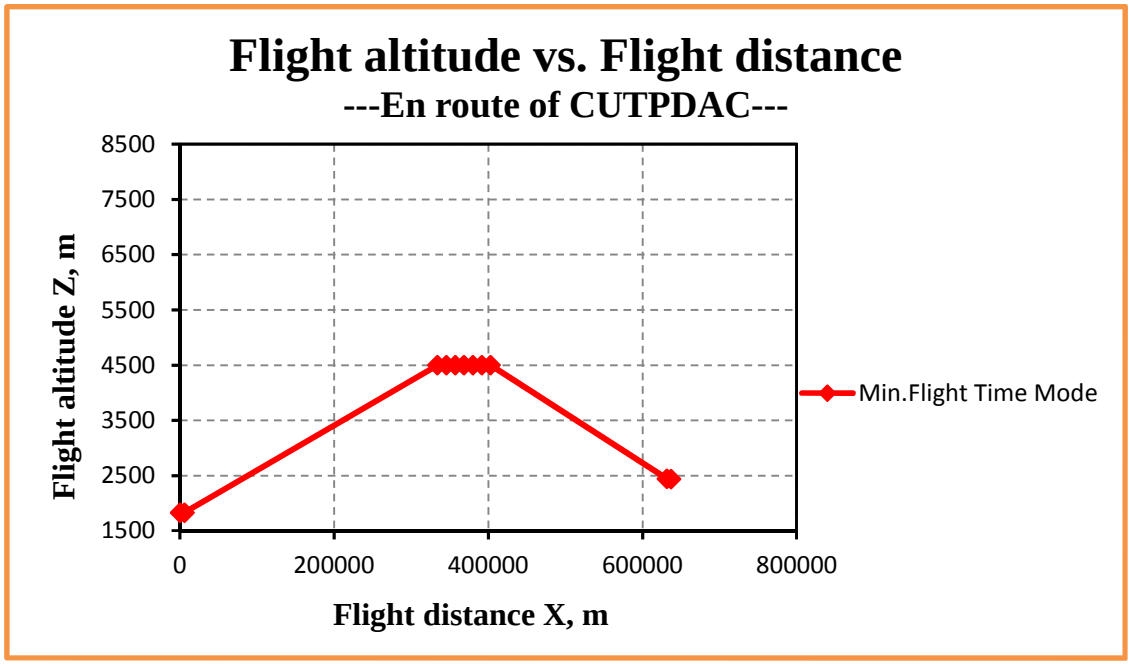

Figure 9-85 Flight altitude vs. Flight distance – 'min. flight time' mode (CUTPDAC-en route)

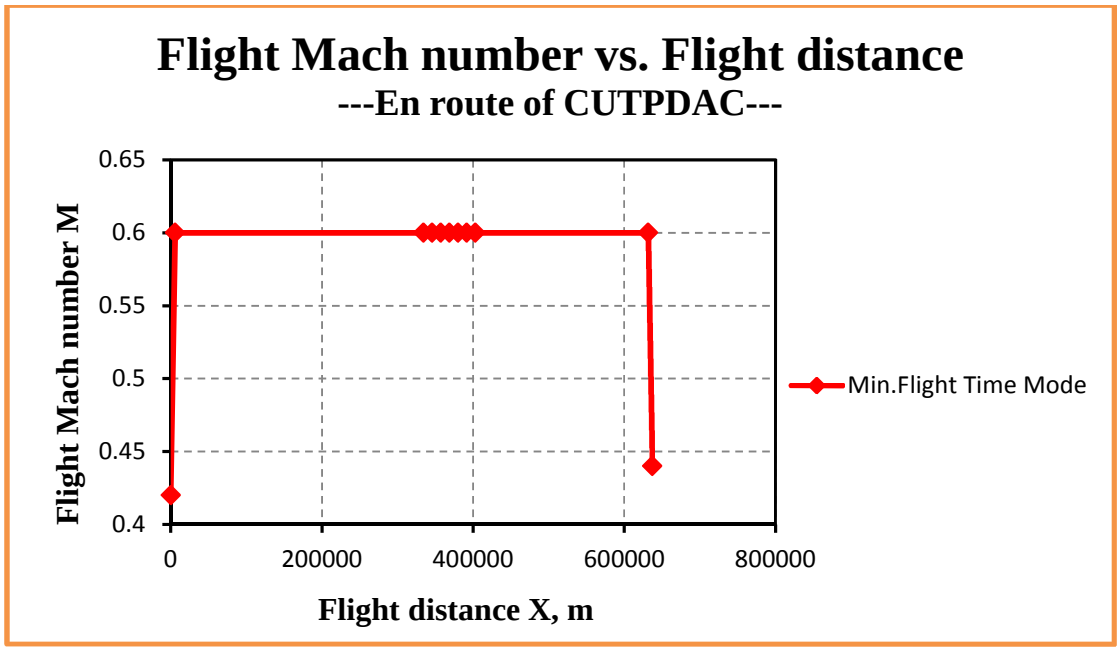

Figure 9-86 Flight Mach number vs. Flight distance – 'min. flight time' mode (CUTPDAC-en route)

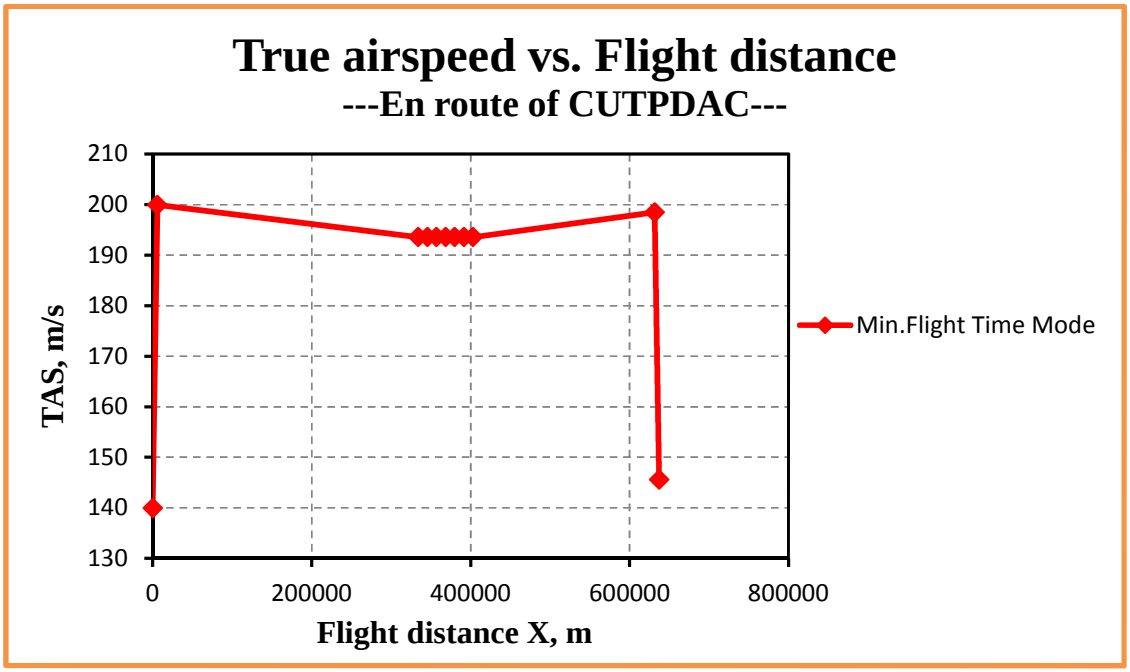

Figure 9-87 True airspeed vs. Flight distance – 'min. flight time' mode (CUTPDAC-en route)

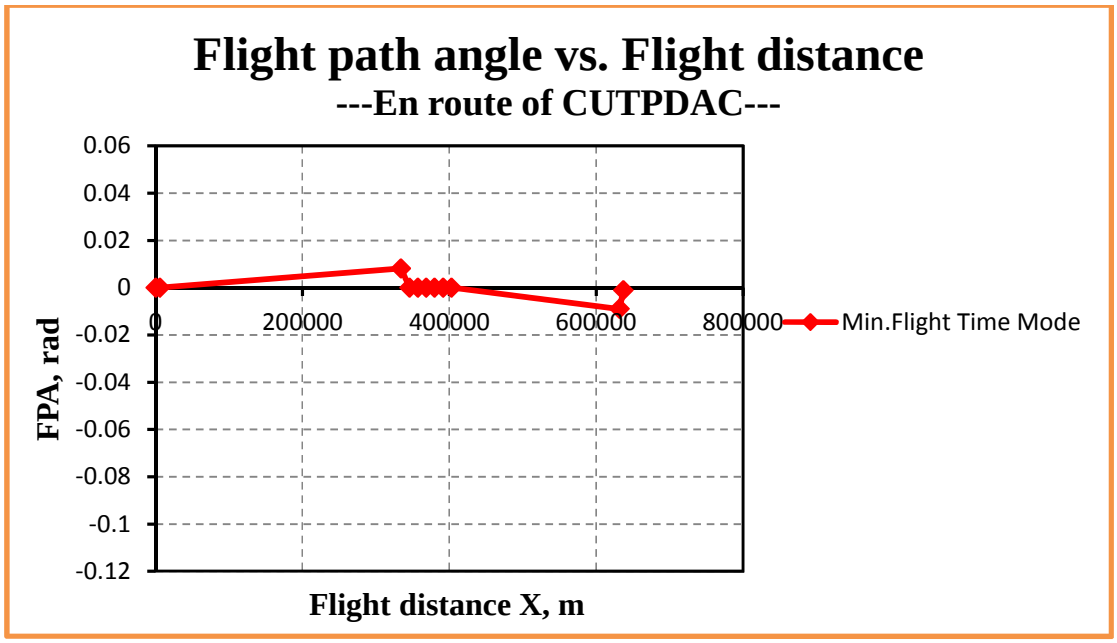

Figure 9-88 Flight path angle vs. Flight distance – 'min. flight time' mode (CUTPDAC-en route)

Table 9-41 Overall performance of two typical flight trajectories (en route-CUTPDAC)

	Fuel burnt	**Flight time**	**CO_2 emission**	**H_2O emission**	**NOx emission**
	(kg)	(s)	(g)	(g)	(g)
Min. Fuel Mode	566.17	3985.93	1810186.01	701333.90	1344.43
Min. Flight Time Mode	1094.47	3256.64	3506091.57	1363040.15	7611.31
Δ	528.30	-729.29	1695905.56	661706.25	6266.89
δ	93.31%	-18.30%	93.69%	94.35%	466.14%

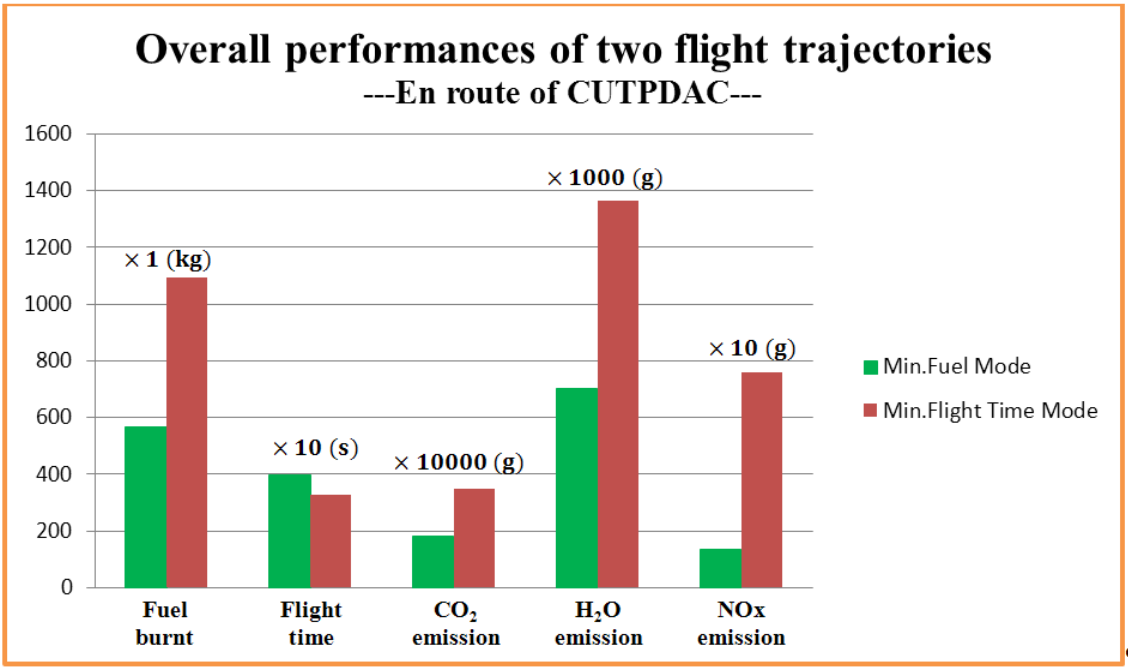

Figure 9-89 Overall performance of two typical flight trajectories (en route-CUTPDAC)

Table 9-42 Parameter segment distributions of 'Min. Fuel Consumption' mode (part) - (En route-CUTPDAC)

Segment	Fn	TET	EINOx	Fuel burnt	Flight time	CO_2 emission	H_2O emission	NOx emission
	(N)	(K)	(g/kg fuel)	(kg)	(s)	(g)	(g)	(g)
1	10081.68	1189.24	3.55	173.40	757.12	553409.29	214899.19	615.07
2	8633.18	1236.89	3.15	31.59	160.34	100569.90	39084.05	99.51
3	6308.56	1128.06	2.14	40.95	262.70	130558.29	50666.31	87.75
4	6261.88	1125.26	2.14	40.75	262.70	129919.01	50415.42	87.06
5	6256.75	1124.95	2.13	40.72	262.70	129819.18	50376.41	86.90
6	6251.64	1124.66	2.13	40.69	262.70	129731.04	50341.97	86.77
7	6246.55	1124.40	2.13	40.66	262.70	129641.05	50306.87	86.64

8	6241.47	1124.03	2.13	40.63	262.70	129524.67	50261.38	86.46
9	1118.07	834.18	0.78	12.98	182.38	41781.63	16079.84	10.13
10	936.39	825.59	0.95	103.79	1309.90	335231.93	128902.47	98.14

Table 9-43 Parameter segment distributions of 'Min. Flight Time' mode' (part) (En route-CUTPDAC)

Segment	**Fn**	**TET**	**EINOx**	**Fuel burnt**	**Flight time**	**CO_2 emission**	**H_2O emission**	**NOx emission**
	(N)	(K)	(g/kg fuel)	(kg)	(s)	(g)	(g)	(g)
1	20334.12	1447.79	17.82	16.60	33.83	53159.78	20692.63	295.77
2	12495.98	1317.70	7.49	597.23	1668.90	1913876.83	744204.79	4473.42
3	10648.34	1282.27	5.59	17.58	59.20	56170.30	21834.87	98.29
4	10211.38	1264.11	5.21	16.98	59.20	54267.11	21090.51	88.49
5	10210.60	1264.07	5.21	16.98	59.20	54263.36	21089.04	88.48
6	10209.82	1264.04	5.21	16.98	59.20	54259.59	21087.57	88.47
7	10209.04	1264.01	5.21	16.97	59.20	54255.83	21086.09	88.44
8	10208.26	1263.92	5.20	16.98	59.20	54259.54	21087.56	88.30
9	11123.23	1275.48	6.13	374.73	1166.80	1200435.79	466572.59	2297.23
10	547.61	887.15	1.28	3.45	31.89	11143.43	4294.50	4.42

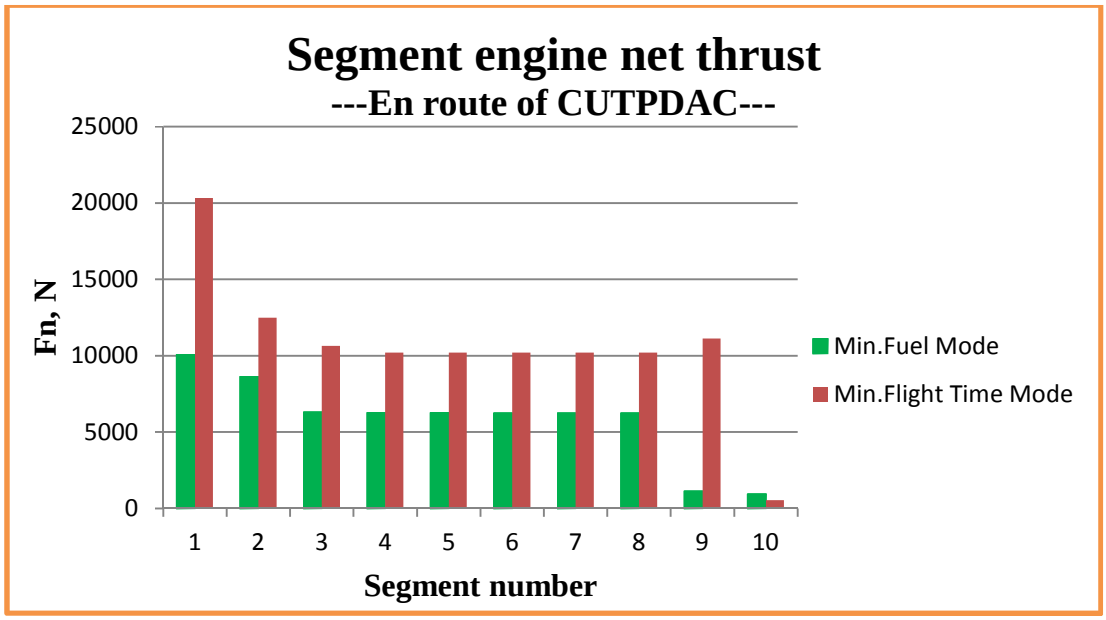

Figure 9-90 Segment engine net thrust (en route-CUTPDAC)

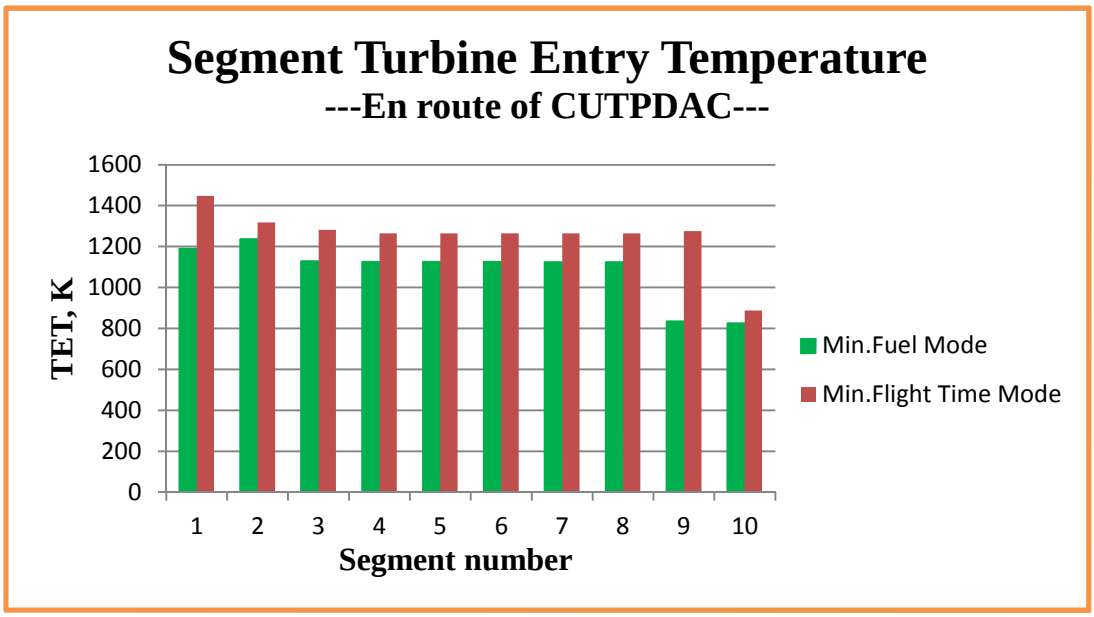

Figure 9-91 Segment engine turbine entry temperature (en route-CUTPDAC)

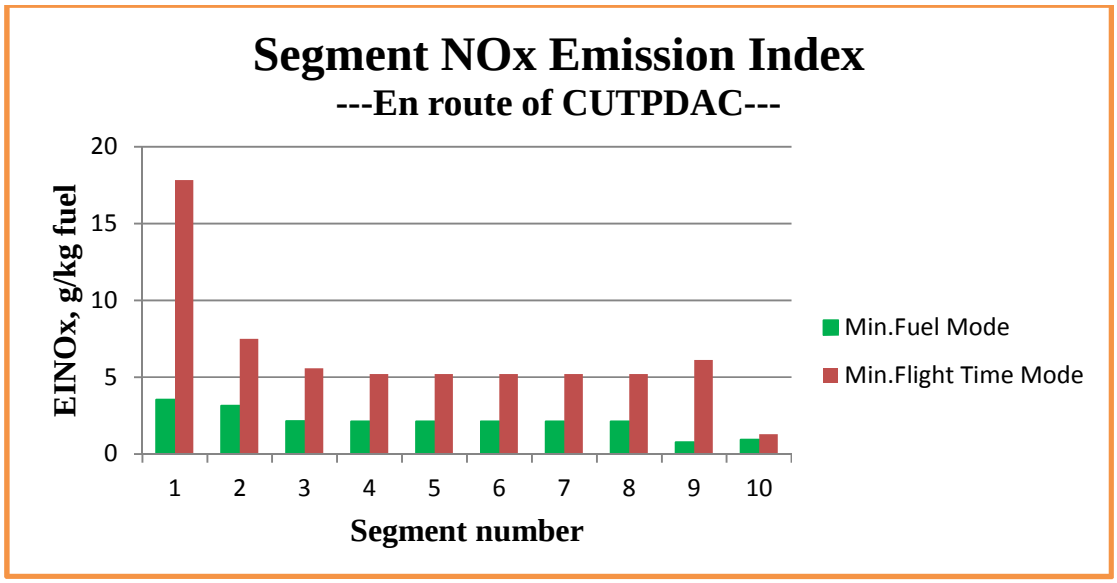

Figure 9-92 Segment NOx emission index (en route-CUTPDAC)

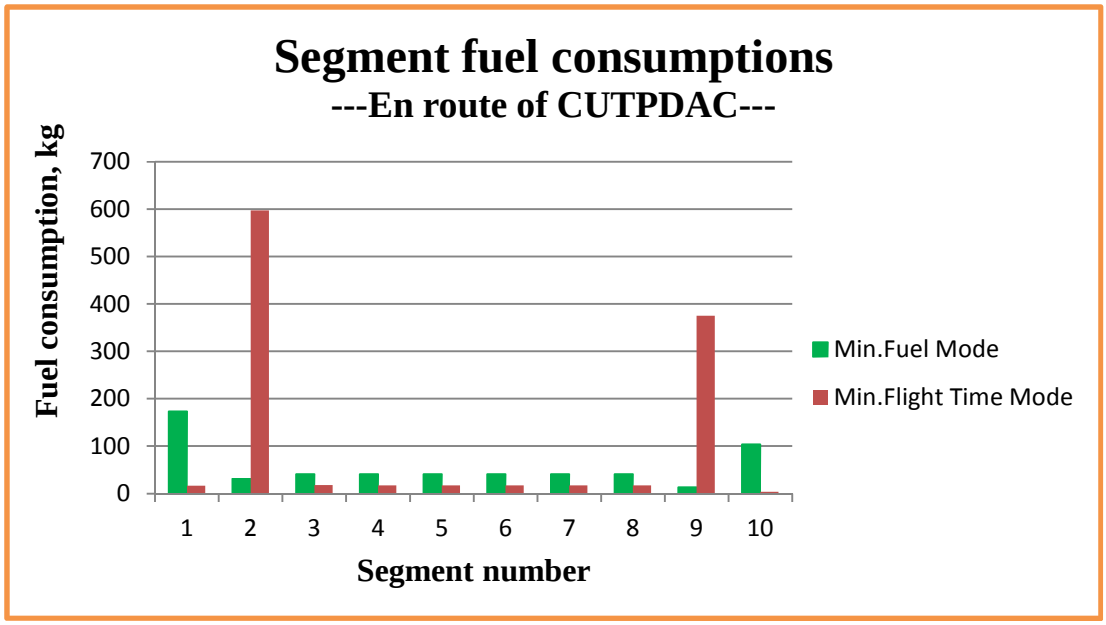

Figure 9-93 Segment fuel consumption (en route-CUTPDAC)

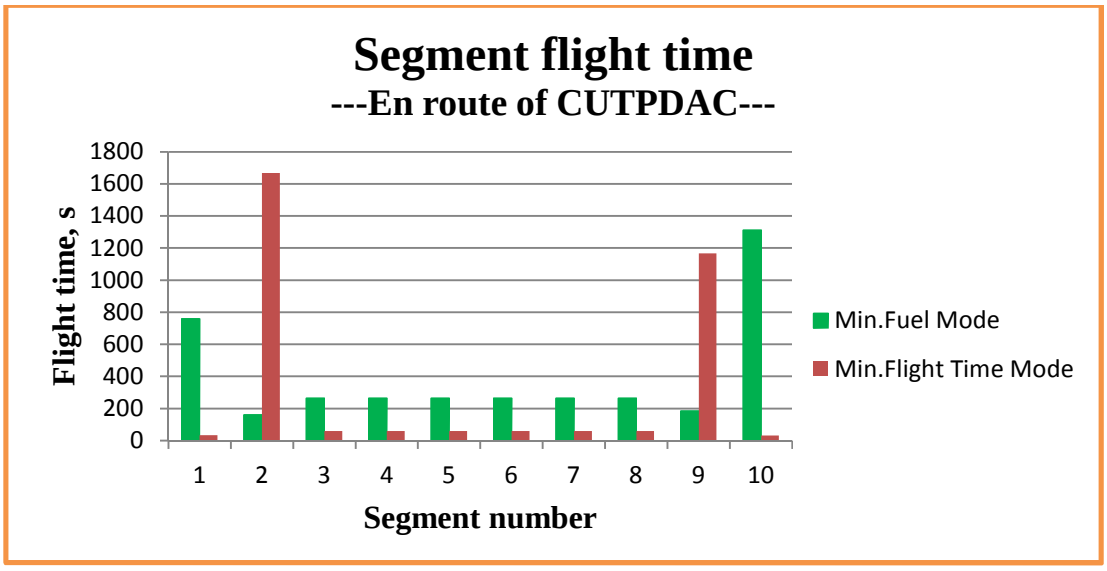

Figure 9-94 Segment flight time (en route-CUTPDAC)

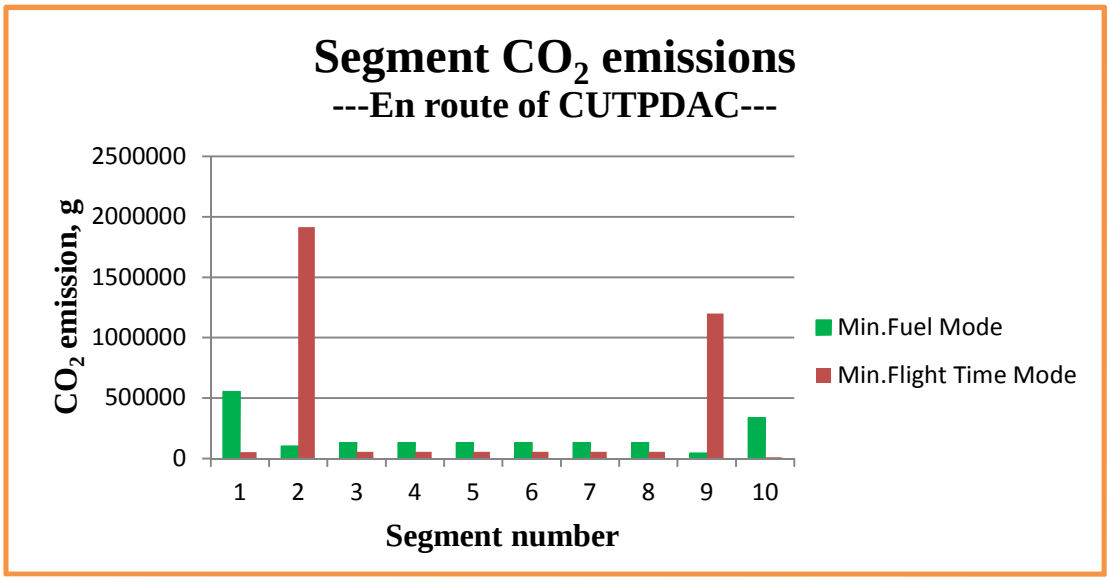

Figure 9-95 Segment CO_2 emission (en route-CUTPDAC)

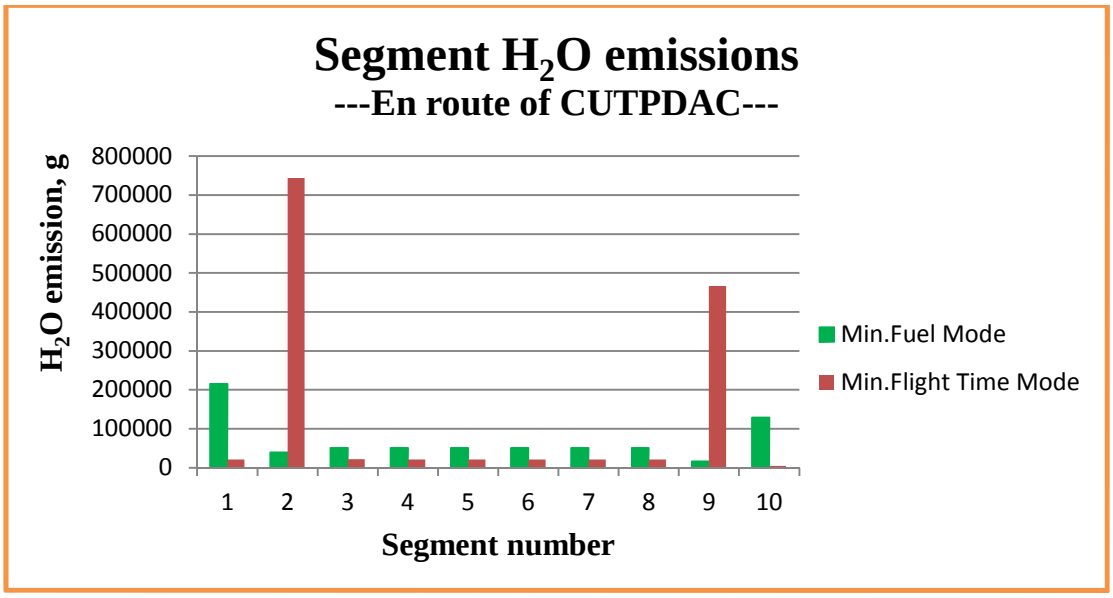

Figure 9-96 Segment H_2O emission (en route-CUTPDAC)

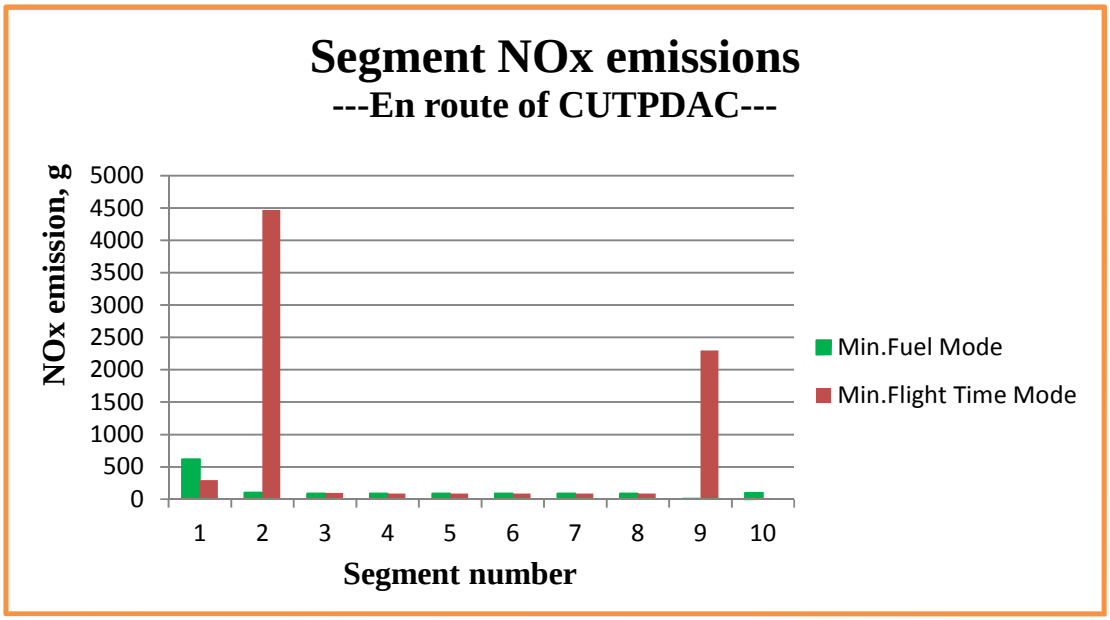

Figure 9-97 Segment NOx emission (en route-CUTPDAC)

As for the en route flight of CUTPDAC (Cranfield University Turboprop-Driven Aircraft), the following points can be observed and summarised:

1) From the plot of normalised Pareto area and the achieved Pareto front line respectively, shown in Figures 9-79 and 9-80, it can be inferred that the

optimisation process has basically converged after the iteration of 450 generations (or 72115 evaluations) listed in Table 9-37.

2) From Table 9-37, the time cost to implement this optimisation process with 450 generations (or 72115 evaluations) is 88 hours 9 minutes 34 seconds, that is, on average, 705.28 seconds/ generation or 4.4 seconds/evaluation.

3) Table 9-39 and Figures 9-81 to 9-84 show the flight trajectory optimised for the flight mode (or purpose) of minimum fuel consumption in terms of horizontal flight distance X, flight altitude Z, flight Mach number, aircraft true airspeed, flight path angle. The optimised results suggest that when the aircraft of CUTPDAC starts its en route flight at the 1st segment, the flight style of acceleration and climb will be used, that is, the flight altitude will be increased from the initial 1828.8 m set by ATC to 7569.34 m and in the meantime the flight Mach number will also go up from the initial 0.42 set by ATC to 0.52. Correspondingly, the true airspeed of the aircraft will reach 161.61 m/s at the end of this segment and the flight path angle will also experience a large increase (from the initial zero radian to 0.0503 radians). To realise the above required acceleration and climb, the aircraft will, in this segment, fly over the horizontal flight distance of around 114 km; When the flight enters into the 2nd segment, although the same flight style as that in the 1st segment will continue to be adopted, only a little increases in both flight altitude and flight speeds will take place, and when the segment completes the flight altitude will reach 7589.28 m, flight Mach number 0.54 and TAS around 166 m/s. The horizontal flight distance covered by this segment will be around 26 km; During the following six segments (i.e., from the 3rd segment to the 8th segment), CUTPDAC will perform the cruise flight with the constant flight altitude (7589.28 m) and constant flight Mach number (0.54). Naturally, the TAS and FPA of this aircraft will also remain their own values (respectively 166.02 m/s and 0 radian) unchanged in the course of the cruise flight. The entire cruise flight will cover the horizontal flight distance of 261672.5 m (i.e. around 262 km); From the 9th segment, CUTPDAC will begin its descent flight. The flight in the 9th segment will cover the horizontal flight distance of around 30 km with the flight altitude decreased to 4177.88 m and the flight Mach number

decreased to 0.52 respectively from their corresponding values in cruise flight. From Table 9-39, it can also be found that although the reduction in the flight Mach number, the TAS of the aircraft at the end of this segment will still be slightly higher than that at the start of this segment (i.e. the value at cruise flight), which is only attributed to the much lower flight altitude at this end point and hence higher ambient temperature and speed of sound offsetting the impact from the reduced flight Mach number; In the last flight segment (i.e., the 10^{th} segment), CUTPDAC will continue to reduce its flight altitude and flight Mach number until the required values (i.e., altitude 2438.4 m and Mach number 0.44 set by ATC) are reached. The descent and deceleration in this segment will be accomplished within the horizontal flight distance of as long as 205 km. Finally, as for the FPA during the last two flight segments, naturally, the negative values will be performed due to the nature of descent flight in the two segments.

4) Table 9-40 and Figures 9-85 to 9-88 illustrate the flight trajectory optimised for the flight mode (or purpose) of minimum flight time. The optimised flight trajectory suggests that when the aircraft of CUTPDAC starts its en route flight in the 1^{st} segment, the level flight and acceleration will be used, that is, the flight altitude will be kept at 1828.8 m same as the initial value set by ATC while the flight Mach number will be increased to 0.60 from the initial value of 0.42, and, as a result, the true airspeed of the aircraft will go up to nearly 200 m/s from the initial 139.94 m/s and the flight path angle will almost remain zero radian. This acceleration process will be performed within the horizontal flight distance of around 5.7 km; When the flight enters into the 2^{nd} segment, the flight style will be shifted to the constant-Mach climb, namely, the flight Mach number 0.60 will remain unchanged and the flight altitude will be increased to 4500 m. Naturally, the TAS will go down slightly during the climb process to 193.55 m/s at the end of this segment due to the increase in the flight altitude and hence the decreases in ambient temperature and the speed of sound. By the calculation, this segment will cover the horizontal flight distance of around 328 km; During the following six flight segments (i.e., from the 3^{rd} segment to the 8^{th} segment), CUTPDAC will perform the cruise flight with the

constant flight altitude (4500.03 m) and constant flight Mach number (0.6), and as a result the TAS as well as the FPA will also keep their own values (193.55 m/s and 0 radian respectively) unchanged. The horizontal flight distance spanned by the entire cruise flight will be nearly 69 km; From the 9^{th} segment, CUTPDAC will begin its descent flight. During the 9^{th} segment, the flight will experience the constant-Mach descent. Following this flight style, the aircraft will keep its flight Mach number (0.60) unchanged but reduce its flight altitude from the cruise value to 2444.34 m on the other hand. Again, due to the decrease in the flight altitude (hence the higher ambient temperature and the speed of sound) and the constant flight Mach number, the TAS of the aircraft will have a slight increase with CUTPDAC's descending in this segment. The horizontal flight distance in this descent segment will amount to nearly 229 km; The last segment (i.e., the 10^{th} segment) will only cover around 5.5 km in the horizontal flight distance, mainly used for the deceleration as well as a little decrease in the flight altitude (therefore, the flight during this segment can be basically considered as the level flight and deceleration). Finally, after the flight in this segment, CUTPDAC will reach the end point of the whole en route flight phase with the required parameter values set by ATC in terms of the flight altitude and flight Mach, that is, the flight altitude will be descended to 2438.4 m and the flight Mach number will be decelerated to 0.44. Naturally, the negative FPA during the last two flight segments will be performed due to the nature of the descent flight in these two segments.

5) Similar to the previous case, for the en route flight of CUTPDAC, the achieved two optimised flight trajectories respectively corresponding to the minimum fuel consumption flight mode and minimum time flight mode show very different flight characteristics as well. The minimum fuel consumption mode requires the aircraft fly at higher flight altitude but with lower flight Mach number so as to effectively reduce the flight drag encountered by the aircraft and hence the power (or energy) consumed by the engines to overcome the drag. Obviously, this flight mode makes the benefit in terms of fuel savings at the cost of longer flight time. On the contrary, when the aircraft flies by the minimum time flight mode, lower flight altitude and higher flight Mach

number will be selected. As a result, the travel time can be reduced but with the increase in the fuel consumption due to higher flight drag which has to be overcome.

6) As the result of the above two different flight trajectories, Table 9-41 and Figure 9-89 further illustrate the quantitative comparisons of the overall performance between the two typical flight modes in terms of fuel consumption, flight time and primary gaseous emissions. The table and figure show that the minimum flight time mode, compared to the minimum fuel consumption mode, will cost 528.30 kg (or 93.31%) more fuel and produce nearly 1696 kg (or 93.69%) more CO_2, nearly 662 kg (or 94.35%) more H_2O and 6.3 kg (or 466.14%) more NOx. As explained in the previous cases, the increases in emissions of CO_2 and H_2O are only due to the increase in the fuel consumption (because the values of the emission index, for both CO_2 and H_2O, will basically keep unchanged respectively during the combustion process) while the significant rise of NOx emission can be attributed to the two factors – higher fuel consumption and higher values of NOx emission index resulted from higher engine operation settings which can be found from Tables 9-42 and 9-43 as well as Figures 9-90 to 9-92. As the return to higher fuel consumption and gaseous emissions, the minimum flight time mode can achieve 729.29 seconds (or 18.30%) less travel time than that from the minimum fuel consumption mode.

9.2.3 CUPFDAC (Cranfield University Propfan-Driven Aircraft)

Table 9-44 Running record of CUPFDAC-En route optimisation

1	Running start time/date	Mon Nov 19 22:22:54 GMT 2012
2	Running end time/date	Fri Nov 23 06:34:27 GMT 2012
3	Total running time	80 hours 11 minutes 33 seconds
4	Generation number	450
5	Total number of evaluations	72139

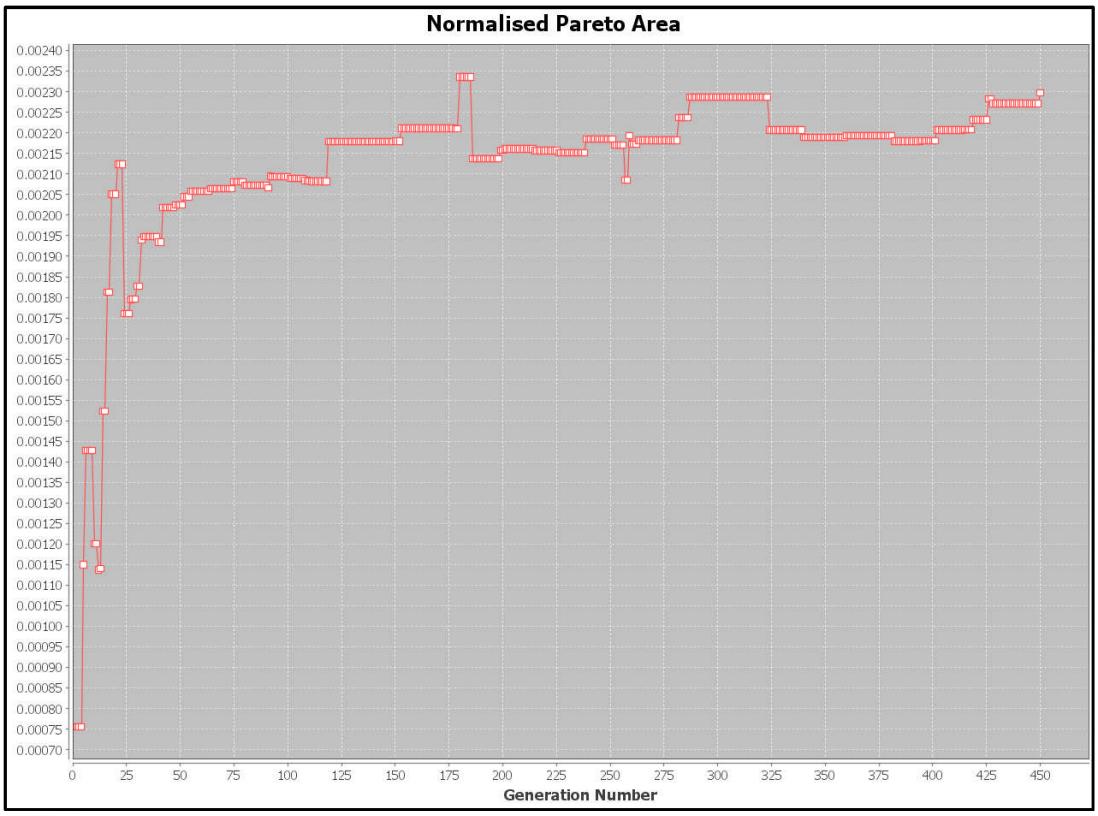

Figure 9-98 Normalised Pareto area (en route-CUPFDAC)

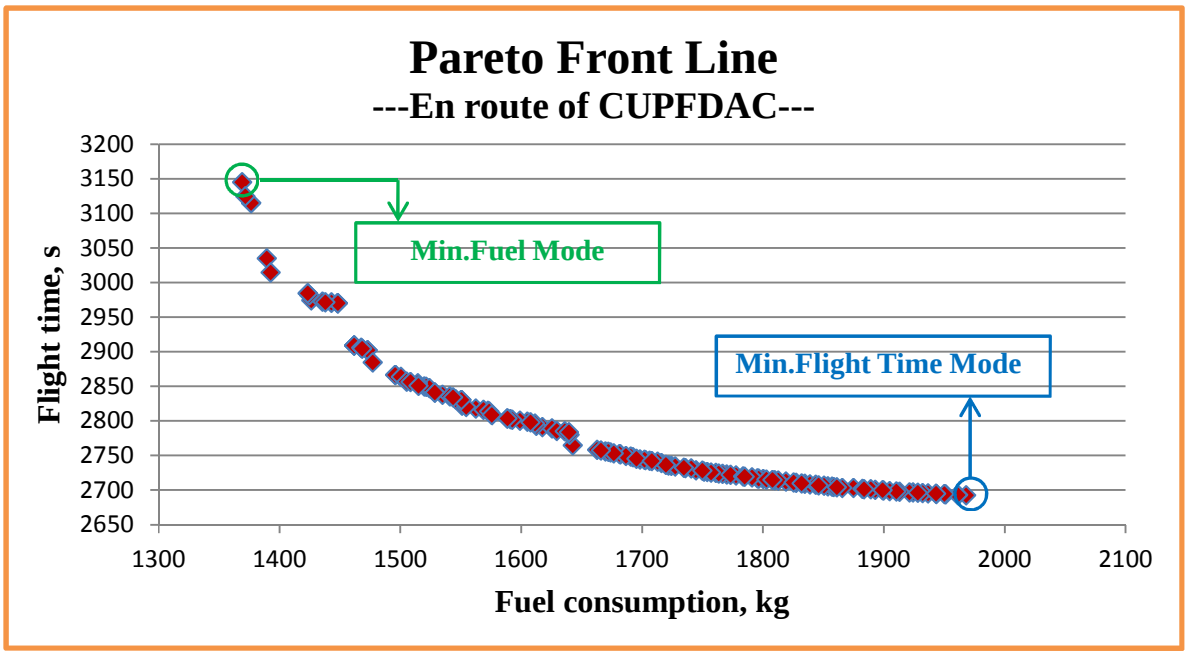

Figure 9-99 Pareto Front line (en route-CUPFDAC)

Table 9-45 Optimised results of two typical flight trajectories (en route-CUPFDAC)

		Minimum Fuel Flight Mode	Minimum Time Flight Mode
Design variables	ALT1, (m)	8439.69	1828.81
	ALT2, (m)	8441.29	7924.8
	ALT9, (m)	4558.86	2438.94
	DIS1, (m)	153457.19	14675.43
	DIS2, (m)	182325.39	335000
	DIS8, (m)	406622.60	471779.95
	DIS9, (m)	459596.15	631205.80
	MACH1, (-)	0.70	0.75
	MACH2, (-)	0.73	0.75
	MACH9, (-)	0.75	0.75
Objective functions	Fuel consumption, (kg)	1369.31	1968.10
	Flight time, (s)	3145.02	2692.56
Optimisation constraints	CA21,(m)	1.60	6095.99
	CX21,(m)	28868.21	320324.57
	CX98,(m)	52973.54	159425.85
	CA89,(m)	3882.43	5485.86
	NOx, (g)	44989.09	113857.68
	CO_2, (g)	4342024.8	6237935.26

Table 9-46 Flight trajectory of 'Min. Fuel Consumption' mode (en route-CUPFDAC)

Point	X (m)	Z (m)	MACH (-)	TAS (m/s)	FPA (rad.)
0	0	1828.8	0.42	139.94	0
1	153457.19	8439.69	0.70	215.25	0.0431
2	182325.39	8441.29	0.73	224.30	5.50×10^{-5}
3	219708.26	8441.29	0.73	224.30	0
4	257091.13	8441.29	0.73	224.30	0
5	294474.00	8441.29	0.73	224.30	0
6	331856.87	8441.29	0.73	224.30	0
7	369239.74	8441.29	0.73	224.30	0
8	406622.60	8441.29	0.73	224.30	0
9	459596.15	4558.86	0.75	240.44	-0.0732
10	637000	2438.4	0.44	145.55	-0.0120

Table 9-47 Flight trajectory of 'Min. Flight Time' mode (en route-CUPFDAC)

Point	X (m)	Z (m)	MACH (-)	TAS (m/s)	FPA (rad.)
0	0	1828.8	0.42	139.94	0
1	14675.43	1828.81	0.75	249.90	0
2	335000	7924.8	0.75	231.35	0.0190
3	357796.66	7924.8	0.75	231.35	0
4	380593.32	7924.8	0.75	231.35	0

5	403389.97	7924.8	0.75	231.35	0
6	426186.63	7924.8	0.75	231.35	0
7	448983.29	7924.8	0.75	231.35	0
8	471779.95	7924.8	0.75	231.35	0
9	631205.80	2438.94	0.75	248.10	-0.0344
10	637000	2438.4	0.44	145.55	-9.40×10^{-5}

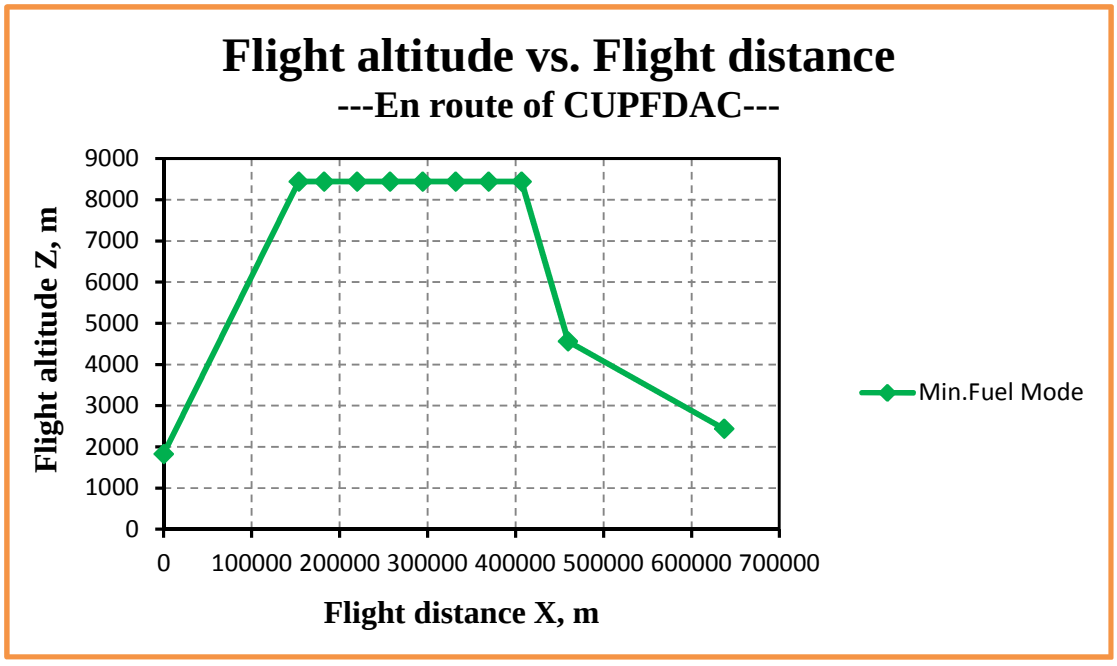

Figure 9-100 Flight altitude vs. Flight distance-'min. fuel' mode (CUPFDAC-en route)

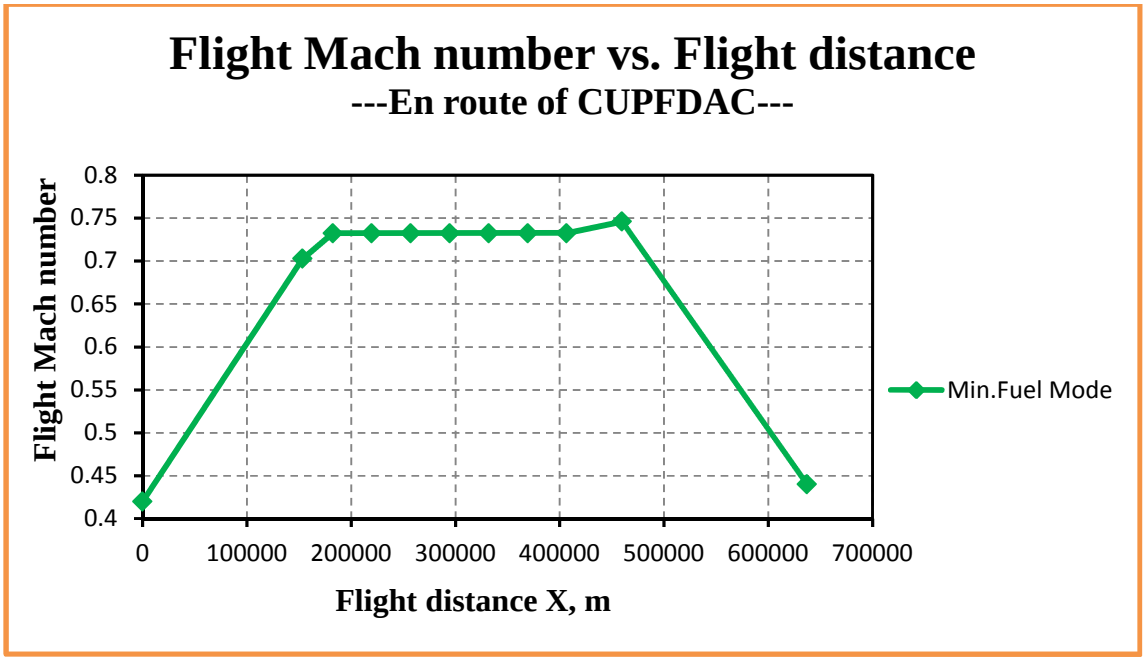

Figure 9-101 Flight Mach number vs. Flight distance-'min. fuel' mode (CUPFDAC-en route)

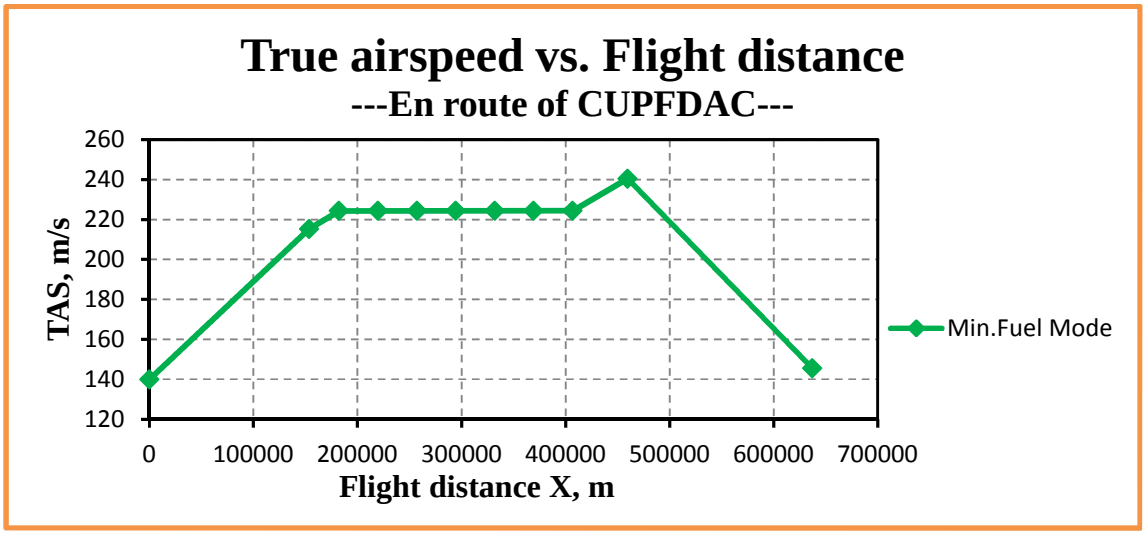

Figure 9-102 True airspeed vs. Flight distance-'min. fuel' mode (CUPFDAC-en route)

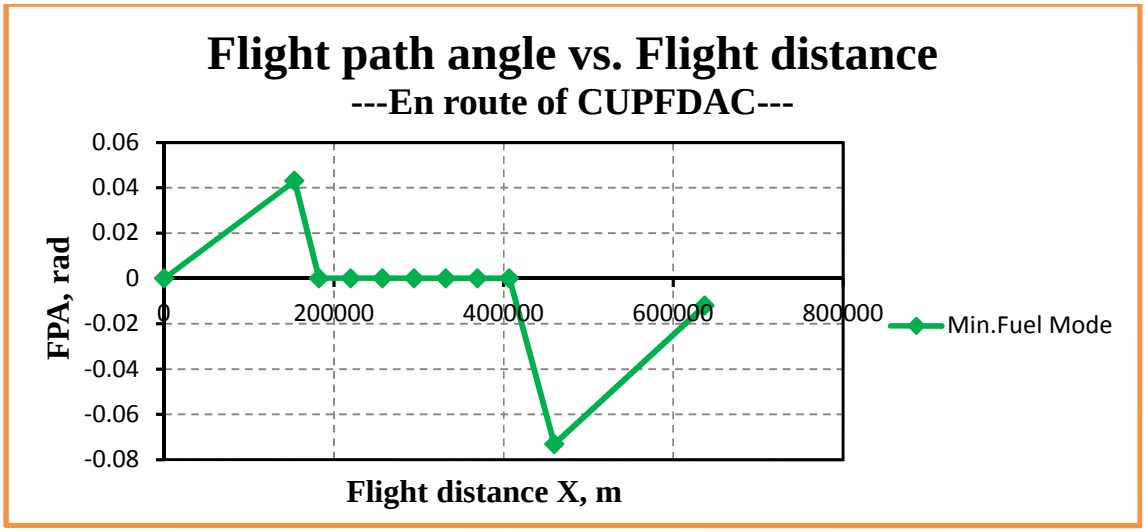

Figure 9-103 Flight path angle vs. Flight distance-‘min. fuel’ mode (CUPFDAC-en route)

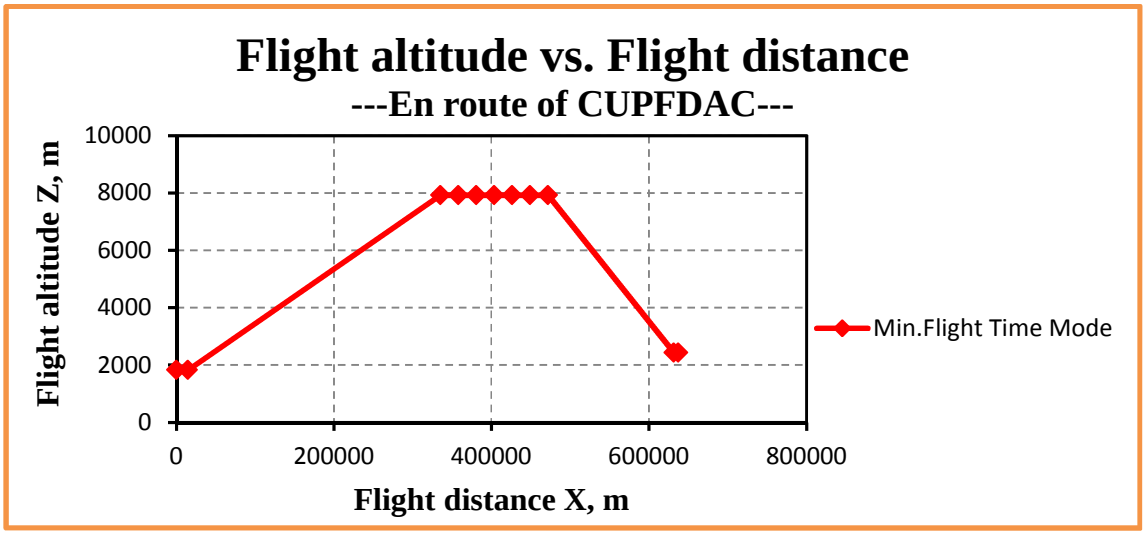

Figure 9-104 Flight altitude vs. Flight distance-‘min. flight time’ mode (CUPFDAC-en route)

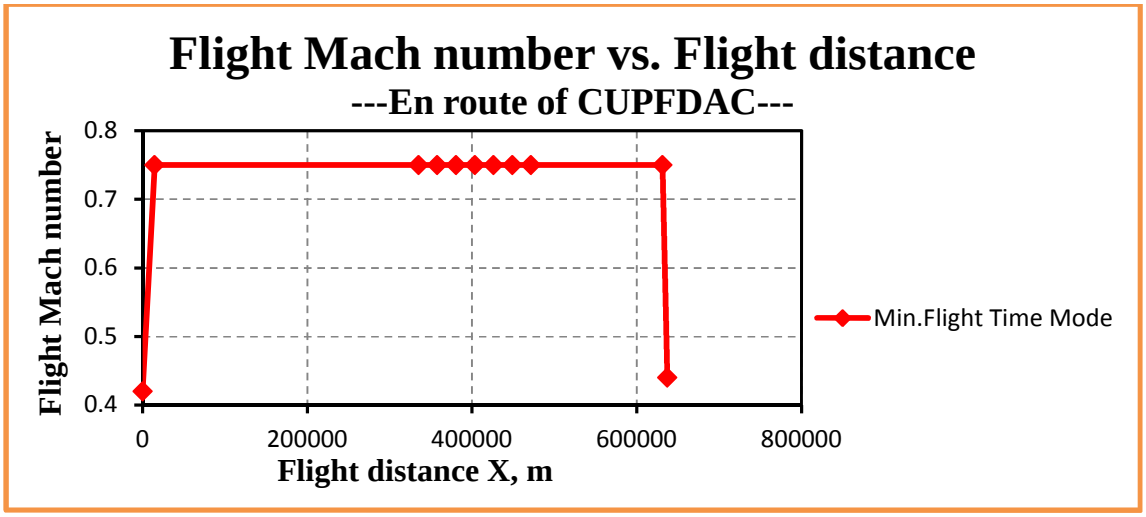

Figure 9-105 Flight Mach number vs. Flight distance-'min. flight time' mode (CUPFDAC-en route)

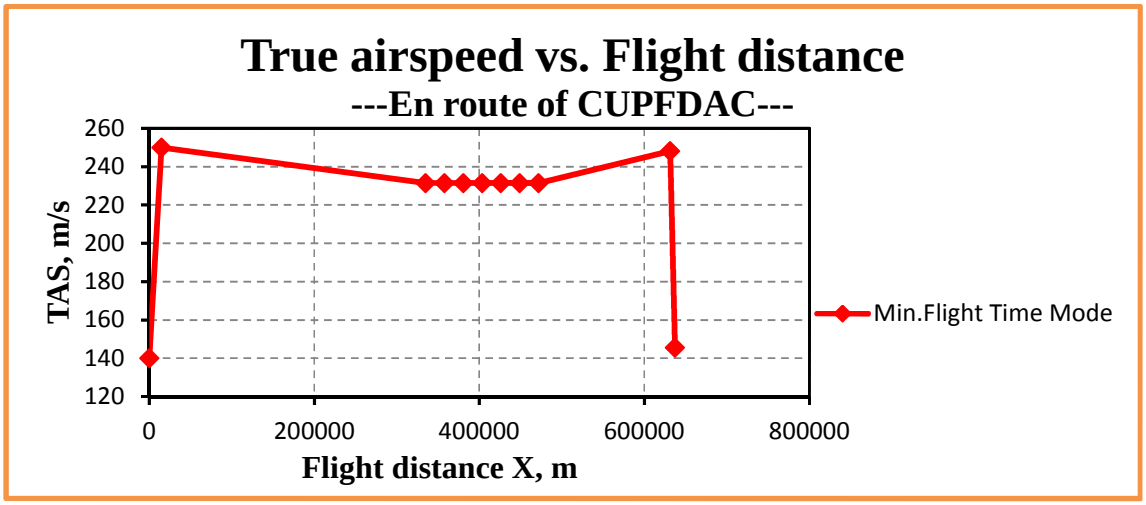

Figure 9-106 True airspeed vs. Flight distance-'min. flight time' mode (CUPFDAC-en route)

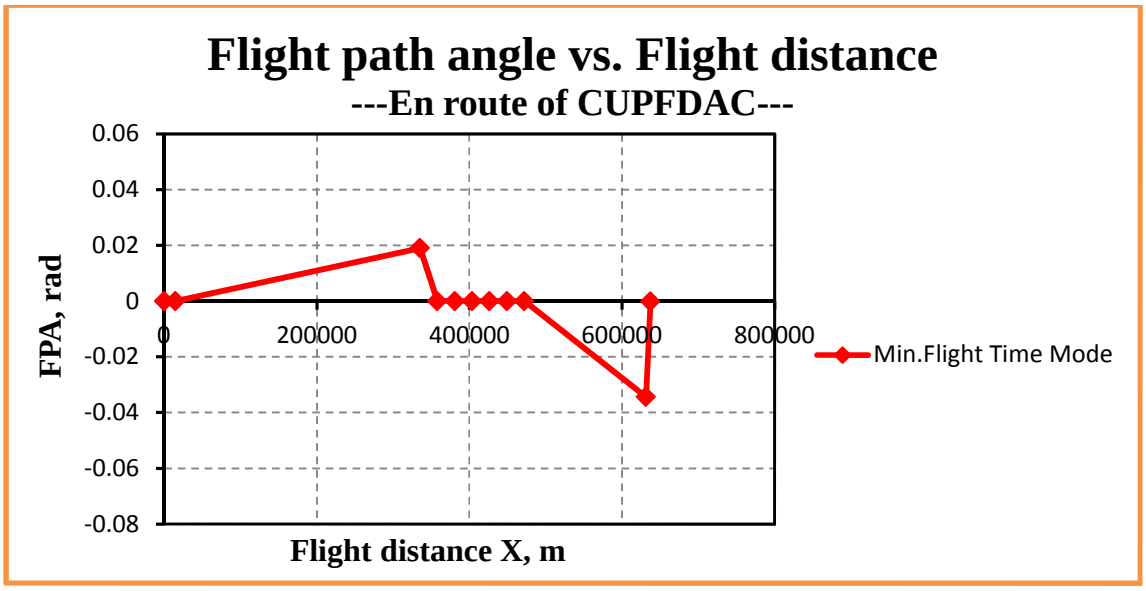

Figure 9-107 Flight path angle vs. Flight distance-'min. flight time' mode (CUPFDAC-en route)

Table 9-48 Overall performance of two typical flight trajectories (CUPFDAC-en route)

	Fuel burnt	**Flight time**	**CO_2 emission**	**H_2O emission**	**NOx emission**
	(kg)	(s)	(g)	(g)	(g)
Min. Fuel Mode	1369.31	3145.02	4342024.8	1691789.37	44989.09
Min. Flight Time Mode	1968.10	2692.56	6237935.26	2430644.64	113857.68
Δ	598.78	-452.46	1895910.46	738855.26	68868.59
δ	43.73%	-14.39%	43.66%	43.67%	153.08%

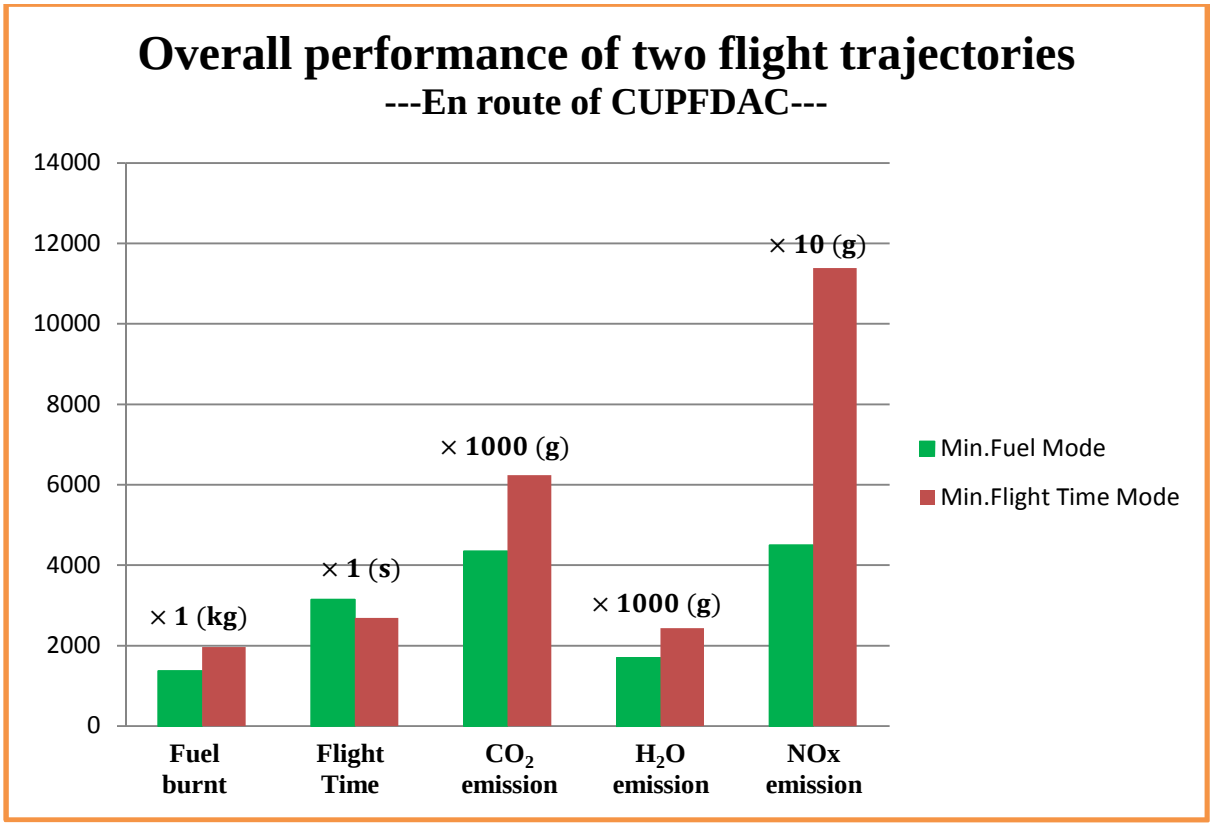

Figure 9-108 Overall performance of two typical flight trajectories (CUPFDAC-en route)

Table 9-49 Parameter segment distributions of 'Min. Fuel Consumption' mode (part) - (CUPFDAC-en route)

Segment	Fn	TET	EINOx	Fuel burnt	Flight time	CO_2 emission	H_2O emission	NOx emission
	(N)	(K)	(g/kg fuel)	(kg)	(s)	(g)	(g)	(g)
1	31322.15	1700.24	45.00	553.81	864.57	1755541.19	684194.83	24923.35
2	26873.22	1763.99	44.89	79.62	131.41	252110.66	98231.84	3574.35
3	20232.22	1654.89	30.19	78.42	166.66	248449.41	96836.46	2367.54
4	20207.80	1654.55	30.15	78.35	166.66	248228.05	96750.21	2362.02
5	20193.48	1654.35	30.12	78.31	166.66	248091.06	96696.84	2358.58

6	20179.19	1654.15	30.09	78.27	166.66	247954.02	96643.45	2355.15
7	20164.92	1653.93	30.07	78.23	166.66	247827.55	96594.17	2351.89
8	20150.68	1653.76	30.04	78.19	166.66	247701.04	96544.89	2348.98
9	10895.29	1533.30	20.01	92.83	228.29	294375.81	114726.70	1857.06
10	2428.40	1227.65	2.83	173.30	920.77	551746.02	214569.97	490.18

Table 9-50 Parameter segment distributions of 'Min. Flight Time' mode' (part) (CUPFDAC-en route)

Segment	**Fn**	**TET**	**EINOx**	**Fuel burnt**	**Flight time**	**CO_2 emission**	**H_2O emission**	**NOx emission**
	(N)	(K)	(g/kg fuel)	(kg)	(s)	(g)	(g)	(g)
1	53033.29	1849.83	88.67	85.45	75.29	271340.71	105680.89	7576.33
2	31592.45	1764.58	64.94	1085.87	1331.35	3441719.67	1340997.87	70520.54
3	24591.86	1710.15	40.43	56.11	98.55	177731.61	69264.71	2268.55
4	21118.08	1664.70	33.74	49.85	98.54	157938.20	61556.54	1681.72
5	21110.36	1664.72	33.74	49.85	98.54	157944.42	61558.97	1681.79
6	21102.65	1664.72	33.70	49.84	98.54	157894.38	61539.50	1679.62
7	21094.95	1664.48	33.69	49.81	98.54	157825.93	61512.82	1678.13
8	21087.26	1664.20	33.69	49.80	98.54	157782.56	61495.91	1677.61
9	21343.89	1749.02	51.64	474.12	665.24	1502494.37	585498.36	24484.97
10	18000.66	1589.26	34.98	17.39	29.45	55263.40	21539.06	608.43

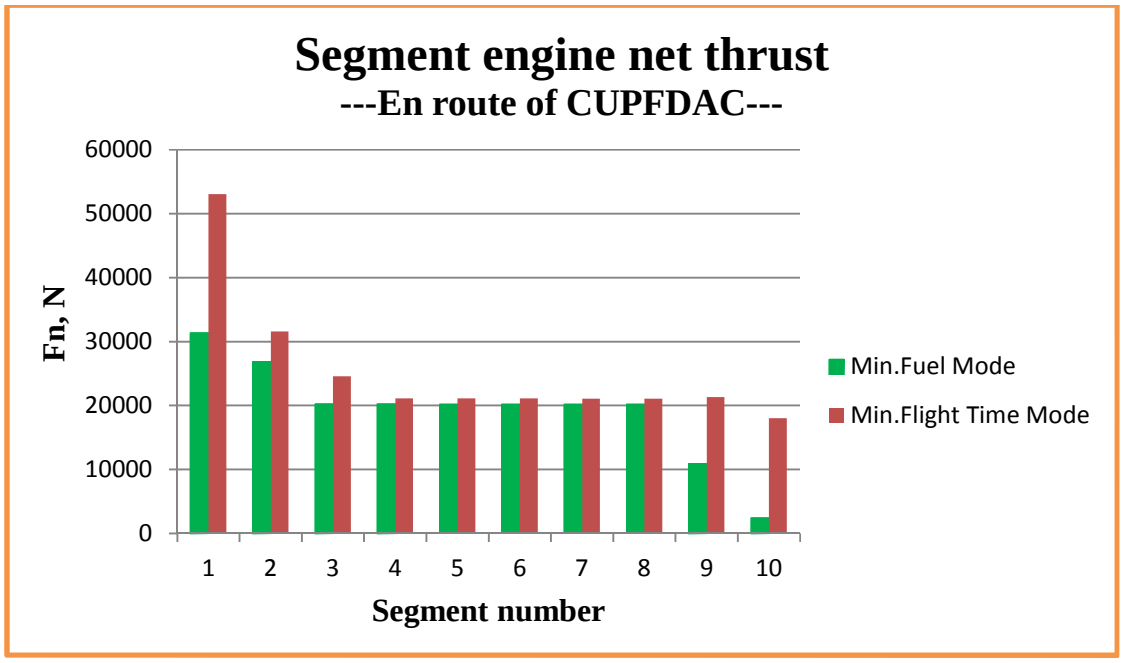

Figure 9-109 Segment engine net thrust (CUPFDAC-en route)

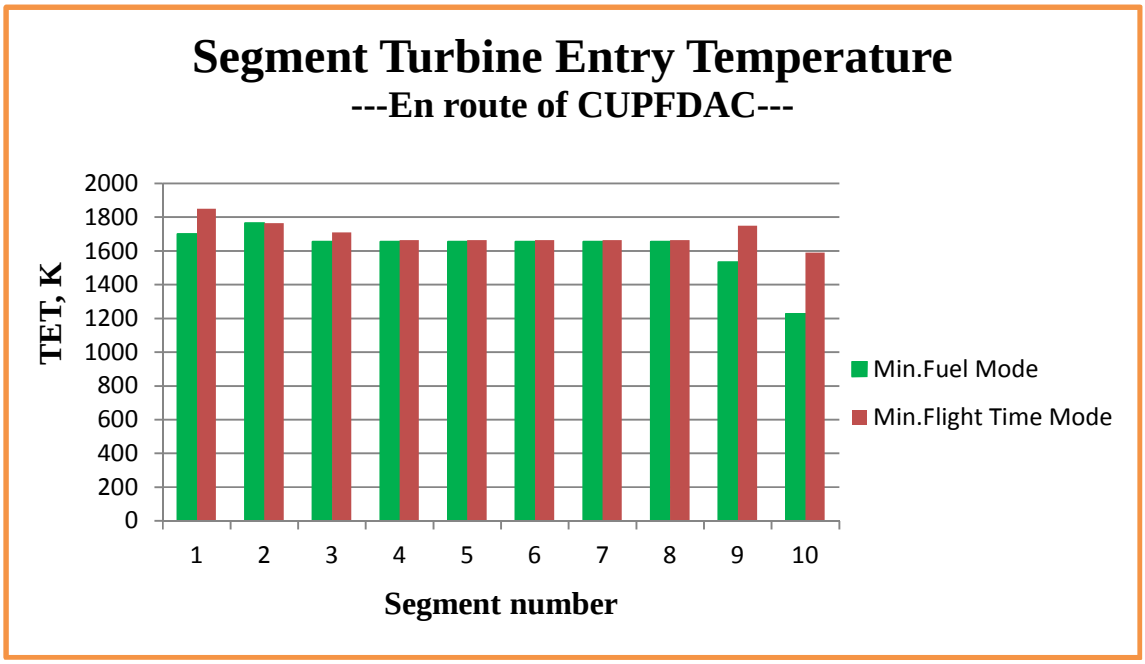

Figure 9-110 Segment engine turbine entry temperature (CUPFDAC-en route)

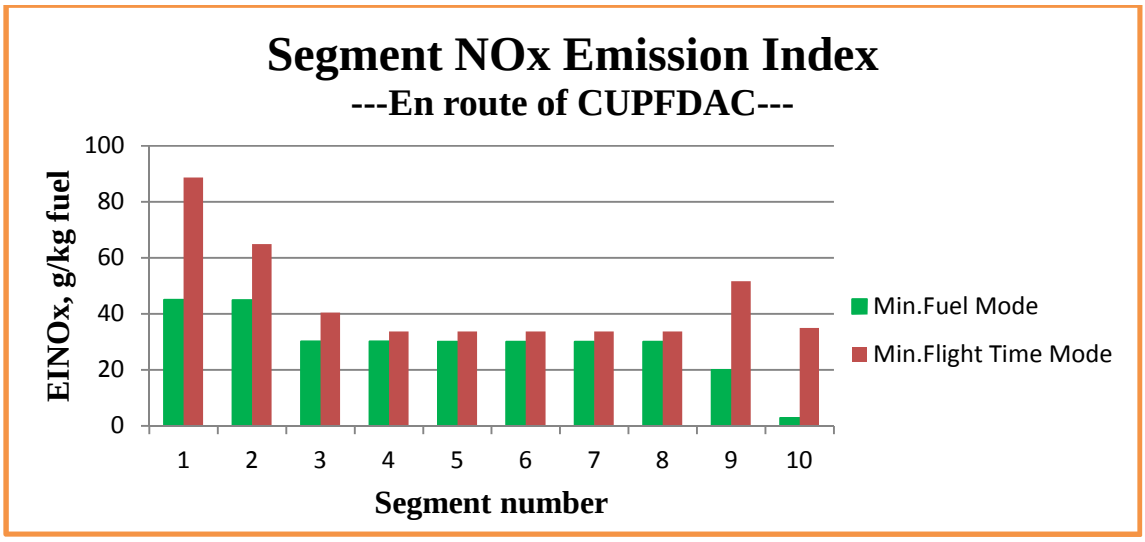

Figure 9-111 Segment NOx emission index (CUPFDAC-en route)

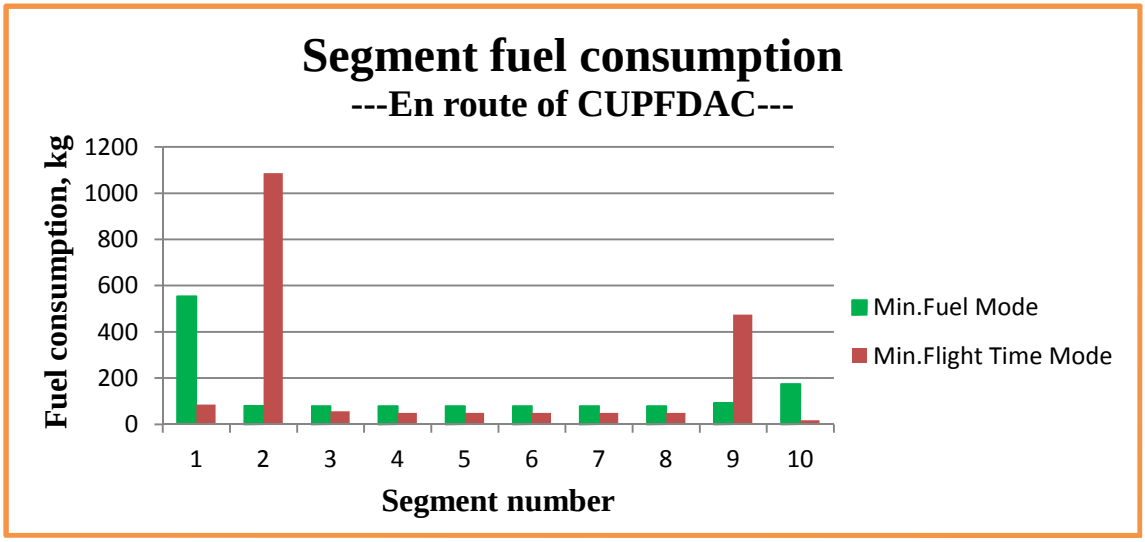

Figure 9-112 Segment fuel consumption (CUPFDAC-en route)

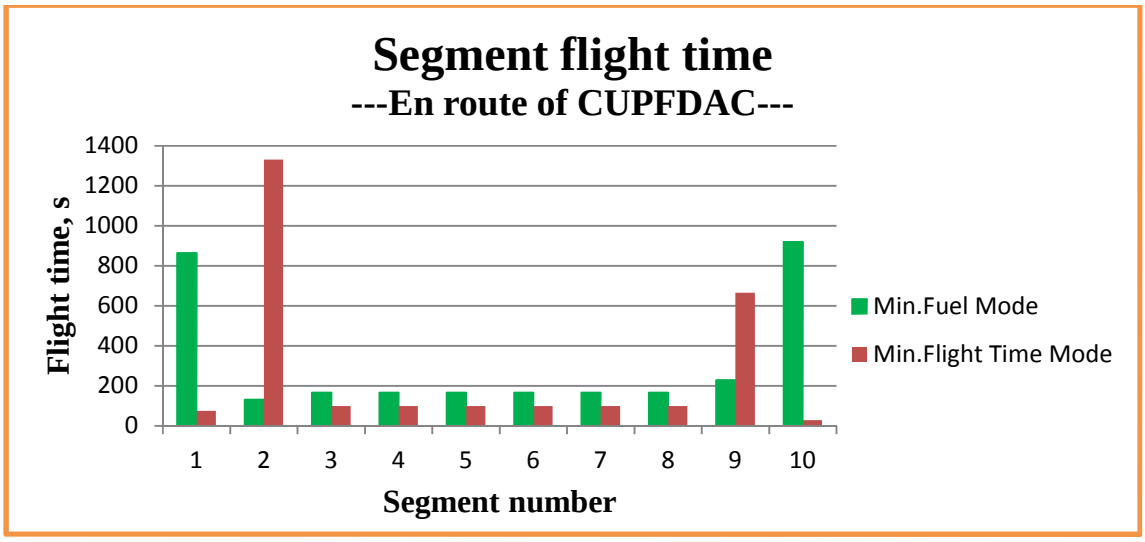

Figure 9-113 Segment flight time (CUPFDAC-en route)

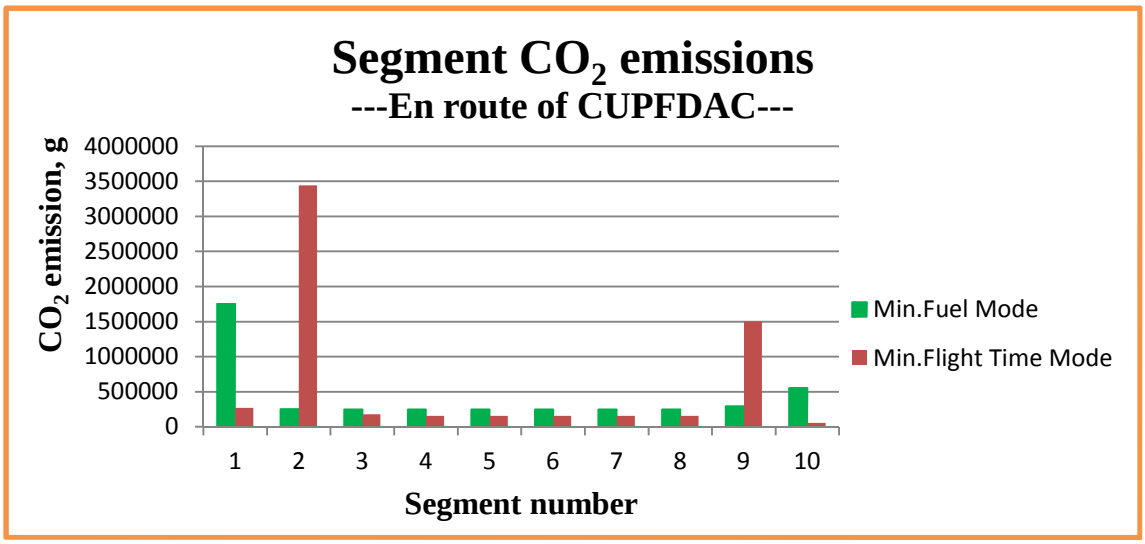

Figure 9-114 Segment CO_2 emissions (CUPFDAC-en route)

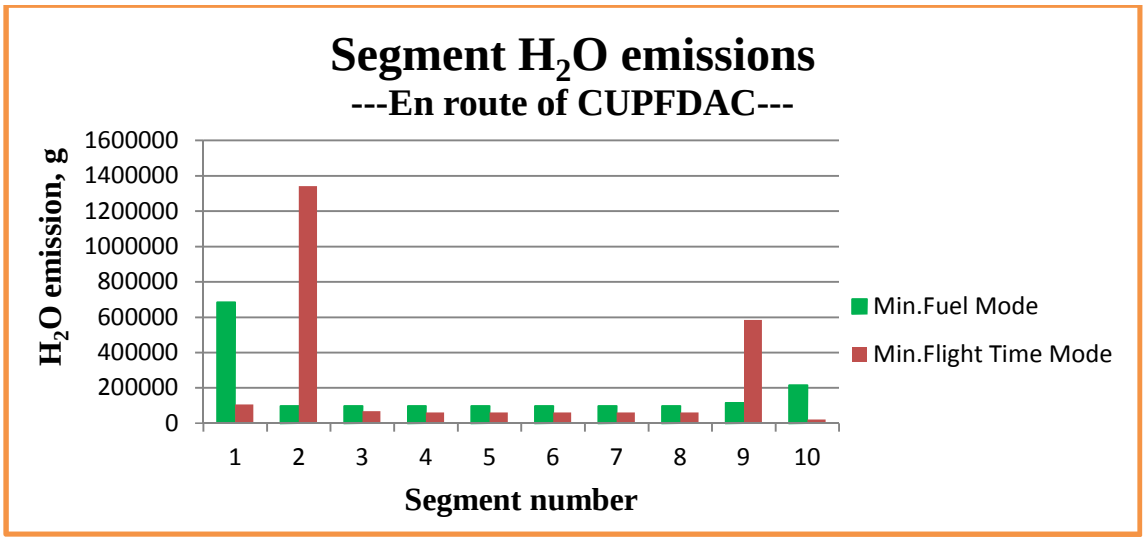

Figure 9-115 Segment H_2O emissions (CUPFDAC-en route)

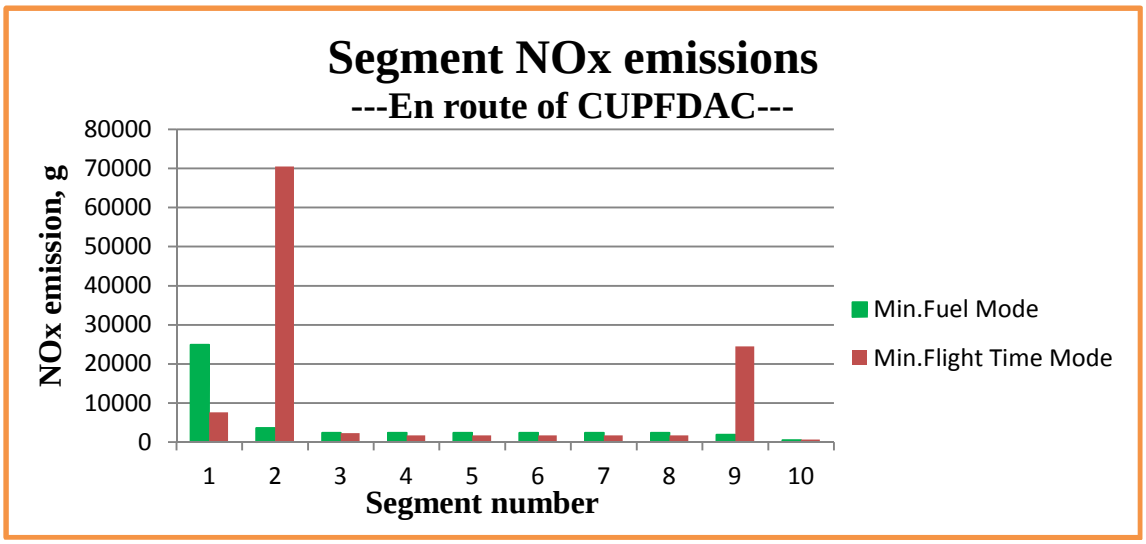

Figure 9-116 Segment NOx emissions (CUPFDAC-en route)

As for the en route flight of CUPFDAC (Cranfield University Propfan-Driven Aircraft), the observations and summaries are as follows:

1) From the plot of normalised Pareto area and the achieved Pareto front line respectively shown in the Figures 9-98 and 9-99, it can be found that although after 450 generations or 72139 evaluations listed in Table 9-44, the convergence

of this optimisation process is not very satisfying and there is still some space to improve (due to time reasons, this improvement will be put into the future work.). However, despite of better convergence expected, the shape of the produced Pareto front line still shows that the optimisation process has basically converged and the two extreme points (or solutions) on this line which will be used and analysed in the following parts have in fact been formed properly. Therefore, the optimised results achieved so far are still effective for the further analysis.

2) Table 9-44 provides the running record of this optimisation process. From this table, it can be found that with the execution of 450 generations or 72139 evaluations, the optimisation process cost totally 80 hours 11 minutes 33 seconds, that is, on average, 641.54 seconds/generation or 4 seconds/evaluation.
3) Table 9-46 and Figures 9-100 to 9-103 illustrate the flight trajectory optimised for the flight mode (or purpose) of minimum fuel consumption when CUPFDAC flies the en route phase, expressed through horizontal flight distance, flight altitude, flight Mach number, true airspeed and flight path angle. According to the optimised results, when CUPFDAC flies in the 1st segment, the climb and acceleration will be implemented simultaneously, that is, after this flight segment, the flight altitude will be required to reach 8439.69 m from the initial value of 1828.8 m and the flight Mach number will be increased to 0.70 from the initial 0.42. Correspondingly, the true airspeed of the aircraft will go up to 215.25 m/s and the flight path angle will also rise to 0.0431 radians from the initial value of zero radian. The 1st segment will cover the horizontal flight distance of around 153 km; Although the flight in the 2nd segment will still adopt the same flight style as in the above 1st segment, namely the climb and acceleration, only relatively small increments in flight altitude and flight speeds are performed. The 2nd-segment flight will cover the horizontal flight distance of around 29 km and when this segment is accomplished the flight altitude will reach 8441.29 m and the flight Mach number will be further increased to 0.73 (correspondingly, TAS will amount to 224.30 m/s); Thereafter, CUPFDAC will enter into the cruise flight by keeping the flight altitude and the flight Mach number unchanged to the end of the 8th segment. Under the flight mode (or

purpose) of minimum fuel consumption, the aircraft's cruise altitude and cruise Mach number are 8441.29 m and 0.73 respectively. The total horizontal flight distance spanned by the entire cruise flight will amount to around 224 km; In the following 9th segment, the aircraft will start to enter into the descent flight. After this segment flight, the flight altitude will be reduced to 4558.86 m from the previous cruise value but the flight Mach number will be unexpectedly accelerated to 0.75 (correspondingly, TAS will also rise to 240.44 m/s from the cruise value of 224.30 m/s). The phenomenon took place ever in the previous en route-flight case of CUTFDAC and similarly more investigation will be done in the future work. The flight in the 9th segment will cover nearly 53 km in terms of the horizontal flight distance; When CUPFDAC operates in the last segment (i.e., the 10th segment), the common flight style of descent and deceleration will be applied, that is, after this segment, the flight altitude and the flight Mach number will be both reduced to 2438.4 m and 0.44 required by ATC. Naturally, same as in the previous segment, a negative FPA will continue to be used due to the descent nature experienced by the last two segments. The flight in the last segment will cover the horizontal flight distance of around 177 km.

4) The flight trajectory optimised for the flight mode (or purpose) of minimum flight time is described by Table 9-47 and Figures 9-104 to 9-107. In light of the achieved optimisation results, when CUPFDAC performs its en route flight in the 1st segment, the level-flight and acceleration will be applied so that with the horizontal flight distance of nearly 15 km spanned by this segment as well as the constant flight altitude 1828.8 m the flight Mach number will be accelerated from the initial value of 0.42 to 0.75 at the end of this segment (and correspondingly, the true airspeed of the aircraft will also go up to nearly 250 m/s). During this flight segment, the flight path angle will keep zero radian same as the initial value; After entering into the 2nd segment, the aircraft will change its flight style into the constant-Mach number climb. That is, during the flight, the flight Mach number will be kept at 0.75 while the flight altitude will be increased to 7924.8 m at the end of this segment. In spite of the constant flight Mach number, the true airspeed of the aircraft will go down to some extent due to the increase in the flight altitude (and hence the reduction in ambient

temperature and the speed of sound). Naturally, the flight path angle in this segment will also experience a large increase from the initial zero radian to 0.0190 radians at the end of this segment. The horizontal flight distance covered by this climb segment will amount to around 320 km; Then, from the 3rd segment, the aircraft will begin its cruise flight to the end of the 8th segment. As required, the aircraft will implement the cruise flight with the constant flight altitude and flight Mach number, i.e., 7924.8 m and 0.75 which are respectively at the lower boundary of the cruise altitude variable and the upper boundary of the cruise flight speed (Mach number) variable. As a result, the TAS and FPA of the aircraft will remain at 231.35 m/s and zero radian respectively. The entire cruise flight comprises totally six segments and will cover nearly 137 km; CUPFDAC will start its descent flight from the 9th segment. During the 9th flight segment, the flight style of the constant-Mach number descent will be adopted, namely, the flight Mach number will be kept at 0.75 while the flight altitude being continuously decreased during the descent, and after the horizontal flight distance of around 159 km covered by this segment, the flight altitude will arrive at 2438.94 m as required; As a matter of fact, the flight altitude reached by the aircraft at the end of the above 9th segment has been almost the same as that value at the end of the 10th segment (i.e., the end of the whole en route flight phase) set by ATC. Therefore, the flight in the 10th segment (i.e., the last segment) will belong to the flight style of the decelerated level flight, that is, the flight altitude will remain at around 2438 m while the flight Mach number being continuously reduced from the cruise value of 0.75 to 0.44 required by ATC (and, correspondingly the TAS will be decreased from 248.10 m/s to 145.55 m/s). This deceleration process will be accomplished within the horizontal flight distance of around 5.8 km and reasonably the negative FPA will be performed in the last two segments due to their descent nature.

5) Just as in the previous en route flights of CUTFDAC and CUTPDAC, there are also significant differences between the minimum fuel consumption flight mode and the minimum time flight mode when performed by CUPFDAC in terms of the achieved flight trajectories and the resultant overall performances such as fuel consumption, flight time as well as gaseous emissions. From the point of

view of flight trajectory, the minimum fuel consumption flight mode asks CUPFDAC to fly at higher cruise altitude and lower cruise Mach number so as to reduce the flight drag encountered by the aircraft and therefore decrease the energy consumption of the power plants. The essence of this flight mode is to achieve the fuel savings by sacrificing its flight time to some extent. On the contrary, when flying at the minimum time flight mode, the aircraft is required to keep the maximum possible flight Mach number as long as possible and select the minimum possible cruise altitude so as to shorten the curve distance flown by the aircraft and increase the true airspeed of the aircraft. Therefore, by this flight mode the travel time can be reduced but at the cost of more fuel consumption and more gaseous emissions due to the higher aircraft drag and higher engine operation ratings. As the result of the above two different flight trajectories implemented by CUPFDAC, the further quantitative comparisons of the overall performance between the two flight modes are provided in Table 9-48 and Figure 9-108. From Table 9-48, it can be found that compared to the minimum fuel consumption flight mode, the minimum time flight mode will make CUPFDAC consume 598.78 kg (or 43.73%) more fuel and produce around 1896 kg (or 43.66%) more CO_2, 739 kg (or 43.67%) more H_2O and 69 kg (or 153.08%) more NOx. As the return to more fuel consumption and gaseous emissions, the minimum time flight mode will achieve 452.46 seconds (or 14.39%) less travel time.

9.2.4 En route flight comparisons between CUPFDAC and CUTFDAC

Table 9-51 Overall comparisons between CUPFDAC and CUTFDAC ('min. fuel consumption' en route flight mode)

	Fuel burnt	**Flight time**	**CO_2 emission**	**H_2O emission**	**NOx emission**
	(kg)	(s)	(g)	(g)	(g)
CUTFDAC	2098.53	3020.51	6624013.66	2598401.20	26522.36
CUPFDAC	1369.31	3145.02	4342024.8	1691789.37	44989.09

Δ	-729.22	124.51	-2281988.86	-906611.83	18466.73
δ	-34.75%	4.12%	-34.45%	-34.89%	69.63%

Table 9-52 Overall comparisons between CUPFDAC and CUTFDAC ('min. flight time' en route flight mode)

	Fuel burnt	**Flight time**	**CO_2 emission**	**H_2O emission**	**NOx emission**
	(kg)	(s)	(g)	(g)	(g)
CUTFDAC	3040.71	2454.41	9598013.85	3765011.97	53652.68
CUPFDAC	1968.10	2692.56	6237935.26	2430644.64	113857.68
Δ	-1072.61	238.15	-3360078.59	-1334367.33	60205
δ	-35.27%	9.70%	-35.01%	-35.44%	112.21%

Table 9-53 TET comparisons between CUPFDAC and CUTFDAC ('min. fuel consumption' en route flight mode)

	TET, K		**Δ**	**δ**
	CUTFDAC	**CUPFDAC**	**K**	**-**
1	1462.59	1700.24	237.65	16.25%
2	1321.39	1763.99	442.6	33.50%
3	1393.16	1654.89	261.73	18.79%
4	1207.46	1654.55	447.09	37.03%
5	1207.08	1654.35	447.27	37.05%
6	1206.71	1654.15	447.44	37.08%

7	1206.34	1653.93	447.59	37.10%
8	1205.97	1653.76	447.79	37.13%
9	1255.81	1533.30	277.49	22.10%
10	1030.05	1227.65	197.6	19.18%

Table 9-54 EINOx comparisons between CUPFDAC and CUTFDAC ('min. fuel consumption' en route flight mode)

	EINOx, g/kg fuel		**Δ**	**δ**
	CUTFDAC	**CUPFDAC**	**g/kg fuel**	**-**
1	22.13	45.00	22.87	103.34%
2	16.29	44.89	28.6	175.57%
3	14.94	30.19	15.25	102.07%
4	10.83	30.15	19.32	178.39%
5	10.82	30.12	19.3	178.37%
6	10.81	30.09	19.28	178.35%
7	10.80	30.07	19.27	178.43%
8	10.79	30.04	19.25	178.41%
9	12.28	20.01	7.73	62.95%
10	7.36	2.83	-4.53	-61.55%

Table 9-55 TET comparisons between CUPFDAC and CUTFDAC ('min. flight time' en route flight mode)

	TET, K		Δ	δ
	CUTFDAC	**CUPFDAC**	**K**	**-**
1	1499.82	1849.83	350.01	23.34%
2	1344.59	1764.58	419.99	31.24%
3	1288.45	1710.15	421.7	32.73%
4	1248.57	1664.70	416.13	33.33%
5	1248.51	1664.72	416.21	33.34%
6	1248.46	1664.72	416.26	33.34%
7	1248.41	1664.48	416.07	33.33%
8	1248.36	1664.20	415.84	33.31%
9	1270.28	1749.02	478.74	37.69%
10	1090.46	1589.26	498.8	45.74%

Table 9-56 EINOx comparisons between CUPFDAC and CUTFDAC ('min. flight time' en route flight mode)

	EINOx, g/kg fuel		Δ	δ
	CUTFDAC	**CUPFDAC**	**g/kg fuel**	**-**
1	24.17	88.67	64.5	266.86%
2	18.61	64.94	46.33	248.95%
3	14.75	40.43	25.68	174.10%
4	13.64	33.74	20.1	147.36%

5	13.63	33.74	20.11	147.54%
6	13.63	33.70	20.07	147.25%
7	13.63	33.69	20.06	147.18%
8	13.63	33.69	20.06	147.18%
9	16.10	51.64	35.54	220.75%
10	10.37	34.98	24.61	237.32%

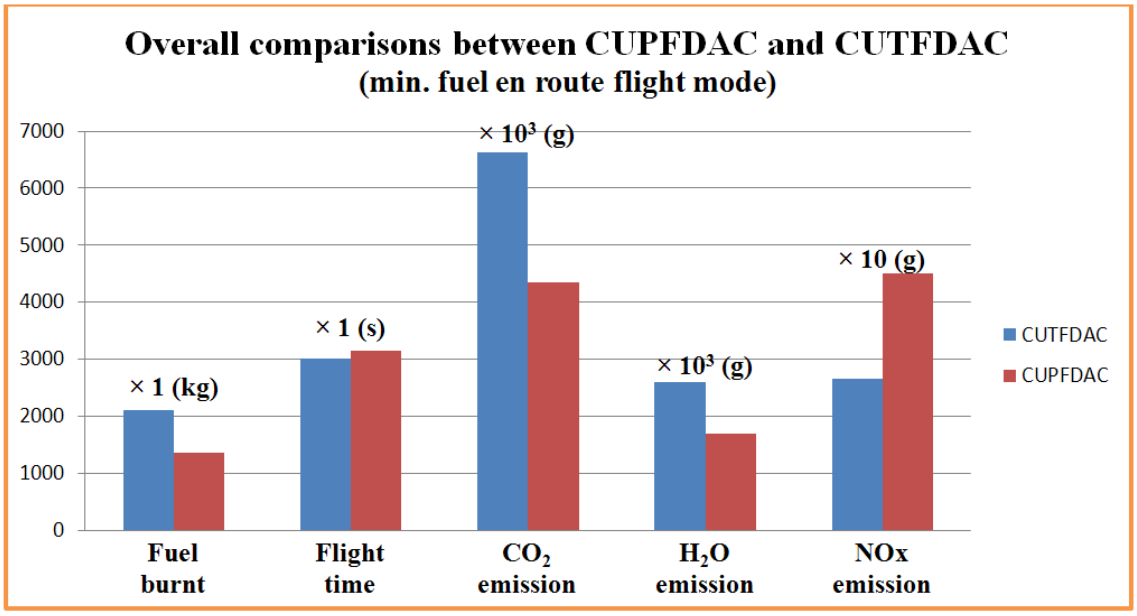

Figure 9-117 Overall comparisons between CUPFDAC and CUTFDAC ('min. fuel consumption' en route flight mode)

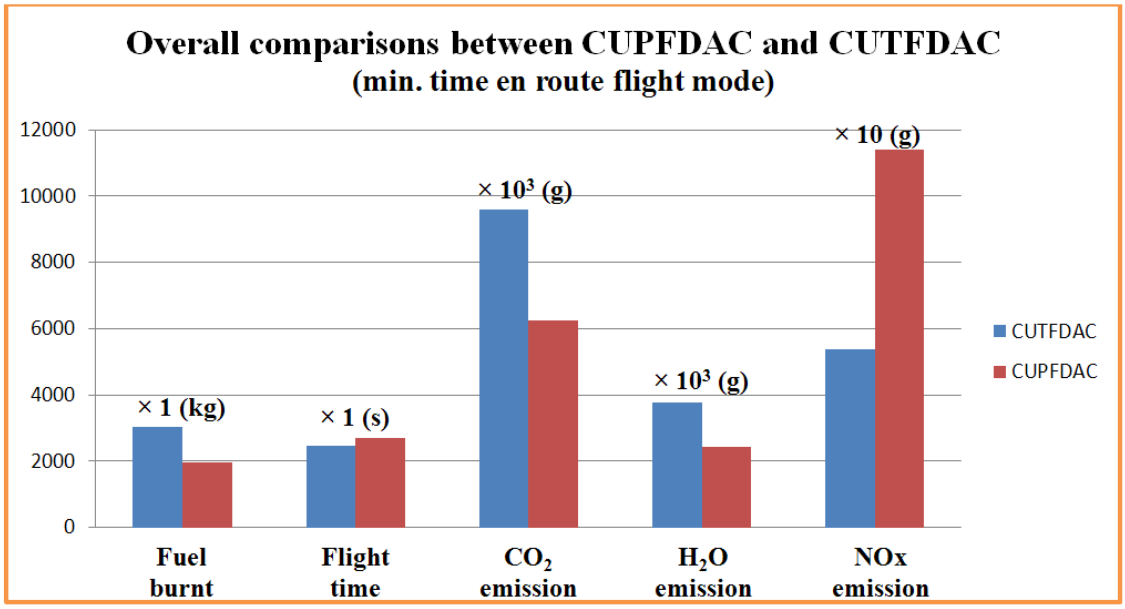

Figure 9-118 Overall comparisons between CUPFDAC and CUTFDAC ('min. flight time' en route flight mode)

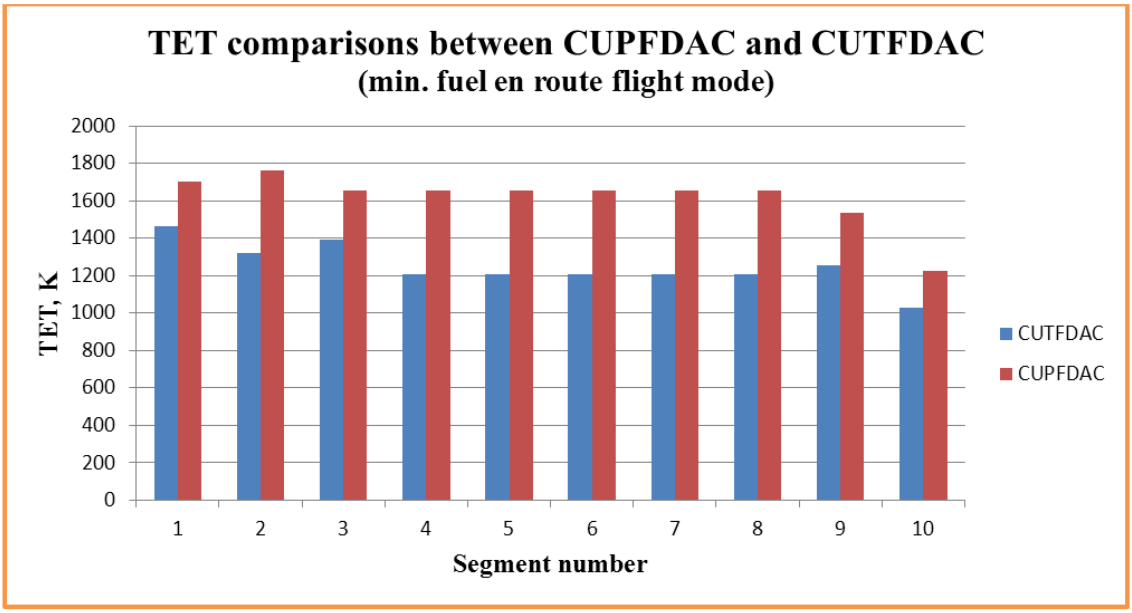

Figure 9-119 TET comparisons between CUPFDAC and CUTFDAC ('min. fuel consumption' en route flight mode)

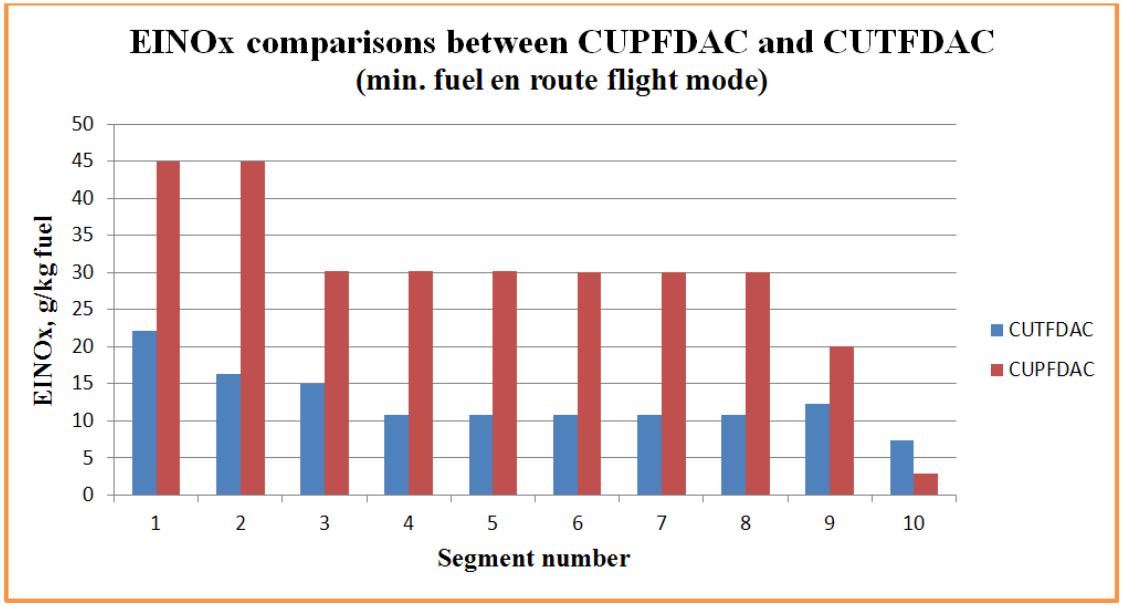

Figure 9-120 EINOx comparisons between CUPFDAC and CUTFDAC ('min. fuel consumption' en route flight mode)

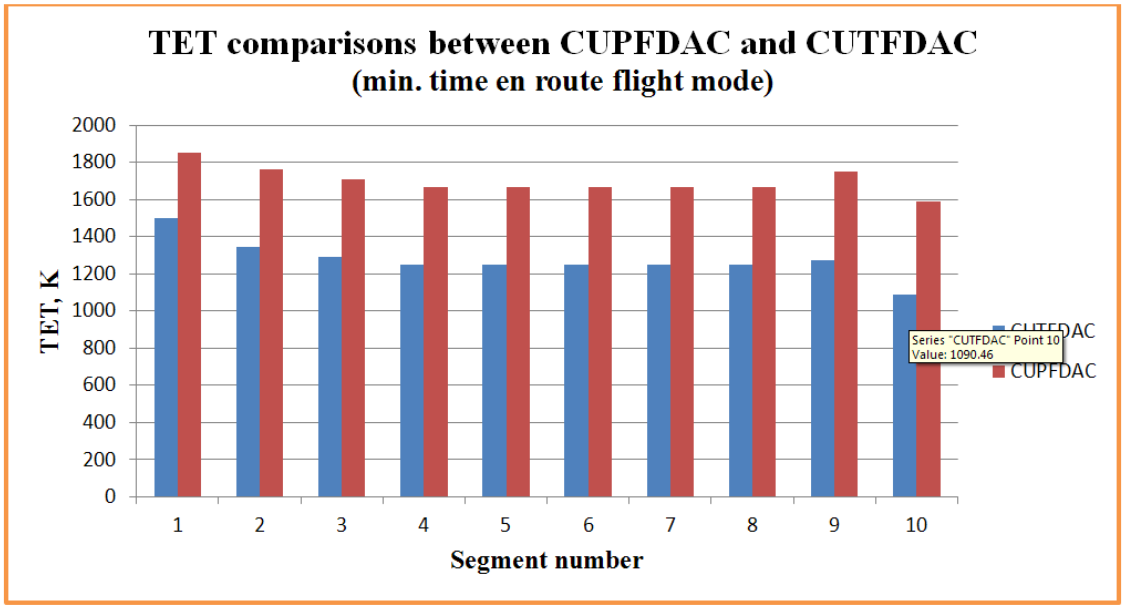

Figure 9-121 TET comparisons between CUPFDAC and CUTFDAC ('min. flight time' en route flight mode)

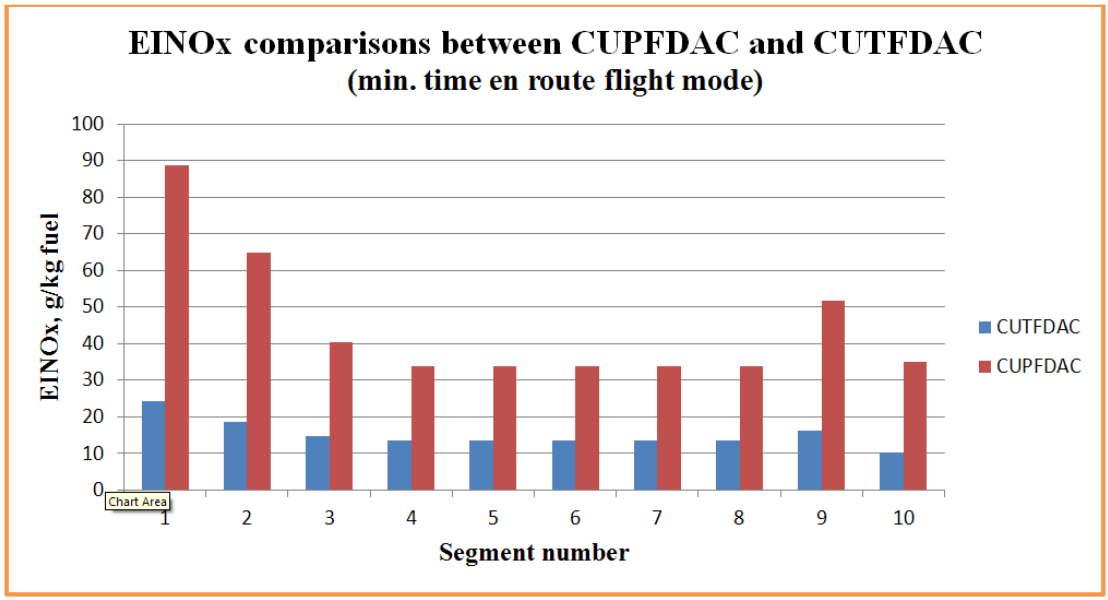

Figure 9-122 EINOx comparisons between CUPFDAC and CUTFDAC ('min. flight time' en route flight mode)

Table 9-51 and Figure 9-117 provide the comparisons of the overall performance in terms of fuel consumption, flight time and main gaseous emissions between CUPFDAC and CUTFDAC under the minimum fuel consumption flight mode for the en route flight phase. From the table and figure, it can be clearly found that, for the same flight mission in terms of the same mission range, the same initial aircraft mass and the same initial flight altitude, flight Mach number and flight path angle, and compared to the aircraft of CUTFDAC propelled by two traditional turbofan engines, the application of the new-generation open rotor engine (or called propfan engine) can save around 729 kg fuel, amounting to nearly 35% less than that consumed by CUTFDAC. A direct consequence of a large amount of fuel saving achieved by CUPFDAC will result in 2282 kg (or 34.45%) less CO_2 emission and 907 kg (or 34.89%) less H_2O produced. Besides, from the point of view of the flight time, although more travel time needed by CUPFDAC, the difference of around 2 minutes when compared to the average mission time of around 51 minutes is completely ignorable. However, in spite of the obvious advantages which the new-generation open rotor has in fuel saving and reduced emissions of CO_2 and H_2O, significant increase in NOx emission (around 18 kg or nearly 70% more than that from CUTFDAC) has been produced by the flight flown by CUPFDAC.

The overall comparisons between CUPFDAC and CUTFDAC under the minimum flight time mode for the en route mission are given in Table 9-52 and Figure 9-118. Similar to the above results from the minimum fuel consumption flight mode, the aircraft driven by the new-generation open rotor engine continues to show the significant superiority in fuel consumption as well as the emissions of CO_2 and H_2O over the CUTFDAC propelled by the conventional turbofan configuration when both aircraft are operated with the minimum flight time mode. According to the comparison results in Table 9-52, nearly 1073 kg (or 35.27%) fuel can be saved and correspondingly around 3360 kg (or 35.01%) CO_2 emission and around 1334 kg (or 35.44%) H_2O emission can be avoided. The difference in the flight time is increased to nearly 4 minutes (certainly more time is required by CUPFDAC to complete the mission), however, compared to the average total mission time of nearly 43 minutes, the slight difference can still be ignored. Higher NOx emission is still a main challenge to the open rotor engine. Under the minimum flight time mode, based on the results from Table 9-52, the flight flown by CUPFDAC will produce around 60 kg (or 112.21%) more NOx than that from the flight by CUTFDAC.

The significant differences in the operation performances described above between CUPFDAC and CUTFDAC for the en route flight mission respectively under two typical flight modes can be explained very well by means of the comparisons of the two different types of power plants adopted in this research, that is, the new-generation open rotor engine and the conventional turbofan engine. From the previous chapter on engine performance modelling, it can be clearly found that the new-generation open rotor engine which drives the aircraft of CUPFDAC is of obvious higher component efficiencies and much higher turbine entry temperature (TET) compared to the technology level represented by the turbofan engine propelling the aircraft of CUTFDAC (besides, Tables 9-53 and 9-55 as well as Figures 9-119 and 9-121 further provide the comparisons of TET between the two engines during the en route flight operation. From these tables and figures, it can be noted that the open rotor engine operates with significantly higher TET than in the case of the traditional turbofan engine under both flight modes. For instance, under the minimum fuel consumption flight mode, the TET used by the open rotor engine will be 197.6 K ~ 447.79 K or 16.25% ~ 37.13% higher than in the case performed by the turbofan engine, while when flying

with the minimum flight time mode, the open rotor engine will operate at the TET levels 350 K~ 498.8 K or 23.34% ~ 45.74% higher), which both make good contributions to the increase in the thermal efficiency of the open rotor engine, and on the other hand, the inherent nature of much higher bypass ratio from open rotor engine (it is reported that the bypass ratio of an open rotor engine can reach 35, while the design value in the bypass ratio of the turbofan in this research is only 5.46) also brings the propulsive efficiency of this type of engine to a higher level due to much lower jet efflux velocity (with such a high bypass ratio, the propulsive efficiency of a modern open rotor engine can amount to above 90 per cent while for a conventional turbofan engine like this used in CUTFDAC, the efficiency value is only around 0.7~0.8). Therefore, as a result, higher engine overall efficiency which equals the product of thermal efficiency and propulsive efficiency and hence lower fuel consumption can be achieved by the new-generation open rotor engine during the operation of this en route flight. The reduction in fuel consumption from CUPFDAC naturally results in the proportionate decreases in both CO_2 and H_2O emissions as well because of the almost unchanged values of emission index in CO_2 and H_2O (total emission (g) = emission index (g/kg fuel) × total fuel consumption (kg)). However, in the case of NOx emission, the situation is completely changed. Here, the NOx emission index will not be any more kept constant as the emission indices of CO_2 and H_2O are and on the contrary experience a significant increase when CUPFDAC is operated for the en route mission (Tables 9-54 and 9-56 as well as Figures 9-120 and 9-122 give the comparisons of NOx emission index between the two different types of power plants during the en route flight under the two typical flight modes. For instance, under the same minimum fuel consumption flight mode, the flight implemented by the open rotor engine will result in 7.73 g/kg fuel ~ 28.6 g/kg fuel or 62.95% ~ 178.43% higher in NOx emission index than in the case of CUTFDAC powered by the turbofan engines, and when flying with the minimum flight time mode, the open rotor engine will bring 20.06 g/kg fuel ~ 64.5 g/kg fuel or 147.18% ~ 266.86% higher in NOx emission index) due to much higher engine operation temperatures described previously. The large increase in NOx emission index plays the dominant role in the production of NOx and finally results in more NOx emission than in the case performed by the turbofan engines in spite of the decreased fuel consumption from the application of open rotor engines. Therefore,

based on the above evaluations about the new-generation open rotor engine for the en route flight, a similar conclusion to that from the previous departure cases can be drawn once more, that is, the application of new-generation open rotor engine with higher component efficiencies and higher turbine entry temperature is one good option to cope with the increasing challenges the aviation industry is facing in terms of economy and environment but only when the effective low-emission combustion technology especially for the reduction in NOx emission is also be adopted in the meantime.

9.3 Arrival Flight Phase

9.3.1 CUTFDAC (Cranfield University Turbofan-Driven Aircraft)

Table 9-57 Running record of CUTFDAC-Arrival optimisation

1	Running start time/date	Mon Oct 15 23:43:19 BST 2012
2	Running end time/date	Tue Oct 16 10:29:13 BST 2012
3	Total running time	10 hours 45 minutes 54 seconds
4	Generation number	350
5	Total number of evaluations	63391

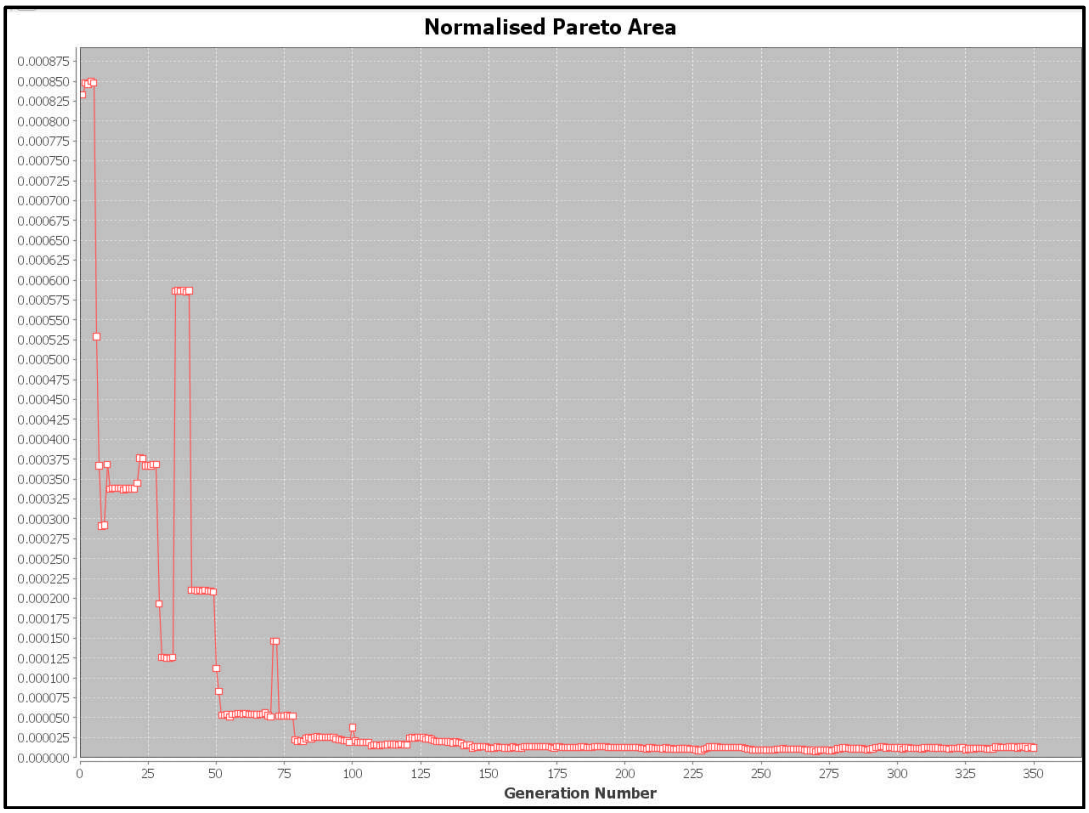

Figure 9-123 Normalised Pareto area (CUTFDAC-arrival)

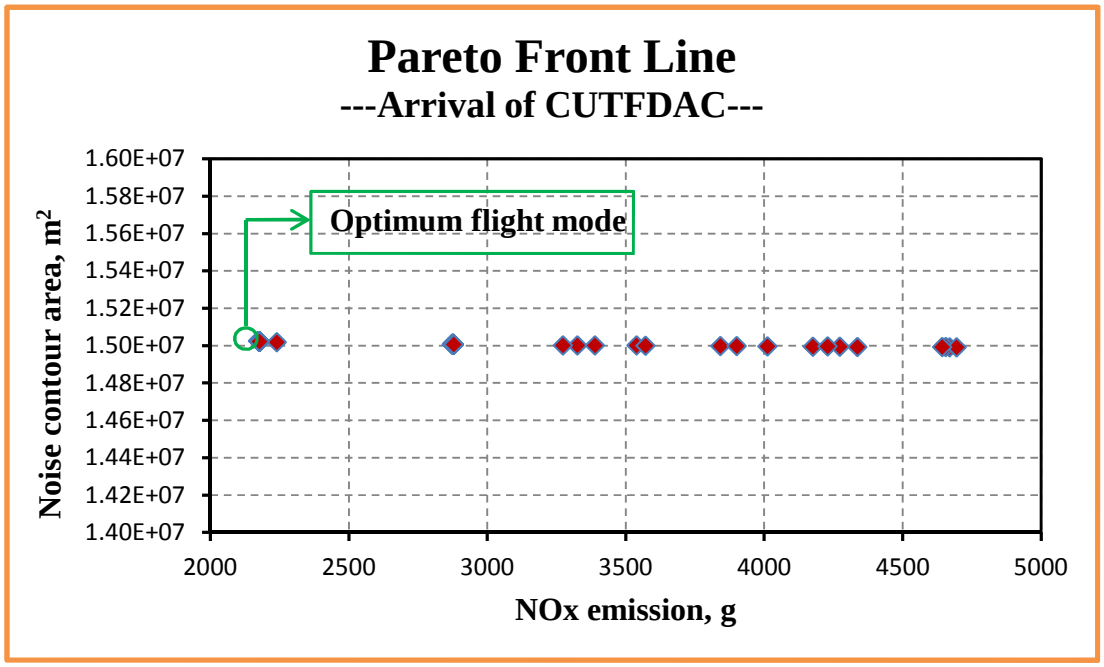

Figure 9-124 Pareto front line (CUTFDAC-arrival)

Table 9-58 Optimised results of the optimum flight trajectory (CUTFDAC-arrival)

		Optimum Flight Mode
Design variables	ALT1, (m)	2393.80
	DIS1, (m)	433.64
	CAS1, (m/s)	128.57
	CAS2, (m/s)	118.24
	CAS3, (m/s)	101.24
	CAS4, (m/s)	91.10
	CAS5, (m/s)	91.10
	CAS6, (m/s)	91.10
Objective functions	NOISE, (m^2)	15024500
	NOx, (g)	2173.66

Table 9-59 Optimum flight trajectory (CUTFDAC-arrival)

Point	**X, m**	**Z, m**	**CAS, m/s**	**TAS, m/s**	**FPA, rad.**
0	0	2438	128.6	147.65	0
1	433.64	2393.80	128.57	147.28	-0.1016
2	47175	1524	118.24	129.31	-0.0186
3	56975	1524	101.24	110.27	0
4	65953	1524	91.10	99.02	0
5	71384	1237.8	91.10	97.63	-0.0526
6	76940	945	91.10	96.23	-0.0527
7	86200	457	77.2	79.43	-0.0527

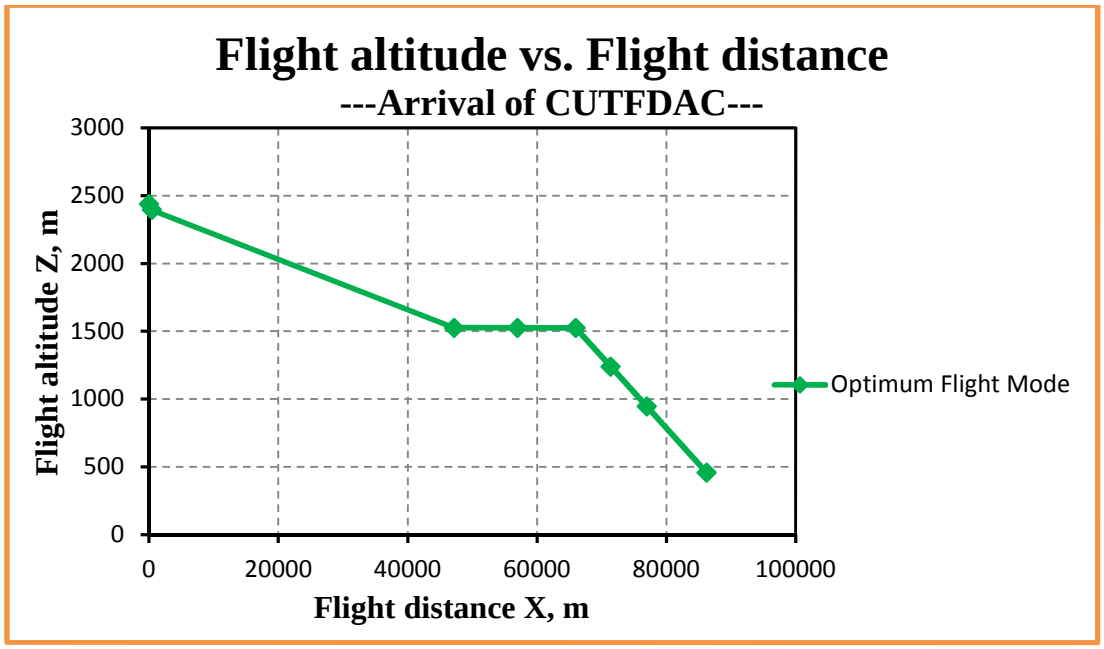

Figure 9-125 Flight altitude vs. Flight distance (the optimum flight trajectory) (CUTFDAC-arrival)

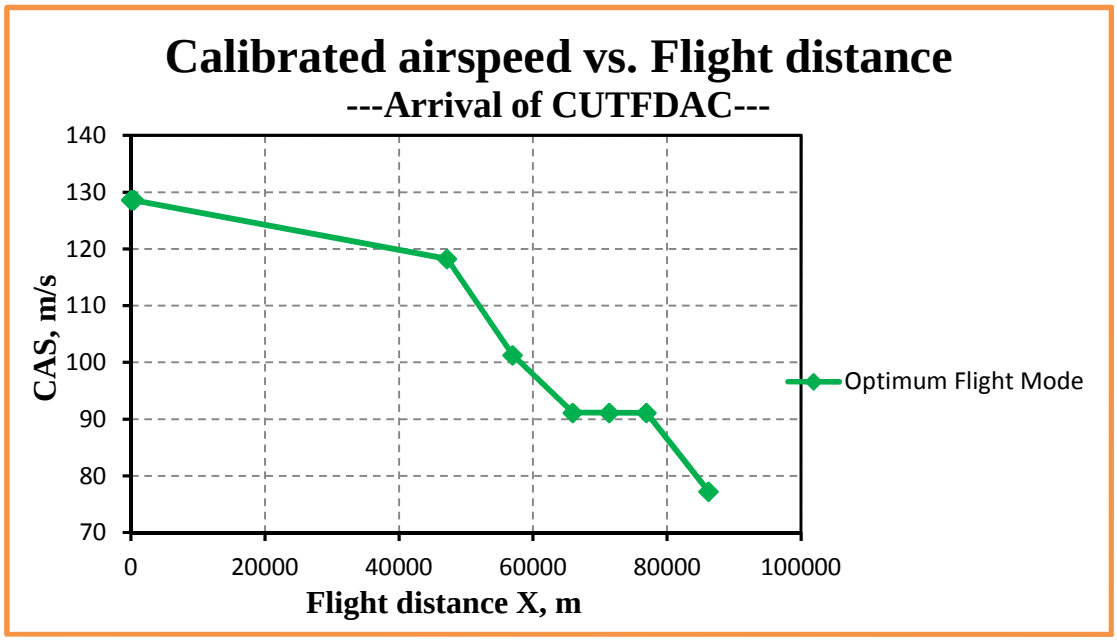

Figure 9-126 Calibrated airspeed vs. Flight distance (the optimum flight trajectory) - (CUTFDAC-arrival)

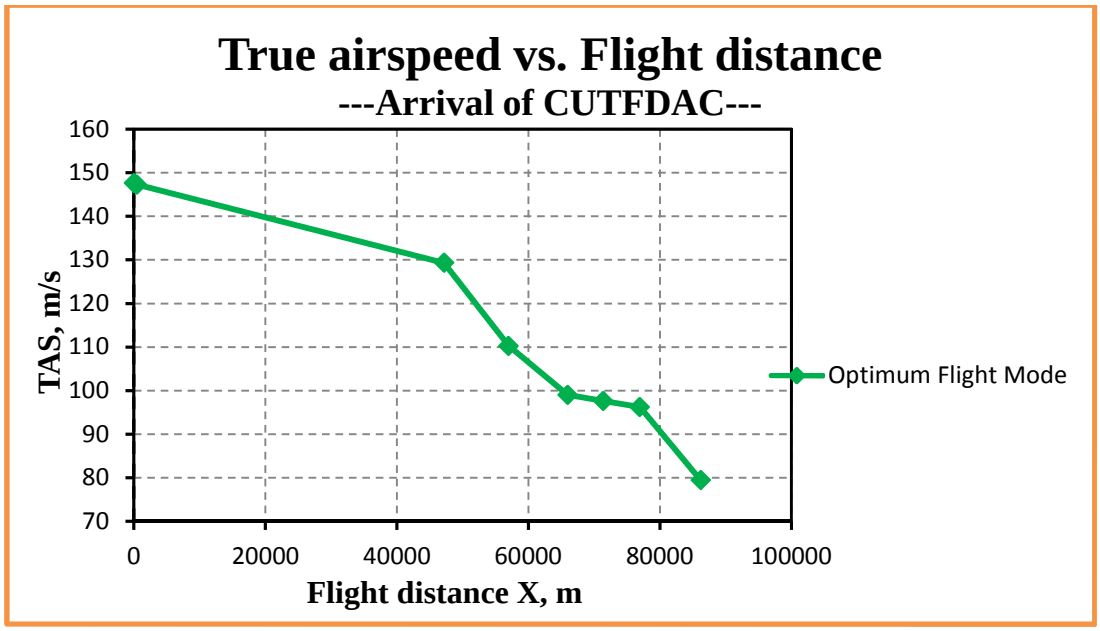

Figure 9-127 True airspeed vs. Flight distance (the optimum flight trajectory) (CUTFDAC-arrival)

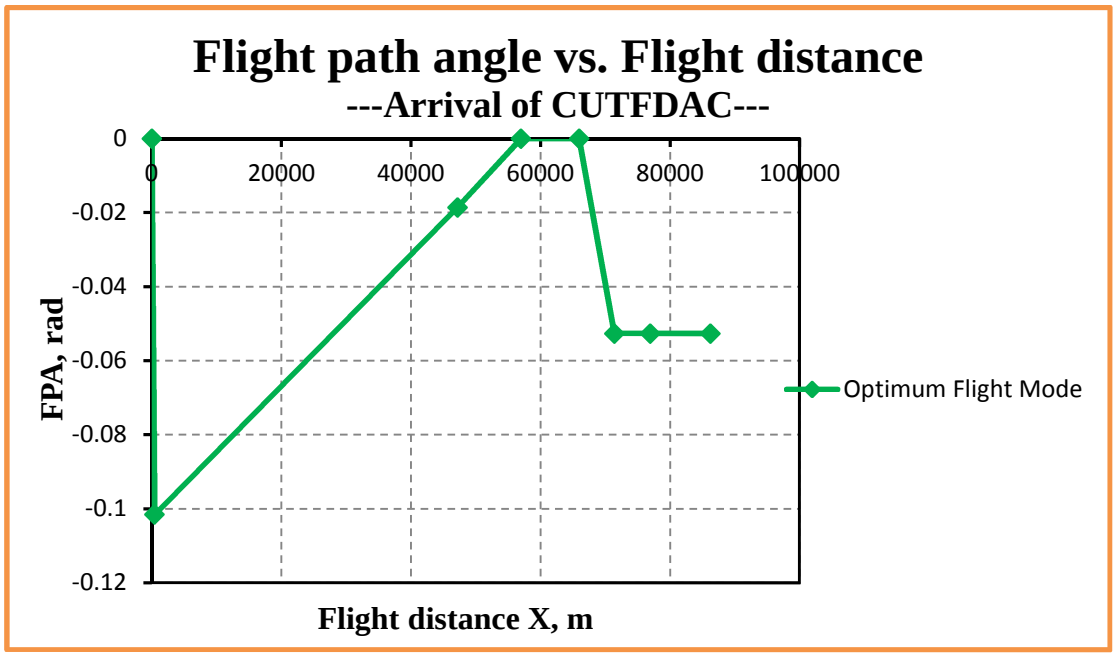

Figure 9-128 Flight path angle vs. Flight distance (the optimum flight trajectory) (CUTFDAC-arrival)

Table 9-60 Overall performance of the optimum flight trajectory (CUTFDAC-arrival)

NOx emission	Noise area	Fuel burnt	Flight time	CO emission	CO_2 emission	H_2O emission	UHC emission
(g)	(m^2)	(kg)	(s)	(g)	(g)	(g)	(g)
2173.66	15024500	317.98	727.74	6010.15	1003714.48	393726.98	340.11

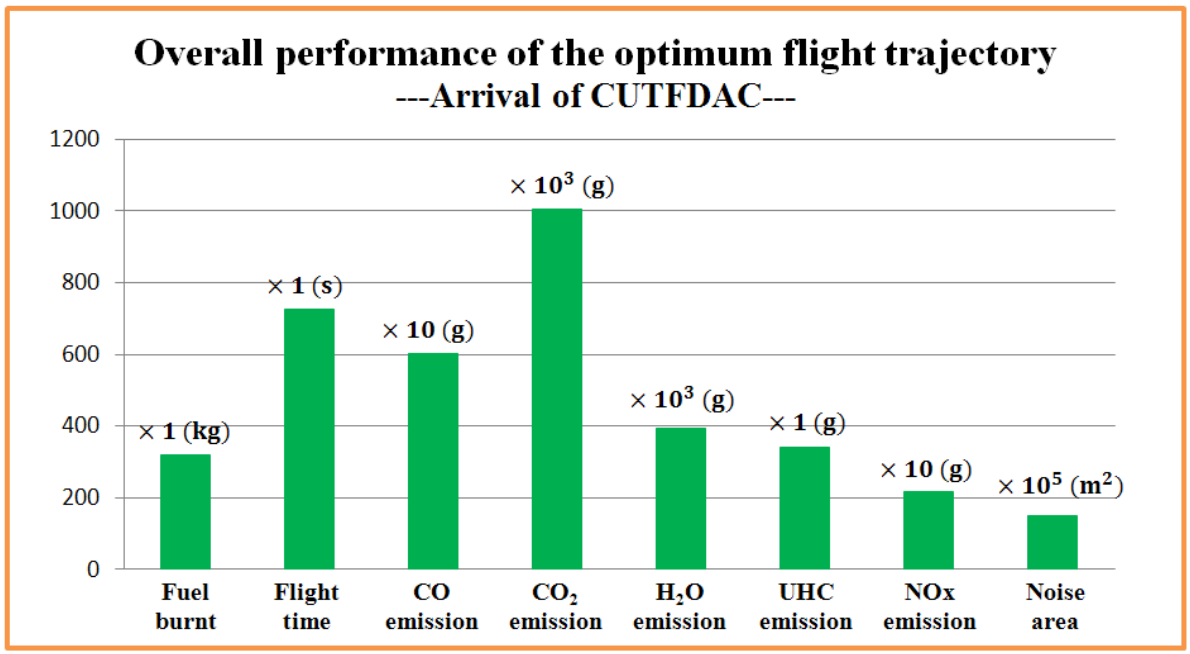

Figure 9-129 Overall performance of the optimum flight trajectory (CUTFDAC-arrival)

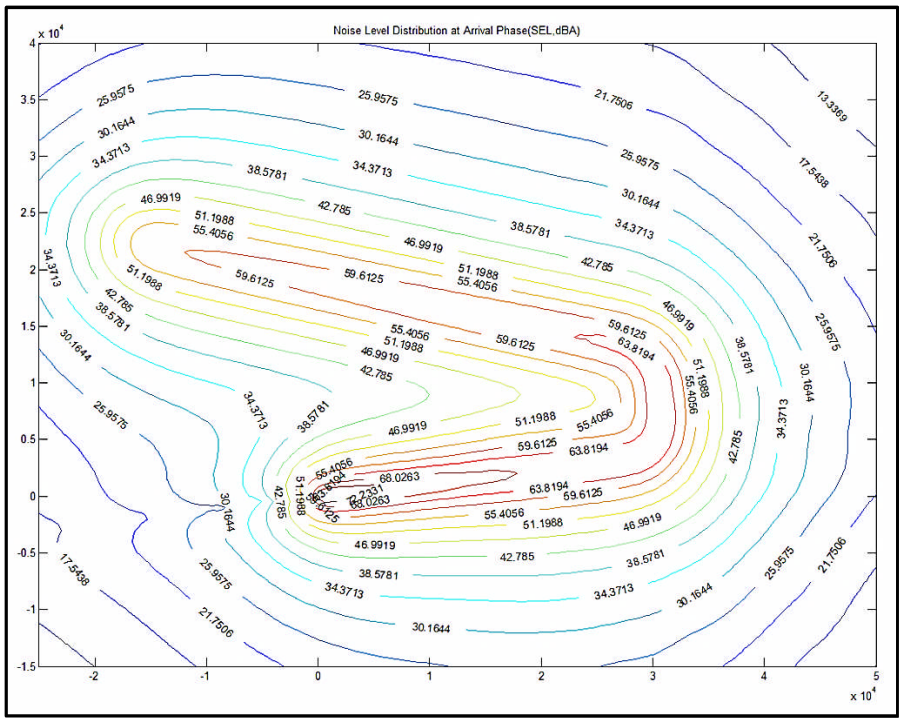

Figure 9-130 (a) Noise-level distribution contour of the optimum flight trajectory (CUTFDAC-arrival)

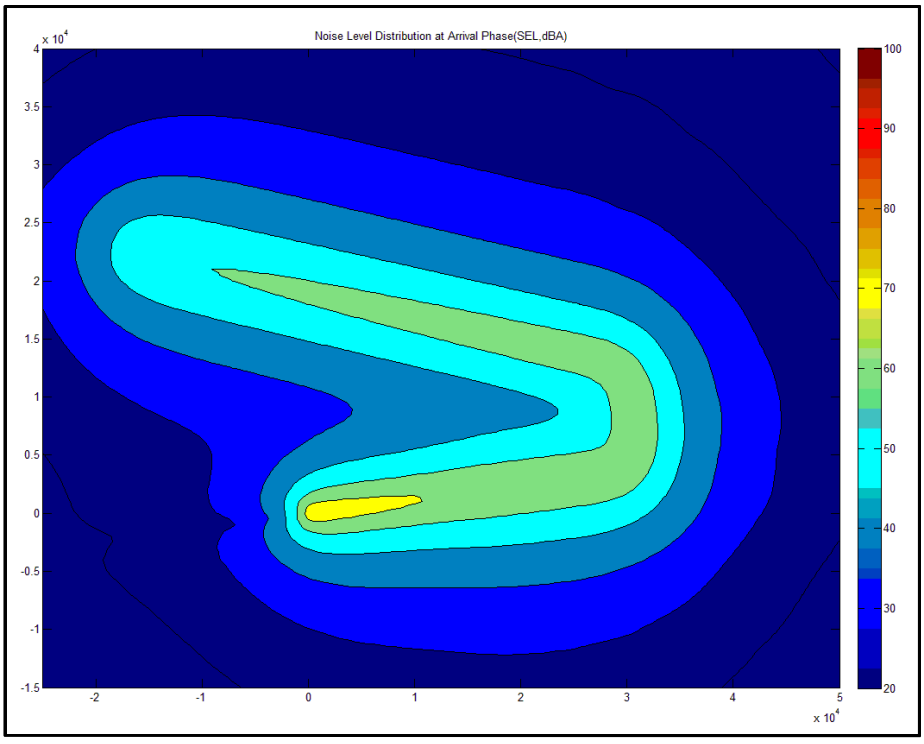

Figure 9-130 (b) Noise-level distribution filled contour of the optimum flight trajectory (CUTFDAC-arrival)

Table 9-61 Parameter segment distributions from the optimum flight trajectory (part) - (CUTFDAC-arrival)

Segment	Fn	TET	EINOx	Fuel burnt	Flight time	CO_2 emission	H_2O emission	NOx emission
	(N)	(K)	(g/kg fuel)	(kg)	(s)	(g)	(g)	(g)
1	6000.00	978.11	5.34	1.06	2.95	3359.44	1317.81	5.69
2	6003.32	971.54	5.18	121.36	338.94	383078.63	150270.22	628.73
3	19106.97	1090.04	9.07	51.56	81.82	162748.03	63841.16	467.81
4	23941.30	1117.95	9.84	59.71	85.79	188478.70	73934.52	587.40
5	17008.07	1055.20	7.63	29.66	55.27	93636.22	36730.67	226.42
6	7808.06	946.57	4.92	20.26	57.40	63945.68	25083.97	99.61
7	6635.16	906.89	4.60	34.36	105.58	108467.78	42548.65	158.01

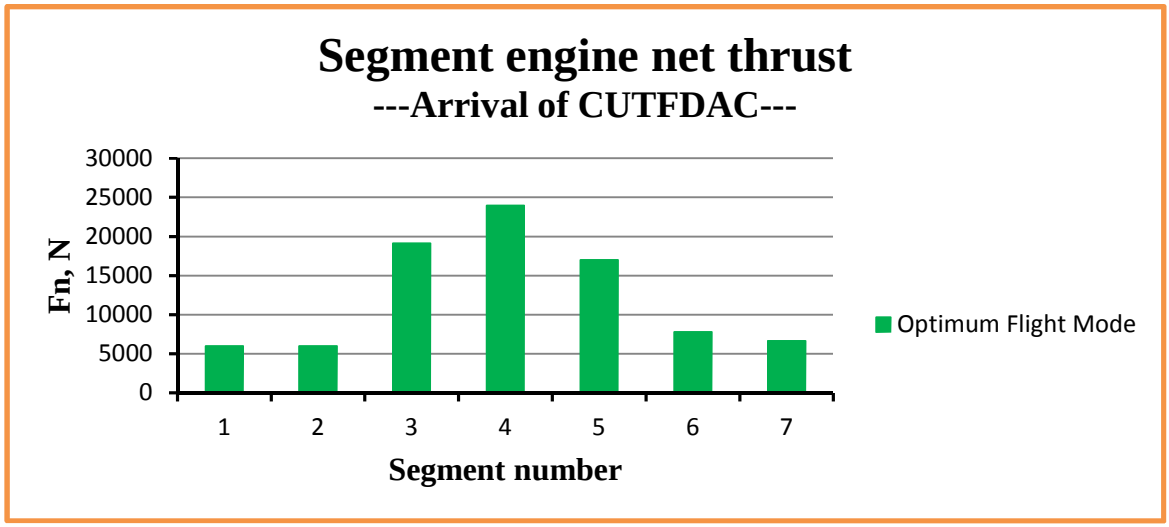

Figure 9-131 Segment engine net thrust (the optimum flight trajectory) (CUTFDAC-arrival)

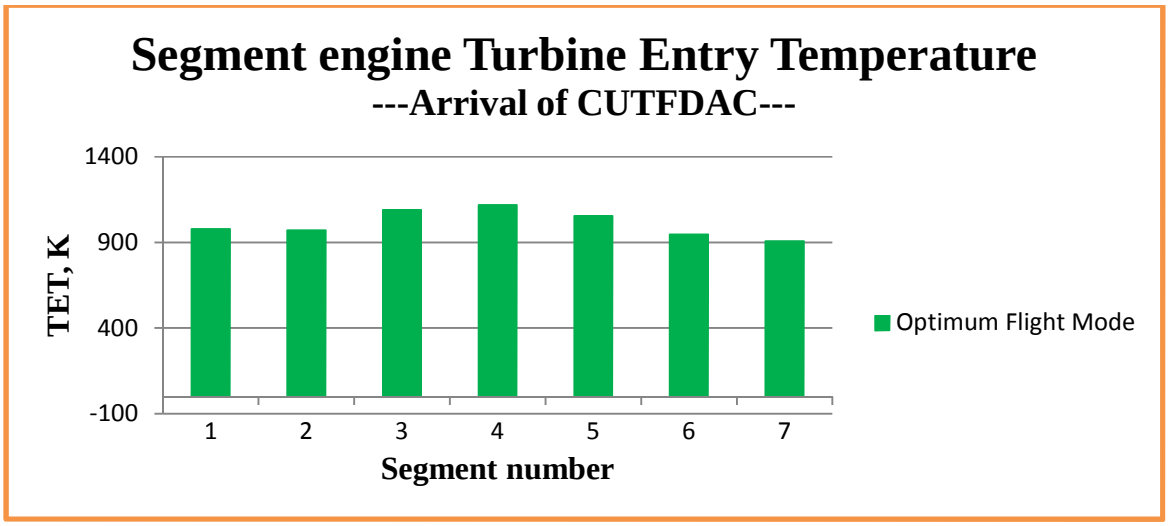

Figure 9-132 Segment engine turbine entry temperature (the optimum flight trajectory) - (CUTFDAC-arrival)

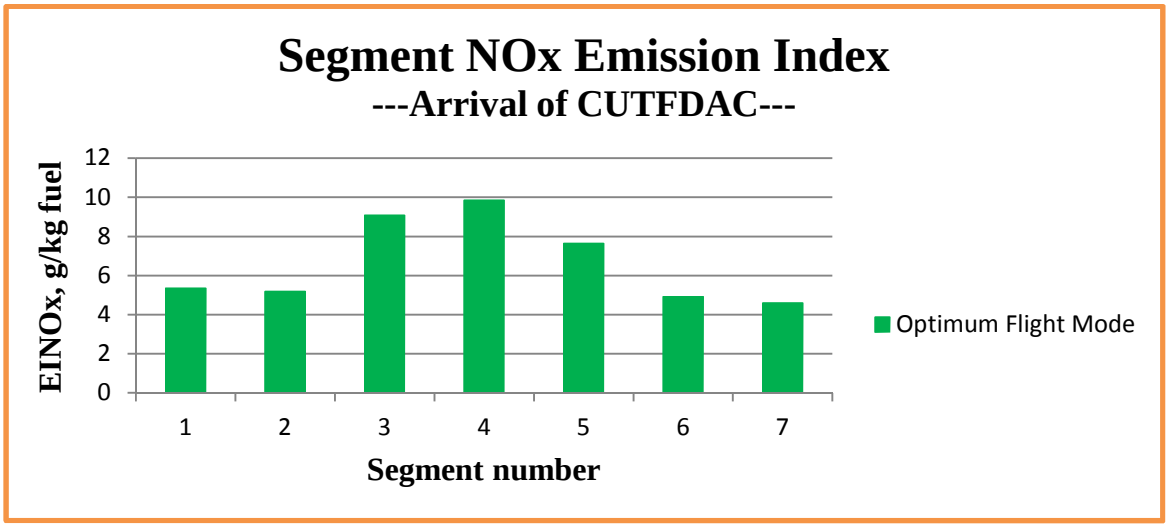

Figure 9-133 Segment NOx emission index (the optimum flight trajectory) (CUTFDAC-arrival)

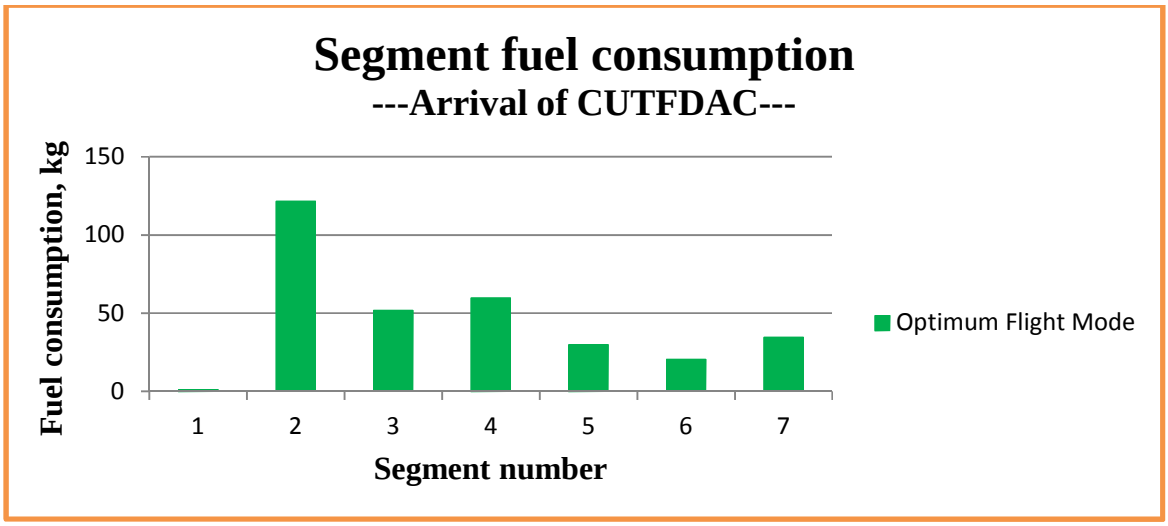

Figure 9-134 Segment fuel consumption (the optimum flight trajectory) (CUTFDAC-arrival)

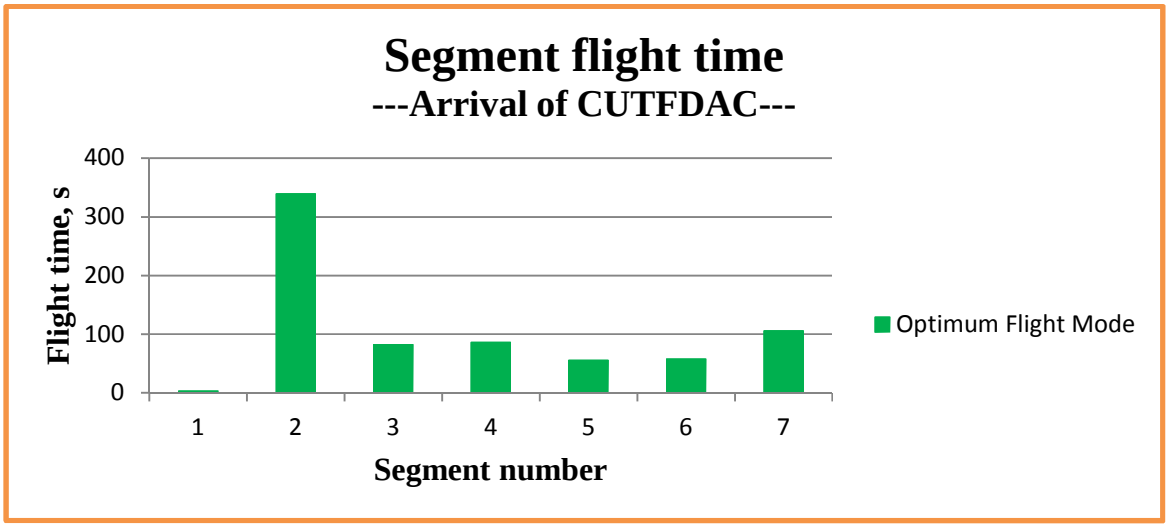

Figure 9-135 Segment flight time (the optimum flight trajectory) (CUTFDAC-arrival)

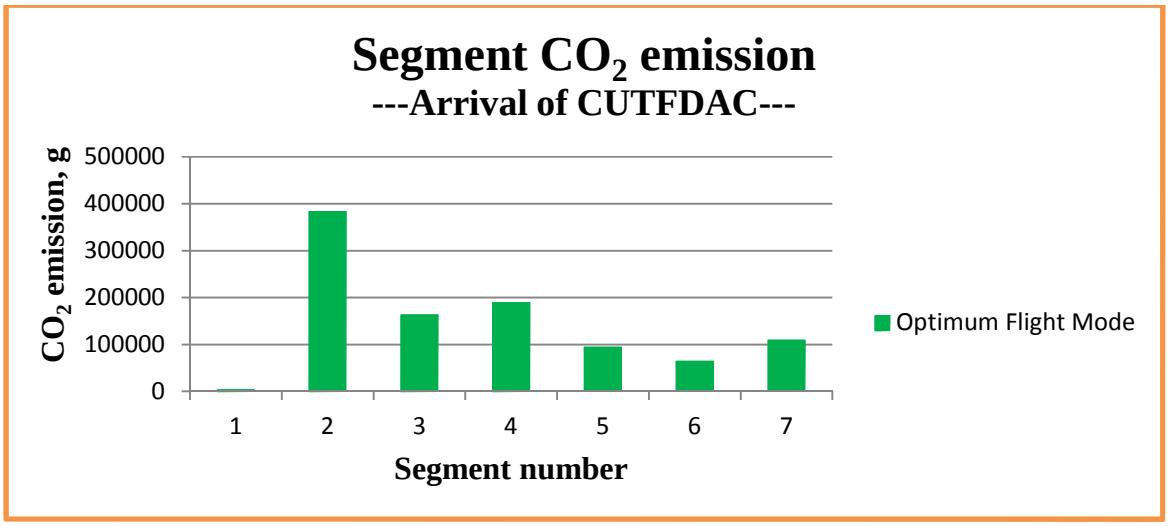

Figure 9-136 Segment CO_2 emission (the optimum flight trajectory) (CUTFDAC-arrival)

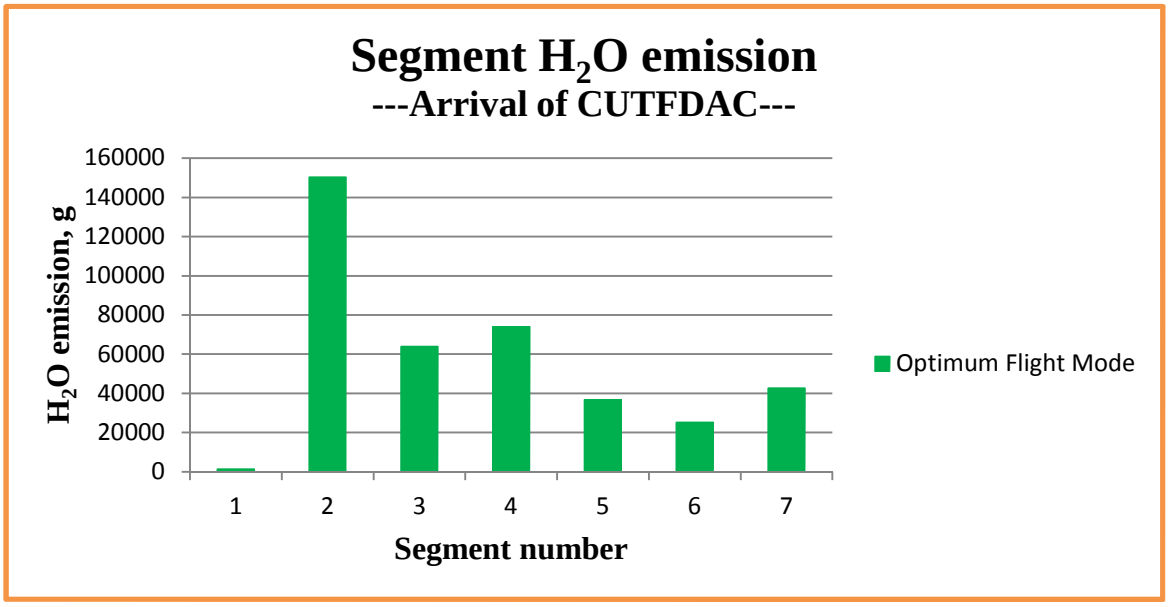

Figure 9-137 Segment H_2O emission (the optimum flight trajectory) (CUTFDAC-arrival)

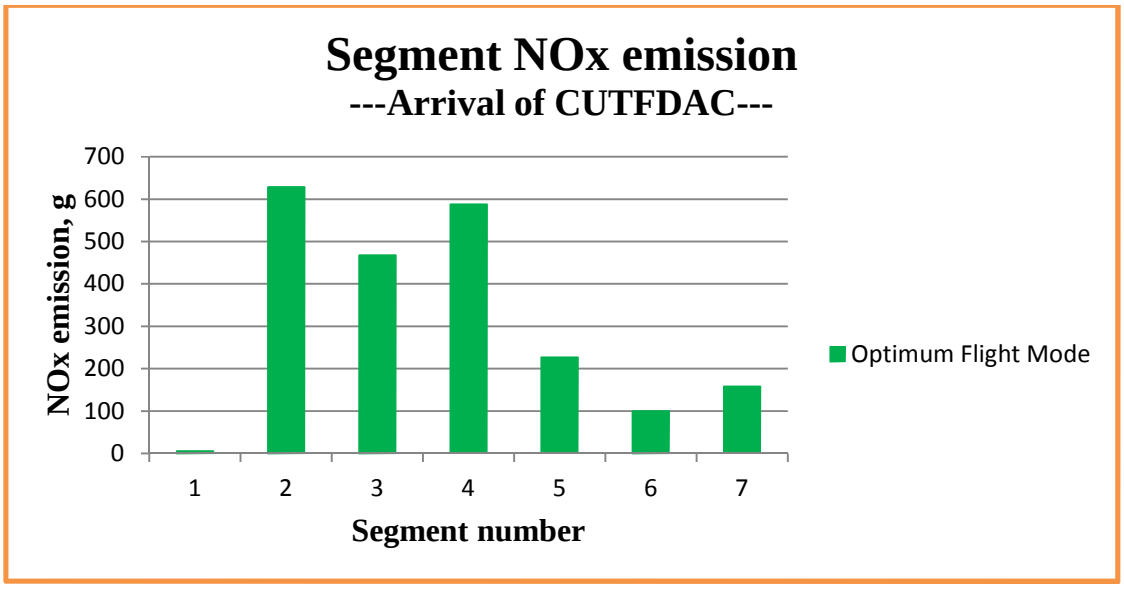

Figure 9-138 Segment NOx emission (the optimum flight trajectory) (CUTFDAC-arrival)

As for the arrival flight performed by CUTFDAC, the observations and summaries based on the above tables and figures are as follows:

1) From the plot of normalised Pareto area (Figure 9-123) and the achieved Pareto front line (Figure 9-124), it can be inferred that the convergence of this optimisation process after 350 generations (totally 63391 evaluations) (see Table 9-57) has been reached.
2) The time cost of the entire optimisation process for this case study is 10 hours 45 minutes 54 seconds (Table 9-57), that is, 110.7 seconds/generation or 0.6 seconds/evaluation on average.
3) From the obtained Pareto front line (Figure 9-124), it can be found that although these achieved optimised solutions are still Pareto efficient (the Pareto line declines slightly from the left side to its right side with the increase in NOx emission), namely, these solutions are unique and not dominant over each other with different trade-offs between the two objectives – NOx emission and noise contour area, the benefit from the reduction in noise contour area at the cost of the increased NOx emission is very small. Therefore, for this specific case study, the actual optimum flight trajectory is that one which produces the least NOx

emission, that is, the leftmost point along the Pareto line which has been marked in green in the Figure 9-124.

4) Table 9-58 gives the optimised results of the optimum arrival trajectory in terms of eight design variables and two objective functions. Based on these results, the optimum arrival trajectory for CUTFDAC operation can be formed as illustrated in Table 9-59 and Figures 9-125 to 9-128. According to these tables and figures, the optimised results suggest that when CUTFDAC starts its arrival phase in the 1st segment, a constant-CAS descent with a very short horizontal flight distance of 433.64 m should be performed, namely, during the flight in this segment, the calibrated airspeed will be kept at 128.6 m/s same as the initial value set by ATC and in the meantime the flight altitude will experience a slight decrease from the initial 2438 m to nearly 2394 m. Correspondingly, the true airspeed will also decrease a little to 147.28 m/s from the original 147.65 m/s and the flight path angles will range from the initial zero radian at the start point to -0.1016 radians at the end of this segment; During the 2nd-segment flight, the aircraft will witness the decreases in both flight altitude and flight speeds. In light of the achieved optimisation results, in this segment, the flight altitude will be reduced to 1524 m and the CAS will decrease to around 118 m/s (correspondingly, the TAS will be also be reduced to around 129 m/s) at the end of this segment. Naturally, the negative FPAs will continue to be applied in this segment. This segment with decelerated descent will span nearly 47 km in horizontal flight distance; In the following 3rd and 4th segments, CUTFDAC will adopt the decelerated level flight. The two segments will totally cover the horizontal flight distance of nearly 19 km, and within the flight distance the flight altitude will remain at 1524 m while the CAS will be continuously reduced from 118.24 m/s at the start of the 3rd segment to 101.24 m/s at the end of the 3rd segment and to 91.10 m/s at the end of the 4th segment (correspondingly, the TAS will decrease from 129.31 m/s to 99.02 m/s as well); Interestingly, opposite to the flight in the above two segments, for the operation in the next two segments, i.e., the 5th and 6th segments, CUTFDAC will be required to fly with the constant-CAS descent, that is, the CAS will be kept at 91.10 m/s while the flight altitude will be continuously reduced to 1237.8 m at the end of the 5th segment and to 945 m at

the end of the 6th segment (correspondingly, the TAS will be reduced to 96.23 m/s when the two flight segments are completed). The horizontal flight distance covered by the two segments will amount to nearly 11 km; The last segment (i.e. the 7th segment) will again experience the reductions in both flight altitude and flight speeds. The flight in this segment will cover the horizontal flight distance of around 9 km and within this distance the flight altitude and the CAS will respectively be decreased to 457 m and 77.2 m/s (correspondingly, the TAS will also fall down to 79.43 m/s) required by ATC.

5) Based on the above optimum arrival trajectory, the corresponding overall performances of the arrival flight are provided in Table 9-60 and Figures 9-129 and 9-130. According to the evaluation results listed in the above table and figures, when the aircraft of CUTFDAC flies its arrival phase by following the above optimum trajectory, around 2 kg NOx, 1004 kg CO_2 and 394 kg H_2O will be produced (the emission of CO will amount to around 6 kg while the emission of UHC is much lower, only around 340 g), and the noise-impact area within which the magnitudes of SEL are not less than 70 dBA will amount to 15 km^2. In order to complete the arrival flight, around 318 kg fuel will be consumed and the entire flight will last nearly 728 seconds (i.e., around 12 minutes).

9.3.2 CUTPDAC (Cranfield University Turboprop-Driven Aircraft)

Table 9-62 Running record of CUTPDAC-Arrival optimisation

1	Running start time/date	Sat Nov 03 12:00:32 GMT 2012
2	Running end time/date	Mon Nov 05 20:41:31 GMT 2012
3	Total running time	56 hours 40 minutes 59 seconds
4	Generation number	450
5	Total number of evaluations	75025

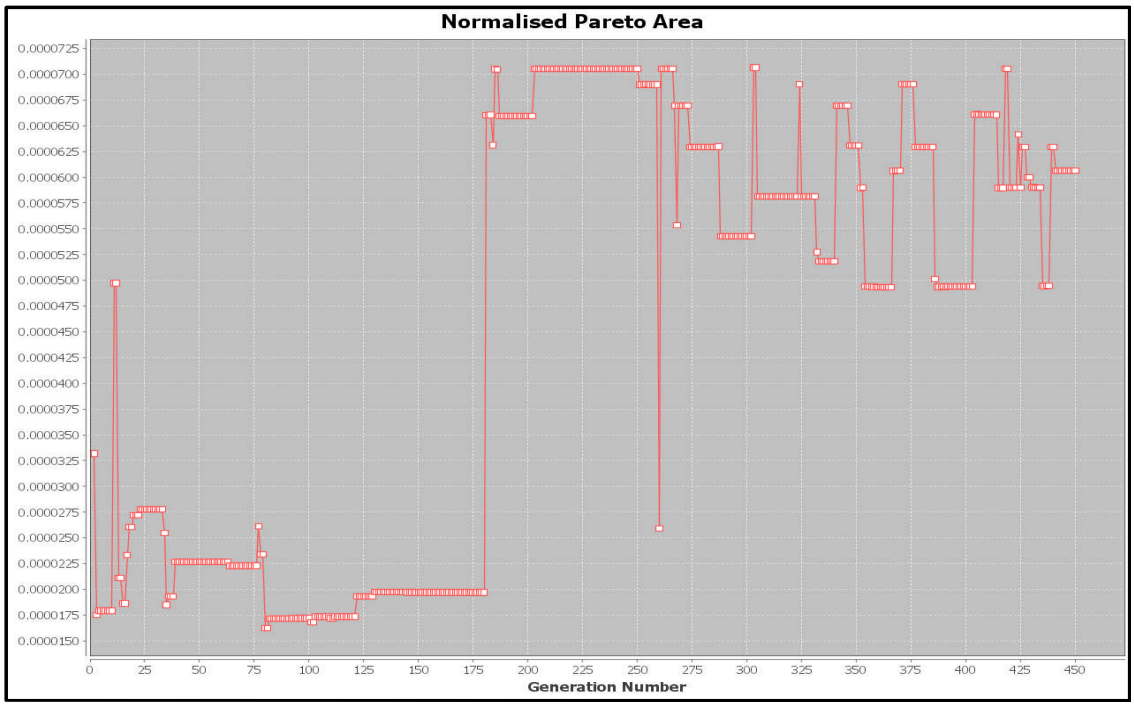

Figure 9-139 Normalised Pareto area (CUTPDAC-arrival)

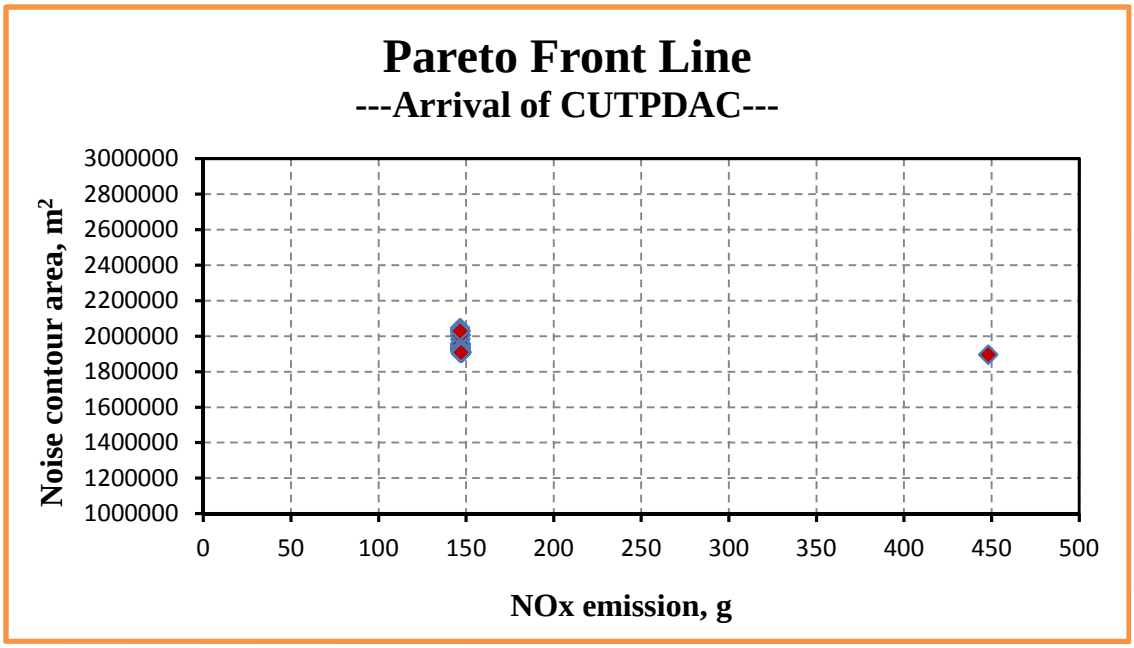

Figure 9-140 Pareto front line (CUTPDAC-arrival)

Table 9-63 Comparisons of optimised results (CUTPDAC-arrival)

	Noise contour area	**NOx emission**
	(m^2)	(g)
Maximum value	2045230	147.11
Minimum value	1907950	146.62
Average value	1928894.87	146.98
Relative deviation	7%	0.3%

Table 9-64 Optimised results of the 'average' flight trajectory (CUTPDAC-arrival)

Design variables	ALT1, (m)	2382.28
	DIS1, (m)	350.58
	CAS1, (m/s)	128.60
	CAS2, (m/s)	106.51
	CAS3, (m/s)	77.20
	CAS4, (m/s)	77.20
	CAS5, (m/s)	77.20
	CAS6, (m/s)	81.43
Objective functions	NOISE, (m^2)	1927080
	NOx, (g)	146.91

Table 9-65 Optimum flight trajectory (CUTPDAC-arrival)

Point	X, m	Z, m	CAS, m/s	TAS, m/s	FPA, rad.
0	0	2438	128.6	147.65	0
1	350.58	2382.28	128.6	147.23	-0.1576
2	47175	1524	106.51	116.15	-0.0183
3	56975	1524	77.20	83.71	0
4	65953	1524	77.20	83.70	0
5	71384	1237.8	77.20	82.53	-0.0526
6	76940	945	81.43	85.86	-0.0527
7	86200	457	77.17	79.40	-0.0527

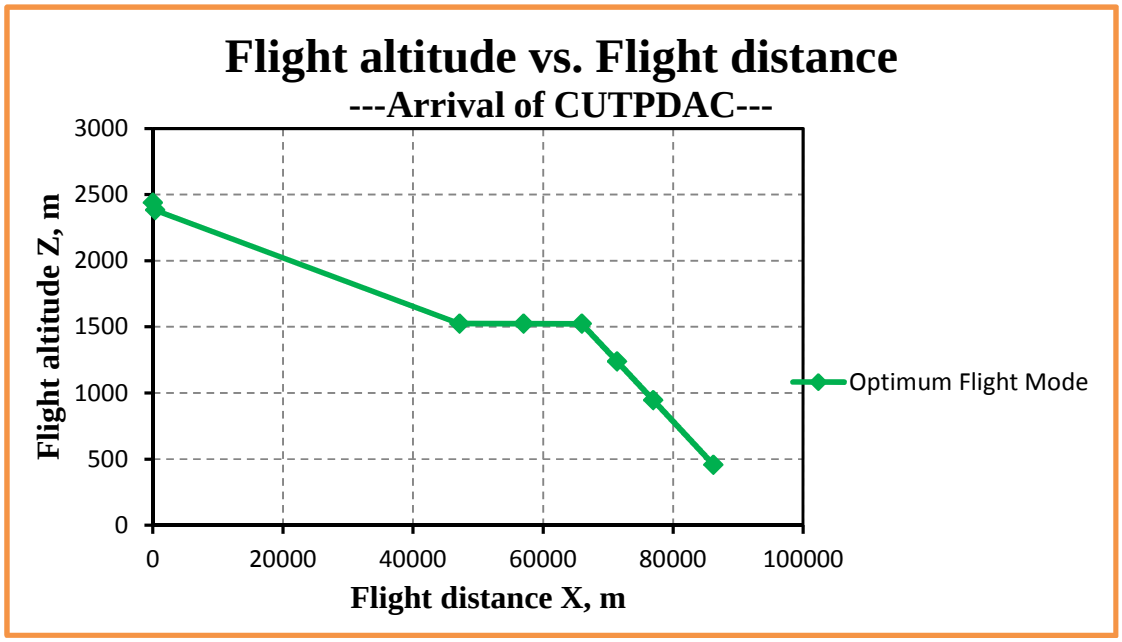

Figure 9-141 Flight altitude vs. Flight distance (CUTPDAC-arrival)

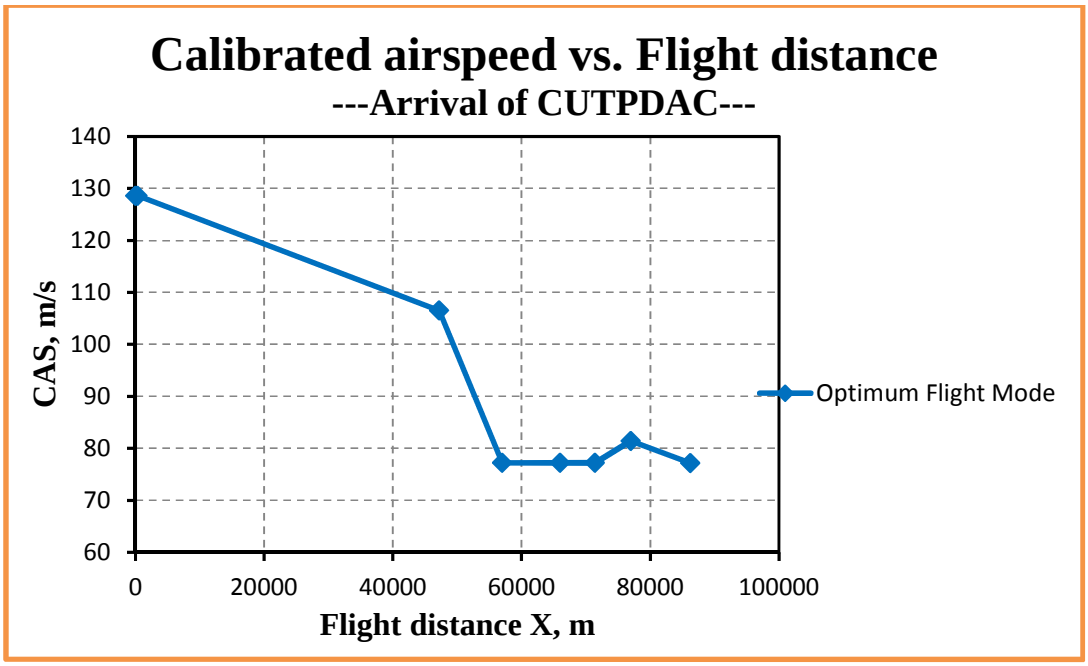

Figure 9-142 Calibrated airspeed vs. Flight distance (CUTPDAC-arrival)

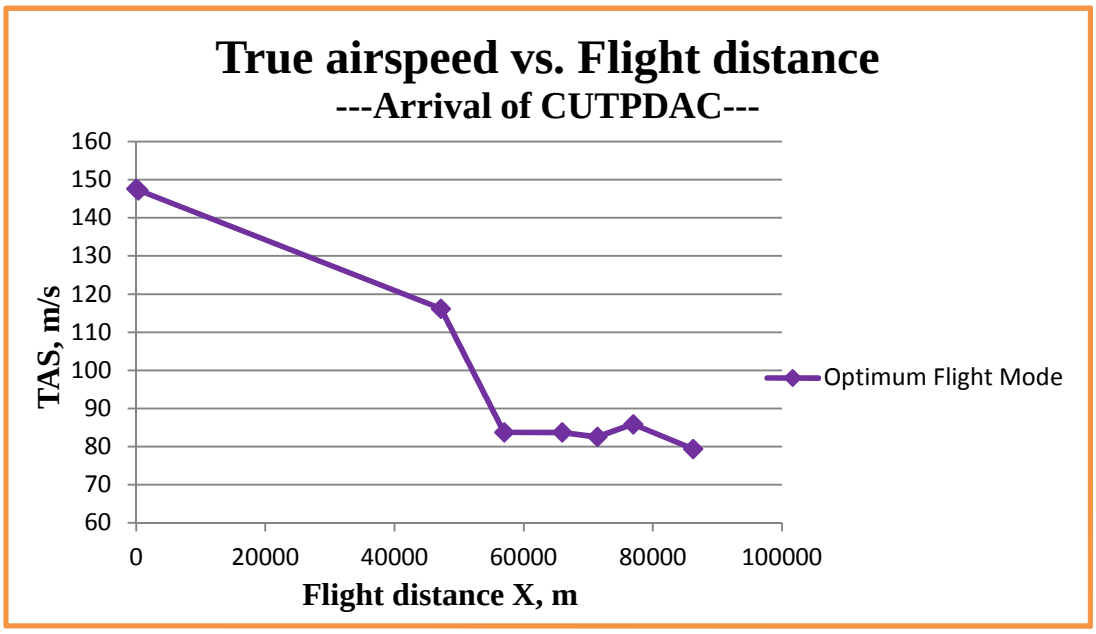

Figure 9-143 True airspeed vs. Flight distance (CUTPDAC-arrival)

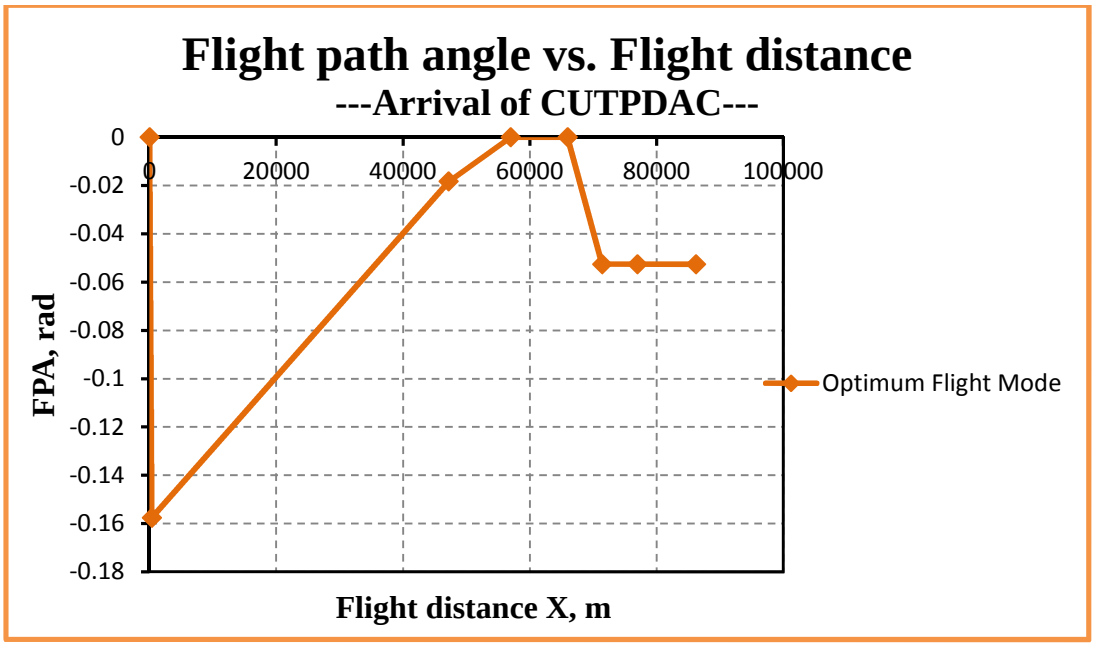

Figure 9-144 Flight path angle vs. Flight distance (CUTPDAC-arrival)

Table 9-66 Overall performance of the optimised flight trajectory (CUTPDAC-arrival)

NOx emission	**Noise area**	**Fuel burnt**	**Flight time**	**CO_2 emission**	**H_2O emission**
(g)	(m^2)	(kg)	(s)	(g)	(g)
146.91	1927080	90.18	809.48	290525.39	112073.40

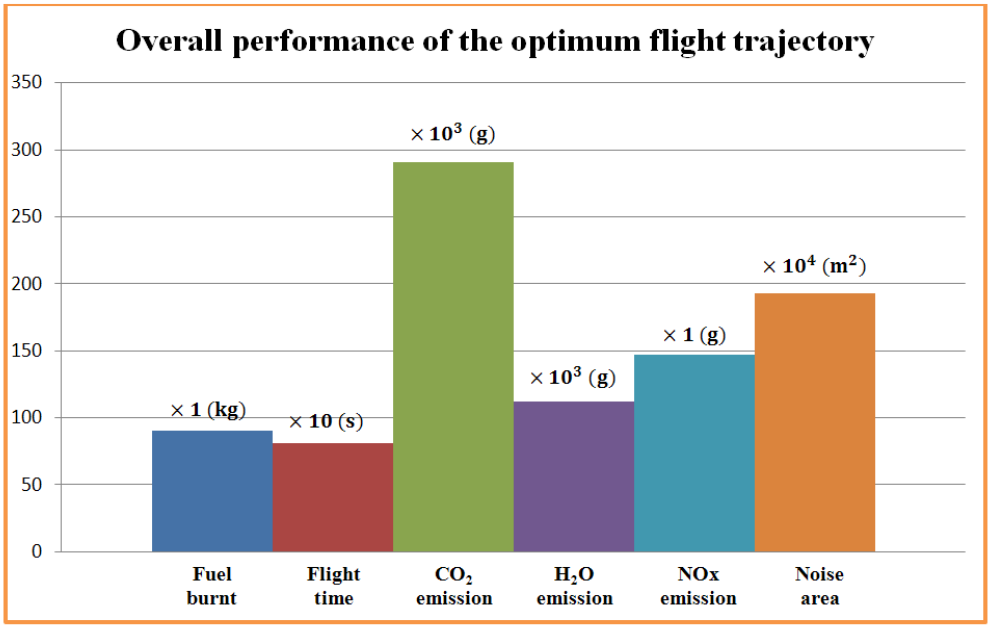

Figure 9-145 Overall performance of the optimum flight trajectory (CUTPDAC-arrival)

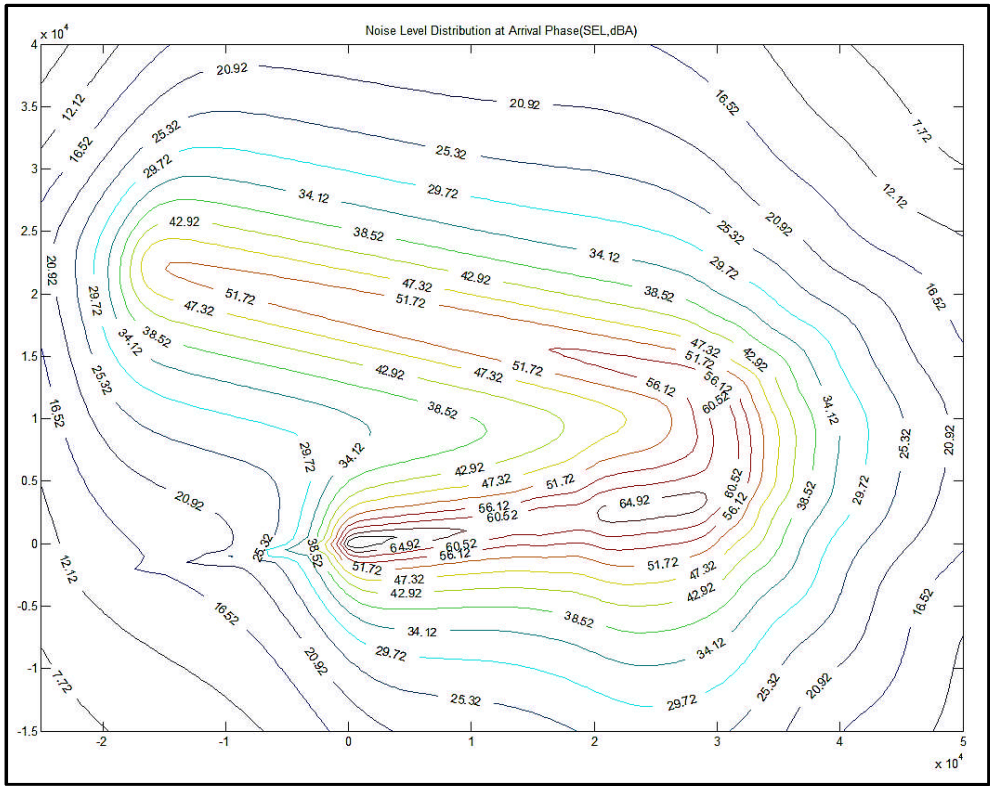

Figure 9-146 (a) Noise-level distribution contour of the optimised flight trajectory (CUTPDAC-arrival)

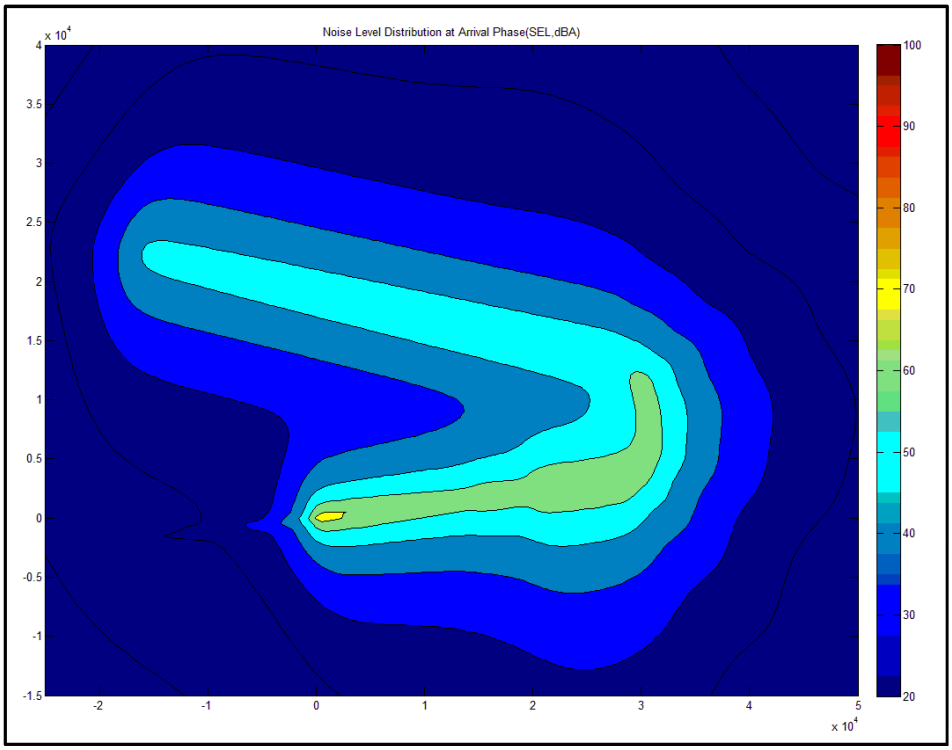

Figure 9-146 (b) Noise-level distribution filled contour of the optimised flight trajectory (CUTPDAC-arrival)

Table 9-67 Parameter segment distributions from the optimum flight trajectory (part) - (CUTPDAC-arrival)

Segment	Fn	TET	EINOx	Fuel burnt	Flight time	CO_2 emission	H_2O emission	NOx emission
	(N)	(K)	(g/kg fuel)	(kg)	(s)	(g)	(g)	(g)
1	702.86	826.25	1.00	0.20	2.39	642.57	247.06	0.20
2	764.97	821.53	1.00	29.62	358.06	95813.03	36832.02	29.70
3	5288.93	1012.59	2.28	16.15	98.08	51837.55	20065.62	36.88
4	7272.85	1041.71	2.47	19.15	107.26	61381.28	23777.09	47.31
5	4337.06	946.71	1.82	8.81	65.39	28333.47	10946.88	16.06
6	1949.06	855.40	1.04	6.44	66.08	20773.16	7999.59	6.71
7	1357.69	823.62	1.02	9.81	112.22	31744.33	12205.14	10.04

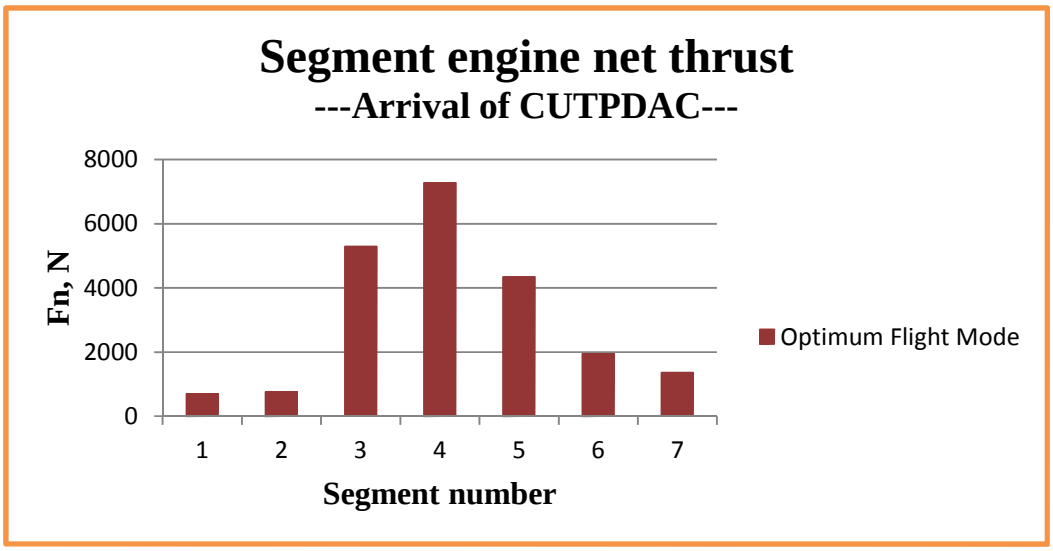

Figure 9-147 Segment engine net thrust (the optimum flight trajectory) (CUTPDAC-arrival)

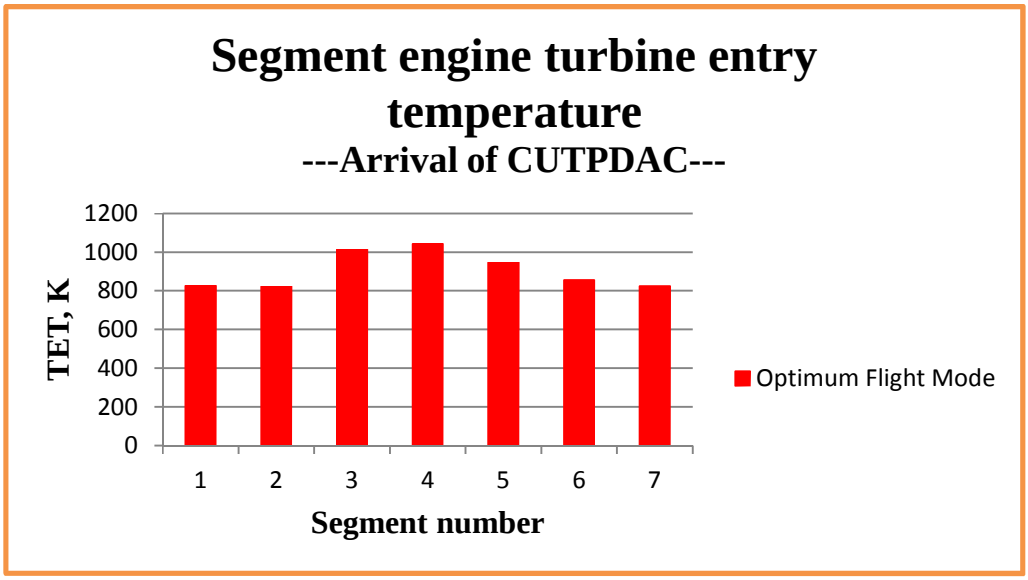

Figure 9-148 Segment engine turbine entry temperature (the optimum flight trajectory) - (CUTPDAC-arrival)

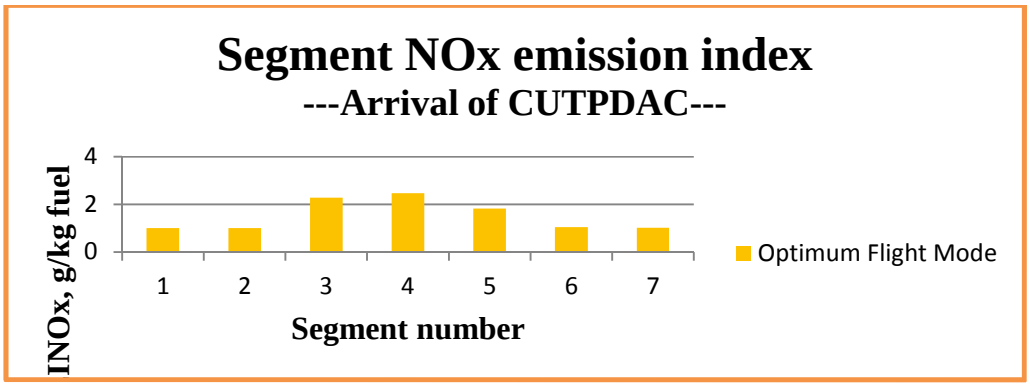

Figure 9-149 Segment NOx emission index (the optimum flight trajectory) (CUTPDAC-arrival)

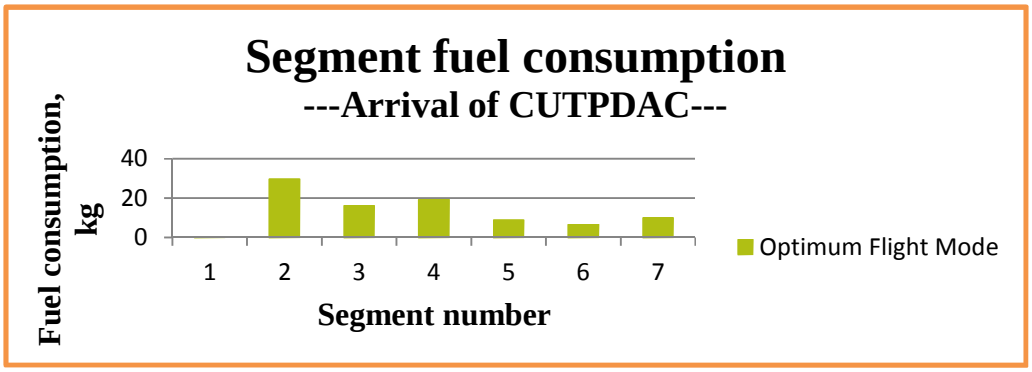

Figure 9-150 Segment fuel consumption (the optimum flight trajectory) (CUTPDAC-arrival)

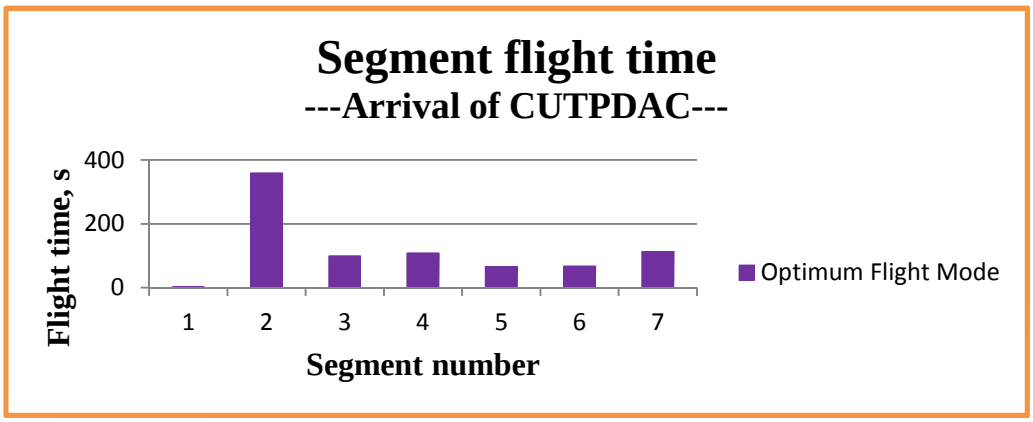

Figure 9-151 Segment flight time (the optimum flight trajectory) (CUTPDAC-arrival)

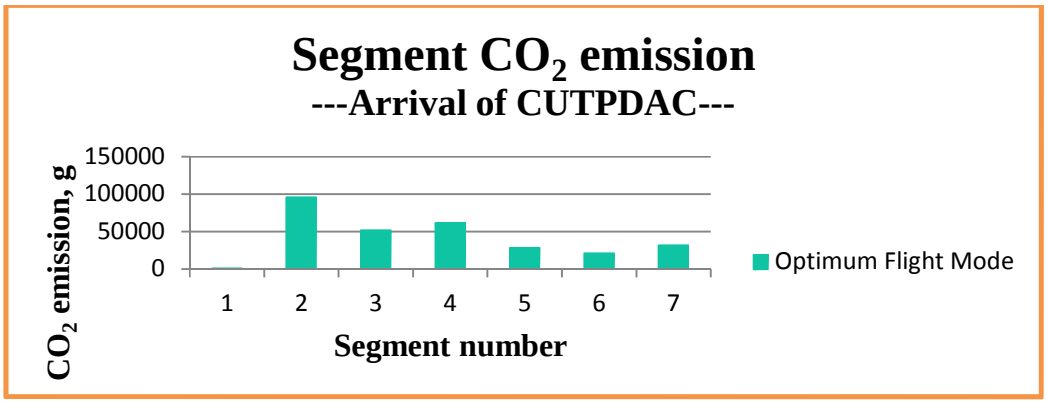

Figure 9-152 Segment CO_2 emission (the optimum flight trajectory) (CUTPDAC-arrival)

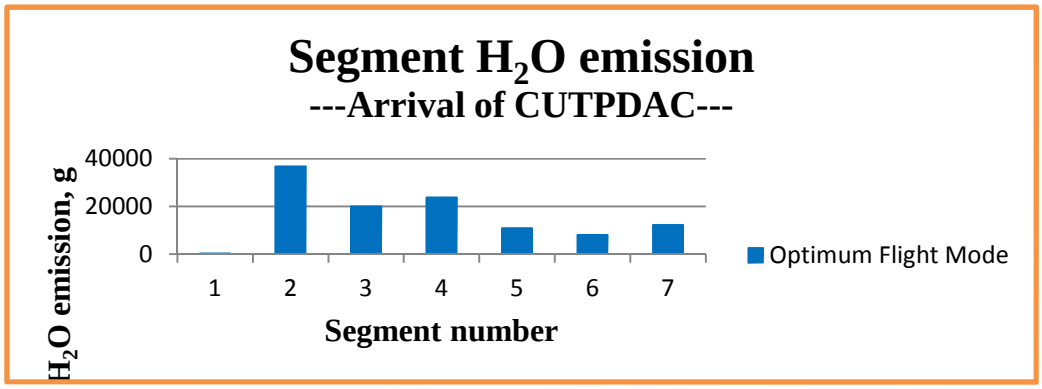

Figure 9-153 Segment H_2O emission (the optimum flight trajectory) (CUTPDAC-arrival)

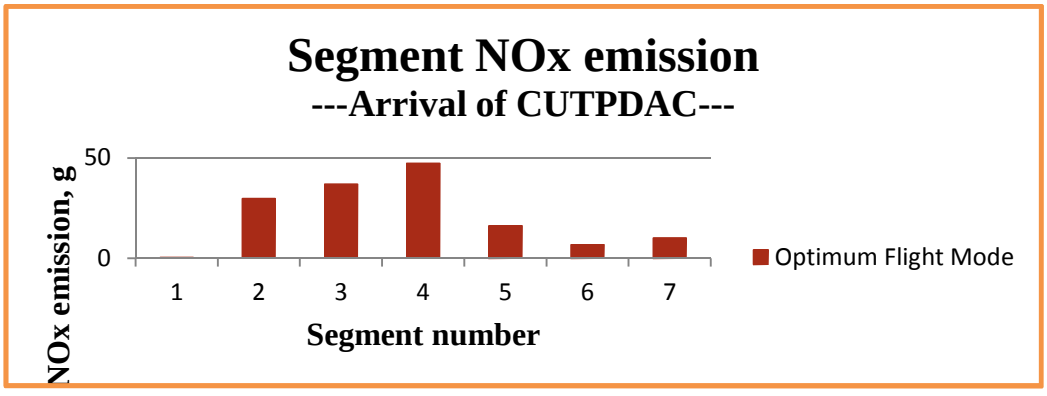

Figure 9-154 Segment NOx emission (the optimum flight trajectory) (CUTPDAC-arrival)

As for the optimisation and evaluations of the arrival case performed by the aircraft of CUTPDAC, the observations and summaries from the above tables and figures can be listed as follows:

1) From the plot of normalised Pareto area (Figure 9-139), it seems to indicate that the convergence of this optimisation process has not been obtained fully yet. However, after careful examination into the scale range of the vertical coordinate in the Figure 9-139 (it varies from the minimum value of 0.0000150 to the maximum value of 0.0000725) and comparisons with the corresponding figures respectively from the previous arrival case of CUTFDAC (see Figure 9-123. In this figure, the scale of the vertical coordinate ranges from the minimum value of 0.000000 to the maximum value of 0.000875) and the next arrival case of CUPFDAC (see Figure 9-155. In this figure, the scale varies from the minimum value of 0.00000 to the maximum value of 0.00023), it can be found that the seemingly obvious fluctuation in values of the normalised Pareto area was actually caused by the relatively narrow scale-range setting. The check and judgment for the convergence can be further made through the achieved optimisation solutions as well as the comparisons among them. The Figure 9-140 illustrates that these achieved optimised solutions have presented some regularity and these results meet the definition of Pareto-efficient solutions, that is, all these achieved optimised solutions with different trade-offs between these two objective functions (i.e., NOx emission and noise-impact area) are unique and not dominant over each other (or, it can be said that the optimisation process has proceeded to the extent that any improvement in one of the objectives will result in degradation in the other, namely, no further Pareto improvements can be available). Therefore, in this sense, the convergence has basically been achieved for the optimisation process. In addition, also from the Figure 9-140, the achieved Pareto-efficient solutions show different distribution characteristics in the objective space spanned by NOx emission and noise contour area (or called noise-impact area) from those from the previous departure and en route cases. Here, most of optimised solutions (except that solution/point on the right side in this space) tend to concentrate from each other. This tendency can also be observed from the comparisons among these optimised solutions (except the

rightmost point/solution in the Figure 9-140) which are shown in Table 9-63. From Table 9-63, it can be found that among these achieved optimised solutions, the available minimum noise-impact area is around 1.9 km^2, while the maximum noise-impact area is only around 2.0 km^2 (the relative difference between the two values which is defined as Max.-Min./Average is 7%), on the other hand, from the point of view of NOx emission, much closer results among these achieved optimised solutions have been obtained. From the same table, it can be observed that the minimum NOx emission is 146.62 g while the maximum value is only 147.11 g and the relative difference is only 0.3%. By the preliminary analysis, the phenomenon of concentration from each other among these achieved optimised solutions may be related to the selection of objective functions. For the arrival case studies in this research project, the noise-impact area and NOx emission were selected as the objective functions for the purpose of optimisation. However, these two objectives are not completely conflicting one another. For instance, the reduced engine power ratings can decrease the NOx emission and in the meantime the noise level and hence the noise-impact area as well, therefore, the optimisation with these two objective functions will to some extent present the nature of single-objective optimisation. Certainly, the two objectives are also not completely consistent because the noise-impact area depends not only on the engine power settings but also on the slant distance between the aircraft (the noise source) and the observer on the ground as well as the exposure duration which the observer on the ground will experience in this noise event. All these factors mentioned above make the contributions to shaping the Pareto frontier in the objective space.

2) Table 9-62 indicates the time cost to implement the optimisation process with 450 generations or 75025 evaluations is 56 hours 40 minutes 59 seconds, that is, around 453.5 seconds/generation or 2.7 seconds/evaluation on average.
3) Based on the above analysis and the fact that these achieved optimised results trend to concentrate from each other and the differences in the two objective functions (i.e., the noise-impact area and NOx emission) among these optimised solutions are relatively small (certainly, the rightmost point/solution in the objective space is not included because the solution, although it is Pareto

efficient, makes the arrival flight operated by CUTPDAC have to pay much more cost in terms of NOx emission to gain the very little benefit in noise-impact area. Therefore, this point/solution has only the academic interests and will not be applied in practice), an 'average' point/solution among these optimisation results which appear on the left side in the Figure 9-140 is selected as the optimum solution for this arrival case flown by CUTPDAC (in fact, alternatively, the solution with the least noise-impact area among the left-side solution cluster can also be selected as the optimum solution. However, the differences between the two 'representative' solutions are small with the deviation in the noise-impact area around 1% and the deviation in the NOx emission less than 0.3%).

4) Table 9-64 provides the optimised results of the optimum arrival trajectory in terms of eight design variables and two objective functions. Based on the optimised results, Table 9-65 and Figures 9-141 to 9-144 further describe the optimum flight trajectory by means of variations of flight altitude (Z), calibrated airspeed (CAS), true airspeed (TAS) and flight path angle (FPA) versus horizontal flight distance (X). According to the table and figures, the optimised results suggest that when CUTPDAC flies in the 1st segment, the constant-CAS descent will be applied, that is, the calibrated airspeed will remain at 128.6 m/s same as the value initially set by ATC while the flight altitude will be reduced from the initial 2438 m to around 2382 m at the end of this segment. Correspondingly, the true airspeed will also slightly decrease to 147.23 m/s from the initial value of 147.65 m/s. This flight segment will only cover around 350 m in the horizontal flight distance; once entering into the 2nd flight segment, the aircraft will experience both deceleration and reduction in flight altitude. In light of the optimisation results, the flight altitude will be decreased to 1524 m and the flight speeds will fall down to 106.51 m/s and 116.15 m/s respectively in terms of CAS and TAS. The flight in the 2nd segment will span around 47 km and negative FPAs are the natural results in this flight segment; in the following 3rd segment, the decelerated level flight (or called constant-altitude deceleration) will be adopted by CUTPDAC. During this flight segment, the aircraft will keep its flight altitude at 1524 m but on the other hand continuously decrease its CAS

to 77.20 m/s when the end of this segment is reached (correspondingly, its TAS will also be reduced to 83.71 m/s). The horizontal flight distance flown in this segment will amount to nearly 10 km; in the coming 4th segment, the flight altitude of 1524 m will continue to be kept as performed in the above 3rd segment and further the flight speeds in both CAS and TAS will also remain at their own levels (i.e., 77.20 m/s and 83.7 m/s respectively). In this segment, FPA will remain at zero radian and the horizontal flight distance flown by the aircraft will be nearly 9 km; when CUTPDAC enters into the 5th flight segment, the descent with constant CAS (77.20 m/s) will be applied again. By the end of this segment, the flight altitude will be decreased to 1237.8 m within the horizontal flight distance of around 5.4 km; the 6th segment will continue to witness the decrease in flight altitude until the altitude of 945 m is reached at the end of this segment. However, this segment will experience a slight increase in the calibrated airspeed from 77.20 m/s to 81.43 m/s (correspondingly, TAS will increase from 82.53 m/s to 85.86 m/s) and the reason for this increase is not very clear so far (therefore more investigation about it will be needed in future). According to the results in Table 9-59, this flight segment will span around 5.6 km; in the last segment (i.e., the 7th segment), the deceleration and descent will be continued by CUTPDAC until the required flight altitude (457 m) and CAS (77.17 m/s) by ATC are reached by the end of this segment. This flight segment will cover the horizontal flight distance of around 9.3 km.

5) Based on the above achieved optimum arrival trajectory, as a result, Table 9-66 and Figures 9-145 to 9-146 give the corresponding overall performances in terms of NOx emission, noise-impact area, noise-level distribution around the runway, fuel consumption, flight time as well as emissions of CO_2 and H_2O. According to the evaluation results listed in Table 9-66, when the aircraft of CUTPDAC flies its arrival phase by following the above optimum trajectory, around 147 g NOx will be emitted and the area of around 1.9 km^2 in the vicinity of the runway will be influenced by noise whose magnitudes in terms of SEL are not less than 70 dBA. The entire flight will last nearly 810 seconds (i.e., 13.5 minutes) with around 90 kg of fuel consumed. Additionally, this arrival flight will produce nearly 291 kg of CO_2 and around 112 kg of H_2O as well.

9.3.3 CUPFDAC (Cranfield University Propfan-Driven Aircraft)

Table 9-68 Running record of CUPFDAC-Arrival optimisation

1	Running start time/date	Sat Nov 24 11:45:41 GMT 2012
2	Running end time/date	Tue Nov 27 01:08:35 GMT 2012
3	Total running time	61 hours 22 minutes 54 seconds
4	Generation number	450
5	Total number of evaluations	75183

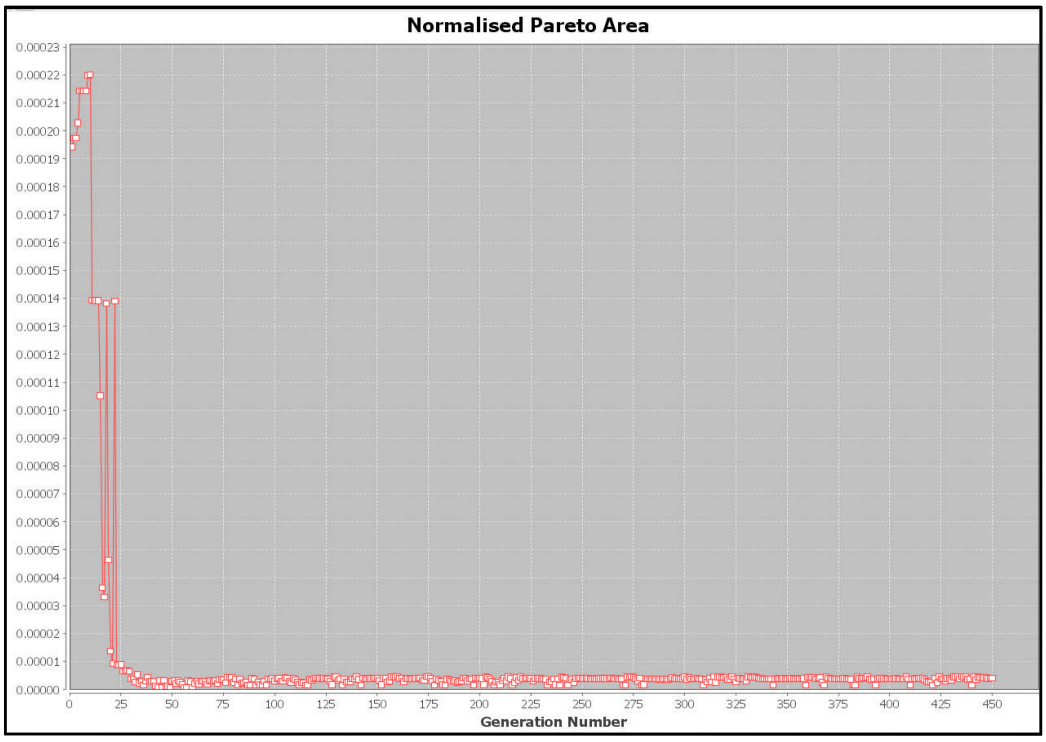

Figure 9-155 Normalised Pareto area (CUPFDAC-arrival)

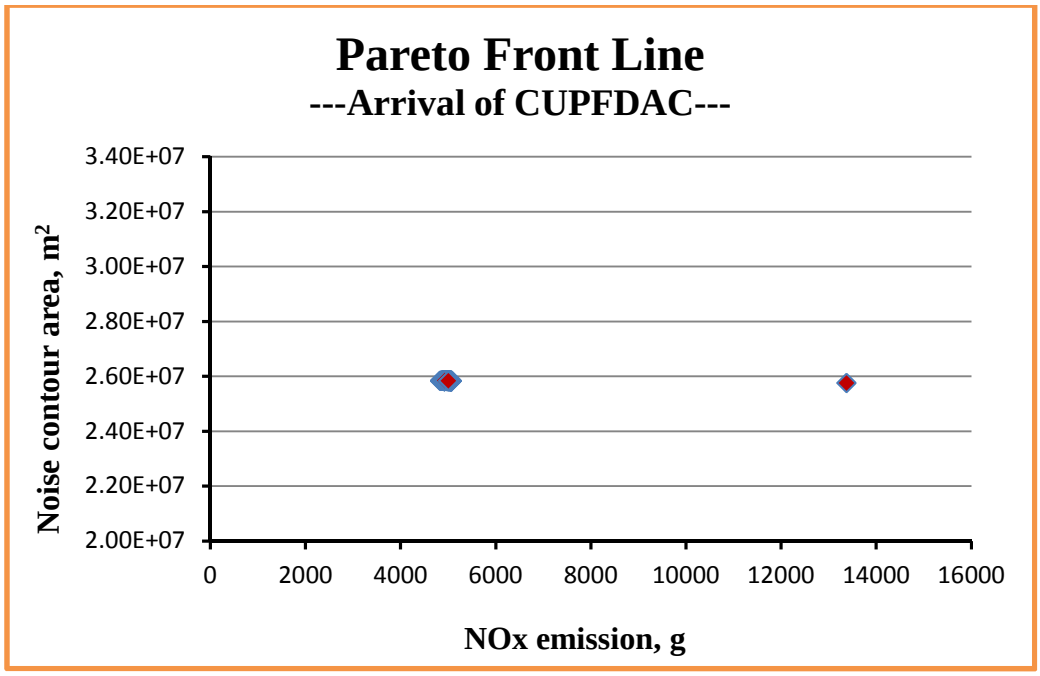

Figure 9-156 Pareto front line (CUPFDAC-arrival)

Table 9-69 Comparisons of optimised results (CUPFDAC-arrival)

	Noise contour area	**NOx emission**
	(m^2)	(g)
Maximum value	25843400	5069.57
Minimum value	25819800	4831.68
Average value	25832000.67	4982.21
Relative deviation	0.09%	4.77%

Table 9-70 Optimised results of the optimum flight trajectory (CUPFDAC-arrival)

Design variables	ALT1, (m)	2235.87
	DIS1, (m)	1206.05
	CAS1, (m/s)	128.53
	CAS2, (m/s)	118.14
	CAS3, (m/s)	102.90
	CAS4, (m/s)	91.09
	CAS5, (m/s)	91.09
	CAS6, (m/s)	90.99
Objective functions	NOISE, (m^2)	25838000
	NOx, (g)	4831.68

Table 9-71 Optimum flight trajectory (CUPFDAC-arrival)

Point	X, m	Z, m	CAS, m/s	TAS, m/s	FPA, rad.
0	0	2438	128.6	147.65	0
1	1206.05	2235.87	128.53	146.06	-0.1661
2	47175	1524	118.14	129.20	-0.0155
3	56975	1524	102.90	112.13	0
4	65953	1524	91.09	99.02	0
5	71384	1237.8	91.09	97.63	-0.0526
6	76940	945	90.99	96.11	-0.0527
7	86200	457	77.17	79.40	-0.0527

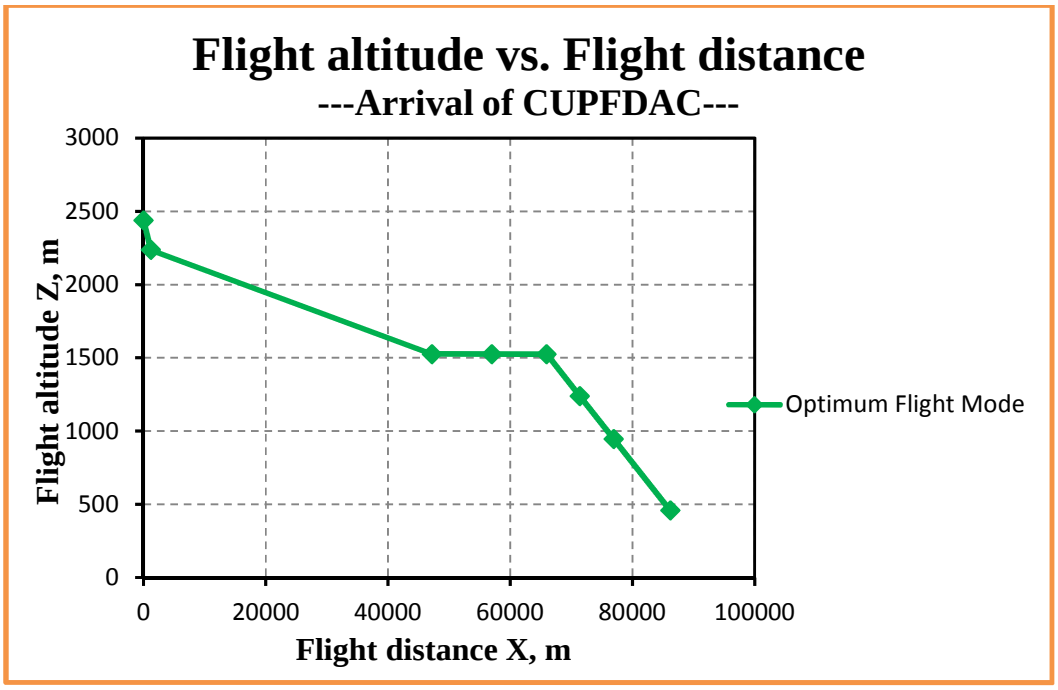

Figure 9-157 Flight altitude vs. Flight distance (the optimum flight trajectory) (CUPFDAC-arrival)

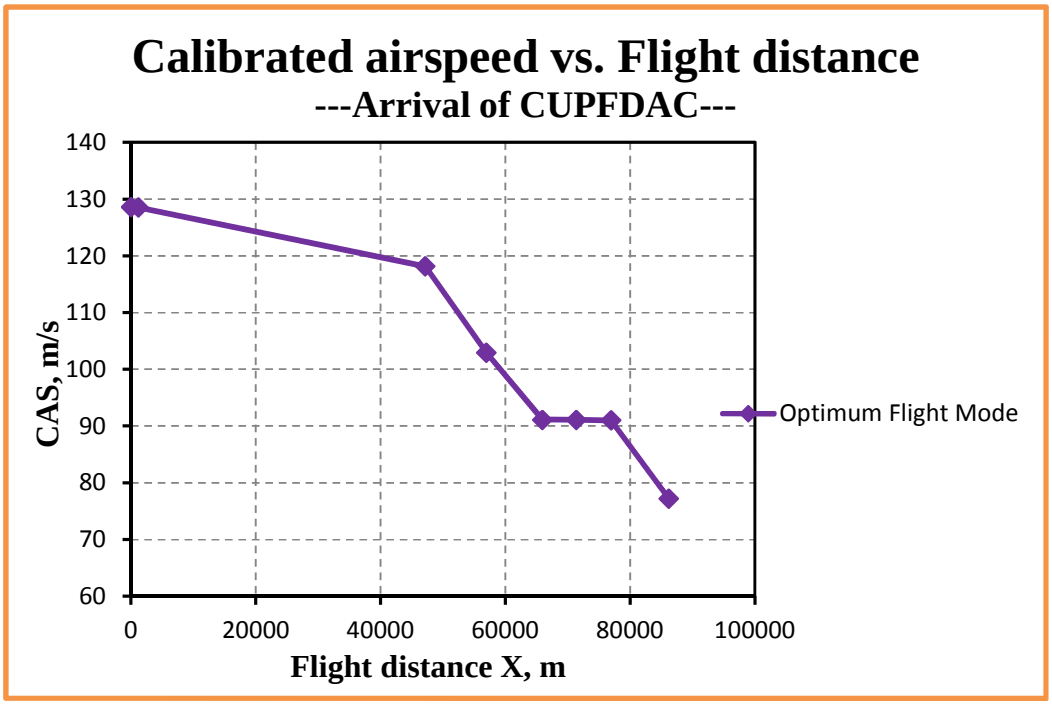

Figure 9-158 Calibrated airspeed vs. Flight distance (the optimum flight trajectory) - (CUPFDAC-arrival)

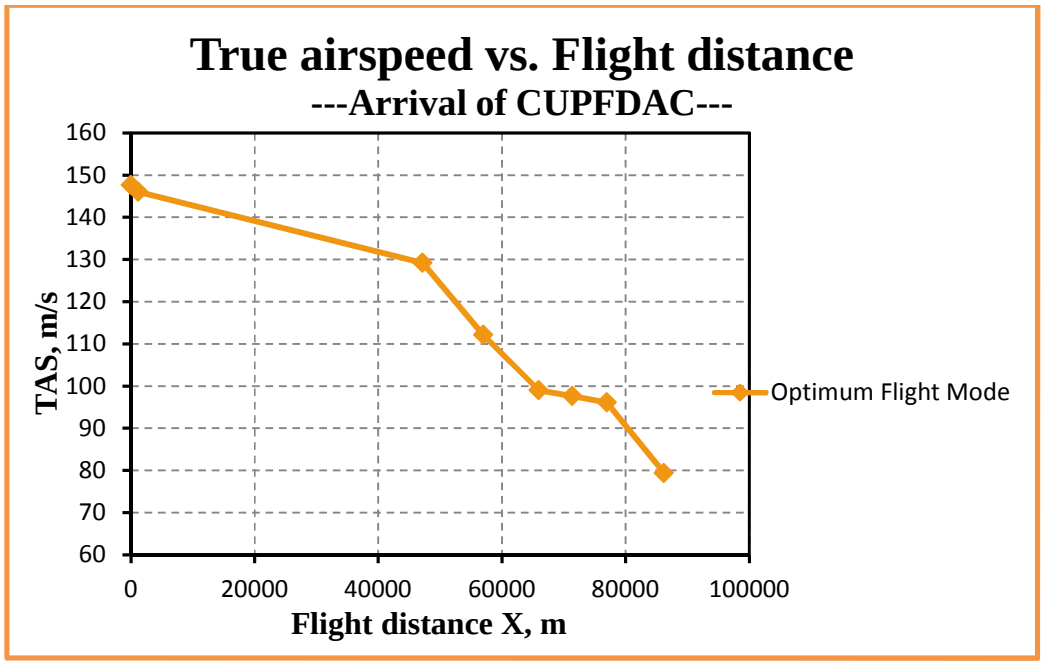

Figure 9-159 True airspeed vs. Flight distance (the optimum flight trajectory) (CUPFDAC-arrival)

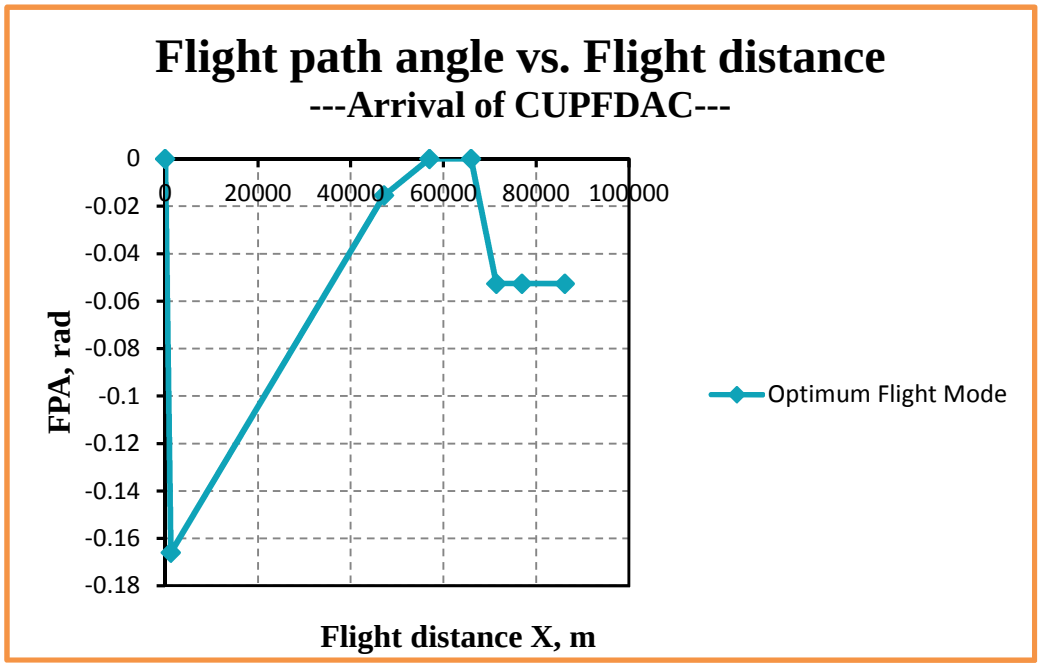

Figure 9-160 Flight path angle vs. Flight distance (the optimum flight trajectory) (CUPFDAC-arrival)

Table 9-72 Overall performance of the optimum flight trajectory (CUPFDAC-arrival)

NOx emission	Noise area	Fuel burnt	Flight time	CO_2 emission	H_2O emission
(g)	(m^2)	(kg)	(s)	(g)	(g)
4831.68	25838000	244.64	729.40	779120.40	303418.85

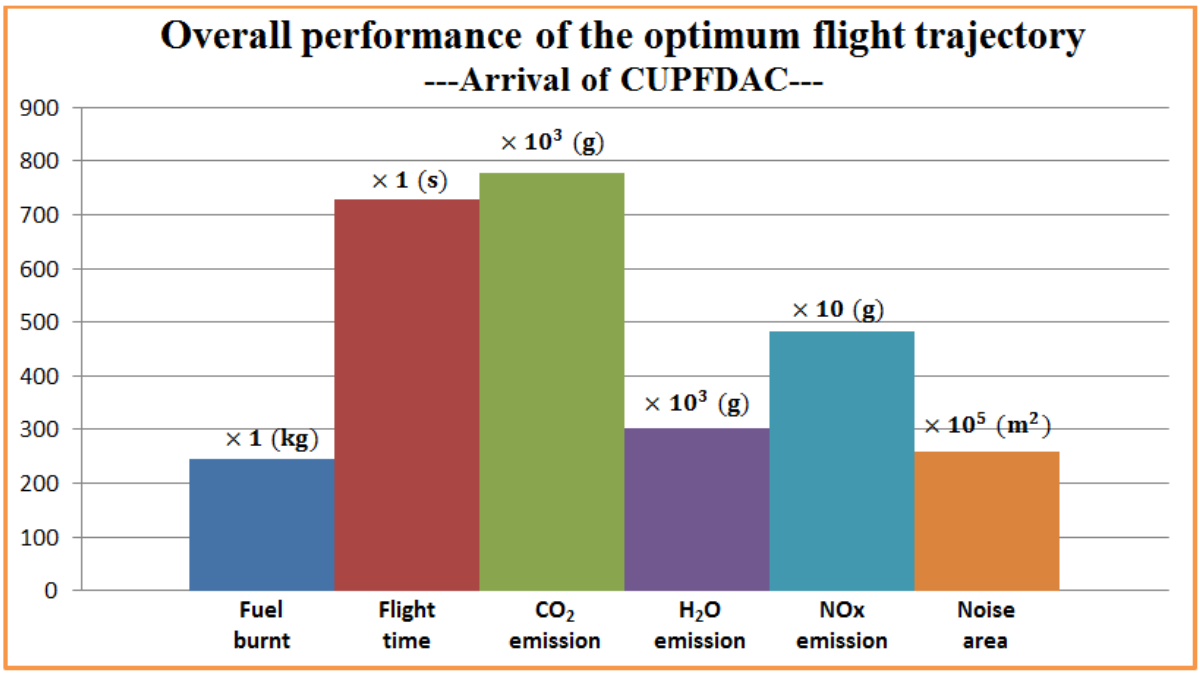

Figure 9-161 Overall performance of the optimum flight trajectory (CUPFDAC-arrival)

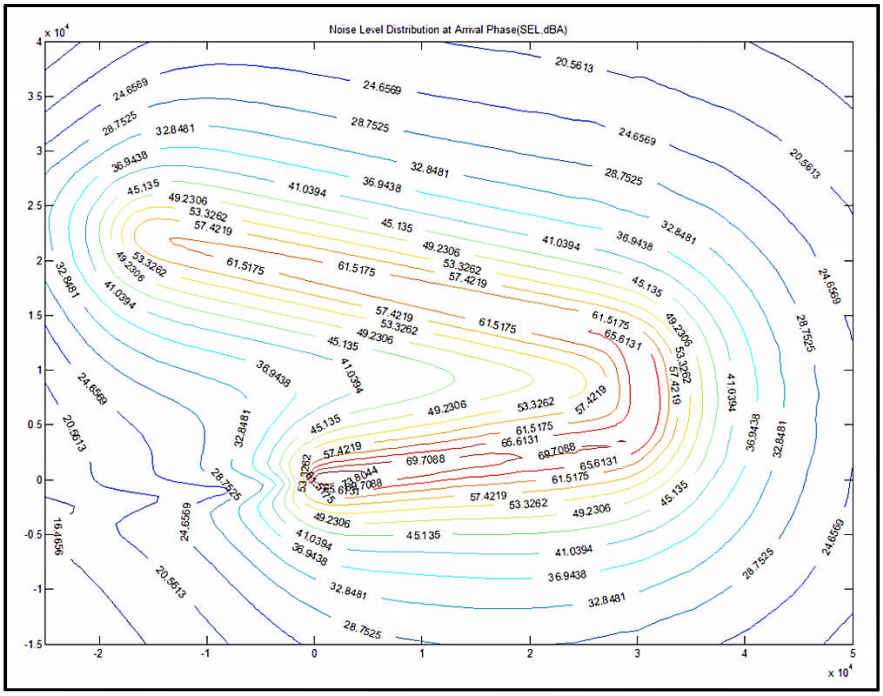

Figure 9-162 (a) Noise-level distribution contour of the optimised flight trajectory (CUPFDAC-arrival)

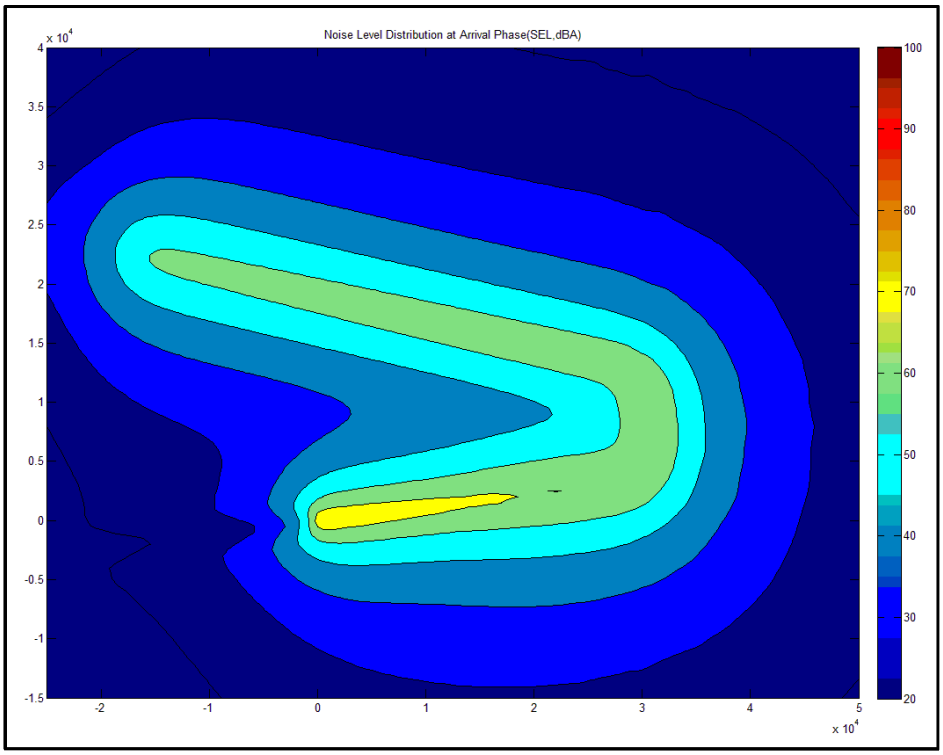

Figure 9-162 (b) Noise-level distribution filled contour of the optimised flight trajectory (CUPFDAC-arrival)

Table 9-73 Parameter segment distributions from the optimised flight trajectory (part) - (CUPFDAC-arrival)

Segment	Fn	TET	EINOx	Fuel burnt	Flight time	CO_2 emission	H_2O emission	NOx emission
	(N)	(K)	(g/kg fuel)	(kg)	(s)	(g)	(g)	(g)
1	3356.00	1238.62	3.05	1.69	8.27	5375.64	2090.88	5.15
2	2714.33	1224.05	2.60	62.36	336.48	198833.15	77331.87	162.45
3	28613.14	1624.85	38.52	51.60	81.22	164097.01	63963.52	1987.81
4	30079.70	1599.63	34.48	50.79	85.04	161531.76	62962.89	1751.18
5	22779.22	1488.43	20.76	26.05	55.28	82930.65	32314.40	540.87
6	13457.03	1357.29	8.78	19.78	57.44	63073.34	24555.98	173.67
7	11605.17	1324.22	6.51	32.37	105.67	103278.85	40199.30	210.56

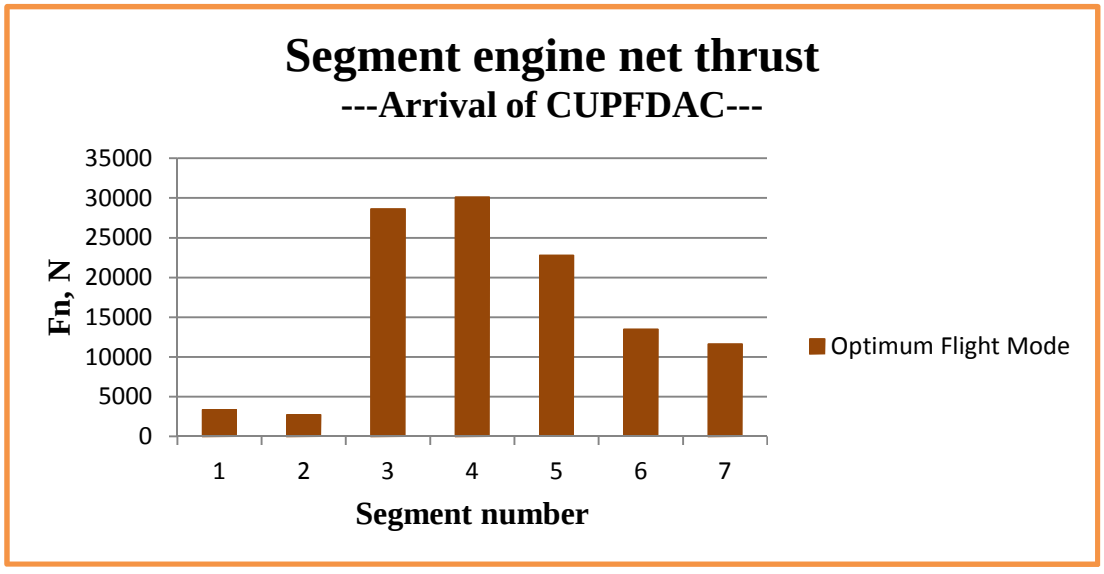

Figure 9-163 Segment engine net thrust (the optimum flight trajectory) (CUPFDAC-arrival)

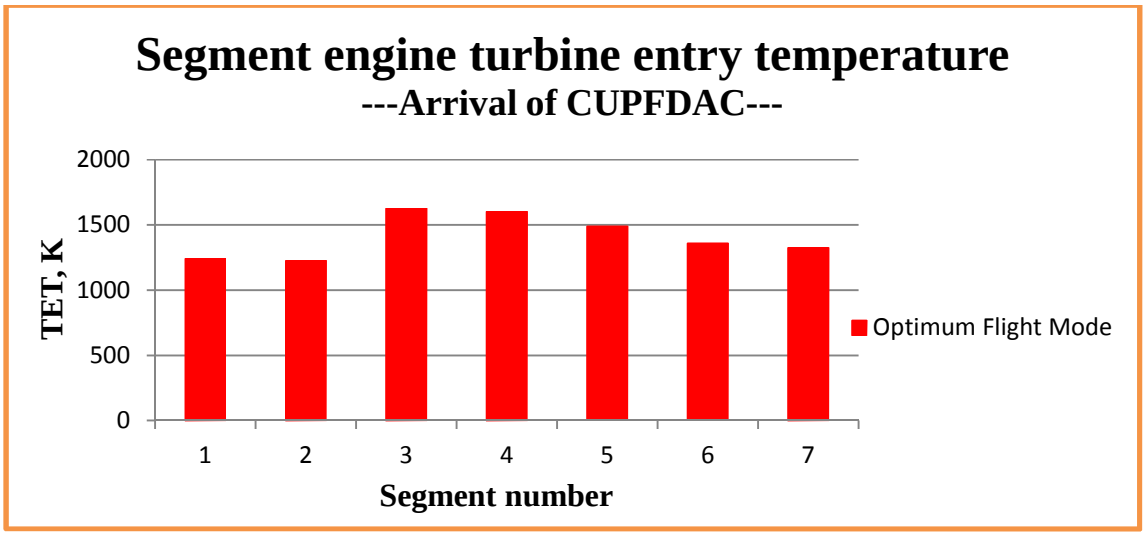

Figure 9-164 Segment engine turbine entry temperature (the optimum flight trajectory) - (CUPFDAC-arrival)

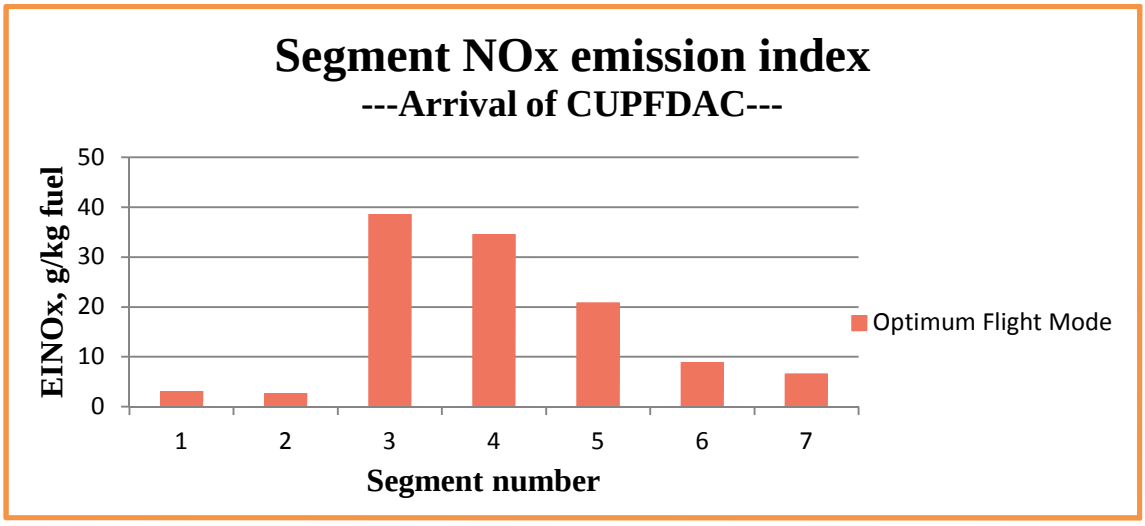

Figure 9-165 Segment NOx emission index (the optimum flight trajectory) (CUPFDAC-arrival)

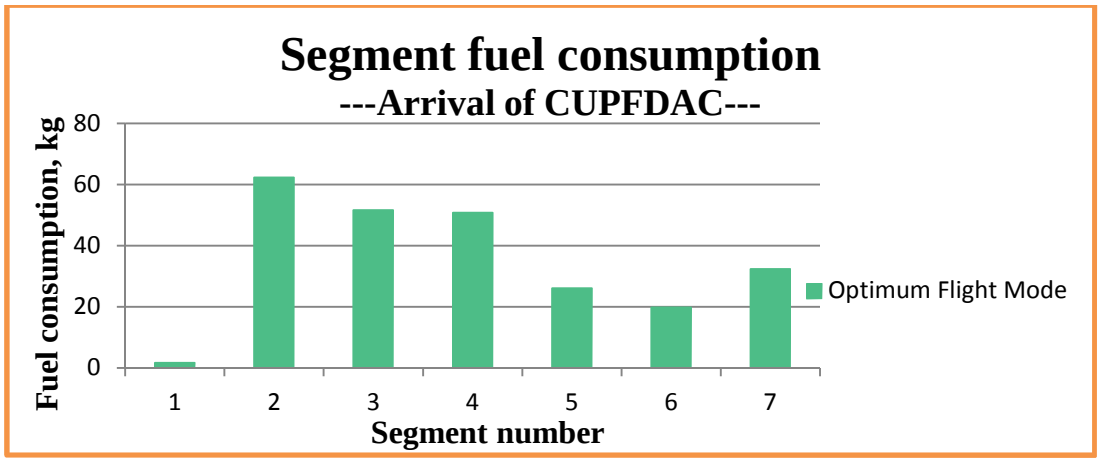

Figure 9-166 Segment fuel consumption (the optimum flight trajectory) (CUPFDAC-arrival)

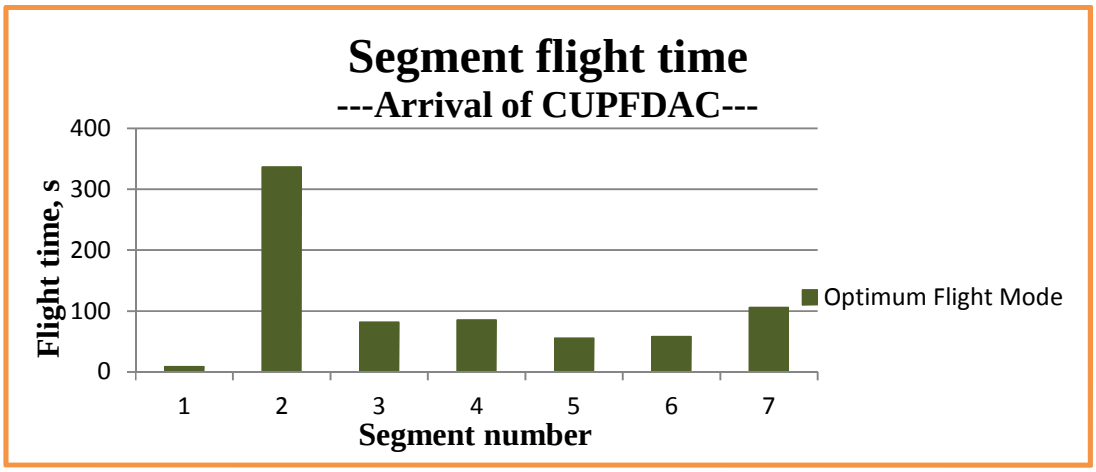

Figure 9-167 Segment flight time (the optimum flight trajectory) (CUPFDAC-arrival)

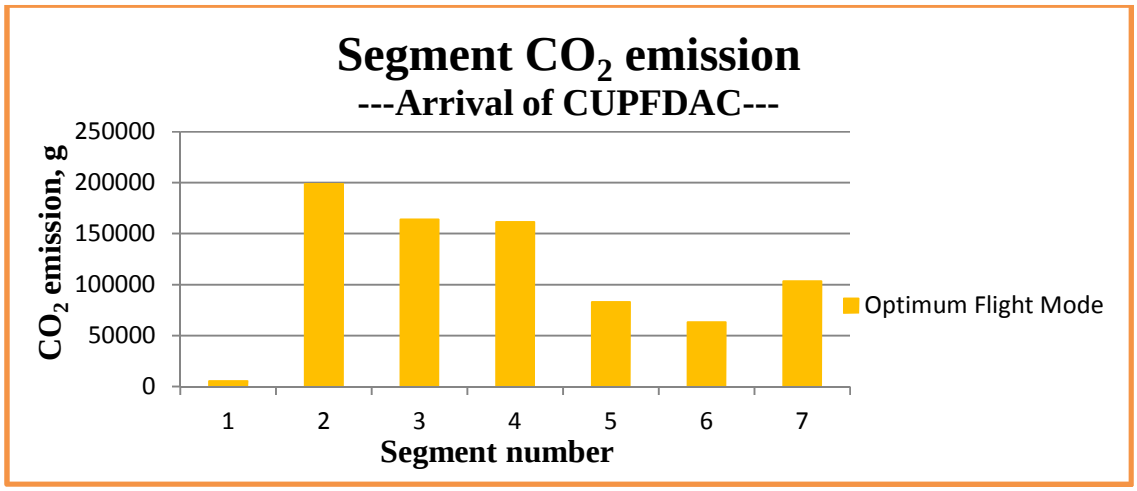

Figure 9-168 Segment CO_2 emission (the optimum flight trajectory) (CUPFDAC-arrival)

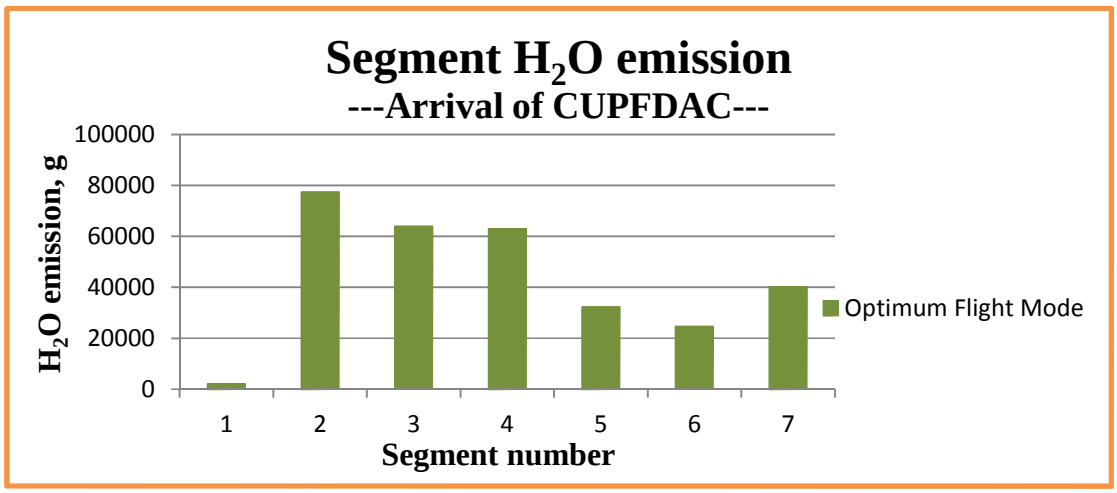

Figure 9-169 Segment H_2O emission (the optimum flight trajectory) (CUPFDAC-arrival)

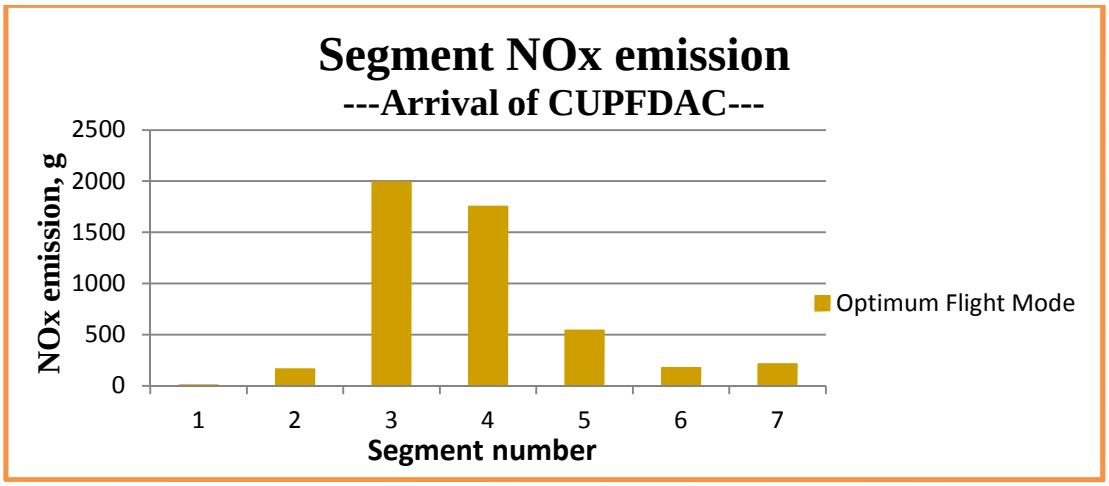

Figure 9-170 Segment NOx emission (the optimum flight trajectory) (CUPFDAC-arrival)

As for the arrival case implemented by the aircraft of CUPFDAC, the observations and summaries from the above figures and tables can be listed as follows:

1) From the plot of normalised Pareto area (see Figure 9-155) and the achieved Pareto frontier (see Figure 9-156), it can be inferred that the optimisation process for the arrival flight case performed by CUPFDAC has basically converged and a set of Pareto-efficient solutions have been achieved.
2) Table 9-68 indicates that the time cost to implement the optimisation process with the 450 generations or 75183 calculation evaluations is 61 hours 22 minutes 54 seconds, that is, 491 seconds/generation or 2.94 seconds/evaluation on average.
3) Compared with the Pareto frontier achieved for the previous arrival case performed by CUTPDAC, the obtained Pareto-efficient solutions in this research case present quite similar distribution characteristics in the objective space spanned by NOx emission and noise contour area (or called noise-impact area), namely, most of the optimised solutions/points tend to converge except for one single solution/point located on the right side and far away from other solutions/points (the reason for this distribution has been explained in the previous section of CUTPDAC's arrival flight case).
4) Table 9-69 describes quantitatively the 'convergence' phenomenon among these optimised solutions/points (except for the rightmost solution/point mentioned

above). From this table, it can be observed that, among these Pareto-efficient solutions, the minimum available noise-impact area is 25.82 km^2 and the maximum value is 25.84 km^2, and the relative difference between the two values which is defined as (Max.-Min.)/Average is only 0.09%. On the other hand, from the point of view of NOx emission, the minimum emission available from these optimised solutions is around 4.8 kg and the maximum value is nearly 5.1 kg, and the relative difference is less than 5%.

5) Therefore, based on the above analysis, a similar treatment to the arrival case of CUTPDAC is adopted here as well, that is, using a certain single solution/point (either the 'average' solution/point or the solution/point with the minimum NOx emission) as the optimum flight trajectory for this arrival flight operated by CUPFDAC (for this case study, the latter solution/point is selected).
6) Table 9-70 gives the optimised results of the optimum flight trajectory for the CUPFDAC's operation in the arrival phase in terms of eight design variables and two objective functions. Based on these results, a further trajectory descriptions by means of variations of flight altitude (Z), calibrated airspeed (CAS), true airspeed (TAS) and flight path angle (FPA) with horizontal flight distance (X) are provided by Table 9-71 and Figures 9-157 to 9-160. According to the achieved optimised results, when the aircraft of CUPFDAC starts its arrival phase in the 1st segment, the constant-CAS descent flight will be applied, that is, the calibrated airspeed will be almost kept at 128.6 m/s same as the initial value required by ATC while the flight altitude will be reduced to nearly 2236 m from the initial value of 2438 m set by ATC. Correspondingly, the true airspeed will also be decreased slightly to around 146 m/s from the initial 147.65 m/s and this flight segment will cover around 1.2 km in the horizontal flight distance; During the 2nd flight segment, the aircraft will experience significant deceleration and descent. By the end of this segment, the flight altitude will be decreased to 1524 m and CAS will fall down to 118.14 m/s (correspondingly, TAS will be also reduced to 129.20 m/s). The flight in this segment will span nearly 46 km in terms of the horizontal flight distance; In the following 3rd and 4th segments, the flight altitude will remain at 1524 m and CAS will be continuously reduced to 102.90 m/s and 91.09 m/s respectively at the end of the

3rd and 4th segments (correspondingly, the TAS will be also reduced to 99.02 m/s when the aircraft arrives at the end of the two segments). The horizontal flight distance covered totally by the two flight segments will amount to nearly 19 km; in the coming 5th and the 6th segments, CUPFDAC will again perform the constant-CAS descent flight as in the 1st segment, namely, the calibrated airspeed will be almost kept at 91 m/s while the flight altitude will be decreased to 1237.8 m and 945 m respectively at the ends of the 5th and 6th segments (correspondingly, the TAS will be reduced to 96.11 m/s as well when the flight in these two segments is accomplished). These two flight segments will cover nearly 11 km in the horizontal flight distance; In the last segment (i.e., the 7th segment), the aircraft of CUPFDAC will continue to reduce its flight altitude and flight speeds (both CAS and TAS) until the required values (457 m in flight altitude and 77.17 m/s in CAS) by ATC are reached within the given horizontal flight distance of 9.3 km.

7) Following the above optimum arrival trajectory, the overall performances which will be available for the operation of CUPFDAC in terms of NOx emission, noise-impact area, noise-level distribution, fuel consumption, flight time and emissions of CO_2 and H_2O are provided in Table 9-72 and Figures 9-161 and 9-162. Additionally, the distributions of some primary parameters along the flight segments such as engine net thrust, turbine entry temperature, NOx emission index as well as the overall performance parameters mentioned above are also given in Table 9-73 and Figures 9-163 to 9-170. From Table 9-72, it can be found that when the aircraft of CUPFDAC which is powered by the new-generation propfan (or called open rotor) engine flies its arrival phase by following the optimum arrival trajectory, around 4.8 kg NOx will be emitted and the noise-impact area (with SEL $\geq$ 70 dBA) in the vicinity of the runway will amount to around 25.8 km^2. The entire arrival flight will last nearly 730 seconds (i.e., 12.2 minutes) and consume nearly 245 kg of fuel. Besides, after this flight, the aircraft will also produce around 779 kg of CO_2 and 303 kg of H_2O.

9.3.4 Arrival-flight comparisons between CUPFDAC and CUTFDAC

Based on the previous descriptions about the optimum arrival trajectories respectively flown by CUPFDAC and CUTFDAC, it is now possible to compare and discuss the performances of these two arrival flights respectively powered by the new-generation propfan (or called open rotor) engine and conventional turbofan engine during the arrival flight phase. The following Tables 9-74 to 9-76 and Figures 9-171 to 9-173 provide the relevant information for this purpose.

Table 9-74 Overall comparisons between CUPFDAC and CUTFDAC (Optimum arrival flight mode)

	NOx emission	**Noise area**	**Fuel burnt**	**Flight time**	**CO_2 emission**	**H_2O emission**
	(g)	(m^2)	(kg)	(s)	(g)	(g)
CUTFDAC	2173.66	15024500	317.98	727.74	1003714.48	393726.98
CUPFDAC	4831.68	25838000	244.64	729.40	779120.40	303418.85
Δ	2658.02	10813500	-73.34	1.66	-224594.08	-90308.13
δ	122.28%	71.97%	-23.06%	0.23%	-22.38%	-22.94%

Table 9-75 TET comparisons between CUPFDAC and CUTFDAC (Optimum arrival flight mode)

	TET, K		**Δ**	**δ**
	CUTFDAC	**CUPFDAC**	**K**	**-**
1	978.11	1238.62	260.51	26.63%
2	971.54	1224.05	252.51	25.99%
3	1090.04	1624.85	534.81	49.06%

4	1117.95	1599.63	481.68	43.09%
5	1055.20	1488.43	433.23	41.06%
6	946.57	1357.29	410.72	43.39%
7	906.89	1324.22	417.33	46.02%

Table 9-76 EINOx comparisons between CUPFDAC and CUTFDAC (Optimum arrival flight mode)

	EINOx, g/kg fuel		**Δ**	**δ**
	CUTFDAC	**CUPFDAC**	**g/kg fuel**	**-**
1	5.34	3.05	-2.29	-42.88%
2	5.18	2.60	-2.58	-49.81%
3	9.07	38.52	29.45	324.70%
4	9.84	34.48	24.64	250.41%
5	7.63	20.76	13.13	172.08%
6	4.92	8.78	3.86	78.46%
7	4.60	6.51	1.91	41.52%

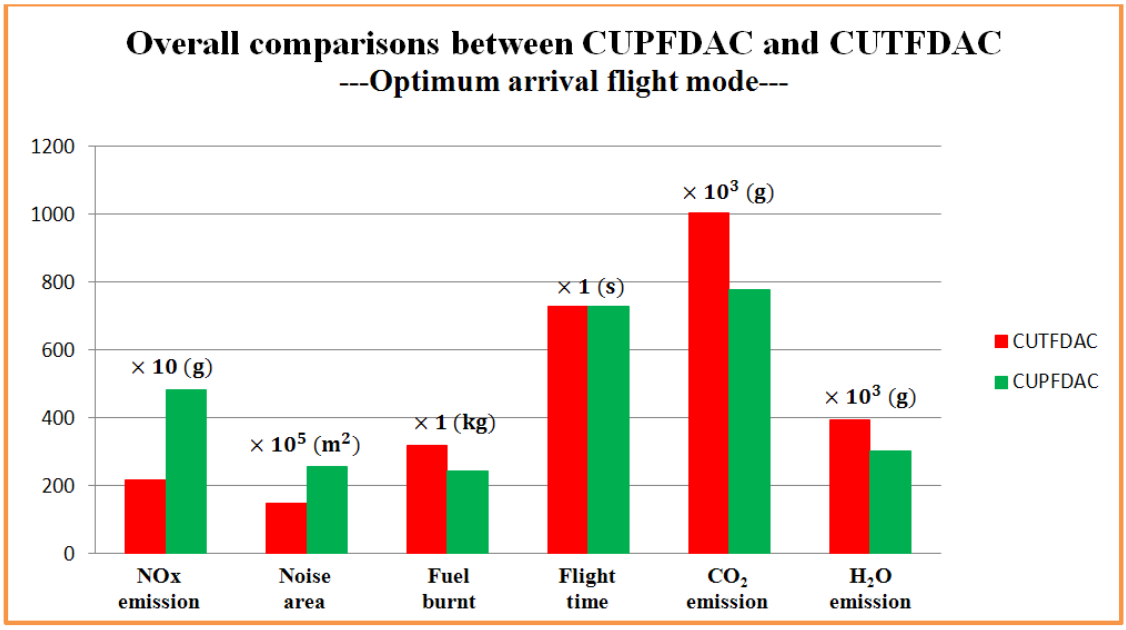

Figure 9-171 Overall comparisons between CUPFDAC and CUTFDAC (Optimum arrival flight mode)

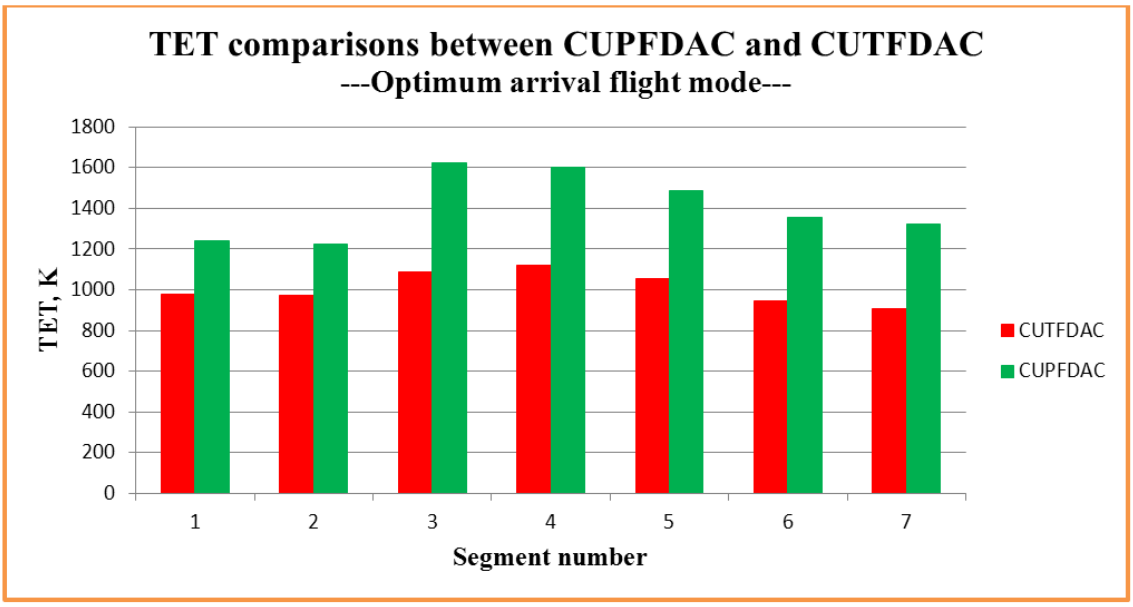

Figure 9-172 TET comparisons between CUPFDAC and CUTFDAC (Optimum arrival flight mode)

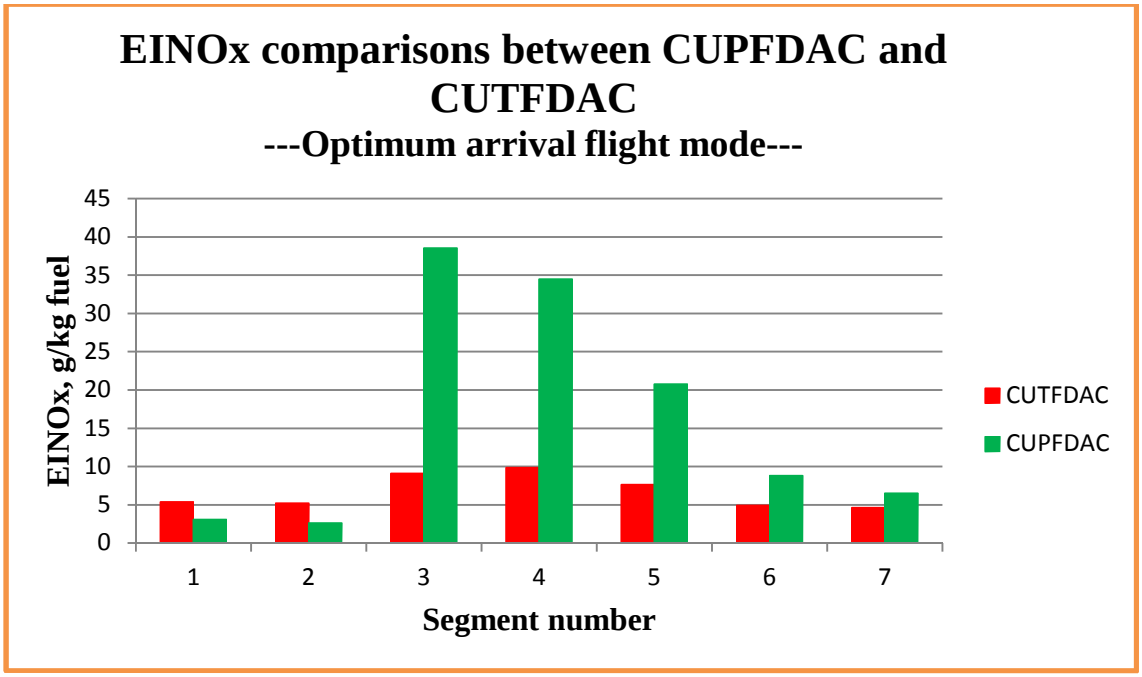

Figure 9-173 EINOx comparisons between CUPFDAC and CUTFDAC (Optimum arrival flight mode)

From the above tables and figures, it can be found that, compared to the arrival flight optimised for the aircraft of CUTFDAC which is propelled by the conventional turbofan engines, the optimum operation for CUPFDAC powered by the new-generation propfan (or called open rotor) engines during the arrival phase will consume 73.34 kg (or around 23%) less fuel and as a result the reductions in the emissions of CO_2 and H_2O will respectively amount to nearly 225 kg (or around 22.4%) and around 90 kg (or around 22.9%). The difference in the flight time is so small (only 1.66 seconds or 0.23%) that it can be ignored completely. However, the application of the new-generation propfan (or called open rotor) engines (but with the traditional combustion chamber) will produce nearly 2.7 kg (or around 122%) more NOx emission and the noise-impact area is also increased to nearly 26 km^2 from the value of 15 km^2 obtained from the operation of the conventional turbofan engines with the values of around 10.8 km^2 and nearly 72% respectively in terms of the absolute and relative increments. As explained in the previous sections in this chapter which involve the comparisons between the new-generation open rotor engine and the traditional turbofan engine respectively for the departure and en route flights, the significant fuel savings as well as corresponding reductions in CO_2 and H_2O can be attributed to the higher engine overall efficiency (and

hence lower specific fuel consumption) resulted from the unique configuration of open rotor engine as well as its much higher component efficiencies and turbine entry temperatures (TETs) adopted in this project research. The significant increases in NOx emission and noise-impact area can be explained by the obviously higher power settings used by the propfan (or called open rotor) engines when compared to the case using the turbofan engines. Table 9-75 and Figure 9-172 provide the comparisons in the turbine entry temperature (TET) when the two aircraft respectively operate along their own optimum arrival trajectories. From the table and figure, it can be found that, over all seven flight segments of the arrival phase, the open rotor engines perform obviously higher TETs (252.51 K ~ 534.81 K higher or 25.99% ~ 49.06% higher). According to the noise models which are used in this project research and have been described in the previous chapter, the noise level perceived by the observer on the ground depends on the engine power ratings and the slant distance between the aircraft (the noise source) and the observer on the ground. In the case studies of flight optimisation for the arrival phase flown respectively by CUPFDAC and CUTFDAC, the flight altitudes, which are closely related to the slant distances, during the arrival flight are mostly fixed and therefore the higher engine power settings, the higher noise levels perceived by the observer on the ground and hence the more noise-impact area (with SEL not less 70 dBA). Similarly, much higher TETs used by the open rotor engines also cause higher values in the emission index of NOx (EINOx). Table 9-76 and Figure 9-173 give the corresponding comparisons from the open rotor engine and the turbofan engine. From the table and figure, it can be found that although CUPFDAC can achieve lower values of EINOx in the first two-segment flight, the other five segments will witness higher EINOx values (1.91 g/kg fuel ~ 29.45 g/kg fuel higher or 41.52% ~ 324.70% higher). Therefore, despite the fuel saving from the open rotor engines, the total NOx emission is still higher than the result from the operation of the conventional turbofan engines due to the significant contributions from the much higher values of EINOx.

CHAPTER TEN CONCLUSIONS AND FUTURE WORKS

Today, the air transport industry has become an essential element of global society by its great contributions to the wide exchanges of cultures and people among different countries as well as the rapid growth in the world economy.

However, on the other hand, the adverse impacts on the environment caused by the air transport, such as air pollution (such as NOx, CO and UHC, etc.), noise and climate change (which is related to emissions of CO_2 and H_2O) are increasingly drawing growing public concern.

With the continuous and steady growth in demand for air travel over the next several decades, it is predicted that the commercial aircraft fleet worldwide will double by 2050 and, as a result, the share in the total man-made CO_2 emissions contributed by air transport is expected to increase to 3% [1].

Besides the above environment concerns, the shortage in fossil-fuel supply is also becoming increasingly severe and will restrict, to a great extent, the increase in the size of air transport industry in future based on the current technology level.

Therefore, the challenges and pressures in terms of environment and economy which commercial aviation is facing up to are unprecedented. Obviously, to address these challenges and pressures, speeding up technological breakthrough and adopting more economical and more environmentally-friendly ways to meet the increasingly growing demand for air travel has become the only option for the future development of the air transport industry.

The Clean Sky JTI is one of the largest European research projects ever launched by the European Union. The main aim of this programme is to achieve a quantum leap in performance through a consistent, coherent and holistic approach, focusing on the integration of advanced technologies and validation of results in a multidisciplinary approach and make major steps towards the environmental goals set by ACARE for 2020.

This project research described in this thesis, and sponsored by the SGO (Systems for Green Operation) ITD (Integrated Technology Demonstrator) of the Clean Sky programme, aims at optimising the two-dimension flight trajectories of commercial

aircraft by means of a new multidisciplinary optimisation method and, in the meantime, evaluating the possible benefits brought by the introduction of the new-generation propfan (open rotor) engine.

Taking the flight from Amsterdam Schiphol airport in the Netherlands to Munich airport in Germany as an example, this research made a detailed investigation into the flight trajectory optimisations for different types of commercial aircraft, including turbofan-propelled aircraft, turboprop-driven aircraft and propfan-powered aircraft, with different optimisation objectives for the different flight phases (namely, for the departure phase, fuel consumption and noise-impact area were selected as objective functions, during the en route flight, fuel consumption and flight time were adopted, and for the final arrival phase NOx emission and noise-impact area were chosen).

Through several rounds of optimisation simulations, a complete set of optimised solutions, aiming at the optimisation problem spectrum spanned by different aircraft types and different optimisation objectives, have been achieved and provided by the research work. These optimised results are Pareto efficient, and based on these optimisation results, customers can be provided with the opportunity and freedom to further make their own choices according to the actual requirements in practice.

Besides, a comprehensive comparison and evaluation, based on the achieved optimisation results, about the new-generation propfan (open rotor) engine with higher component efficiencies and higher turbine entry temperature (TET), has been made in this research project as well, in terms of fuel consumption, flight time, noise-impact area, gaseous emissions (NOx, CO_2 and H_2O, etc.) by reference to the conventional turbofan engine with 1990's technology level.

10.1 Main Optimisation Results

The achieved main results in flight trajectory multidisciplinary optimisation can be briefly summarised as follows:

1) The sets of Pareto-efficient solutions respectively for the nine research examples spanned by aircraft types and flight phases with different optimisation objectives have been achieved basically.

2) For the departure flight performed by the aircraft of CUTFDAC, two typical optimum solutions were selected for the purpose of analysis, namely, the ‘min. fuel consumption’ flight mode and the ‘min. noise area’ flight mode. Optimisation results show the different optimum flight trajectories achieved for these two modes. Compared to the ‘min. fuel consumption’ mode, the ‘min. noise area’ mode chooses to climb to higher flight altitudes at earlier segments of the departure phase. Naturally, this choice can effectively increase the distances between the aircraft (noise source) and the ground (observers) as soon as possible and hence reduce the noise-impact area. Additionally, during the departure flight by ‘min. noise area’ mode, a reduced flight speed is also introduced at the 4^{th} segment. The reduced flight speed can result in decreased engine power settings in terms of engine net thrust, and therefore the lower noise-impact area as well because engine power setting, besides the distance between noise source and observer, is also a prime contributor to noise levels according to the flight noise model. Therefore, as a result, when CUTFDAC flies in the ‘min. noise area’ mode, a significant reduction in the noise-impact area (amounting to around 25 km^2 or 37%) can be obtained compared to the noise area resulted from ‘min. fuel consumption’ flight mode. However, on the other hand, ‘min. noise area’ flight mode, compared to ‘min. fuel consumption’ flight mode, does consume more fuel (38.42 kg or 12.6%) and produce more gaseous emissions, for instance, the emissions of CO_2 and H_2O will increase around 121 kg and around 48 kg respectively (amounting to 12.6%), and NOx emission also increases by 685 g, amounting to 15.48% due to higher values of NOx emission index (resulted from higher engine operation temperatures) and more fuel consumption, but the latter one is the main contributor.
3) The optimisation of the departure case flown by the aircraft of CUTPDAC shows the different characteristics from those achieved respectively from the above CUTFDAC case and the following CUPFDAC case, that is, achieved optimum solutions tend to converge from each other (among these optimum solutions, the maximum relative difference in noise-impact area is 2.07% and the maximum relative difference in fuel consumption is only 0.84%.). As a result, an ‘average’ optimum solution was used as the representative for the

purpose of trajectory analysis. Optimisation results indicate that when the 'average' optimum trajectory is followed during the departure phase, CUTPDAC will consume around 77 kg fuel and produce around 247 kg CO_2, 96 kg H_2O and 375 g NOx, and besides, noise-impact area (with SEL $\geq$ 70 dBA) will amount to around 93 km^2 and the entire departure flight will last for 5 minutes.

4) The optimisation results of CUPFDAC departure flight present high similarities to those from the CUTFDAC departure case, in terms of the shape of Pareto frontier and the characteristics of optimum departure trajectories respectively for the 'min. fuel consumption' flight mode and 'min. noise area' flight mode. The optimisation indicates that compared to the 'min. fuel consumption' flight mode, when CUPFDAC flies along the departure profile prescribed by the 'min. noise area' flight mode, the lower noise-impact area (around 15 km^2 or 25% less than the result from the 'min. fuel consumption' mode) can be achieved, but with more fuel consumption (around 25 kg or 13% more) and higher gaseous emissions in terms of CO_2 (around 78 kg or 13% higher), H_2O (around 30 kg or 13% higher) and NOx (around 2.5 kg or 29% higher).
5) The optimisation of en route flight flown by the aircraft of CUTFDAC shows that compared to the results from minimum-fuel-consumption flight, the minimum-time flight will consume 942.18 kg (or 44.90%) more fuel and produce 2974 kg (or 44.90%) more CO_2, around 1167 kg (or 44.90%) more H_2O and around 27 kg (or 102.29%) more NOx but with 566 seconds (or 18.74%) less flight time.
6) The optimisation of en route flight flown by the aircraft of CUTPDAC shows that the minimum flight time mode, compared to the minimum fuel consumption mode, will cost 528.30 kg (or 93.31%) more fuel and produce nearly 1696 kg (or 93.69%) more CO_2, nearly 662 kg (or 94.35%) more H_2O and 6.3 kg (or 466.14%) more NOx. As the return to higher fuel consumption and gaseous emissions, the minimum flight time mode can achieve 729.29 seconds (or 18.30%) less travel time than that from the minimum fuel consumption mode.
7) The optimisation of en route flight flown by the aircraft of CUPFDAC shows that compared to the minimum fuel consumption flight mode, the minimum time

flight mode will make CUPFDAC consume 598.78 kg (or 43.73%) more fuel and produce around 1896 kg (or 43.66%) more CO_2, 739 kg (or 43.67%) more H_2O and 69 kg (or 153.08%) more NOx. As the return to more fuel consumption and gaseous emissions, the minimum time flight mode will achieve 452.46 seconds (or 14.39%) less travel time.

8) The trajectory optimisation results for the arrival phases, respectively flown by CUTFDAC, CUTPDAC and CUPFDAC, show a common feature, namely, for each optimisation case one representative optimum solution can be found. For the CUTFDAC case, when the aircraft flies its arrival phase by following the representative optimum trajectory, around 2 kg NOx, 1004 kg CO_2 and 394 kg H_2O will be produced, and the noise-impact area (SEL $\geq$ 70 dBA) will amount to 15 km^2. In the meantime, in order to complete the arrival flight, around 318 kg fuels will be consumed and the entire flight will last around 12 minutes. When the aircraft of CUTPDAC flies its arrival phase by following the representative optimum trajectory, around 147 g NOx will be emitted and the area of around 1.9 km^2 in the vicinity of the runway will be influenced by noise whose magnitudes in terms of SEL are not less than 70 dBA. The entire flight will last nearly 13.5 minutes with around 90 kg of fuel consumed. Additionally, this arrival flight will produce nearly 291 kg of CO_2 and around 112 kg of H_2O as well. For the arrival case of CUPFDAC, under the condition of its representative optimum flight trajectory, around 4.8 kg NOx will be emitted and the noise-impact area (with SEL $\geq$ 70 dBA) in the vicinity of the runway will amount to around 25.8 km^2. The entire arrival flight will last nearly 12.2 minutes and consume nearly 245 kg of fuel. Besides, this flight will also produce around 779 kg of CO_2 and 303 kg of H_2O.

9) With the same ‘min. fuel consumption’ departure flight mode, the much lower value of fuel consumption (around 120 kg or 39% less) and hence much better operation economy can be achieved when the propfan (open rotor) engine is applied compared to the turbofan case. Consequently, the emissions of CO_2 and H_2O can also be greatly reduced, the decreased magnitudes respectively amounting to 372 kg (39%) and 148 kg (39%). The flight times separately spent by CUPFDAC and CUTFDAC are very close to each other and the slight

difference in flight time (less than 7 seconds) can be ignored. Unfortunately, an obvious problem CUPFDAC is facing in this case study is its very high level of NOx emission (4 kg or 96% more than the emission from CUTFDAC) due to much higher values of NOx emission index in the CUPFDAC case caused by higher engine power settings during the departure phase.

10) Under the same minimum fuel consumption flight mode for the en route flight phase, the application of the new-generation propfan (or open rotor) engine can, compared to the traditional turbofan engine, save around 729 kg fuel (nearly 35% less) and correspondingly will result in 2282 kg (or 34.45%) less CO_2 emission and 907 kg (or 34.89%) less H_2O produced. Besides, from the point of view of the flight time, although more travel time was needed by CUPFDAC, the difference of around 2 minutes, when compared to the average mission time of around 51 minutes, is completely ignorable. However, in spite of the obvious advantages which the new-generation open rotor has in fuel saving and reduced emissions of CO_2 and H_2O, significant increase in NOx emission (around 18 kg or nearly 70% more than that from CUTFDAC) has been produced by the flight flown by CUPFDAC.

11) Under the condition of arrival flights, compared to the arrival flight optimised for the aircraft of CUTFDAC which is propelled by the conventional turbofan engines, the optimum operation for CUPFDAC powered by the new-generation propfan (or called open rotor) engines during the arrival phase will consume 73.34 kg (or around 23%) less fuel and, as a result, the reductions in the emissions of CO_2 and H_2O will respectively amount to nearly 225 kg (or around 22.4%) and around 90 kg (or around 22.9%). The difference in the flight time is so small (only 1.66 seconds or 0.23%) that it can be ignored completely. However, the application of the new-generation propfan (or called open rotor) engines (but with the traditional combustion chamber) will produce nearly 2.7 kg (or around 122%) more NOx emission and the noise-impact area is also increased to nearly 26 km^2 from the value of 15 km^2 obtained from the operation of the conventional turbofan engines with the values of around 10.8 km^2 and nearly 72% respectively in terms of the absolute and relative increments.

12) Therefore, according to the above comparisons between CUPFDAC and CUTFDAC, such a conclusion can be derived, that is, the adoption of the new-generation propfan (or open rotor) engine, whose technologies will be ready around 2025 to 2030, can significantly reduce the fuel consumption and the emissions of CO_2 and H_2O when compared to the 1990s' technology level represented by the conventional turbofan engine in CUTFDAC, because of the combination of higher engine thermal efficiency (due to the applications of higher turbine entry temperature, higher component efficiencies) and higher propulsive efficiency which propfan engine has inherently. On the other hand, the challenge from NOx emission will be increasingly severe with higher operation temperatures of the future propfan engine, and traditional combustion technology and combustor design cannot any longer meet the requirements from this novel engine, hence new low emission technologies under high engine power settings, such as fuel staged combustor and LPP (Lean Premix-Prevapourize) combustor, etc., will have to be explored and applied.

10.2 Main Contributions to Knowledge

Through the research work described in this thesis, the main contributions to knowledge are summarised briefly again as follows:

1) From the known literature published openly so far, it is the first time that the flight trajectories flown respectively by turboprop-driven aircraft and propfan-powered aircraft for the purpose of city-pair air transport are optimised based on multi-disciplines with the optimisation methodology and multi-objective Genetic Algorithms introduced in this thesis, as well as actual constraints from the local airports.
2) From the known literature published openly so far, it is the first time that a relative complete set of models involving aircraft performance, engine performance, gaseous emissions and noise are included when flight trajectories are optimised with the multidisciplinary optimisation method and optimisation constraints mentioned in item 1) above.
3) From the known literature published openly so far, it is the first time that the combination of the new-generation propfan (or called open rotor) engine, which

is planned into commercial service in 2030, with the optimised flight trajectory achieved by a new multidisciplinary optimisation method is tried and evaluated to achieve more economical and greener commercial flight.

4) Inside the SGO ITD project of the Clean Sky programme, it is one of quite few cases that used Neural Networks (NNs) and P3T3 method to replace the complicated and time-consuming simulation models of engine performance and engine gaseous emissions, in order to alleviate the challenge in optimisation time cost brought by GAs and speed up the optimisation processes. By the actual application comparisons, the significant benefit in terms of the optimisation time consumption has been achieved. For a long time, much longer optimisation time caused by GAs has been a main problem/obstacle for the wide application of this optimisation method. The successful application of NNs in engine performance modelling and multidisciplinary optimisation cases in this research project provides one promising solution.
5) Inside the SGO ITD project of the Clean Sky programme, it is the first time that compressor variable geometry and bleeding was dynamically introduced into engine off-design operations (that is, these anti-surge measures can be implemented when required). As a result, the optimisation of flight trajectory and the achieved optimised solutions (mainly for the arrival flights) have been improved greatly compared to those cases studies performed with engine performance models which were not equipped with such characteristics.
6) Compared with previous work in case modelling by the author, an obvious progress has been achieved in this research work described in this thesis, that is, when optimisation cases being modelled, horizontal flight distance X, flight altitude Z and flight speed (CAS or Mach number) can all become the options of optimisation/design variables. This improvement greatly enhanced the modelling flexibility in the optimisation studies of flight trajectory, so that some better and applicable optimum solutions which were not available from the previous case modelling technology can be achieved now.

10.3 Future Works

Although significant progress has been achieved by the research works described in this thesis, these works are only preliminary and there are still many investigations in this technology domain of multidisciplinary optimisation of flight trajectory which need to be performed further in future. These investigations can be briefly summarised and suggested as follows:

1) *Improvements (or refinements) of aircraft performance models*

   Firstly, in the present modelling method of aircraft lift characteristics (i.e., lift coefficient vs. angle of attack), the slopes of the lift curves were obtained based on the corrections to the theoretical value of 2π which is derived from the 2D thin aerofoil theory by means of taking the influences of the actual 3D flow over finite wing, compressibility from high speed flight and sweep angle of wing into account, and the values of zero-lift angle of attack were determined according to some statistical data (or based on the assumptions that the aerofoil will be kept unchanged along the wing span and the value of zero-lift angle of attack for 3D finite wing is the same as that from 2D aerofoil, which can be determined through aerofoil wind-tunnel tests). However, in practice, the wing designs are much complicated with 'twist' and varied aerofoils from the wing root to the wing tip, for instance. How do these features in wing geometry affect the aircraft lift characteristics and how should these impacts be taken into account during the modelling process? Secondly, when the lift-drag characteristics (i.e., the drag polar) were modelled in this research, only the typical cruise flight condition (in terms of flight altitude and flight Mach number) and turbulent flow over the investigated aircraft components were considered to calculate the value of Reynolds number and, accordingly, estimate the zero-lift drag coefficient of each aircraft component. However, actually, aircraft fly under wide flight conditions which will result in the varied values in Reynolds number for each of the aircraft components, and in the meantime, the flows over aircraft components are often of the feature of mixture of laminar flow and turbulent flow which will lead to the different formula for the friction calculation. How should these impact factors be taken into account in future works? Thirdly, for the current modelling method and calculation software available from SGO ITD of the Clean Sky programme (i.e., APM) for aircraft performance simulation, the variation of

COG (centre of gravity) due to fuel consumption during flight was not considered. For a short flight, the impact may not be primary. However with the increase in flight range, the influence will emerge gradually and corresponding measures for this issue have to be taken into account in future works as well. Fourthly, the aircraft performance modelling, software development and performance simulation should be expanded further to include the ground operations of aircraft, such as ground roll, take-off and landing, so that the multidisciplinary optimisation with a complete flight profile can be performed in future. Lastly, the correlations between the optimised flight parameters achieved through the optimisation operations, described in this thesis, and corresponding operation (or control) parameters of aircraft/engine combination should be established so that expected optimum flight trajectories can be realised further (see the Figure 1-3 in Chapter One).

2) *Improvements (or refinements) of engine performance models*

Firstly, in a practical engine system, bleed from compressors is not only used for the purpose of cooling of turbine blades but also used for sealing, turbine disk cooling as well as adjustment of axial loads of bearings, etc. In addition, these air is usually bled from different locations of a compressor (for instance, from the front stages, middle stages or the compressor exit) depending on the applications, and returns the main gas flow path in different ways as well. However, in the present engine performance models built in this research work, the complicated bleeding system has been simplified with bleed only from the exit of high pressure compressor and for the purpose of HPT blade cooling. Secondly, the requirements about power extraction and customer bleed from aircraft side have not been considered fully. Thirdly, more attention should be paid to the usage of the anti-surge measures besides the present consideration of engine performance, in terms of net thrust and SFC, because of its significant importance to the descent or arrival flights of aircraft, although the preliminary application has been made in this research work. Fourthly, the representative performance characteristics of the propeller for the new-generation propfan engine can be obtained and applied in the future, instead of some fixed values for propeller efficiency adopted in the current research work, and in the meantime, the results of pitch angle of propeller blade can also be output besides others when the engine performance simulation with the propeller characteristic map

is implemented, so that the combination of the pitch angle with other operation parameters from aircraft and engine achieved through the training/calibration process (see the Figure 1-3 in the Chapter One) can be executed to realise the expected optimum flight trajectories. These issues discussed above should be considered in the future works.

3) *Improvements (or refinements) of engine gaseous emission models*

Firstly, more investigation is needed for the 'interpolation' method when P_3T_3 emission estimation equations and the experiment data from ICAO emission databank are used. From the ICAO databank, the discrete values of emission indices of gaseous pollutants, such as NOx, CO and UHC under the typical operation conditions including TAKE-OFF, CLIMB OUT, APPROACH and IDLE, can be obtained. Based on these data, a formulated correlation between emission index and engine power ratings should be built for the purpose of convenient application. At present, in this research, the correlation was approximated by a set of straight lines which in turn link the adjacent points among the above emission data from ICAO and linear interpolation was adopted when needed for the purpose of simplicity. However, it is not the only way to express this correlation, and other approaches such as spline curve, etc. can also be tried and the differences from the above different 'interpolation' methods can be compared and evaluated. Secondly, although the predictions of main gaseous emissions from turboprop and propfan engines in this research work were made by means of the chemical-reaction based stirred reactor models, rather than the empirical correlation formulas, the main difficulties to use such models lay in determining the values of some combustor geometry parameters (such as the inlet and outlet areas and lengths of Primary Zone, Intermediate Zone and Dilution Zone), as well as the distributions of fuel and gas (or/and air) along the combustor (usually, these parameter values involve design details of combustors and are very hard to be obtained from the manufacturers unless the evaluated combustors are not self-designed). Therefore, how to solve this problem so as to apply this modelling method in flight trajectory optimisation or other relevant emission evaluations better, will be one of the future research works. Thirdly, on the other hand, the simulation capability of the stirred reactor models can also be improved by the additional modelling of other phenomena which take

place during the combustion process, such as flow recirculation and fuel evaporation. Lastly, the modelling emphasis of gaseous emission prediction (either empirical correlations or stirred reactor based models or even other methods) should be shifted gradually to new low-emission combustors such as staged combustor and LPP (Lean Premix- Prevapourize) combustor, etc., in order to reflect the advance in the combustion technology.

4) *Improvements of noise prediction and impact evaluation*

In the project research described in this thesis, the noise characteristic of a turbofan engine with the technology level of the 1980s-1990s had to be used as a replacement to estimate the noise level and the noise-impact area resulted from a new-generation propfan engine (based on the assumption that the noise levels from both types of power plants are roughly of the same order when the technology advance is considered for the new-generation propfan engine in spite of its 'unducted' configuration), because the actual noise characteristics representing the state-of-the-art designs in aero acoustics for propfan engines is not available so far. Therefore, once such a characteristic is available by either numerical simulation or wind-tunnel test, the updated optimisation should be performed accordingly. In addition, the present evaluation about the flight noise impact only involved the noise-impact area and other evaluation ways, such as noise-impact population or noise-impact households, may be made as well in future when these distribution data in the vicinity of the local airports are available.

5) *Improvements of multi-objective optimisation algorithms*

Firstly, the capability of the genetic algorithms used in this research work to cope with more design (or called optimisation) variables should be improved. Based on the present trajectory optimisation methodology and performance simulation methods of aircraft and engine, a flight trajectory is divided into a number of flight segments, and during the flight at each segment the aircraft mass is assumed unchanged and the average flight altitude and Mach number from each segment are used as the inputs for the subsequent engine performance simulation. Therefore, in order to improve trajectory optimisation results as well as the accuracy of performance simulation, the division with more segments (i.e., shorter segment length and more points can be available for the trajectory description) will be

expected. However, the requirement of more segments from the above sides of performance simulations and trajectory optimisation means that more design (or optimisation) variables will be involved during the optimisation process (i.e., the dimensional number of the search space spanned by these design variables will be increased greatly) and, therefore, achieving converged optimisation results by the present GAs under this condition is very difficult and time-consuming. Secondly, the capability of the genetic algorithms used in this research work to cope with more optimisation objectives should be developed further in the future works. Thirdly, new optimisation technologies such as Hybrid GAs and Adaptive GAs should be tried and developed in future works. Hybrid GAs are actually the combination of GAs with other optimisation/search techniques, and by means of this combination different advantages from different optimisation technologies can be made full use of for the different demands or characteristics from different phases of an optimisation process. When this optimisation technology is implemented, GAs are responsible for determining the region where the optimum solutions are located through its global search capability, and then the local optimisation techniques take over to find these optimums. Different from the present GAs used in this research work which adopts fixed values in some key parameters such as population size, crossover ratio, and mutation ratio, etc., Adaptive GAs can dynamically adjust the values of these key GAs' parameters according to the progress of the search or optimisation process and, as a result, the optimisation performance can be improved in terms of convergence and calculation efficiency.

6) *New models and new researches in flight trajectory optimisation*

Based on the present work undertaken in this research project, some new models should be introduced and, accordingly, new investigations into multidisciplinary flight trajectory optimisation should be implemented.

These new models include the weather model, the ATC (air traffic control) model, the cost model of aircraft/engine maintenance, the cost model of flight/cabin crew salary, and the cost model of emission taxes (including gaseous emissions and noise emission), etc. The first two models can further impose some practical and new constraints to the trajectory optimisation problems of interest through adverse weather conditions, such as thunderstorms, strong winds and volcanic ash, etc., or

some limitations to commercial air transport, for example, no-fly zone, etc. The latter three cost models are used to estimate the additional expenses from a flight besides the cost resulted from the fuel consumption. In the present research works described in this thesis, fuel consumption was regarded as the indicator of flight economy (or flight cost) and was treated as one of the objective functions for the minimisation. However, this representation for operation economy by fuel consumption is not the best way. Actually, the three expenses mentioned above all make contributions to the overall flight cost and are related to the flight trajectory optimisation. Especially, the maintenance expenses of aircraft and engine as well as the crew salaries hold relatively greater percentages in the operation cost structure. In addition, compared to the large, narrow or wide jet aircraft, the importance of fuel cost in the overall operation cost will decrease while the contribution from the maintenance cost will increase for the regional flights performed by either Regional Jet or turboprop due to the frequent take-off and landing. Therefore, based on the above analysis, taking only the fuel consumption as the indicator of flight economy is not enough, and a better option is to build a comprehensive economy indicator from fuel cost, maintenance expenses, crew salaries and emission taxes for the purpose of flight trajectory optimisation.

Once all the improvements suggested above are accomplished and new models are built, new research in the multidisciplinary optimisation of flight trajectory can be carried out. The new trajectory optimisation will comprise the following features:

a) Three-dimension (3D);
b) Involving a complete flight profile: take-off, climb, cruise, descent, approach and landing;
c) Multi-objective (number of objective functions ≥ 2);
d) Using more trajectory design variables;
e) Practical and relative complete optimisation constraints;
f) Building the correlations between optimised flight parameters and operation parameters and forming the corresponding control laws;
g) Better simulation accuracies and less optimisation time.

Further, in future, the above practical flight trajectory optimisations can be accomplished by means of an on-board computer quickly enough so that any revisions

or updates to the original flight plans due to the possible changes in flight constraints from, for instance, unexpected changes in weather, air traffic controls or other reasons can be realised in time, which will certainly put higher requirements in the multidisciplinary optimisation technology and the performance of computer devices.

REFERENCES

1 Clean Sky Joint Undertaking (2012), available at: http://www.cleansky.eu/ (accessed 20th October 2012).

2 Clean Sky Joint Undertaking (2010), Annual Activity Report 2010, available at: http://www.cleansky.eu/content/document/annual-activity-report-2010 (accessed 20th October 2012).

3 Clean Sky Joint Undertaking (2011), Green Regional Aircraft (GRA), Annual Report 2011 – Summary, available at: http://www.cleansky.eu/content/document/itds-annual-reports-summary-2011 (accessed 20th October 2012).

4 Clean Sky Joint Undertaking (2011), Smart Fixed Wing Aircraft (SFWA), Annual Report 2011 – Summary, available at: http://www.cleansky.eu/content/document/itds-annual-reports-summary-2011 (accessed 20th October 2012).

5 Clean Sky Joint Undertaking (2011), Green Rotorcraft (GRC), Annual Report 2011 – Summary, available at: http://www.cleansky.eu/content/document/itds-annual-reports-summary-2011 (accessed 21st October 2012).

6 Clean Sky Joint Undertaking (2011), Sustainable and Green Engine IT, Annual Report 2011 – Summary, available at: http://www.cleansky.eu/content/document/itds-annual-reports-summary-2011 (accessed 21st October 2012).

7 Clean Sky Joint Undertaking (2011), System for Green Operations (SGO), Annual Report 2011 – Summary, available at: http://www.cleansky.eu/content/document/itds-annual-reports-summary-2011 (accessed 22nd October 2012).

8 Clean Sky Joint Undertaking (2011), Eco-Design ITD, Annual Report 2011 – Summary, available at: http://www.cleansky.eu/content/document/itds-annual-reports-summary-2011 (accessed 22nd October 2012).

9 Pervier, H., Nalianda, D., et al. (2011), Application of Genetic Algorithm for Preliminary Trajectory Optimization, SAE Int. J. Aerosp. Vol. 4, No. 2, p. 973-987.

10 Navaratne, R., Tessaro, M. et al. (2012), Generic Framework for Multi-Disciplinary Trajectory Optimization of Aircraft and Power Plant Integrated Systems, J Aeronaut Aerospace Eng, Vol. 1, No. 3, available at: http://dx.doi.org/10.4172/2168-9792.1000103 (accessed 1st February 2013).

11 Tessaro, M. (2011), Multi-disciplinary long-range aircraft trajectory assessments (MSc Thesis), Cranfield University, Cranfield.

12 Yu, Y. (2012), Long range aircraft trajectory optimisation with city hop considerations (MSc Thesis), Cranfield University, Cranfield.

13 Deidewig, F., Doepelheuer, A. and Lecht, M. (1996), Methods to Assess Aircraft Engine Emissions in Flight, in: 20th Congress of the Int. Council of the Aeronautical Sciences 1996 (ICAS), 8-13 September 1996, Sorrento, Italy, American Institute of Aeronautics & Astronautics, Reston, V.A.

14 Deb, K. (2002), A Fast and Elitist Multiobjective Genetic Algorithm: NSGA-II, IEEE Transactions on Evolutionary Computation, Vol. 6, No. 2.

15 Gu, W. et al. (2012), Towards the development of a multi-disciplinary flight trajectory optimization tool - GATAC, in: ASME Turbo Expo 2012, Vol. 1, GT2012-69862, p. 415-424.

16 Hendricks, E. S. and Tong, M. T. (2012), Performance and Weight Estimates for an Advanced Open Rotor Engine, NASA/TM—2012-217710, AIAA–2012–3911, Glenn Research Centre, Cleveland, Ohio.

17 Cavcar, M., The International Standard Atmosphere (ISA) Anadolu University, Eskishehir, Turkey (unpublished report).

18 Wikipedia (2011), Atmospheric models, available at: http://en.wikipedia.org/wiki/Atmospheric_models (accessed 9th May 2011).

19 Wikipedia (2011), International Standard Atmosphere, available at: http://en.wikipedia.org/wiki/International_Standard_Atmosphere (accessed 9th May 2011).

20 Walsh, P. P. and Fletcher, P. (2004), Gas Turbine Performance (2nd ed), Blackwell Publishing.

21 DuBois, D. and Paynter, G. (2006), "Fuel Flow Method2" for Estimating Aircraft Emissions, SAE Technical Paper 2006-01-1987, 2006, doi: 10.4271/2006-01-1987.

22 Pan, J. (1989), Basis for aerodynamics (revised ed.), National Defence Industry Press, Beijing, China.

23 Jenkinson, L. et al. (1999), *Civil jet aircraft design*, Arnold, London.

24 Jackson, P. (ed) (2011), Jane's All the World's Aircraft 2011-2012, Jane's Information Group.

25 Jenkinson, L. et al. (1999), Data Sets, Civil jet aircraft design, available at: http://www.elsevierdirect.com/companions/9780340741528/appendices/default.htm (accessed 6th November 2011).

26 Wetted Area Calculations, available at: http://adg.stanford.edu/aa241/drag/wettedarea.html (accessed 7th November 2011).

27 Anon. (1986), "Aerodynamically speaking", Flight International, 1st August 1986, p. 90.

28 Li, W. (2004), Aircraft Conceptual Design, Northwestern Polytechnical University Press, Xi'an, China.

29 Anderson, J. D. (2001), Fundamentals of Aerodynamics (3rd ed), McGraw Hill, New York.

30 Brandt, S. A. (2004), Introduction to Aeronautics: A Design Perspective (2nd ed), American Institute of Aeronautics and Astronautics, Reston, VA.

31 Torenbeek, E. (1982), Synthesis of subsonic airplane design: an introduction to the preliminary design, of subsonic general aviation and transport aircraft, with

emphasis on layout, aerodynamic design, propulsion, and performance, Delft University Press. Delft.

32 BADA dataset, (2011) A320__.OPF, Creation_date: 30 April 2002, Modification_date: 30 March 2011.

33 Camilleri, W. (2010), Specific Aircraft Performance Model, O_3.1_19-a / SGO-WP 3.1-C-U-SPEC-0104, Cranfield University, Cranfield (confidential and not available for the general public).

34 BADA dataset (2008), MD82__.OPF, Creation_date: 16 October 2008, Modification_date: 16 October 2008.

35 Niţă, M. F. (2008), Aircraft Design Studies Based on the ATR 72, Hamburg University of Applied Sciences, Hamburg.

36 BADA dataset (2011), AT75__.OPF, Creation_date: 31 March 2011, Modification_date: 31 March 2011.

37 Raziq, U. (2011), Turboprop Aircraft Model, SGO-WP 3.1-C-U-SPEC-0140, Cranfield University, Cranfield (confidential and not available for the general public).

38 Gunston, B. (ed) (2007), Jane's Aero Engines, (Issue 21), Jane's Information Group, USA.

39 Najafi, E. et al. (2009), Preliminary Specification of the CUTSTF Engine Performance Model for Use in GATAC V1, DI-3.1.2-1, Cranfield University, Cranfield (confidential and not available for public).

40 Pachidis, V. (2008), Gas Turbine Performance Simulation, Cranfield University, Cranfield, Simulation and Diagnostics lecture.

41 Gas Turbine Engineering Group (2008), The TURBOMATCH Scheme, TURBOMATCH User's Manual, Cranfield University, Cranfield.

42 VIVACE Project, Official Website (2012), available at: http://www.vivaceproject.com/ (accessed 5th September 2012).

43 PROOSIS, Official Website (2012), available at: http:// www.proosis.com/ (accessed 5th September 2012).

44 VITAL Project, Official Website (2012), available at: http://www.project-vital.org/ (accessed 6th September 2012).

45 NEWAC Project, Official Website (2012), available at: http://www.newac.eu/ (accessed 6th September 2012).

46 Pilidis, P. et al. (2008), Gas Turbine Theory and Performance, Cranfield University, Cranfield, Gas Turbine Performance lecture.

47 Francis, L. (2001), The Basics of Neural Networks Demystified.

48 MATLAB R2012a, Product help.

49 Daly, M. and Gunston, B. (2006), Jane's Aero Engines, Jane's Information Group, USA.

50 Jackson, P. (2006), Jane's All The World's Aircraft, Jane's Information Group.

51 Ziemianski, J. A. and Willis, E. A. (1991), NASA aeropropulsion research in support of propulsion systems of the 21st century, NASA-TM-104403, E-6226, NAS 1.15:104403, in: The 36th International Gas Turbine and Aeroengine Congress and Exposition, Orlando, FL, 3-6 Jun. 1991.

52 Ludemann, S. (1982), Prop-Fan Powered Aircraft - An Overview, SAE Technical Paper 820957, 1982, doi: 10.4271/820957.

53 Ziemianski, J. A. and Whitlow, Jr. J. B. (1988), NASA/Industry Advanced Turboprop Technology Program, in: 16th Congress of the International Council of Aeronautical Sciences – ICAS '88, Jerusalem, Israel, Lewis Research Centre, Cleveland, Ohio.

54 Hughes, C. and Zeug, T. (2008), NASA / GE Aviation Collaborative Partnership Research in Ultra High Bypass Cycle Propulsion Concepts, in: Fundamental Aeronautics Program, 2nd Annual Meeting, Atlanta, GA.

55 Hendricks, E. S. (2011), Development of an Open Rotor Cycle Model in NPSS Using a Multi-Design Point Approach, in: ASME 2011 Turbo Expo, No. GT2011-46694, p. 441-450, doi: 10.1115/GT2011-46694.

56 Guynn, M. D. et al. (2011), Initial Assessment of Open Rotor Propulsion Applied to an Advanced Single-Aisle Aircraft, in: 11th AIAA Aviation Technology, Integration, and Operations (ATIO) Conference, VA, AIAA 2011-7058.

57 Graber, E. J. (1990), Overview of NASA PTA propfan flight test program, in: Aeropropulsion 1987, p 363-382.

58 NASA (1987), Full scale technology demonstration of a modern counterrotating unducted fan engine concept. Engine test, NASA-CR-180869, NAS 1.26:180869.

59 Chapman, D. C., Godston, J. and Smith, D. E. (1988), Testing of the 578-DX propfan propulsion system, in: AIAA-88-2804, AIAA/ASME/SAE/ASEE 24th Joint Propulsion Conference, Boston, Massachusetts, 11-13 July 1988.

60 Nalianda, D. K. (2011), Specification of Propfan Engine Model -V1, O_3.1_38-a/ SGO-WP 3.1-C-U-OUT -0138-A1, Cranfield University, Cranfield (confidential and not available for the general public).

61 Singh, R., (2009), Gas Turbine Combustors, Volume 1, Cranfield University, Cranfield, MSc. lecture notes.

62 Moss, J. B. (2001), Predictive Methods for Gas Turbine Combustor Emissions, in: IMechE Seminar Publications on Gas Turbine Pollutant Emissions, Professional Engineering Publishing, London, UK.

63 Allaire, D. L. (2006), A Physics-Based Emissions Model for Aircraft Gas Turbine Combustors (MSc thesis), Massachusetts Institute of Technology, USA.

64 Osgerby, I. T. (1974), Literature Review of Turbine Combustor Modeling and Emissions, AIAA Journal, Vol. 12, No. 6, p. 743-752.

65 Celis, C. (2010), Evaluation and optimisation of environmentally friendly aircraft propulsion systems (PhD thesis), Cranfield University, Cranfield.

66 Lefebvre, A. H. (1983), Fuel Effects on Gas Turbine Combustion, AFWAL-TR-83-2004, Purdue University, West Lafayette, Indiana, USA.

67 Norman, P. D., Lister, D. H. et al. (2003), Development of the technical basis for a New Emissions Parameter covering the whole AIRcraft operation: NEPAIR - Final Technical Report, NEPAIR/WP4/WPR/01, QinetiQ.

68 Pearce, D. and Wrobel, L. (2010), Deliverable D1, Technical Specifications, CS-GA-2009-255674-TURBOGAS, Brunel University, U.K.

69 Allaire, D. L., Waitz, I. A. and Willcox, K. E. (2007), A Comparison of Two Methods for Predicting Emissions from Aircraft Gas Turbine Combustors, GT2007-28346, in: Proceedings of GT2007, ASME Turbo Expo 2007: Power for Land, Sea and Air, Montreal, Canada.

70 Visser, W. P. J. and Kluiters, S. C. A. (1998), Modelling the Effects of Operating Conditions and Alternative Fuels on Gas Turbine Performance and Emissions, RTO AVT Symposium on Gas Turbine Performance and Emissions, Lisbon, Portugal.

71 Shakariyants, S. A., van Buijtenen, J. P., Visser, W. P. J. and Tarasov, A. (2006), A Multidisciplinary Aero-Engine Exhaust Emission Study, in: Proceedings of GT2006, ASME Turbo Expo 2006: Power for Land, Sea and Air, Barcelona, Spain.

72 Mohamed, H., Ticha, H. B. and Mohamed, S. (2004), Simulation of Pollutant Emissions from a Gas-Turbine Combustor, Combustion Science and Technology, Vol. 176, No. 5, p. 819-834.

73 Turner, M. G., Norris, A. and Veres, J. P. (2003), High Fidelity 3D Simulation of the GE90, AIAA 2003-3996.

74 Veres, J. P. (2002), Overview of High-Fidelity Modeling Activities in the Numerical Propulsion System Simulations (NPSS) Project, NASA/TM—2002-211351, Glenn Research Center, Cleveland, Ohio.

75 Jella, S. E. (2008), Emissions Predictions in Turbulent Reacting Industrial Gas Turbine Combustor Flows using RANS and LES methods (MSc thesis), Concordia University, Montreal, Quebec, Canada.

76 Benelli, G., Brunetti, J., Carrai, L. and Sigali, S. (2007), RANS simulation of a gas turbine combustor: a study on aerodynamics, mixing and heat transfer in combustive conditions, Third European Combustion Meeting, ECM 2007.

77 Su, K. and Zhou, C. Q. (1999), Numerical Study of Parametric Effects on Gas Turbine Combustion NOx Emissions Using a Reduced Mechanism, Purdue University Calumet, Hammond, USA.

78 ICAO (2007), ICAO engine exhaust emissions data bank – subsonic engines – CFM56-5B4/3 – 8CM055.

79 Pervier, H. (2010), Turboprop Engine Emissions Model Specification, O_3.1_35-a / SGO-WP 3.1-C-U-SPEC-0100-A, Cranfield University, Cranfield (confidential and not available for the general public).

80 Pervier, H. (2011), Propfan Engine Emissions Model Specification, O_3.1_39-a / SGO-WP 3.1-C-U-SPEC-0132-A, Cranfield University, Cranfield (confidential and not available for the general public).

81 Smith, M. J. T. (1989), Aircraft noise, Cambridge University Press, Cambridge.

82 Powell, C. A. and Preisser, J. S. (2000), NASA's Subsonic Jet Transport Noise Reduction Research, NASA Langley Research Centre.

83 Leifsson, L. T. (2005), Multidisciplinary Design Optimization of Low-Noise Transport Aircraft, The Virginia Polytechnic Institute and State University.

84 ECAC.CEAC Doc 29 (2005), Report on Standard Method of Computing Noise Contours around Civil Airports, in: European Civil Aviation Conference, Volume 1: Applications Guide, December 2005.

85 Burton, N. J. S. (2004), Methods of Assessment of Aircraft Noise (MSc thesis), London South Bank University, London.

86 Ollerhead, J. B. and Rhodes, D. P. (1999), The UK Civil Aircraft Noise Contour Model ANCON: Improvements in Version 2, R&D REPORT 9842, Environmental Research and Consultancy Department, Civil Aviation Authority, available at: http://www.caa.co.uk/ (accessed 7th March 2012).

87 Hartjes, S. (2010), INMTM v3 Noise Calculation Tool Specification, SGO-WP 3.1.2-TUD-SPEC-0053-A, Delft University of Technology, Delft (confidential and not available for the general public).

88 Hartjes, S. (2010), NoiseLAss v2.0 Noise Level Assessment Tool Specification and Validation, SGO-WP 3.1.2-TUD-SPEC-0056-A, Delft University of Technology, Delft (confidential and not available for the general public).

89 Federal Aviation Administration (2012), Integrated Noise Model (INM), available at: http://www.faa.gov/about/office_org/headquarters_offices/apl/research/models/inm_model/ (accessed 1st July 2012).

90 Connor, T. Hinckley, R. et al. (1979), INM, Integrated Noise Model, Version 2 – Programmer's Guide, FAA-EE-79-10, Department of Transportation, Federal Aviation Administration, USA.

91 Forsyth, D. W., Gulding, J. and DiPardo, J. (2003), Review of Integrated Noise Model (INM) Equations and Processes, NASA/CR-2003-212414, Boeing Commercial Airplane Company, Federal Aviation Administration, USA.

92 Croft, J. (2012), Open rotor noise not a barrier to entry: GE, available at: http://www.flightglobal.com/news/articles/open-rotor-noise-not-a-barrier-to-entry-ge-373817/ (accessed 12th July 2012).

93 Envia, E. (2010), NASA Open Rotor Noise Research, 14th CEAS-ASC Workshop & 5th Scientific Workshop of X3-Noise Aeroacoustics of High-Speed Aircraft Propellers and Open Rotors, Institute of Aviation, Warsaw, Poland, 2010.

94 EASA (2012), Type-Certificate Data Sheet For Noise (No. EASA.IM.A.211 for MD-90-30, 717-200).

95 Wikipedia (2011), Multidisciplinary design optimization, available at: http://en.wikipedia.org/wiki/Multidisciplinary_design_optimization (accessed 11th June 2011).

96 Wikipedia (2011), Multi-objective optimization, available at: http://en.wikipedia.org/wiki/Multi-objective_optimization (accessed 12th June 2011).

97 Rao, S. S. (1996), Engineering Optimization: Theory and Practice (3rd ed), John Wiley, New York, US.

98 Russell, S. and Norvig, P. (2003), Artificial Intelligence: A Modern Approach (2nd ed), Prentice Hall, New Jersey, US.

99 Quagliarella, D. (1998), Genetic Algorithms and Evolution Strategy in Engineering and Computer Science, Recent Advances and Industrial Applications, John Wiley & Sons Ltd., Chichester, UK.

100 Gen, M. and Cheng, R. (2000), Genetic Algorithms and Engineering Optimization, John Wiley & Sons Inc., Chichester, UK.

101 Eshelman, L. J. and Schaffer, J. D. (1993), Real-coded Genetic Algorithms and Interval-schemata, in: Whitley, D. L. (editor), Foundations of Genetic Algorithms, Vol. 2, Morgan Kaufmann Publishers, San Francisco, US.

102 Deb, K. and Agrawal, R. B. (1994), Simulated Binary Crossover for Continuous Search Space Export, Complex Systems, Vol. 9, p. 1-34.

103 Eiben, A. E. and Smith, J. E. (2003), Introduction to Evolutionary Computing, Springer-Verlag, New York, US.

104 Rogero, J. M. (2002), A Genetic Algorithms-based Optimisation Tool for the Preliminary Design of Gas Turbine Combustors (Ph.D. thesis), Cranfield University, Cranfield.

105 Deb, K., Agrawal, S., Pratap, A. and Meyarivan, T. (2000), A Fast Elitist Non-Dominated Sorting Genetic Algorithm for Multi-Objective Optimization: NSGA-II, KanGAL Report No. 200001, Kanpur Genetic Algorithms Laboratory (KanGAL), Indian Institute of Technology Kanpur, Kanpur, India.

106 Sammut, M., Muscat, R. et al. (2012), GATAC V2.1.1 User Manual, University of Malta, Malta and Cranfield University, UK.

107 Charts. Aero (2012), Airport Charts for EHAM/AMS - Amsterdam Airport Schiphol, Haarlemmermeer, Netherlands, available at: http://charts.aero/airport/EHAM (accessed 7th April 2012).

108 Charts. Aero (2012), Airport Charts for EDDM/MUC - Munich International Airport, Munich, Germany, available at: http://charts.aero/airport/EDDM (accessed 7th April 2012).

APPENDICES

Appendix A Coefficient Matrices from Artificial Neural Network Training

1) Neural Network Training for Function $P_3 = f_1(H, M, F_N)$

Table A-1 Matrix $W1i_{,p3}$ (10×3)

w1i <10x3 double>

	1	2	3
1	1.3059	-0.3294	2.2358
2	0.1563	0.3164	-0.2909
3	0.6799	2.1898	5.0089
4	1.2262	-0.7180	2.9801
5	0.2426	0.3556	0.6910
6	0.2979	-0.7921	0.5973
7	-0.5054	-0.8676	0.2001
8	0.1979	0.1732	0.2224
9	1.1055	0.3998	5.2583
10	0.2057	-0.2824	-0.1283

Table A-2 Matrix $b1_{,p3}$ (10×1)

b1 <10x1 double>

	1
1	-0.0543
2	-0.8142
3	6.9563
4	-0.7649
5	-0.2788
6	1.6672
7	-1.0275
8	-0.0419
9	4.7598
10	0.9869

Table A-3 Matrix $W21_{,p3}$ (10×10)

w21 <10x10 double>

	1	2	3	4	5	6	7	8	9	10
1	-1.8539	-1.3704	0.9217	0.9627	0.5286	-0.6236	-0.0029	0.3689	0.1737	-1.9652
2	0.6876	8.3720e-04	-3.5077	1.5106	7.0988	0.1506	-5.1811	-6.1351	-0.7152	6.7240
3	0.5338	1.4931	-0.1519	-0.3359	1.7143	0.1036	-0.1946	-4.7769	-0.0338	1.8354
4	1.0531	-7.0116	-2.3995	-1.5001	0.9353	0.7747	-0.6461	7.0835	0.5001	-6.6982
5	2.0146	18.9455	6.3901	0.3855	-9.2428	18.5055	1.9952	-16.2519	-1.9412	-17.4059
6	-0.4529	-0.9391	0.0791	0.2917	-1.5499	-0.1019	0.1466	3.8031	0.0414	-1.0870
7	0.2895	2.7112	-4.1007	-0.9268	-9.5639	2.7908	-0.8389	-1.3420	0.3522	-6.9218
8	0.2555	-0.0344	-0.4269	-2.2734	-1.1885	5.5381	-0.2273	0.7402	-0.6654	-2.6323
9	2.3132	-2.2648	-2.5081	-0.8296	-3.2506	1.8543	-2.8857	0.8464	2.4033	-4.9780
10	0.6039	-0.6373	-3.9474	1.5293	7.8734	-0.0575	-5.2717	-6.0179	-0.5159	8.4270

Table A-4 Matrix $b2_{,p3}$ (10×1)

b2 <10x1 double>

	1
1	-1.8459
2	-3.6535
3	-0.5629
4	6.2220
5	-1.9068
6	0.2374
7	-0.0596
8	1.6441
9	0.4039
10	-4.2846

Table A-5 Matrix $W32_{,p3}$ (1×10)

w32 <1x10 double>

	1	2	3	4	5	6	7	8	9	10
1	0.8539	8.2822	-5.0585	0.2721	-0.0061	-5.8796	0.0487	1.9075	0.0097	-3.8827

Table A-6 Matrix $b3_{,p3}$ (1×1)

b3 <1x1 double>

	1
1	2.4794
2	

2) Neural Network Training for Function $T_3 = f_2(H, M, F_N)$

Table A-7 W1i,$_{T3}$ (10×3)

w1i <10x3 double>

	1	2	3
1	2.2973	0.1469	2.8618
2	0.0382	0.0872	-5.3036
3	0.3894	0.8159	1.2427
4	3.5878	0.9011	6.0533
5	2.2470	0.6866	3.0608
6	-10.5955	0.0276	0.2401
7	-0.1173	0.2828	0.2286
8	0.3089	0.5680	0.2855
9	-0.0176	0.1936	1.2265
10	0.3841	-0.2237	-0.4084

Table A-8 b1$_{,T3}$ (10×1)

b1 <10x1 double>

	1
1	-0.3808
2	-5.6809
3	1.4187
4	1.3198
5	0.0181
6	8.1433
7	-0.2399
8	0.7562
9	1.5991
10	0.8155

Table A-9 $W21_{,T3}$ (10×10)

w21 <10x10 double>

	1	2	3	4	5	6	7	8	9	10
1	-0.0986	-0.5302	-0.0697	0.3841	0.9707	-0.0347	-1.3726	0.1793	1.2855	-1.2696
2	0.3597	0.9423	-0.7554	-0.5236	-1.0716	0.0918	1.0596	0.4115	-0.7635	1.2216
3	-0.6299	0.5298	0.4874	-0.2796	-0.2368	-0.1033	1.8427	-0.6379	-1.0647	-0.1175
4	0.3976	-0.5176	-0.6012	0.3190	0.1087	0.0516	-1.6950	0.8756	1.0554	0.1698
5	0.3571	-0.0981	1.5620	-0.6943	0.0108	-0.0358	2.0324	-3.8746	-2.5670	-0.9326
6	-0.5355	1.5159	0.4515	1.6151	-1.5020	-0.0357	-3.9261	0.4972	3.3415	-1.9101
7	-5.1955	-1.0363	4.9685	-1.1136	5.1317	5.6516	-5.0835	-7.5369	0.4140	0.5872
8	-0.5142	0.8058	-1.1509	0.3681	1.6467	0.0248	-3.4266	3.1006	2.8545	-0.8628
9	-1.0841	0.4625	2.7986	-0.8951	1.9127	-0.0470	2.3175	-3.9261	-6.7517	-0.4527
10	0.4871	0.6358	-1.1406	-1.0565	0.9879	0.1748	0.6253	1.8411	-0.3987	0.9331

Table A-10 $b2_{,T3}$ (10×1)

b2 <10x1 double>

	1
1	-2.6993
2	3.5791
3	0.8094
4	-1.0735
5	4.2057
6	-1.2678
7	-8.1386
8	-0.2656
9	6.9047
10	-0.4091

Table A-11 $W32_{,T3}$ (1×10)

w32 <1x10 double>

	1	2	3	4	5	6	7	8	9	10
1	8.2304	10.9462	-5.9011	-7.9866	-0.5282	-0.6988	0.0133	1.1741	-0.4494	-1.6831

Table A-12 $b3_{,T3}$ (1×1)

b3 <1x1 double>

	1
1	-3.7573

3) Neural Network Training for Function $TET = f_3(H, M, F_N)$

Table A-13 $W1i_{,TET}$ (10×3)

w1i <10x3 double>

	1	2	3
1	13.3532	0.0630	0.2797
2	-0.2605	-0.0324	-2.5794
3	0.8311	1.3101	5.4007
4	4.1318	0.4218	7.4024
5	0.7519	0.8636	1.0310
6	-0.0496	-0.3640	1.0946
7	-1.2702	0.0880	0.2893
8	0.2342	0.5210	0.8232
9	0.8485	0.3095	0.3107
10	0.0485	0.1099	-0.7673

Table A-14 $b1_{,TET}$ (10×1)

b1 <10x1 double>

	1
1	-9.8373
2	-3.4027
3	5.6936
4	2.0711
5	-0.1190
6	0.8718
7	1.4381
8	1.8096
9	0.3450
10	-0.6031

Table A-15 $W21_{,TET}$ (10×10)

w21 <10x10 double>

	1	2	3	4	5	6	7	8	9	10
1	-0.0050	-0.0648	2.2701	-1.7963	1.7908	-0.8756	-3.4737	-11.1118	-2.7291	2.3649
2	-0.0301	15.8577	2.3302	-0.1950	0.3539	-2.3847	0.8559	-9.4660	-2.3324	-0.5533
3	-0.0610	5.9045	1.7074	-0.2202	0.7419	-1.3419	0.0978	-5.0296	-0.4948	-2.7925
4	0.0573	-1.0874	0.5079	0.3680	-0.6795	2.5553	1.0071	1.2068	0.4118	4.5079
5	0.0516	6.3207	-12.0043	0.7702	-0.1374	14.4088	1.2101	29.1111	7.7434	10.7625
6	-0.0231	-0.7925	-1.4100	0.0760	-0.4078	1.0702	0.5165	3.0010	0.7158	2.4794
7	0.0071	1.0033	1.3084	0.0712	0.4029	-0.7922	-0.2936	-2.4499	-0.7090	-1.8269
8	-0.2824	4.1243	0.3130	0.0689	0.7271	2.9797	-0.8060	2.2302	-0.3346	4.0143
9	2.3260	8.7215	1.2092	0.6715	0.4194	1.5947	-1.3003	-0.3820	-2.5709	5.3853
10	0.0015	-0.8784	-1.0752	-0.1395	-0.3157	0.7386	0.0435	1.9501	0.6022	1.4810

Table A-16 $b2_{,TET}$ (10×1)

b2 <10x1 double>

	1
1	8.3925
2	23.7995
3	8.3682
4	-2.2967
5	-15.5955
6	-2.3699
7	2.1995
8	4.1066
9	13.1093
10	-1.7780

Table A-17 $W32_{,TET}$ (1×10)

w32 <1x10 double>

	1	2	3	4	5	6	7	8	9	10
1	-0.0980	-1.3131	-1.1353	-0.5785	-0.1532	-6.6697	-14.3702	2.9807	-0.1484	-9.9998

Table A-18 $b3_{,TET}$ (1×1)

b3 <1x1 double>

	1
1	-1.3015

4) Neural Network Training for Function $W_f = f_4(H, M, F_N)$

Table A-19 $W1i_{,wf}$ (10×3)

w1i <10x3 double>

	1	2	3
1	0.2042	-0.1407	0.4586
2	0.2058	0.1848	-0.9624
3	-2.3956	-0.0375	-3.5081
4	2.2018	0.4441	3.0311
5	0.0511	0.2336	0.2859
6	-0.1606	-0.1608	1.1707
7	-0.1991	0.1701	-0.3017
8	-2.4795	0.1739	-4.2608
9	-0.0165	0.2879	0.0611
10	-0.0666	-0.0703	-0.1668

Table A-20 $b1_{,wf}$ (10×1)

b1 <10x1 doub

	1
1	-0.7836
2	-1.2801
3	-1.0800
4	-0.0242
5	-0.4657
6	1.3133
7	-0.6196
8	-0.7947
9	-0.2308
10	-0.6093

Table A-21 $W21_{,wf}$ (10×10)

w21 <10x10 double>

	1	2	3	4	5	6	7	8	9	10
1	-4.6881	-1.0548	-0.3521	0.0659	3.5121	-0.4015	7.5634	0.0930	-9.0068	-16.9842
2	15.6549	-59.8885	0.3793	0.9301	-79.1729	-42.2666	-91.8280	-0.4735	123.2526	69.7731
3	27.3333	-39.9692	0.5092	-5.7791	23.4239	-26.1558	0.3141	1.4065	3.4157	-19.7257
4	27.2825	-23.7033	-0.2227	3.6263	-62.3003	-14.9218	-15.9273	0.9212	57.8223	-23.2067
5	-1.8057	4.0786	0.1519	-0.2486	-4.5220	2.4540	-5.8991	-0.1182	5.5338	8.5904
6	2.9378	8.1474	0.0077	-0.3366	-0.4852	7.5771	-6.6664	-0.4644	8.7725	34.8263
7	-19.1341	13.6746	0.0493	-2.5493	52.4845	7.9094	7.3484	-0.5453	-39.4235	35.7804
8	12.0196	8.9038	-1.8982	-6.3215	1.2750	5.4741	1.3474	-2.6937	11.9187	39.9402
9	-5.4144	-24.5698	0.6748	4.2672	-29.9967	-15.8886	-53.3454	-0.7105	68.6865	80.7837
10	-5.7319	-0.7589	-0.3765	0.0587	3.4799	-0.3080	7.1028	0.1116	-8.7655	-16.0829

Table A-22 $b2_{,wf}$ (10×1)

b2 <10x1 double>

	1
1	-10.4184
2	-18.9079
3	14.5770
4	-18.9720
5	-0.0769
6	19.6576
7	25.8405
8	37.5674
9	10.5958
10	-10.8700

Table A-23 $W32_{,wf}$ (1×10)

w32 <1x10 double>

	1	2	3	4	5	6	7	8	9	10
1	8.9318	-0.0145	-0.0030	0.0672	-0.3899	-0.4099	0.1269	-5.7435	0.0282	-8.8649

Table A-24 $b3_{,wf}$ (1×1)

b3 <1x1 double>

	1
1	5.3373